frontiers | Research Topics

# Preparation, bioactivity evaluation, and quality control of natural products and their derivatives

**Edited by**
Xi Zheng, Xuetao Xu and Xiping Cui

**Published in**
Frontiers in Pharmacology
Frontiers in Chemistry

FRONTIERS EBOOK COPYRIGHT STATEMENT

The copyright in the text of individual articles in this ebook is the property of their respective authors or their respective institutions or funders. The copyright in graphics and images within each article may be subject to copyright of other parties. In both cases this is subject to a license granted to Frontiers.

The compilation of articles constituting this ebook is the property of Frontiers.

Each article within this ebook, and the ebook itself, are published under the most recent version of the Creative Commons CC-BY licence. The version current at the date of publication of this ebook is CC-BY 4.0. If the CC-BY licence is updated, the licence granted by Frontiers is automatically updated to the new version.

When exercising any right under the CC-BY licence, Frontiers must be attributed as the original publisher of the article or ebook, as applicable.

Authors have the responsibility of ensuring that any graphics or other materials which are the property of others may be included in the CC-BY licence, but this should be checked before relying on the CC-BY licence to reproduce those materials. Any copyright notices relating to those materials must be complied with.

Copyright and source acknowledgement notices may not be removed and must be displayed in any copy, derivative work or partial copy which includes the elements in question.

All copyright, and all rights therein, are protected by national and international copyright laws. The above represents a summary only. For further information please read Frontiers' Conditions for Website Use and Copyright Statement, and the applicable CC-BY licence.

ISSN 1664-8714
ISBN 978-2-8325-6057-0
DOI 10.3389/978-2-8325-6057-0

## About Frontiers

Frontiers is more than just an open access publisher of scholarly articles: it is a pioneering approach to the world of academia, radically improving the way scholarly research is managed. The grand vision of Frontiers is a world where all people have an equal opportunity to seek, share and generate knowledge. Frontiers provides immediate and permanent online open access to all its publications, but this alone is not enough to realize our grand goals.

## Frontiers journal series

The Frontiers journal series is a multi-tier and interdisciplinary set of open-access, online journals, promising a paradigm shift from the current review, selection and dissemination processes in academic publishing. All Frontiers journals are driven by researchers for researchers; therefore, they constitute a service to the scholarly community. At the same time, the *Frontiers journal series* operates on a revolutionary invention, the tiered publishing system, initially addressing specific communities of scholars, and gradually climbing up to broader public understanding, thus serving the interests of the lay society, too.

## Dedication to quality

Each Frontiers article is a landmark of the highest quality, thanks to genuinely collaborative interactions between authors and review editors, who include some of the world's best academicians. Research must be certified by peers before entering a stream of knowledge that may eventually reach the public - and shape society; therefore, Frontiers only applies the most rigorous and unbiased reviews. Frontiers revolutionizes research publishing by freely delivering the most outstanding research, evaluated with no bias from both the academic and social point of view. By applying the most advanced information technologies, Frontiers is catapulting scholarly publishing into a new generation.

## What are Frontiers Research Topics?

Frontiers Research Topics are very popular trademarks of the *Frontiers journals series*: they are collections of at least ten articles, all centered on a particular subject. With their unique mix of varied contributions from Original Research to Review Articles, Frontiers Research Topics unify the most influential researchers, the latest key findings and historical advances in a hot research area.

Find out more on how to host your own Frontiers Research Topic or contribute to one as an author by contacting the Frontiers editorial office: frontiersin.org/about/contact

# Preparation, bioactivity evaluation, and quality control of natural products and their derivatives

**Topic editors**
Xi Zheng — Rutgers, The State University of New Jersey, United States
Xuetao Xu — Wuyi University, China
Xiping Cui — Guangdong University of Technology, China

**Citation**
Zheng, X., Xu, X., Cui, X., eds. (2025). *Preparation, bioactivity evaluation, and quality control of natural products and their derivatives*. Lausanne: Frontiers Media SA.
doi: 10.3389/978-2-8325-6057-0

# Table of contents

05 Identification of potential anti-inflammatory components in Moutan Cortex by bio-affinity ultrafiltration coupled with ultra-performance liquid chromatography mass spectrometry
Caomin Zou, Qianru Chen, Jiasheng Li, Xiguang Lin, Xingyang Xue, Xinhang Cai, Yicheng Chen, Yue Sun, Shumei Wang, Ying Zhang and Jiang Meng

20 Exploring pyrrolidinyl-spirooxindole natural products as promising platforms for the synthesis of novel spirooxindoles as EGFR/CDK2 inhibitors for halting breast cancer cells
Mohamed S. Nafie, Abdullah Mohammed Al-Majid, M. Ali, Abdulmajeed Abdullah Alayyaf, Matti Haukka, Sajda Ashraf, Zaheer Ul-Haq, Ayman El-Faham and Assem Barakat

38 Discovery of novel melatonin–mydroxyquinoline hybrids as multitarget strategies for Alzheimer's disease therapy
Wei Wang, Tingting Pan, Rui Su, Mingbin Chen, Wandi Xiong, Congjun Xu and Ling Huang

49 N-*p*-coumaroyloctopamine ameliorates hepatic glucose metabolism and oxidative stress involved in a PI3K/AKT/GSK3β pathway
Yuechang Huang, Xingmin Zhang, Qian Li, Wende Zheng, Panpan Wu, Rihui Wu, Wen-Hua Chen and Chen Li

63 Natural product nobiletin-loaded Pickering emulsion stabilized by bovine serum albumin/carboxymethyl inulin complexes: preparation and digestive characteristics
Guiying Huang, Man Zhang, Konglong Feng, Jie Xiao, Qingrong Huang, Chi-Tang Ho and Jun Liu

75 Hovendulcisic acid A-D: four novel ceanothane-type triterpenoids from *Hovenia dulcis* stems with anticancer properties
Jianzhan Yang, Wanna Cai, Fan Wu, Shengmei Xu, Xiaoqi Zhang, Bo Liu and Fangfang Xu

86 Seasonal influence on the essential oil chemical composition of *Hyptis crenata* Pohl ex Benth.: a valuable plant from Marajó, Brazil
Maria Nancy Norat de Lima, Paulo Vinicius Lima Santos, Lucas Botelho Jerônimo, Rian Martins Viana, Joyce Kelly da Silva, William N. Setzer, José Guilherme S. Maia and Pablo Luis B. Figueiredo

96 Inhibition mechanism investigation of quercetagetin as a potential tyrosinase inhibitor
Faliang Liang

104 Zn(II)–curcumin prevents cadmium-aggravated diabetic nephropathy by regulating gut microbiota and zinc homeostasis
Wenjia Sun, Xueting Mei, Jiasheng Wang, Zhicong Mai and Donghui Xu

120 Honokiol as an α-glucosidase inhibitor
Hua Zhu and Xin Zhong

128 Water decoction of *Pericarpium citri reticulatae* and *Amomi fructus* ameliorates alcohol-induced liver disease involved in the modulation of gut microbiota and TLR4/NF-κB pathway
Xing-Min Zhang, Yue-Chang Huang, Bai-Zhong Chen, Qian Li, Pan-Pan Wu, Wen-Hua Chen, Ri-Hui Wu and Chen Li

146 Prenylated flavonoids from *Sophora flavescens* inhibit mushroom tyrosinase activity and modulate melanogenesis in murine melanoma cells and zebrafish
Fenling Fan, Lanqing Chen, Caihong Chen, Song Ang, Justin Gutkowski, Navindra P. Seeram, Hang Ma and Dongli Li

162 Screening of anti-inflammatory activities components of *Angelica dahurica* root based on spectrum-effect relationship analysis and NF-κB pathway
Huan Shi, Qianqian Wang, Yaqing Chang, Yuguang Zheng, Dan Zhang, Yunsheng Zhao and Long Guo

176 Impact of baicalin and components of Scutellaria baicalensis on renal fibrosis of diabetic kidney disease
Jiarui Li, Yuan Zhuang, Guoyong Fan, Simeng Wang, Enhui Yan, Jianpeng Guo, Chi Zhang and Shicui Jiang

187 Discovery of quality markers of *Meconopsis quintuplinervia* based on an absorption-based metabolite approach and rapid quantification using polarity-switching UPLC-QQQ-MS/MS
Yifan Tian, Yuan Liu, Yuanlin Kong, Limin Li, Zhengming Yang, Wenbin Li, Qiang Li, Chaoqin Ren, Wenxia Sun and Yanfei Huang

202 The isolation, bioactivity, and synthesis of natural products from *Litsea verticillate* with anti-HIV activities
Jia-Lei Yan, Huiru Nan, Xiaoyu Fang, Xiong-En Long, Yu Jiang and Junyang Liu

frontiers | Frontiers in Pharmacology

TYPE Original Research
PUBLISHED 07 February 2024
DOI 10.3389/fphar.2024.1358640

Check for updates

OPEN ACCESS

EDITED BY
Xuetao Xu,
Wuyi University, China

REVIEWED BY
Lin Zhu,
The Chinese University of Hong Kong, China
Tao Yi,
Hong Kong Baptist University, Hong Kong SAR, China

*CORRESPONDENCE
Jiang Meng,
jiangmeng666@126.com
Ying Zhang,
157099926@qq.com
Shumei Wang,
2395903468@qq.com

†These authors have contributed equally to this work

RECEIVED 20 December 2023
ACCEPTED 15 January 2024
PUBLISHED 07 February 2024

CITATION
Zou C, Chen Q, Li J, Lin X, Xue X, Cai X, Chen Y, Sun Y, Wang S, Zhang Y and Meng J (2024), Identification of potential anti-inflammatory components in Moutan Cortex by bio-affinity ultrafiltration coupled with ultra-performance liquid chromatography mass spectrometry. *Front. Pharmacol.* 15:1358640.
doi: 10.3389/fphar.2024.1358640

COPYRIGHT
© 2024 Zou, Chen, Li, Lin, Xue, Cai, Chen, Sun, Wang, Zhang and Meng. This is an open-access article distributed under the terms of the Creative Commons Attribution License (CC BY). The use, distribution or reproduction in other forums is permitted, provided the original author(s) and the copyright owner(s) are credited and that the original publication in this journal is cited, in accordance with accepted academic practice. No use, distribution or reproduction is permitted which does not comply with these terms.

# Identification of potential anti-inflammatory components in Moutan Cortex by bio-affinity ultrafiltration coupled with ultra-performance liquid chromatography mass spectrometry

Caomin Zou[1†], Qianru Chen[1†], Jiasheng Li[1†], Xiguang Lin[1†], Xingyang Xue[2], Xinhang Cai[1], Yicheng Chen[1], Yue Sun[1], Shumei Wang[1]*, Ying Zhang[3]* and Jiang Meng[1]*

[1]School of Traditional Chinese Medicine, Guangdong Pharmaceutical University, Key Laboratory of Digital Quality Evaluation of Chinese Materia Medica, State Administration of Traditional Chinese Medicine (TCM), Engineering Technology Research Center for Chinese Materia Medica Quality of Universities in Guangdong Province, Guangdong Provincial Key Laboratory of Traditional Chinese Medicine Informatization, Guangzhou, China, [2]Affiliated Cancer Hospital and Institute of Guangzhou Medical University, Guangzhou, China, [3]College of Pharmacy, Jinan University, Guangzhou, China

Moutan Cortex (MC) has been used in treating inflammation-associated diseases and conditions in China and other Southeast Asian countries. However, the active components of its anti-inflammatory effect are still unclear. The study aimed to screen and identify potential cyclooxygenase-2 (COX-2) inhibitors in MC extract. The effect of MC on COX-2 was determined *in vitro* by COX-2 inhibitory assays, followed by bio-affinity ultrafiltration in combination with ultra-performance liquid chromatography-mass spectrometry (BAUF-UPLC-MS). To verify the reliability of the constructed approach, celecoxib was applied as the positive control, in contrast to adenosine which served as the negative control in this study. The bioactivity of the MC components was validated *in vitro* by COX-2 inhibitor assay and RAW264.7 cells. Their *in vivo* anti-inflammatory activity was also evaluated using LPS-induced zebrafish inflammation models. Finally, molecular docking was hired to further explore the internal interactions between the components and COX-2 residues. The MC extract showed an evident COX-2-inhibitory effect in a concentration-dependent manner. A total of 11 potential COX-2 inhibitors were eventually identified in MC extract. The COX-2 inhibitory activity of five components, namely, gallic acid (GA), methyl gallate (MG), galloylpaeoniflorin (GP), 1,2,3,6-Tetra-O-galloyl-β-D-glucose (TGG), and 1,2,3,4,6-Penta-O-galloyl-β-D-glucopyranose (PGG), were

**Abbreviations:** MC, Moutan Cortex; COX-2, cyclooxygenase-2; BAUF-UPLC-MS, bio-affinity ultrafiltration coupled with ultra-performance liquid chromatography-mass; GA, gallic acid; MG, methyl gallate; GP, galloylpaeoniflorin; TGG, 1,2,3,6-Tetra-O-galloyl-β-D-glucose; PGG, 1,2,3,4,6-Penta-O-galloyl-β-D-glucopyranose; DMSO, Dimethyl sulfoxide; TCM, Traditional Chinese Medicine; ESI, electrospray ion; DAD, diode array detector; BD, binding degree; BCA, bicchoninic acid; SDS-PAGE, SDS-polyacrylamide gel electrophoresis; ECL, enhanced chemiluminescent.

validated through both *in vitro* assays and experiments using zebrafish models. Besides, the molecular docking analysis revealed that the potential inhibitors in MC could effectively inhibit COX-2 by interacting with specific residues, similar to the mechanism of action exhibited by celecoxib. In conclusion, BAUF-UPLC-MS combining the molecular docking is an efficient approach to discover enzyme inhibitors from traditional herbs and understand the mechanism of action.

KEYWORDS

**Moutan cortex, cox-2 inhibitors, bio-affinity ultrafiltration, UPLC-MS, anti-inflammatory**

# 1 Introduction

To date, an increasing body of evidence has suggested that chronic inflammation may be directly associated with the occurrence of cancer through its ability to induce tumorigenic transformation in susceptible cells (Federico et al., 2007). Typically, inflammatory process involves with injury and/or infection, as well as tissue regeneration and repair prior to inflamation resolution. Upon initiation of the inflammatory response, neutrophils and macrophages, which are inflammatory cells, undergo aggregation followed by the release of specific factors that facilitate the progression of inflammation (Fitzpatrick, 2001; Aggarwal et al., 2006; Bartsch and Nair, 2006). Cyclooxygenase-2 (COX-2), a crucial factor associated with inflammation that is less frequently expressed in normal organisms, has been observed to be induced by cytokines, mitogens, and endotoxins in inflammatory cells. It plays a pivotal role in the development of inflammation by increasing prostaglandin levels *in vivo* (Huai, et al., 2019). Moreover, epidemiological studies have underscored COX-2 as a pivotal area of interest in the development of cancer prevention strategies, and Nonsteroidal anti-inflammatory drugs (NSAIDs) have exhibited broad effectiveness by competitively suppressing the activity of cyclooxygenase enzymes. (Smalley and DuBois, 1997). While the long-term use of anti-inflammatory medications, particularly NSAIDs and corticosteroids, may lead to some side effects, ranging from cardiovascular issues to gastrointestinal discomfort and potential impacts on liver and kidney function (Bindu et al., 2020; Braun et al., 2020; Watanabe et al., 2020). Traditional Chinese Medicine (TCM) has been recognized for its anti-inflammatory efficacy with a relatively low incidence of side effects (Zhang et al., 2017). Consequently, it is important to systematically identify and validate the anti-inflammatory components from TCM with high-throughput and reliable methodologies.

Moutan Cortex (MC), the root bark of *Paeonia suffruticosa* Andr., is a traditional Chinese herb widely utilized in clinical settings for its analgesic, sedative, and anti-inflammatory properties. It is also used as a remedy for cardiovascular diseases, conditions with a manifestation of extravasated blood or stagnated blood, as well as female diseases such as menstruation disorders and uteritis (Yun et al., 2013). In-depth research on MC has unveiled its potential anti-inflammatory and antiviral properties (Sheehan and Atherton, 1994; Au et al., 2001; Hsiang et al., 2001). For example, Chun et al. discovered that the anti-inflammatory activity of MC could potentially be attributed to its inhibition of NO and PGE2 productional. Apart from that, it also led to a reduction in the concentration of TNF-α, IL-1β and IL-6 in LPS-activated cells by suppressing the expression of iNOS, COX-2, p-IκBα and NF-κB (Chun et al., 2007). However, despite the reports delineating the association between the anti-inflammatory activity and certain monomeric compounds in MC, there have been limited studies conducted to identify the active anti-inflammatory components with a COX-2-inhibitory effect. Nevertheless, it is undeniably of great significance to identify the COX-2-inhibiting compounds in MC and elucidate their underlying mechanism for further research and clinical applications.

The biologically active constituents derived from natural herbs possess potential applications in novel drug development or as lead compounds for structural modification and optimization (Mohan et al., 2021). The current methodology employed for the identification of active ingredients in natural plants primarily involves chemical separation and structure elucidation. However, this approach is often criticized for its lengthy cycle time and susceptibility to loss of active components, thus rendering it inherently flawed (Wolfender et al., 2015). So far, bio-affinity ultrafiltration coupled with ultra-performance liquid chromatography-mass spectrometry (BAUF-UPLC-MS) has been regarded as an efficient tool commonly used for rapid and efficient screening of active ingredients from complex natural product systems (Wei et al., 2016). Having a high affinity with the target molecules which can be traced by UPLC-MS, the active compounds are able to be separated from the solution system for further identification. For example, Lan successfully identified potential thrombin inhibitors from Curcuma Rhizoma using UPLC-Q-Exactive Orbitrap/MS and subsequently validated their thrombin-inhibiting efficacy through *in vivo* and *in vitro* assays (Lan et al., 2021).

In this study, our aim was to identify the potential active anti-inflammatory compounds of MC and elucidate their underlying mechanisms. The inhibitory effect of MC on COX-2 was determined through COX-2-inhibitory assays, followed by BAUF-UPLC-MS analysis to identify potential components responsible for COX-2 inhibition in the MC extract. These components' COX-2 inhibiting effects were further validated through additional COX-2 inhibitory assays and *in vivo* experiments using established zebrafish inflammation models to evaluate their anti-inflammatory efficacy. Finally, molecular docking techniques were employed to investigate the interaction between the identified components and COX-2. The procedure was illustrates in Figure 1.

# 2 Materials and methods

## 2.1 Materials and animals

Gallic acid (GA, batch number: CHB180114), 1,2,3,4,6-Penta-O-galloyl-β-D-glucopyranose (PGG, batch number: CHB190125),

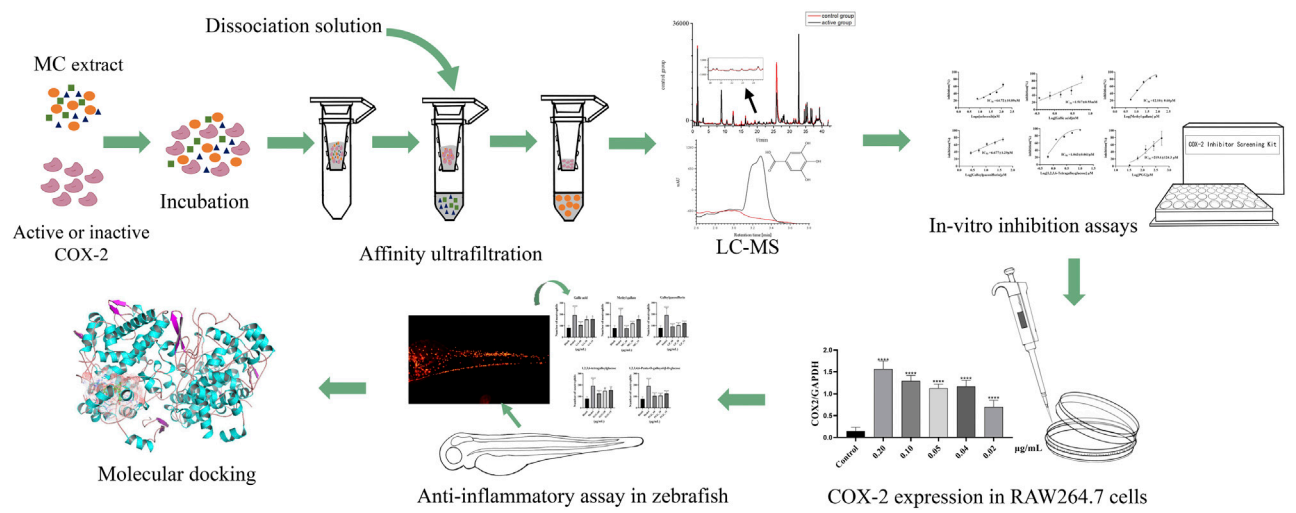


FIGURE 1
Schematic diagram of screening COX-2 inhibitors from MC by BAUF-UPLC-Q-Exactive Orbitrap-MS.

and 1,2,3,6-Tetra-O-galloyl-β-D-glucose (TGG, batch number: CHB201224) were purchased from Chengdu Chroma-Biotechnology Co., Ltd (Chengdu, China). Methyl gallate (MG, batch number: AF20061051) was obtained from Chengdu Alfa Biotechnology Co., Ltd (Chengdu, China). Galloylpaeoniflorin (GP, batch number: 220319) was from Chengdu Herb Substance Bio-Technology Co., Ltd (Chengdu, China). Celecoxib (batch number: D11A6S2151) was from Shanghai Yuanye Bio-Technology Co., Ltd (Shanghai, China). Adenosine (batch number: CSN23524-003) was purchased from CSNpharm, Inc (Chicago, United States). All the reagents were of HPLC grade.

MC (batch number: YPA7H0001) was obtained from Caizhilin Pharmaceutical Co., Ltd (Guangzhou, China) and identified by Professor Jizhu Liu from the School of Traditional Chinese Medical Materials, Guangdong Pharmaceutical University. The voucher specimens were preserved at the Herbarium Centre, Guangdong Pharmaceutical University. The samples, after transferred to a rocking pulverizer (DFy-400-D) and crushed into small pieces, were passed through an 80-mesh sieve and sealed for preservation. The herb powder was ultrasonically extracted once with 50% methanol (1:10, w/v), and then processed by a rotary evaporator as well as a freeze dryer to harvest the MC extract, which was sealed and then preserved under 4°C.

The COX-2 Inhibitor Screening Kits were procured from Beyotime Biotechnology (Shanghai, China). Human recombinant COX-2 (No.60122, 5000U) was obtained from Cayman Chemicals (Ann Arbor, MI, United States). Lipopolysaccharides (LPS, batch number: L118716) from *Escherichia coli* O55:B5 was provided by Shanghai Aladdin Biochemical Technology Co., Ltd. (Shanghai, China). Centrifugal ultrafiltration filters (Amico Ultra-0.5, 10 kDa) were from Millipore Co., Ltd. (Bed Ford, MA, United States).

Tg (lyz:DsRed2) zebrafish larvae from the National Zebrafish Resource Center were processed under lysozyme C (lyz) promoter to establish zebrafish models containing DsRed-labeled neutrophils (Xu et al., 2018). The models were employed in this experiment to assess the anti-inflammatory efficacy of the compounds based on the premise that zebrafish neutrophil count exhibited a positive correlation with proinflammatory substance concentration (Chen et al., 2019). The experiment was conducted in the major laboratory of digital quality evaluation of Chinese Materia Medica in Guangdong Pharmaceutical University (Guangzhou, China), where the zebrafish were kept in an automatic circulating tank system, with live brine shrimp as the feed twice a day. The conditions were maintained as a 14 h light/10 h dark cycle, with the water temperature controlled at 28°C ± 0.5°C and pH at 7.0 ± 0.5. After the zebrafish produced embryos naturally, the fertilized zebrafish eggs were gathered and processed with culture water. All procedures involving with Zebrafish experiments in this study were under the approval by the Institutional Ethics Committee (IEC) of Guangdong Pharmaceutical University (Ethics Approval number: GDPULAC2021121), and carried out according to the requirements of the International AAALAC certification (certification No. 001458).

## 2.2 Determination of COX-2 inhibitory activity

In this experiment, the inhibitory effect was determined by using COX-2 Inhibitor Screening Kits. A 96-well black plate was employed, where COX-2 cofactor working solution (5 μL), COX-2 assay buffer (75 μL), test solution (5 μL), and COX-2 working solution (5 uL) were mixed and incubated for 10 min at 37°C in the dark. Then 5 μL of probe solution, together with 5 μL of COX-2 substrate solution, was added immediately. After a 37°C incubation in the dark for another 5 min, the fluorescence value was determined at an excitation wavelength of 560 nm and emission wavelength of 590 nm. In this experiment, Celecoxib, a widely used COX-2 inhibitor, was employed in the positive control group for method validation, while 5 μL of dimethyl sulfoxide (DMSO), as the substitute of the test solution, was applied in the 100% enzyme activity control group. Besides, COX-2 Assay Buffer was used in the blank control group to replace COX-2 working solution. MC extract

or potential inhibitors were dissolved with DMSO as the test solution in the sample groups. The inhibition rate of the samples was obtained by the formula shown as below:

$$\text{Inhibition activity (\%)} = (F_1 - F_2) / (F_1 - F_3) \times 100\%$$

Where, $F_1$, $F_2$, and $F_3$ respectively indicate the fluorescence value of the three groups—100% enzyme activity control group, sample group and blank control group.

## 2.3 Screening procedures of BAUF-UPLC-MS

The screening procedure was performed by referring to the previous report (Jiao et al., 2019). An experimental group and inactivated enzyme group were set up in this study for comparison. 40 μL of 100 mg/mL MC extract as well as 280 μL of COX-2 (100 U/mL) was transferred to EP tube in the experimental group, in contrast to the control group where 280 μL of inactivated COX-2 (boiled in the water bath for 30 min) was used as the substitute of the activated enzyme. The tubes from both groups were incubated at 37°C in the dark for 40 min, aiming to create an optimal condition under which the potentially suitable ligands would completely combined with the enzyme. A centrifugal filter was employed for ultrafiltration at 15000 × g for 15 min. Afterwards, 300 μL of PBS was added to the samples, and the unbound small molecules were removed by 15000 × g centrifugation for 15 min. To avoid interference caused by non-specific binding, the target-ligand compounds were shifted to new ultrafiltration membranes, where 300 μL of methanol was added to the complexes and the compounds were subsequently maintained at room temperature for 15 min to allow dissociation of the ligands from COX-2. The procedure was repeated for three times. The samples, under a gentle stream of nitrogen, were evaporated to dryness at room temperature and redissolved in methanol for UPLC-MS analysis.

UPLC-Q-Exactive-Orbitrap-MS was performed to analyze the compounds in the filtrate using Thermo Scientific Orbitrap Fusion Tribrid Mass Spectrometer (Thermo Fisher Scientific, United States) and Ultimate 3,000 Ultra-performance liquid chromatograph, at the same time with Waters ACQUITY UPLC BEH RP18 (2.1 mm × 100 mm, 1.7 μm) employed for chromatographic analysis. The UPLC was conducted under such conditions: Gradient elution was carried out at a flow rate of 0.2 mL/min with water (containing 0.1% formic acid; A) and acetonitrile (B) as the mobile phases. The gradient program was set as 0–10 min, 5%–8% B; 10–12 min, 8%–12% B; 12–15 min, 12%–14% B; 15–20 min, 14%–16% B; 20–25 min, 16%–18% B; 25–30 min, 18%–22% B; 30–35 min, 22%–40% B; 35–38 min, 40%–95% B; 38–40 min, 95%–5% B; 40–42 min, 5% B. The column temperature was adjusted to 35°C and the injection volume of the samples was determined as 2 μL. The measurements were read at the detection wavelength of 254 nm. In the MS test, electrospray ion (ESI) sources were hired to analyze the compounds, with Full MS/dd $MS^2$ used as the scanning mode; The other parameters of MS analysis were as follows: nebulizer voltage, 4.0 kV; sheath gas pressure, 35 arb; aux gas pressure, 15 arb; ion transport temperature, 320°C; evaporation temperature, 320°C; and CES, 10 eV. The average EPI scanning spectrum was observed at a CE of 15, 35 and 45, respectively. In addition, mass spectrometry as well as data acquisition was conducted by Orbitrap Fusion Tune and Xcalibur 4.0. By comparing peak areas of two groups, specific ligands binding to COX-2 were determined. Relative binding degree (BD) of COX-2 ligands were calculated by the following formula: BD (%) = (A1–A2)/A1×100%, Where A1and A2 were the peak area of compounds in the active enzyme group and the control denatured enzyme group, respectively (Qin et al., 2015; Cai et al., 2020).

## 2.4 Method validation

To evaluate the specificity of the established approach, a solution of celecoxib (specific COX-2 inhibitor) was prepared as the positive control, in contrast to adenosine which was used as the negative control, both at a concentration of 20 μM. The control samples were prepared with inactivated COX-2. Besides, comparison of the peak area of the ultrafiltrate was performed between the active and inactivated enzyme groups to determine the specific binding between ligands and COX-2.

HPLC condition: HPLC (Shimadzu Corporation, Japan) furnished with a binary pump, vacuum degasser, diode array detector (DAD), and automatic sampler, was employed in combination with the usage of an Ultimatetm XB-C18 (250 × 4.6 mm, 5 μm) to verify the affinity ultrafiltration approach. With reference to the modified approach recorded in the previous study (Jadhav and Shingare, 2005), the conditions for HPLC were set as follows: mobile phases, water (containing 0.1% formic acid; A) and acetonitrile (B); elution program, 0–30 min, 5%–95% B; column temperature, 35°C; sample injection volume, 20 μL; detection wavelength, 254 nm; and the flow rate, 1.0 mL/min.

## 2.5 COX-2 expression assay

### 2.5.1 Cell culture

RAW264.7 cells originated from mouse macrophage cell line were purchased from the American Type Culture Collection. DMEM medium containing 5% fetal bovine serum and 1% Penicillin G Streptomycin was used to culture the cells under 37°C in a humidified atmosphere of 5% $CO_2$.

### 2.5.2 Cell viability assay (MTT)

Cell viability was determined by MTT assay, where RAW264.7 cells ($6 \times 10^5$ cells/well), after mixed with LPS or potential COX-2 inhibitors, were cultured in a 96-well plate for 12 h. Then DEME with 20% MTT solution was added, followed by a 37°C incubation for extra 4 h. After the supernatant was removed, DMSO was added to dissolve the insoluble formazan product. The optical density was measured by a microplate reader at 490 nm. In this experiment, the formula used to calculate cell viability was as follows:

$$\text{Cell viability (\%)} = \left(OD_{\text{experimental group}} - OD_{\text{blank group}}\right) \Big/ \left(OD_{\text{control group}} - OD_{\text{blank group}}\right) \times 100\%$$

### 2.5.3 RT-qPCR test

RAW264.7 cells were seeded in a 6-well plate and cultured until they sticked to the wall. After a 12-h pretreatment with 0.2 μg/mL LPS, the cells were further treated with the potential inhibitors at a

series of concentrations for 12 h till they were lysed. Then AG RNAex Pro Reagent was used to isolate the total RNA. A reverse transcription kit (Evo M M-LV RT Mix with gDNA Clean for qPCR, Accurate Biology China) was employed to convert RNA to cDNA. SYBR Green Premix Pro Taq HS qPCR kit (Accurate Biology, China) was applied to carry out q-PCR where the relative amount of mRNA was calculated with $2^{-\triangle\triangle t}$ method. The primer sequences were as follows:

GAPDH:
5′-ACTCCACTCACGGCAAATTCAAC-3′ (Forward)
5′-ACACCAGTAGACTCCACGACATAC-3′ (Reverse)
COX-2:
5′-CACATTTGATTGACAGCCCACCAAC-3′ (Forward)
5′-AGTCATCAGCCACAGGAGGAAGG-3′ (Reverse)

### 2.5.4 Western blot analysis

RAW264.7 cells were resuspended over ice in 98% ice-cold radioimmunoprecipitation assay (RIPA) lysis buffer (Meilunbio, Shanghai, China) supplemented with 1% EDTA-free protease and 1% PMSF for 30 min, followed by a 25-min centrifugation at 12000 r/min, 4°C. Then the supernatant was removed, and bicchoninic acid (BCA) protein assay kit (Biosharp, Shanghai, China) was employed to measure the concentration of proteins. Afterwards, 5 × SDS-PAGE loading buffer (Biosharp, Shanghai, China) was added into the mixture, which was subsequently boiled to denature the proteins. Meanwhile, 7.5% SDS-polyacrylamide gel electrophoresis (SDS-PAGE) was used to separate equal amount of proteins for electroblotting on a 0.2 μM PVDF membrane (Millipore). The samples were then blocked with 5% BCA blocking buffer for 1 h, followed by an overnight 4°C incubation with the primary antibodies against COX-2 (RT1159, Huabio) and GAPDH (60004-1-lg, Proteintech). Thereafter, TBST was used to wash the membranes for four times, and HRP-labelled goat anti-mouse IgG (A2016, Beyotime, China) secondary antibody was transferred to the membranes for another 37°C incubation for 40 min. The expression was determined by enhanced chemiluminescent (ECL) reagent (MA0186-1, Meilunbio) in Gel Analyzer—a fully automated chemiluminescence image analysis system, and the intensity of the protein bands was evaluated by densitometry and quantified using ImageJ software with GAPDH as an internal reference.

### 2.5.5 Statistical analysis

In the study, the data were mostly presented as mean ± SD. GraphPad Prism software was employed for statistical analysis, with one-way ANOVA applied for inter-group comparison among multiple groups, and *t*-test for comparison between pair groups.

## 2.6 Anti-inflammatory assay in zebrafish

With an attempt to further verify whether the compounds bear an *in vivo* anti-inflammatory effect, LPS was used to construct zebrafish inflammatory models for anti-inflammatory test. According to the method of model construction proposed in previous study (Li et al., 2018), healthy transgenic Tg (lyz: DsRed2) zebrafish larvae were randomly collected and transferred into a 12-well plate (n = 20/well) at 72 hpf. The samples were treated with the following protocols: (1) The control group was treated with 4 mL of 0.1% DMSO for 24 h; (2) The model group, 4 mL of 0.025 mg/mL LPS (dissolved in 0.1% DMSO); (3) The drug groups, in the wake of a treatment with 0.025 mg/mL LPS for 30 min, were supplemented with MC to a working concentration of 15, 30 and 60 μg/mL, respectively, and maintained for 24 h. The concentration gradient was designed based on the maximum tolerable concentration. Afterwards, approximately 15 zebrafish were respectively transferred from each of the groups to fresh water for observation and imaging using a fluorescence microscope (Olympus, Tokyo, Japan). In addition, Image-Pro Plus was also used to record the number of neutrophils.

## 2.7 Molecular docking

To obtain a three-dimensional view visualizing the interaction between COX-2 and the potential inhibitors, molecular docking technology was adopted to perform a computer simulation. The crystal structure of COX-2 (code ID:1CVU, resolution:2.40 Å) was obtained from the RCSB Protein Data Bank in PDB format (Kiefer et al., 2000). By submitting the PDB file to the "build/check/repair model" and "Prepare PDB file for docking programs" modules, some repair work was further completed, such as modeling the missing side chains, performing a small regularization, correcting water positions and symmetry, and adding hydrogen. The fixed PDB file was then assessed and submitted to AutodockTools (ADT ver.1.5.6) to prepare PDBQT file, and Gasteiger charges were computed for protein atoms. Then, the central coordination of the docking box was positioned at x = 24.952; y = 23.300; z = 48.666, and the size of the box was set at 60 × 60×60, 0.375 Å spacing. Created by ChemDraw, the ligand compounds from MC extract were then converted to mol2 format by Chem3D. Docking simulations were performed by ADT. The searching work, with lamarckian genetic algorithm (GALS) as the engine, was carried out in 100 runs. The docking procedure was run by Autodock4 using the region of the grid box, which was also employed by Autogrid4 to prepare affinity grid maps. The most stable docking model, which was identified for each of the components based on the beat-scored conformation under the ADT prediction, was applied to further analyze the binding mode of the molecular docking. PyMOL was used for analysis of the docking sites so that the interaction between enzymes and inhibitors could be observed and evaluated.

# 3 Result and discussion

## 3.1 Determination of the COX-2-inhibitory activity of MC extract

To characterize the *in vitro* inhibitory effect of MC on COX-2, the inhibitory rate of MC extract was assessed at various concentrations using COX-2 Inhibitor Screening Kits. The resulting $IC_{50}$ curve was generated using GraphPad Prism 9 software. The $IC_{50}$ of MC extract is 77.43 ± 3.12 μg/mL. As depicted in Figure 2, an increase in the concentration of MC extract corresponded to a proportional elevation in its COX-2 inhibition rate, suggesting that the MC extract likely contains concentration-dependent potential COX-2 inhibitors.

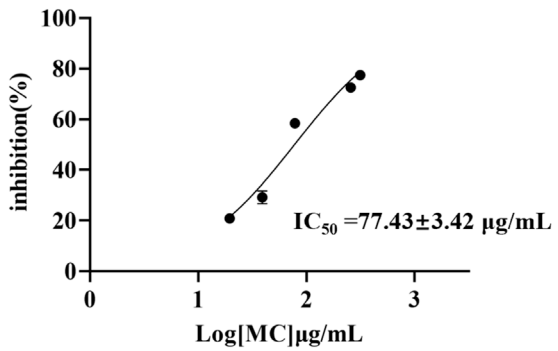


FIGURE 2
Dose-response curve of *in vitro* inhibition assay for Moutan Cortex extract.

## 3.2 Validation of affinity ultrafiltration method

Celecoxib, a selective COX-2 inhibitor commonly used in clinical practice, was applied as the positive control in this study, while adenosine was used as the negative control. The two agents were mixed and subjected to affinity ultrafiltration aiming to verify the feasibility of the established approach. As shown in Figure 3, Celecoxib and adenosine were detected at 28.2 min and 5.5 min, respectively. Compared with the control group, the response value of celecoxib significantly increased in the active group. By contrast, there was no evident change in the response value of adenosine, suggesting that the established affinity ultrafiltration approach harbored a satisfying specificity for COX-2 test.

## 3.3 Screening potential COX-2 inhibitors by BAUF-UPLC-MS

The potential COX-2 inhibitors preliminarily identified in the experiment for determining COX-2-inhibitory activity of MC extract were further screened by BAUF-UPLC-MS. Following affinity ultrafiltration, the chromatographic peak areas were compared between the active-enzyme group and inactive-enzyme group, in an attempt to identify the bioactive components in the extract. Moreover, the reliability of the established approach was verified by setting up positive and negative control groups, which were also used to eliminate the possible disturbance produced by other inactive compounds.

The UPLC chromatogram showed distinct differences in the two groups of the activated enzyme group (Figure 4A), and components in the activated group exhibited bigger peak areas than those in the inactivated enzyme group, which suggested possible COX-2 ligands in MC. The binding degree (BD) is defined to rank the affinity binding between the ligands and the enzyme. A higher BD value indicates stronger binding with the receptor and consequently greater inhibitory effect on the enzyme activity. Through analyzing the peak areas of two groups, the BDs for these identified compounds were calculated (Table 1), and the results showed that the BDs of 11 components more than 30%, which suggested that these compounds might be effective COX-2 ligands. However, it was also observed that some of the peak areas in the inactivated enzyme group were larger than those of the active enzyme group, which could possibly attribute to the fact that the protein spatial structure (about 74 kDa) was modified during inactivation of the enzyme in the boiling water bath. Therefore, when the inactivated enzyme was incubated with the extract, the pores in the ultrafiltration membrane were blocked and certain small unbound molecules were retained on the ultrafiltration membrane during the elution process (Zhang et al., 2021).

## 3.4 Identification of the potential COX-2 inhibitors by UPLC-Q-TOF-MS

By referring to standard compounds and relevant findings from previous literature (He et al., 2006; He et al., 2010), the components of the BAUF ultrafiltrate were identified and characterized in this study based on their precise mass and fragment ions. The structure and the major data of the compounds, which were identified as monoterpene glycosides, galloyl glucoses, gallic acid, and their derivatives, were shown in Figure 4B; Figure 5; Table 1, respectively. Compund 1 and

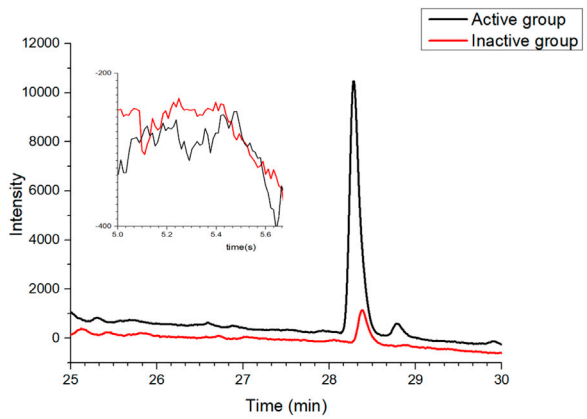


FIGURE 3
Validation of the affinity ultrafiltration in which mixtures of positive and negative drugs were tested to verify the feasibility of the established method: red line, control group with the inactivated enzyme; black line, experimental group with the active enzyme.

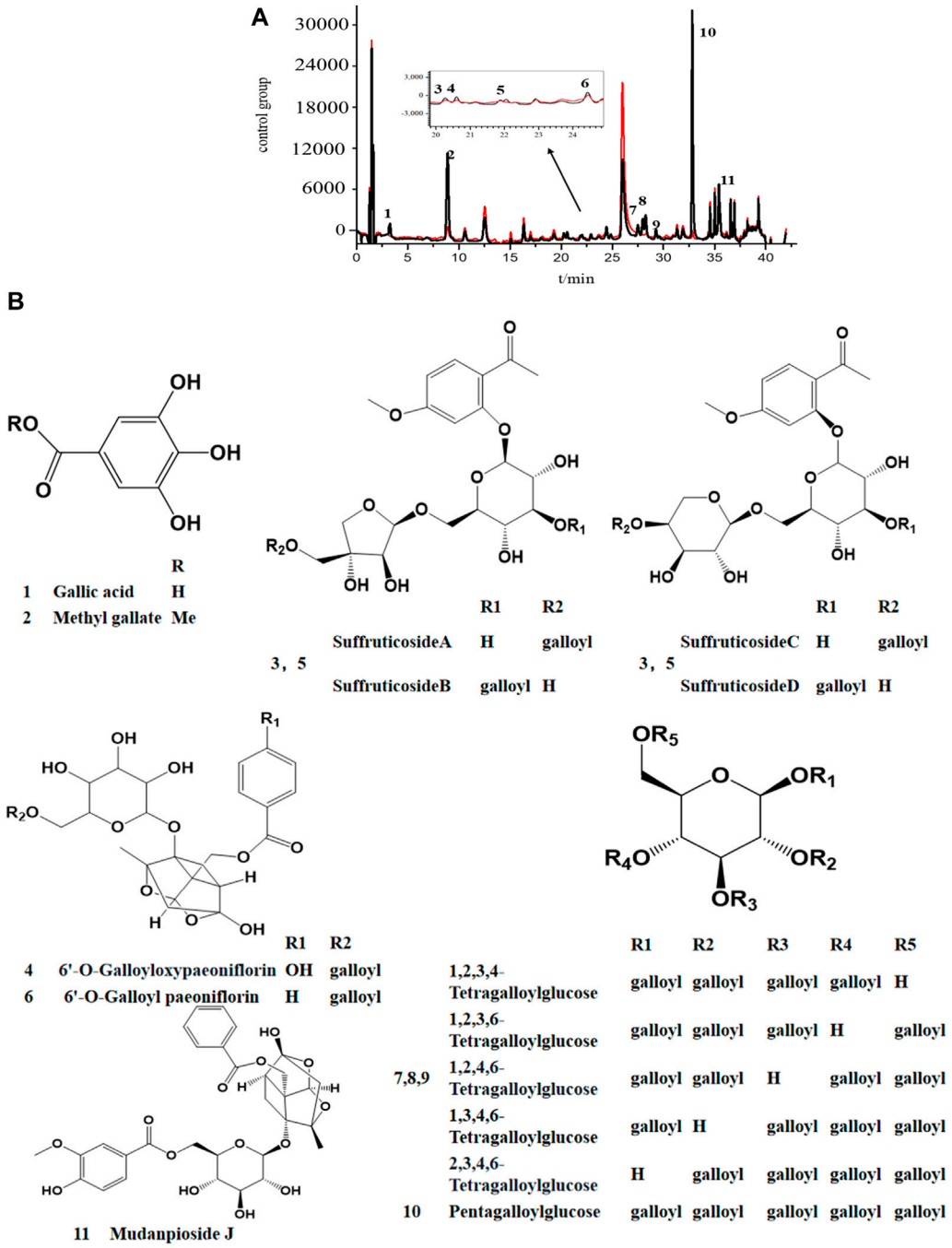


FIGURE 4
UPLC chromatogram **(A)** and the stuctures of potential COX-2 inhibitors **(B)** in MC by AUC. black line, the experimental group with active enzyme; red line, control group with denatured enzyme. **1**. Galic acide; **2**. Methy gallate; **3**. Suffruticoside A/B/C/D; **4**. 6′-O-Galloyloxypaeoniflorin; **5**. Suffruticoside A/B/C/D; **6**. 6′-O-Galloyl paeoniflorin; **7**. TGG; **8.** TGG; **9**. TGG; **10**. PGG; **11**. Mudanpioside J.

2 wer derivatives of agllic acid; Compound 3, 4, 5, 6 and 11 were monoterpene glycosides; compund 7, 8, 9 and 10 are galloyl glucoses.

The mass spectrometry analysis revealed the loss of a higher number of water molecules, as well as small CO2 and CO molecules. Additionally, gallic acid and galloyl fragments were found to be easily detached from these compounds, which can be attributed to the presence of hydroxyl and carboxyl groups in the structure of gallic acid (Fernandes et al., 2022; Liu et al., 2023).

Taking compound 10 as an example, it yielded a quasi-molecular ion peak of m/z 939.1109 $[M-H]^-$ according to its MS/MS spectrum, and its molecular formula was identified as $[C_{41}H_{31}O_{26}]^-$ (1.164 ppm) by Xcalilbur. Successive loss of the fragment ions of galloyl (m/z 151.0027 $[C_7H_3O_4]^-$ (0.761 ppm)) and gallic acid (m/z 169.0133 $[C_7H_5O_5]^-$ (0.899 ppm)) were observed, in addition to subsequently identified fragments m/z 787.10040 ($[M\text{-galloyl}]^-$) (1.971 ppm) and m/z 769.08936 ($[M\text{-gallic acid}]^-$) (1.399 ppm).

TABLE 1 Identification of potential COX-2 inhibitors in Moutan Cortex by UHPLC-Q-Exactive Orbitrap/MS.

| No. | $t_R$ (min) | Molecular formula | m/z | Measured ions | Mass error/ppm | Fragment ions | Tentative identification |
|---|---|---|---|---|---|---|---|
| 1 | 3.44 | $C_7H_6O_5$ | 169.0134 | $[C_7H_5O_5]^-$ | 1.362 | 125.0232 | Gallic acid |
| 2 | 8.99 | $C_8H_8O_5$ | 183.0291 | $[C_8H_7O_5]^-$ | 1.367 | 168.0056, 124.0153 | Methyl gallate |
| 3 | 20.25 | $C_{27}H_{32}O_{16}$ | 611.1618 | $[C_{27}H_{31}O_{16}]^-$ | 1.978 | 445.0986, 343.0666, 169.0133 | Suffruticoside A/B/C/D |
| 4 | 20.71 | $C_{30}H_{32}O_{16}$ | 647.1620 | $[C_{30}H_{31}O_{15}]^-$ | 2.146 | 399.0931, 313.0564, 271.0459, 169.0133 | 6-O-Galloyloxy-paeoniflorin |
| 5 | 21.97 | $C_{27}H_{32}O_{16}$ | 611.1618 | $[C_{27}H_{31}O_{16}]^-$ | 1.863 | 445.0986, 301.0563, 169.0132, 165.0547 | Suffruticoside A/B/C/D |
| 6 | 24.94 | $C_{30}H_{32}O_{15}$ | 631.1668 | $[C_{30}H_{31}O_{15}]^-$ | 1.685 | 613.1564, 313.0565, 177.0547, 169.0132 | Galloylpaeoniflorin |
| 7 | 27.40 | $C_{34}H_{28}O_{22}$ | 787.1001 | $[C_{34}H_{27}O_{22}]^-$ | 1.666 | 635.0888, 617.0781, 483.0779, 465.0672, 447.0570, 169.0132 | Tetragalloyl glucose |
| 8 | 28.05 | $C_{34}H_{28}O_{22}$ | 787.1000 | $[C_{34}H_{27}O_{22}]^-$ | 1.514 | 635.0888, 617.0784, 483.0781, 465.0671, 447.0566, 169.0132 | Tetragalloyl glucose |
| 9 | 28.33 | $C_{34}H_{28}O_{22}$ | 787.0998 | $[C_{34}H_{27}O_{22}]^-$ | 1.272 | 635.0891, 617.0782, 483.0777, 65.0675, 447.0571, 169.0133 | Tetragalloyl glucose |
| 10 | 32.88 | $C_{41}H_{32}O_{26}$ | 939.1109 | $[C_{41}H_{31}O_{26}]^-$ | 1.164 | 769.0892, 617.0784, 635.0894, 169.0133 | 1,2,3,4,6-Penta-O-galloyl-β-D-glucose |
| 11 | 35.42 | $C_{31}H_{34}O_{14}$ | 629.1874 | $[C_{31}H_{33}O_{14}]^-$ | 1.523 | 477.1401, 431.1346, 281.0665, 137.0232 | Muddanpioside J |

Therefore, the structure of compound 10 could be deduced as PGG (1,2,3,4,6-Penta-O-galloyl -β-D-glucopyranose)[27]. The proposed fragmentation pathway of PGG was shown in Figure 6.

The acetal-caged pinane skeleton is known as the characteristic construction in monoterpene glycosides. Various pinane backbone ion fragments can be seen in paeoniflorin compounds. The bonds attaching to glucosyl moiety, the ester group attaching to pinane backbone, as well as the ketal, methoxyl and carbonyl groups on aglycone are the sites where cleavage typically occurs, thereby, the neutral fragments of benzoic acid, glucose, CO, $H_2O$, and formaldehyde are easily lost. compound 6 serves as a representative example, compound 6 yielded a quasi-molecular ion peak of m/z 631.1668 $[M-H]^-$ ($[C_{30}H_{31}O_{15}]^-$). The fragment ions at m/z 613.1565 ($[C_{30}H_{29}O_{14}]^-$), 331.0671 ($[C_{13}H_{13}O_9]^-$) and 121.0295 ($[C_7H_6O_2]^-$) were indicative of the successive loss of H2O, galloyl glucose, and a benzoyl group, respectively. Then the fragment at m/z 331.0671 gave rise to 169.0134 ($[M-C_6H_{12}O_5]^-$) by successive loss of a glucose reside. by comparing its MS/MS behaviors with the reference standard and literature, the composition 6 was identified as galloylpaeoniflorin (Xiong et al., 2021). The proposed fragmentation pathway of galloylpaeoniflorin was shown in Figure 6.

Some studies have indicated that galloylate derivatives have antifungal property and also act as an antioxidant *in vivo* (Strippoli et al., 2000; Ow and Stupans, 2003). PGG has proved to have a potential to relieve pain and accelerate the recovery of voluntary movement that was constrained due to inflammatory pain, which was achieved by inhibiting generation of cellular NO in RAW 264.7 cells (Chun et al., 2016). Monoterpene glycosides, the main class of compounds in MC, have been recognized as a major contribution to the therapeutic effects of MC (Ding et al., 2012a; Ding et al., 2012b). Galloylpaeoniflorin attenuated osteoclast genesis and alleviates ovariectomy-induced osteoporosis by supressing ROS and MAPKs/c-Fos/NFATc1 signaling pathways (Liu et al., 2021). Plus, suffruticoside A/C have shown the potence associated with radical scavenging (Matsuda et al., 2001). These findings suggest that these potential COX-2 inhibitors could be used as leading compounds for a variety of biologically active products.

## 3.5 *In Vitro* COX-2 inhibition assays

To validate the experimental results of affinity ultrafiltration, the compounds identified in this study-gallic acid, methyl gallate, TGG, galloylpaeoniflorin, and PGG, as well as the positive control celecoxib, were also purchased from commercial marketsand. The COX-2 inhibiting activity of thees components were determined by COX-2 inhibitor screening kits. The dose-response curves as well as the half-maximal inhibitory concentrations ($IC_{50}$ values) of each compound were shown in Figure 7. With Celecoxib as the positive control ($IC_{50}$ = 0.0647 μM), TGG exhibited the most potent inhibitory effect on COX-2 activity ($IC_{50}$ = 1.043 μM) among the five compounds screened in the affinity ultrafiltration study. Meanwhile, galloylpaeoniflorin ($IC_{50}$ = 6.77 μM) and Methyl gallate (IC50 = 12.10 μM) demonstrated stronger inhibitory activities, while PGG and gallic acid displayed weaker inhibitory effects with $IC_{50}$ values of 219.6 μM and 1.5170 mM, respectively. Unfortunately, due to the low content in this plant and difficulties in the process of enrichment and purification, there was not enough Suffruticoside A/B/C/D, Galloyloxypaeoniflorin and Muddanpioside J in our laboratory for the bioassay. The COX-2 inhibitory results suggest that BAUF-UPLC-MS, as an approach for identifying potential COX-2 inhibitors from MC extract, is capable and effective.

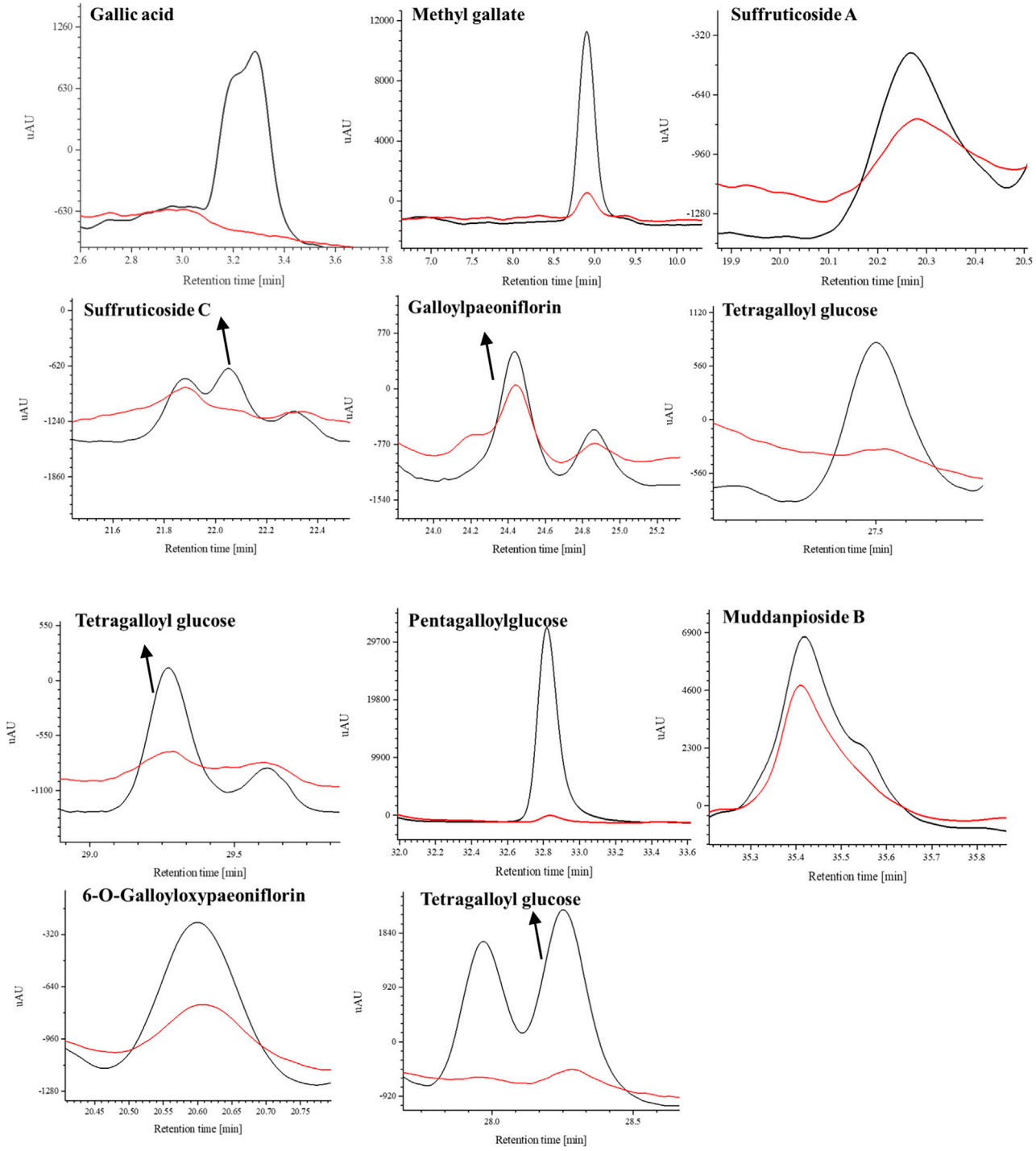


FIGURE 5
The selective ion monitoring (SIR) chromatograms (blue line, experimental group with active COX-2 enzyme; red line, control group with inactive COX-2 enzyme).

## 3.6 Anti-inflammatory assay in cells

The cell-based study aimed to elucidate the anti-inflammatory effect of the potential inhibitors in MC extract by exploring their activity in modulating COX-2 mRNA and protein expression using LPS-induced RAW264.7 cells. The anti-inflammatory activity was evaluated following the MTT assay, which was utilized to determine the cytotoxic concentration of LPS and potential inhibitors. Figure 8A demonstrated that Gallic acid (≤250 μM), Methyl gallate (≤10 μM), Galloylpaeoniflorin (≤100 μM), TGG (≤20 μM), PGG (≤150 μM), and LPS (≤0.5 μg/mL) exhibited no cytotoxicity against RAW264.7 cells. To identify the appropriate concentration for modeling, COX-2 expression in RAW264.7 cells was assessed by western blotting using LPS at a series of concentrations. Figure 8B

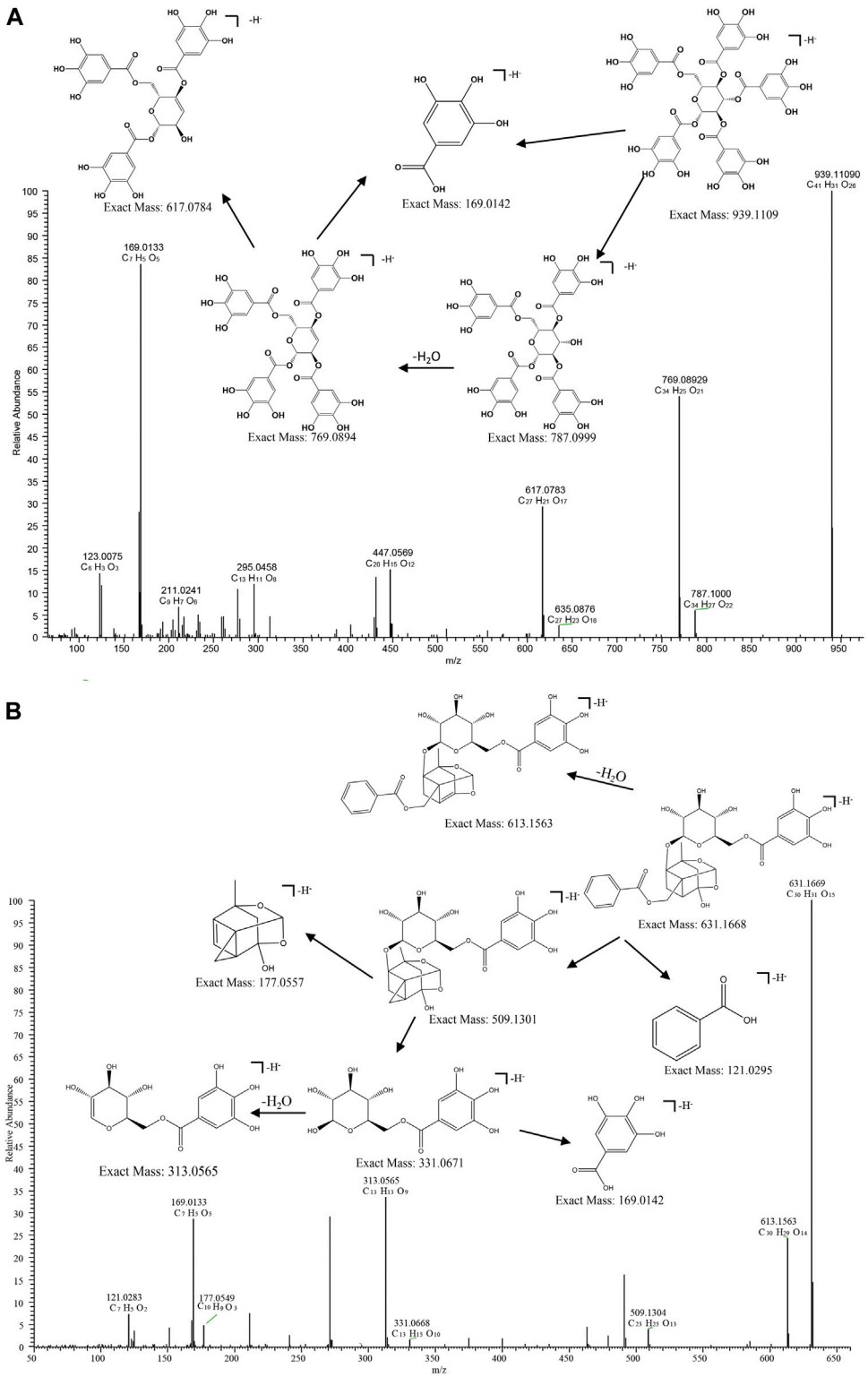


FIGURE 6
MS/MS spectrum and fragmentation pattern of PGG **(A)** and Galloylpaeoniflorin **(B)** from MC in negative ion mode.

showed that COX-2 protein expression was upregulated as the LPS concentration elevated, with the highest protein expression observed at 0.2 μg/mL. Subsequently, the effects of potential inhibitors on COX-2 mRNA and protein expressions were evaluated in LPS-treated RAW264.7 cells by RT-qPCR and western blotting technique. Figure 8C revealed that according to RT-qPCR, the COX-2 mRNA expression of the model group was evidently higher than that of the blank group. However, the COX-2 mRNA expression in groups

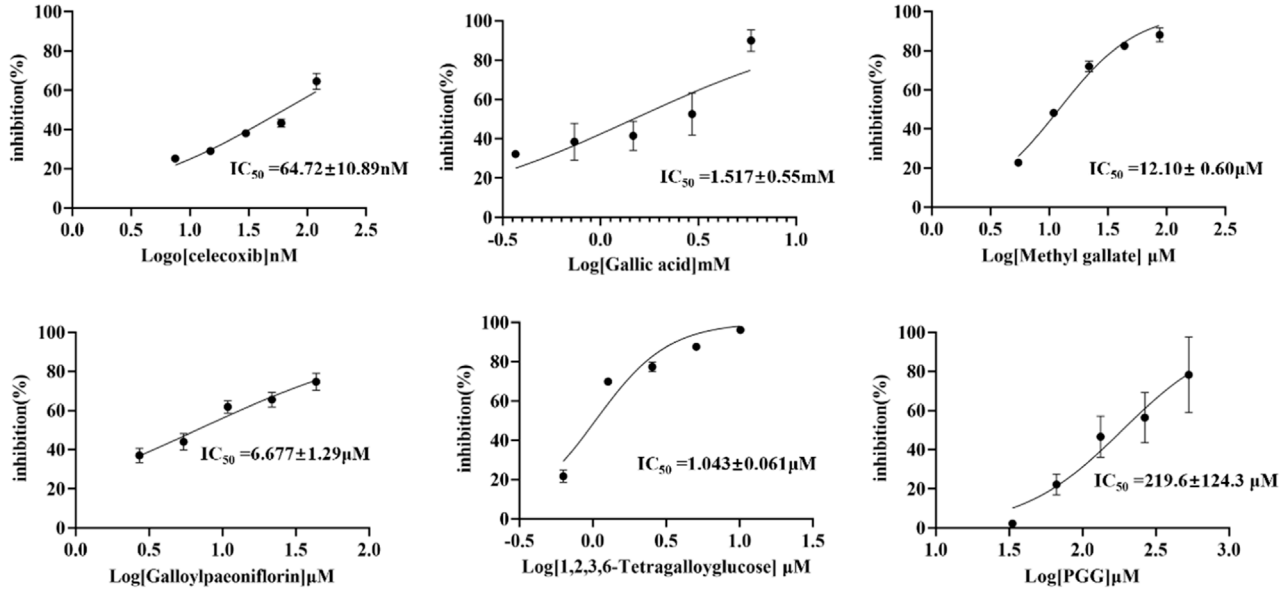


FIGURE 7
Dose-response curves of *in vitro* inhibition assays for celecoxib and five COX-2-inhibitory compounds.

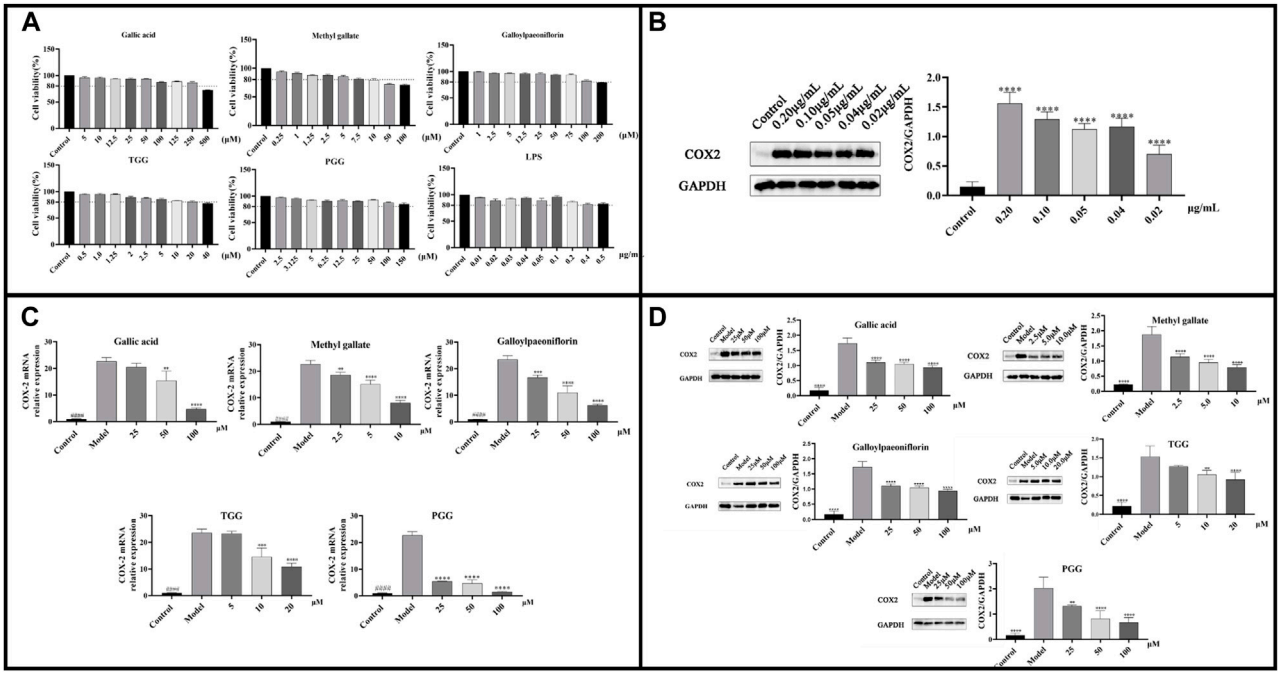


FIGURE 8
**(A)** Cell viability of LPS and each potential inhibitors by MTT assay; **(B)** COX-2 protein expression at different concentrations of LPS-induced RAW264.7; **(C)** COX-2 mRNA expressions in LPS-stimulated RAW264.7 cells following treatment by the potential inhibitors; **(D)** COX-2 Protein expressions in LPS-stimulated RAW264.7 cells following treatment by the potential inhibitors. $^{\#\#\#\#}p < 0.0001$ model group vs. blank group; $^{****}p < 0.0001$, $^{***}p < 0.001$, $^{**}p < 0.01$ experimental group vs. model group.

treated with the potential inhibitors was lower as compared to that in the model group, indicating that these inhibitors showed a dose-dependent suppression on the expression of COX-2 gene. Figure 8D illustrated that COX-2 protein expression was dramatically higher in the model group compared with the blank group. Moreover, the COX-2 protein expression of the potential inhibitors groups was lower in comparison to that of the model group, which was consistent with the findings from RT-qPCR. These results suggested that the potential inhibitors were likely to exert anti-inflammatory effect by modulating LPS-mediated signaling pathways associated with COX-2.

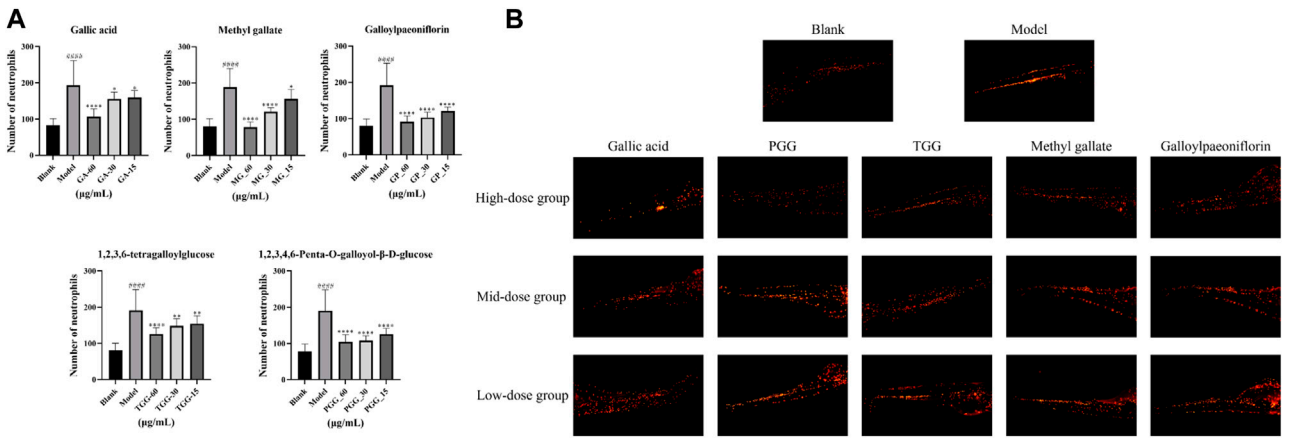


FIGURE 9
Anti-inflammatory activity of potential inhibitors in zebrafish ($n$ = 15, mean ± standard deviation). **(A)** The number of neutrophils in zebrafish was counted under a fluorescence microscope. **(B)** The neutrophils picture of each zebrafish group under the fluorescence microscope. $^{\#\#\#\#}p < 0.0001$, the model group vs. the blank group; $^{****}p < 0.0001$, $^{**}p < 0.01$, $^{*}p < 0.05$, potential inhibitors group vs. the model group.

## 3.7 Anti-inflammatory assay in zebrafish

In the present study, potential COX-2 inhibitors in MC were preliminarily identified by affinity ultrafiltration and further validated by *in vitro* inhibitory assays. To examine whether the compounds (GA, MG, GP, TGG, PGG) boast *in vivo* anti-inflammatory effect, biological model with LPS-induced inflammation was constructed using transgenic zebrafish. The toxicity of RMC at a series of concentrations was evaluated in 5 days, and a 100% survival rate was attained at 60 μg/mL. Therefore, a gradient consisting of three concentrations (15 μg/mL, 30 μg/mL and 60 μg/mL) was applied for the administration group based on the maximum tolerated concentration. The *in vivo* Anti-inflammatory effect of the compounds were characterized by counting the number of neutrophils in zebrafish. The fluorescence of neutrophils in each group of zebrafish was shown in Figure 9. The results revealed that the number of neutrophils in the model group showed a dramatic rise in comparison to the blank group, indicating that the zebrafish inflammation models were successfully established. Meanwhile, all the experimental groups exhibited a reduction in the number of neutrophils in zebrafish compared with the model group, suggesting that the all the five compounds harbor an *in vivo* anti-inflammatory activity by inhibiting the inflammatory response caused by LPS.

## 3.8 Molecular docking analysis

COX-2 is an active enzyme functioning as cyclooxygenase and peroxidase due to its structure containing the relevant activation sites, each of which is functionally connected by a bridged hemoglobin part (Lucido et al., 2016). According to the literature, when COX-2 produce pro-inflammatory effect, the substrate will form strong hydrogen bonds with Tyr385 and Ser530, as well as van der Waals forces with Arg120. Meanwhile, Trp 387 plays a key role in stabilizing the substrate conformation during the generation of PGG2. Other residues involved in the substrate catalytic process include residues 520-535, Tyr348, Phe381, Tyr385, and Ser530 (Kurumbail et al., 1996; Kiefer et al., 2000). To observe the interaction between the compounds and COX-2, computer simulation-based molecular docking technique was employed in this study. The results of molecular docking in this study were shown in Figure 10, and a summary of the residues interacting with the compound was presented in Table 2. The binding free energy of celecoxib was −9.39 kcal/mol indicating that celecoxib and COX-2 had strong interactions, which indirectly proved that the protein active pocket established in this study was reasonable. The positive drug forms hydrogen bonds with the key residue Arg120 mentioned earlier, while also interacting hydrophobically with Trp387, Tyr355, Val523, Met522, and Ala527. This indicated that celecoxib could enter the active pocket of COX-2, obstructing the entry of substrates and exerting anti-inflammatory effects. Similarly, in the potential anti-inflammatory active compounds in this experiment, GA, MG, GP, and TGG could form hydrogen bonds, van der Waals forces, or hydrophobic interactions with Tyr355, Val523, Ser530, Ala527, Tyr387, and Arg120, respectively. Based on these results, it was speculated that the above compounds, like the positive drug, could enter the active pocket of COX-2 and exerted similar anti-inflammatory effects. While PGG in Figure 10F showed conformations and docking residues indicating that it did not fully enter the interior of the active pocket, the residues with which PGG forms hydrogen bond and van der Waals interactions were mostly located at the entrance of the pocket. This implied that the anti-inflammatory effect produced by PGG was not directly interacting with the key positions in the active pocket, but rather achieving the anti-inflammatory purpose by interacting with residues at the entrance, preventing the substrate from entering the active pocket. Mealwhile, TGG also had lower binding energy with COX-2, but it showed a better *in vitro* COX-2-inhibitory activity in comparison to other inhibitors. The possible explanation was that TGG and PGG, with a larger molecular weight in simulated docking, inevitably had a higher torsional free energy, thus leading to the discrepancy

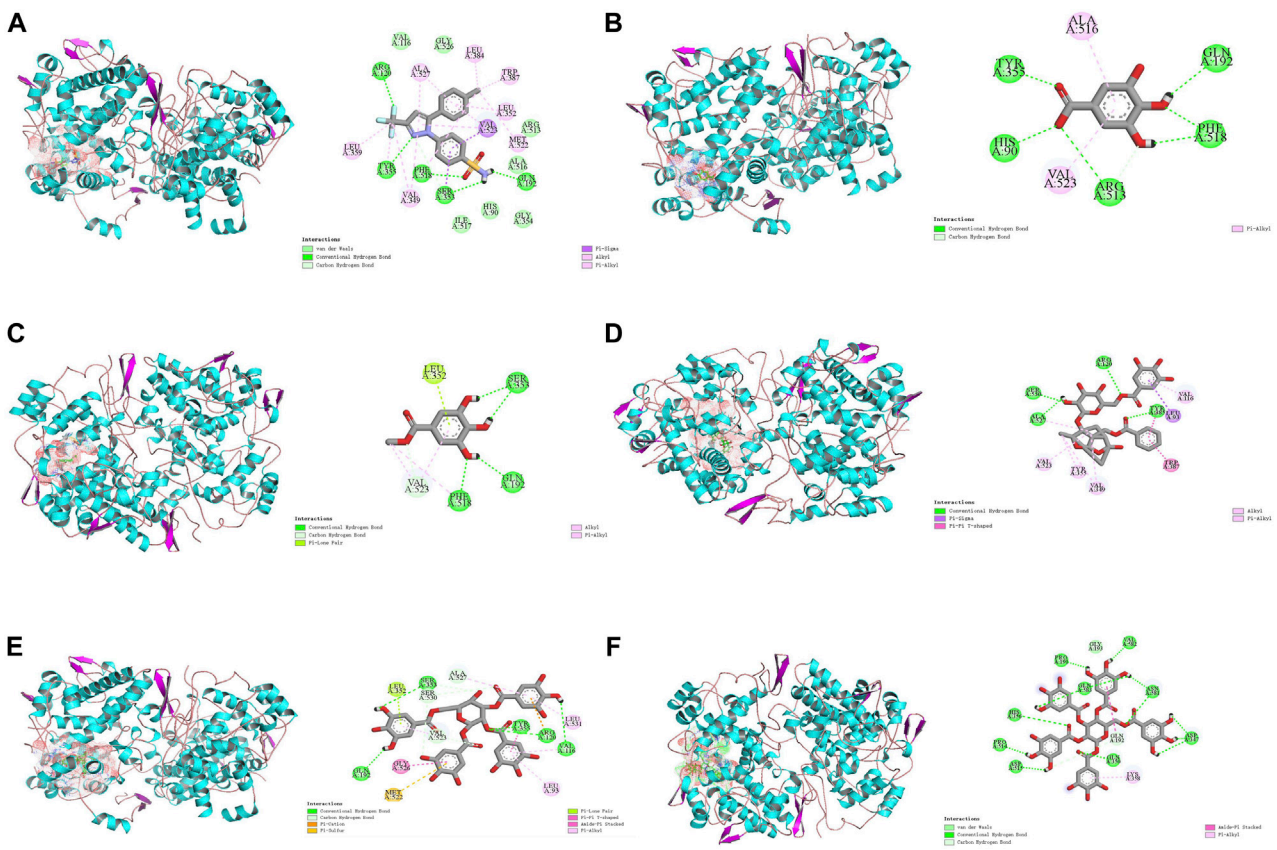


FIGURE 10
Docking models of screened inhibitors in COX-2 active site. **(A)** celecoxib, **(B)** gallic acid **(C)** methyl gallate, **(D)** galloylpaeonflorin, **(E)** TGG, and **(F)** PGG (Van der Waals are colored in light green; Hydrogen bonds are colored in deep green; Yellow, purple, deep pink, and light pink indicate hydrophobic interactions and represent Pi-Sulful, Pi-sigma, Amide-Pi Stacked, and Pi-Alkyl, respectively).

**TABLE 2** Free energy of binding as well as interaction between amino acids and the compounds.

| Compound | Estimated free energy of binding (kcal/mol) | Hydrogen bond and pi-pi interaction amino acids | Hydrophobic interaction amino acids |
|---|---|---|---|
| Celecoxib | −9.33 | Arg120, Tyr355, Phe518, Ser353, Gln192 | Ala527, Leu384, Trp387, Leu352, Val523, Met522, Ser353, Phe518, Val349, Tyr355, Leu359 |
| Gallic acid | −5.46 | Tyr355, Arg513, His90, Gln192, Phe518 | Val523, Ala516 |
| Methyl gallate | −4.9 | Ser353, Gln192, Phe518 | Phe518, Val523 |
| Galloylpaeoniflorin | −9.36 | Ser530, Ala527, Arg120 | Val116, Leu93, Tyr385, Trp387 Val349, Tyr355, Val523 |
| 1,2,3,6-Tetra-O-galloyl-β-D-glucose | −4.29 | Val116, Gln192, Arg120, Tyr355, Ala527, Ser353, Ser530 | Leu93, Leu531, Val523, Leu352, Gly526, Ser530, Met522, Arg120, Tyr355 |
| 1,2,3,4,6-Penta-O-galloyl-β-D-glucose | −3.96 | Asp515, Pro514, His356, Gln583, Pro191, Val582, Asn581, Asp347, Gln350 | Gln192, Lys358 |

between the results from molecular docking and *in vitro* inhibition assays. Likewise, inconsistent results between the two techniques also occurred in GA, which was associated with the fact that GA was more likely to enter the grid box and interact with the residues during docking due to its smaller molecular weight (Agarwal and Mehrotra, 2016).

## 4 Conclusion

In this study, an BAUF-UPLC-MS approach on the basis of COX-2 affinity analysis was successfully developed for a rapid, efficient, and targeted screening and identification of the bioactive components in MC. A total of 11 components with potential COX-2-inhibitory activity

were discovered. Among them, five compounds—GC, MG, GP, TGG, and PGG—were validated to be bioactive by *in vitro* COX-2-inhibitory experiments. Subsequently, the anti-inflammatory effect of the five components were also assessed with a cell model *in vitro* and zebrafish model *in vivo*. Also, molecular docking was performed to further explore the structure-activity association of the components. Finally, the mechanisms underlying their anti-inflammatory effects were elucidated using network pharmacology approaches. Our results demonstrate that BAUF-UPLC-MS is an effective method for screening active ingredients in complex Chinese medicines. The method is simple, fast, inexpensive, and requires less sample, and can be used for other enzymes to highthroughput screen complex natural products. Also, analyzing these bioactive compounds are useful for quality assessment and clinical application of natural products.

## Data availability statement

The original contributions presented in the study are included in the article/Supplementary material, further inquiries can be directed to the corresponding authors.

## Ethics statement

The animal study was approved by the Institutional Ethics Committee (IEC) of Guangdong Pharmaceutical University and the International AAALAC certification. The study was conducted in accordance with the local legislation and institutional requirements.

## Author contributions

CZ: Writing–review and editing, Writing–original draft. QC: Investigation, Software, Writing–original draft. JL: Writing–original draft, Data curation, Methodology. XL: Data curation, Methodology, Writing–original draft. XX: Writing–original draft. XC: Writing–original draft, Writing–review and editing. YC: Writing–original draft, Investigation, Software. YS: Project administration, Resources, Writing–original draft. SW: Project administration, Resources, Writing–original draft. YZ: Writing–original draft. JM: Conceptualization, Resources, Supervision, Writing–original draft, Writing–review and editing.

## Funding

The author(s) declare financial support was received for the research, authorship, and/or publication of this article. This work was co-financed by grants National Natural Science Foundation of China (Nos 82173973 and 81473352), Key project of Guangdong Education Department (2018KZDXM040) and Guangdong Provincial Key Laboratory of Traditional Chinese Medicine Informatization (2021B1212040007).

## Conflict of interest

The authors declare that the research was conducted in the absence of any commercial or financial relationships that could be construed as a potential conflict of interest.

## Publisher's note

All claims expressed in this article are solely those of the authors and do not necessarily represent those of their affiliated organizations, or those of the publisher, the editors and the reviewers. Any product that may be evaluated in this article, or claim that may be made by its manufacturer, is not guaranteed or endorsed by the publisher.

## References

Agarwal, S., and Mehrotra, R. J. J. C. (2016). An overview of molecular docking. *JSM Chem.* 4 (2), 1024–1028. doi:10.47739/2334-1831/1024

Aggarwal, B. B., Shishodia, S., Sandur, S. K., Pandey, M. K., and Sethi, G. (2006). Inflammation and cancer: how hot is the link? *Biochem. Pharmacol.* 72 (11), 1605–1621. doi:10.1016/j.bcp.2006.06.029

Au, T. K., Lam, T. L., Ng, T. B., Fong, W. P., and Wan, D. C. C. (2001). A comparison of HIV-1 integrase inhibition by aqueous and methanol extracts of Chinese medicinal herbs. *Life Sci.* 68 (14), 1687–1694. doi:10.1016/S0024-3205(01)00945-6

Bartsch, H., and Nair, J. (2006). Chronic inflammation and oxidative stress in the genesis and perpetuation of cancer: role of lipid peroxidation, DNA damage, and repair. *Langenbecks Arch. Surg.* 391 (5), 499–510. doi:10.1007/s00423-006-0073-1

Bindu, S., Mazumder, S., and Bandyopadhyay, U. (2020). Non-steroidal anti-inflammatory drugs (NSAIDs) and organ damage: a current perspective. *Biochem. Pharmacol.* 180, 114147. doi:10.1016/j.bcp.2020.114147

Braun, J., Baraliakos, X., and Westhoff, T. (2020). Nonsteroidal anti-inflammatory drugs and cardiovascular risk – a matter of indication. *Semin. Arthritis Rheum.* 50 (2), 285–288. doi:10.1016/j.semarthrit.2019.07.012

Cai, Q., Meng, J., Ge, Y., Gao, Y., Zeng, Y., Li, H., et al. (2020). Fishing antitumor ingredients by G-quadruplex affinity from herbal extract on a three-phase-laminar-flow microfluidic chip. *Talanta* 220, 121368. doi:10.1016/j.talanta.2020.121368

Chen, S., Dang, Y., Gong, Z., Letcher, R. J., and Liu, C. (2019). Progression of liver tumor was promoted by tris(1,3-dichloro-2-propyl) phosphate through the induction of inflammatory responses in krasV12 transgenic zebrafish. *Environ. Pollut.* 255, 113315. doi:10.1016/j.envpol.2019.113315

Chun, K., Kim, S. O., and Lee, S. H. (2016). Analgesic effects of 1,2,3,4,6-penta-O-galloyl-β-D-glucose in an animal model of lipopolysaccharide-induced pain. *Int. J. Mol. Med.* 38 (4), 1264–1270. doi:10.3892/ijmm.2016.2726

Chun, S. C., Jee, S. Y., Lee, S. G., Park, S. J., Lee, J. R., and Kim, S. C. (2007). Anti-inflammatory activity of the methanol extract of moutan cortex in LPS-activated Raw264. 7 cells. *Evid. Based Complement. Altern. Med.* 4 (3), 327–333. doi:10.1093/ecam/nel093

Ding, L., Jiang, Z., Liu, Y., Chen, L., Zhao, Q., Yao, X., et al. (2012a). Monoterpenoid inhibitors of NO production from Paeonia suffruticosa. *Fitoterapia* 83 (8), 1598–1603. doi:10.1016/j.fitote.2012.09.008

Ding, L., Zhao, F., Chen, L., Jiang, Z., Liu, Y., Li, Z., et al. (2012b). New monoterpene glycosides from Paeonia suffruticosa Andrews and their inhibition on NO production in LPS-induced RAW 264.7 cells. *Bioorg Med. Chem. Lett.* 22 (23), 7243–7247. doi:10.1016/j.bmcl.2012.09.034

Federico, A., Morgillo, F., Tuccillo, C., Ciardiello, F., and Loguercio, C. (2007). Chronic inflammation and oxidative stress in human carcinogenesis. *Int. J. Cancer.* 121 (11), 2381–2386. doi:10.1002/ijc.23192

Fernandes, T. A., Antunes, A. M. M., Caldeira, I., Anjos, O., de Freitas, V., Fargeton, L., et al. (2022). Identification of gallotannins and ellagitannins in aged wine spirits: a new perspective using alternative ageing technology and high-resolution mass spectrometry. *Food Chem.* 382, 132322. doi:10.1016/j.foodchem.2022.132322

Fitzpatrick, F. A. (2001). Inflammation, carcinogenesis and cancer. *Int. Immunopharmacol.* 1 (9-10), 1651–1667. doi:10.1016/s1567-5769(01)00102-3

He, C. N., Peng, Y., Zhang, Y. C., Xu, L. J., Gu, J., and Xiao, P. G. (2010). ChemInform abstract: phytochemical and biological studies of paeoniaceae. *Chem. Biodivers.* 7 (4), 805–838. doi:10.1002/cbdv.200800341

He, Q., Ge, Z. W., Song, Y., and Cheng, Y. Y. (2006). Quality evaluation of cortex moutan by high performance liquid chromatography coupled with diode array detector and electrospary ionization tandem mass spectrometry. *Chem. Pharm. Bull.* 54 (9), 1271–1275. doi:10.1248/cpb.54.1271

Hsiang, C. Y., Hsieh, C. L., Wu, S. L., Lai, I. L., and Ho, T. Y. (2001). Inhibitory effect of anti-pyretic and anti-inflammatory herbs on herpes simplex virus replication. *Am. J. Chin. Med.* 29 (3-4), 459–467. doi:10.1142/S0192415X01000472

Huai, J., Zhao, X., Wang, S., Xie, L., Li, Y., Zhang, T., et al. (2019). Characterization and screening of cyclooxygenase-2 inhibitors from Zi-shen pill by affinity ultrafiltration-ultra performance liquid chromatography mass spectrometry. *J. Ethnopharmacol.* 241, 111900. doi:10.1016/j.jep.2019.111900

Jadhav, A. S., and Shingare, M. S. (2005). A new stability–indicating RP-HPLC method to determine assay and known impurity of celecoxib API. *Drug Dev. Ind. Pharm.* 31 (8), 779–783. doi:10.1080/03639040500216378

Jiao, J. J., Yang, Y. Z., Wu, Z. F., Li, B. T., Zheng, Q., Wei, S. F., et al. (2019). Screening cyclooxygenase-2 inhibitors from Andrographis paniculata to treat inflammation based on bio-affinity ultrafiltration coupled with UPLC-Q-TOF-MS. *Fitoterapia* 137, 104259. doi:10.1016/j.fitote.2019.104259

Kiefer, J. R., Pawlitz, J. L., Moreland, K. T., Stegeman, R. A., Hood, W. F., Gierse, J. K., et al. (2000). Structural insights into the stereochemistry of the cyclooxygenase reaction. *Nature* 405 (6782), 97–101. doi:10.1038/35011103

Kurumbail, R. G., Stevens, A. M., Gierse, J. K., McDonald, J. J., Stegeman, R. A., Pak, J. Y., et al. (1996). Structural basis for selective inhibition of cyclooxygenase-2 by anti-inflammatory agents. *Nature* 384 (6610), 644–648. doi:10.1038/384644a0

Lan, Z., Zhang, Y., Sun, Y., Wang, L., Huang, Y., Cao, H., et al. (2021). Identifying of anti-thrombin active components from curcumae rhizoma by affinity-ultrafiltration coupled with UPLC-Q-exactive Orbitrap/MS. *Front. Pharmacol.* 12, 769021. doi:10.3389/fphar.2021.769021

Li, J. J., Zhang, Y., Han, L. W., Tian, Q. P., He, Q. X., Wang, X. M., et al. (2018). Tenacissoside H exerts an anti-inflammatory effect by regulating the nf-κb and p38 pathways in zebrafish. *Fish. Shellfish Immunol.* 83, 205–212. doi:10.1016/j.fsi.2018.09.032

Liu, S., Guo, S., Hou, Y., Zhang, S., Bai, L., Ho, C., et al. (2023). Chemical fingerprinting and multivariate analysis of Paeonia ostii leaves based on HPLC-DAD and UPLC-ESI-Q/TOF-MS/MS. *Microchem. J.* 184, 108169. doi:10.1016/j.microc.2022.108169

Liu, W., Xie, G., Yuan, G., Xie, D., Lian, Z., Lin, Z., et al. (2021). 6 ’-O-galloylpaeoniflorin attenuates osteoclasto-genesis and relieves ovariectomy-induced osteoporosis by inhibiting reactive oxygen species and MAPKs/c-fos/NFATc1 signaling pathway. *Front. Pharmacol.* 12, 641277. doi:10.3389/fphar.2021.641277

Lucido, M. J., Orlando, B. J., Vecchio, A. J., and Malkowski, M. G. (2016). Crystal structure of aspirin-acetylated human cyclooxygenase-2: insight into the formation of products with reversed stereochemistry. *Biochemistry* 55 (8), 1226–1238. doi:10.1021/acs.biochem.5b01378

Matsuda, H., Ohta, T., Kawaguchi, A., and Yoshikawa, M. (2001). Bioactive constituents of Chinese natural medicines. VI. Moutan cortex. (2): structures and radical scavenging effects of suffruticosides A, B, C, D, and E and galloyl-oxypaeoniflorin. *Chem. Pharm. Bull.* 49 (1), 69–72. doi:10.1248/cpb.49.69

Mohan, M., Hussain, M. A., Khan, F. A., and Anindya, R. (2021). Symmetrical and un-symmetrical curcumin analogues as selective COX-1 and COX-2 inhibitor. *Eur. J. Pharm. Sci.* 160, 105743. doi:10.1016/j.ejps.2021.105743

Ow, Y. Y., and Stupans, I. (2003). Gallic acid and gallic acid derivatives: effects on drug metabolizing enzymes. *Curr. Drug Metab.* 4 (3), 241–248. doi:10.2174/1389200033489479

Qin, S., Ren, Y., Fu, X., Shen, J., Chen, X., Wang, Q., et al. (2015). Multiple ligand detection and affinity measurement by ultrafiltration and mass spectrometry analysis applied to fragment mixture screening. *Anal. Chim. Acta* 886, 98–106. doi:10.1016/j.aca.2015.06.017

Sheehan, M. P., and Atherton, D. J. (1994). One-year follow up of children treated with Chinese medicinal herbs for atopic eczema. *Brit J. Dermatol* 130 (4), 488–493. doi:10.1111/j.1365-2133.1994.tb03383.x

Smalley, W. E., and DuBois, R. N. (1997). Colorectal cancer and nonsteroidal anti-inflammatory drugs. *Adv. Pharmacol.* 39, 1–20. doi:10.1016/s1054-3589(08)60067-8

Strippoli, V., D’Auria, F. D., Tecca, M., Callari, A., and Simonetti, G. (2000). Propyl gallate increases *in vitro* antifungal imidazole activity against Candida albicans. *Int. J. Antimicrob. Ag.* 16 (1), 73–76. doi:10.1016/S0924-8579(00)00200-4

Watanabe, T., Fujiwara, Y., and Chan, F. K. L. (2020). Current knowledge on non-steroidal anti-inflammatory drug-induced small-bowel damage: a comprehensive review. *J. Gastroenterol.* 55 (5), 481–495. doi:10.1007/s00535-019-01657-8

Wei, H., Zhang, X., Tian, X., and Wu, G. (2016). Pharmaceutical applications of affinity-ultrafiltration mass spectrometry: recent advances and future prospects. *J. Pharm. Biomed.* 131, 444–453. doi:10.1016/j.jpba.2016.09.021

Wolfender, J. L., Marti, G., Thomas, A., and Bertrand, S. (2015). Current approaches and challenges for the metabolite profiling of complex natural extracts. *J. Chromatogr. A* 1382, 136–164. doi:10.1016/j.chroma.2014.10.091

Xiong, P., Qin, S., Li, K., Liu, M., Zhu, L., Peng, J., et al. (2021). Identification of the tannins in traditional Chinese medicine paeoniae radix alba by UHPLC-Q-exactive Orbitrap MS. *Arab. J. Chem.* 14, 103398. doi:10.1016/j.arabjc.2021.103398

Xu, H., Zhang, X., Li, H., Li, C., Huo, X. J., Hou, L. P., et al. (2018). Immune response induced by major environmental pollutants through altering neutrophils in zebrafish larvae. *Aquat. Toxicol.* 201, 99–108. doi:10.1016/j.aquatox.2018.06.002

Yun, C. S., Choi, Y. G., Jeong, M. Y., Lee, J. H., and Lim, S. (2013). Moutan Cortex Radicis inhibits inflammatory changes of gene expression in lipopolysaccharide-stimulated gingival fibroblasts. *J. Nat. Med.* 67 (3), 576–589. doi:10.1007/s11418-012-0714-3

Zhang, X., Wei, J., Que, Z., and Chen, Y. (2017). Research progress on anti-inflammatory effects of traditional Chinese medicine. *Chin. J. Ethnomedicine Ethnopharmacy* 26 (21), 67–69.

Zhang, X. Y., Wei, Z. J., Qiao, W. L., Sun, X. M., Jin, Z. L., Gong, W., et al. (2021). Discovery of cyclooxygenase-2 inhibitors from Kadsura coccinea by affinity ultrafiltration mass spectrometry and the anti-inflammatory activity. *Fitoterapia* 151, 104872. doi:10.1016/j.fitote.2021.104872

frontiers | Frontiers in Chemistry

TYPE Original Research
PUBLISHED 29 February 2024
DOI 10.3389/fchem.2024.1364378

Check for updates

OPEN ACCESS

EDITED BY
Xuetao Xu,
Wuyi University, China

REVIEWED BY
Eman Nossier,
Al-Azhar University, Egypt
Ibrahim F. Nassar,
Ain Shams University, Egypt

*CORRESPONDENCE
Ayman El-Faham,
ayman.elfaham@alexu.edu.eg
Assem Barakat,
ambarakat@ksu.edu.sa

RECEIVED 02 January 2024
ACCEPTED 15 February 2024
PUBLISHED 29 February 2024

CITATION
Nafie MS, Al-Majid AM, Ali M, Alayyaf AA, Haukka M, Ashraf S, Ul-Haq Z, El-Faham A and Barakat A (2024), Exploring pyrrolidinyl-spirooxindole natural products as promising platforms for the synthesis of novel spirooxindoles as EGFR/CDK2 inhibitors for halting breast cancer cells.
*Front. Chem.* 12:1364378.
doi: 10.3389/fchem.2024.1364378

COPYRIGHT
© 2024 Nafie, Al-Majid, Ali, Alayyaf, Haukka, Ashraf, Ul-Haq, El-Faham and Barakat. This is an open-access article distributed under the terms of the Creative Commons Attribution License (CC BY). The use, distribution or reproduction in other forums is permitted, provided the original author(s) and the copyright owner(s) are credited and that the original publication in this journal is cited, in accordance with accepted academic practice. No use, distribution or reproduction is permitted which does not comply with these terms.

# Exploring pyrrolidinyl-spirooxindole natural products as promising platforms for the synthesis of novel spirooxindoles as EGFR/CDK2 inhibitors for halting breast cancer cells

Mohamed S. Nafie[1,2], Abdullah Mohammed Al-Majid[3], M. Ali[3], Abdulmajeed Abdullah Alayyaf[3], Matti Haukka[4], Sajda Ashraf[5], Zaheer Ul-Haq[5], Ayman El-Faham[6]* and Assem Barakat[3]*

[1]Department of Chemistry, College of Sciences, University of Sharjah, Sharjah, United Arab Emirates, [2]Chemistry Department, Faculty of Science, Suez Canal University, Ismailia, Egypt, [3]Department of Chemistry, College of Science, King Saud University, Riyadh, Saudi Arabia, [4]Department of Chemistry, University of Jyväskylä, Jyväskylä, Finland, [5]Dr. Panjwani Center for Molecular medicine and Drug Research, International Center for Chemical and Biological Sciences, University of Karachi, Karachi, Pakistan, [6]Department of Chemistry, Faculty of Science, Alexandria University, Alexandria, Egypt

Cancer represents a global challenge, and the pursuit of developing new cancer treatments that are potent, safe, less prone to drug resistance, and associated with fewer side effects poses a significant challenge in cancer research and drug discovery. Drawing inspiration from pyrrolidinyl-spirooxindole natural products, a novel series of spirooxindoles has been synthesized through a one-pot three-component reaction, involving a [3 + 2] cycloaddition reaction. The cytotoxicity against breast cancer cells (MCF-7 and MDA-MB-231) and safety profile against WISH cells of the newly developed library were assessed using the MTT assay. Compounds **5l** and **5o** exhibited notable cytotoxicity against MCF-7 cells ($IC_{50}$ = 3.4 and 4.12 μM, respectively) and MDA-MB-231 cells ($IC_{50}$ = 8.45 and 4.32 μM, respectively) compared to Erlotinib. Conversely, compounds **5a-f** displayed promising cytotoxicity against MCF-7 cells with $IC_{50}$ values range ($IC_{50}$ = 5.87–18.5 μM) with selective activity against MDA-MB-231 cancer cells. Compound **5g** demonstrated the highest cytotoxicity ($IC_{50}$ = 2.8 μM) among the tested compounds. Additionally, compounds **5g**, **5l**, and **5n** were found to be safe (non-cytotoxic) against WISH cells with higher $IC_{50}$ values ranging from 39.33 to 47.2 μM. Compounds **5g**, **5l**, and **5n** underwent testing for their inhibitory effects against EGFR and CDK-2. Remarkably, they demonstrated potent EGFR inhibition, with $IC_{50}$ values of 0.026, 0.067, and 0.04 μM and inhibition percentages of 92.6%, 89.8%, and 91.2%, respectively, when compared to Erlotinib ($IC_{50}$ = 0.03 μM, 95.4%). Furthermore, these compounds exhibited potent CDK-2 inhibition, with $IC_{50}$ values of 0.301, 0.345, and 0.557 μM and inhibition percentages of 91.9%, 89.4%, and 88.7%, respectively, in contrast to Roscovitine ($IC_{50}$ = 0.556 μM, 92.1%). RT-PCR analysis was performed on both untreated and **5g**-treated MCF-7 cells to confirm apoptotic cell death. Treatment with **5g** increased the gene expression of pro-apoptotic genes P53, Bax, caspases

3, 8, and 9 with notable fold changes while decreasing the expression of the anti-apoptotic gene Bcl-2. Molecular docking and dynamic simulations (100 ns simulation using AMBER22) were conducted to investigate the binding mode of the most potent candidates, namely, **5g**, **5l**, and **5n**, within the active sites of EGFR and CDK-2.

KEYWORDS

**spirooxindole, [3+2] cycloaddition, breast cancer (MCF-7 and MDA-MB-231), EGFR, CDK-2, molecular dynamics**

## Introduction

Cancer, a widespread and intricate group of diseases, presents a significant challenge in global healthcare, impacting millions of lives (Sung et al., 2021). Characterized by uncontrolled cell growth, it forms malignant tumors and persists as a major public health concern despite medical advancements. The multifaceted nature of cancer involves diverse forms and complex interactions of genetic, environmental, and lifestyle factors. The problem's gravity is highlighted by its global prevalence and substantial emotional, economic, and healthcare burdens on individuals and communities. Urgency is fueled by rising incidence rates and the ongoing search for effective treatments and prevention. The introduction emphasizes the need to understand cancer's intricacies for developing innovative therapies and prevention strategies, setting the stage for exploring its multifaceted aspects and addressing the challenges it poses to public health improvement.

Among women globally, breast cancer stood out as the predominant form of cancer, comprising 30% of the total newly diagnosed cases in the year 2021 (Sung et al., 2021). Breast cancer cell lines, such as MCF-7 and MDA-MB-231, play a crucial role in cancer research. Derived from breast cancer tumors, these cell lines serve as invaluable tools for studying the disease's biology, testing treatments and understanding molecular mechanisms. They are cultured in laboratories, allowing researchers to investigate various aspects of breast cancer, including genetic makeup, treatment responses, and drug resistance. These cell lines are vital for the preclinical testing of new therapies, contributing to developing more effective treatments for breast cancer patients.

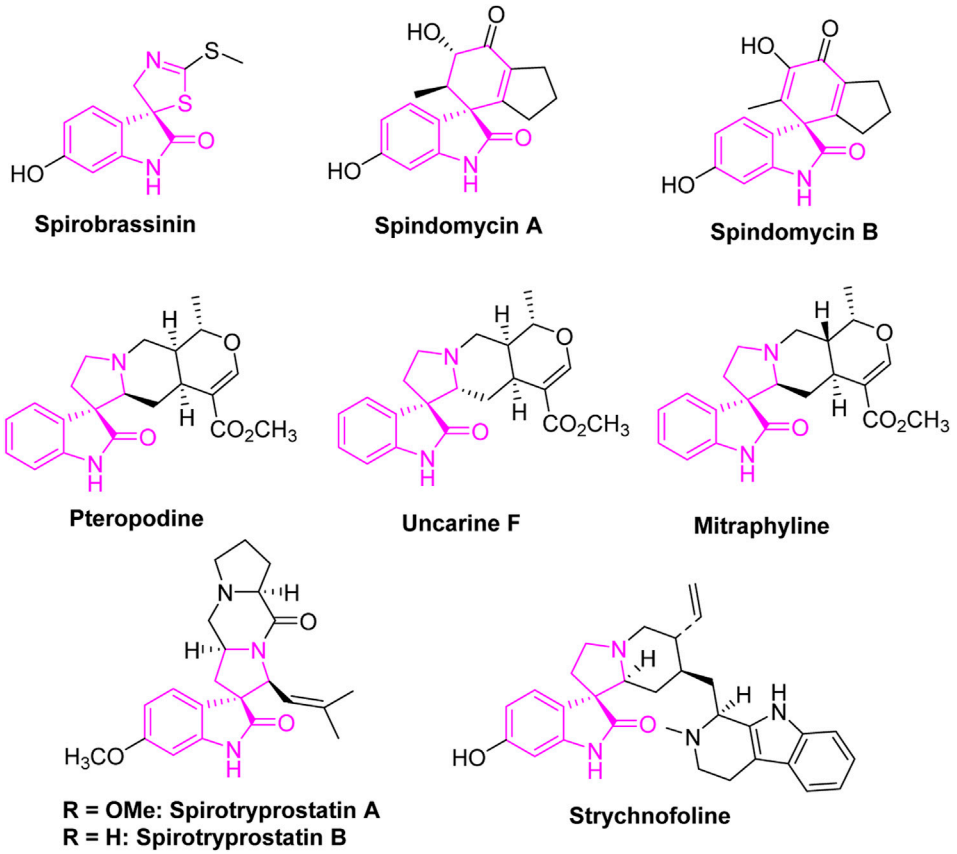


FIGURE 1
Naturally occurring spirooxindole compounds possessing anti-tumor properties.

The distinct structural framework of these compounds, characterized by a spiro ring fusion at position-3 of the oxindole, gives rise to their diverse biological activities. This arrangement enables the oxindole moiety to serve as either a hydrogen bond donor or acceptor, thereby augmenting its interactions with diverse biological targets. Furthermore, their adaptability in forming combinations with various bioactive cycloalkyl or heterocyclic motifs substantially boosts their effectiveness across various applications (Zhou et al., 2020).

Figure 1 depicts diverse spirooxindole frameworks sourced from nature, showcasing potent anti-cancer activity (Yu et al., 2015). Of particular note is Spirobrassinin, an oxindole alkaloid renowned for its robust anti-tumor properties (Budovská et al., 2020), along with spindomycins A and B, identified as potential inhibitors of the tyrosine kinase Bcr-Abl (Guo et al., 2014). Spirotryprostatins A and B exhibit noteworthy inhibitory effects against mouse breast cancer, specifically targeting tsFT210 (Ding et al., 2005; Al-Rashood et al., 2020). Pteropodine and Uncarine F have shown robust inhibitory effects against CEM-C7H2 cells, whereas Mitraphylline has exhibited significant inhibitory activity against various cancer cell lines, including neuroblastoma SKN-BE, glioma GAMG, human Ewing's sarcoma MHH-ES-1, and breast cancer MT-3 cells in a dose-dependent manner (García Giménez et al., 2010). Strychnofoline is an additional example, demonstrating efficacy against melanoma and Ehrlich tumor cells (Yu et al., 2018; Yuenyongsawad et al., 2013). Mitraphylline, Uncarine F, and Pteropodine represent natural spirooxindole alkaloids extracted from Uncaria tomentosa (Bacher et al., 2006).

Spirotryprostatin A (Cui, et al., 1996; Edmondson et al., 1999) is an example of a neutrally occurring spirooxindole scaffold targeting breast cancer cells. Derived from the tryprostatin alkaloid family (Islam et al., 2023; Marti and Carreira, 2003), this compound exhibits notable inhibitory effects against breast cancer cell lines. The unique structural features of the spirooxindole scaffold, including a spiro ring fusion at position-3 of the oxindole, contribute to its ability to interact with biological targets in breast cancer cells. Studies suggest that Spirotryprostatin A hinders breast cancer cell proliferation and induces apoptosis, making it a potential candidate for further exploration in the development of targeted breast cancer therapies. The compound exemplifies the potential of spirooxindole scaffolds in the quest for innovative and effective treatments for breast cancer.

Cyclin-Dependent Kinase 2 (CDK2) (Tadesse, et al., 2018; Golsteyn, 2005) is a compelling target in cancer therapy due to its crucial role in regulating the cell cycle, particularly the transition from G1 to S phase. Aberrant activation of CDK2 is associated with uncontrolled cell proliferation in various cancers. Inhibitors designed to selectively target CDK2 have shown promise in preclinical and clinical settings by inducing cell cycle arrest and triggering apoptosis in cancer cells. Targeting CDK2 offers a strategic approach to impede cancer cell division, and ongoing research aims to optimize CDK2 inhibitors for enhanced efficacy and reduced side effects, highlighting its potential as an innovative avenue in cancer therapy. We built upon the groundwork established by benchmark oxindole-based CDK2 inhibitors (**I**) (Luk, 2004; Venkanna, et al., 2020; Bramson, et al., 2001) and spiro (Al-Jassas, et al., 2023; Barakat, et al., 2023) anti-cancer agents recognized for their kinase inhibition, specifically those aimed at CDK2. This rational study involved a detailed exploration of the CDK2 inhibitory potential within the investigated series, as depicted in Figure 2.

Al-Jassas (Al-Jassas, et al., 2023) designed, synthesized, and assessed a novel spirooxindole scaffold for its dual inhibitory properties against CDK2 and EGFR. Compound **II** exhibited notable inhibition, with $IC_{50}$ values of 0.189 ± 0.01 μM (MCF-7) and 1.04 ± 0.21 μM (HepG2). Additionally, it demonstrated potent CDK-2 inhibition (34.98 nM) and an $IC_{50}$ of 96.6 nM for EGFR inhibition. Compound **II** also effectively modulated the expression of pro-apoptotic genes (P53, Bax, caspases-3, 8, and 9) while downregulating the anti-apoptotic gene Bcl-2.

Barakat research group has reported a combinatorial stereoselective synthesis of rationally designed spiroindeno [1,2-*b*] quinoxaline-based CDK2 inhibitors **III** for non-small cell lung cancer (NSCLC) therapy (Barakat, et al., 2023). Among the derivatives tested, hit **III** emerged as the most promising, exhibiting potent inhibitory effects against A549 cells and normal lung fibroblasts Wi-38, with an $IC_{50}$ value of 54 nM and a selectivity index (SI) of 6.64.

Biao Wang et al. (Wang, et al., 2020) identified the THN-fused spirooxindole derivative, **IV**, as a potent inhibitor using a rational drug design approach, complemented by the asymmetric synthesis of the designed compounds. Notably, **IV** exhibited robust inhibitory effects on both MDM2 and CDK4 in glioblastoma cells expressing either wild-type or mutant P53. Molecular dynamics simulations suggested a tight binding affinity of **IV** to both MDM2 and CDK4. Furthermore, **IV** demonstrated the ability to induce substantial apoptosis and G1 phase cell cycle arrest.

Based on the aforementioned findings, this study explores the realm of pyrrolidinyl-spirooxindole natural products, drawing inspiration from their distinctive chemical structures for the potential development of therapeutic agents. These naturally occurring compounds serve as intriguing templates, providing valuable insights into the design of novel medications. The investigation aims to unveil the therapeutic potential inherent in pyrrolidinyl-spirooxindoles, with the goal of developing innovative and effective therapeutic agents for diverse medical applications (Galliford and Scheidt., 2007). The study involves the synthesis and evaluation of a new set of spirooxindoles against breast cancer cells, along with an assessment of their inhibitory activities against CDK2 and EGFR. Additionally, the study explores apoptotic cell death, pro-apoptotic genes, and anti-apoptotic gene assays. Finally, molecular docking and dynamic simulations are employed to investigate the binding modes of the most potent candidates within the active sites of EGFR and CDK-2.

## Results and discussion

Scheme 1 illustrates the efficient and highly selective synthesis of the targeted bi-spirooxindole-incorporated rhodanine analog. The starting material chalcones based rhodanine motif **4a-f**, was synthesized following a literature-reported method (Barakat et al., 2021). Employing a one-pot multicomponent 32CA reaction, the arylidene rhodanine analogue **4a-f**, isatin derivatives **2a-e**, and

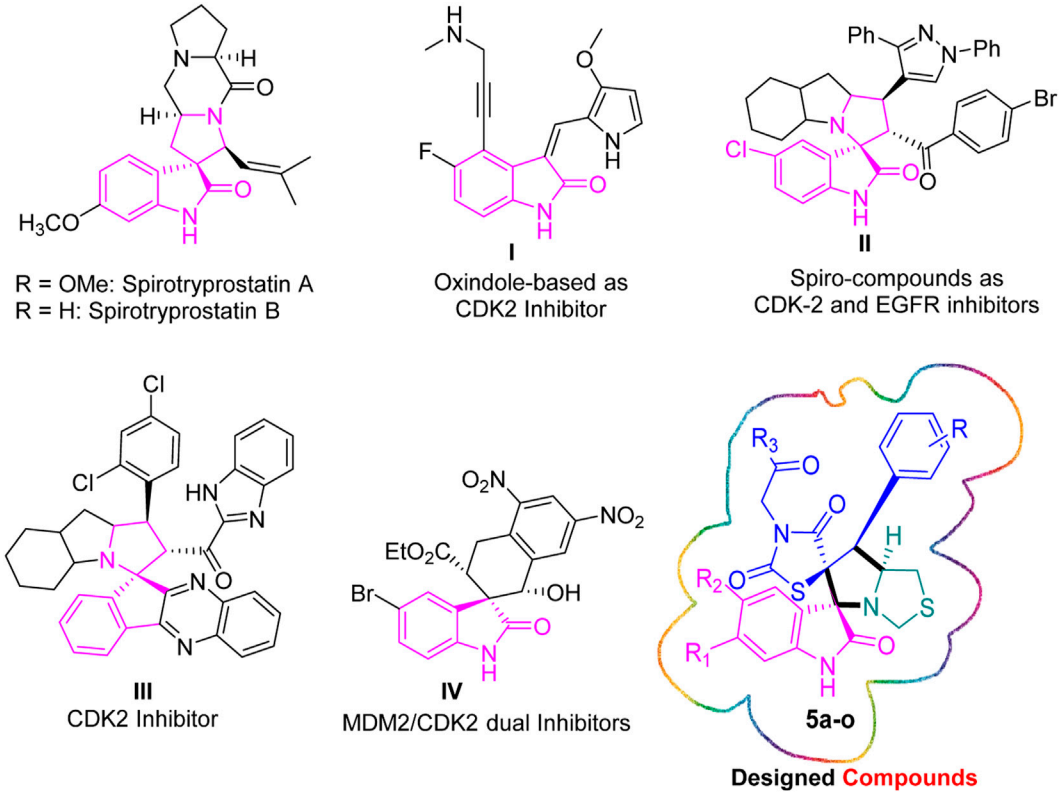


FIGURE 2
Rational design inspired by both natural products and novel synthetic spirooxindoles.

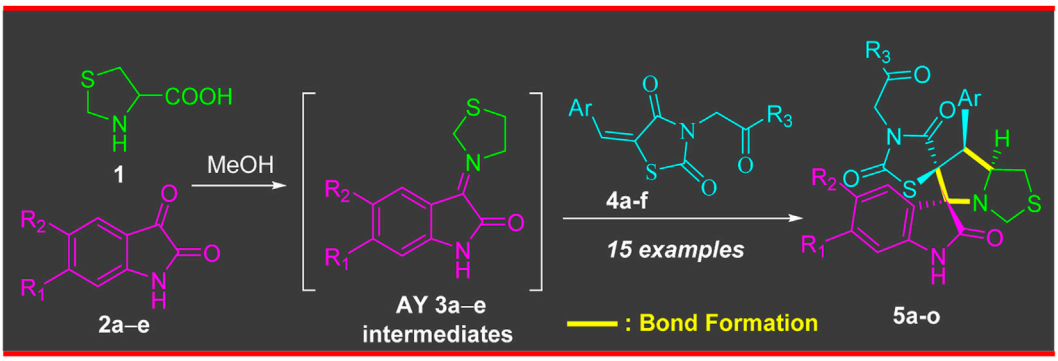


SCHEME 1
Synthesis of compounds **5a-o** *via* a 32CA reaction of AY **3a-e** with ethylene derivative **4a-f**.

thioproline **1** were reacted under refluxed conditions in MeOH for 2 h, resulting in the desired stereo-selective bi-spirooxindole-incorporated rhodanine analog **5a-o**. The reaction proceeded in two steps: first, isatin derivatives **2a-e** reacted with secondary amino acid (thioproline) **1** to generate the azomethine ylide (AY). In the second step, the generated azomethine ylide (AY 3) reacted with arylidene rhodanine analog **4a-f** through completely *ortho* regioselective and *exo* stereoiselective. Spectral data analysis and elucidation confirmed the proposed structure, and single crystal X-ray diffraction analysis further validated the chemical structure.

## Crystal structure description

The X-ray structure of the studied compound **5e** (Figure 3) revealed the formation of the target organic hybrid, which crystallized with one molecule of methanol as a crystal solvent. It crystallized in monoclinic crystal system and $P2_1/n$ as a space group. The unit cell parameters are $a$ = 11.5475 (3), $b$ = 15.7550 (4) $c$ = 14.6493 (3) Å and $\beta$ = 104.655 (2)°. There is one molecule as asymmetric formula while $z$ = 4. It is evident from the reported X-ray structure the presence of four stereogenic centers located at

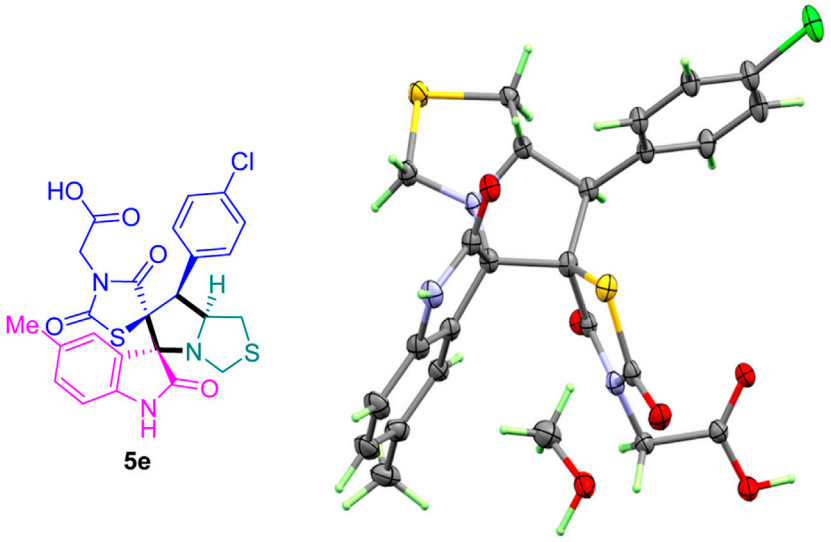


FIGURE 3
ORTEP for compound **5e**.

C9, C12, C13 and C14 atoms. This indicated and assigned the absolute configuration of the final spiroxindoles adduct.

## Cytotoxic activity

The cytotoxicity of the synthesized compounds was tested using the MTT assay on breast cancer cells (MCF-7 and MDA-MB-231). As seen in Table 1, compounds **5l-5o** showed potent cytotoxicity against MCF-7 cells with $IC_{50}$ values range of 3.4–4.5 μM compared to Erlotinib ($IC_{50}$ = 2.14 μM), and they exhibited potent cytotoxicity against MDA-MB-231 with $IC_{50}$ values range of 4.3–8.4 μM compared Erlotinib ($IC_{50}$ = 3.25 μM). Compounds **5a-f** showed promising cytotoxicity against MCF-7 cells with $IC_{50}$ values range of 5.87–18.5 μM, with selective cytotoxicity against MDA-MB-231 cancer cells with higher $IC_{50}$ values. Interestingly, compound **5g** had the highest cytotoxicity among the tested compounds, with $IC_{50}$ value of 2.8 μM. Furthermore, potent compounds **5g**, **5l,** and **5n** were safe (non-cytotoxic) against the WISH cells with higher $IC_{50}$ values with an $IC_{50}$ value range of 39.33–47.2 μM.

## EGFR/CDK-2 inhibition

Inhibitory activities of **5g, 5l,** and **5n** were tested against EGFR and CDK-2. Interestingly, as seen in Table 2, they exhibited potent EGFR inhibition, with $IC_{50}$ values of 0.026, 0.067, and 0.04 μM with percentages of inhibition of 92.6%, 89.8%, 91.2% compared to Erlotinib ($IC_{50}$ = 0.03 μM, 95.4%). Additionally, they exhibited potent CDK-2 inhibition, with $IC_{50}$ values of 0.301, 0.345, and 0.557 μM with percentages of inhibition of 91.9%, 89.4%, 88.7% compared to Roscovitine ($IC_{50}$ = 0.556 μM, 92.1%). These findings highlight the promising EGFR/CDK-2 enzyme inhibition.

## Apoptotic investigation

### Annexin V/PI staining with cell cycle analysis

The apoptotic activity of compounds **5g** was determined by flow cytometric analysis of Annexin V/PI staining of untreated and treated MCF-7 cells. Figure 4A) showed that compounds **5g** significantly activated apoptotic cell death, increasing the cell population in total apoptosis by 31.9% (10.15% late and 21.87% early apoptosis) compared to the untreated control group (1.98%). Additionally, they induced necrotic cell death by 5.43% compared to 2.12% in the untreated control. Hence, compound **5g**-treatment induced apoptosis more than necrotic cell death.

Additionally, As can be shown in Figure 4B), the cell population in the G0-G1-phase was considerably raised by 39.8% after treatment with compound **5g**, compared to the control 31%, whereas the cell population in the S-phase was significantly increased by 45.2% after treatment compared to the control 32.1%, hence, in contrast, cells population at G2/M phase were decreased upon treatment.

### RT-PCR gene expression of apoptosis-related genes

Both the untreated and treated MCF-7 cells were subjected to RT-PCR to confirm apoptotic cell death (Figure 5). The expression of pro-apoptotic genes P53, Bax, caspases 3, 8, and 9 was upregulated by **5g** treatment, with corresponding fold changes of 4.1, 6.26, 9.2, 1.7, and 6.13, respectively. Concurrently, it resulted in a 0.39-fold reduction in the expression of the anti-apoptotic gene Bcl-2. These findings are in line with the possibility of triggering cell death by blocking enzymes. Activation of the intrinsic apoptotic pathway leads to mitochondrial potential loss and cytochrome c release. When the ratio of proteins that promote cell death to those that prevent it rises, a cascade reaction involving caspases 3 and 9 is set in motion, leading to cell death by caspase-dependent apoptosis.

10.3389/fchem.2024.1364378

TABLE 1 Cytotoxicity of the tested compounds against MCF-7 and MDA-MB-231 breast cancer cells using the MTT assay.

| Chemical structures | $IC_{50}$ ± SD [μM] | | |
|---|---|---|---|
| | MCF-7 | MDA-MB-231 | WISH |
| 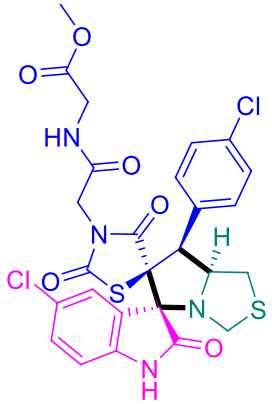 **5a** | 5.87 ± 0.5 | 29.5 ± 1.3 | NT |
| 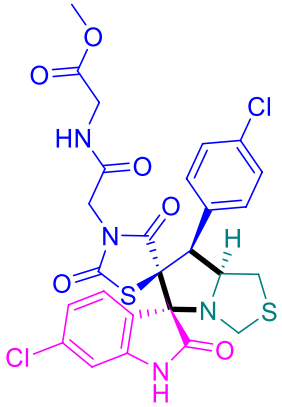 **5b** | 7.8 ± 0.32 | 32.5 ± 0.42 | NT |
| 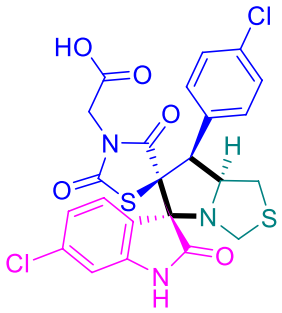 **5c** | 15.8 ± 0.4 | 24.2 ± 1.1 | NT |
| 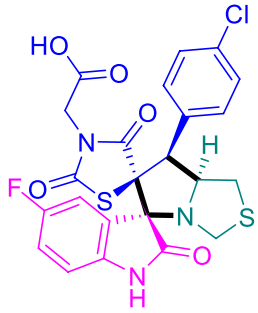 **5d** | 19.4 ± 0.4 | 9.8 ± 0.35 | NT |

(Continued on following page)

10.3389/fchem.2024.1364378

TABLE 1 (*Continued*) Cytotoxicity of the tested compounds against MCF-7 and MDA-MB-231 breast cancer cells using the MTT assay.

| Chemical structures | $IC_{50}$ ± SD [μM] | | |
|---|---|---|---|
| | MCF-7 | MDA-MB-231 | WISH |
| 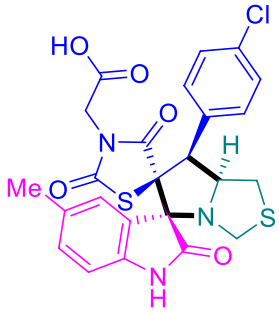 **5e** | 9.8 ± 0.7 | 5.4 ± 0.6 | NT |
| 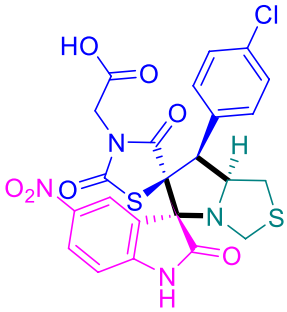 **5f** | 18.5 ± 0.6 | 35.5 ± 1.1 | NT |
| 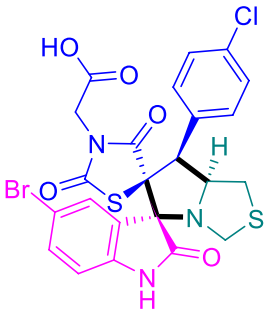 **5g** | 2.8 ± 0.4 | 23.5 ± 0.9 | 39.33 ± 1.8 |
| 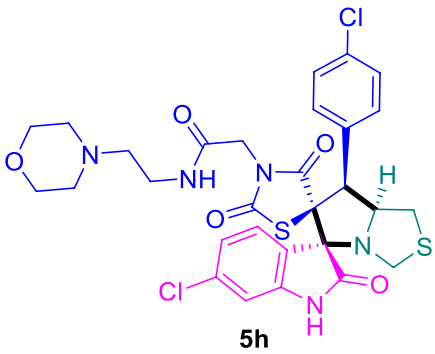 **5h** | 24.3 ± 0.9 | 31.5 ± 1.0 | NT |

(Continued on following page)

TABLE 1 (*Continued*) Cytotoxicity of the tested compounds against MCF-7 and MDA-MB-231 breast cancer cells using the MTT assay.

| Chemical structures | $IC_{50}$ ± SD [μM] | | |
|---|---|---|---|
| | MCF-7 | MDA-MB-231 | WISH |
| 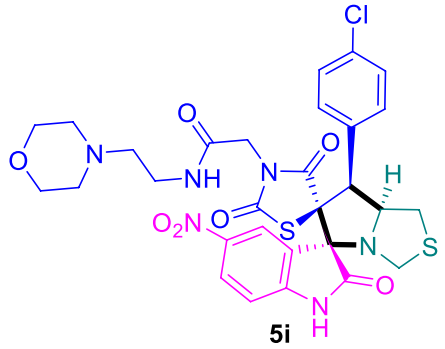 **5i** | 28.7 ± 0.8 | 35.3 ± 1.2 | NT |
| 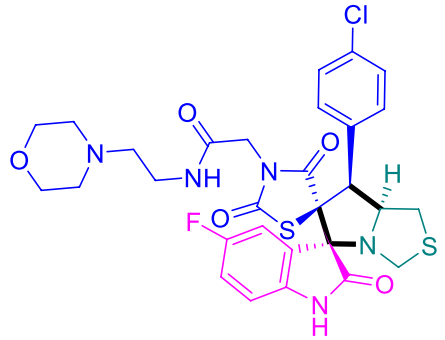 **5j** | 23.4 ± 1.2 | 21.4 ± 0.8 | NT |
| 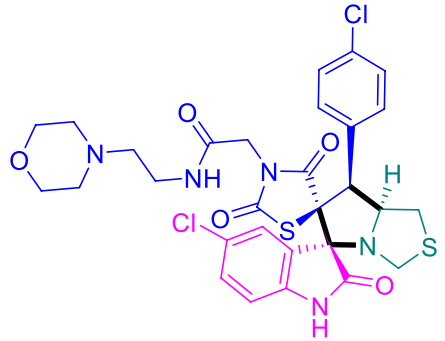 **5k** | 21.4 ± 0.9 | 19.5 ± 0.7 | NT |
| 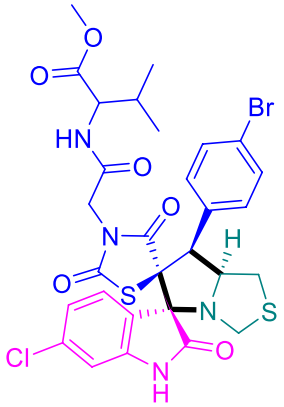 **5l** | 3.4 ± 0.5 | 8.43 ± 0.6 | 43.5 ± 2.0 |

(Continued on following page)

TABLE 1 (*Continued*) Cytotoxicity of the tested compounds against MCF-7 and MDA-MB-231 breast cancer cells using the MTT assay.

| Chemical structures | $IC_{50}$ ± SD [μM] | | |
|---|---|---|---|
| | MCF-7 | MDA-MB-231 | WISH |
| 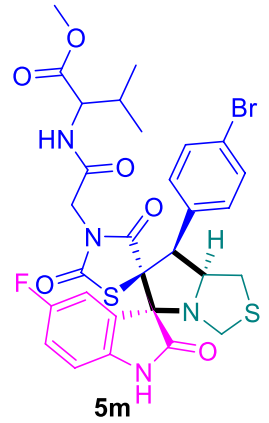 **5m** | 4.5 ± 0.4 | 6.3 ± 0.3 | NT |
| 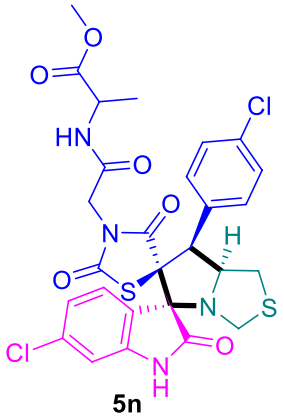 **5n** | 3.9 ± 0.3 | 5.3 ± 0.4 | 47.2 ± 2.1 |
| 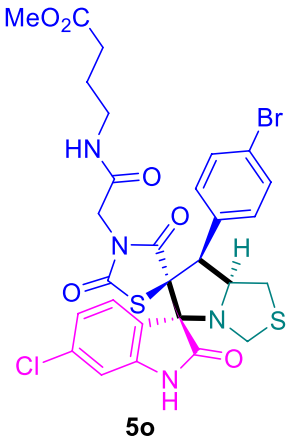 **5o** | 4.12 ± 0.4 | 4.32 ± 0.5 | NT |
| Standard: Erlotinib | 2.14 ± 0.3 | 3.25 ± 0.5 | NT |

*Values are expressed as Mean ± SD, of three independent trials. NT: non tested.

Structure-Activity Relationship (SAR) analysis is pivotal in understanding the correlation between the structural features of the synthesized spirooxindoles and their biological activities. In the case of these compounds inspired by pyrrolidinyl-spirooxindole natural products, SAR exploration involves assessing how variations in the molecular structure impact cytotoxicity against specific cancer cell lines, inhibitory activities against enzymes like EGFR and CDK-2, and safety profiles. The goal is to identify key structural elements that contribute to therapeutic efficacy, guiding further optimization for the development of more effective compounds. The results indicate that among the synthesized library of inspired spiroxindoles, compound **5g** stands out as the most active. Notably, it features a *p*-Cl-substituted benzene, 5-Cl-substituted oxindole, and *N*-substituted acid in its chemical structure (Figure 6).

### Molecular docking study

Using the MOE docking suite, the most active compound of the series and the reference anti-cancer drugs roscovitine and erlotinib were docked into the active sites of the target proteins CDK2 (PDB ID 6Q4G) (Wood et al., 2019) and EGFR (PDB ID 1M17) (Stamos et al., 2002), respectively, to explore the anti-cancer potential of spirooxindole engrafted rhodanine derivatives. The binding modes of the most active compounds, **5g**, **5l**, and **5n**, were established using MOE with binding energies ranging from −5.3 to −7.6 kcal mol-1. Figure 7A depicts the binding pose of compound **5g**, where the oxygen of the dioxothiazolidin ring is involved in a hydrogen bond interaction with the nitrogen of the side chain of Lys9 at a distance of 3.2Å. The protein-ligand interactions are further stabilized by hydrophobic interactions between the ligand and Ile10, Lys88, and Val163 of the CDK2 protein. In the case of compound **5l**, a strong hydrogen bond interaction is observed between the oxygen of the dioxothiazolidin ring and the side chain of Glu12 at a distance of 2.1Å (Figure 7B). Meanwhile, in the case of compound **5n**, which is the most active compound of the series, two hydrogen bond interactions are exhibited with the main chain of Glu12 at distances of 1.9 and 3.4Å (Figure 7C). Another hydrogen bond is observed between the oxygen of the dioxothiazolidin ring and the side chain of Lys89 at a distance of 3.4Å. Apart from the H-bond interactions, an oxygen atom of compounds **5l** and **5n** participates in a salt bridge interaction with the positively charged Lys33 residue. These compounds also exhibit hydrophobic interactions with Val18, Gln131, and Val163.

In EGFR docking, the conformation exhibiting the most favorable binding energy (approximately −7.4 to −8.3 kcal mol-1) substantiates the notion that the compounds are effectively incorporated within the binding pocket. The binding patterns are also slightly different, which may be responsible for the variations in activity. It is important to mention that the reference inhibitor forms a hydrogen bond with the backbone NH of Met769 in the Hinge region, while the compound is deeply embedded into the EGFR active site *via* hydrophobic interactions that are conserved in the majority of the structures. In the case of compound **5g**, in addition to hydrophobic interactions, a salt bridge interaction is also observed with Lys721 (Figure 8A). The plausible binding mode of compound **5l** is depicted in Figure 8B. The nitrogen of the thiazole and indolin ring is involved in a hydrogen bond interaction with the oxygen of Leu694 and Arg817 at distances of 3.3 and 3.5 Å, respectively. Another hydrogen bond interaction is observed between the oxygen of the dioxothiazolidin ring and the side chain of Gly772 at a distance of 3.3 Å. Figure 8C presents the binding mode of compound **5n**. This compound also exhibits three hydrogen bond interactions with Leu694, Gly772, and Arg817 at distances of 3.4, 3.3, and 2.5 Å, respectively. Further, anchorage is provided by hydrophobic interactions with Leu694, Val702, Leu768, and Leu820.

A 100 ns simulation using AMBER22 was conducted to understand the dynamic behavior of the active chemical. An evaluation of the system's overall stability and simulation quality was conducted using the RMSD, RMSF, and RG (radius of gyration) as metrics for quantitative analysis (RoG).

The RMSD of the heavy atoms in the main chain of the proteins was computed using the "rms" tool in CPPTRAJ. Figures 9, 10; Supplementary Figure S10 illustrate the RMSD of the heavy atoms in the protein backbone. Figures 7, 8 clearly demonstrate the system's stability, as indicated by an average RMSD value of 2.7 Å in the case of CDK2. In the case of EGFR, higher RMSD is observed due to flexibility in its domain. This observation was further corroborated by examining the RoG, indicating that the systems were tightly compressed (Figures 7, 8). In addition, to comprehend the behavior of the side chains of residues, the RMSF of the protein was computed over time (Figures 9, 10). The results indicated that the amino acid residues in the protein-ligand complex remained stable upon interaction with the active chemical of the series.

Regarding EGFR, a visual examination of the paths shows that **5n** engages in hydrophobic interactions with Leu694, Val702, Leu768, and Leu820. Compound **5n** demonstrates a significant affinity for the "hinge region key residue," Met769, of the EGFR target. This residue is essential for the active site and is occupied 68% of the time. Throughout the simulation, the majority of the protein-ligand interactions were observed to align with the docking position.

## Materials and methods

### General notes

> "Isatin derivatives **2a-e** and thioproline **1** are commercially available. $^{1}$H-NMR and $^{13}$C-NMR are recorded in DMSO-$d_6$ (JEOL Spectrometer (400 MHz). The X-ray diffraction data was collected on a Rigaku Oxford Diffraction Supernova diffractometer using Cu Kα radiation. The desired starting material **4a-f** was synthesized according to reported literature Abd Alhameed et al., 2020). The desired sprio-compounds derived rhodanine amino-acids **5h-k** was synthesized according to previous reported literature (Barakat et al., 2021)".

### General procedure for the synthesis of spiro compounds analogues 5a-o

A mixture of three components reaction including substituted isatin **2a-e** (0.5 mmol), L-thioproline **1** (66.5 mg, 0.5 mmol), and compounds **4a-f** (0.5 mmol) were refluxed on oil bath for 2 h. After completion of the reaction, as evident from (TLC Eluent: Ethyl acetate: *n*-Hexane 40%), Without additional purification, the reaction mixture was left at room temperature overnight to slowly evaporate. The solid crystalline components were filtered out to give compounds **5a-o**, which were solid compounds with a light faint yellow color and an 80%–90% chemical yield.

### Methyl (2-((3*S*,6′*S*,7′*S*,7a′*S*)-5-chloro-7′-(4-chlorophenyl)-2,2″,4″-trioxo-7′,7a′-dihydro-1′*H*,3′*H*-dispiro [indoline-3,5′-pyrrolo [1,2-c]thiazole-6′,5″-thiazolidin]-3″-yl)acetyl)glycinate 5a

The 5-chloro-isatin **2a** (90.5 mg) and **4a** (192.0 mg) were utilized according to the general method, and the sprio-compound **5a** was obtained in 90% yield.

$^{1}$H NMR (400 MHz, DMSO-$d_6$) δ 11.17 (s, 1H), 8.65 (t, $J$ = 5.8 Hz, 1H), 7.69 (d, $J$ = 8.7 Hz, 1H), 7.63 (d, $J$ = 8.7 Hz, 1H), 7.52–7.36 (m, 4H), 7.20 (d, $J$ = 2.5 Hz, 1H), 6.90 (d, $J$ = 8.2 Hz, 1H), 4.81 (q, $J$ = 7.8 Hz, 1H), 4.35 (s, 1H), 4.19–4.06 (m, 2H), 4.00 (d, $J$ = 16.2 Hz, 1H), 3.91 (dd, $J$ = 6.1, 3.0 Hz, 3H), 3.78 (d, $J$ = 6.0 Hz, 1H), 3.45 (d, $J$ = 5.9 Hz, 1H), 2.99 (dd, $J$ = 9.5, 5.7 Hz, 1H), 2.82–2.71 (m, 1H).$^{13}$C-NMR (100 Hz, DMSO-$d_6$): δ 176.1, 174.5, 168.6, 164.7, 158.2, 154.2, 151.1, 145.4, 135.9, 135.6, 133.4, 132.3, 131.5, 129.1, 121.6, 110.8, 76.2, 75.5, 70.1, 66.7, 57.7, 55.9, 53.8, 47.1, 43.9, 36.7, 33.3; Chemical Formula: $C_{26}H_{22}Cl_2N_4O_6S_2$; LCMS ($m/z$): 622.54 [M + H]$^+$, Elemental Analysis: [Calculated: C, 50.25; H, 3.57; N, 9.01; S, 10.32; Found: C, 50.30; H, 3.60; N, 9.11; S, 10.40].

## Methyl (2-((3*S*,6′*S*,7′*S*,7a′*S*)-6-chloro-7′-(4-chlorophenyl)-2,2″,4″-trioxo-7′,7a′-dihydro-1′*H*,3′*H*-dispiro [indoline-3,5′-pyrrolo [1,2-*c*]thiazole-6′,5″-thiazolidin]-3″-yl)acetyl)glycinate 5b

The 6-chloro-isatin **2b** (90.5 mg) and **4a** (192.0 mg) were utilized according to the general method, and the spiro compound **5b** was obtained in 91% yield.

$^{1}$H NMR (400 MHz, DMSO-$d_6$) δ 11.18 (s, 1H), 8.61 (t, $J$ = 5.8 Hz, 1H), 7.51–7.37 (m, 5H), 7.25 (d, $J$ = 8.1 Hz, 1H), 7.05 (dd, $J$ = 8.3, 2.2 Hz, 1H), 6.90 (d, $J$ = 2.1 Hz, 1H), 4.88–4.76 (m, 1H), 4.35 (s, 1H), 4.17 (d, $J$ = 9.4 Hz, 1H), 4.04 (d, $J$ = 6.7 Hz, 2H), 3.89 (d, $J$ = 6.0 Hz, 2H), 3.82 (d, $J$ = 6.4 Hz, 1H), 3.45 (d, $J$ = 6.0 Hz, 1H), 3.01 (dd, $J$ = 9.6, 5.7 Hz, 1H);$^{13}$C NMR (101 MHz, DMSO-$d_6$) δ 207.15, 178.72, 176.21, 174.69, 170.53, 169.03, 168.67, 164.42, 146.26, 145.35, 138.13, 135.92, 133.48, 132.21, 130.31, 129.29, 121.47, 105.91, 104.02, 95.33, 94.30, 76.20, 75.51, 74.09, 60.51, 40.68, 40.47, 40.26, 40.15, 40.05, 39.84, 39.63, 39.43, 31.34; Chemical Formula: $C_{26}H_{22}Cl_2N_4O_6S_2$; LCMS ($m/z$): 622.54 [M + H]$^+$, Elemental Analysis: [Calculated: C, 50.25; H, 3.57; N, 9.01; S, 10.32; Found: C, 50.31; H, 3.60; N, 9.12; S, 10.39].

## 2-((3*S*,6′*S*,7′*S*,7a′*S*)-6-chloro-7′-(4-chlorophenyl)-2,2″,4″-trioxo-7′,7a′-dihydro-1′H,3′H-dispiro [indoline-3,5′-pyrrolo [1,2-*c*]thiazole-6′,5″-thiazolidin]-3″-yl)acetic acid 5c

The 6-chloro-isatin **2b** (90.5 mg) and **4b** (156.0 mg) were utilized according to the general method, and the spiro-compound **5c** was obtained in 89% yield.

$^{1}$H NMR (400 MHz, DMSO-$d_6$) δ 11.19 (s, 1H), 7.50–7.36 (m, 5H), 7.29 (d, $J$ = 8.5 Hz, 1H), 7.06 (d, $J$ = 8.6 Hz, 1H), 6.90 (s, 1H), 4.88–4.77 (m, 1H), 4.22–4.11 (m, 2H), 4.05 (d, $J$ = 17.4 Hz, 1H), 3.84 (d, $J$ = 6.3 Hz, 1H), 3.47 (d, $J$ = 6.0 Hz, 1H), 3.00 (d, $J$ = 5.7 Hz, 1H), 2.78 (dd, $J$ = 9.9, 7.3 Hz, 1H); $^{13}$C NMR (101 MHz, DMSO-$d_6$) δ 176.18, 174.57, 174.10, 174.06, 168.68, 167.87, 153.13, 152.58, 145.27, 137.10, 135.98, 135.43, 134.50, 133.47, 132.44, 125.81, 124.78, 121.44, 118.15, 111.68, 107.49, 106.78, 86.80, 79.46, 76.26, 75.62; Chemical Formula: $C_{23}H_{17}Cl_2N_3O_5S_2$; LCMS ($m/z$): 551.40 [M + H]$^+$, Elemental Analysis: [Calculated: C, 50.19; H, 3.11; N, 7.63; S, 11.65; Found: C, 50.18; H, 3.09; N, 7.659; S, 11.60].

## 2-((3*S*,6′*S*,7′*S*,7a′*S*)-7′-(4-Chlorophenyl)-5-fluoro-2,2″,4″-trioxo-7′,7a′-dihydro-1′*H*,3′*H*-dispiro [indoline-3,5′-pyrrolo [1,2-*c*] thiazole-6′,5″-thiazolidin]-3″-yl)acetic acid 5d

The 5-fluoro-isatin **2c** (82.5 mg) and **4b** (156.0 mg) were utilized according to the general method, and the spiro-compound **5d** was obtained in 85% yield.

$^{1}$H NMR (400 MHz, DMSO-$d_6$) δ 11.06 (s, 1H), 7.50–7.37 (m, 5H), 7.17 (td, $J$ = 8.9, 2.7 Hz, 1H), 7.07 (dd, $J$ = 9.1, 2.7 Hz, 1H), 6.88 (dd, $J$ = 8.5, 4.6 Hz, 1H), 4.89–4.78 (m, 1H), 4.23–4.13 (m, 2H), 4.05 (d, $J$ = 17.4 Hz, 1H), 3.82 (d, $J$ = 6.0 Hz, 1H), 3.47 (d, $J$ = 6.1 Hz, 1H), 3.00 (dd, $J$ = 9.6, 5.8 Hz, 1H);$^{13}$C NMR (101 MHz, DMSO-$d_6$) δ 176.22, 174.50, 168.78, 167.82, 164.98, 160.63, 157.47, 139.96, 137.26, 136.95, 135.39, 134.18, 133.47, 132.30, 129.84, 129.38, 124.15, 121.31, 116.73, 112.07, 110.97, 84.14, 79.14, 76.48, 75.81, 66.90, 56.67, 47.04, 42.99, 40.79, 40.68, 40.59, 40.47, 40.37, 40.26, 40.16, 40.05, 39.84, 39.63, 39.52, 39.43, 32.17, 31.31, 31.21; Chemical Formula: $C_{23}H_{17}ClFN_3O_5S_2$; LCMS ($m/z$): 534.94 [M + H]$^+$, Elemental Analysis: [Calculated: C, 51.74; H, 3.21; N, 7.87; S, 12.01; Found: C, 51.76; H, 3.23; N, 7.92; S, 12.00].

## 2-((3*S*,6′*S*,7′*S*,7a′*S*)-7′-(4-Chlorophenyl)-5-methyl-2,2″,4″-trioxo-7′,7a′-dihydro-1′*H*,3′*H*-dispiro [indoline-3,5′-pyrrolo [1,2-*c*] thiazole-6′,5″-thiazolidin]-3″-yl)acetic acid 5e

The 5-methyl-isatin **2d** (80.5 mg) and **4b** (156.0 mg) were utilized according to the general method, and the spiro-compound **5e** was obtained in 87% yield.

$^{1}$H NMR (400 MHz, DMSO-$d_6$) δ 10.93 (s, 1H), 7.50–7.38 (m, 5H), 7.16–7.04 (m, 2H), 6.76 (d, $J$ = 8.0 Hz, 1H), 4.91–4.80 (m, 1H), 4.22–4.09 (m, 2H), 4.02 (d, $J$ = 17.5 Hz, 1H), 3.85 (d, $J$ = 5.9 Hz, 1H), 3.45 (d, $J$ = 5.9 Hz, 1H), 3.01 (dd, $J$ = 9.6, 5.7 Hz, 1H), 2.77 (d, $J$ = 7.3 Hz, 0H); $^{13}$C NMR (101 MHz, DMSO-$d_6$) δ 176.16, 174.99, 168.90, 167.84, 165.29, 141.27, 139.39, 135.86, 133.39, 132.20, 129.29, 127.99, 127.39, 126.84, 122.57, 112.70, 110.78, 95.65, 92.01, 89.01, 76.36, 75.94, 70.22, 70.09, 56.40, 47.04, 41.87, 40.68, 40.56, 40.47, 40.36, 40.26, 40.15, 40.05, 39.84, 39.63, 39.42, 32.28, 30.03, 18.89; Chemical Formula: $C_{24}H_{20}ClN_3O_5S_2$; LCMS ($m/z$): 531.01 [M + H]$^+$, Elemental Analysis: [Calculated: C, 54.39; H, 3.80; N, 7.93; S, 12.10; Found: C, 54.39; H, 3.80; N, 7.93; S, 12.10].

## 2-((3*S*,6′*S*,7′*S*,7a′*S*)-7′-(4-Chlorophenyl)-5-nitro-2,2″,4″-trioxo-7′,7a′-dihydro-1′*H*,3′*H*-dispiro [indoline-3,5′-pyrrolo [1,2-*c*] thiazole-6′,5″-thiazolidin]-3″-yl)acetic acid 5f

The 5-nitro-isatin **2e** (96.0 mg) and **4b** (156.0 mg) were utilized according to the general method, and the Spiro-compound **5f** was obtained in 82% yield.

$^{1}$H NMR (400 MHz, DMSO-$d_6$) δ 13.24 (s, 1H), 11.71 (s, 1H), 8.27 (dd, $J$ = 8.8, 2.6 Hz, 1H), 8.13 (d, $J$ = 2.7 Hz, 1H), 7.51–7.39 (m, 5H), 7.08 (d, $J$ = 8.4 Hz, 1H), 4.85–4.74 (m, 1H), 4.25–4.13 (m, 2H), 4.01 (d, $J$ = 17.5 Hz, 1H), 3.85 (d, $J$ = 6.1 Hz, 1H), 3.49 (d, $J$ = 6.0 Hz, 1H), 3.02 (dd, $J$ = 9.6, 5.7 Hz, 1H); $^{13}$C NMR (101 MHz, DMSO-$d_6$) δ

TABLE 2 $IC_{50}$ values of EGFR and CDK-2 kinase activities of the tested compounds.

| Compound | EGFR kinase | | CDK-2 kinase | |
|---|---|---|---|---|
| | $IC_{50}$ [μM][a] | % Of EGFR inhibition | $IC_{50}$ [μM][a] | % Of CDK-2 inhibition |
| 5 g | 0.026 ± 0.006 | 92.6 ± 1.9 | 0.301 ± 0.011 | 91.9 ± 2.1 |
| 5l | 0.067 ± 0.001 | 89.8 ± 2.8 | 0.345 ± 0.011 | 89.4 ± 2.8 |
| 5n | 0.04 ± 0.001 | 91.2 ± 2.1 | 0.557 ± 0.017 | 88.7 ± 1,9 |
| Erlotinib | 0.03 ± 0.002 | 95.4 ± 2.7 | -- | -- |
| Roscovitine | -- | -- | 0.556 ± 0.001 | 92.1 ± 2.7 |

[a]Values are expressed as an average of three independent replicates. $IC_{50}$ values were calculated using sigmoidal non-linear regression curve fit of percentage inhibition against five concentrations of each compound.

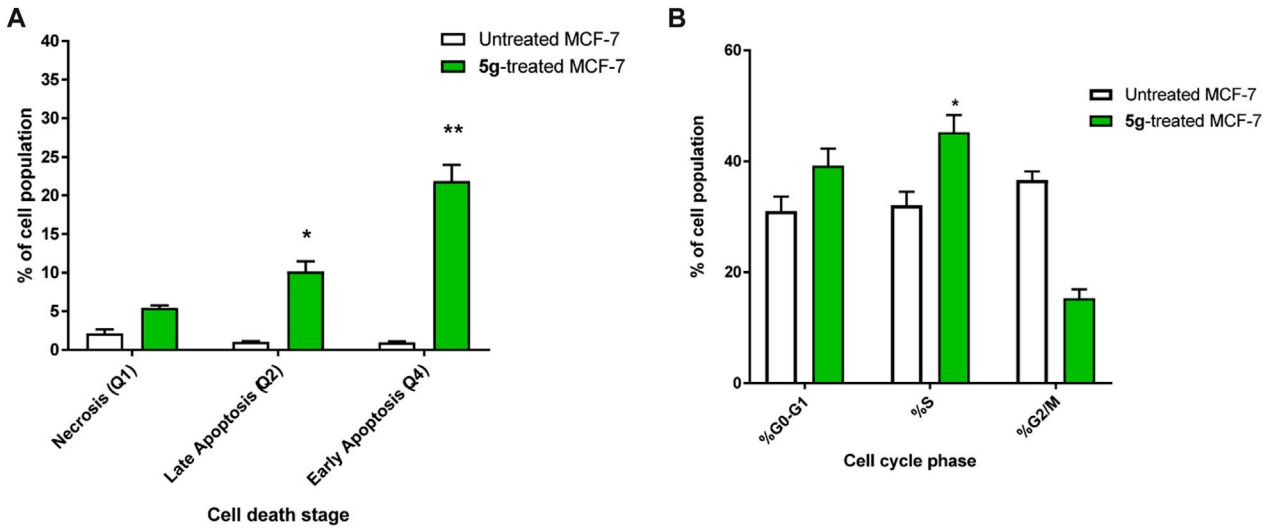


FIGURE 4
**(A)** Bar representation of the percentage of apoptosis (early and late apoptotic cell population) using Annexin V/Propidium Iodide staining. **(B)** Bar representation of the percentage of percentage of cell population at each cell phase in untreated and **5g**-treated MCF-7 cells, at the $IC_{50}$ value at 48 h "Data shown are the average of three independent experimental runs (Mean ± SD). *$p \leq 0.05$ and **$p < 0.001$ compared to untreated control".

176.75, 174.20, 168.40, 167.73, 159.45, 149.95, 143.45, 135.24, 133.56, 132.43, 130.71, 129.02, 128.48, 124.17, 124.06, 123.25, 115.86, 113.97, 111.40, 111.26, 76.46, 75.17, 70.37, 56.26, 46.89, 40.71, 40.50, 40.29, 40.08, 39.87, 39.66, 39.46, 32.22; Chemical Formula: $C_{23}H_{17}ClN_4O_7S_2$; LCMS (*m*/*z*): 561.93 $[M + H]^+$, Elemental Analysis: [Calculated: C, 49.24; H, 3.05; N, 9.99; S, 11.43; Found: C, 49.26; H, 3.10; N, 10.9; S, 11.45].

## 2-((3*S*,6′*S*,7′S,7a′*S*)-5-bromo-7′-(4-chlorophenyl)-2,2″,4″-trioxo-7′,7a′-dihydro-1′*H*,3′*H*-dispiro [indoline-3,5′-pyrrolo [1,2-*c*]thiazole-6′,5″-thiazolidin]-3″-yl)acetic acid 5g

The 5-bromo-isatin **2f** (96.0 mg) and **4b** (156.0 mg) were utilized according to the general method, and the final compound **5g** was obtained in 86% yield.

$^1$H NMR (400 MHz, DMSO-$d_6$) δ 13.34 (s, 1H), 11.17 (s, 1H), 7.54–7.35 (m, 7H), 6.84 (d, *J* = 8.6 Hz, 1H), 4.80 (q, *J* = 7.7 Hz, 1H), 4.26–4.14 (m, 2H), 3.97 (d, *J* = 17.0 Hz, 1H), 3.77 (d, *J* = 6.0 Hz, 1H), 3.47 (d, *J* = 6.3 Hz, 1H), 2.99 (dd, *J* = 9.9, 5.5 Hz, 1H);$^{13}$C NMR (101 MHz, DMSO-$d_6$) δ 175.80, 174.40, 168.58, 167.67, 143.04, 135.36, 134.42, 134.01, 133.50, 132.30, 130.58, 130.39, 129.21, 124.90, 114.83, 113.06, 110.51, 76.67, 75.52, 68.59, 56.28, 56.20, 49.23, 46.98, 44.35, 40.71, 40.50, 40.29, 40.09, 39.88, 39.67, 39.54, 39.46, 32.86; Chemical Formula: $C_{23}H_{17}BrClN_3O_5S_2$; LCMS (*m*/*z*): 595.97 $[M + H]^+$, Elemental Analysis: [Calculated: C, 49.24; H, 3.05; N, 9.99; S, 11.43; Found: C, 46.50; H, 3.00; N, 7.12; S, 10.83].

## Methyl (2-((3*S*,6′*S*,7′*S*,7a′*S*)-7′-(4-bromophenyl)-6-chloro-2,2″,4″-trioxo-7′,7a′-dihydro-1′*H*,3′*H*-dispiro [indoline-3,5′-pyrrolo [1,2-*c*]thiazole-6′,5″-thiazolidin]-3″-yl)acetyl)valinate 5l

The 6-chloro-isatin **2b** (90.5 mg) and **4c** (235.0 mg) were utilized according to the general method, and the spiro-compound **5l** was obtained in 80% yield.

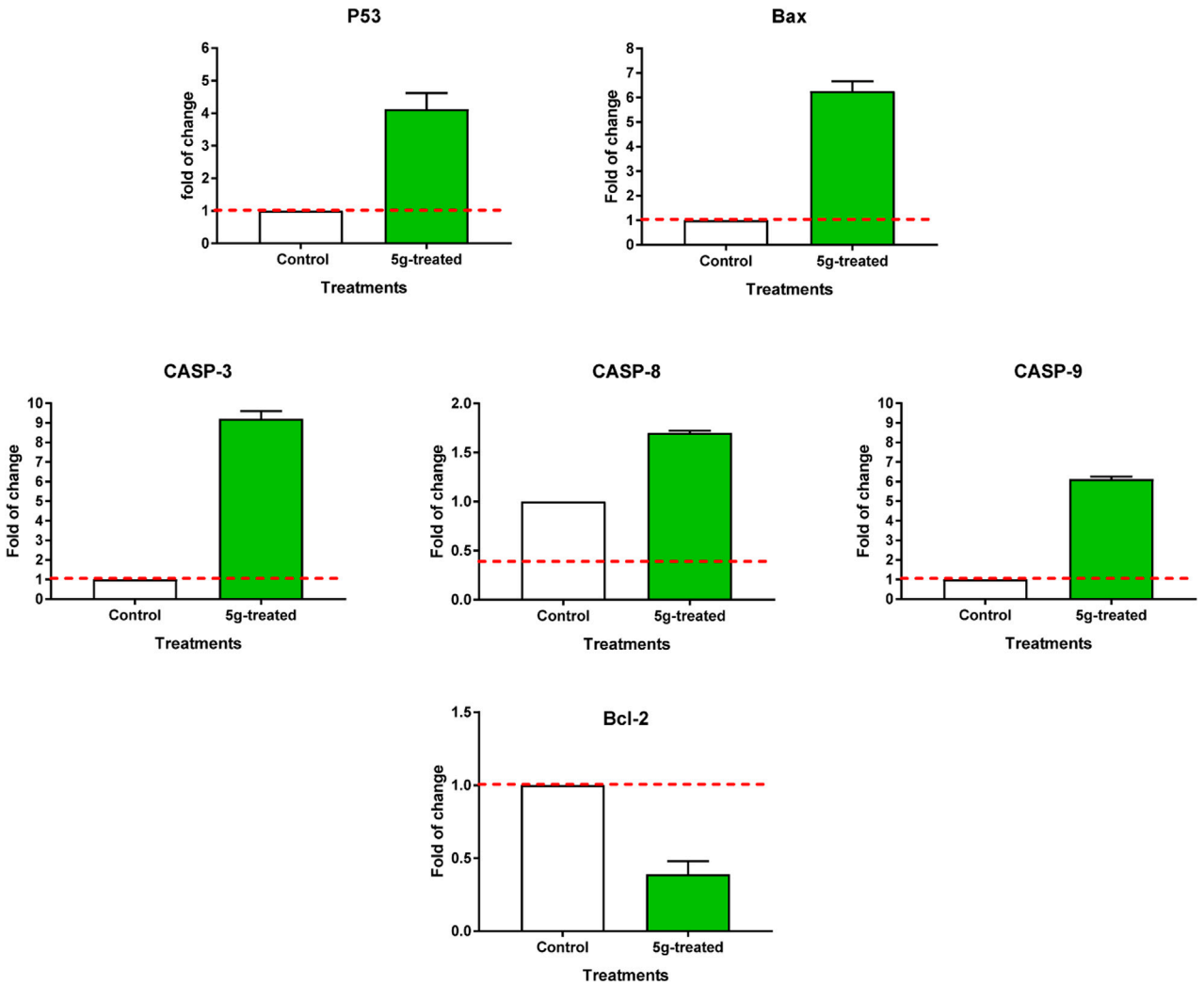


FIGURE 5
RT-PCR of apoptosis-related genes of untreated and **5g**-treated MCF-7 cells at the $IC_{50}$ value. "Values are expressed as Mean ± SD of three independent replicates". "Data were normalized using β-actin as house-keeping gene. The dashed line represents the gene expression level of untreated control. Fold change was calculated using $2^{-\Delta\Delta CT}$".

$^{1}$H NMR (400 MHz, DMSO-$d_6$) δ 11.18 (d, $J$ = 3.9 Hz, 1H), 8.51 (dd, $J$ = 8.8, 5.3 Hz, 1H), 7.71–7.58 (m, 1H), 7.50–7.36 (m, 4H), 7.26 (dd, $J$ = 8.4, 4.0 Hz, 1H), 7.04 (dd, $J$ = 8.1, 2.2 Hz, 1H), 6.91 (s, 1H), 4.82 (dt, $J$ = 13.1, 5.2 Hz, 1H), 4.18 (td, $J$ = 9.3, 4.2 Hz, 2H), 4.07 (d, $J$ = 6.1 Hz, 1H), 4.05 (s, 0H), 3.82 (dd, $J$ = 6.0, 2.2 Hz, 1H), 3.69–3.61 (m, 3H), 3.46 (dd, $J$ = 6.1, 3.2 Hz, 1H), 3.01 (dd, $J$ = 9.6, 5.8 Hz, 1H), 2.84–2.73 (m, 1H), 2.16–2.09 (m, 1H), 0.86 (ddd, $J$ = 18.5, 6.9, 4.2 Hz, 7H); $^{13}$C NMR (101 MHz, DMSO-$d_6$) δ 207.05, 176.20, 174.73, 174.60, 172.19, 168.65, 166.00, 165.16, 165.07, 145.35, 135.99, 135.61, 133.42, 132.25, 129.28, 121.57, 106.62, 106.31, 76.29, 76.20, 75.59, 75.52, 57.92, 55.53, 52.37, 47.06, 43.66, 40.67, 40.58, 40.46, 40.37, 40.25, 40.16, 40.04, 39.95, 39.83, 39.63, 39.42, 32.27, 31.37, 31.26, 31.15, 31.04, 30.81, 19.40, 18.46; Chemical Formula: $C_{29}H_{28}BrClN_4O_6S_2$; LCMS ($m/z$): 709.01 $[M + H]^+$, Elemental Analysis: [Calculated: C, 49.19; H, 3.99; N, 7.91; 56; S, 9.06; Found: C, 49.16; H, 4.01; N, 7.99; 56; S, 9.02].

## Methyl (2-((3*S*,6′*S*,7′*S*,7a′*S*)-7′-(4-bromophenyl)-5-fluoro-2,2″,4″-trioxo-7′,7a′-dihydro-1′*H*,3′*H*-dispiro [indoline-3,5′-pyrrolo [1,2-*c*]thiazole-6′,5″-thiazolidin]-3″-yl)acetyl)valinate 5m

The 5-Fluoro-isatin **2c** (82.5 mg) and **4c** (235.0 mg) were utilized according to the general method, and the spiro-compound **5m** was obtained in 82% yield.

$^{1}$H NMR (400 MHz, DMSO-$d_6$) δ 11.06 (s, 1H), 8.53 (t, $J$ = 9.0 Hz, 1H), 7.72–7.58 (m, 1H), 7.51–7.37 (m, 4H), 7.19 (td, $J$ = 8.9, 2.7 Hz, 1H), 7.02 (dt, $J$ = 8.8, 3.0 Hz, 1H), 6.89 (dd, $J$ = 8.7, 4.5 Hz, 1H), 4.83 (d, $J$ = 7.6 Hz, 1H), 4.24–4.05 (m, 4H), 3.81 (d, $J$ = 6.0 Hz, 1H), 3.65 (d, $J$ = 10.5 Hz, 3H), 3.46 (s, 1H), 2.99 (dd, $J$ = 9.6, 5.7 Hz, 1H), 2.15–2.07 (m, 2H), 0.92–0.80 (m, 7H);$^{13}$C NMR (101 MHz, DMSO-$d_6$) δ 207.11, 192.69, 176.19, 174.76, 172.15, 170.54, 168.73, 165.73, 165.14, 140.04,

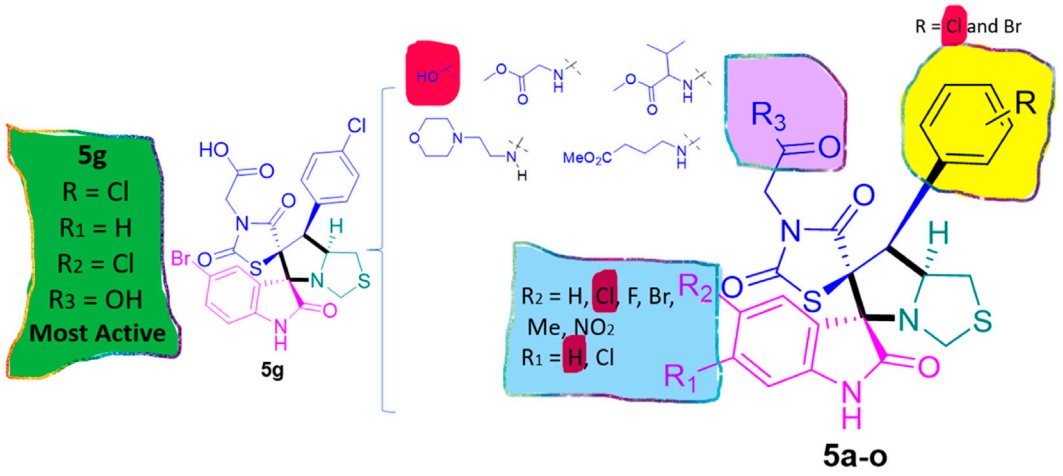


FIGURE 6
Structure reactivity relationship (SAR) of the synthesized compounds.

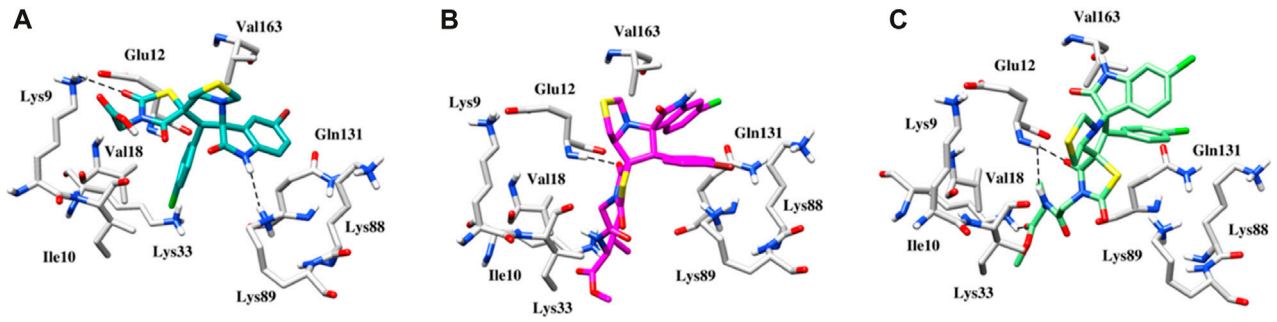


FIGURE 7
**(A)** Binding pose of the **5g** within the active site of CDK2 protein. **(B)** Binding pose of the **5l** within the active site of CDK2 protein. **(C)** Binding pose of the **5n** within the active site of CDK2 protein. Interactions between hydrogen bonds are shown by the dashed black lines.

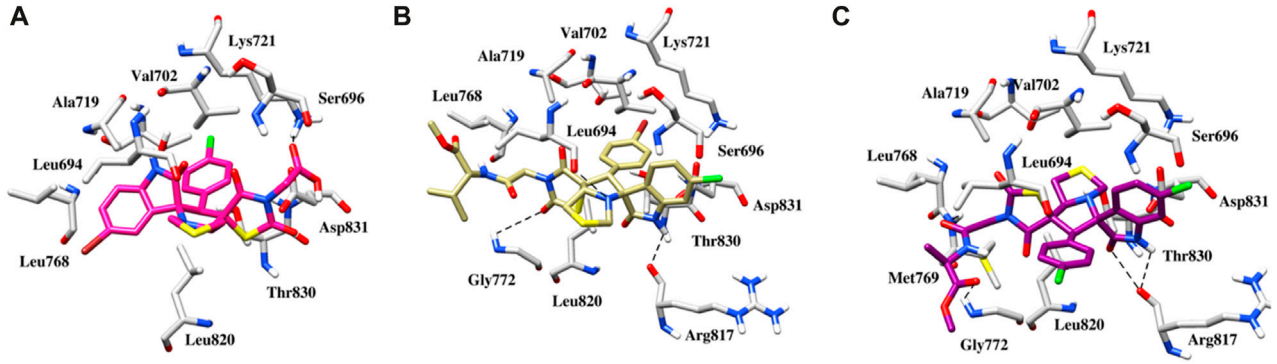


FIGURE 8
**(A)** Binding pose of the **5g** within the active site of EGFR protein. **(B)** Binding pose of the **5l** within the active site of EGFR protein. **(C)** Binding pose of the **5n** within the active site of EGFR protein. The dashed black line depicts hydrogen bond interaction.

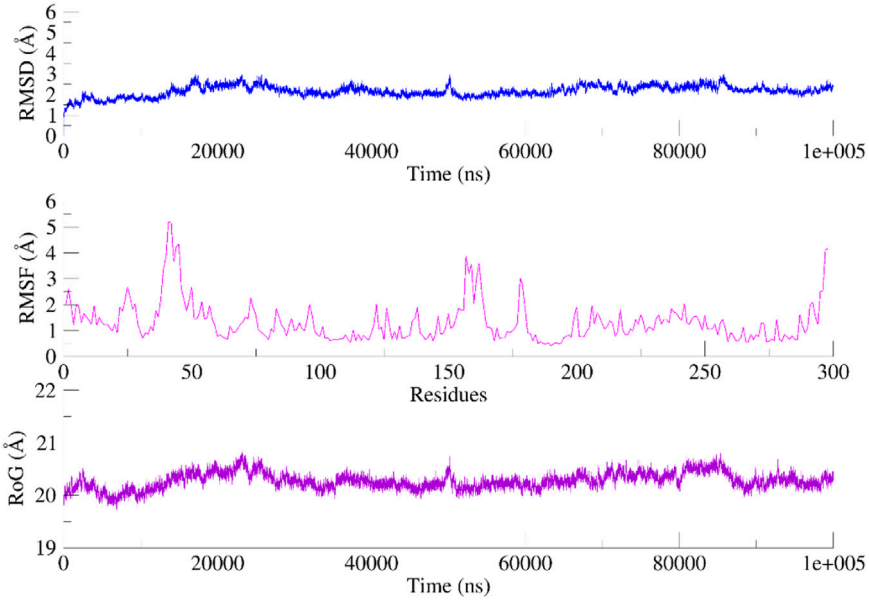


FIGURE 9
RMSD, RMSF and RoG of the CDK2 systems calculated as a function of time.

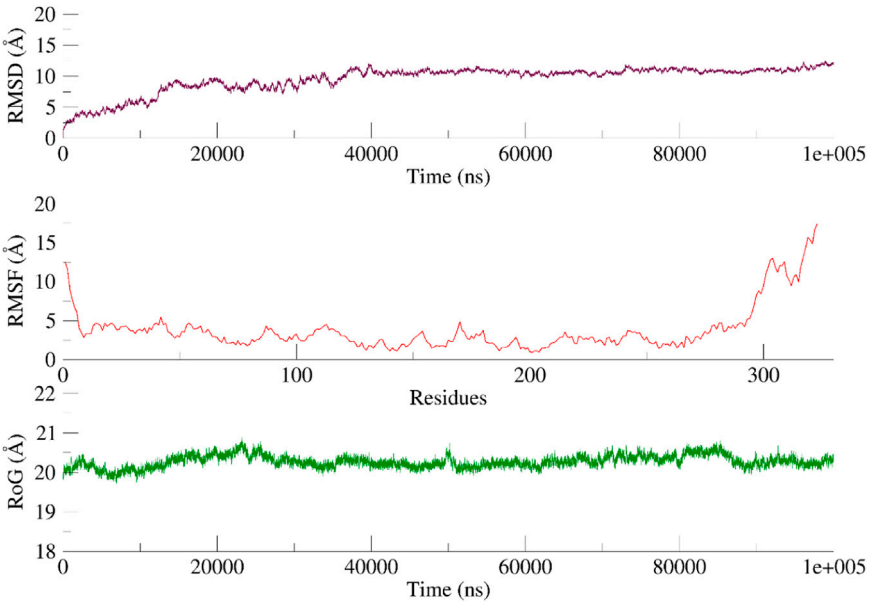


FIGURE 10
RMSD, RMSF and RoG of the EGFR systems calculated as a function of time Based on the visual examination of simulation trajectories, it can be inferred that compound **5n** achieves stability within the cavity of CDK2 and EGFR by effectively facilitating hydrophobic and hydrophilic contacts with the active site residue. The examination of time-varying paths of **5n** reveals intriguing findings. The polar atoms of the dioxothiazolidin moiety maintain contact with the protein through polar interactions with Glu12 and Lys89, with occupancies of 65% and 55%, respectively.

135.57, 133.42, 131.58, 129.60, 125.81, 123.36, 92.33, 79.20, 76.28, 75.75, 59.09, 58.38, 55.59, 52.35, 52.30, 46.85, 40.80, 40.68, 40.59, 40.48, 40.38, 40.27, 40.17, 40.06, 39.85, 39.72, 39.64, 39.43, 31.40, 31.30, 31.20, 31.10; Chemical Formula: $C_{29}H_{28}BrFN_4O_6S_2$; LCMS (*m/z*): 692.59 $[M + H]^+$, Elemental Analysis: [Calculated: C, 50.37; H, 4.08; N, 8.10; S, 9.27; Found: C, 50.36; H, 4.09; N, 8.07; S, 9.29].

### Methyl (2-((3*S*,6′*S*,7′*S*,7a′*S*)-6-chloro-7′-(4-chlorophenyl)-2,2″,4″-trioxo-7′,7a′-dihydro-1′H,3′H-dispiro [indoline-3,5′-pyrrolo [1,2-*c*]thiazole-6′,5″-thiazolidin]-3″-yl)acetyl)alaninate 5n

The 6-chloro-isatin **2b** (90.5 mg) and **4d** (221.5 mg) were utilized according to the general method, and the spiro-compound **5n** was obtained in 84% yield.

$^{1}$H NMR (400 MHz, DMSO-$d_6$) δ 11.18 (d, $J$ = 5.0 Hz, 1H), 8.63 (t, $J$ = 6.8 Hz, 1H), 7.72–7.59 (m, 1H), 7.47 (d, $J$ = 8.1 Hz, 2H), 7.41 (d, $J$ = 8.2 Hz, 2H), 7.25 (t, $J$ = 8.9 Hz, 1H), 7.05 (t, $J$ = 9.4 Hz, 1H), 6.90 (s, 1H), 4.82 (q, $J$ = 7.9, 7.4 Hz, 1H), 4.35–4.23 (m, 1H), 4.21–4.12 (m, 1H), 4.10–3.91 (m, 2H), 3.82 (d, $J$ = 6.0 Hz, 1H), 3.64 (d, $J$ = 6.7 Hz, 3H), 3.49–3.41 (m, 1H), 3.01 (t, $J$ = 7.7 Hz, 1H), 1.28 (q, $J$ = 7.1 Hz, 3H); $^{13}$C NMR (101 MHz, DMSO-$d_6$) δ 181.16, 176.20, 174.37, 172.16, 169.71, 167.74, 164.67, 151.40, 143.74, 135.98, 135.63, 135.05, 133.41, 132.31, 131.02, 126.13, 125.81, 123.05, 112.07, 94.30, 84.51, 76.27, 75.58, 59.25, 54.52, 52.58, 48.11, 46.69, 40.71, 40.63, 40.51, 40.30, 40.09, 39.88, 39.67, 39.46, 17.74; Chemical Formula: $C_{27}H_{24}Cl_2N_4O_6S_2$; LCMS ($m/z$): 636.59 [M + H]$^+$, Elemental Analysis: [Calculated: C, 51.03; H, 3.81; N, 8.82; S, 10.09; Found: C, 51.03; H, 3.81; N, 8.82; S, 10.09].

### Methyl 4-(2-((3*S*,6′*S*,7′*S*,7a′*S*)-7′-(4-bromophenyl)-6-chloro-2,2″,4″-trioxo-7′,7a′-dihydro-1′*H*,3′*H*-dispiro [indoline-3,5′-pyrrolo [1,2-*c*]thiazole-6′,5″-thiazolidin]-3″-yl)acetamido)butanoate 5o

The 6-chloro-isatin **2b** (90.5 mg) and **4e** (228.5 mg) were utilized according to the general method, and the spiro-compound **5o** was obtained in 81% yield.

$^{1}$H NMR (400 MHz, DMSO-$d_6$) δ 11.18 (s, 1H), 8.16 (t, $J$ = 5.6 Hz, 1H), 7.68 (d, $J$ = 8.6 Hz, 0H), 7.63 (d, $J$ = 8.7 Hz, 0H), 7.52–7.38 (m, 5H), 7.26 (d, $J$ = 8.5 Hz, 1H), 7.06 (dd, $J$ = 8.4, 2.3 Hz, 1H), 6.90 (d, $J$ = 2.1 Hz, 1H), 4.82 (q, $J$ = 7.7, 7.2 Hz, 1H), 4.29–4.12 (m, 2H), 4.07–3.77 (m, 3H), 3.45 (d, $J$ = 6.1 Hz, 1H), 3.13–3.00 (m, 3H), 3.05–2.96 (m, 1H), 2.77 (dd, $J$ = 9.8, 7.6 Hz, 1H), 1.72–1.57 (m, 3H); $^{13}$C NMR (101 MHz, DMSO-$d_6$) δ 176.22, 174.78, 173.62, 173.08, 168.74, 167.22, 165.52, 164.72, 145.38, 136.00, 135.64, 133.40, 132.33, 129.46, 129.42, 123.04, 121.61, 112.52, 112.22, 76.19, 75.48, 70.60, 63.64, 56.11, 51.86, 50.22, 48.78, 47.03, 43.86, 40.71, 40.63, 40.50, 40.47, 40.29, 40.09, 39.88, 39.67, 39.54, 39.46, 38.62, 32.26, 31.11, 24.92; Chemical Formula: $C_{28}H_{26}BrClN_4O_6S_2$; LCMS ($m/z$): 695.02 [M + H]$^+$, Elemental Analysis: [Calculated: C, 48.46; H, 3.78; N, 8.07; S, 9.24; Found: C, 48.49; H, 3.80; N, 8.11; S, 9.25].

## Crystal structure determination

The technical protocol and data manipulation software details (Rikagu Oxford Diffraction CrysAlisPro, 2020; Sheldrick. 2015; Hübschle et al., 2011) are available in the Supplementary Material S1.

## Biological investigations

The methods for the Cytotoxic activity (Mosmann, 1983; Nafie et al., 2020a); EGFR/CDK-2 enzyme inhibition (Nafie et al., 2022a); Flow cytometry using Annexin V/PI staining; Gene expression analysis using RT-PCR (Nafie et al., 2022b); are amended in the Supplementary Material S1.

## Molecular docking and molecular dynamic simulation

The protcol for the Molecular docking and Molecular dynamic simulation are provided in in the Supplementary Material S1 ((Wood et al., 2019; Stamos et al., 2002; Chemical Computing Group, 2013; Case et al., 2023; Khalil et al., 2019; Roe and Cheatham, 2013).

# Conclusion

In conclusion, the synthesized compounds, particularly **5g**, **5l**, and **5n**, exhibited remarkable cytotoxicity against cancer cells, with noteworthy potency against both MCF-7 and MDA-MB-231 cells. Additionally, these compounds demonstrated promising inhibitory activities against EGFR and CDK-2, showcasing their potential as dual inhibitors. The RT-PCR results further confirmed their impact on promoting apoptotic cell death by modulating the expression of key pro-apoptotic and anti-apoptotic genes. Molecular docking and dynamic simulations provided insights into the binding modes of these compounds within the active sites of EGFR and CDK-2, reinforcing their potential as therapeutic agents. Overall, this comprehensive study underscores the multifaceted potential of these compounds in cancer treatment, warranting further investigation and development.

# Data availability statement

The original contributions presented in the study are included in the article/Supplementary Material, further inquiries can be directed to the corresponding authors.

# Author contributions

MN: Formal Analysis, Methodology, Software, Writing–review and editing. AA-M: Supervision, Visualization, Writing–review and editing. MA: Investigation, Methodology, Writing–review and editing. AA: Investigation, Methodology, Writing–review and editing. MH: Data curation, Formal Analysis, Software, Writing–review and editing. SA: Data curation, Investigation, Software, Validation, Writing–review and editing. ZU-H: Data curation, Investigation, Software, Validation, Writing–review and editing. AE-F: Methodology, Supervision, Writing–review and editing. AB: Funding acquisition, Methodology, Project administration, Writing–original draft, Writing–review and editing.

## Funding

The author(s) declare financial support was received for the research, authorship, publication of this article. The authors would like to extend their sincere appreciation to the Researchers Supporting Project (RSP 2024R64), King Saud University, Riyadh, Saudi Arabia.

## Conflict of interest

The authors declare that the research was conducted in the absence of any commercial or financial relationships that could be construed as a potential conflict of interest.

## Publisher's note

All claims expressed in this article are solely those of the authors and do not necessarily represent those of their affiliated organizations, or those of the publisher, the editors and the reviewers. Any product that may be evaluated in this article, or claim that may be made by its manufacturer, is not guaranteed or endorsed by the publisher.

## Supplementary material

The Supplementary Material for this article can be found online at: https://www.frontiersin.org/articles/10.3389/fchem.2024.1364378/full#supplementary-material

## References

Abd Alhameed, R., Almarhoon, Z., Bukhari, S. I., El-Faham, A., de la Torre, B. G., and Albericio, F. (2020). Synthesis and antimicrobial activity of a new series of thiazolidine-2,4-diones carboxamide and amino acid derivatives. *Molecules* 25, 105. doi:10.3390/molecules25010105

Al-Jassas, R. M., Islam, M. S., Al-Majid, A. M., Nafie, M. S., Haukka, M., Rahman, A. M., et al. (2023). Synthesis and SARs study of novel spiro-oxindoles as potent antiproliferative agents with CDK-2 inhibitory activities. *Arch. Pharm.* 356, e2300185. doi:10.1002/ardp.202300185

Al-Rashood, S. T., Hamed, A. R., Hassan, G. S., Alkahtani, H. M., Almehizia, A. A., Alharbi, A., et al. (2020). Anti-tumor properties of certain spirooxindoles towards hepatocellular carcinoma endowed with antioxidant activity. *J. Enzyme Inhib. Med. Chem.* 35 (1), 831–839. doi:10.1080/14756366.2020.1743281

Bacher, N., Tiefenthaler, M., Sturm, S., Stuppner, H., Ausserlechner, M. J., Kofler, R., et al. (2006). Oxindole alkaloids from Uncaria tomentosa induce apoptosis in proliferating, G0/G1-arrested and bcl-2-expressing acute lymphoblastic leukaemia cells. *Br. J. Haematol.* 132 (5), 615–622. doi:10.1111/j.1365-2141.2005.05907.x

Barakat, A., Alshahrani, S., Al-Majid, A. M., Alamary, A. S., Haukka, M., Abu-Serie, M. M., et al. (2023). New spiro-indeno[1,2-b]quinoxalines clubbed with benzimidazole scaffold as CDK2 inhibitors for halting non-small cell lung cancer; stereoselective synthesis, molecular dynamics and structural insights. *J. Enzyme Inhib. Med. Chem.* 38 (1), 2281260. doi:10.1080/14756366.2023.2281260

Barakat, A., Haukka, M., Soliman, S. M., Ali, M., Al-Majid, A. M., El-Faham, A., et al. (2021). Straightforward regio- and diastereoselective synthesis, molecular structure, intermolecular interactions and mechanistic study of spirooxindole-engrafted rhodanine analogs. *Molecules* 26, 7276. doi:10.3390/molecules26237276

Bramson, H. N., Corona, J., Davis, S. T., Dickerson, S. H., Edelstein, M., Frye, S. V., et al. (2001). Oxindole-based inhibitors of cyclin-dependent kinase 2 (CDK2): design, synthesis, enzymatic activities, and X-ray crystallographic analysis. *J. Med. Chem.* 44 (25), 4339–4358. doi:10.1021/jm010117d

Budovská, M., Tischlerová, V., Mojžiš, J., Kozlov, O., and Gondová, T. (2020). An alternative approach to the synthesis of anti-cancer molecule Spirobrassinin and its 2′-amino analogues. *Monatsh. Chem.* 151 (1), 63–77. doi:10.1007/s00706-019-02528-x

Case, D. A. A., Belfon, K., Ben-Shalom, I. Y., Berryman, J. T., Brozell, S. R., Cerutti, D. S., et al. (2023). *Amber 2023*. San Francisco: University of California.

Chemical Computing Group (2013). *Molecular operating environment (MOE)*. Sherbooke St. West, Montreal, QC, Canada.

Cui, C. B., Kakeya, H., and Osada, H. (1996). Spirotryprostatin B, a novel mammalian cell cycle inhibitor produced by Aspergillus fumigatus. *J. Antibiot.* 49 (8), 832–835. doi:10.7164/antibiotics.49.832

Ding, K., Lu, Y., Nikolovska-Coleska, Z., Qiu, S., Ding, Y., Gao, W., et al. (2005). Structure-based design of potent non-peptide MDM2 inhibitors. *J. Am. Chem. Soc.* 127 (29), 10130–10131. doi:10.1021/ja051147z

Edmondson, S., Danishefsky, S. J., Sepp-Lorenzino, L., and Rosen, N. (1999). Total synthesis of spirotryprostatin A, leading to the discovery of some biologically promising analogues. *J. Am. Chem. Soc.* 121 (10), 2147–2155. doi:10.1021/ja983788i

Galliford, C. V., and Scheidt, K. A. (2007). Pyrrolidinyl-spirooxindole natural products as inspirations for the development of potential therapeutic agents. *Angew. Chem. Int. Ed. Engl.* 46 (46), 8748–8758. doi:10.1002/anie.200701342

García Giménez, D., García Prado, E., Sáenz Rodríguez, T., Fernández Arche, A., and De La Puerta, R. (2010). Cytotoxic effect of the pentacyclic oxindole alkaloid mitraphylline isolated from Uncaria tomentosa bark on human ewing's sarcoma and breast cancer cell lines. *Planta Med.* 76 (2), 133–136. doi:10.1055/s-0029-1186048

Golsteyn, R. M. (2005). Cdk1 and Cdk2 complexes (cyclin dependent kinases) in apoptosis: a role beyond the cell cycle. *Cancer Lett.* 217 (2), 129–138. doi:10.1016/j.canlet.2004.08.005

Guo, K., Fang, T., Wang, J., Wu, A. A., Wang, Y., Jiang, J., et al. (2014). Two new spirooxindole alkaloids from rhizosphere strain streptomyces sp. Xzqh-9. *Bioorg. Med. Chem. Lett.* 24 (21), 4995–4998. doi:10.1016/j.bmcl.2014.09.026

Hübschle, C. B., Sheldrick, G. M., and Dittrich, B. (2011). ShelXle: a Qt graphical user interface for SHELXL. *J. Appl. Cryst.* 44, 1281–1284. doi:10.1107/S0021889811043202

Islam, F., Dehbia, Z., Zehravi, M., Das, R., Sivakumar, M., Krishnan, K., et al. (2023). Indole alkaloids from marine resources: understandings from therapeutic point of view to treat cancers. *Chem. Biol. Interact.* 383, 110682. doi:10.1016/j.cbi.2023.110682

Khalil, R., Ashraf, S., Khalid, A., and Ul-Haq, Z. (2019). Exploring novel N-myristoyltransferase inhibitors: a molecular dynamics simulation approach. *ACS omega* 15 (9), 13658–13670. doi:10.1021/acsomega.9b00843

Luk, K.-C., Simcox, M. E., Schutt, A., Rowan, K., Thompson, T., Chen, Y., et al. (2004). A new series of potent oxindole inhibitors of CDK2. *Bioorg. Med. Chem. Lett.* 14 (4), 913–917. doi:10.1016/j.bmcl.2003.12.009

Marti, C., and Carreira, E. M. (2003). Construction of Spiro [pyrrolidine-3, 3′-oxindoles]– recent applications to the synthesis of oxindole alkaloids. *EurJOC* 2003 (12), 2209–2219. doi:10.1002/ejoc.200300050

Mosmann, T. (1983). Rapid colorimetric assay for cellular growth and survival: Application to proliferation and cytotoxicity assays. *J. Immunol. Methods.* 65, 55–63. doi:10.1016/0022-1759(83)90303-4

Nafie, M. S., Amer, A. M., Mohamed, A. K., and Tantawy, E. S. (2020b). Discovery of novel pyrazolo[3,4-b]pyridine scaffold-based derivatives as potential PIM-1 kinase inhibitors in breast cancer MCF-7 cells. *Bioorg. Med. Chem.* 28, 115828. doi:10.1016/j.bmc.2020.115828

Nafie, M. S., Arafa, K., Sedky, N. K., Alakhdar, A. A., and Arafa, R. K. (2020a). Triaryl dicationic DNA minor-groove binders with antioxidant activity display cytotoxicity and induce apoptosis in breast cancer. *Chem. Biol. Interact.* 324, 109087. doi:10.1016/j.cbi.2020.109087

Nafie, M. S., and Boraei, A. T. A. (2022). Exploration of novel VEGFR2 tyrosine kinase inhibitors via design and synthesis of new alkylated indolyl-triazole Schiff bases for targeting breast cancer. *Bioorg. Chem.* 122, 105708. doi:10.1016/j.bioorg.2022.105708

Nafie, M. S., Elghazawy, N. H., Owf, S. M., Arafa, K., Abdel-Rahman, M. A., and Arafa, R. K. (2022b). Control of ER-positive breast cancer by ERα expression inhibition, apoptosis induction, cell cycle arrest using semisynthetic isoeugenol derivatives. *Chem. Biol. Interact.* 351, 109753. doi:10.1016/j.cbi.2021.109753

Nafie, M. S., Kishk, S. M., Mahgoub, S., and Amer, A. M. (2022a). Quinoline-based thiazolidinone derivatives as potent cytotoxic and apoptosis-inducing agents through EGFR inhibition. *Chem. Biol. Drug Des.* 99, 547–560. doi:10.1111/cbdd.13997

Rikagu Oxford Diffraction CrysAlisPro (2020) *CrysAlisPro*, Yarnton, Oxfordshire, England: Rikagu Oxford Diffraction inc.,

Roe, D. R., and Cheatham, T. E., III (2013). PTRAJ and CPPTRAJ: software for processing and analysis of molecular dynamics trajectory data. *J. Chem. theory Comput.* 9 (7), 3084–3095. doi:10.1021/ct400341p

Sheldrick, G. M. (2015). Crystal structure refinement with SHELXL. *Acta Cryst.* C71, 3–8. doi:10.1107/S2053229614024218

Sheldrick, G. M. (2015). SHELXT – integrated space-group and crystal-structure determination. *Acta Cryst.* A71, 3–8. doi:10.1107/S2053273314026370

Stamos, J., Sliwkowski, M. X., and Eigenbrot, C. (2002). Structure of the epidermal growth factor receptor kinase domain alone and in complex with a 4-anilinoquinazoline inhibitor. *J. Biol. Chem.* 277 (48), 46265–46272. doi:10.1074/jbc.M207135200

Sung, H., Ferlay, J., Siegel, R. L., Laversanne, M., Soerjomataram, I., Jemal, A., et al. (2021). Global cancer statistics 2020: GLOBOCAN estimates of incidence and mortality worldwide for 36 cancers in 185 countries. *Ca. Cancer J. Clin.* 71 (3), 209–249. doi:10.3322/caac.21660

Tadesse, S., Caldon, E. C., Tilley, W., and Wang, S. (2018). Cyclin-dependent kinase 2 inhibitors in cancer therapy: an update. *J. Med. Chem.* 62 (9), 4233–4251. doi:10.1021/acs.jmedchem.8b01469

Venkanna, A., Subedi, L., Teli, M. K., Lama, P. D., Nangunuri, B. G., Lee, S.-Y., et al. (2020). Positioning of an unprecedented spiro [5.5] undeca ring system into kinase inhibitor space. *Sci. Rep.* 10 (1), 21265. doi:10.1038/s41598-020-78158-9

Wang, B., Peng, F., Huang, W., Zhou, J., Zhang, N., Sheng, J., et al. (2020). Rational drug design, synthesis, and biological evaluation of novel chiral tetrahydronaphthalene-fused spirooxindole as MDM2-CDK4 dual inhibitor against glioblastoma. *Acta Pharm. Sin. B* 10 (8), 1492–1510. doi:10.1016/j.apsb.2019.12.013

Wood, D. J., Lopez-Fernandez, J. D., Knight, L. E., Al-Khawaldeh, I., Gai, C., Lin, S., et al. (2019). FragLites—minimal, halogenated fragments displaying pharmacophore doublets. An efficient approach to druggability assessment and hit generation. *J. Med. Chem.* 62 (7), 3741–3752. doi:10.1021/acs.jmedchem.9b00304

World Cancer Research Fund (2021). *Cancer facts and figures 2021*. London, United Kingdom: World Cancer Research Fund International, 1–4.

Yu, B., Yu, D. Q., and Liu, H. M. (2015). Spirooxindoles: promising scaffolds for anti-cancer agents. *Eur. J. Med. Chem.* 97, 673–698. doi:10.1016/j.ejmech.2014.06.056

Yu, Q., Guo, P., Jian, J., Chen, Y., and Xu, J. (2018). Nine-step total synthesis of (-)-Strychnofoline. *Chem. Commun.* 54 (9), 1125–1128. doi:10.1039/c7cc08938d

Yuenyongsawad, S., Bunluepuech, K., Wattanapiromsakul, C., and Tewtrakul, S. (2013). Anti-cancer activity of compounds from Bauhinia strychnifolia stem. *J. Ethnopharmacol.* 150 (2), 765–769. doi:10.1016/j.jep.2013.09.025

Zhou, L. M., Qu, R. Y., and Yang, G. F. (2020). An overview of spirooxindole as a promising scaffold for novel drug discovery. *Expert Opin. Drug Discov.* 15 (5), 603–625. doi:10.1080/17460441.2020.1733526

frontiers | Frontiers in Chemistry

TYPE Original Research
PUBLISHED 16 April 2024
DOI 10.3389/fchem.2024.1374930

Check for updates

OPEN ACCESS

EDITED BY
Xuetao Xu,
Wuyi University, China

REVIEWED BY
Wenbao Wang,
Qiqihar Medical University, China
Yunlei Hou,
Shenyang Pharmaceutical University, China
Zhenghui Kang,
Chinese Academy of Sciences (CAS), China
Gaofei Wei,
Northwestern Polytechnical University, China

*CORRESPONDENCE
Congjun Xu,
congjunxu@hainanu.edu.cn
Ling Huang,
linghuang@hainanu.edu.cn

RECEIVED 02 February 2024
ACCEPTED 02 April 2024
PUBLISHED 16 April 2024

CITATION
Wang W, Pan T, Su R, Chen M, Xiong W, Xu C and Huang L (2024), Discovery of novel melatonin–mydroxyquinoline hybrids as multitarget strategies for Alzheimer's disease therapy.
*Front. Chem.* 12:1374930.
doi: 10.3389/fchem.2024.1374930

COPYRIGHT
© 2024 Wang, Pan, Su, Chen, Xiong, Xu and Huang. This is an open-access article distributed under the terms of the Creative Commons Attribution License (CC BY). The use, distribution or reproduction in other forums is permitted, provided the original author(s) and the copyright owner(s) are credited and that the original publication in this journal is cited, in accordance with accepted academic practice. No use, distribution or reproduction is permitted which does not comply with these terms.

# Discovery of novel melatonin–mydroxyquinoline hybrids as multitarget strategies for Alzheimer's disease therapy

Wei Wang[1], Tingting Pan[2], Rui Su[1], Mingbin Chen[1], Wandi Xiong[1], Congjun Xu[1]* and Ling Huang[1]*

[1]Key Laboratory of Tropical Biological Resources of Ministry of Education, School of Pharmaceutical Sciences, Hainan University, Haikou, China, [2]School of Pharmaceutical Sciences, Sun Yat-Sen University, Guangzhou, China

Alzheimer's disease (AD) is a neurodegenerative disease that seriously affects human health, and current treatment strategies are far from meeting clinical needs. Inspired by multi-target drug design strategies, a series of novel natural products-based melatonin–hydroxyquinoline hybrids were designed and synthesized, targeting anti-oxidation and metal-chelating at the same time. Most of the compounds showed significant oxygen radical absorbance capacity and $A\beta_{1-42}$ aggregation inhibition. Moreover, the compounds possess good blood-brain barrier permeability. **6b** and **6c** have a good ability to alleviate oxidative stress induced by hydrogen peroxide. **6b** and **6c** possess metal-chelating properties with the chelation ratio being 2:1. Furthermore, **6b** can significantly mitigate metal-induced Aβ aggregation. This work may provide a new multi-target treatment strategy for Alzheimer's disease.

KEYWORDS

**melatonin, Alzheimer's disease, natural products, multitarget strategies, hydrids**

## 1 Introduction

Alzheimer's disease (AD) is a neurodegenerative disease characterized by memory loss and cognitive impairment, whose impact will be even more profound as the global population continues to age (Scheltens et al., 2021; Author Anonymous, 2023). The number of people affected by AD worldwide is estimated to rise from 55 million in 2020 to 135 million by 2050 (Author Anonymous, 2023). The global cost of treating AD is estimated at approximately 2.8 trillion dollars, which will create a huge social burden. The development of safe and effective anti-AD drugs has always been the hot spot in medical chemistry.

The pathogenesis of AD is complex, and many hypotheses were proposed, including the cholinergic hypothesis, the beta-amyloid cascade hypothesis, the oxidative stress hypothesis, the metal ion disorder hypothesis, etc. In the past years, major research institutions and pharmaceutical companies have invested hundreds of billions of dollars in AD. At present, the drugs that have been approved, such as AChE inhibitors and NMDAR inhibitors, only alleviate the symptoms or make them slightly better, and there is no specific drug that can completely cure AD (Cerejeira et al., 2012; Marcinkowska et al., 2021). Therefore, more and more researchers have turned their attention to the multi-target

design strategy. Multi-target drugs are expected to become a breakthrough in the treatment of AD (Rossi et al., 2021; Babaei et al., 2022; Turgutalp et al., 2022).

Melatonin (MT) is a neurohormone secreted by the pineal gland (Somalo-Barranco et al., 2022). As an endogenous natural active substance of the human body, accumulating reports suggest that melatonin has excellent antioxidant activity and a protective effect on nerve cells (He et al., 2022). Besides, MT can also chelate heavy metals, including lead, cadmium, and aluminum, while chelating iron and copper can reduce oxidative stress in the body (Reiter et al., 2016). Furthermore, clinical studies have shown that melatonin can improve cognition and mood in Alzheimer's patients (Dowling et al., 2008). In the meantime, the imbalance of metal ions in the brain will accelerate the aggregation of Aβ and Tau proteins resulting in cognitive decline. Hence, metal ion chelators, such as hydroxyquinoline derivative clioquinol (CQ) are considered potential drugs for the treatment of AD (Adlard et al., 2008; Faux et al., 2010). From this, a hypothesis can be proposed that simultaneously targeting oxidative stress and metal ion disorder may be an effective strategy for treating AD.

In this study, a series of novel melatonin–hydroxyquinoline hybrids were designed and synthesized, targeting anti-oxidation and metal ion chelation at the same time. In detail, melatonin and hydroxyquinoline were coupled by amide or amine linkage, and the connecting linker's length and the hydroxyquinoline's link location were investigated for their impact on bioactivity (Figure 1).

# 2 Results and discussion

## 2.1 Synthesis

Routes for synthesizing the target compounds (**3a-d**, **4**, **6a-d**, **11a-b** and **13a-c**) are demonstrated in Schemes 1–4. Commercially available 2-methyl-8-hydroxyquinoline (**1**) was reacted with $SeO_2$ in the presence of 1,4-dioxane to produce compound **2**. Dissolving different amines, compound **2** and isopropanol, they were reacted at room temperature for 3 h, then $NaBH_4$ was added and kept stirring for 12 h to obtain **3a-d**. Target compound **4** was obtained by the *N*-methylationst of **3a**.

The synthetic route of **6a-d** *via* a tow-step produce is shown in Scheme 2. Commercially available 2-methyl-8-hydroxyquinoline was reacted with $SeO_2$ in pyridine to produce compound **5**, followed by treatment with amines, HATU and DIPEA to mediate amine formation, so **6a-d** were obtained.

The synthesis of the target compounds **11a-b** is summarized in Scheme 3. Using $ZnCl_2$ as a catalyst, 8-hydroxyquinoline was reacted with formaldehyde and hydrochloric acid to produce **8**. Compound **8** was refluxed in DMF for 8 h. Then refluxed in hydrochloric acid for 9 h to obtain compound **10**. Followed by treatment with different substituted carboxylic acids, HATU and DIPEA to produce target **11a-b**.

As showed in Scheme 4, treatment of the commercially available 8-hydroxyquinoline-7-carboxylic acid and different amines in the presence of HATU and DIPEA afforded the target compounds **13a-b**.

## 2.2 Activity evaluation and structure-activity relationships

### 2.2.1 The oxygen radical absorbance capacity (ORAC)

Oxidative stress is involved in various pathological processes of AD and is one of the crucial adjective pathogeneses of AD. Therefore, it is essential to test the scavenging ability of target compounds. The oxygen radical absorbance capacity (ORAC) (Wang et al., 2014; Wang et al., 2015) was tested to evaluate the effects of compounds on oxidative stress. As shown in Table 1, MT has a satisfactory antioxidant effect, with the ORAC values of 2.38, whereas CQ had almost no antioxidant effect. Compared with the melatonin, most of the target compounds, such as 3a~3d, 4, 6a~6d, and 11a~11b, which ORAC values were greater than 2.3. while compound **13a~13c**, which is linked at position **7** of hydroxyquinoline, have weaker oxygen radical scavenging ability. This suggests that the position of the junction on CQ has a large effect on the activity. Furthermore, the change in the connecting linker's length has a slight effect on the ORAC, just as 3a and 3d have different lengths while having similar antioxidant activity.

### 2.2.2 Inhibition of $A\beta_{1-42}$ aggregation

Self-mediated Aβ1–42 aggregation inhibition was assessed via thioflavin T (ThT) fluorescence assay (Rosini et al., 2008; Wang et al., 2018; Babaei et al., 2022). As shown in Table 1, both CQ and MT showed good anti-aggregation effect. Most of the target compounds showed good inhibition of $A\beta_{1-42}$ aggregation. Among them, **3c**, **4**, **6a**, **6b**, **6c**, **11a**, and **13a** showed better activity than melatonin (38.96 ± 9.35) and CQ (30.76 ± 1.08). When the connection is amine, compounds with -OH substituents on the indole ring have the highest inhibitory activity against $A\beta_{1-42}$ aggregation. Compound **3c** containing hydroxyl-substituted indole ring fragments has the highest inhibitory rate against $A\beta_{1-42}$ self-aggregation (40.23%), which is much higher than the inhibition rate of methoxy-substituted and unsubstituted indole ring fragment compounds (18.23% and 27.10% respectively). When the connection mode is an amide, compound **6b** with a methoxy group on the indole ring has the highest inhibition rate (63.24%). This shows that the different substituents at position 5 on the indole ring and the different link methods between melatonin and hydroxyquinoline play an important role in inhibiting the self-aggregation of $A\beta_{1-42}$. Compared **3a** (27.10%) with **4** (52.54%), it can be found that methylation of nitrogen atoms leads to increased activity. On the whole when the connection mode is amide, the inhibitory activity is better. The length of the connected chain is shortened, and the activity decreases to different degrees. In addition, the compounds obtained at positions 2, 5 and 7 of the quinoline ring had no significant effect on the self-aggregation of $A\beta_{1-42}$ such as **6a** (45.45%), **11a** (44.74%) and **13a** (46.98%).

### 2.2.3 Blood–brain barrier permeability assay

The blood-brain barrier permeability of central nervous drugs is a crucial drug-like property. In this work, the parallel artificial membrane permeability assay (PAMPA) (Di et al., 2003; Wang et al., 2014) was used to evaluate the ability of compounds to cross the blood-brain barrier. 13 commercial drugs were chosen to establish the evaluation system (Supplementary Table S1). Most of the target compounds can cross the blood-brain barrier with the

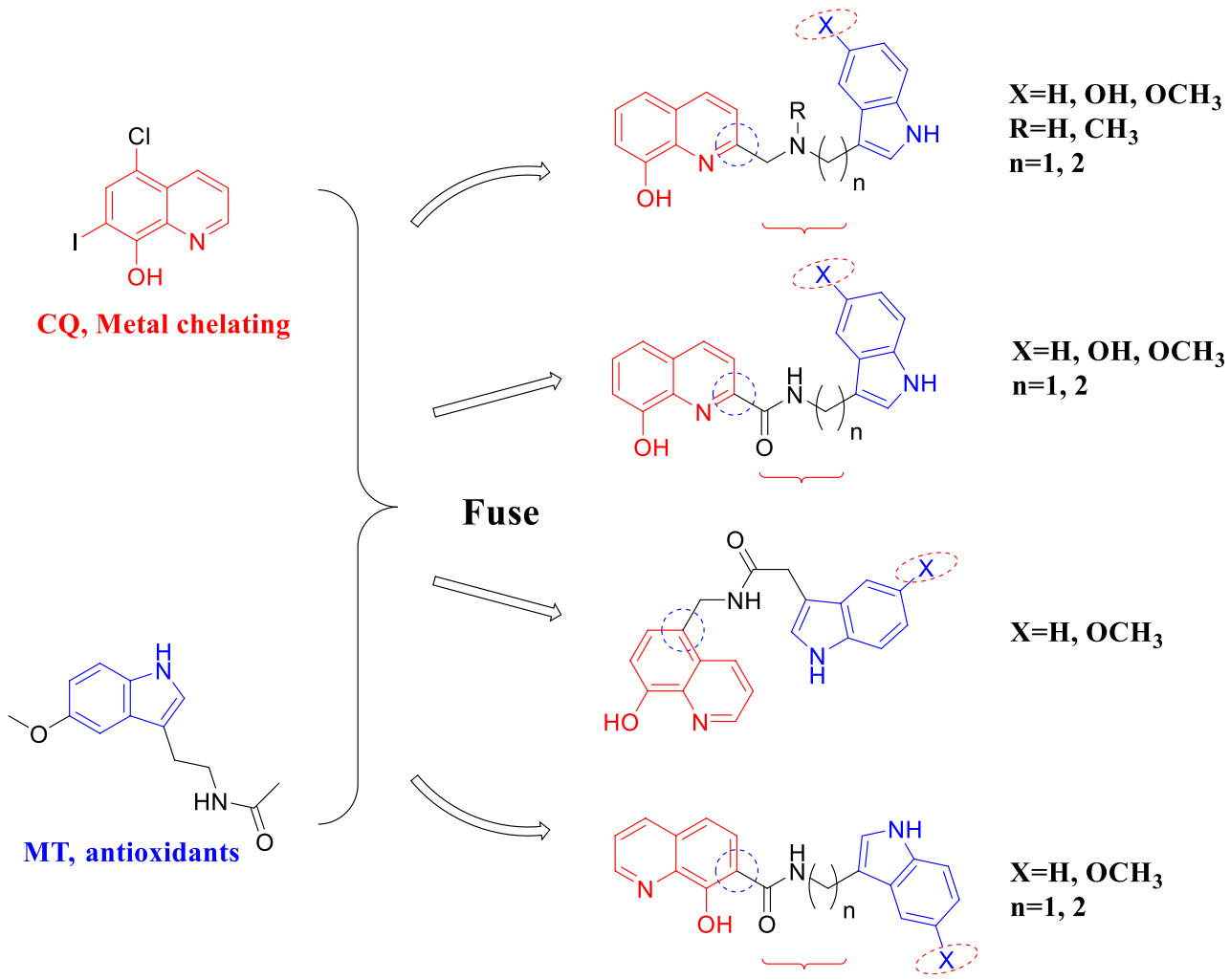


FIGURE 1
The design strategy of melatonin–hydroxyquinoline hybrids.

$P_e$ > 4.7, such as **3a**, **3b**, **3c**, **3d**, **4**, **6a**, **6b** and **6d**. The compounds with hydroxyl groups exhibit poor BBB permeability, possibly due to increased hydrophilia.

### 2.2.4 Cytotoxicity assay

To further investigate the bioactivity of the compounds, cytotoxicity was evaluated on SH-SY5Y and BV2 cell lines (Figures 2A, B). The results showed that **6b** and **6c** exhibit no cytotoxicity at 5 μM in SH-SY5H cell lines while showing slight toxicity at concentrations of 10 μM. As for BV2 cells, **6b** and **6c** also showed no significant cytotoxicity at 20 μM concentration.

### 2.2.5 Alleviating oxidative stress induced by hydrogen peroxide

The effect of **6b** and **6c** on the oxidative stress of SH-SY5H cells induced by hydrogen peroxide was investigated using DCFH-DA as the fluorescent probe (Xu et al., 2021). The results showed that the ROS increased sharply in SH-SY5H cells treated with 400 μM hydrogen peroxide for 12 h. Pretreatment with **6b** or **6c** reduced ROS production in a dose-dependent manner, suggesting that **6b** and **6c** have a good ability to alleviate oxidative stress (Figure 2C).

### 2.2.6 Metal-chelating property

To further evaluate multi-target anti-AD potential, the metal-chelating properties of **6b** and **6c** were determined by UV spectrophotometry (Geng et al., 2012; Lu et al., 2013; Hu et al., 2019). As shown in Figures 3A, C, **6b** exhibited a maximum absorption peak at 255 nm, and the maximum absorption peak showed a significant redshift and the intensity decreased when **6b** co-incubated with $Cu^{2+}$ or $Zn^{2+}$. While co-incubated with $Fe^{3+}$ or $Fe^{2+}$, the intensity at 255 nm was in different degrees decreased. The same result occurred for **6c**. Those results suggested that **6b** and **6c** possess metal-chelating properties. Next, the chelation ratios of **6b** and **6c** to $Cu^{2+}$ were measured and calculated using the inflection point method (Figures 3B, D). The inflection point appears when the concentration ratio of compound $Cu^{2+}$ to **6b** or **6c** is 0.5, so it can be inferred that the chelation ratio of compound **6b** and **6c** to $Cu^{2+}$ is 2:1.

### 2.2.7 Effect of $Cu^{2+}$-induced Aβ aggregation

To further detect the ability of compounds **6b**, CQ and MT to disaggregate or inhibit the $Cu^{2+}$-induced $A\beta_{1-42}$ aggregation, we conducted thioflavin T fluorometric detection (Hu et al., 2019). The results showed that compounds **6b** and CQ both significantly

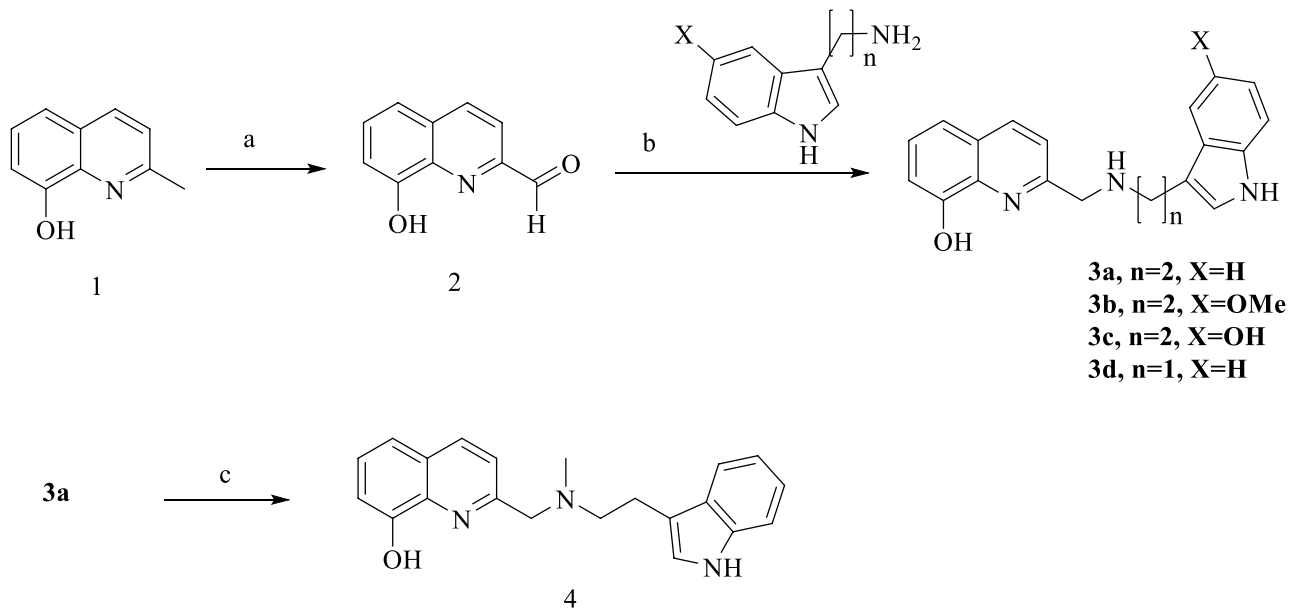


SCHEME 1
Synthesis of **3a-d** and **4**. Reagent and conditions: (a) $SeO_2$/1,4-dioxane, 60°C to reflux; 86%. (b) $NaBH_4$, isopropanol, room temperature, overnight, 62%–67%; (c) $CH_3I$, $K_2CO_3$, acetone, 60%.

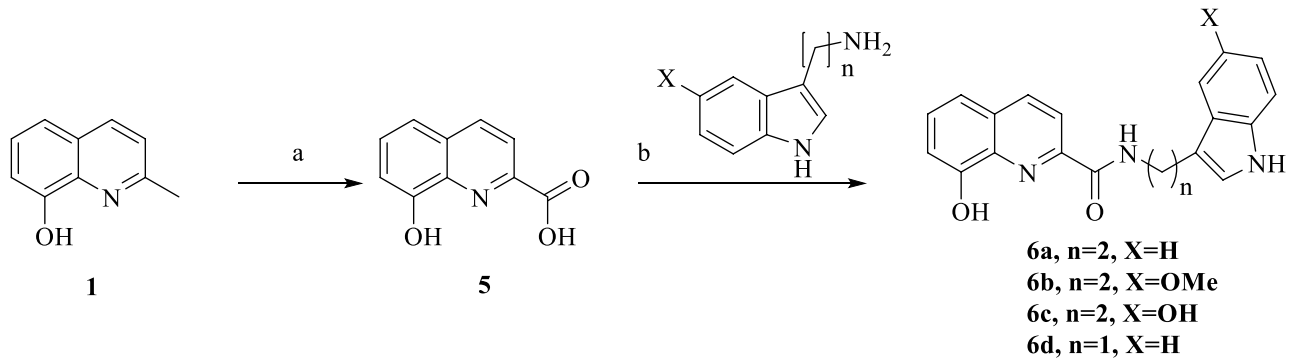


SCHEME 2
Synthesis of **6a-d**. Reagent and conditions: (a) $SeO_2$, pyridine, 120°C, 12 h, 50%; (b) HATU, DIPEA, anhydrous $CH_2Cl_2$, room temperature, overnight, 60%–70%.

disaggregated $Cu^{2+}$-induced $A\beta_{1-42}$ aggregation, also with the mild disaggregated effect of MT (Figure 4A). As shown in Figure 4B, **6b** exhibited a distinct inhibitory effect on $Cu^{2+}$-induced $A\beta_{1-42}$ aggregation, which was superior to the reference compound CQ, while MT exhibited weak inhibitory activity. Those results suggest that **6b** can significantly mitigate metal ion induced Aβ aggregation.

# 3 Experimental

## 3.1 Chemistry

### 3.1.1 8-hydroxyquinoline-2-carbaldehyde (**2**)

At 60°C, 10 mL dioxane solution of 2-methyl-8-hydroxyquinoline (10 mmol) was added to 50 mL dioxane solution of $SeO_2$ (20 mmol). After half an hour of drip adding, the reaction reflux for 4 h. Yield 86%. $^1$H NMR (400 MHz, Acetone-$d_6$) $\delta$ 10.16 (s, 1H), 9.22 (s, 1H), 8.55 (d, $J$ = 8.5 Hz, 1H), 8.04 (d, $J$ = 8.5 Hz, 1H), 7.69 (t, $J$ = 8.0 Hz, 1H), 7.57 (dd, $J$ = 8.2, 0.9 Hz, 1H), 7.28 (dd, $J$ = 7.7, 1.0 Hz, 1H).

### 3.1.2 8-hydroxyquinoline-2-carboxylic acid (5)

**1** (20 mmol) was dissolved in pyridine (50 mL), and $SeO_2$ (20 mmol) was added followed by stirring at 120°C for 12 h, after the completion of the reaction (monitored by TLC). The reaction mixture was filtered off first. The solvent was distilled off and the residue was dissolved in an aqueous KOH solution (10%), Then filtered and the filtered liquid was acidified with hydrochloric acid (10%). Last the filtered crude product was purified by silica-column chromatography. yellow solid, yield 50%.$^1$H NMR (400 MHz,

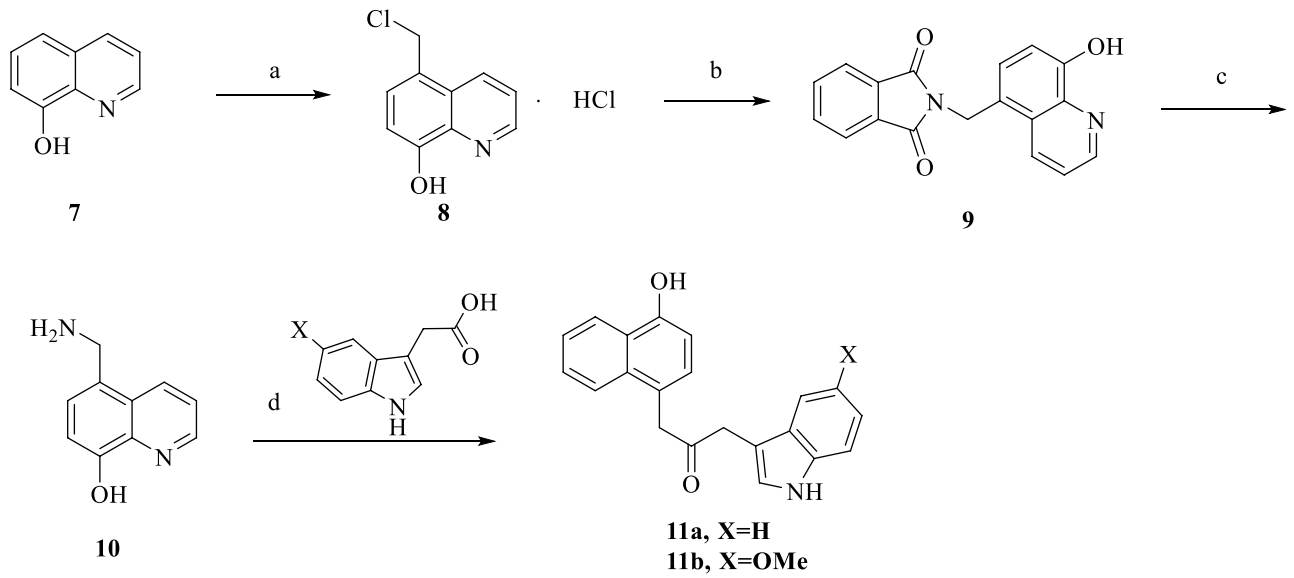


SCHEME 3
Synthesis of **11a-b**. Reagent and conditions: (a) $ZnCl_2$, HCl, formaldehyde, room temperature, 12 h, 85%; (b) DMF, reflux, 8 h, 50%; (c) HCl, reflux, 9 h, 75%; (d) HATU, DIPEA, anhydrous $CH_2Cl_2$, room temperature, overnight, 58%–60%.

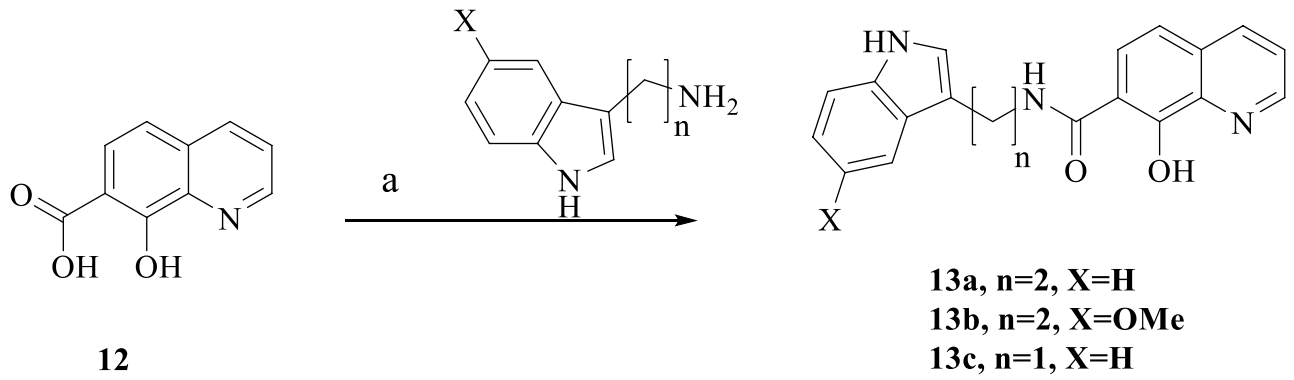


SCHEME 4
Synthesis of **13a-c**. Reagent and conditions: (a) HATU, DIPEA, anhydrous $CH_2Cl_2$, room temperature, overnight, 40%–55%.

Acetone-$d_6$) $\delta$ 9.68 (s, 1H), 8.63 (d, $J$ = 8.5 Hz, 1H), 8.27 (d, $J$ = 8.5 Hz, 1H), 7.70 (t, $J$ = 7.9 Hz, 1H), 7.60 (d, $J$ = 8.2 Hz, 1H), 7.28 (d, $J$ = 7.6 Hz, 1H).

### 3.1.3 5-(Chloromethyl)quinolin-8-ol hydrochloride (8·HCl)

Compound **8** was synthesized according to the literature. Pale yellow solid, yield 98%. $^1$H NMR (400 MHz, DMSO-$d_6$) $\delta$ 9.22 (d, $J$ = 7.9 Hz, 1H), 9.13 (dd, $J$ = 5.0, 1.1 Hz, 1H), 8.12 (dd, $J$ = 8.6, 5.1 Hz, 1H), 7.87 (d, $J$ = 8.0 Hz, 1H), 7.51 (d, $J$ = 8.0 Hz, 1H), 5.33 (s, 2H).

### 3.1.4 2-(hydroxyquinoline-5-yl-methyl)-isoquinoline-1,3-diketone (9)

Under the nitrogen atmosphere. A mixture of phthalimide potassium (4.5 mmol), 5-(Chloromethyl)quinolin-8-ol Hydrochloride (3 mmol) and DMF (10 mL) was heated to 150°C, and refluxed for 8 h. After cooling to room temperature, the white potassium chloride residue was formed at the bottom of the flask, which was filtered. The filtrate was poured into water (400 mL), and filtered to obtain compound **9**. White solid, yields 73%. $^1$H NMR (400 MHz, DMSO-$d_6$) $\delta$ 9.82 (s, 1H), 8.88 (dd, $J$ = 4.1, 1.2 Hz, 1H), 8.73 (dd, $J$ = 8.6, 1.3 Hz, 1H), 7.92–7.87 (m, 2H), 7.87–7.82 (m, 2H), 7.65 (dd, $J$ = 8.6, 4.1 Hz, 1H), 7.45 (d, $J$ = 7.9 Hz, 1H), 7.03 (d, $J$ = 7.9 Hz, 1H), 5.14 (s, 2H).

### 3.1.5 5-aminomethyl-8-hydroxyquinoline (10)

To a stirred concentrated hydrochloric acid (20 mL), compound **9** (2.19 mmol) was added, refluxed for 9 h until the mixture became transparent after cooling to room temperature. The solvent was distilled off and the residue was dissolved in water, then the solution pH to produce a solid. Greenish solid, yield 75%. $^1$H NMR (400 MHz, DMSO-$d_6$) $\delta$ 8.85 (dd, $J$ = 4.1, 1.4 Hz, 1H), 8.56 (dd, $J$ = 8.5, 1.4 Hz, 1H), 7.57 (dd, $J$ = 8.5, 4.1 Hz, 1H), 7.42 (d, $J$ = 7.8 Hz, 1H), 7.01 (d, $J$ = 7.8 Hz, 1H), 4.08 (s, 2H).

TABLE 1 Oxygen radical absorbance capacity, PAMPA assay and inhibition of $A\beta_{1-42}$ self-aggregation for target compounds.

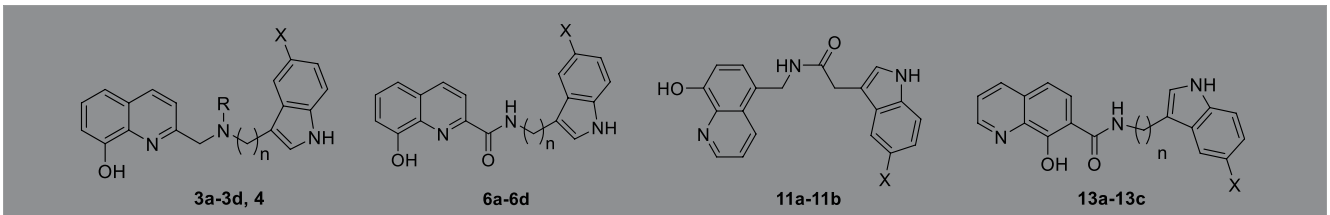


| Compound | n | X | R | ORAC[a] | Inhibition of $A\beta_{1-42}$ aggregation (%)[b] | $P_e$ (× $10^{-6}$ cm $s^{-1}$)[c] | pred |
|---|---|---|---|---|---|---|---|
| 3a | 2 | H | H | 3.50 ± 0.12 | 27.10 ± 5.01 | 8.08 ± 0.56 | CNS+ |
| 3b | 2 | OMe | H | 3.25 ± 0.10 | 18.23 ± 2.02 | 6.61 ± 0.22 | CNS+ |
| 3c | 2 | OH | H | 4.47 ± 0.18 | 40.23 ± 2.89 | 4.81 ± 0.87 | CNS+ |
| 3d | 1 | H | H | 2.60 ± 0.20 | 20.47 ± 4.72 | 5.09 ± 1.32 | CNS+ |
| 4 | 2 | H | Me | 2.93 ± 0.15 | 52.54 ± 6.47 | 9.87 ± 0.66 | CNS+ |
| 6a | 2 | H | — | 2.49 ± 0.22 | 45.45 ± 0.41 | 7.71 ± 0.61 | CNS+ |
| 6b | 2 | OMe | — | 2.76 ± 0.01 | 63.24 ± 2.02 | 6.91 ± 0.92 | CNS+ |
| 6c | 2 | OH | — | 3.23 ± 0.02 | 40.33 ± 2.09 | 2.96 ± 0.58 | CNS± |
| 6d | 1 | H | — | 2.32 ± 0.17 | 19.25 ± 5.85 | 6.81 ± 1.13 | CNS+ |
| 11a | 2 | H | — | 2.91 ± 0.16 | 44.74 ± 5.18 | 2.82 ± 0.42 | CNS± |
| 11b | 2 | OMe | — | 3.58 ± 0.12 | 34.94 ± 2.91 | 1.35 ± 0.25 | CNS− |
| 13a | 2 | H | — | 1.06 ± 0.07 | 46.98 ± 6.25 | 3.98 ± 0.45 | CNS± |
| 13b | 2 | OMe | — | 1.33 ± 0.02 | 19.66 ± 2.06 | 1.12 ± 0.42 | CNS− |
| 13c | 1 | H | — | 0.94 ± 0.02 | 38.58 ± 5.12 | 2.65 ± 0.46 | CNS± |
| CQ | — | — | | 0.54 ± 0.17 | 30.76 ± 1.08 | NT | NT |
| Melatonin | — | — | | 2.38 ± 0.12 | 38.96 ± 9.35 | NT | NT |
| Curcumin | — | — | | NT | 52.88 ± 6.38 | NT | NT |
| Chlorpromazinne | — | — | | NT | NT | 6.63 ± 0.81 | CNS+ |
| Hydrocortisone | — | — | | NT | NT | 1.13 ± 0.15 | CNS− |

[a]Result is the mean of three independent experiments ($n$ = 3) ± SD.
[b]Result are the mean of three independent experiments ($n$ = 3) ± SD., The concentration of all compounds was 20 μM.
[c]Result are the mean of three independent experiments ($n$ = 3) ± SD., Compounds could potentially cross the BBB, when Pe > 4.7 × 10−6 cm s−1.
NT, not tested.

#### 3.1.5.1 General method for the preparation of compounds 3a-3d

To a solution of **2** (1 mmol) and different indole (1 mmol) in isopropyl alcohol. After stirring at room temperature for 3 h, the $NaBH_4$ (2 mmol) was added and kept stirring for 12 h. Quenched with water, extracted with ethyl acetate, the organic layer was dried with $Na_2SO_4$ and concentrated under reduced pressure. The residue was purified by silica gel chromatography to afford **3a**-**3d** ($CH_2Cl_2$/$CH_3OH$ = 50:1).

### 3.1.6 2-(((2-(1H-indol-3-yl)ethyl)amino)methyl) quinolin-8-ol (3a)

Yellow solid, yield 65%. $^1$H NMR (400 MHz, DMSO-$d_6$) $\delta$ 10.76 (s, 1H), 8.24 (d, $J$ = 8.5 Hz, 1H), 7.56 (d, $J$ = 8.5 Hz, 1H), 7.51 (d, $J$ = 7.8 Hz, 1H), 7.42–7.37 (m, 1H), 7.37–7.33 (m, 1H), 7.32 (d, $J$ = 8.1 Hz, 1H), 7.14 (d, $J$ = 1.8 Hz, 1H), 7.09–7.06 (m, 1H), 7.06–7.01 (m, 1H), 6.94 (t, $J$ = 7.4 Hz, 1H), 4.07 (s, 2H), 2.91 (s, 2H), 2.90 (s, 2H). $^{13}$C NMR (126 MHz, DMSO-$d_6$) $\delta$ 159.23, 153.23, 137.91, 136.69, 136.66, 128.05, 127.75, 127.23, 122.96, 121.45, 121.28, 118.76, 118.58, 117.98, 113.10, 111.79, 111.46, 55.13, 50.53, 26.04. HRMS (ESI) m/z calcd for $C_{20}H_{19}N_3O$ $[M + H]^+$, 318.1562; found, 318.1562. HPLC purity: 99.6%, retention time: 8.8 min.

### 3.1.7 2-(((2-(5-methoxy-1H-indol-3-yl)ethyl) amino)methyl)quinolin-8-ol (3b)

Yellow solid, yield 67%. $^1$H NMR (400 MHz, DMSO-$d_6$) $\delta$ 10.61 (s, 1H), 8.25 (d, $J$ = 8.5 Hz, 1H), 7.57 (d, $J$ = 8.5 Hz, 1H), 7.42–7.37 (m, 1H), 7.37–7.31 (m, 1H), 7.20 (d, $J$ = 8.7 Hz, 1H), 7.10 (d, $J$ = 2.1 Hz, 1H), 7.07 (dd, $J$ = 7.0, 1.6 Hz, 1H), 6.94 (d, $J$ = 2.2 Hz, 1H), 6.68 (dd, $J$ = 8.7, 2.3 Hz, 1H), 4.08 (s, 2H), 3.68 (s, 3H), 2.88 (s, 4H). $^{13}$C NMR (126 MHz, DMSO-$d_6$) $\delta$ 159.19, 153.34, 153.24, 137.91, 136.66, 131.83, 128.05, 128.01, 127.24, 123.67, 121.45, 117.97, 112.85, 112.45, 111.48, 111.46, 100.47, 55.70, 55.06, 50.38, 26.05. HRMS (ESI) m/z calcd for $C_{21}H_{21}N_3O_2$

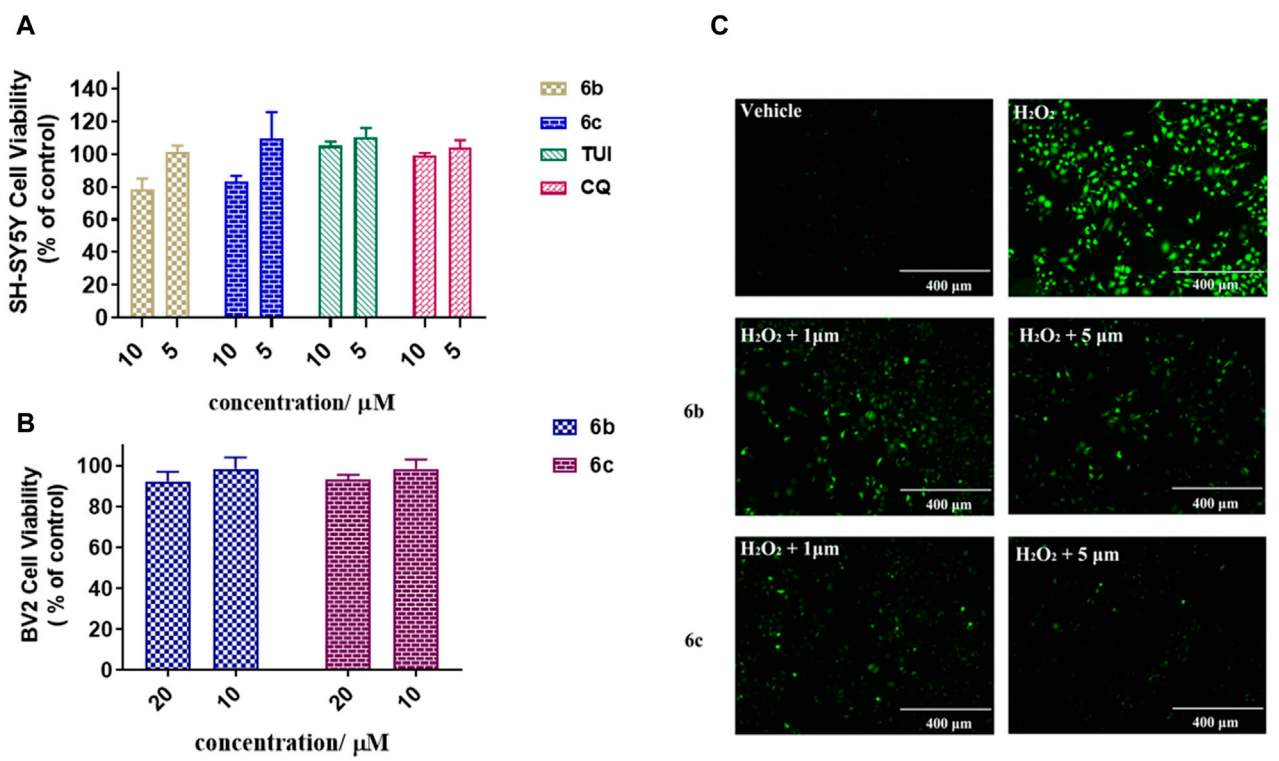


FIGURE 2
Cytotoxicity assay of 6b and 6c on SH-SY5Y **(A)** and BV2 **(B)**. Protective effect of **6b** and **6c** against $H_2O_2$ induced SH-SY5Y oxidative stress **(C)**.

[M + H]$^+$, 348.1678; found,348.1667. HPLC purity: 98.6%. Retention time: 8.7 min.

### 3.1.8 2-(((2-(5-hydroxy-1H-indol-3-yl)ethyl)amino) methyl)quinolin-8-ol (3c)

Yellow solid, yield 62%. $^1$H NMR (400 MHz, DMSO-$d_6$) $\delta$ 10.45 (s, 1H), 8.26 (d, $J$ = 8.5 Hz, 1H), 7.57 (d, $J$ = 8.5 Hz, 1H), 7.45–7.38 (m, 1H), 7.38–7.33 (m, 1H), 7.12 (d, $J$ = 8.6 Hz, 1H), 7.08 (dd, $J$ = 7.0, 1.4 Hz, 1H), 7.04 (d, $J$ = 1.7 Hz, 1H), 6.83 (d, $J$ = 1.9 Hz, 1H), 6.58 (dd, $J$ = 8.6, 2.1 Hz, 1H), 4.10 (s, 2H), 3.00 (d, J = 6.8 Hz, s), 2.85 (d, $J$ = 6.6 Hz, 2H). $^{13}$C NMR (126 MHz, DMSO-$d_6$) $\delta$ 158.84, 153.22, 150.59, 137.88, 136.73, 131.29, 128.42, 128.06, 127.29, 123.46, 121.40, 118.00, 112.11, 111.96, 111.68, 111.51, 102.73, 55.01, 50.37, 26.01. HRMS (ESI) m/z calcd for $C_{20}H_{19}N_3O_2$ [M + H]$^+$, 348.1678; found,348.1667. HPLC purity: 98.1%. Retention time: 8.4 min.

### 3.1.9 2-((((1H-indol-3-yl)methyl)amino)methyl) quinolin-8-ol (3d)

Yellow solid, yield 64%. $^1$H NMR (400 MHz, DMSO-$d_6$) $\delta$ 10.90 (s, 1H), 8.25 (d, $J$ = 8.5 Hz, 1H), 7.65 (d, $J$ = 7.8 Hz, 1H), 7.58 (d, $J$ = 8.5 Hz, 1H), 7.41–7.38 (m, 1H), 7.38–7.36 (m, 1H), 7.36–7.34 (m, 1H), 7.30 (s, 1H), 7.10–7.08 (m, 1H), 7.08–7.06 (m, 1H), 6.97 (t, J = 7.2 Hz, 1H), 4.07 (s, 2H), 3.99 (s, 2H). $^{13}$C NMR (126 MHz, DMSO-$d_6$) $\delta$ 158.77, 153.24, 137.89, 136.82, 136.68, 128.06, 127.52, 127.26, 124.32, 121.49, 121.43, 119.34, 118.79, 117.98, 113.49, 111.80, 111.50, 54.35, 44.43. HRMS (ESI) m/z calcd for $C_{19}H_{17}N_3O$ [M + H]$^+$, 304.1423; found,304.1405. HPLC purity: 98. Retention time: 13.7 min.

### 3.1.10 2-(((2-(1H-indol-3-yl)ethyl)(methyl)amino) methyl)quinolin-8-ol (4)

To a solution of **3a** (0.5 mmol) and $K_2CO_3$ (1 mmol) in acetone, $CH_3I$ (0.5 mmol) was added slowly. After being stirred at room temperature overnight, the solvent was evaporated, followed by extraction with $CH_2Cl_2$. The combined organic layer was dried over anhydrous $Na_2SO_4$ and concentrated under reduced pressure. The residue was purified by silica gel chromatography to afford yellow oil ($CH_2Cl_2$/$CH_3OH$ = 30: 1). Yellow solid, yield 66%. $^1$H NMR (400 MHz, MeOD) $\delta$ 8.16 (d, $J$ = 8.5 Hz, 1H), 7.44 (d, $J$ = 8.4 Hz, 1H), 7.41 (s, 1H), 7.39 (s, 1H), 7.33 (d, $J$ = 7.6 Hz, 1H), 7.29 (d, $J$ = 8.1 Hz, 1H), 7.10 (d, $J$ = 7.5 Hz, 1H), 7.04 (d, $J$ = 7.6 Hz, 1H), 7.02 (s, 1H), 6.88 (t, $J$ = 7.5 Hz, 1H), 4.00 (s, 2H), 3.06 (dd, $J$ = 9.8, 6.4 Hz, 2H), 2.87 (dd, $J$ = 9.7, 6.4 Hz, 2H), 2.50 (s, 3H).$^{13}$C NMR (126 MHz, MeOD) $\delta$ 156.15, 153.00, 138.01, 136.73, 136.46, 128.00, 127.22, 127.04, 121.74, 121.40, 120.87, 118.10, 117.80, 117.40, 112.18, 110.83, 110.66, 62.75, 58.27, 41.63, 22.31. HRMS (ESI) m/z calcd for $C_{21}H_{21}N_3O$ [M + H]$^+$, 332.1732; found, 332.1718. HPLC purity: 97.8%. Retention time: 11.6 min.

#### 3.1.10.1 General method for the preparation of compounds 6a-6d, 11a-11b and 13a-13c

To a solution of quinoline acid or quinoline amine (1 mmol) and indole amine or indole acid (1.3 mmol) in anhydrous $CH_2Cl_2$, HATU (1 mmol) and DIPEA (2 mmol) were added. After stirred at room temperature overnight, the reaction was extracted with $CH_2Cl_2$. The combined organic phase was dried and evaporated, the target compounds were purified by column chromatography *via* $CH_2Cl_2$/MeOH mixture. ($CH_2Cl_2$: MeOH = 50:1.)

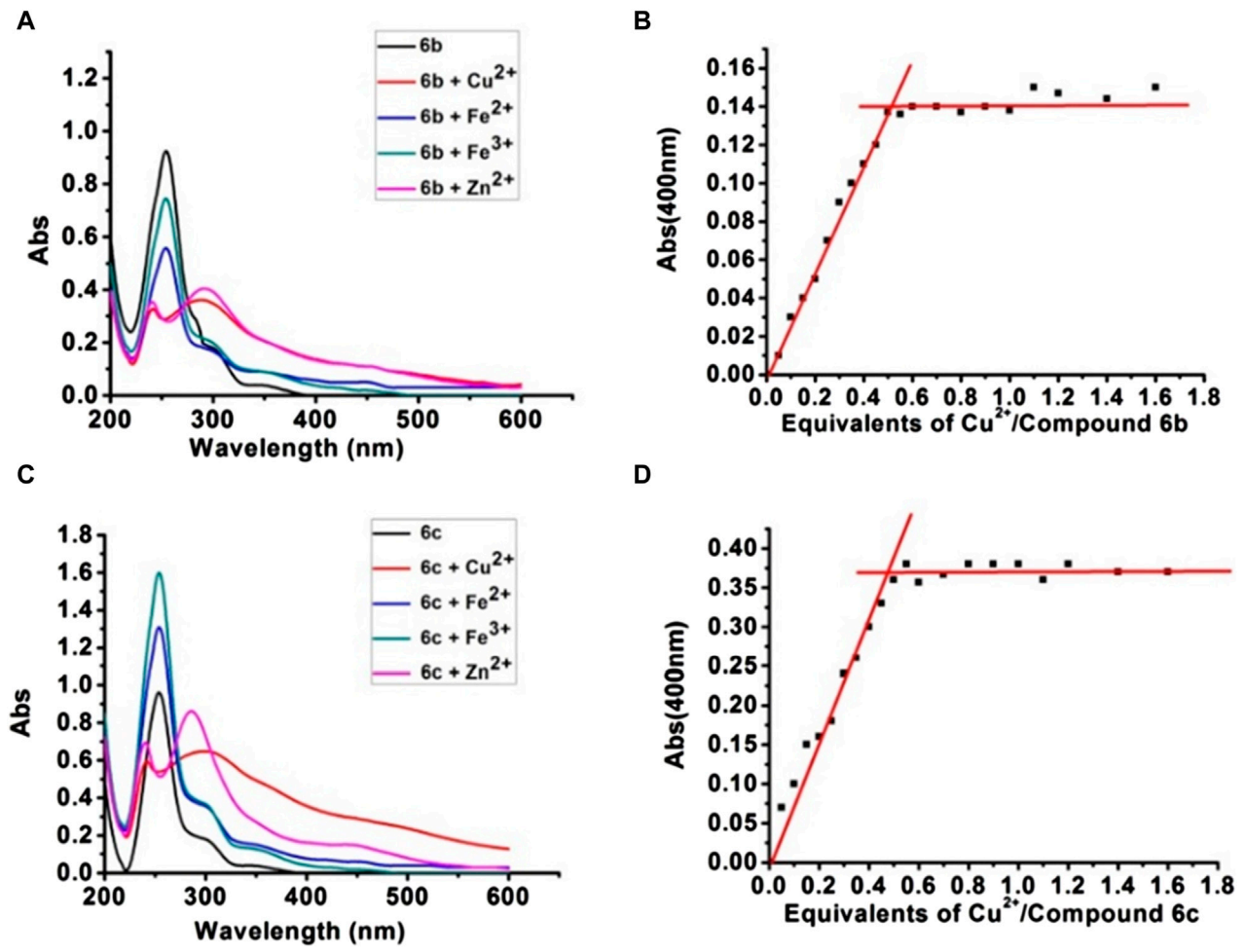


FIGURE 3
UV-vis absorption spectra of compounds **6b**, **6c** with $Cu^{2+}$, $Zn^{2+}$, $Fe^{2+}$, and $Fe^{3+}$ **(A, C)**. The chelation ratios of **6b** and **6c** to $Cu^{2+}$ **(B, D)**.

### 3.1.11 N-(2-(1H-indol-3-yl) ethyl)-8-hydroxyquinoline-2-carboxamide (6a)

Pale yellow solid, yield 60%. $^{1}$H NMR (500 MHz, DMSO-$d_6$) $\delta$ 10.85 (s, 1H), 10.13 (s, 1H), 9.82 (t, $J$ = 6.0 Hz, 1H), 8.51 (d, $J$ = 8.5 Hz, 1H), 8.17 (d, $J$ = 8.5 Hz, 1H), 7.63 (d, $J$ = 7.8 Hz, 1H), 7.57 (t, $J$ = 7.9 Hz, 1H), 7.52–7.45 (m, 1H), 7.35 (d, $J$ = 8.1 Hz, 1H), 7.22 (d, $J$ = 2.1 Hz, 1H), 7.18 (dd, $J$ = 7.6, 0.9 Hz, 1H), 7.07 (t, $J$ = 7.5 Hz, 1H), 6.99 (t, $J$ = 7.4 Hz, 1H), 3.69 (dd, $J$ = 14.7, 6.6 Hz, 2H), 3.05 (t, $J$ = 7.6 Hz, 2H). $^{13}$C NMR (126 MHz, DMSO-$d_6$) $\delta$ 164.11, 154.08, 148.09, 138.19, 136.88, 136.72, 129.92, 129.81, 127.70, 123.15, 121.44, 119.29, 118.75, 118.64, 118.01, 112.22, 111.99, 111.89, 25.90. HRMS (ESI) m/z calcd for $C_{20}H_{17}N_3O_2$ [M + H]$^+$, 332.1732; found,332.1354. HPLC purity: 98.3%. Retention time: 15.4 min.

### 3.1.12 8-hydroxy-N-(2-(5-methoxy-1H-indol-3-yl) ethyl)quinoline-2-carboxamide (6b)

Pale yellow solid, yield 62%. $^{1}$H NMR (500 MHz, DMSO-$d_6$) $\delta$ 10.69 (s, 1H), 10.15 (s, 1H), 9.83 (s, 1H), 8.50 (d, $J$ = 8.3 Hz, 1H), 8.19 (d, $J$ = 8.3 Hz, 1H), 7.57 (t, $J$ = 7.6 Hz, 1H), 7.49 (d, $J$ = 7.8 Hz, 1H), 7.25 (d, $J$ = 8.5 Hz, 1H), 7.20 (s, 1H), 7.18 (s, 1H), 7.12 (s, 1H), 6.72 (d, $J$ = 8.0 Hz, 1H), 3.72 (s, 3H), 3.69 (s, 2H), 3.04 (s, 2H). $^{13}$C NMR (126 MHz, DMSO-$d_6$) $\delta$ 164.12, 154.08, 153.48, 148.11, 138.17, 136.89, 131.84, 129.91, 129.81, 128.05, 123.83, 119.29, 118.00, 112.52, 112.12, 111.99, 111.63, 100.56, 55.71, 25.90. HRMS (ESI) m/z calcd for $C_{21}H_{19}N_3O_3$ [M + H]$^+$, 362.1471; found, 362.1460. HPLC purity: 99.6%. Retention time: 13.4 min.

### 3.1.13 8-hydroxy-N-(2-(5-hydroxy-1H-indol-3-yl) ethyl)quinoline-2-carboxamide (6c)

Pale yellow solid, yield 60%. $^{1}$H NMR (400 MHz, DMSO-$d_6$) $\delta$ 10.50 (s, 1H), 10.11 (s, 1H), 9.78 (t, $J$ = 5.8 Hz, 1H), 8.60 (s, 1H), 8.51 (d, $J$ = 8.5 Hz, 1H), 8.18 (d, $J$ = 8.5 Hz, 1H), 7.57 (t, $J$ = 7.9 Hz, 1H), 7.49 (d, $J$ = 8.0 Hz, 1H), 7.18 (d, $J$ = 7.5 Hz, 1H), 7.14 (d, $J$ = 8.6 Hz, 1H), 7.11 (d, $J$ = 1.8 Hz, 1H), 6.93 (d, $J$ = 1.9 Hz, 1H), 6.61 (dd, $J$ = 8.6, 2.1 Hz, 1H), 3.65 (dd, $J$ = 14.8, 6.6 Hz, 2H), 2.99–2.93 (m, 2H). $^{13}$C NMR (126 MHz, DMSO-$d_6$) $\delta$ 164.09, 154.07, 150.72, 148.12, 138.18, 136.89, 131.30, 129.92, 129.81, 128.37, 123.57, 119.29, 118.01, 112.18, 111.99, 111.82, 111.24, 102.70, 26.03. HRMS (ESI) m/z calcd for $C_{20}H_{17}N_3O_3$ [M + H]$^+$, 348.1313; found, 348.1303. HPLC purity: 99.5%. Retention time: 8.0 min.

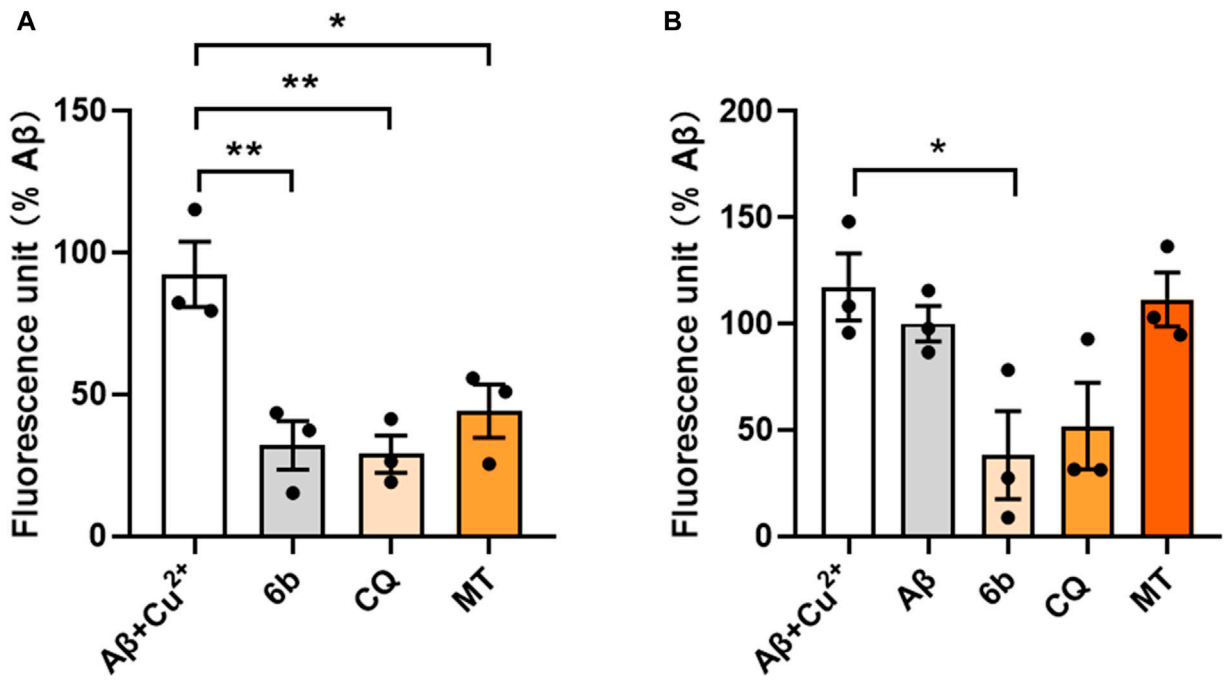


FIGURE 4
Thioflavin T fluorometric detection. Compounds were incubated before **(A)** or after **(B)** the pre-fibrillation of $A\beta_{1-42}$ and $Cu^{2+}$ at 37°C for 24 h.

### 3.1.14 N-((1H-indol-3-yl)methyl)-8 -hydroxyquinoline-2-carboxamide (6d)

Pink solid, yield 60%. $^{1}$H NMR (400 MHz, DMSO-$d_6$) $\delta$ 10.96 (s, 1H), 10.14 (s, 1H), 9.89 (t, $J$ = 5.9 Hz, 1H), 8.50 (d, $J$ = 8.6 Hz, 1H), 8.23 (t, $J$ = 8.3 Hz, 1H), 7.65 (d, $J$ = 7.9 Hz, 1H), 7.54 (t, $J$ = 7.9 Hz, 1H), 7.46 (d, $J$ = 8.1 Hz, 1H), 7.39–7.37 (m, 1H), 7.37–7.35 (m, 1H), 7.13 (d, $J$ = 7.5 Hz, 1H), 7.07 (t, $J$ = 7.5 Hz, 1H), 6.97 (t, $J$ = 7.5 Hz, 1H), 4.77 (d, $J$ = 5.9 Hz, 2H). $^{13}$C NMR (126 MHz, DMSO-$d_6$) $\delta$ 163.90, 154.13, 148.13, 138.16, 136.91, 136.87, 129.91, 129.80, 126.96, 124.49, 121.67, 119.47, 119.23, 119.07, 117.96, 112.77, 112.01, 111.98, 34.80. HRMS (ESI) m/z calcd for $C_{19}H_{15}N_3O_2$ [M + H]$^+$, 318.1573; found, 318.1198. HPLC purity: 97.9%. Retention time: 16.5 min.

### 3.1.15 N-((8-hydroxyquinolin-5-yl)methyl)-2-(1H-indol-3-yl)acetamide (11a)

Pale white solid, yield 58%. $^{1}$H NMR (400 MHz, DMSO-$d_6$) $\delta$ 10.83 (s, 1H), 9.72 (s, 1H), 8.85 (d, $J$ = 3.8 Hz, 1H), 8.43 (d, $J$ = 8.6 Hz, 1H), 8.35 (t, J = 5.1 Hz, 1H), 7.53–7.48 (m, 1H), 7.48–7.43 (m, 1H), 7.37 (d, $J$ = 7.8 Hz, 1H), 7.32 (d, $J$ = 8.1 Hz, 1H), 7.15 (s, 1H), 7.05 (t, $J$ = 7.5 Hz, 1H), 6.99 (d, $J$ = 7.7 Hz, 1H), 6.90 (t, $J$ = 7.4 Hz, 1H), 4.62 (d, $J$ = 5.5 Hz, 2H), 3.54 (s, 2H). $^{13}$C NMR (126 MHz, DMSO-$d_6$) $\delta$ 170.93, 153.21, 148.24, 139.12, 136.56, 133.23, 128.21, 127.66, 127.30, 125.53, 124.24, 122.14, 121.38, 119.19, 118.65, 111.74, 110.66, 109.32, 54.05, 33.16. HRMS (ESI) m/z calcd for $C_{20}H_{17}N_3O_2$ [M + H]$^+$, 332.1364; found, 332.1354. HPLC purity: 95.2%. Retention time: 8.2 min.

### 3.1.16 N-((8-hydroxyquinolin-5-yl)methyl)-2-(5-methoxy-1H-indol-3-yl)acetamide (11b)

Pale white solid, yield 60%. $^{1}$H NMR (400 MHz, DMSO-$d_6$) $\delta$ 10.68 (s, 1H), 9.71 (s, 1H), 8.84 (dd, $J$ = 4.0, 1.3 Hz, 1H), 8.42 (dd, $J$ = 8.5, 1.2 Hz, 1H), 8.35 (t, $J$ = 5.3 Hz, 1H), 7.47 (dd, $J$ = 8.6, 4.1 Hz, 1H), 7.38 (d, $J$ = 7.8 Hz, 1H), 7.22 (d, $J$ = 8.7 Hz, 1H), 7.12 (d, $J$ = 2.1 Hz, 1H), 6.99 (d, $J$ = 5.7 Hz, 1H), 6.98 (s, 1H), 6.70 (dd, $J$ = 8.7, 2.4 Hz, 1H), 4.63 (d, $J$ = 5.6 Hz, 2H), 3.62 (s, 3H), 3.51 (s, 2H). $^{13}$C NMR (126 MHz, MeOD) $\delta$ 173.08, 153.64, 152.64, 147.53, 138.78, 132.55, 131.89, 127.87, 127.29, 127.08, 124.42, 124.33, 121.35, 111.63, 111.50, 109.58, 107.81, 99.89, 54.63, 40.20, 32.85. HRMS (ESI) m/z calcd for $C_{21}H_{19}N_3O_3$ [M + H]$^+$, 362.1469; found, 362.1460. HPLC purity: 96.2%. Retention time: 7.5 min.

### 3.1.17 N-(2-(1H-indol-3-yl)ethyl)-8 -hydroxyquinoline-7-carboxamide (13a)

Orange solid, yield 40%. $^{1}$H NMR (400 MHz, DMSO-$d_6$) $\delta$ 10.83 (s, 1H), 9.01 (t, $J$ = 5.2 Hz, 1H), 8.92 (d, $J$ = 3.0 Hz, 1H), 8.34 (d, $J$ = 8.2 Hz, 1H), 7.99 (d, $J$ = 8.8 Hz, 1H), 7.67–7.63 (m, 1H), 7.62 (d, $J$ = 8.6 Hz, 1H), 7.42 (d, $J$ = 8.8 Hz, 1H), 7.35 (d, $J$ = 8.0 Hz, 1H), 7.22 (s, 1H), 7.08 (t, $J$ = 7.4 Hz, 1H), 6.99 (t, $J$ = 7.3 Hz, 1H), 3.66 (dd, $J$ = 13.4, 6.9 Hz, 2H), 3.03 (t, $J$ = 7.3 Hz, 2H). $^{13}$C NMR (126 MHz, DMSO-$d_6$) $\delta$ 168.62, 157.48, 149.58, 139.71, 136.75, 136.45, 131.12, 130.11, 127.68, 125.38, 123.95, 123.27, 121.45, 118.77, 117.35, 112.96, 112.08, 111.89, 40.60, 25.51. HRMS (ESI) m/z calcd for $C_{20}H_{17}N_3O_2$ [M + H]$^+$, 332.1373; found, 332.1354. HPLC purity: 98.9%. Retention time: 5.0 min.

### 3.1.18 8-hydroxy-N-(2-(5-methoxy-1H-indol-3-yl)ethyl)quinoline-7-carboxamide (13b)

Orange solid, yield 45%. $^{1}$H NMR (400 MHz, DMSO-$d_6$) $\delta$ 10.67 (s, 1H), 9.00 (t, $J$ = 5.4 Hz, 1H), 8.92 (dd, $J$ = 4.1, 1.5 Hz, 1H), 8.35 (dd, $J$ = 8.3, 1.4 Hz, 1H), 8.00 (d, $J$ = 8.8 Hz, 1H), 7.65 (dd, $J$ = 8.3, 4.2 Hz, 1H), 7.42 (d, $J$ = 8.8 Hz, 1H), 7.24 (d, $J$ = 8.7 Hz, 1H), 7.18 (d, $J$ = 2.1 Hz, 1H), 7.09 (d, $J$ = 2.2 Hz, 1H), 6.72 (dd, $J$ = 8.7, 2.3 Hz, 1H), 3.66 (dd, $J$ = 13.2, 7.0 Hz, 2H), 3.00 (t, $J$ = 7.3 Hz, 2H). $^{13}$C NMR

(126 MHz, DMSO-$d_6$) $\delta$ 168.62, 157.44, 153.48, 149.58, 139.67, 136.47, 131.87, 131.11, 128.03, 125.38, 123.96, 123.93, 117.35, 112.96, 112.53, 111.93, 111.62, 100.58, 55.71, 40.61, 25.48. HRMS (ESI) m/z calcd for $C_{21}H_{19}N_3O_3$ [M + H]$^+$, 362.1466; found, 362.1460. HPLC purity: 97.5%. Retention time: 5.1 min.

#### 3.1.19 N-((1H-indol-3-yl)methyl) -8-hydroxyquinoline-7-carboxamide (13c)

Orange solid, yield 50%. $^1$H NMR (400 MHz, DMSO-$d_6$) $\delta$ 11.00 (s, 1H), 9.12 (t, $J$ = 5.2 Hz, 1H), 8.90 (dd, $J$ = 4.1, 1.4 Hz, 1H), 8.34 (dd, $J$ = 8.3, 1.4 Hz, 1H), 8.06 (d, $J$ = 8.8 Hz, 1H), 7.70–7.65 (m, 1H), 7.65–7.62 (m, 1H), 7.41 (d, $J$ = 8.8 Hz, 1H), 7.41–7.38 (m, 1H), 7.38–7.36 (m, 1H), 4.75 (d, $J$ = 5.4 Hz, 2H). $^{13}$C NMR (126 MHz, DMSO-$d_6$) $\delta$ 167.89, 157.00, 149.47, 139.58, 136.81, 136.51, 131.06, 126.94, 125.77, 124.75, 123.93, 121.70, 119.17, 119.10, 117.36, 113.23, 112.19, 112.01, 35.04. HRMS (ESI) m/z calcd for $C_{19}H_{15}N_3O_2$ [M + H]$^+$, 318.1219; found, 318.1198. HPLC purity: 99.5%. Retention time: 4.7 min.

### 3.2 Thioflavin T fluorometric detection

Detection of the compounds for disaggregated and inhibitory effects on $Cu^{2+}$ induced $A\beta_{1\text{-}42}$ aggregation. $A\beta_{1\text{-}42}$ (Sigma-Aldrich A9810, 20 μM) was dissolved in HEPES buffer (pH = 6.6, containing 1% ammonium hydroxide). 10 μL of $A\beta_{1\text{-}42}$ was previously incubated with or without $Cu^{2+}$ at 37°C for 3 days to pre-fibrillation. 10 μL of **6b**, CQ, and MT (150 μM, in DMSO) were incubated before or after the pre-fibrillation of $A\beta_{1\text{-}42}$ at 37°C for 1 day. After incubation, 170 μL of thioflavin T (5 μM, in 50 mM glycine-NaOH buffer) was added to mix well. After incubation for 5 min, the $A\beta_{1\text{-}42}$ aggregation was detected by Microplate Reader (HITACHI, F-4700) with excitation/emission at 450/485 nm.

#### 3.2.1 Oxygen radical absorbance capacity (ORAC-FL) assay

The testes compounds and fluorescein (FL) stock solution were diluted with 75 mM phosphate buffer (pH 7.4) to 5 μM and 0.117 μM, respectively (Wang et al., 2018). The solution of Trolox was diluted with 75 mM phosphate buffer to 40, 20, 10, 5, 2.5, and 1.25 μM. The solution of 2,2′-azobis- (amidinopropane) dihydrochloride (AAPH) was prepared to a final concentration of 40 mM. The mixture of the tested compounds (20 μL) and FL (120 μL; 70 nM) was pre-incubated for 10 min at 37°C, 60 μL of the AAPH solution was added. The fluorescence was recorded every minute for 120 min (excitation, 485 nm; emission, 520 nm). The antioxidant curves (fluorescence versus time) were normalized to the curve of the blank. The area under the fluorescence decay curve (AUC) was calculated as the following equation:

$$\mathrm{AUC} = 1 + \sum_{i=1}^{i=120} fi/f0$$

Where $f0$ is the initial fluorescence reading at 0 min and $fi$ is the fluorescence reading at time i. The net AUC was calculated by the expression: $AUC_{sample}$—$AUC_{blank}$. Regression equations between net AUC and Trolox concentration were calculated. ORAC-FL value of the tested compound expressed as Trolox equivalents.

#### 3.2.2 Inhibition of $A\beta_{1-42}$ aggregation assay

Following the previous literature (Rosini et al., 2008; Wang et al., 2018), $A\beta_{1-42}$ (Sigma-Aldrich) was dissolved in $NH_4OH$ (1% v/v) to get a stock solution, which was aliquoted into small samples and stored at −80°C.

#### 3.2.3 Metal-chelating study

**6b** and **6c** (50 μM) were incubated with $CuSO_4$, $FeSO_4$, $FeCl_3$, or $ZnCl_2$ (50 μM) in buffer (20 mM HEPES, 150 mM NaCl, pH 7.4) for 30 min, and the absorption spectras were recorded at room temperature. For the stoichiometry of the compound–$Cu^{2+}$ complex, a fixed amount of **6b** and **6c** (50 μM) was mixed with growing amounts of copper ion (0–100 μM), and the difference UV–vis spectra were examined to investigate the ratio of ligand/metal in the complex.

#### 3.2.4 Statistical analysis

Data were presented as mean ± standard deviation (SD) (represented by error bars). All the experiments had three replicates ($n$ = 3). *In vivo* anti-tumor Student's $t$-test was used for comparing two groups, and significant differences were indicated by $^*p < 0.05$, $^*p < 0.01$, $^{***}p < 0.001$. The statistical analysis was performed with GraphPad Prism 8.0.1.

## 4 Conclusion

In this study, a series of novel melatonin–hydroxyquinoline hybrids were designed and synthesized, simultaneously targeting anti-oxidation and metal-chelating. Most of the compounds possess good blood-brain barrier permeability and showed significant oxygen radical absorbance capacity and $A\beta_{1-42}$ aggregation inhibition. Among them, **6b** and **6c** have a good ability to alleviate oxidative stress (Figure 2C) induced by hydrogen peroxide and exhibit metal-chelating properties with the chelation ratio being 2:1. Furthermore, **6b** can significantly mitigate metal ion induced Aβ aggregation.

## Data availability statement

The datasets presented in this study can be found in online repositories. The names of the repository/repositories and accession number(s) can be found in the article/Supplementary Material.

## Author contributions

WW: Writing–original draft, Investigation, Methodology, Validation. TP: Investigation, Methodology, Writing–original draft. RS: Methodology, Writing–original draft, Formal Analysis. MC: Writing–original draft, Data curation. WX: Writing–original draft, Methodology. CX: Writing–original draft, Conceptualization, Funding acquisition, Writing–review and editing. LH: Conceptualization, Supervision, Writing–review and editing.

## Funding

The author(s) declare financial support was received for the research, authorship, and/or publication of this article. This study was supported by the National Natural Science Foundation of China (82160653 to LH and 82204193 to CX), Hainan Provincial Natural Science Foundation of China (822MS052 to CX), Natural Science Foundation of Guangdong Province (2022A1515012527 to CX).

## Conflict of interest

The authors declare that the research was conducted in the absence of any commercial or financial relationships that could be construed as a potential conflict of interest.

## Publisher's note

All claims expressed in this article are solely those of the authors and do not necessarily represent those of their affiliated organizations, or those of the publisher, the editors and the reviewers. Any product that may be evaluated in this article, or claim that may be made by its manufacturer, is not guaranteed or endorsed by the publisher.

## Supplementary material

The Supplementary Material for this article can be found online at: https://www.frontiersin.org/articles/10.3389/fchem.2024.1374930/full#supplementary-material

## References

Adlard, P. A., Cherny, R. A., Finkelstein, D. I., Gautier, E., Robb, E., Cortes, M., et al. (2008). Rapid restoration of cognition in Alzheimer's transgenic mice with 8-hydroxy quinoline analogs is associated with decreased interstitial Aβ. *Neuron* 59, 43–55. doi:10.1016/j.neuron.2008.06.018

Author Anonymous (2023). Alzheimer's disease facts and figures. *Alzheimers Dement.* 19, 1598–1695. doi:10.1002/alz.12328

Babaei, E., Kucukkilinc, T. T., Jalili-Baleh, L., Nadri, H., Oz, E., Forootanfar, H., et al. (2022). Novel coumarin-pyridine hybrids as potent multi-target directed ligands aiming at symptoms of Alzheimer's disease. *Front. Chem.* 10, 895483. doi:10.3389/fchem.2022.895483

Cerejeira, J., Lagarto, L., and Mukaetova-Ladinska, E. B. (2012). Behavioral and psychological symptoms of dementia. *Front. Neurol.* 3, 73. doi:10.3389/fneur.2012.00073

Di, L., Kerns, E. H., Fan, K., McConnell, O. J., and Carter, G. T. (2003). High throughput artificial membrane permeability assay for blood-brain barrier. *Eur. J. Med. Chem.* 38, 223–232. doi:10.1016/s0223-5234(03)00012-6

Dowling, G. A., Burr, R. L., Van Someren, E. J., Hubbard, E. M., Luxenberg, J. S., Mastick, J., et al. (2008). Melatonin and bright-light treatment for rest-activity disruption in institutionalized patients with Alzheimer's disease. *J. Am. Geriatr. Soc.* 56, 239–246. doi:10.1111/j.1532-5415.2007.01543.x

Faux, N. G., Ritchie, C. W., Gunn, A., Rembach, A., Tsatsanis, A., Bedo, J., et al. (2010). PBT2 rapidly improves cognition in Alzheimer's disease: additional phase II analyses. *J. Alzheimers. Dis.* 20, 509–516. doi:10.3233/jad-2010-1390

Geng, J., Li, M., Wu, L., Ren, J., and Qu, X. (2012). Liberation of copper from amyloid plaques: making a risk factor useful for Alzheimer's disease treatment. *J. Med. Chem.* 55, 9146–9155. doi:10.1021/jm3003813

He, L., Du, J. J., Zhou, J. J., Chen, M. T., Luo, L., Li, B. Q., et al. (2022). Synthesis of melatonin derivatives and the neuroprotective effects on Parkinson's disease models of *Caenorhabditis elegans*. *Front. Chem.* 10, 918116. doi:10.3389/fchem.2022.918116

Hu, J., Pan, T., An, B., Li, Z., Li, X., and Huang, L. (2019). Synthesis and evaluation of clioquinol-rolipram/roflumilast hybrids as multitarget-directed ligands for the treatment of Alzheimer's disease. *Eur. J. Med. Chem.* 163, 512–526. doi:10.1016/j.ejmech.2018.12.013

Lu, C., Guo, Y., Yan, J., Luo, Z., Luo, H. B., Yan, M., et al. (2013). Design, synthesis, and evaluation of multitarget-directed resveratrol derivatives for the treatment of Alzheimer's disease. *J. Med. Chem.* 56, 5843–5859. doi:10.1021/jm400567s

Marcinkowska, M., Bucki, A., Sniecikowska, J., Zagórska, A., Fajkis-Zajączkowska, N., Siwek, A., et al. (2021). Multifunctional arylsulfone and arylsulfonamide-based ligands with prominent mood-modulating activity and benign safety profile, targeting neuropsychiatric symptoms of dementia. *J. Med. Chem.* 64, 12603–12629. doi:10.1021/acs.jmedchem.1c00497

Reiter, R. J., Mayo, J. C., Tan, D. X., Sainz, R. M., Alatorre-Jimenez, M., and Qin, L. L. (2016). Melatonin as an antioxidant: under promises but over delivers. *J. Pineal Res.* 61, 253–278. doi:10.1111/jpi.12360

Rosini, M., Simoni, E., Bartolini, M., Cavalli, A., Ceccarini, L., Pascu, N., et al. (2008). Inhibition of acetylcholinesterase, β-amyloid aggregation, and nmda receptors in Alzheimer's disease: a promising direction for the multi-target-directed ligands gold rush. *J. Med. Chem.* 51, 4381–4384. doi:10.1021/jm800577j

Rossi, M., Freschi, M., de Camargo Nascente, L., Salerno, A., de Melo Viana Teixeira, S., Nachon, F., et al. (2021). Sustainable drug discovery of multi-target-directed ligands for Alzheimer's disease. *J. Med. Chem.* 64, 4972–4990. doi:10.1021/acs.jmedchem.1c00048

Scheltens, P., De Strooper, B., Kivipelto, M., Holstege, H., Chételat, G., Teunissen, C. E., et al. (2021). Alzheimer's disease. *Lancet* 397, 1577–1590. doi:10.1016/s0140-6736(20)32205-4

Somalo-Barranco, G., Serra, C., Lyons, D., Piggins, H. D., Jockers, R., and Llebaria, A. (2022). Design and validation of the first family of photo-activatable ligands for melatonin receptors. *J. Med. Chem.* 65, 11229–11240. doi:10.1021/acs.jmedchem.2c00717

Turgutalp, B., Bhattarai, P., Ercetin, T., Luise, C., Reis, R., Gurdal, E. E., et al. (2022). Discovery of potent cholinesterase inhibition-based multi-target-directed lead compounds for synaptoprotection in Alzheimer's disease. *J. Med. Chem.* 65, 12292–12318. doi:10.1021/acs.jmedchem.2c01003

Wang, Z., Hu, J., Yang, X., Feng, X., Li, X., Huang, L., et al. (2018). Design, synthesis, and evaluation of orally bioavailable quinoline–indole derivatives as innovative multitarget-directed ligands: promotion of cell proliferation in the adult murine Hippocampus for the treatment of Alzheimer's disease. *J. Med. Chem.* 61, 1871–1894. doi:10.1021/acs.jmedchem.7b01417

Wang, Z., Wang, Y., Li, W., Mao, F., Sun, Y., Huang, L., et al. (2014). Design, synthesis, and evaluation of multitarget-directed selenium-containing clioquinol derivatives for the treatment of Alzheimer's disease. *ACS Chem. Neurosci.* 5, 952–962. doi:10.1021/cn500119g

Wang, Z., Wang, Y., Wang, B., Li, W., Huang, L., and Li, X. (2015). Design, synthesis, and evaluation of orally available clioquinol-moracin M hybrids as multitarget-directed ligands for cognitive improvement in a rat model of neurodegeneration in Alzheimer's disease. *J. Med. Chem.* 58, 8616–8637. doi:10.1021/acs.jmedchem.5b01222

Xu, C., Yang, H., Xiao, Z., Zhang, T., Guan, Z., Chen, J., et al. (2021). Reduction-responsive dehydroepiandrosterone prodrug nanoparticles loaded with camptothecin for cancer therapy by enhancing oxidation therapy and cell replication inhibition. *Int. J. Pharm.* 603, 120671. doi:10.1016/j.ijpharm.2021.120671

frontiers | Frontiers in Pharmacology

TYPE Original Research
PUBLISHED 25 April 2024
DOI 10.3389/fphar.2024.1396641

Check for updates

OPEN ACCESS

EDITED BY
Xi Zheng,
Rutgers, The State University of New Jersey, United States

REVIEWED BY
Xiaohu Kang,
Lanzhou Jiaotong University, China
Huaichun Yang,
Shanghai Jiao Tong University, China

*CORRESPONDENCE
Rihui Wu,
wyuchemwrh@126.com
Wen-Hua Chen,
whchen@wyu.edu.cn
Chen Li,
chenli@wyu.edu.cn

†These authors have contributed equally to this work

RECEIVED 06 March 2024
ACCEPTED 09 April 2024
PUBLISHED 25 April 2024

CITATION
Huang Y, Zhang X, Li Q, Zheng W, Wu P, Wu R, Chen W-H and Li C (2024), N-*p*-coumaroyloctopamine ameliorates hepatic glucose metabolism and oxidative stress involved in a PI3K/AKT/GSK3β pathway. *Front. Pharmacol.* 15:1396641. doi: 10.3389/fphar.2024.1396641

COPYRIGHT
© 2024 Huang, Zhang, Li, Zheng, Wu, Wu, Chen and Li. This is an open-access article distributed under the terms of the Creative Commons Attribution License (CC BY). The use, distribution or reproduction in other forums is permitted, provided the original author(s) and the copyright owner(s) are credited and that the original publication in this journal is cited, in accordance with accepted academic practice. No use, distribution or reproduction is permitted which does not comply with these terms.

# N-*p*-coumaroyloctopamine ameliorates hepatic glucose metabolism and oxidative stress involved in a PI3K/AKT/GSK3β pathway

Yuechang Huang[1,2,3†], Xingmin Zhang[1,2,3†], Qian Li[1,2,3], Wende Zheng[1,2,3], Panpan Wu[1,2,3], Rihui Wu[1,2,3*], Wen-Hua Chen[1,2,3*] and Chen Li[1,2,3*]

[1]School of Pharmacy and Food Engineering, Wuyi University, Jiangmen, China, [2]International Healthcare Innovation Institute (Jiangmen), Jiangmen, China, [3]Guangdong Provincial Key Laboratory of Large Animal Models for Biomedicine, Wuyi University, Jiangmen, China

Type 2 diabetes mellitus is regarded as a chronic metabolic disease characterized by hyperglycemia. Long-term hyperglycemia may result in oxidative stress, damage pancreatic β-cell function and induce insulin resistance. Herein we explored the anti-hypoglycemic effects and mechanisms of action of N-*p*-coumaroyloctopamine (N-p-CO) *in vitro* and *in vivo*. N-p-CO exhibited high antioxidant activity, as indicated by the increased activity of SOD, GSH and GSH-Px in HL-7702 cells induced by both high glucose (HG) and palmitic acid (PA). N-p-CO treatment significantly augmented glucose uptake and glycogen synthesis in HG/PA-treated HL-7702 cells. Moreover, administration of N-p-CO in diabetic mice induced by both high-fat diet (HFD) and streptozotocin (STZ) not only significantly increased the antioxidant levels of GSH-PX, SOD and GSH, but also dramatically alleviated hyperglycemia and hepatic glucose metabolism in a dose-dependent manner. More importantly, N-p-CO upregulated the expressions of PI3K, AKT and GSK3β proteins in both HG/PA-induced HL-7702 cells and HFD/STZ-induced mice. These findings clearly suggest that N-p-CO exerts anti-hypoglycemic and anti-oxidant effects, most probably via the regulation of a PI3K/AKT/GSK3β signaling pathway. Thus, N-p-CO may have high potentials as a new candidate for the prevention and treatment of diabetes.

KEYWORDS

**N-p-coumaroyloctopamine, diabetes, oxidative stress, hyperglycemia, mechanism of action**

## 1 Introduction

Diabetes is a chronic metabolic disorder characterized by persistent dysregulation of glucose and lipid metabolism (Huang et al., 2023; Hu et al., 2024). Currently, type 2 diabetes (T2DM) accounts for approximately 90% of the global diabetes cases, which significantly exacerbates physical and economic burdens for individuals (Kane et al., 2018). More and more evidences have suggested that diabetes is a multifactorial disease accompanied by the dysregulation of lipid and glucose metabolism, and oxidative stress,

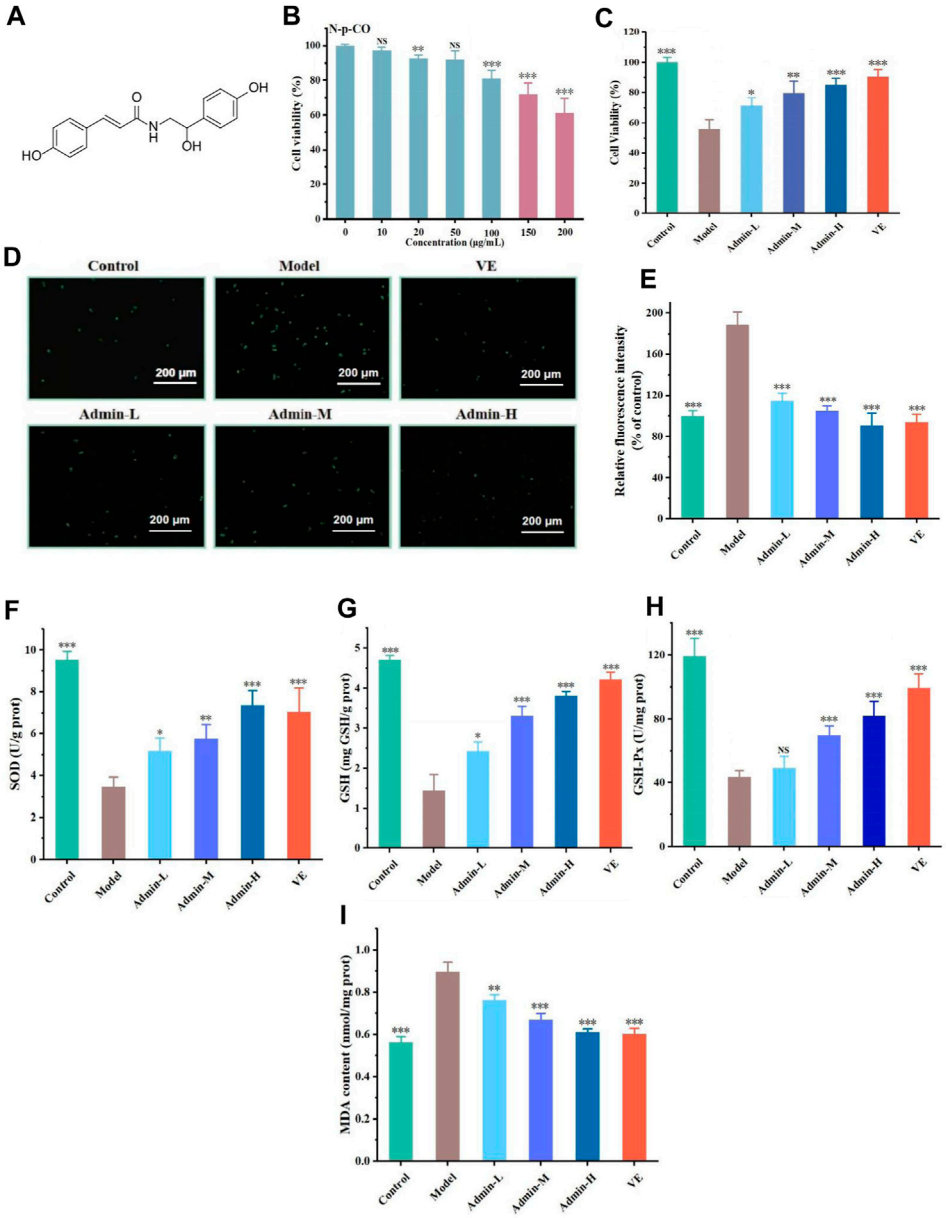


FIGURE 1
N-p-CO treatment increased the antioxidant capacity in HL-7702 cells exposed to both HG and PA. **(A)** Structure of N-p-CO; **(B)** Cytotoxicity of N-p-CO on HL-7702 cells; **(C)** Effects of different concentrations of N-p-CO on the viability of HG/PA-induced HL-7702 cells; **(D)** Representative images of ROS fluorescence staining; **(E)** Relative fluorescence intensity of ROS; **(F–I)** Contents of SOD, GSH, GSH-Px and MDA in HG/PA-induced HL-7702 cells. Data were represented as mean ± SD ($n$ = 3). *$p$ < 0.05, **$p$ < 0.01 and ***$p$ < 0.001 compared with the model group.

which plays an important role in the occurrence and development of diabetes (Maria and Mattias, 2017; Hu et al., 2020; Sourbh and Jeena, 2022). The long-term hyperglycemia in patients with diabetes may lead to chronic injury and dysfunction of various tissues (Satman et al., 2023; Min et al., 2024). Although the commonly used hypoglycemic clinical agents, such as metformin and glibenclamide can lower blood glucose, they often induce a range of side effects including diarrhea, intestinal flatulence, hemolytic anemia, lactic acidosis and congestive heart failure (Xing et al., 2021; Elkhalifa et al., 2024). Therefore, it is imperative to develop novel hypoglycemic agents with low adverse effects.

It is known that oxidative stress has been regarded as a pathological mechanism that contributes to the initiation and progression of T2DM and related complications (Jiang et al., 2020; Argaev-Frenkel and Rosenzweig, 2023). It is a cytotoxic consequence of excessive reactive oxygen species (ROS) production and inhibition of ROS elimination in antioxidant defense systems (Hasandeep et al., 2023). Chronic long-term exposure of hyperglycemia may result in oxidative stress, activate several pathways including protein kinase C (PKC), phosphatidylinositol 3-kinase (PI3K) and serine/threonine protein kinase AKT, and facilitate the formation of advanced glycation end-products (AGEs). The activation of these signaling

pathways eventually alters gene expressions and physiological metabolism, leading to organ dysfunction (Hasandeep et al., 2023). Liver is the major regulator for carbohydrate metabolism and lipid biosynthesis (Adeva-Andany et al., 2016). In the setting of T2DM, the disordered oxidation of these substrates can induce excessive levels of systemic glucose and lipid and oxidative stress. These alterations are also accompanied by the disturbance in the metabolism of hepatocellular glucose. Thus, targeting hepatic glucose and glycogen metabolism has been considered as a strategy for the treatment of T2DM (Rines et al., 2016). Several studies have reported that remission of oxidative stress by natural products from plants, such as polyphenols, polysaccharides and flavones, contributes to the improvement of glycolipid metabolism and diabetic phenotype (Chen et al., 2022; He et al., 2022; Zhou et al., 2023). As a naturally-occurring hydroxycinnamoyl amide compound, N-p-coumaroyloctopamine (N-p-CO, Figure 1A) widely exists in alliums, eggplants, potatoes and the like (Hisashi et al., 1998). N-p-CO-enriched allium crude extracts have been found to effectively inhibit the activity of α-glucosidase *in vitro* (Jeppe et al., 2014). In addition, N-p-CO exhibits excellent antioxidant activity (Ayanlowo et al., 2020) and anti-inflammatory activity to reduce the levels of inflammatory cytokines in lipopolysaccharide (LPS)-induced human peripheral blood mononuclear cell (Nchiozem-Ngnitedem et al., 2020). Both biological effects are helpful for the mitigation of diabetes. Thus, it is of great significance to reveal the potential anti-diabetic effects and mechanisms of action of N-p-CO.

In the work reported herein, we sought to evaluate the antioxidant and hypoglycemic effects of N-p-CO in both high glucose (HG)/palmitic acid (PA)-induced HL-7702 cells and high-fat diet (HFD)/treptozotocin (STZ)-induced mice, and recovered the PI3K/AKT/GSK3β pathway involved in the alleviation of N-p-CO on hepatic glucose metabolism.

# 2 Materials and methods

## 2.1 Cell culture

HL-7702 cells were originally obtained from the American Type Culture Collection (ATCC), and cultured in Dulbecco's Modification of Eagle's Medium (DMEM, Servicebio, Wuhan, China) supplemented with 10% fetal bovine serum (FBS, PAN, German) and 100 U/mL penicillin and 100 μg/mL streptomycin (HyClone, Logan, United States) at 37°C with 5% carbon dioxide in a humidified incubator prior to treatment.

## 2.2 Cell treatment and bioactivity assay

HL-7702 cells were plated in a 96-well plate with a density of $1 \times 10^5$ cells per well for 24 h and incubated for an additional 24 h with serum-free medium in combination with or without 30 mM glucose, 0.2 mM PA, or 0–200 μg/mL N-p-CO (Macklin, Shanghai, China). The cytotoxicity of N-p-CO was measured using a 3-[4,5-dimethylthiazol-2-yl]-2,5-diphenyltetrazolium bromide (MTT, Biofroxx, Einhausen, German) assay according to previous methods (Wang et al., 2020). Briefly, after treatment with N-p-CO, MTT (5 mg/mL, 20 μL) was added to each well for 4 h and then dimethyl sulfoxide (DMSO, 150 μL) was added. The absorbance was determined at 490 nm on a Microplate Reader (BioTek, Vermont, United States).

## 2.3 Assessment of cellular glucose consumption and uptake

For the consumption of cellular glucose, after treatment with or without N-p-CO (10 μg/mL, 20 μg/mL and 50 μg/mL) or Metformin (Met, HPLC >97%, Macklin, Shanghai, China; 50 μg/mL), the culture supernatant of HL-7702 cells induced by both PA (0.2 mM) and glucose (30 mM) was collected and quantified using a sulfate-anthrone method. The concentration of glucose was determined using a standard curve of glucose under an absorbance of 620 nm.

The glucose uptake was measured according to a previous method (Ye et al., 2022). In brief, after treatments with N-p-CO of varying concentrations, the HL-7702 cells were washed with PBS (Adamas life, Shanghai, China) and then incubated with fluorescent deoxyglucose derivative (2-NBDG, Invivochem, Guangzhou, China; 100 μM) at 37°C for 30 min. Subsequently, fluorescence microscopy (Olympus, Nagano, Japan) was used to detect cellular fluorescence intensity.

## 2.4 Determination of cell glycogen

The content of glycogen in cells was determined using the method described before (Huang et al., 2015). Briefly, cells supernatant was air-dried naturally and the mass was quantified. A solution containing 30% KOH (Aladdin, Shanghai, China) was added and heated in a water bath for 30 min. Then anhydrous ethanol (1.5 mL) was added and centrifuged at 12,000 g for 15 min at 4°C. The glucose content was determined using a sulfuric acid-anthrone (Macklin, Shanghai, China) method.

## 2.5 Animal model and experimental design

6–8 Week-old C57BL/6 healthy male mice (20 ± 2 g) were obtained from BesTest Biotechnology Co., LTD (Zhuhai, Guangdong, China) and housed under standard specific pathogen-free (SPF) conditions with a constant temperature of 25°C and a 12-h light/dark cycle. To induce T2DM, the mice were adapted for 7 days and treated with both high-fat and high-sugar diets (D12492, Xiao Shu You Tai, Beijing, China) and intraperitoneal STZ (Biofiven, Guangzhou, China). The mice in a control group received a normal diet. The mice in the other groups were fed with a high-fat and high-sugar diet. The mice in the experimental groups were fasted for 12 h and intraperitoneally injected with 40 mg/kg STZ dissolved in sodium citrate buffer solution (pH 4.4) (Xu et al., 2020). The mice in normal control group was administered with an equal

volume of citric acid-sodium citrate buffer solution instead of STZ injection. Mice with T2DM were identified using fasting blood glucose levels at ≥ 16 mmol/L after 5 days and selected for further treatment. Diabetic mice were randomly divided into four groups ($n$ = 5), that is, diabetic model group (DM), positive control group (*i.p.* 200 mg/kg metformin, DM-Met), low-dose group (*i.p.* 5 mg/kg N-p-CO, DM-L) and high-dose group (*i.p.* 10 mg/kg N-p-CO, DM-H). The mice in normal control and diabetic model groups received an equal volume of normal saline for 5 weeks.

## 2.6 Oral glucose tolerance test (OGTT)

After treatment for 5 weeks, mice were fasted overnight and given 2 g/kg glucose by oral gavage. The blood glucose of mice was measured with a blood glucose meter (Sinocare, Shenzhen, China) after glucose administration for 0, 30, 60, 90, and 120 min. The area under the curve (AUC) was calculated to give the OGTT of mice.

## 2.7 Oxidation detection

The antioxidant activity of N-p-CO was assessed by measuring the contents of ROS, superoxide dismutase (SOD), glutathione (GSH), glutathione peroxidases GSH-px and malondialdehyde (MDA). For the detection of cellular antioxidant activity, the level of ROS was measured by using a 2,7-dichlorodihdrofluorescein diacetate (DCFH-DA) probe staining method in lined with previous reports (Sun et al., 2021; Zhang et al., 2021). Briefly, HL-7702 cells were plated in a 96-well plate with a density of $1 \times 10^5$ cells per well for 24 h and incubated for an additional 24 h with serum-free medium, 30 mM glucose, 0.2 mM PA, or 0, 10, 20 and 50 μg/mL N-p-CO (Ye et al., 2024). The content of ROS was measured using a ROS detection kit and observed with fluorescence microscope.

For the detection of SOD, GSH, GSH-px and MDA in cells and liver, cell culture supernatant or heptic homogenate was determined by using commercial reagent kits (Nanjing Jiancheng Bioengineering Institute, Nanjing, China) following the manufacturer's instructions with mild modifications (Sun et al., 2020; Zhang et al., 2021).

## 2.8 Serum biochemical analysis

Serum and hepatic levels of alanine aminotransferase (ALT), aspartate transaminase (AST) and glycated serum protein (GSP) were detected by commercial assay kits in line with the manufacturer's protocol with mild adjustments (Qi et al., 2022).

## 2.9 Histopathological examination

Histopathological examination of liver was performed with a standard process with mild modifications (Ma et al., 2023; Zhang et al., 2023). The liver tissue from the mice was fixed with 4% paraformaldehyde solution for 24 h, dehydrated with gradient ethanol solution and embedded in paraffin. Sections (4 μm) were prepared and stained with hematoxylin and eosin (H&E) and periodic acid-schiff (PAS) staining, respectively. The morphology was obtained with a light microscope (Olympus, Nagano, Japan).

## 2.10 Western blot assay

The western blot assay was performed using the procedures previously described (Tao et al., 2020; Wang et al., 2021; Sun et al., 2023). The total protein of liver or cells was extracted with the RIPA lysis buffer and quantified with a BCA protein detection kit (Aidlab, Beijing, China). Each sample was loaded with 1 μL protein, separated with 10% SDS-PAGE and transferred onto a PVDF membrane (Millipore, Massachusetts, United States). Membrane binding proteins were blocked with 10% milk (Yili, Neimenggu, China) at room temperature for 1 h. Subsequently, primary antibodies including AMPK (1:1,000, Cell Signaling Technology, MA, United States), GLUT2 (1:1,000, Cell Signaling Technology, MA, United States), PI3K (1:1,000, Cell Signaling Technology, MA, United States), AKT (1:1,000, Cell Signaling Technology, MA, United States), GSK3β (1:1,000, Cell Signaling Technology, MA, United States), p-GSK3β (1:1,000, Cell Signaling Technology, MA, United States) and β-actin (1:1,000, Cell Signaling Technology, MA, United States), were incubated overnight at 4°C followed by three washes with Tris-buffered saline Tween-20 (TBST) (Sinopharm, Beijing, China). The membrane was then incubated with a horseradish peroxidase-labeled secondary antibody (1:2000, Sarvicebio, Wuhan, China) at room temperature for another 1 h and washed three times with TBST. Finally, the membrane-bound proteins were detected using an ECL detection reagent (Beyotime, Shanghai, China) and visualized on an Image Quant LAS-4000 digital imaging system (GE Healthcare Bio-Sciences, Uppsala, Sweden).

## 2.11 qPCR analysis

The relative expressions of genes were conducted according to established protocols (Wang and Mu, 2021; Hao et al., 2022; Liu et al., 2022). Total RNA from the cells was extracted using a Trizol extraction reagent (Biosharp, Guangzhou, China). The RNA was reversed into c-DNA using an RT reagent kit (ThermoFisher, Massachusetts, United States). qRT-PCR was performed using a TB Green kit (Servicebio, Wuhan, China) on the Applied Biosystems Step One RT-PCR system (Applied Biosystems, Forster city, United States). The primer sequences of the target genes are listed in Table 1.

## 2.12 Statistical analysis

Data are presented as mean ± standard deviation. One-way analysis of variance (ANOVA) was performed to analyze the significant differences among groups by IBM SPSS Statistics 26.0 (SPSS Inc., Chicago, United States). Results were visualized using

TABLE 1 Primers for the PCR assay.

| Name | Forward primer (5′-3′) | Reverse primer (5′-3′) |
|---|---|---|
| GSK3β | GACAGTGGTGTGGATCAGTTGGTG | GCGATTGCCTCTGGTGGAGTTC |
| GLUT2 | CACCAGCACATACGACACCAGAC | CCCAAGCCACCCACCAAAGAAC |
| PI3K | AGGATGCCCAACTTGATGCTGATG | CCCGTTCATATAGGGTGTCGCTGTG |
| AMPKα | CAACTATCGATCTTGCCAAAGG | AACAGGAGAAGAGTCAAGTGAG |
| AKT | TGACCATGAACGAGTTTGAGTA | GAGGATCTTCATGGCGTAGTAG |
| β-Actin | ATGTGGATCAGCAAGCAGGA | ATGTGGATCAGCAAGCAGGA |

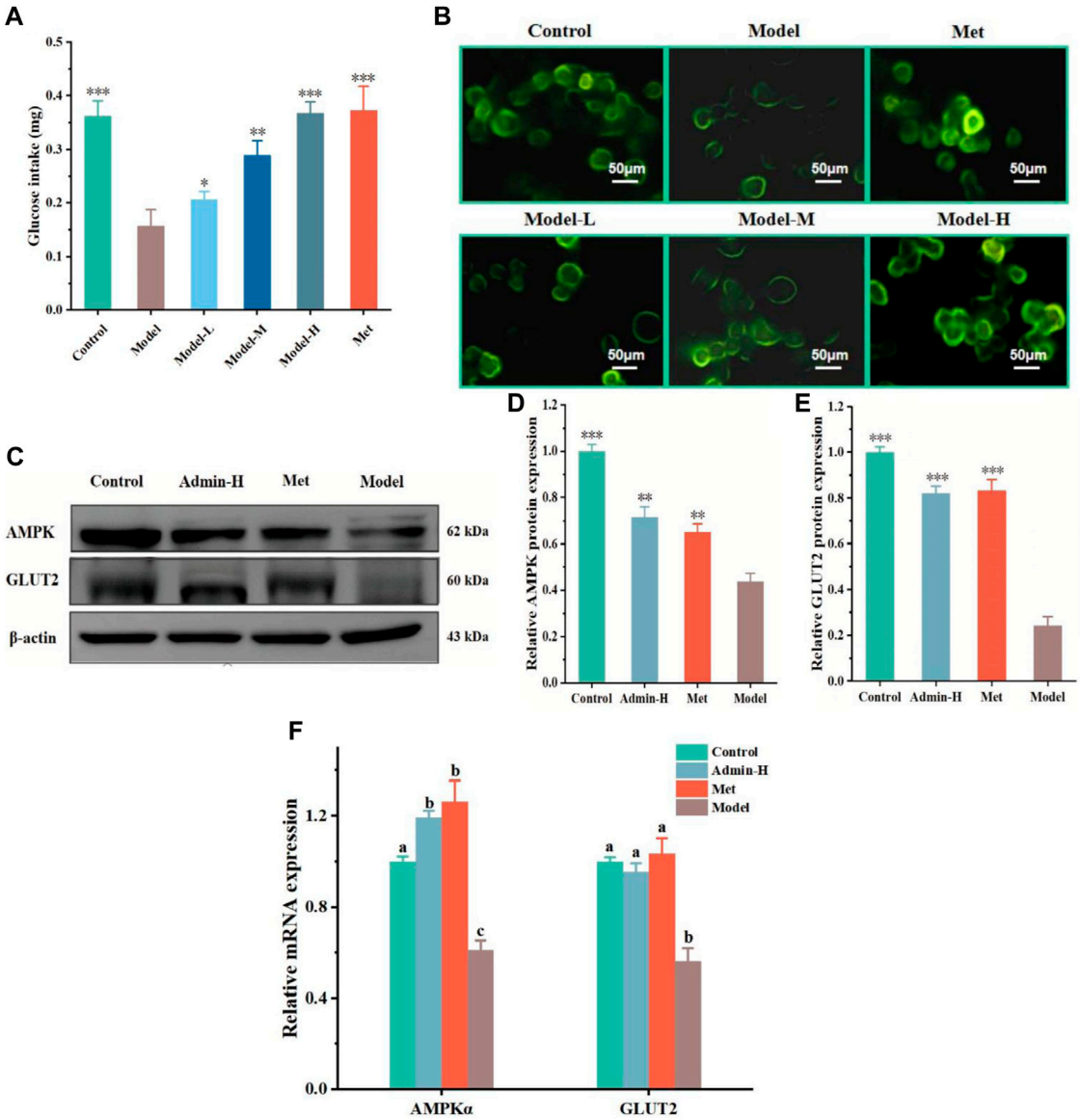


FIGURE 2
N-p-CO increases cellular glucose uptake in HG/PA-induced HL-7702 cells. **(A)** The glucose uptake of HG/PA-induced HL-7702 cells was determined by an anthrone-sulfuric method; **(B)** Representative images of 2-NBDG fluorescence staining; **(C)** Representative bands of GLUT2 and AMPK determined by western blot; **(D,E)** Relative expressions of AMPK and GLUT2 proteins; **(F)** Relative mRNA expression of AMPKα and GLUT2. Data were represented as mean ± SD ($n$ = 3). *$p$ < 0.05, **$p$ < 0.01 and ***$p$ < 0.001 compared with the model group.

Origin 2022 software (OriginLab, Electronic Arts Inc., United States). Statistical significance is indicated by $^{*}p < 0.05$, $^{**}p < 0.01$ and $^{***}p < 0.001$.

# 3 Result

## 3.1 N-p-CO ameliorated oxidative stress of HG/PA-induced HL-7702 cells

To assess the antioxidant capacity of N-p-CO, a model of HL-7702 cells was established in the absence or presence of HG/PA. The concentrations of 10 μg/mL, 20 μg/mL and 50 μg/mL without any effect on the cell viability were selected for subsequent experiments according to the cytotoxicity induced by N-p-CO in HL-7702 cells (Figure 1B). Exposure of HL-7702 cells to N-p-CO led to a significant decrease in the cell viability in a dose-dependent manner. The viability was significantly decreased to 81.02% ± 4.65% at the concentration of 50 μg/mL of HG/PA (Figure 1B). Compared with the cell viability of HL-7702 cells exposed to HG/PA, treatment with N-p-CO significantly increased the viability of HG/PA-induced cells in a dose-dependent manner (Figures 1C–I). Furthermore, ROS fluorescence staining showed that the content of intracellular ROS in the model group was significantly higher than that in the control group. Supplementation with N-p-CO significantly reduced the ROS levels elevated by HG/PA in a dose dependent manner (Figures 1D, E). N-p-CO also significantly increased the levels of SOD, GSH and GSH-px, and decreased the contents of MDA in HG/PA-incued HL-7702 cells in a dose dependent manner (Figures 1F–I). These results indicate that N-p-CO has the potential to alleviate HG/PA-induced oxidative damage.

## 3.2 N-p-CO increased glucose uptake of HL-7702 cells induced by HG/PA

High sugar exposure can promote the generation of ROS and in turn activates AMPKα to reduce the cellular glucose uptake capacity, eventually resulting in metabolic disorders (Jiang et al., 2021). Glucose uptake was measured, with met as the positive control drug which had been a clear mechanism that met can increase GLUT2 expression. The glucose uptake capacity of HG/PA-treated HL-7702 cells was significantly lower than that of the control group. The glucose uptake capacity of HL-7702 cells was significantly improved after treatment with metformin and different doses of N-p-CO (Figures 2A, B). As cellular glucose uptake is mainly regulated by GLUT2 (Rathinam and Pari, 2016), we conducted western blot analysis to observe the effects of N-p-CO on the expression of GLUT2 protein. Compared with the control cells, cells exposed to HG/PA presented a clear downregulation of GLUT2 protein. Treatment with N-p-CO or an AMPK agonist metformin (Sun Y. et al., 2023) significantly upregulated the expression of GLUT2 in the HG/PA-treated HL-7702 cells. Interestingly, the upregulation of GLUT2 and the enhancement of glucose uptake capacity by N-p-CO were significantly reversed by metformin treatment. This result suggests that N-p-CO effectively increases glucose uptake, which may be related to the upregulation of GLUT2 and the activation of AMPK (Figures 2C–F).

## 3.3 N-p-CO upregulated the PI3K/AKT/GSK3β pathway and increased the content of glycogen in HG/PA-induced HL-7702 cells

As the uptake of glucose is mainly stored in the form of glycogen in liver (M. et al., 2016), we next tested whether N-p-CO could affect the generation of glycogen in hepatocytes. It was observed that the content of glycogen in HG/PA-induced HL-7701 cells was significantly lower than that of controls. Treatment with N-p-CO could effectively increase the content of intracellular glycogen in HG/PA-induced HL-7701 cells when compared with the model group (Figure 3A). The production of glycogen has been suggested to be associated with the inhibition of glycogen synthase kinase 3β (GSK3β) (Yan et al., 2023). Then we characterized the protein expressions of GSK3β involved signaling pathway using western blot. Significant downregulations of p-GSK3β proteins and its upstream gene PI3K and AKT were observed in the model group when compared with the control group. After intervention with N-p-CO, the expressions of these proteins were significantly upregulated in HG/PA-induced HL-7701 cells (Figures 3B–F). These findings reveal that N-p-CO could activate the PI3K/AKT/GSK3β pathway and increase the content of glycogen in HG/PA-induced HL-7702 cells, which may hold great potentials for the mitigation of hyperglycemia.

## 3.4 N-p-CO decreased blood glucose and improved physical phenotypes in HFD/STZ-induced T2DM mice

Because administration of N-p-CO could ameliorate glucose uptake and glycogen production *in vitro*, we then tested whether N-p-CO exhibited these effects in mice treated with HFD/STZ. Mice were treated with HFD/STZ with or without N-p-CO for 8 weeks (Figure 4A). It could be found that mice in the DM group exhibited significantly reduced sizes, disheveled and dull hair (Figure 4B). As expected, these physical appearances of DM mice characterized by soft and lustrous hair, were significantly restored after intervention with N-p-CO or Met (Figure 4B). Compared with the control mice, HFD/STZ treatment induced an obvious decrease in the body weight of mice in the DM group, while relatively slow decline in mice administrated with either N-p-CO or Met (Figures 4C, D). Furthermore, the fasting blood sugar (FBG) of the HFD/STZ-induced mice was significantly higher than that in the NC group. Compared with the DM group, treatment with N-p-CO significantly reduced the level of FBG in HFD/STZ-induced mice in a dose-dependent manner (Figure 4E). Additionally, DM mice displayed significantly increased consumption of water and food when compared with the controls, which was improved after treatment with either N-p-CO or Met (Figures 4F, G). These results indicate that N-p-CO could effectively improve the

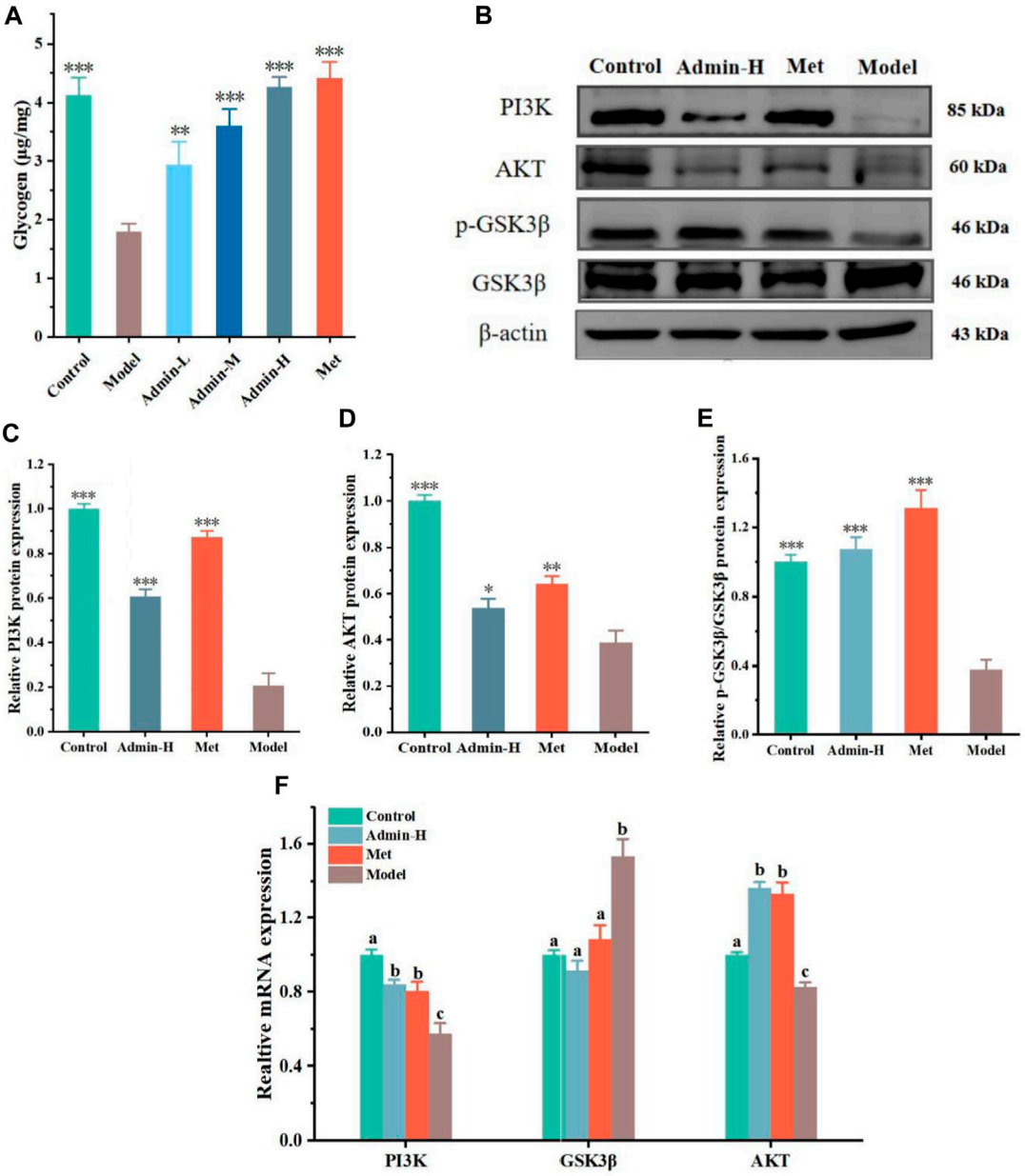


FIGURE 3
N-p-CO promoted glycogen production related to the PI3K/AKT/GSK3β pathway in HG/PA-induced HL-7702 cells. **(A)** Content of glycogen in HG/PA-induced HL-7702 cells; **(B)** Representative western blot bands of PI3K, AKT and GSK3β proteins; **(C–E)** The relative expressions of PI3K, AKT and GSK3β proteins; **(F)** Relative mRNA expression of PI3K, AKT and GSK3β. Data were represented as mean ± SD ($n$ = 3). *$p$ < 0.05, **$p$ < 0.01 and ***$p$ < 0.001 compared with the model group.

phenotypes of hyperglycemia in mice with diabetes induced by HFD/STZ.

## 3.5 N-p-CO enhanced antioxidant ability in mice treated by HFD/STZ

As the above data have shown that N-p-CO supplementation could prevent oxidative damage induced by HG/PA in liver cells, the antioxidant effect of N-p-CO was further determined in mice treated by HFD/STZ. Compared with mice in the NC group, mice treated with HFD/STZ presented a significant decrease in the levels of GSH, GSH-Px and SOD in the serum. Administration with N-p-CO significantly increased the serum levels of GSH, GSH-Px and SOD in mice induced by HFD/STZ (Figures 5A–C). The content of MDA in serum of DM group was significantly higher than that in the control groups. Compared with the DM group, treatment with N-p-CO reduced the serum content of MDA in HFD/STZ-induced mice. Meanwhile, the hepatic levels of GSH, GSH-Px and SOD were

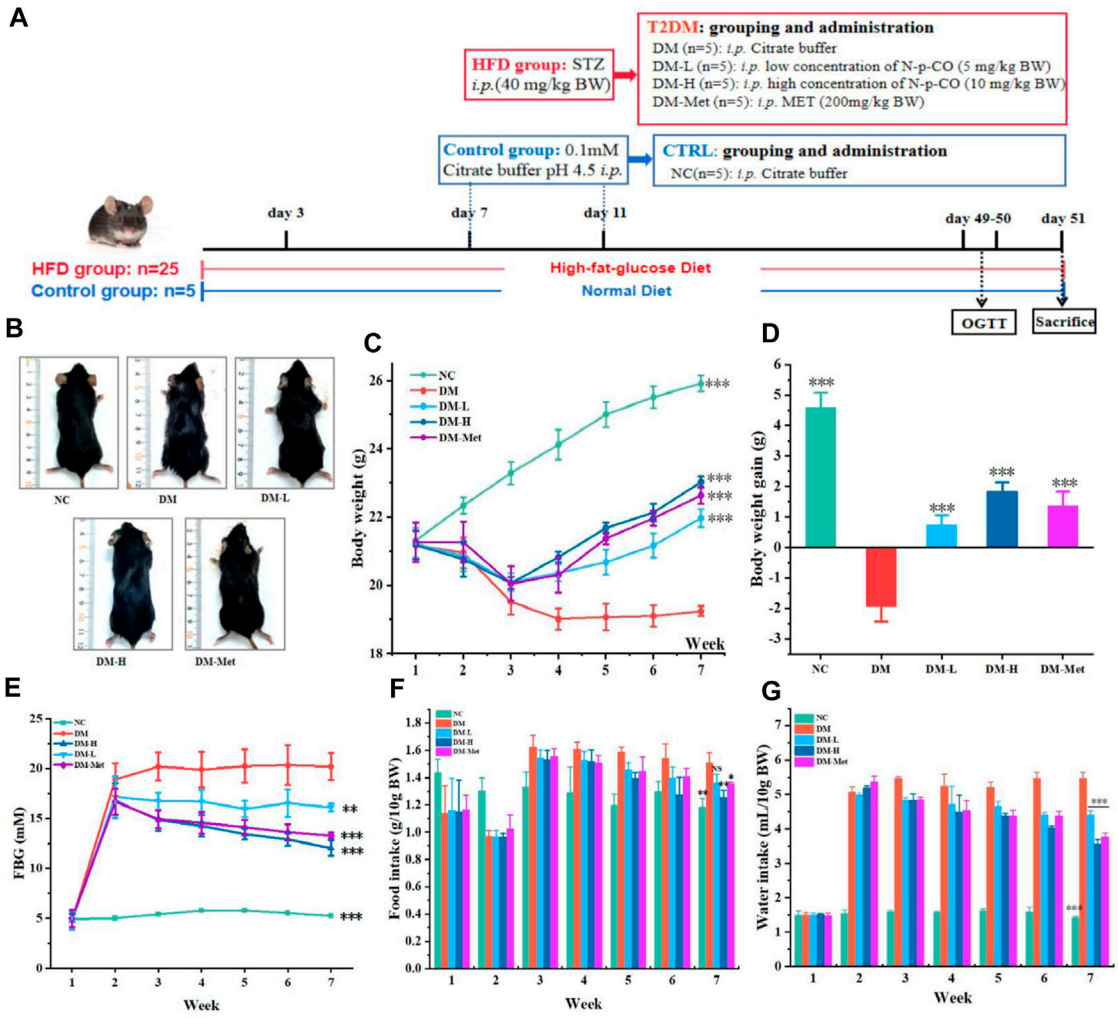


FIGURE 4
N-p-CO improved the phenotypes of hyperglycemia in HFD/STZ-induced mice. **(A)** Experimental process and employed groups; **(B)** Representative images of mice; **(C)** The changes in the body weight of mice; **(D)** The body weight gain of mice; **(E)** The changes of fasting blood glucose of mice; **(F)** Food intake of mice; **(G)** Water intake of mice. Data were represented as mean ± SD ($n$ = 5). *$p$ < 0.05, **$p$ < 0.01 and ***$p$ < 0.001 compared with the DM group.

significantly decreased in the mice induced by HFD/STZ when compared with the NC group. The levels of these antioxidant enzymes in the liver of HFD/STZ-induced mice were remarkably increased by N-p-CO treatment in a dose-dependent manner (Figures 5E–G). Compared with the NC group, HFD/STZ-induced mice displayed evaluated content of MDA in the liver, which was significantly decreased after treatment with N-p-CO (Figure 5H). These results suggest that N-p-CO could effectively enhance the antioxidant capacity of mice induced by HFD/STZ.

## 3.6 N-p-CO improved liver function in HFD/STZ-induced mice

As liver acts as a vital organ involved in the metabolism of glucose, we evaluated the protective effect of N-p-CO on liver function and morphology. Compared with the NC group, the ratio of liver weight and body weight, and the levels of ALT and AST in the liver of mice induced by HFD/STZ were significantly increased. N-p-CO treatment significantly reduced liver index and the hepatic levels of ALT and AST in HFD/STZ-induced mice (Figures 6A–C). The H&E staining of liver showed that hepatocytes exhibited intact architecture with well-defined boundaries, uniform sizes, and abundant cytoplasm in liver from the NC group. The hepatic sinuses displayed a regular arrangement with clear sinusoidal spaces occasionally accompanied by a few inflammatory cells in the control mice. Conversely, in relative to the control mice, the hepatocytes in the DM group showed hypertrophy, vacuolar degeneration, and cytoplasmic accumulation of numerous round lipid droplets of varying sizes (Figure 6D). Moreover, there was significant infiltration of inflammatory cells, hepatocyte necrosis along with indistinct hepatic lobular boundaries and disorganized arrangement of hepatic cords. Additionally, a great number of red blood cells were observed within the hepatic cords, indicating severe cellular damage. N-p-CO treatment induced a significant reduction

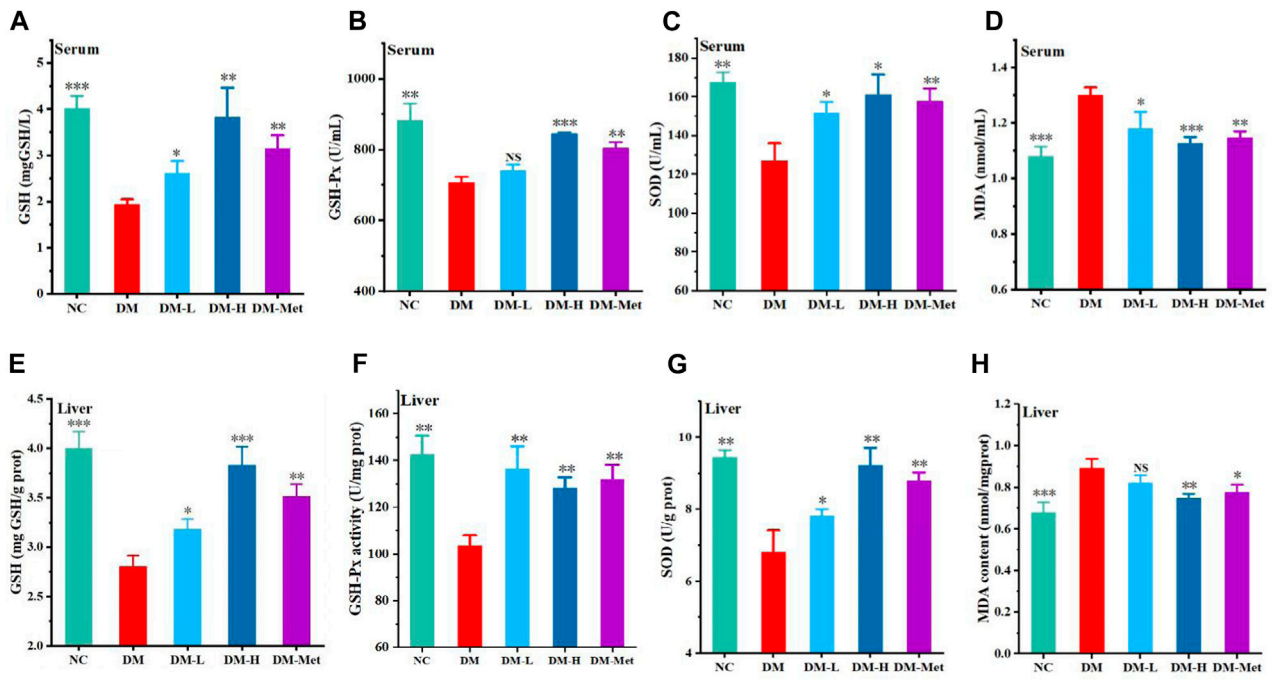


FIGURE 5
N-p-CO enhanced systemic and hepatic antioxidant ability in HFD/STZ-induced mice. **(A–C)** The levels of GSH, GSH-Px and SOD in serum; **(D)** The content of MDA in serum; **(E–G)** The hepatic levels of GSH, GSH-Px and SOD; **(H)** The content of MDA in liver. Data were represented as mean ± SD ($n$ = 3). *$p$ < 0.05, **$p$ < 0.01 and ***$p$ < 0.001 compared with the DM group.

in hepatic steatosis and improvement of glomerular morphology in the HFD/STZ-induced mice. These findings indicate that N-p-CO may have high potentials in improving hepatic function and metabolic activity, which may contribute to the remission of diabetes.

## 3.7 N-p-CO activated PI3K/AKT/GSK3β pathway and improved the metabolism of hepatic glucose in mice

The above results indicated that N-p-CO could improve the function of liver in mice induced by HFD/STZ and glucose metabolism in HL-7702 cells induced by HG/PA. We next evaluated whether N-p-CO could also improve the metabolism of glucose in the liver of diabetic mice. A significant increase in the level of blood glucose was found in HFD/STZ-induced mice when compared with the mice in NC group, suggesting that HFD/STZ treatment induced an impaired glucose tolerance in mice. Oral glucose tolerance was significantly improved by the decrease in the blood glucose level by administration with either Met or N-p-CO in HFD/STZ-induced mice (Figures 7A, B). Serum level of GSP in HFD/STZ-induced DM mice was significantly higher than that in the NC group. Supplementation with either N-p-CO or Met significantly reduced the content of GSP in mice induced by HFD/STZ (Figure 7C). Furthermore, glycogen production in liver was determined using periodic PAS staining. The content of glycogen in liver in HFD/STZ-induced DM mice was decreased when compared with the NC group. Administration with either N-p-CO or Met significantly increased the production of glycogen in the liver of mice induced by HFD/STZ (Figures 7D, E). Importantly, in line with the changes in cells, the downregulations of hepatic PI3K, AKT and GSK3β expressions by HFD/STZ exposure were significantly restored in mice by treatment with either N-p-CO or Met. Notably, HFD/STZ exposure caused a clear downregulation of hepatic GLUT2 protein in mice, which was significantly increased after treatment with either N-p-CO or Met. These findings suggest that administration with N-p-CO effectively improved hepatic glucose metabolism, which may be related to the activation of a PI3K/AKT/GSK3β pathway in mice (Figures 7F–L).

# 4 Discussion

It has been suggested that chronic or intermittent hyperglycemia is linked to the development of diabetic complications (Volpe et al., 2018; Wu et al., 2023). Several signaling pathways involved in diabetic complications may be directly triggered by hyperglycemia in different tissues, due to the production of ROS, the formation of AGEs and the secretion of pro-inflammatory cytokines (Song et al., 2022; Yoshikawa et al., 2022). Thus, reduction of ROS has been proposed as an effective strategy for mitigating inflammation and complications associated with diabetes (Cheng et al., 2019). Several natural antioxidants including polyphenols, have been shown to reduce the risk of T2DM via increasing the antioxidant defense, regulating inflammatory response and decreasing blood glucose and insulin resistance (Shah et al., 2022; Kukavica et al., 2024). Therefore, it is in need to further discover high-efficiency, low-toxicity and multi-target antioxidants for diabetes and its complications. In this study, we found that as a natural polyphenol compound, N-p-CO exhibited strong

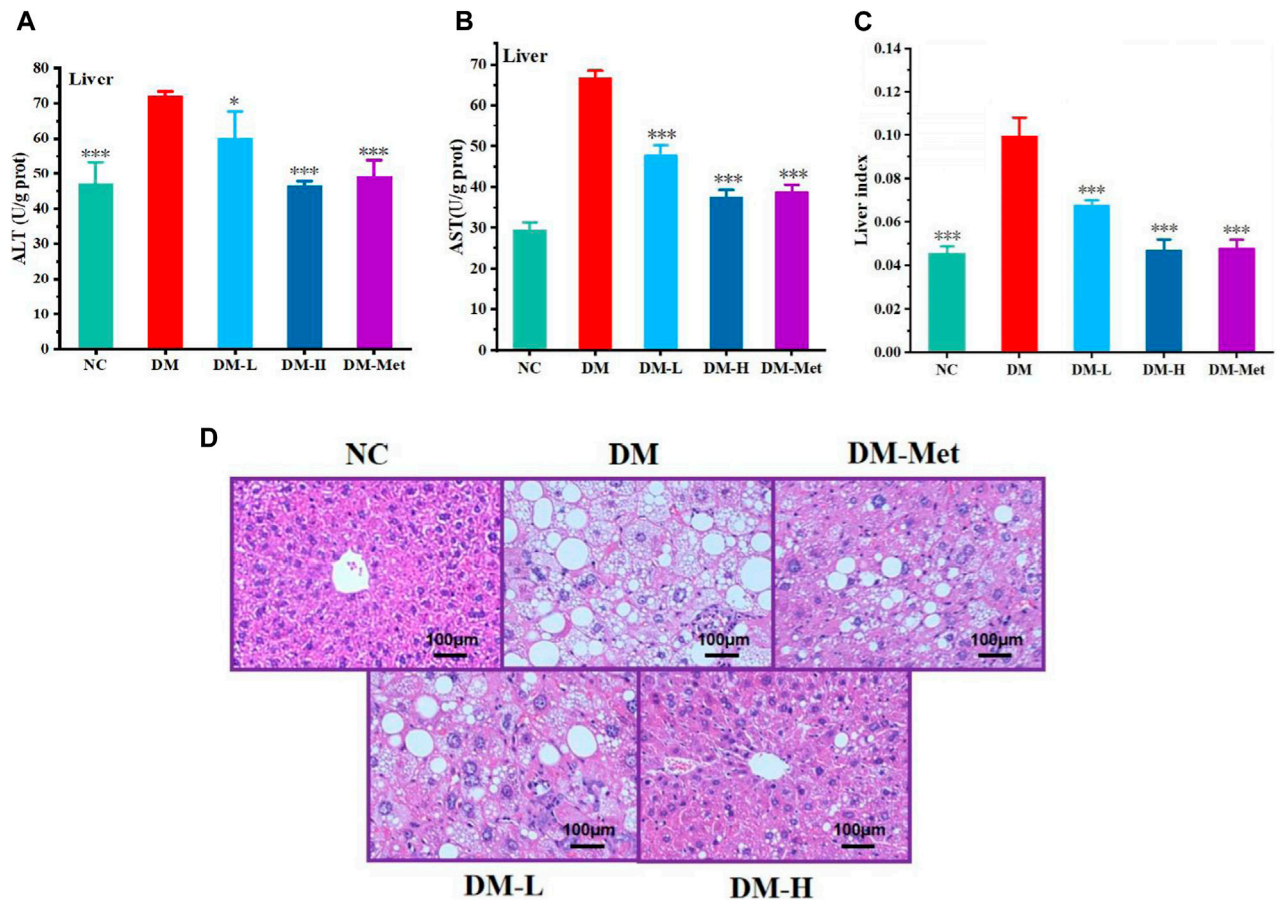


FIGURE 6
N-p-CO improved the function of liver in HFD/STZ induced mice. **(A)** Content of ALT; **(B)** Content of AST; **(C)** Liver index; **(D)** H&E staining of liver. Bars represent mean ± SD ($n$ = 5). *$p$ < 0.05, **$p$ < 0.01 and ***$p$ < 0.001 compared with the DM group.

antioxidant ability and hypoglycemic effect in both HG/PA-induced HL-7702 cells and HFD/STZ-induced mice. Furthermore, supplementation with N-p-CO significantly activated the hepatic PI3K/AKT/GSK3β signaling pathway, which may participate in the metabolism of glucose in liver. N-p-CO may serve as an antioxidant and regulator of hepatic glucose metabolism in diabetes, which may provide a theoretical basis for the clinical use of N-p-CO.

Liver is an important organ for the maintenance of glucose homeostasis via controlling glycogenesis, glycogenolysis, glycolysis, gluconeogenesis and other pathways (Ding et al., 2018). However, these hepatic processes are dysregulated in diabetes mellitus, which may contribute to high hepatic glucose production and hyperglycaemia (Petersen et al., 2017). It is reported that high glucose can induce apoptosis and oxidative stress injury for different cells, and hepatic glucose and glycogen metabolism have been considered to be related to the hepatic glucose output (Ding et al., 2021). The enhancement of hepatic glucose and glycogen metabolism has been proposed as a potential avenue for the development of anti-diabetic therapy. However, this aspect remains largely unexplored (Rines et al., 2016). The dysregulation of hepatic glucose metabolism probably results from the oxidative damage to enzymes that are related to the glycolysis, tricarboxylic acid cycle and ATP biosynthesis (Jha and Mazumder, 2019). Therefore, targeting oxidative stress to improve the metabolism of glucose in liver has been suggested as a strategy for the treatment of hepatotoxicity, diabetes and its complications (Sun et al., 2020b). For example, dapagliflozin protects hyperglycemia-induced cardiomyocytes damage through inhibiting NADPH oxidase-mediated oxidative stress (Xing et al., 2021). Notably, polyphenols have been considered to have the potential to treat diabetes due to their strong antioxidant ability (Krawczyk et al., 2023). Rutin and quercetin have been found to enhance glucose uptake by decreasing oxidative stress in L6 myotubes induced by tertiary butyl hydrogen peroxide (Dhanya et al., 2014). Resveratrol could afford advantageous effects for glucose uptake and metabolism by activating the AKT pathway and reducing the oxidative injury in the context of insulin resistance related with pre-diabetes and T2DM (Brasnyó et al., 2011).

Consistent with the strong anti-oxidant effects of these polyphenols in T2DM, we found that N-p-CO treatment significantly increased the activity of GSH-PX, SOD and GSH in both HG/PA-induced HL-7702 cells and HFD/STZ-induced mice, indicating a lowered degree of the hydroxyl free radical production induced by N-p-CO. In other words, the strong antioxidant properties of N-p-CO may result from the ability to activate antioxidant enzymes and other mechanisms. Notably, administration with N-p-CO not

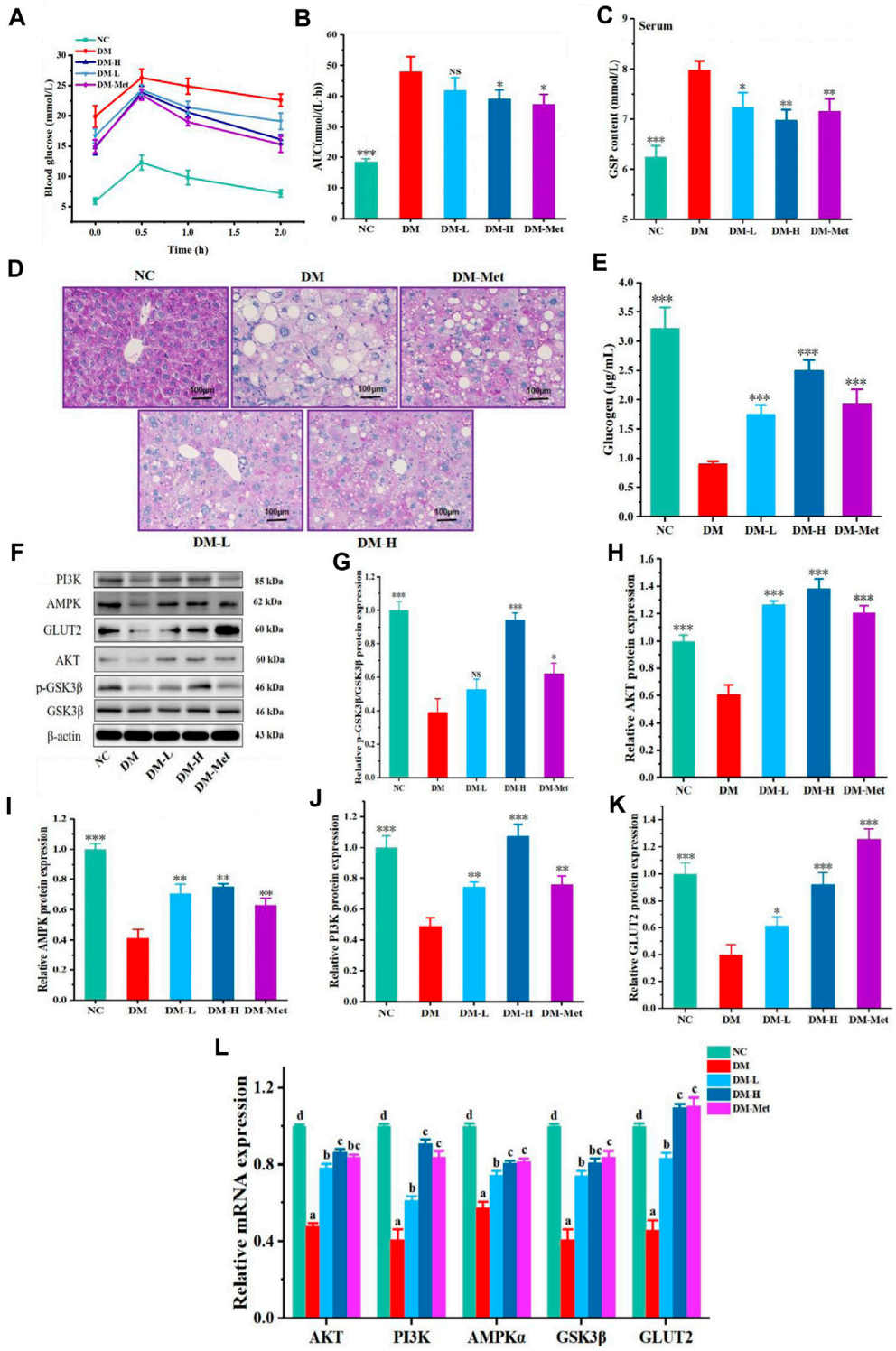


FIGURE 7
N-p-CO improved hepatic glucose metabolism and activated a PI3K/AKT/GSK3β pathway in HFD/STZ-treated mice. **(A)** The curve of oral glucose tolerance; **(B)** AUC of blood glucose; **(C)** Content of GSP in serum; **(D)** PAS staining of liver; **(E)** Content of glucogen in liver; **(F)** Representative western blot bands of PI3K, AKT, GSK3β, AMPK and GLUT2 proteins; **(G–K)** Relative expressions of PI3K, AKT, GSK3β, AMPK and GLUT2 proteins; **(L)** Relative mRNA expression of AKT, PI3K, AMPKα, GSK3β and GLUT2. Data were represented as mean ± SD ($n$ = 5). *$p$ < 0.05, **$p$ < 0.01 and ***$p$ < 0.001 compared with the DM group.

only dramatically augmented glucose uptake and glycogen synthesis in HG/PA-treated HL-7702 cells, but also significantly alleviated hyperglycemia and hepatic glucose metabolism in a dose-dependent manner in diabetic mice induced by HFD/STZ. This result suggests that the consumption of N-p-CO could effectively improve hepatocellular glucose homeostasis in T2DM. These findings

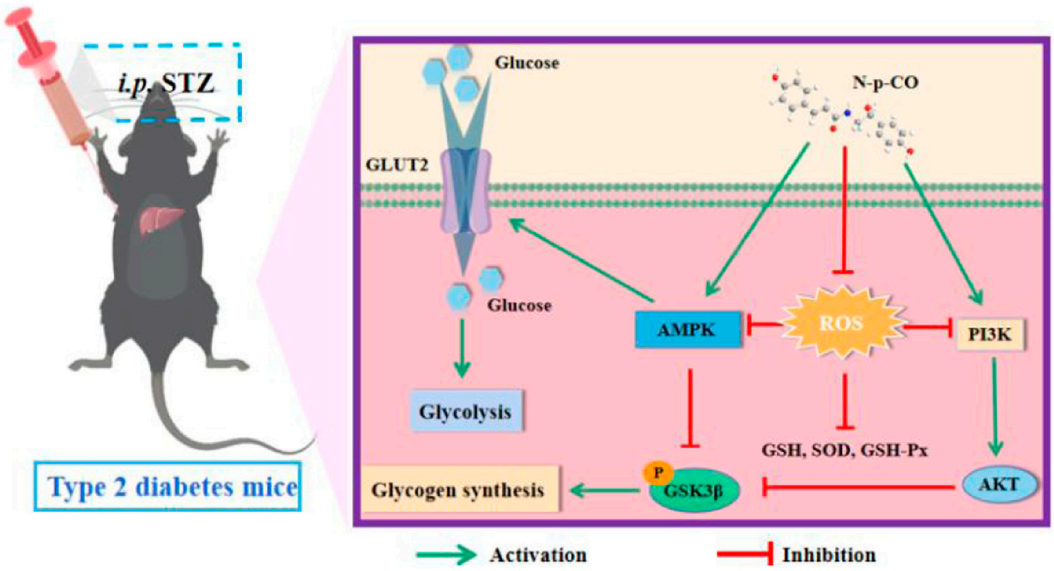


FIGURE 8
Hypoglycemic effects and possible mechanisms of N-p-CO *in vivo* and *in vitro*.

also demonstrate that the amelioration of dysregulation of hepatic glucose metabolism by N-p-CO was, at least in part, owing to the increase in the antioxidant defense.

The regulation of hepatic glucose and lipid metabolism is controlled by the intrinsic molecular signaling pathways, such as PI3K/AKT, MAPK and AMPK pathways (Kumar et al., 2021). For instance, the PI3K pathway has been identified as a critical pathway for the actions of insulin in liver, which can be differentially regulated by AKT and PKC λ/ξ and induced differential actions of insulin and PI3K (Taniguchi et al., 2006). The PI3K-dependent activation of AKT is helpful for the regulation of hepatic glucose metabolism induced by insulin. Impaired phosphorylation of AKT and its substrate GSK3β suppresses gluconeogenesis and increases glycogen synthesis (Ge et al., 2015). Previous studies have reported that upregulation of PI3K/AKT and AMPK proteins by polyphenols is able to inhibit intestinal glucose absorption by sodium-dependent glucose transporter 1 (SGLT1), enhance insulin-dependent glucose uptake, activate PI3K-dependent insulin and AMPK signaling pathways, and reduce hepatic glucose output (Munir et al., 2013). In line with these findings, we found that supplementation with N-p-CO could significantly activate PI3K/AKT/GSK3β pathways, upregulate the expression of GLUT2, and improve the hepatocellular glycometabolism in both HG/PA-induced HL-7702 cells and diabetic mice (Figure 8). These findings indicate that the ability of N-p-CO to stimulate hepatocellular glycogenesis production and glucose consumption may be mediated by AKT pathway activation via PI3K phosphorylation, leading to increased p-GSK3β levels and subsequent promotion of glycogen. In other words, the regulation of hepatic glucose metabolism by N-p-CO may be, at least in part, related to the PI3K-dependent activation of AKT. However, the precise mechanism underlying the amelioration of hepatic glucose metabolism dysregulation by N-p-CO through the AKT pathway remains to be further elucidated *in vivo* and *in vitro* utilizing AKT-deficient or CRISPR-Cas9 modified mice models.

## 5 Conclusion

In conclusion, administration with N-p-CO effectively activated a PI3K/AKT/GSK3β signaling pathway and ameliorated oxidative stress in both HG/PA-induced HL-7702 cells and HFD/STZ-induced mice. N-p-CO treatment not only significantly promoted glucose uptake and glycogen synthesis in HG/PA-induced HL-7702 cells, but also exhibited significant hypoglycemic effects by reducing fasting blood glucose and increasing hepatic glycogen production in HFD/STZ-induced mice. These effects demonstrated the significant mitigation of the dysregulation of hepatic glucose metabolism induced by N-p-CO supplementation, and may be attributed to the reduction of the hydroxyl free radical and the activation of a PI3K/AKT/GSK3β signaling pathway. Though more work will be needed to reveal the PI3K/AKT/GSK3β-involved accurate mechanism of action regulated by N-p-CO, the present findings clearly demonstrate that N-p-CO is exploitable as a new candidate for the prevention and treatment of diabetes.

## Data availability statement

The raw data supporting the conclusion of this article will be made available by the authors, without undue reservation.

## Ethics statement

The animal study was approved by Experimental Animal Management Committee of Jiangmen Health International Innovation Research Institute. The study was conducted in accordance with the local legislation and institutional requirements.

## Author contributions

YH: Conceptualization, Data curation, Formal Analysis, Investigation, Methodology, Software, Validation, Visualization, Writing–original draft. XZ: Conceptualization, Data curation, Formal Analysis, Methodology, Software, Visualization, Writing–original draft. QL: Conceptualization, Formal Analysis, Methodology, Writing–review and editing. WZ: Conceptualization, Investigation, Writing–review and editing. PW: Conceptualization, Methodology, Supervision, Writing–review and editing. RW: Conceptualization, Methodology, Writing–review and editing. W-HC: Writing–review and editing, Supervision, Validation. CL: Conceptualization, Funding acquisition, Project administration, Resources, Supervision, Visualization, Writing–review and editing.

## Funding

The author(s) declare that financial support was received for the research, authorship, and/or publication of this article. This work was financially supported by the National Natural Science Foundation of China (Nos 81803390 and 22077020), Natural Science Foundation of Guangdong Province, China (No. 2021A1515010221), Guangdong and Macao Cooperation Project from the Department of Science and Technology of Guangdong Province and Jiangmen Science and Technology Bureau (2022A0505020026) and Department of Education of Guangdong Province, China (Nos 2021ZDZX4041 and 2020KZDZX1202) and Jiangmen Science and Technology Plan Project (No. 2021030102620004497), the Science and Technology Planning Project of Guangdong Province, China (2021B1212040016).

## Conflict of interest

The authors declare that the research was conducted in the absence of any commercial or financial relationships that could be construed as a potential conflict of interest.

## Publisher's note

All claims expressed in this article are solely those of the authors and do not necessarily represent those of their affiliated organizations, or those of the publisher, the editors and the reviewers. Any product that may be evaluated in this article, or claim that may be made by its manufacturer, is not guaranteed or endorsed by the publisher.

## References

Adeva-Andany, A., Noemi, P. F., Carlos, F. F., Cristóbal, D. G., and Cristina, P. G. (2016). Liver glucose metabolism in humans. *Biosci. Rep.* 36, e00416. doi:10.1042/BSR20160385

Argaev-Frenkel, L., and Rosenzweig, T. (2023). Redox balance in type 2 diabetes: therapeutic potential and the challenge of antioxidant-based therapy. *Antioxidants* 12, 994. doi:10.3390/antiox12050994

Ayanlowo, A. G., Garádi, Z., Boldizsár, I., Darcsi, A., Nedves, A. N., Varjas, B., et al. (2020). UHPLC-DPPH method reveals antioxidant tyramine and octopamine derivatives in Celtis occidentalis. *J. Pharm. Biomed. Anal.* 191, 113612. doi:10.1016/j.jpba.2020.113612

Brasnyó, P., Molnár, G. A., Mohás, M., Markó, L., Laczy, B., Cseh, J., et al. (2011). Resveratrol improves insulin sensitivity, reduces oxidative stress and activates the Akt pathway in type 2 diabetic patients. *Br. J. Nutr.* 106, 383–389. doi:10.1017/S0007114511000316

Chen, J., Cao, D., Jiang, S., Liu, X., Pan, W., Cui, H., et al. (2022). Triterpenoid saponins from Ilex pubescens promote blood circulation in blood stasis syndrome by regulating sphingolipid metabolism and the PI3K/AKT/eNOS signaling pathway. *Phytomedicine* 104, 154242. doi:10.1016/j.phymed.2022.154242

Cheng, Y. S., Chao, J., Chen, C., Lv, L. L., Han, Y. C., and Liu, B. C. (2019). The PKCβ-p66shc-NADPH oxidase pathway plays a crucial role in diabetic nephropathy. *J. Pharm. Pharmacol.* 71, 338–347. doi:10.1111/jphp.13043

Dhanya, R., Arun, K. B., Syama, H. P., Nisha, P., Sundaresan, A., Santhosh Kumar, T. R., et al. (2014). Rutin and quercetin enhance glucose uptake in L6 myotubes under oxidative stress induced by tertiary butyl hydrogen peroxide. *Food Chem.* 158, 546–554. doi:10.1016/j.foodchem.2014.02.151

Ding, H. R., Wang, J. L., Ren, H. Z., and Shi, X. L. (2018). Lipometabolism and glycometabolism in liver diseases. *Biomed. Res. Int.* 2018, 1287127. doi:10.1155/2018/1287127

Ding, M., Tang, Z., Liu, W., Shao, T., Yuan, P., Chen, K., et al. (2021). Burdock fructooligosaccharide attenuates high glucose-induced apoptosis and oxidative stress injury in renal tubular epithelial cells. *Front. Pharmacol.* 12, 784187. doi:10.3389/fphar.2021.784187

Elkhalifa, A. M. E., Nazar, M., Ali, S. I., Khursheed, I., Taifa, S., Ahmad Mir, M., et al. (2024). Novel therapeutic agents for management of diabetes mellitus: a hope for drug designing against diabetes mellitus. *Life* 14, 99. doi:10.3390/life14010099

Ge, Z., Zhang, P., Hong, T., Tang, S., Meng, R., Bi, Y., et al. (2015). Erythropoietin alleviates hepatic insulin resistance via PPARγ-dependent AKT activation. *Sci. Rep.* 8, 17878. doi:10.1038/srep17878

Hao, J., Bei, J., Li, Z., Han, M., Ma, B., Ma, P., et al. (2022). Qing`e Pill inhibits osteoblast ferroptosis via ATM serine/threonine kinase (ATM) and the PI3K/AKT pathway in primary osteoporosis. *Front. Pharmacol.* 13, 902102. doi:10.3389/fphar.2022.902102

Hasandeep, S., Rajanpreet, S., Arshdeep, S., Harshbir, S., Gurpreet, S., Sarabjit, K., et al. (2023). Role of oxidative stress in diabetes-induced complications and their management with antioxidants. *Arch. Biochem. Biophys.* 2023, 2243651. doi:10.1080/13813455.2023.2243651

He, C., Wang, D., Wang, R., Huang, Y., Huang, X., Shen, S., et al. (2022). Epigallocatechin gallate induces the demethylation of actinin alpha 4 to inhibit diabetic nephropathy renal fibrosis via the NF-KB signaling pathway *in vitro*. *Dose Response* 20 (2), 15593258221105704. doi:10.1177/15593258221105704

Hisashi, M., Atsuhi, I., Lim, C. H., Tamio, U., and Naotaka, F. (1998). Induction of N-p-coumaroyloctopamine in potato tuber disks by 3-1, 3-glucooligosaccharide. *J. Pestic. Sci.* 23, 49–53. doi:10.1584/jpestics.23.49

Hu, C. L., Wang, C. Y., X, Y., and Yao, X. M. (2020). Dapagliflozin therapy curative effect observation on nonalcoholic fatty liver disease in patients with type 2 diabetes mellitus. *Indian J. Pharm. Sci.* 82, 122–129. doi:10.36468/pharmaceutical-sciences.spl.155

Hu, C. M., Liang, B. W., Sun, J. P., Li, J. Y., Xiong, Z., Wang, S. H., et al. (2024). Synthesis and biological evaluation of indole derivatives containing thiazolidine-2,4-dione as α-glucosidase inhibitors with antidiabetic activity. *Eur. J. Med. Chem.* 264, 115957. doi:10.1016/j.ejmech.2023.115957

Huang, Q., Chen, L., Teng, H., Song, H. B., Wu, X. Q., and Xu, M. Y. (2015). Phenolic compounds ameliorate the glucose uptake in HepG2 cells' insulin resistance via activating AMPK: anti-diabetic effect of phenolic compounds in HepG2 cells. *J. Funct.* 19, 487–494. doi:10.1016/j.jff.2015.09.020

Huang, T. S., Wu, T., Wu, Y. D., Li, X. H., Tan, J., Shen, C. H., et al. (2023). Long-term statins administration exacerbates diabetic nephropathy via ectopic fat deposition in diabetic mice. *Nat. Commun.* 14, 390. doi:10.1038/s41467-023-35944-z

Jeppe, S. S., Nils T, N., and Dan, S. (2014). Assessment of constituents in Allium by multivariate data analysis, high-resolution α-glucosidase inhibition assay and HPLC-SPE-NMR. *Food Chem.* 161, 192–198. doi:10.1016/j.foodchem.2014.03.062

Jha, D., and Mazumder, P. M. (2019). High fat diet administration leads to the mitochondrial dysfunction and selectively alters the expression of class 1 GLUT protein in mice. *Mol. Biol. Rep.* 46, 1727–1736. doi:10.1007/s11033-019-04623-y

Jiang, P., Ren, L. J., Zhi, L., Yu, Z., Lv, F., Xu, F., et al. (2021). Negative regulation of AMPK signaling by high glucose via E3 ubiquitin ligase MG53. *Mol. Cell* 81, 629–637.e5. doi:10.1016/j.molcel.2020.12.008

Jiang, Y. X., Li, W., Wang, J., and Wang, G. G. (2020). Cardiac dysfunction is attenuated by ginkgolide B via reducing oxidative stress and fibrosis in diabetic rats. *Iran. J. Basic Med. Sci.* 23, 1078–1084. doi:10.22038/ijbms.2020.44210.10358

Kane, N. S., Hoogendoorn, C. J., Tanenbaum, M. L., and Gonzalez, J. S. (2018). Physical symptom complaints, cognitive emotion regulation strategies, self-compassion and diabetes distress among adults with Type 2 diabetes. *Diabet. Med.* 35, 1671–1677. doi:10.1111/dme.13830

Krawczyk, M., Burzynska-Pedziwiatr, I., Wozniak, L. A., and Bukowiecka-Matusiak, M. (2023). Impact of polyphenols on inflammatory and oxidative stress factors in diabetes mellitus: nutritional antioxidants and their application in improving antidiabetic therapy. *Biomolecules* 13, 1402. doi:10.3390/biom13091402

Kukavica, B., Škondrić, S., Trifković, T., Mišić, D., Gašić, U., Topalić-Trivunović, L., et al. (2024). Comparative polyphenolic profiling of five ethnomedicinal plants and their applicative potential in the treatment of type 2 diabetes. *J. Ethnopharmacol.* 320, 117377. doi:10.1016/j.jep.2023.117377

Kumar, S., Behl, T., Sachdeva, M., Sehgal, A., Kumari, S., Kumar, A., et al. (2021). Implicating the effect of ketogenic diet as a preventive measure to obesity and diabetes mellitus. *Life Sci.* 264, 118661. doi:10.1016/j.lfs.2020.118661

Liu, W. B., Wang, H. L., Chen, L., Tang, B., Ke, G., Wang, S., et al. (2022). Cucurbitacin E inhibits cellular proliferation and induces apoptosis in melanoma by suppressing HSDL2 expression. *Chin. Med.* 17 (1), 28. doi:10.1186/s13020-022-00582-y

Ma, M. Y., Wei, N., Yang, J. R., Ding, T. T., Song, A. P., Chen, L. R., et al. (2023). Schisandrin B promotes senescence of activated hepatic stellate cell via NCOA4-mediated ferritinophagy. *Pharm. Biol.* 61, 621–629. doi:10.1080/13880209.2023.2189908

Maria, P., and Mattias, C. (2017). Adenosine signaling in diabetes mellitus and associated cardiovascular and renal complications. *Mol. Asp. Med.* 55, 62–74. doi:10.1016/j.mam.2016.12.001

Min, X. F., Guo, S. Q., Lu, Y. J., and Xu, X. T. (2024). Investigation on the inhibition mechanism and binding behavior of cryptolepine to α-glucosidase and its hypoglycemic activity by multi-spectroscopic method. *J. Lumin* 269, 120437. doi:10.1016/j.jlumin.2024.120437

Munir, K. M., Chandrasekaran, S., Gao, F., and Quon, M. J. (2013). Mechanisms for food polyphenols to ameliorate insulin resistance and endothelial dysfunction: therapeutic implications for diabetes and its cardiovascular complications. *Am. J. Physiol. Endocrinol. Metab.* 305, E679–E686. doi:10.1152/ajpendo.00377.2013

Nchiozem-Ngnitedem, V. A., Omosa, L. K., Bedane, K. G., Derese, S., Brieger, L., Strohmann, C., et al. (2020). Anti-inflammatory steroidal sapogenins and a conjugated chalcone-stilbene from Dracaena usambarensis Engl. *Fitoterapia* 146, 104717. doi:10.1016/j.fitote.2020.104717

Petersen, M. C., Vatner, D. F., and Shulman, G. I. (2017). Regulation of hepatic glucose metabolism in health and disease. *Nat. Rev. Endocrinol.* 13, 572–587. doi:10.1038/nrendo.2017.80

Qi, X., Zheng, S., Ma, M., Lian, N., Wang, H., Chen, L., et al. (2022). Curcumol Suppresses CCF-mediated hepatocyte senescence through blocking LC3B-Lamin B1 interaction in alcoholic fatty liver disease. *Front. Pharmacol.* 13, 912825. doi:10.3389/fphar.2022.912825

Rathinam, A., and Pari, L. (2016). Myrtenal ameliorates hyperglycemia by enhancing GLUT2 through Akt in the skeletal muscle and liver of diabetic rats. *Chem. Biol. Interact.* 256, 161–166. doi:10.1016/j.cbi.2016.07.009

Rines, A. K., Sharabi, K., Tavares, C. D., and Puigserver, P. (2016). Targeting hepatic glucose metabolism in the treatment of type 2 diabetes. *Nat. Rev. Drug Discov.* 15, 786–804. doi:10.1038/nrd.2016.151

Satman, I., Bayirlioglu, S., Okumus, F., Erturk, N., Yemenici, M., Cinemre, S., et al. (2023). Estimates and forecasts on the burden of prediabetes and diabetes in adult and elderly population in Turkiye. *Eur. J. Epidemiol.* 38, 313–323. doi:10.1007/s10654-022-00960-8

Shah, M. A., Haris, M., Faheem, H. I., Hamid, A., Yousaf, R., Rasul, A., et al. (2022). Cross-talk between obesity and diabetes: introducing polyphenols as an effective phytomedicine to combat the dual sword diabesity. *Curr. Pharm. Des.* 28, 1523–1542. doi:10.2174/1381612828666220628123224

Song, J., Xu, H. F., Zhang, W., Yang, C. Y., Li, L., and Luan, J. J. (2022). Impact of solute carrier family 47 member 1 gene polymorphism detection on therapeutic effect of diabetes. *Int. J. Pharmacol.* 18, 398–406. doi:10.3923/ijp.2022.398.406

Sourbh, S. G., and Jeena, G. (2022). Polyol pathway and redox balance in diabetes. *Pharmacol. Res.* 182, 106326. doi:10.1016/j.phrs.2022.106326

Sun, S., Li, S., Du, Y., Wu, C., Zhang, M., Li, J., et al. (2020a). Anti-inflammatory effects of the root, stem and leaf extracts of Chloranthus serratus on adjuvant-induced arthritis in rats. *Pharm. Biol.* 58, 528–537. doi:10.1080/13880209.2020.1767159

Sun, S., Wang, Y., Du, Y., Sun, Q., He, L., Zhu, E., et al. (2020b). Oxidative stress-mediated hepatotoxicity in rats induced by ethanol extracts of different parts of Chloranthus serratus. *Pharm. Biol.* 58, 1277–1289. doi:10.1080/13880209.2020.1859552

Sun, S., Zhang, J., Li, H., Du, Y., Li, S., Li, A., et al. (2021). Anti-inflammatory activity of the water extract of Chloranthus serratus roots in LPS-stimulated RAW264.7 cells mediated by the Nrf2/HO-1, MAPK and NF-κB signaling pathways. *J. Ethnopharmacol.* 271, 113880. doi:10.1016/j.jep.2021.113880

Sun, X., Zheng, Y. Q., Tian, Y. Q., Xu, Q. X., Liu, S. C., Li, H. H., et al. (2023a). Astragalus polysaccharide alleviates alcoholic-induced hepatic fibrosis by inhibiting polymerase I and transcript release factor and the TLR4/JNK/NF-κB/MyD88 pathway. *J. Ethnopharmacol.* 314, 116662. doi:10.1016/j.jep.2023.116662

Sun, Y., Guo, L. Q., Wang, D. G., Xing, Y. J., Bai, Y. P., Zhang, T., et al. (2023b). Metformin alleviates glucolipotoxicity-induced pancreatic β cell ferroptosis through regulation of the GPX4/ACSL4 axis. *Eur. J. Pharmacol.* 956, 175967. doi:10.1016/j.ejphar.2023.175967

Taniguchi, C. M., Kondo, T., Sajan, M., Luo, J., Bronson, R., Asano, T., et al. (2006). Divergent regulation of hepatic glucose and lipid metabolism by phosphoinositide 3-kinase via Akt and PKClambda/zeta. *Cell Metab.* 3, 343–353. doi:10.1016/j.cmet.2006.04.005

Tao, Z. S., Zhou, W. S., Xu, H. G., and Yang, M. (2020). Simvastatin can enhance the osseointegration of titanium rods in ovariectomized rats maintenance treatment with valproic acid. *Biomed. Pharmacother.* 132, 110745. doi:10.1016/j.biopha.2020.110745

Volpe, C. M. O., Villar-Delfino, P. H., Dos Anjos, P. M. F., and Nogueira-Machado, J. A. (2018). Cellular death, reactive oxygen species (ROS) and diabetic complications. *Cell Death Dis.* 9, 119. doi:10.1038/s41419-017-0135-z

Wang, L., Wang, P., Wang, D., Tao, M., Xu, W., and Olatunji, O. J. (2020). Anti-inflammatory activities of kukoamine A from the root bark of lycium chinense Miller. *Nat. Prod. Commun.* 15, 1934578X2091208. doi:10.1177/1934578X20912088

Wang, R., and Mu, J. (2021). Arbutin attenuates ethanol-induced acute hepatic injury by the modulation of oxidative stress and Nrf-2/HO-1 signaling pathway. *J. Biochem. Mol. Toxicol.* 35, e22872. doi:10.1002/jbt.22872

Wang, S., Chen, X., Cheng, J., Cai, T., Wu, X., Cheng, Z., et al. (2021). Calunduloside E inhibits HepG2 cell proliferation and migration via p38/JNK-HMGB1 signalling axis. *J. Pharmacol. Sci.* 147, 18–26. doi:10.1016/j.jphs.2021.05.005

Wu, X. Z., Zhu, W. J., Lu, L., Hu, C. M., Zheng, Y. Y., Zhang, X., et al. (2023). Synthesis and anti-α-glucosidase activity evaluation of betulinic acid derivatives. *Arab. J. Chem.* 16, 104659. doi:10.1016/j.arabjc.2023.104659

Xing, Y. J., Liu, B. H., Wan, S. J., Cheng, Y., Zhou, S. M., Sun, Y., et al. (2021). A SGLT2 inhibitor dapagliflozin alleviates diabetic cardiomyopathy by suppressing high glucose-induced oxidative stress *in vivo* and *in vitro*. *Front. Pharmacol.* 12, 708177. doi:10.3389/fphar.2021.708177

Xu, S., He, L., Ding, K., Zhang, L., Xu, X., Wang, S., et al. (2020). Tanshinone IIA ameliorates streptozotocin-induced diabetic nephropathy, partly by attenuating PERK pathway-induced fibrosis. *Drug Des. Devel Ther.* 14, 5773–5782. doi:10.2147/DDDT.S257734

Yan, Z., Cao, X. J., Sun, S. X., Sun, B., and Gao, J. (2023). Inhibition of GSK3B phosphorylation improves glucose and lipid metabolism disorder. *Biochim. Biophys. Acta Mol. Basis Dis.* 1869, 166726. doi:10.1016/j.bbadis.2023.166726

Ye, X., Chen, W., Huang, X. F., Yan, F. J., Deng, S. G., Zheng, X. D., et al. (2024). Anti-diabetic effect of anthocyanin cyanidin-3-O-glucoside: data from insulin resistant hepatocyte and diabetic mouse. *Nutr. Diabetes* 14, 7. doi:10.1038/s41387-024-00265-7

Ye, X., Chen, W., Tu, P., Jia, R., Liu, Y. Q. T., Tang, Q., et al. (2022). Antihyperglycemic effect of an anthocyanin, cyanidin-3-O-glucoside, is achieved by regulating GLUT-1 via the Wnt/β-catenin-WISP1 signaling pathway. *Food Funct.* 13, 4612–4623. doi:10.1039/d1fo03730g

Yoshikawa, T., Mifune, Y., Inui, A., Nishimoto, H., Yamaura, K., Mukohara, S., et al. (2022). Influence of diabetes-induced glycation and oxidative stress on the human rotator cuff. *Antioxidants* 11, 743. doi:10.3390/antiox11040743

Zhang, L., Ren, X. H., He, J., Li, W. N., Hao, J. W., Jing, Y. R., et al. (2021). Protective effect of Phaeoporus obliquus polysaccharide against acute liver injury induced by carbon tetrachloride and alcohol in mice. *Pak J. Pharm. Sci.* 34, 649–656. doi:10.36721/PJPS.2021.34.2.REG.649-656.1

Zhang, S. P., Zhu, P., Yuan, J. N., Cheng, K. M., Xu, Q. X., Chen, W., et al. (2023). Non-alcoholic fatty liver disease combined with rheumatoid arthritis exacerbates liver fibrosis by stimulating co-localization of PTRF and TLR4 in rats. *Front. Pharmacol.* 14, 1149665. doi:10.3389/fphar.2023.1149665

Zhang, X. S., Lu, Y., Li, W., Tao, T., Peng, L., Wang, W. H., et al. (2021). Astaxanthin ameliorates oxidative stress and neuronal apoptosis via SIRT1/NRF2/Prx2/ASK1/p38 after traumatic brain injury in mice. *Brit J. Pharmacol.* 178, 1114–1132. doi:10.1111/bph.15346

Zhou, Y., Liu, L., Xiang, R., Bu, X., Qin, G. Z., Dai, J. J., et al. (2023). Arctigenin mitigates insulin resistance by modulating the IRS2/GLUT4 pathway via TLR4 in type 2 diabetes mellitus mice. *Int. Immunopharmacol.* 114, 109529. doi:10.1016/j.intimp.2022.109529

frontiers | Frontiers in Pharmacology

TYPE Original Research
PUBLISHED 01 May 2024
DOI 10.3389/fphar.2024.1375779

Check for updates

OPEN ACCESS

EDITED BY
Xiping Cui,
Guangdong University of Technology, China

REVIEWED BY
Jiangfeng Song,
Jiangsu Academy of Agricultural Sciences (JAAS), China
Changxing Jiang,
Huaiyin Institute of Technology, China

*CORRESPONDENCE
Qingrong Huang,
qhuang@sebs.rutgers.edu
Chi-Tang Ho,
ctho@sebs.rutgers.edu

RECEIVED 24 January 2024
ACCEPTED 29 February 2024
PUBLISHED 01 May 2024

CITATION
Huang G, Zhang M, Feng K, Xiao J, Huang Q, Ho C-T and Liu J (2024), Natural product nobiletin-loaded Pickering emulsion stabilized by bovine serum albumin/carboxymethyl inulin complexes: preparation and digestive characteristics.
*Front. Pharmacol.* 15:1375779.
doi: 10.3389/fphar.2024.1375779

COPYRIGHT
© 2024 Huang, Zhang, Feng, Xiao, Huang, Ho and Liu. This is an open-access article distributed under the terms of the Creative Commons Attribution License (CC BY). The use, distribution or reproduction in other forums is permitted, provided the original author(s) and the copyright owner(s) are credited and that the original publication in this journal is cited, in accordance with accepted academic practice. No use, distribution or reproduction is permitted which does not comply with these terms.

# Natural product nobiletin-loaded Pickering emulsion stabilized by bovine serum albumin/carboxymethyl inulin complexes: preparation and digestive characteristics

Guiying Huang[1], Man Zhang[2], Konglong Feng[3], Jie Xiao[3], Qingrong Huang[2]*, Chi-Tang Ho[2]* and Jun Liu[4]

[1]College of Light Industry and Food Science, Zhongkai University of Agriculture and Engineering, Guangzhou, Guangdong, China, [2]Department of Food Science, Rutgers University, New Brunswick, NJ, United States, [3]College of Food Science, South China Agricultural University, Guangzhou, Guangdong, China, [4]College of Food Science and Engineering, Yangzhou University, Yangzhou, Jiangsu, China

To expand the application of nobiletin (NOB) in semi-solid functional foods, bovine serum albumin (BSA)/carboxymethyl inulin (CMI) complexes-stabilized Pickering emulsion (BCPE) ($\varphi_{oil}$ = 60%, v/v) was fabricated, and the swallowing index and bioavailability of the NOB-loaded Pickering emulsion was evaluated. Confocal laser scanning microscope (CLSM) and cryo-scanning electron microscopy (cryo-SEM) images revealed that BSA/CMI complexes attached to the oil–water interface. NOB-loaded BCPE exhibited a viscoelastic and shear-thinning behavior. Fork drip test results suggested that the textural value of unloaded and NOB-loaded emulsions was International Dysphagia Diet Standardisation Initiative Level 4, which could be swallowed directly without chewing. The *in vitro* lipolysis model suggested that NOB had a faster digestive profile and a higher bioaccessibility in the BCPE than in the oil suspension. The *in vivo* rat model revealed that the oral bioavailability of NOB was increased by 2.07 folds in BCPE compared to its bioavailability in unformulated oil. Moreover, BCPE led to a higher plasma concentration of the major demethylated metabolite of NOB (4′-demethylnobiletin) than the unformulated oil. Accordingly, BCPE enhanced the oral bioavailability of NOB by improving bioaccessibility, absorption, and biotransformation.

KEYWORDS

**complexes, Pickering emulsion, nobiletin, 4-demethylnobiletin, bioavailability**

## Highlights

- A bovine serum albumin/carboxymethyl inulin complexes-stabilized Pickering emulsion (BCPE) with a 60% oil content was fabricated. The textural values of unloaded and nobiletin (NOB)-loaded BCPE were International Dysphagia Diet Standardisation Initiative (IDDSI) Level 4.
- BCPE enhanced the oral bioavailability of NOB in rats compared to oil suspension.
- BCPE improved the biotransformation of 4′-demethylnobiletin *in vivo* during 24 h.

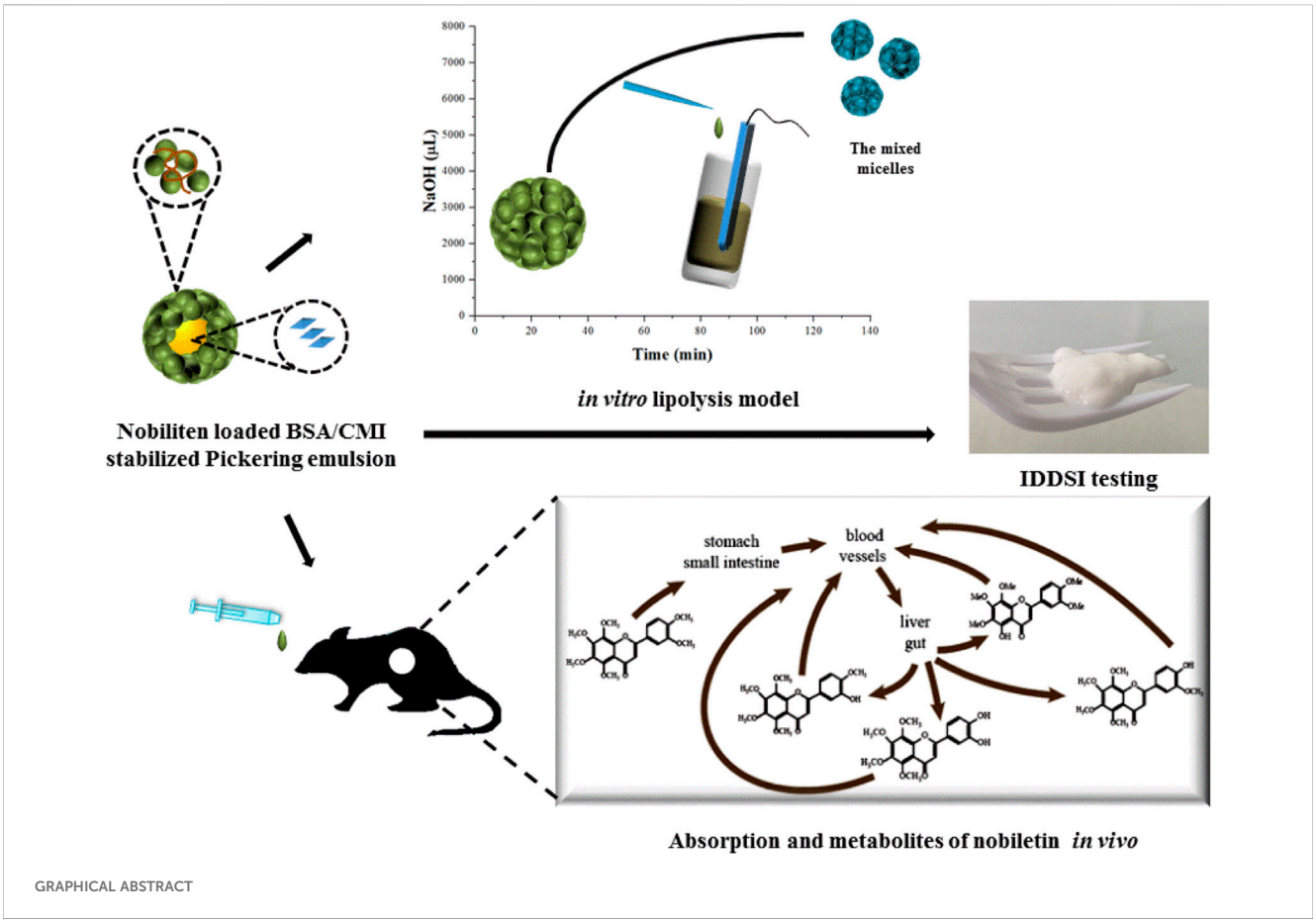


GRAPHICAL ABSTRACT

## 1 Introduction

Natural products are important sources of clinical drugs and functional food owing to their bioactivities and low toxicity (Li et al., 2022; Zhang et al., 2022; Wu et al., 2023). Nobiletin (NOB; 5,6,7,8,3′,4′-hexamethoxyflavone) is a major component of citrus polymethoxyflavones (PMFs), which are a group of flavonoids predominately found in citrus peels (Li et al., 2006a; Zhang et al., 2021). NOB has healthcare functions due to its profound bioactivities, such as anticancer, anti-inflammation, anti-atherosclerosis, anti-viral, and neuroprotective effects, and its ability to prevent neurodegenerative diseases and regulate lipid metabolism, glucose metabolism, mitochondrial function, and muscle physiology (Gao et al., 2018; Nakajima and Ohizumi, 2019; Nohara et al., 2019). These bioactivities can be achieved by the blood circulation system *in vitro* (Chen et al., 2020; Min et al., 2024). *In vivo* experiments infer that NOB and its metabolites are distributed to different tissues via the blood circulation system and ultimately excreted in urine. NOB undergoes phase I and II reactions in the small intestine; the major metabolites of NOB in the urine of mice are demethylated products of B-ring methoxyl groups, including 4′-demethylnobiletin (4′-DMN), 3′-demethylnobiletin (3′-DMN), and 3′,4′-didemethylnobiletin (3′,4′-DDMN; Zhang et al., 2020). Among these metabolites, 4′-DMN is the major metabolite of NOB and has a higher anti-inflammatory and immunomodulatory therapeutic effect than the parent NOB (Li et al., 2006b; Li et al., 2014; Wu et al., 2015; Zheng et al., 2015; Huang et al., 2016; Wu et al., 2018). Therefore, NOB is suitable for the functional enhancement of food. However, NOB exhibits a bitter taste that hampers its product acceptance and limits its application in the functional food area (Batenburg et al., 2016). Specific food formulations must be developed to expand the application of NOB in semi-solid functional foods. Although formulation can reduce the bitterness of NOB, it changes the oral bioavailability of NOB. Evaluation of the oral and digestive characteristics of any novel formulations of NOB should be performed.

A complexes-stabilized Pickering emulsion is one type of emulsion stabilized by particles. The complexes are formed by electrostatic interactions, which are physical reactions that do not change the structure of raw materials. A complexes-stabilized Pickering emulsion has various advantages, such as high loading, high biocompatibility, and desired viscoelasticity, and it is being composed of functional biopolymers and small molecules (Dickinson, 1998; Jie et al., 2016). Owing to nutrient density, remodeling ability, and easy-to-swallow. Complexes-stabilized Pickering emulsion may be a novel food matrix for special populations (Goldstein et al., 2017; Kerien et al., 2020). A complexes-stabilized Pickering emulsion is made with a simple process, and its textural properties can be shifted by adjusting the raw materials (Ming et al., 2023).

Complexes-stabilized Pickering emulsions can be fabricated in two steps. First, complexes are prepared via electrostatic interaction between two types of biomacromolecules with opposite charges.

Then, the complexes stabilize the Pickering emulsion by providing steric and electrostatic repulsion or reducing interface tension. Although many studies focus on the development of complexes-stabilized Pickering emulsions, the texture and digestive characteristics of the resulting emulsions have rarely been reported. Emulsion systems used to obscure the bitterness of natural products have been reported. Some emulsions can distract off-flavor or trigeminal effects by their ingredients, while others can reduce the contact time between natural products and taste buds by being swallowed directly without chewing (Batenburg et al., 2016). To define the swallowing characteristics of foods, the International Dysphagia Diet Standardisation Initiative (IDDSI) developed the IDDSI framework. This framework can be applied to evaluate the swallowing characteristics of emulsions.

Inulin is a fructan-type plant polysaccharide derived from inulin or chicory. Inulin has many biological activities, such as antioxidant and anticancer effects; regulation of blood sugar, blood lipids, and the immune system; and improvement of intestinal health, and benefits for metabolic syndromes (Wan et al., 2020). Moreover, because inulin has low non-specific absorption in most tissues and can be easily filtered by kidneys, it has been used in the pharmaceutical and food industries for decades. Carboxymethyl inulin (CMI) is a derivative of inulin that changes surface electric charge, increases solubility, and decreases viscosity (Joshi et al., 2017).

Our previous work revealed that CMI and bovine serum albumin (BSA) could form complexes induced by physical interactions (Huang et al., 2019). In this study, we used BSA/CMI complexes to stabilize a Pickering emulsion. The resulting BSA/CMI complexes-stabilized Pickering emulsion (BCPE) was applied to encapsulate NOB. The bioaccessibility of NOB-loaded in BCPE was measured using an *in vitro* lipolysis model. The oral bioavailability of NOB was monitored using a rat model to compare the formulated form and an unformulated oil suspension. In addition to evaluating the oral bioavailability of NOB *in vitro* and *in vivo*, the biotransformation of NOB in rats is discussed.

# 2 Materials and methods

## 2.1 Materials

BSA (>98%) was purchased from Sigma-Aldrich Chemical Co. (St. Louis, MO, USA). CMI was synthesized in our laboratory (Rutgers University, NJ, USA) (Huang et al., 2019). Medium-chain triglyceride (MCT) was requested from Stepan Company (Northfield, IL, USA). NOB and tangeretin (98% purity) were obtained from Shanxi Huike Plant Development Co., Ltd. (Shanxi, China). 3′,4′-DDMN, 3′-DMN, and 4′-DMN were synthesized and identified using LC-QTOF-MS/MS (Zhang et al., 2020). Hydrochloric acid (HCl) was purchased from Fisher Scientific (Waltham, MA, USA) (Zhang et al., 2020). Tris was purchased from Saiguo Biotechnology Co., Ltd. (Guangdong, China). Maleic acid was purchased from America SECOMA Biotechnology Co., Ltd. (Beijing, China). Calcium chloride was purchased from Damao Chemical Co., Ltd. (Tianjin, China). Sodium taurodeoxycholate (NaTDC) was purchased from Ruiyong Biotechnology Co., Ltd. (Shanghai, China). Lecithin from soybean, pancreatin, and Tween 80 were purchased from Macklin Biochemical Co., Ltd. (Shanghai, China). HPLC-grade acetonitrile (ACN) and methanol were purchased from Gris Pharmaceutical Chemical Technology Co., Ltd. (Tianjin, China). HPLC-grade tetrahydrofuran, ammonium acetate, trifluoroacetic acid (TFA), and acetic acid were purchased from Yien Chemical Technology Co., Ltd. (Shanghai, China). Dimethyl sulfoxide (DMSO), β-D-glucuronidase, and sulfatase were purchased from Sigma-Aldrich Chemical Co. (St. Louis, MO, USA). Milli-Q distilled water was used in all experiments.

## 2.2 Formation of BSA/CMI complexes

BSA (1% w/v) and CMI (0.2% w/v) were mixed in water solutions free from NaCl. After being fully dissolved for 1 h using a magnetic stirrer, the solution was adjusted to pH 4.0 using HCl solution, and a suspension of BSA/CMI complexes was obtained. The mean particle size of the BSA/CMI complexes was determined using a Brookhaven 90 Plus/BI-MAS instrument equipped with a 15-mW solid-state laser for multi-angle particle sizing. The BSA/CMI complexes were diluted 10 times using water (pH 4.0) and dispersed for 30 min using an ultrasonic oscillator (40 kHz) before particle size measurement.

## 2.3 Fabrication of unloaded and NOB-loaded BSA/CMI complexes-stabilized Pickering emulsion

The aqueous phase was prepared as follows. BSA (10 mg/mL) and CMI (2 mg/mL) were fully dissolved in 5 mL distilled water, and the solution was adjusted to pH 4.0. The aqueous phase was homogenized for 2 min at 10,000 rpm using a T25 digital ULTRA-TURRAX® homogenizer (IKA-Werke GmbH & Co. KG, Germany) equipped with an S25N-10G dispersing rotor. The oil phase was slowly added to the aqueous phase. Then, the BCPE with an oil fraction of 60% was obtained after homogenization for 3 min at 10,000 rpm.

The oil phase of NOB-loaded BCPE was prepared as follows. NOB powder of 2% (w/v) was added into 10 mL MCT and stirred at 90°C using an oil bath until the NOB was completely dissolved. Then the MCT solution was cooled to 35°C before being added to the water phase. The concentrations of NOB, BSA, CMI, and MCT were set at 1.2%, 1%, 0.2%, and 60% (w/v), respectively.

## 2.4 Microstructure measurement of BCPE

The microstructures of the BCPE samples were observed on a Zeiss FV120 confocal laser scanning microscope (CLSM) with an inverted microscope (model Leica DM IRB). The oil and the aqueous phases were stained with curcumin (green) and rhodamine B (red), respectively. The CLSM was performed using two laser excitation sources (488 and 543 nm).

Freeze fracture scanning electron microscopy (cryo-SEM) was used to examine the interfacial structure of BCPE droplets. A small sample volume was placed onto a Cu sample stub and snap-frozen in a liquid nitrogen bath. The frozen sample was transferred to a preparation chamber (PP3010T Cryo-SEM preparation system, USA). After being fractured with a cooled knife and subjected to sublimation at 95°C for 9 min, the sample was sputtered and coated with platinum. SEM measurement of the sample was performed using a cold-field emission scanning electron microscope (S-4800 Hitachi, Japan).

## 2.5 Microstructure analysis of NOB-loaded BCPE

The microstructure of NOB-loaded BCPE was analyzed using an inverted microscope with a refrigeration charge-coupled device (CCD) camera (OPTEC DV330). Images (40×) were captured after the sample was placed on a glass microscopic slide.

## 2.6 Rheological properties of NOB-loaded BCPE

Rheological measurement of complexes and *Pickering* emulsion was performed following the method described in Zou (2018). The shear viscosities were determined at 25°C using a TA ARES-G2 rheometer (TA Instruments, New Castle, DE, USA) with parallel plates (d = 20 mm). The shear rate range was set to 1–100 $s^{-1}$. Frequency sweeps were performed from 0.08 to 10 Hz at the strain of the identified linear viscoelastic region. Dynamic strain scanning was performed in the range of 0.01%–100%. All the samples were loaded onto the parallel plate with the gap at 1 mm for 10 min before analysis.

## 2.7 Fork drip test of unloaded or NOB-loaded BCPE

A fork drip test was performed using the IDDSI testing methods (Hadde and Chen, 2020). The IDDSI framework consists of a continuum of eight levels (0–7), where flow tests are used in levels 0–3, while fork drip tests are applied in levels 4–7. Ten participants were provided with pictures and descriptions of IDDSI Levels 3–5. The participants then assigned each sample to an IDDSI category. Each judgment was determined individually without discussion.

## 2.8 Lipolysis analysis of NOB in BCPE and MCT suspension

An *in vitro* lipolysis study was performed using the Ting et al. (2015) method. The lipolysis buffer consisted of tris maleate (50 mM), sodium chloride (150 mM), calcium chloride (5 mM), NaTDC (5 mM), and phosphatidylcholine (5 mM). Pancreatin powder (1 g) was added into 5 mL of lipolysis buffer, and then the well-mixed solution was centrifuged at 2000 rpm for 10 min. The obtained supernatant was stored on ice until further use. The simulated small intestinal fluid (SSIF) was mixed with 1 mL of pancreatin suspension and 9 mL of lipolysis buffer.

For the *in vitro* lipolysis study, a sample containing 250 mg of the oil phase was injected into 10 mL of the SSIF. The mixture was maintained at 37°C ± 1°C and stirred in an oil bath. The pH of the mixture was adjusted to 7.50 ± 0.02 by titrating with 0.25 N sodium hydroxide solution. The temperature and pH were kept constant for 2 h. The consumption of sodium hydroxide solution was recorded at each time point.

After the 2-h lipolysis, the final mixture was ultracentrifuged at 4°C for 60 min at 50,000 rpm using an Optima XE-100 ultracentrifuge (Beckman Coulter Life Sciences, Indianapolis, IN, USA). After ultracentrifugation, the mixture was separated into three layers. The upper layer was the undigested oil phase, the middle transparent layer was the micelle phase containing soluble NOB, and the bottom was the solid precipitant. The micelle phase was tested for NOB concentration by HLPC, and its volume was measured.

A 100-μL aliquot of the micelle phase sample was filtered and added to 400 μL of methanol. The content of NOB in the micelle phase was analyzed using HPLC. The bioaccessibility (%) of NOB was calculated using the following equation:

$$\text{Bioaccessibility (\%)} = \frac{\text{total mass of solubilized NOB (g)}}{\text{total mass of NOB in original lipid samples (g)}} \times 100\%$$

## 2.9 Animal experiment

The animal experiment was performed according to the previously reported method of Zhang et al. (2020). Young (6 weeks old) healthy male Sprague-Dawley rats were purchased from Southern Medical University (Guangdong, China). During a week of acclimation, all rats were housed in a controlled environment (about 25°C and 40%–60% relative humidity) with a 12-h light–dark cycle. All rats were fed with Purina Laboratory Chow 5001 and *ad libitum* water. Care of the rats followed the Chinese Government's Guide for the Care and Use of Laboratory Animals. The experimental protocol (protocol number: 2019048) was approved by the Institutional Animal Care and Use Committee of South China Agricultural University.

Before conducting a pharmacokinetics study, the rats (around 250 g) were fasted overnight and randomly divided into four groups (five rats in each group). Rats in the first group were orally administered 100 mg/kg NOB-loaded BCPE using oral gavage, while rats in the second group were orally administered 100 mg/kg NOB in MCT. Blood samples from eyeballs were collected at 0.5, 1, 2, 4, 6, 10, and 24 h. The whole-blood samples were immediately centrifuged at 5,000 rpm at 4°C for 15 min, and the plasma samples were collected and stored at −80°C before HPLC analysis.

Prior to HPLC analysis, a plasma sample of 200 μL was mixed with 20 μL tangeretin (10 μg/mL, methanol solution) as an internal standard and 20 μL enzymes of β-D-glucuronidase (500 U) and sulfatase (10 U). The mixture was incubated at 37.8°C for 45 min.

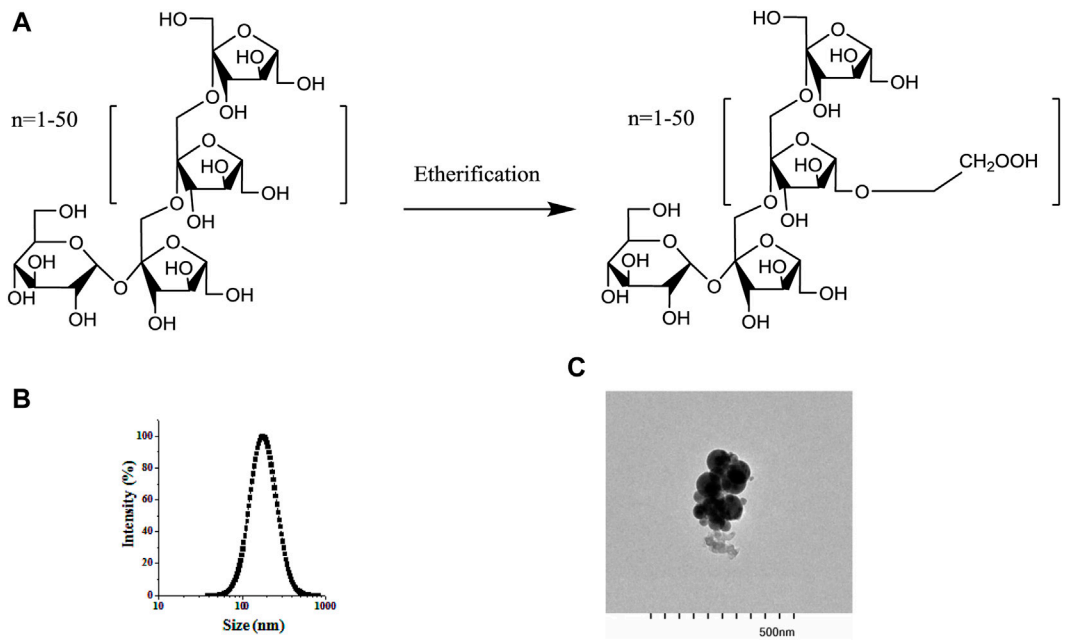


FIGURE 1
Structure of inulin and CMI **(A)**, particle size distribution of BSA/CMI complexes **(B)**, and TEM images of BSA/CMI complexes (bar scale = 500 nm) **(C)**.

Then, ethyl acetate of 400 μL was added, and the suspension was vortexed at 3,000 rpm for 3 min. After centrifugation at 10,000 rpm for 5 min, the supernatant was transferred to a centrifuge tube. After repeating the steps, the combined supernatant was dried using flowing nitrogen. Dried samples were dissolved in 150 μL of 80% methanol in water containing 0.2% acetic acid. The solution was filtered with a 0.22-μm filter membrane before HPLC analysis.

## 2.10 UPCL–MS/MS analysis of NOB in plasma of rat

NOB and its metabolites in the rat plasma were identified using UPLC–MS/MS (Shimadzu, Kyoto, Japan) consisting of an LC-30AD and a triple quadrupole linear ion trap mass spectrometer (model QTRAP 4500) (AB SCIEX, Concord, Canada) based on multiple reaction monitoring (MRM). An Agilent Poroshell 120 PFP (4.6 × 150 mm, 2.7 μm) column was used in the detection. The measurement was performed according to the method previously reported by Zhang et al. (2020).

## 2.11 HPLC analysis of NOB in rat plasma

The measurement of NOB concentration in plasma samples was conducted using an LC-20A HPLC system equipped with a PDA (UV-VIS) absorption detector (Shimadzu Corporation, Kyoto, Japan) and an Ascentis RP-Amide reversed-phase HPLC column (15 cm × 4.6 mm id, 3 μm; Sigma-Aldrich, St. Louis, MO, USA), according to the previously reported method of Zheng et al. (2015) with minor modifications. Detection wavelength, column temperature, flow rate, and injection volume were set to 320 nm, 20°C, 1 mL/min, and 30 μm, respectively. The detection of NOB was performed using a gradient elution of two complex mobile phases, A and B. A was 75% water, 20% ACN, 5% THF, and 50 mM ammonium acetate; B was 50% water, 40% ACN, 10% THF, and 50 mM ammonium acetate. The pH values of both mobile phases were adjusted to 3.0 using TFA. The gradient elution using phases A and B began with 10% B, and then increased to 20%, 40%, 60%, 70%, and 100% B at 3, 8, 23, 29, and 32 min, respectively. Then, the volume percent of phase B was reduced to 10% in 3 min, and detection was stopped after 1 min. The total elution time was 36 min.

## 2.12 Statistical analysis

Experiments were conducted in duplicate, and results were expressed as the mean ± standard deviation (SD). Error bars on figures represent standard deviations. The Q test with 90% confidence interval was applied in the rat experiments.

# 3 Results and discussion

## 3.1 Fabrication of BCPE

BSA/CMI complexes were prepared before the BCPE was fabricated. CMI samples with 0.5 degrees of substitution were synthesized by etherification technology (Figure 1A). A mixed solution of BSA and CMI complexes at a 5:1 ratio was prepared at pH 4. DLS analysis showed that the average size of the complexes was 200.33 nm. The transmission electron microscope photograph of the complex indicated that the complexes were formed by the aggregation of spherical particles. In our previous study, isothermal titration

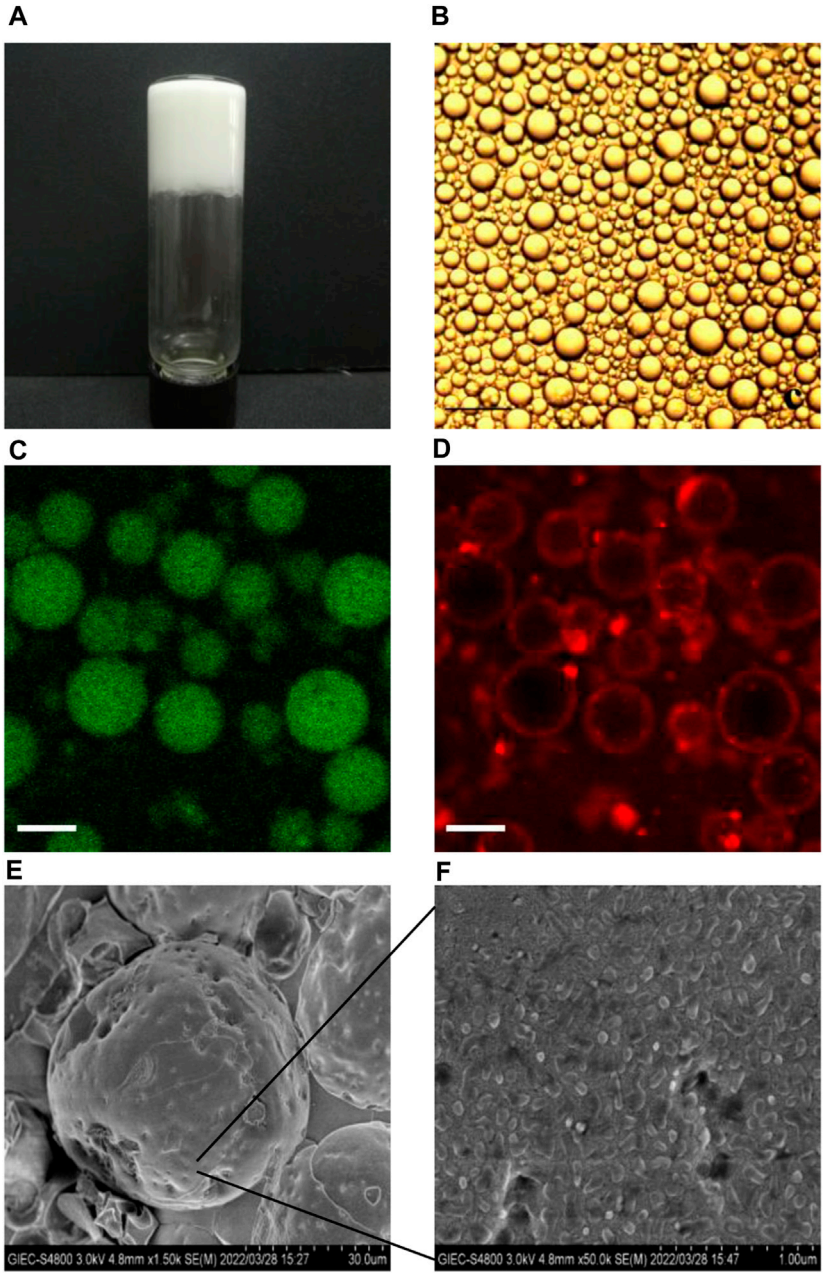


FIGURE 2
Visual photograph **(A)** and microscopic image **(B)** of NOB BSA/CMI-PE (bar scale = 25 μm); CLSM images of BSA/CMI-PE: excitation at 488 nm **(C)** and excitation at 543 nm **(D).** The oil and water phases were stained with curcumin (green) and rhodamine B (red), respectively (bar scale = 30 μm); cryo-SEM images of BSA/CMI-PE particles **(E)** and the surface of BSA/CMI-PE particles **(F)**.

microcalorimetry (ITC) data revealed that BSA/CMI complexes were dominated by enthalpy changes ($\Delta H < 0$, $\Delta S < 0$). Therefore, electrostatic and hydrogen bonding interactions occurred between BSA and CMI. CMI was the bridge for the connection of BSA particles. Raman spectra suggested that the formation of complexes led to the change in the secondary structure of BSA and to the aggregation of BSA (Huang et al., 2019). The BSA/CMI complexes were used to stabilize the Pickering emulsion with an oil phase of 60% (Li and Huang, 2015). Therefore, BCPE was fabricated based on the combined mechanisms of BSA and CMI to prevent flocculation and coalescence (Bouyer et al., 2012).

## 3.2 Microstructures of BCPE

Figure 2A shows the photographs of BCPEs after 7 days of preservation. A uniform milky gel-like material was observed, suggesting that a stable emulsion was fabricated. The microscope image shows BCPE droplets with an average droplet size of 28 μm. CLSM measurement of BCPE was performed. The oil and aqueous phases were stained with curcumin (green) and rhodamine B (red), respectively. The green globes in Figure 2C indicated that the Pickering emulsion is an O/W emulsion Figure 2D showed that a certain thickness aggregated around the oil droplets. This evidence

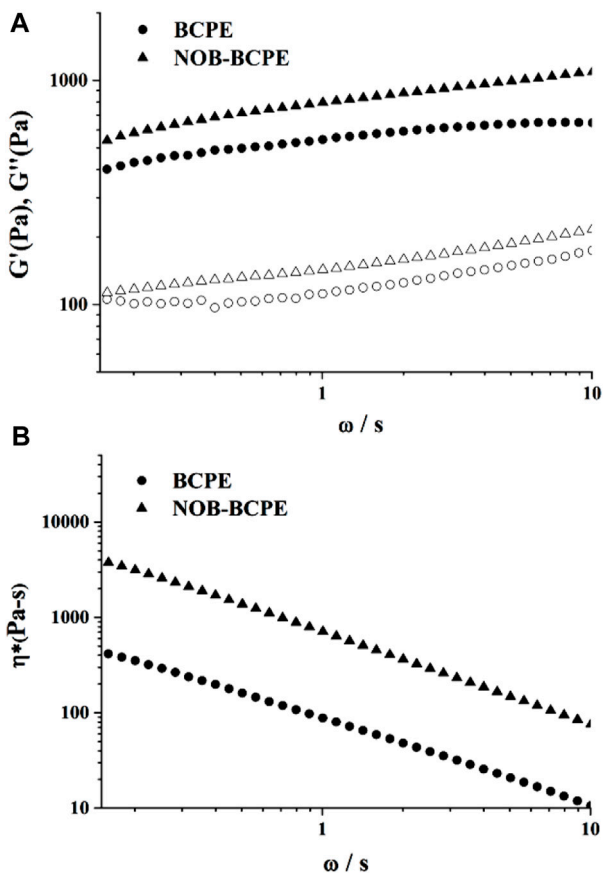


FIGURE 3
Plots of storage modulus (G′) and loss modulus (G″) *versus* angular frequency for NOB-loaded BSA/CMI-PE **(A)**. Plots of tan δ *versus* angular frequency for NOB-loaded BSA/CMI-PE **(B)**.

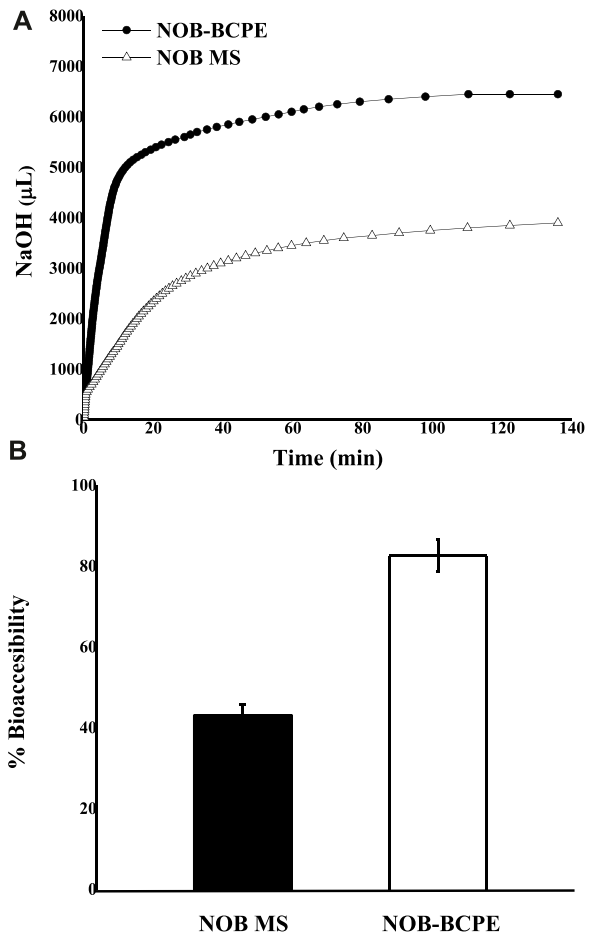


FIGURE 4
*In vitro* comparison of the lipid digestion kinetics of NOB BCPE and MS expressed as the amount of NaOH added as a function of time **(A)**. Comparison of NOB percent bioaccessibility relative to the original dose in BCPE and MS **(B)**. Data are presented as mean ± standard deviation (n = 3).

suggests that the BSA/CMI complexes adsorbed on the surface of oil droplets, and the complexes provided the steric hindrance to stabilize BCPE (Jiang et al., 2021).

The emulsion samples were quickly frozen using liquid nitrogen. The water in the samples cooled rapidly and formed amorphous ice. The emulsion samples were embedded in amorphous ice, and their state was captured in cryo-SEM images. Typical emulsion droplets stabilized by BSA/CMI complexes with indentations are exhibited in Figure 2E. When observed under higher magnification, rod-like nanoscale particles were absorbed onto the surface of emulsion droplets (Figure 2F; Xiao et al., 2016). These particles were larger than pure BSA particles, suggesting that the nanoparticles on the surface of oil droplets were BSA/CMI complexes. Based on the high oil content and droplet density, the distance between the oil droplets is relatively close. The BSA/CMI complexes stabilized the Pickering emulsion by reducing interfacial energy and shielding oil droplets from coalescence.

## 3.3 Textural properties of unloaded and NOB-loaded BCPEs

An optimal BCPE formulation was used to encapsulate 1% (w/v) NOB. Its stability was evaluated using rheological measurements. Dynamic (oscillatory) measurements of BCPE and NOB-loaded BCPE (NOB-BCPE) were carried out as a function of frequency. Both the storage modulus G′ and the loss modulus G″ of BCPE and NOB-BCPE slightly increased with increased frequency, revealing little dependence on frequency (Figures 3A,B). The significantly higher G′ than G″ at all frequencies indicated that the BCPE and the NOB-BCPE formed an interconnected gel-like network microstructure. The viscoelastic properties of this microstructure led to the uniform distribution of NOB in BCPE (Sun et al., 2018). The complex viscosity of BCPE decreased nearly linearly with frequency, suggesting shear-thinning behaviors. A similar phenomenon was observed in the rheological properties of a NOB-loaded nanoemulsion (Zhang et al., 2020). However, this result was in contrast to the result found with a tangeretin- or a 5-demethyltangeretin-loaded nanoemulsion or a PMF (tangeretin of 66% and NOB of 23%)-loaded whey protein isolate/pectin complexes-stabilized Pickering emulsion (Ting et al., 2013; Wijaya et al., 2021). Therefore, the rheological properties of PMFs-loaded emulsion were probably associated with the type and concentration of PMFs and the different kinds of emulsion systems.

The 10 participants in the fork drip test experiments identified the texture values of unloaded and NOB-loaded BCPEs as IDDSI Level 4. The flowability of the unloaded BCPE was better than that of the NOB-loaded BCPE. The emulsions could be brought to the back of the mouth by the tongue for swallowing without being bitten or chewed. The oral chewing properties of the emulsions could be ignored.

## 3.4 *In vitro* lipolysis model analysis of NOB in BCPE and MCT suspensions

The bioaccessibility of NOB loaded in BCPE and MCT suspensions was evaluated using an *in vitro* lipolysis model study. The absorption of hydrophobic bioactives was positively related to their water solubility and stability in the GI tract (Ting et al., 2015). Lipid-based formulations are developed to improve the water dispersity and enhance the absorption of hydrophobic compounds. After digestion in the GI tract, the lipids would be hydrolyzed and then released as free fatty acids (FFAs). The release of FFAs promoted the formation of mixed micelles. The mixed micelles generated in the small intestine, which consist of FFAs and bile salts, could solubilize hydrophobic compounds for intestinal transport. The solubilization capacity for NOB was enhanced by the increase of mixed micelles.

In this *in vitro* model, the existing FFAs led to decreased pH in the SSIF. The addition of NaOH could neutralize the FFAs and maintain the pH at an initial value of 7.50 ± 0.02. The consumption of NaOH as a function of time can be used to indicate the rate of lipid digestion (McClements and Li, 2010). Figure 4A shows the consumption of NaOH solution as a function of time; most of the lipid digestion of NOB-loaded BCPE occurred within the first 10 min. By contrast, the BCPE consumed more than three times the amount of NaOH within the first 10 min. After 2 h, the final consumption of NaOH in the BCPE was nearly twice that in the MCT suspension. Figure 4B shows that the bioaccessibility of NOB was much higher in the BCPE (82.55% ± 3.97%) than it was in the MCT (43.04% ± 2.84%). The higher bioaccessibility of NOB in the BCPE resulted from the higher surface area-to-volume ratio and, thus, the greater extent of lipid hydrolysis of the BCPE than of the MCT suspension.

Three major factors caused the difference in FFA release from the BCPE and MCT suspensions. First, BCPE increased the contact area between the oil droplets and the SSIF. Second, the interfacial properties were altered by the BSA/CMI complexes. The complexes absorbed on the droplet surfaces and formed a thicker layer to prevent the flocculation and coalescence of oil droplets in the small intestine digestion fluid (McClements, 2018; Wijaya et al., 2021). Third, although the digested BSA probably released peptides, amino acids, and some protons ($H^+$), which might lead to an over-estimate of the actual value of released FFA, the peptides or amino acids could favor the formation of mixed micelles (Wijaya et al., 2020). Accordingly, BCPE could enhance the bioaccessibility of NOB proportionally to the rate and extent of lipid digestion (Ting et al., 2015). Due to the liposolubility at the concentration of 1.2% (w/v), the first-pass effect of NOB could be enhanced.

## 3.5 *In vivo* animal model analysis of NOB in BCPE and MCT suspensions

The biological activity of NOB is associated with intake and bioavailability, depending on its absorption, metabolism, and excretion in the human body. After absorption in the small intestine, NOB underwent phase I and II metabolisms. In these two phases, NOB was converted into sulfates, glucuronides, and methylated metabolites in the small intestine. The metabolites of NOB, consisting of 3′,4′-DDMN, 3′-DMN, and 4′-DMN, formed. The metabolites pass to the portal vein and liver before entering the blood and being excreted in urine (Arshad et al., 2023). Because the Pickering emulsion might lead to a slow release and because its ingredients could affect enzymatic activity, NOB and its major metabolites were identified and detected in serum (Ting et al., 2015; Wan et al., 2020). After a single oral administration of NOB (100 mg/kg) in either BCPE or MCT suspension, the distinctive pharmacokinetic profiles of NOB and its metabolites of 4′-DMN, 3′-DMN, 3′,4′-DDMN, and 5-demethylnobiletin in rats were confirmed by UPLC-MS/MS at 6 h. 3′-DMN and 4′-DMN were further identified by HPLC-DAD. NOB and its metabolites were detected by HPLC-DAD at 0.5, 1, 2, 4, 6, 10, and 24 h.

After the conjugates of NOB and its metabolites were treated by enzymes, mass spectral data were obtained with the ESI positive-ion mode under different collision voltages. NOB and its metabolites were observed at 0.5 h after oral administration, suggesting the absorption and metabolism of NOB. NOB and 4′-DMN had the highest concentrations within 24 h in all plasma samples, compared to the other metabolites, illustrating that 4′-DMN was the major metabolite. This result was similar to the metabolites identified in the urine of mice fed with NOB after absorption in the small intestine and liver metabolism (Li et al., 2006b; Zheng et al., 2013). 4′-DMN, 3′-DMN, and 5-demethylnobiletin were converted from NOB directly, while 3′,4′-DDMN was converted from 4′-DMN and 3′-DMN (Figure 5). The MRM LC-MS/MS spectrum indicated that a small amount of 5,4′-didemethylnobiletin (8.8 min) and an unknown demethylated NOB (5.3 min) were present.

The concentration kinetics of NOB and its major metabolite, 4′-DMN, in rat plasma after oral administration of NOB were monitored for 24 h (Figure 6). The pharmacokinetic parameters are summarized in Table 1. The highest peak appeared at a similar time in the NOB-loaded MCT suspension (1.216 ± 0.422 h) and the BCPE (1.152 ± 0.378 h), suggesting that the rates of absorption, metabolism, and excretion were about the same at $T_{max}$. However, the plasma $C_{max}$ of NOB-loaded BCPE (0.936 ± 0.220 μg/mL) was much higher than that of the NOB-loaded MCT suspension (0.532 ± 0.094 μg/mL) at this time. Combined with the *in vitro* results, these findings suggest that BCPE might enhance bioavailability by improving aqueous solubility and controlling release. The plasma concentration of NOB delivered by the MCT suspension dropped dramatically at around 4 h, while the plasma concentration of NOB delivered by BCPE had little change. Then, the plasma concentration of the NOB-loaded BCPE reached a second peak at 6 h. In the TIM-1 GI study of the PMF-loaded whey protein isolate/pectin complexes-stabilized Pickering emulsion, the concentration of NOB in the emulsion reached a peak after 3 h of digestion and then decreased (Wijaya et al., 2020). This

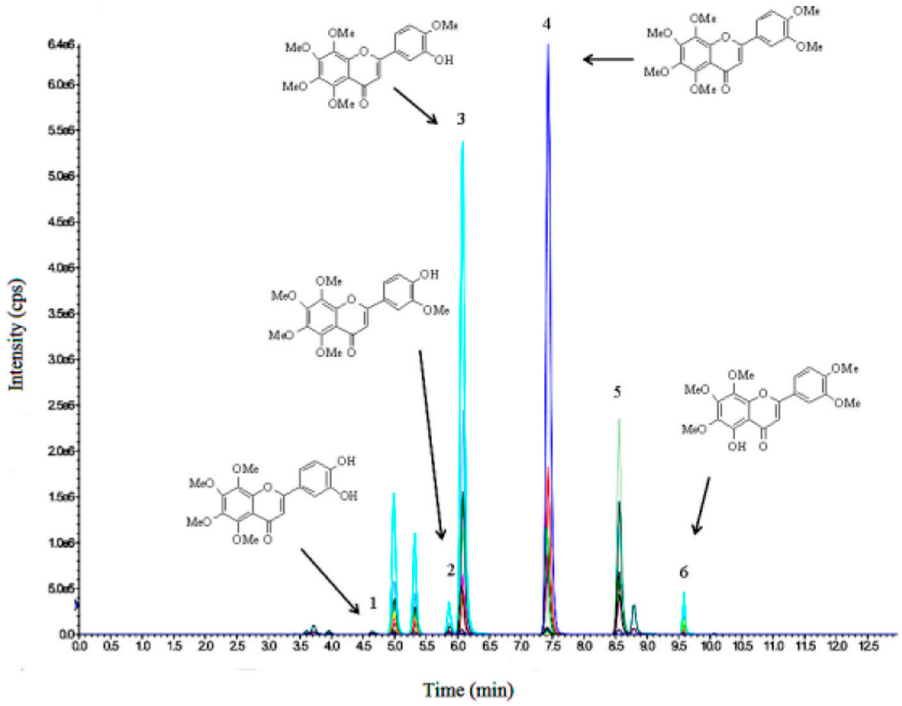


FIGURE 5
LC-MS/MS profile of 3′,4′-DDMN (1), 3′-DMN (2), 4′-DMN (3), NOB (4), tangeretin (5), and 5-demethylnobiletin (6) in plasma at 6 h after oral administration.

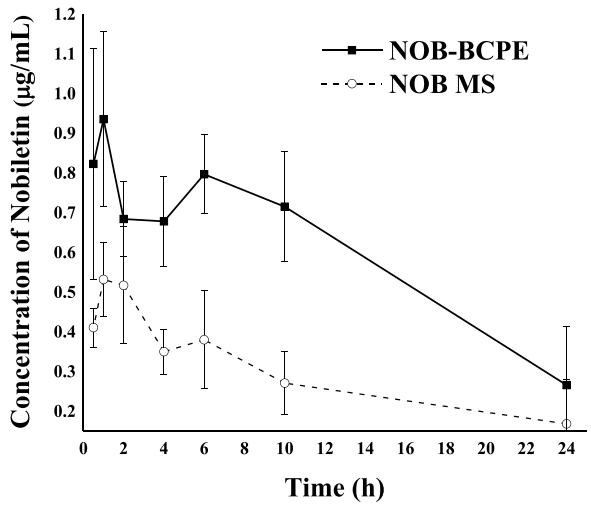


FIGURE 6
Profiles of plasma concentration of NOB as a function of time after oral administration of 100 mg/kg in the form of BCPE (solid line) and MS (dashed line). Data from five rats are presented as mean ± standard deviation.

phenomenon revealed that BCPE had a sustained release effect. The $AUC_{0-24}$ of NOB in the MCT suspension (6.84 ± 1.48 h*μg/mL) and BCPE (14.19 ± 1.67 h*μg/mL) were significantly different. The relative bioavailability of NOB loaded in BCPE was 2.07 times higher than that suspended in MCT over 24 h. Plasma concentrations of NOB in both BCPE and MCT suspensions returned to similar levels at 24 h.

In the plasma concentration–time curve, the plasma concentration data suggest a two-compartment model. The extended release of NOB delivered by BCPE could be associated with the viscoelasticity and viscosity of BCPE (Ting et al., 2015). In addition, the composition of the emulsion stabilizer might contribute to different absorption and metabolism rates of NOB (Dickinson, 2009).

The clearance of 4′-DMN in the plasma might be due to 1) further biotransformation to other metabolites, 2) delivery into targeted organs, and 3) excretion in urine. Compared with the *in vivo* biotransformation results of NOB in conventional emulsion, the different pattern of 4′-DMN in rat plasma observed in this study suggested that the emulsion types could be an important factor for the biotransformation *in vivo* (Zhang et al., 2020). Due to the properties of the Pickering emulsion, the particles or complexes were difficult to detach from the interface of water and oil. Therefore, the Pickering emulsion was considered to have a higher stability than conventional emulsions. The complexes consisted of CMI, an anionic derivative of inulin. Given that CMI could be digested by gut microbiota, the upward trend of plasma 4′-DMN within 10–24 h might result from microbial biotransformation and reabsorption from the colon. Future encapsulation strategies might utilize prebiotics as the building blocks of delivery systems to benefit the gut microbiota.

Figure 7 shows the plasma concentration of 4′-DMN after oral administration of NOB in BCPE and unformulated MCT over

TABLE 1 Pharmacokinetic parameters of NOB in rats after oral administration.

| Formulation | NOB dose (mg/kg) | $T_{max}$ (hr) | $C_{max}$ (μg/mL) | $AUC_{0-24}$ (hr × μg/mL) | Relative bioavailability |
|---|---|---|---|---|---|
| MCT suspension | 100 | 1.216 ± 0.422 | 0.532 ± 0.094 | 6.84 ± 1.48 | 2.07 |
| Emulsion | 100 | 1.152 ± 0.378 | 0.936 ± 0.220 | 14.19 ± 1.67 | |

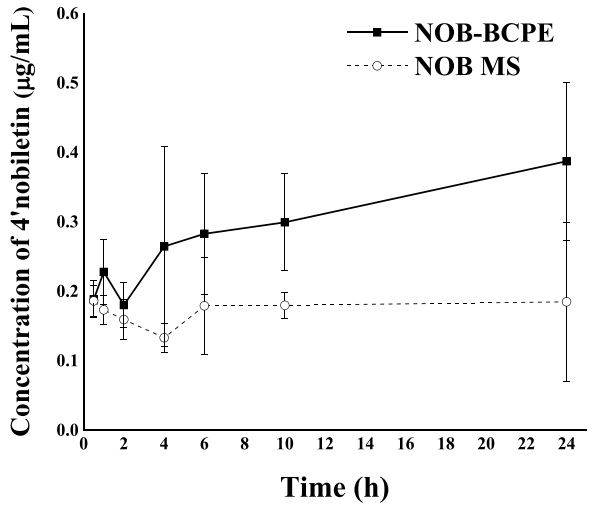


FIGURE 7
Profiles of plasma concentration of 4′-DMN as a function of time after oral administration of 100 mg/kg in the form of BCPE (solid line) and MS (dashed line), respectively. Data from five rats are presented as mean ± standard deviation.

24 h. A much higher level of 4′-DMN was observed in rats receiving BCPE than in rats receiving the MCT suspension, suggesting a higher metabolic rate for NOB-loaded in BCPE than for the MCT suspension. In particular, the concentration of 4′-DMN exhibited an upward trend from 10 h to 24 h. This trend was different from the result of *in vivo* experiments of untreated NOB; the concentration of 4′-DMN sharply decreased from 10 h to 24 h, and 4′-DMN could not be detected in any organ after 24 h, suggesting that BCPE could prolong the residence time of 4′-DMN (Murakami et al., 2002). Such an upward trend of 4′-DMN was not observed in rats receiving the NOB-loaded conventional emulsion (Ting et al., 2015; Zhang et al., 2020). This pattern was probably attributed to the biotransformation of NOB in serum at 6 h, which was the second peak of digestion (Figure 6). Therefore, BCPE could alter the host's biotransformation of NOB.

## 4 Conclusion

NOB-loaded BCPE was fabricated, and its swallowing and digestive characteristics were evaluated in this study. The characteristics of NOB-loaded BCPE were observed as follows: 1) based on the IDDSI framework, NOB-loaded BCPE was semi-solid and could be swallowed without being chewed. This property could reduce the contact time between NOB and the taste buds to lower the impact of bitterness. In addition, NOB was distributed inside the emulsion, and the ingredients in the water phase might distract from any off-flavor or trigeminal effect. 2) The *in vitro* digestion model revealed that BCPE could enhance the bioaccessibility of NOB by accelerating lipid digestion and micelle formation. 3) The *in vivo* animal study revealed that the plasma concentration of NOB in rats was enhanced after the oral administration of NOB-loaded BCPE. CMI could not be degraded by pepsin, CMI protected BSA from proteolysis, and sustained release of NOB-loaded in BCPE was achieved. 4) The biotransformation content of the major metabolite (4′-DMN) in rat plasma was promoted. BCPE might enhance the bioavailability and promote the biotransformation content of major metabolites by adjusting the micelle formation and intestinal permeability.

The swallowing and digestive profile of BCPE was characterized by the IDDSI framework model, an *in vitro* digestion model, and an *in vivo* animal model, which is useful for precisely applying the system to natural products. According to the results, BCPE might be a potential functional food matrix that can be shaped as needed. It might be a good delivery system for hydrophobic and bitter natural products.

## Data availability statement

The original contributions presented in the study are included in the article/Supplementary Material; further inquiries can be directed to the corresponding authors.

## Ethics statement

The animal study was approved by the Chinese Government's Guide for the Care and Use of Laboratory Animals. The study was conducted in accordance with the local legislation and institutional requirements.

## Author contributions

GH: writing–review and editing, writing–original draft, visualization, and funding acquisition. MZ: writing–original draft, validation, and data curation. KF: writing–original draft, visualization, software, and methodology. JX: writing–review and editing, visualization, and resources. QH: writing–review and editing, resources, project administration, and methodology. C-TH: writing–review and editing, validation, project administration, and methodology. JL: writing–review and editing, methodology, investigation, and data curation. MZ: resources, investigation, writing–review and editing, and funding acquisition.

## Funding

The author(s) declare that financial support was received for the research, authorship, and/or publication of this article from the Guangdong Provincial Key Laboratory of Lingnan Specialty Food Science and Technology (2021B1212040013), the Jiangmen Program for Innovative Research Team (2018630100180019806), and the Program for Guangdong Introducing Innovative and Entrepreneurial Teams (2019ZT08N291).

## Acknowledgments

We appreciate the support of the Laboratory of Sensory Characteristics and Sensory Analysis of Lingnan Specialty Food (22097155302141). We are also grateful for the help of Kun MZ, Suqing Zhao, Shuwen JL, Weiping Jin, Yujing Lu, Yuanxin Qiu, Qin Wang, Chan Wang, Yangping Xin, Yan Luo, Xiaorong Chen, Jian JL, Winnie Huang, and Zhihui Lin.

## Conflict of interest

The authors declare that the research was conducted in the absence of any commercial or financial relationships that could be construed as a potential conflict of interest.

The reviewer JS declared a past co-authorship with the author JL to the handling editor.

## Publisher's note

All claims expressed in this article are solely those of the authors and do not necessarily represent those of their affiliated organizations, or those of the publisher, the editors, and the reviewers. Any product that may be evaluated in this article, or claim that may be made by its manufacturer, is not guaranteed or endorsed by the publisher.

## References

Arshad, R., Masood, S., Sharif, H. R., Goksen, G., Xu, B., and Faisal Manzoor, M. (2023). New insights into health-promoting effects of nobiletin from citrus fruits. *Food Rev. Int.*, 1–20. doi:10.1080/87559129.2023.2212047

Batenburg, A. M., de Joode, T., and Gouka, R. J. (2016). Characterization and modulation of the bitterness of polymethoxyflavones using sensory and receptor-based methods. *J. Agric. food Chem.* 64 (12), 2619–2626. doi:10.1021/acs.jafc.5b05833

Bouyer, E., Mekhloufi, G., Rosilio, V., Grossiord, J. L., and Agnely, F. (2012). Proteins, polysaccharides, and their complexes used as stabilizers for emulsions: alternatives to synthetic surfactants in the pharmaceutical field? *Int. J. Pharm.* 436 (1-2), 359–378. doi:10.1016/j.ijpharm.2012.06.052

Chen, J., Li, D.-L., Xie, L.-N., Ma, Y.-r., Wu, P.-P., Li, C., et al. (2020). Synergistic anti-inflammatory effects of silibinin and thymol combination on LPS-induced RAW264. 7 cells by inhibition of NF-κB and MAPK activation. *Phytomedicine* 78, 153309. doi:10. 1016/j.phymed.2020.153309

Dickinson, E. (1998). Stability and rheological implications of electrostatic milk protein - polysaccharide interactions. *Trends Food Sci. Technol.* 9 (10), 347–354. doi:10. 1016/s0924-2244(98)00057-0

Dickinson, E. (2009). Hydrocolloids as emulsifiers and emulsion stabilizers. *Food Hydrocoll.* 23 (6), 1473–1482. doi:10.1016/j.foodhyd.2008.08.005

Gao, Z., Gao, W., Zeng, S.-L., Li, P., and Liu, E.-H. (2018). Chemical structures, bioactivities and molecular mechanisms of citrus polymethoxyflavones. *J. Funct. Foods* 40, 498–509. doi:10.1016/j.jff.2017.11.036

Goldstein, N., Lesmes, U., Portmann, R., and Levi, C. (2017). Emulsion and protein degradation in the elderly: qualitative insights from a study coupling a dynamic *in vitro* digestion model with proteomic analyses. *Food Hydrocoll.* 69 (Aug), 393–401. doi:10. 1016/j.foodhyd.2017.02.017

Hadde, E. K., and Chen, J. (2020). Texture and texture assessment of thickened fluids and texture-modified food for dysphagia management. *J. Texture Stud.* 52, 4–15. doi:10. 1111/jtxs.12567

Huang, G., Liu, J., Jin, W., Wei, Z., Ho, C.-T., Zhao, S., et al. (2019). Formation of nanocomplexes between carboxymethyl inulin and bovine serum albumin via pH-induced electrostatic interaction. *Molecules* 24 (17), 3056. doi:10.3390/molecules24173056

Huang, H., Li, L., Shi, W., Liu, H., Yang, J., Yuan, X., et al. (2016). The multifunctional effects of nobiletin and its metabolites *in vivo* and *in vitro*. *Evidence-Based Complementary Altern. Med.* 2016, 2918796–2918814. doi:10.1155/2016/2918796

Jiang, Y., Zhang, C., Yuan, J., Wu, Y., Huang, Q., I N Waterhouse, G., et al. (2021). Exploiting the robust network structure of zein/low-acyl gellan gum nanocomplexes to create pickering emulsion gels with favorable properties. *Food Chem.* 349 (6), 129112. doi:10.1016/j.foodchem.2021.129112

Jie, X., Yunqi, Li, and Qingrong, H. (2016). Recent advances on food-grade particles stabilized Pickering emulsions: fabrication, characterization and research trends. *Trends Food Sci. Technol.* 55, 48–60. doi:10.1016/j.tifs.2016.05.010

Joshi, P. N., Agawane, S., Athalye, M. C., Jadhav, V., and Prakash, R. (2017). Multifunctional inulin tethered silver-graphene quantum dots nanotheranostic module for pancreatic cancer therapy. *Mater. Sci. Eng. C* 78, 1203–1211. doi:10. 1016/j.msec.2017.03.176

Kerien, M., Jasutien, I., Eisinait, V., Venskutonis, P. R., and Leskauskait, D. (2020). Designing multiple bioactives loaded emulsions for the formulations for diets of elderly. *Food and Funct.* 11 (3), 2195–2207. doi:10.1039/d0fo00021c

Li, S., Lo, C.-Y., and Ho, C.-T. (2006a). Hydroxylated polymethoxyflavones and methylated flavonoids in sweet orange (Citrus sinensis) peel. *J. Agric. Food Chem.* 54 (12), 4176–4185. doi:10.1021/jf060234n

Li, S., Wang, H., Guo, L., Zhao, H., and Ho, C.-T. (2014). Chemistry and bioactivity of nobiletin and its metabolites. *J. Funct. foods* 6, 2–10. doi:10.1016/ j.jff.2013.12.011

Li, S., Wang, Z., Sang, S., Huang, M. T., and Ho, C. T. (2006b). Identification of nobiletin metabolites in mouse urine. *Mol. Nutr. food Res.* 50 (3), 291–299. doi:10.1002/ mnfr.200500214

Li, S., Zhang, L., Wan, X., Zhan, J., and Ho, C.-T. (2022). Focusing on the recent progress of tea polyphenol chemistry and perspectives. *Food Sci. Hum. Wellness* 11 (3), 437–444. doi:10.1016/j.fshw.2021.12.033

Li, Y., and Huang, Q. (2015). Protein-polysaccharide complexes for effective delivery of bioactive functional food ingredients. *Nano-and Micro-Scale Veh. Eff. Deliv. Bioact. Ingredients Funct. Foods*, 224–246. doi:10.1002/9781118462157.ch14

McClements, D. J. (2018). Enhanced delivery of lipophilic bioactives using emulsions: a review of major factors affecting vitamin, nutraceutical, and lipid bioaccessibility. *Food and Funct.* 9 (1), 22–41. doi:10.1039/c7fo01515a

McClements, D. J., and Li, Y. (2010). Structured emulsion-based delivery systems: controlling the digestion and release of lipophilic food components. *Adv. colloid interface Sci.* 159 (2), 213–228. doi:10.1016/j.cis.2010.06.010

Min, X., Guo, S., Lu, Y., and Xu, X. (2024). Investigation on the inhibition mechanism and binding behavior of cryptolepine to α-glucosidase and its hypoglycemic activity by multi-spectroscopic method. *J. Luminescence* 269, 120437. doi:10.1016/j.jlumin.2024. 120437

Ming, L., Wu, H., Liu, A., Naeem, A., Dong, Z., Fan, Q., et al. (2023). Evolution and critical roles of particle properties in Pickering emulsion: a review. *J. Mol. Liq.* 388, 122775. doi:10.1016/j.molliq.2023.122775

Murakami, A., Koshimizu, K., Ohigashi, H., Kuwahara, S., Kuki, W., Takahashi, Y., et al. (2002). Characteristic rat tissue accumulation of nobiletin, a chemopreventive polymethoxyflavonoid, in comparison with luteolin. *BioFactors* 16, 73–82. doi:10.1002/ biof.5520160303

Nakajima, A., and Ohizumi, Y. (2019). Potential benefits of nobiletin, A citrus flavonoid, against alzheimer's disease and Parkinson's disease. *Int. J. Mol. Sci.* 20 (14), 3380. doi:10.3390/ijms20143380

Nohara, K., Mallampalli, V., Nemkov, T., Wirianto, M., Yang, J., Ye, Y., et al. (2019). Nobiletin fortifies mitochondrial respiration in skeletal muscle to promote healthy aging against metabolic challenge. *Nat. Commun.* 10 (1), 3923–4015. doi:10.1038/s41467-019-11926-y

Sun, G., Lei, L., Chen, H., Li, B., Cao, Y., and Li, Y. (2018). Tailoring of structured hydroxypropyl methylcellulose-stabilized emulsions for encapsulation of nobiletin: modification of the oil and aqueous phases. *Food and Funct.* 9 (7), 3657–3664. doi:10.1039/c7fo02068f

Ting, Y., Jiang, Y., Lan, Y., Xia, C., Lin, Z., Rogers, M. A., et al. (2015). Viscoelastic emulsion improved the bioaccessibility and oral bioavailability of crystalline compound: a mechanistic study using *in vitro* and *in vivo* models. *Mol. Pharm.* 12 (7), 2229–2236. doi:10.1021/mp5007322

Ting, Y., Xia, Q., Li, S., Ho, C.-T., and Huang, Q. (2013). Design of high-loading and high-stability viscoelastic emulsions for polymethoxyflavones. *Food Res. Int.* 54 (1), 633–640. doi:10.1016/j.foodres.2013.07.047

Wan, X., Guo, H., Liang, Y., Zhou, C., Wang, L., Li, K., et al. (2020). The physiological functions and pharmaceutical applications of inulin: a review. *Carbohydr. Polym.* 246, 116589. doi:10.1016/j.carbpol.2020.116589

Wijaya, W., Zheng, H., Patel, A. R., Van der Meeren, P., and Huang, Q. (2021). Crystallization of polymethoxyflavones in high internal phase emulsions stabilized using biopolymeric complexes: implications for microstructure and *in vitro* digestion properties. *Food Biosci.* 40, 100876. doi:10.1016/j.fbio.2021.100876

Wijaya, W., Zheng, H., Zheng, T., Su, S., Patel, A. R., Van der Meeren, P., et al. (2020). Improved bioaccessibility of polymethoxyflavones loaded into high internal phase emulsions stabilized by biopolymeric complexes: a dynamic digestion study via TNO's gastrointestinal model. *Curr. Res. food Sci.* 2, 11–19. doi:10.1016/j.crfs.2019.11.007

Wu, X., Song, M., Qiu, P., Li, F., Wang, M., Zheng, J., et al. (2018). A metabolite of nobiletin, 4′-demethylnobiletin and atorvastatin synergistically inhibits human colon cancer cell growth by inducing G0/G1 cell cycle arrest and apoptosis. *Food and Funct.* 9 (1), 87–95. doi:10.1039/c7fo01155e

Wu, X., Song, M., Rakariyatham, K., Zheng, J., Guo, S., Tang, Z., et al. (2015). Anti-inflammatory effects of 4′-demethylnobiletin, a major metabolite of nobiletin. *J. Funct. foods* 19, 278–287. doi:10.1016/j.jff.2015.09.035

Wu, X.-Z., Zhu, W.-J., Lu, L., Hu, C.-M., Zheng, Y.-Y., Zhang, X., et al. (2023). Synthesis and anti-α-glucosidase activity evaluation of betulinic acid derivatives. *Arabian J. Chem.* 16 (5), 104659. doi:10.1016/j.arabjc.2023.104659

Xiao, J., Wang, X., Gonzalez, A., and Huang, Q. (2016). Kafirin nanoparticles-stabilized Pickering emulsions: microstructure and rheological behavior. *Food Hydrocoll.* 54, 30–39. doi:10.1016/j.foodhyd.2015.09.008

Zhang, C. T., Zhu, S., and Huang, Q. (2021). Citrus polymethoxyflavones as regulators of metabolic homoeostasis: recent advances for possible mechanisms. *Trends Food Sci. Technol.* 110 (1), 743–753. doi:10.1016/j.tifs.2021.02.046

Zhang, M., Feng, K., Huang, G., Xin, Y., Huang, Q., Cao, Y., et al. (2020). Assessment of oral bioavailability and biotransformation of emulsified nobiletin using *in vitro* and *in vivo* models. *J. Agric. Food Chem.* 68 (41), 11412–11420. doi:10.1021/acs.jafc.0c04450

Zhang, X., Zheng, Y.-Y., Hu, C.-M., Wu, X.-Z., Lin, J., Xiong, Z., et al. (2022). Synthesis and biological evaluation of coumarin derivatives containing oxime ester as α-glucosidase inhibitors. *Arabian J. Chem.* 15 (9), 104072. doi:10.1016/j.arabjc.2022.104072

Zheng, J., Bi, J., Johnson, D., Sun, Y., Song, M., Qiu, P., et al. (2015). Analysis of 10 metabolites of polymethoxyflavones with high sensitivity by electrochemical detection in high-performance liquid chromatography. *J. Agric. food Chem.* 63 (2), 509–516. doi:10.1021/jf505545x

Zheng, J., Song, M., Dong, P., Qiu, P., Guo, S., Zhong, Z., et al. (2013). Identification of novel bioactive metabolites of 5-demethylnobiletin in mice. *Mol. Nutr. food Res.* 57 (11), 1999–2007. doi:10.1002/mnfr.201300211

frontiers | Frontiers in Chemistry

TYPE Original Research
PUBLISHED 14 May 2024
DOI 10.3389/fchem.2024.1383886

Check for updates

OPEN ACCESS

EDITED BY
Xuetao Xu,
Wuyi University, China

REVIEWED BY
Li-She Gan,
Zhejiang Chinese Medical University, China
Xiaoxiao Huang,
Shenyang Pharmaceutical University, China

*CORRESPONDENCE
Fangfang Xu,
xudubfang@163.com
Bo Liu,
doctliu@263.net
Xiaoqi Zhang,
tzhxq01@jnu.edu.cn

†These authors have contributed equally to this work

RECEIVED 08 February 2024
ACCEPTED 12 April 2024
PUBLISHED 14 May 2024

CITATION
Yang J, Cai W, Wu F, Xu S, Zhang X, Liu B and Xu F (2024), Hovendulcisic acid A-D: four novel ceanothane-type triterpenoids from *Hovenia dulcis* stems with anticancer properties. *Front. Chem.* 12:1383886.
doi: 10.3389/fchem.2024.1383886

COPYRIGHT
© 2024 Yang, Cai, Wu, Xu, Zhang, Liu and Xu. This is an open-access article distributed under the terms of the Creative Commons Attribution License (CC BY). The use, distribution or reproduction in other forums is permitted, provided the original author(s) and the copyright owner(s) are credited and that the original publication in this journal is cited, in accordance with accepted academic practice. No use, distribution or reproduction is permitted which does not comply with these terms.

# Hovendulcisic acid A-D: four novel ceanothane-type triterpenoids from *Hovenia dulcis* stems with anticancer properties

Jianzhan Yang[1†], Wanna Cai[1,2†], Fan Wu[1], Shengmei Xu[1], Xiaoqi Zhang[3]*, Bo Liu[1]* and Fangfang Xu[1]*

[1]Guangdong Provincial Key Laboratory of Research on Emergency in TCM, the Second Clinical College of Guangzhou University of Chinese Medicine, Guangzhou, China, [2]Department of Pharmacy, The First Affiliated Hospital of Shantou University Medical College, Shantou, China, [3]Guangdong Provincial Engineering Research Center for Modernization of TCM, College of Pharmacy, Jinan University, Guangzhou, China

Sixteen ceanothane-type triterpenoids, including four new compounds—hovendulcisic acids A–D (**1**–**4**) —were purified from the stems of *Hovenia dulcis* Thunb. The structures of **1**–**4** were confirmed by comprehensive means including ECD and quantum chemical calculations. Putative biosynthetic pathways of **1**–**16** were proposed, and **3**, **5**, and **15** exhibited antitumor activity on A549 and MDA-MB-231 cells.

KEYWORDS

***Hovenia dulcis* Thunb, ceanothane-type triterpenoids, hovendulcisic acid, antitumor activity, quantum chemical calculations**

## Introduction

*Hovenia dulcis* Thunb (Rhamnaceae family) is a traditional Chinese medicine, and many parts of this herb, including seeds, fruit, leaves, and stem, have been used to relieve alcohol toxicity and protect the liver in ancient medical books (Wang, 1958; Su, 1985; Flora of China Editorial Committee, 1982; Chinese materia medica editorial board, 1999; Wu, 2000). Research on the *Hovenia* genus has revealed its anti-tumor efficacy (Ji, 2003; Ji, et al., 2003; Zhang, 2017), with triterpenoids and flavonoids as their main bioactive constituents (Yoshikawa et al., 1992; Yoshikawa et al., 1998a; Kang et al., 2017; Xu, et al., 2020a; Xu, et al., 2020b; Cai, et al., 2021).

Previous studies revealed that the triterpenoid saponins from *H. dulcis* inhibited Nrf2 expression (Cai, et al., 2021), indicated potential anti-tumor sensitization activity (Lin et al., 2020). This discovery piqued our interest about the triterpenoid constituents of the *Hovenia* genus. We found the stems of *Hovenia* genus to be rich in triterpenoids by LC-MS experimentation. The chemical constituents from the stem of *H. dulcis* were thus isolated and identified in this study. As a result, four new triterpenoids of hovendulcisic acid A-D (**1**–**4**) were isolated from 70% alcohol extract by multi-column chromatography and HPLC methods. The activity of **1**–**4** on Nrf2 were measured by luciferase reporter gene assay, and the cell viability of **1**–**4** on MDA-MB-231 and A549 cells were tested by CCK8 method. This research serves as a reference for further study on the pharmacological effects and drug active substance basis of *H. dulcis*.

# Materials and methods

## General experimental procedures

NMR data were obtained with a Bruker AMX-600 (Germany). HRESIMS was performed on a Thermo LTQ Orbitrap-Discovery (United States). Acid hydrolysis results were analyzed by Agilent GC 7890A/5975C (United States). UV was recorded on a Hitachi U-2910 (Japan). IR were acquired using a Perkin Elmer Spectrum 400 (United States). Preparative HPLC used an Agilent 1260 instrument equipped with a Cosmosil ODS $C_{18}$ column (5 $\mu$m, 10 mm × 250 mm). Optical rotations were measured on a Rodolph Autopol I Polarimeter (United States); column chromatographies were performed with 80–100 and 200–300 mesh silica gel (Qingdao Haiyang) and Sephadex LH-20 (Pharmacia, United States). TLC was carried out on GF254 plates (Qingdao Haiyang). Human MDA-MB-231 cells were purchased from ATCC (VA, United States). D-(+)-glucose and tert-butylhydroquinone (tBHQ) were bought from Sigma Chemical (MO, United States).

## Plant materials

The stems of *H. dulcis* Thunb. were collected in December 2020 in Zhen-an City, Shanxi Province and identified by pharmacist Ganshu She in the Guangdong Provincial Hospital of Chinese Medicine. The samples were authenticated as voucher number (202012001) and stored at the TCM storehouse in the Second Clinical College of the Guangzhou University of Chinese Medicine.

## Extraction and Isolation

A total of 30.0 kg of air-dried and mechanically powdered stems of *H. dulcis* were extracted by reflux using ethanol-$H_2O$ solvent (70:30, *v*/*v*) thrice and then concentrated to obtain residue. The crude extract was then suspended with water and successively extracted by EtOAc and n-BuOH. The EtOAc fraction (382.9 g) was isolated on a silica gel column and eluted with $CHCl_2$/MeOH solvent system to obtain seven fractions (E1 – E7). Fraction E1 (0.77 g) was isolated via ODS column [MeOH/$H_2O$ (40 : 60–100 : 0)], obtaining four subfractions (E1–1 – E1-4). Subfraction E1-2 was separated on a semi-prepared HPLC [aqueous acetonitrile (3.0 mL/min, 99 : 1, *v*/*v*)] and obtained **15** (2 mg, $t_R$ = 18.9 min). Fraction E2 (62.37 g) was isolated on a silica gel (300–400 mesh) column [PE/EtOAc (1:0, 10:1, 9:1, 6:1, 5:1, 4:1, 3:1, 2:1, 1:1, and 0:1)] with 15 subfractions (E2–1 – E2-15). E2-2 was repeatedly dissolved and recrystallized in $CHCl_2$ and MeOH to obtain compound **16** (35.1 mg). E2-4 (201.0 mg) was separated on a Sephadex LH-20 column (MeOH) and then separated on a ODS column [MeOH/$H_2O$ solvent (2:3–1:0)] to divide into four subfractions (E2-4–1 – E2-4–4). Compound **3** (19.1 mg, $t_R$ = 12.1 min) was isolated from subfraction E2-4-2 by semi-prepared HPLC using aqueous acetonitrile (3.0 mL/min, 99 : 1, *v*/*v*). E2-6 (781.0 mg) was separated on a Sephadex LH-20 column (MeOH), and compound **5** (66 mg) was obtained by MeOH redissolution. E2-9 (1.11 g) fractions were separated by a silica gel column with $CHCl_2$/MeOH (100:0, 250:1, 200:1, 150:1, 100:1, 50:1, 30:1, 10:1, 0:100). Compound **11** (38 mg, $t_R$ = 20.5 min) was obtained from E2-9-6 by semi-prepared HPLC (acetonitrile: water, 65:35, *v*/*v*). E2-10 (2.60 g) was separated on a Sephadex LH-20 column (MeOH), obtaining five subfractions E2-10–1 – E2-10–5. E2-10–2 (268 mg) was isolated on an ODS column eluted with gradient MeOH/$H_2O$ solvent (20:80–100:0, *v*/*v*) to divide into six subfractions (E2-10-2–1 – E2-10-2–6). Compound **12** (2.2 mg, $t_R$ = 9.0 min) was obtained from E2-10–2-2 by semi-prepared HPLC (acetonitrile: water, 67 : 33, *v*/*v*), and compound **8** (9.1 mg, $t_R$ = 18.4 min) was obtained from E2-10–2-5 by semi-prepared HPLC (acetonitrile: water, 70 : 30, *v*/*v*). E2-12 (2.65 g) was separated on an ODS column [MeOH/$H_2O$ solvent (30:70–100:0, *v*/*v*)] to divide into six subfractions (E2-12–1 – E2-12–6). Compound **2** (5.1 mg, $t_R$ = 10.6 min) was obtained from E2-12-4 by semi-prepared HPLC (acetonitrile: water, 75 : 25, *v*/*v*). Compound **7** (54 mg) was obtained from E2-12-5 by repeatedly dissolving and recrystallizing in MeOH. E2-13 (5.86 g) was separated on an ODS column [MeOH/$H_2O$ solvent (20 : 80–100 : 0, *v*/*v*)] to divide into eight subfractions (E2-13–1 – E2-13–8). Compound **9** (228.1 mg, $t_R$ = 8.0 min) was obtained from E2-13-4 by semi-prepared HPLC (acetonitrile: water, 60 : 40, *v*/*v*). E2-13–6 was separated by silica gel column chromatography ($CHCl_2$/MeOH, 100:0, 50:1, 40:1, 25:1, 15:1, 10:1, 5:1), obtaining five subfractions (E2-13-6–1 – E2-13-6–5). We obtained **10** (33.2 mg, $t_R$ = 7.2 min) by semi-prepared HPLC (acetonitrile: water, 65:35, *v*/*v*) from E2-13-6–3. Fraction E3 (41.53 g) was separated on a silica gel (300–400 mesh) column eluted by $CHCl_2$/MeOH (100:0, 25:1, 15:1, 10:1, 6:1, 4:1, 0:100) to obtain ten subfractions (E3–1 – E3-15). Subfraction E3-6 (2.73 g) was further separated on a Sephadex LH-20 column (MeOH) into eight subfractions (E3-6–1 – E3-6–8). Subfraction E3-6–2 (519.1 mg) was purified on an ODS column eluted with gradient MeOH/$H_2O$ (1:4–1:0), followed by semi-prepared HPLC eluted with acetonitrile/0.1% formic acid water (3.0 mL/min, 57 : 43, *v*/*v*) to obtain **4** (9.0 mg, $t_R$ = 12.8 min). Compound **1** (5.1 mg) was isolated from subfraction E3-6–3 (591.1 mg) by an ODS column eluted with MeOH/$H_2O$ (1:4–1:0). Compound **13** (2.2 mg) was obtained from E3-6-5 by repeated dissolving and recrystallizing in MeOH. E3-8 (2.47 g) was separated on a Sephadex LH-20 column (MeOH) and semi-prepared HPLC (acetonitrile: water, 70 : 30, *v*/*v*), obtaining compound **14** (13.2 mg, $t_R$ = 16 min).

## Spectroscopic data

Hovendulcisic acid A (**1**): white powder; m.p. 340–342°C; $[\alpha]^{25}_D$ +11.20 (c 0.8, MeOH); UV (MeOH) $\lambda_{max}$: 201.0 nm; IR ($\nu_{max}$ $cm^{-1}$): 3330.0, 2955.3, 2868.3, 1457.3, 1392.8, 1241.0, 1715.6, 1682.6, 1644.6, 1174.0, and 883.5. HR-ESI-MS: *m/z* 533.3124 $[M-H]^-$ ($C_{30}H_{45}O_8$, calcd. for 533.3109). 1D NMR see Table 1 and Table 2.

Hovendulcisic acid B (**2**): white powder; m.p. 324–326°C; $[\alpha]^{25}_D$ +16.0 (c 0.1, MeOH); UV (MeOH) $\lambda_{max}$: 203.5 nm; IR ($\nu_{max}$ $cm^{-1}$): 3475.3, 2968.4, 2937.8, 2868.3, 1454.1, 1402.4, 1379.8, 1722.0, 1718.9, 1687.9, 1644.6, 1235.4, and 883.5. HR-ESI-MS: *m/z* 499.3060 $[M-H]^-$ ($C_{30}H_{43}O_6$, calcd. for 499.3054). 1D NMR see Table 1 and Table 2.

Hovendulcisic acid C (**3**): white powder; m.p. 326–328°C; $[\alpha]^{25}_D$ −11.8 (c 0.1, MeOH); UV (MeOH) $\lambda_{max}$: 204.0 nm; IR ($\nu_{max}$ $cm^{-1}$): 3397.0, 2944.8, 2869.0, 1739.6, 1701.3, 1458.2, 1375.0, 1235.1,

10.3389/fchem.2024.1383886

TABLE 1 $^{1}$H NMR data of 1–4 ($CD_3OD$, 600 MHz, $\delta$ in ppm, $J$ in Hz).

| Position | 1[a] | 2 | 3 | 4 |
|---|---|---|---|---|
| | $\delta_H$ | $\delta_H$ | $\delta_H$ | $\delta_H$ |
| 1 | 3.30, s | 2.50, s | 1.86, td, (8.2, 4.6) | 2.48, s |
| 2 | - | - | 4.47, dd, (11.5,4.5) | - |
| | | | 4.04, dd, (11.5,7.8) | |
| 3 | 4.87, s | 4.08, s | 4.94, d, (8.7) | 4.07, s |
| 5 | 2.22, m | 1.56, m | 1.22, m | 1.58, m |
| 6 | 1.50, m | 1.43, m | 1.46, m | 1.39, m |
| | 1.42, m | 1.35, m | 1.36, m | 1.33, m |
| 7 | 1.03, m | 2.25, dt, (13.2, 3.3) | 1.44, m | 1.84, m |
| | 1.94, m | 1.06, m | 1.42, m | 1.81, m |
| 9 | 2.80, d, (10.5) | 1.61, m | 1.69, dd, (12.9, 3.6) | 1.52, m |
| 11 | 2.38, m | 1.78, m | 1.57, m | 1.64, m |
| | 1.70, td, (9.0, 3.6) | 1.67, m | 1.53, m | 1.77, m |
| 12 | 3.20, m | 1.82, m | 1.75, m | 1.55, m |
| | 2.19, m | 1.84, m | 1.19, m | 1.43, m |
| 13 | 3.13, m | 2.53, td, (12, 5.6) | 2.30, td, (12.9,3.7) | 2.52, td, (12.1, 5.3) |
| 15 | 2.64, d, (12.4) | 1.92, m | 1.56, m | 1.88, m |
| | 2.01, m | 1.42, m | 1.16, m | 1.49, m |
| 16 | 2.16, m | 1.59, m | 2.25, dt, (12.8, 3.2) | 2.35, dd, (10.1, 3.2) |
| | 1.76, m | 1.44, m | 1.44, m | 1.09, m |
| 18 | 2.89, t, (8.6) | 1.55, m | 1.61, t, (11.4) | 1.67, m |
| 19 | 2.25, m | 3.04, td, (10.8, 4.2) | 3.02, td, (10.9, 4.7) | 3.03, m |
| 21 | 2.35, m | 1.38, m | 1.95, m | 1.96, m |
| | 1.99, m | 1.94, m | 1.40, m | 1.37, m |
| 22 | 2.99, d, (11.8) | 1.36, m | 1.90, m | 1.36, m |
| | 2.06, m | 1.90, m | 1.49, m | 1.92, m |
| 23 | 1.30, s | 1.05, s | 0.82, s | 1.04, s |
| 24 | 1.25, s | 0.89, s | 1.01, s | 0.87, s |
| 25 | 1.48, s | 1.09, s | 0.89, s | 1.07, s |
| 26 | 1.30, s | 1.04, s | 0.95, s | 1.01, s |
| 27 | - | 10.13, s | 1.05, s | 10.12, s |
| 29 | 1.47, s | 4.74, s | 4.73, s | 4.74, s |
| | | 4.63, s | 4.61, s | 4.62, s |
| 30 | 1.39, s | 1.70, s | 1.71, s | 1.69, s |
| 1′ | | | - | 5.50, d, (8.0) |
| 2′ | | | 2.05, s | 3.31, m |
| 3′ | | | - | 3.41, m |
| 4′ | | | 1.98, s | 3.36, m |
| 5′ | | | | 3.36, m |
| 6′ | | | | 3.82, m |
| | | | | 3.69, m |

[a]The solvent used was Pyridine-d5.

TABLE 2 $^{13}C$ NMR data of 1–4 ($CD_3OD$, 150 MHz, $\delta$ in ppm).

| Position | 1[a] | 2 | 3 | 4 |
|---|---|---|---|---|
| | $\delta_C$ type | $\delta_C$ type | $\delta_C$ type | $\delta_C$ type |
| 1 | 67.6, CH | 66.6, CH | 57.6, CH | 66.9, CH |
| 2 | 178.4, C=O | 178.2, C=O | 66.6, $CH_2$ | 178.6, C=O |
| 3 | 84.9, CH | 85.5, CH | 88.1, CH | 85.6, CH |
| 4 | 44.1, C | 44.2, C | 40.8, C | 44.2, C |
| 5 | 57.4, CH | 57.8, CH | 63.1, CH | 57.8, CH |
| 6 | 19.5, $CH_2$ | 19.5, $CH_2$ | 19.0, $CH_2$ | 19.5, $CH_2$ |
| 7 | 38.8, $CH_2$ | 33.7, $CH_2$ | 35.5, $CH_2$ | 26.2, $CH_2$ |
| 8 | 42.4, C | 44.1, C | 43.1, C | 44.2, C |
| 9 | 46.5, CH | 51.9, CH | 51.8, CH | 49.6, CH |
| 10 | 50.6, C | 50.4, C | 46.0, C | 50.3, C |
| 11 | 25.4, $CH_2$ | 24.9, $CH_2$ | 24.8, $CH_2$ | 24.9, $CH_2$ |
| 12 | 30.9, $CH_2$ | 26.2, $CH_2$ | 26.4, $CH_2$ | 35.4, $CH_2$ |
| 13 | 41.4, CH | 39.6, CH | 39.3, CH | 39.3, CH |
| 14 | 60.1, C | 59.0, C | 43.9, C | 58.9, C |
| 15 | 29.7, $CH_2$ | 25.5, $CH_2$ | 31.0, $CH_2$ | 25.4, $CH_2$ |
| 16 | 38.1, $CH_2$ | 35.6, $CH_2$ | 33.4, $CH_2$ | 33.1, $CH_2$ |
| 17 | 61.3, C | 56.9, C | 57.3, C | 57.4, C |
| 18 | 50.4, CH | 49.5, CH | 50.5, CH | 52.0, CH |
| 19 | 52.7, CH | 48.8, CH | 48.6, CH | 48.6, CH |
| 20 | 72.9, C | 151.4, C | 151.9,C | 151.3, C |
| 21 | 29.6, $CH_2$ | 31.5, $CH_2$ | 31.7, $CH_2$ | 37.4, $CH_2$ |
| 22 | 35.6, $CH_2$ | 38.1, $CH_2$ | 38.2, $CH_2$ | 31.3, $CH_2$ |
| 23 | 31.7, $CH_3$ | 31.2, $CH_3$ | 25.6, $CH_3$ | 31.3, $CH_3$ |
| 24 | 20.6, $CH_3$ | 19.7, $CH_3$ | 24.9, $CH_3$ | 19.7, $CH_3$ |
| 25 | 20.1, $CH_3$ | 19.4, $CH_3$ | 14.9, $CH_3$ | 19.6, $CH_3$ |
| 26 | 19.2, $CH_3$ | 17.9, $CH_3$ | 17.4, $CH_3$ | 17.9, $CH_3$ |
| 27 | 179.2, C=O | 211.3, C=O | 15.1, $CH_3$ | 211.4, CH |
| 28 | 180.1, C=O | 179.4, C=O | 179.9,C=O | 175.7, C=O |
| 29 | 30.8, $CH_3$ | 110.7, $CH_2$ | 110.3, $CH_2$ | 110.8, $CH_2$ |
| 30 | 28.9, $CH_3$ | 19.4, $CH_3$ | 19.6, $CH_3$ | 19.3, $CH_3$ |
| 1′ | | | 172.8, C=O | 95.2, CH |
| 2′ | | | 21.0, $CH_3$ | 74.1, CH |
| 3′ | | | 172.7, C=O | 78.4, CH |
| 4′ | | | 20.9, $CH_3$ | 71.1, CH |
| 5′ | | | | 78.9, CH |
| 6′ | | | | 62.3, $CH_2$ |

[a]The solvent used was Pyridine-d5.

1186.2, 1029.0, and 774.7. HR-ESI-MS: *m/z* 555.3699 $[M-H]^-$ ($C_{34}H_{51}O_6$, calcd. for 555.3680). 1D NMR see Table 1 and Table 2.

Hovendulcisic acid D (**4**): white powder; m.p. 243.6–245.1°C; $[\alpha]^{25}_D$ +15.12 (c 0.5, MeOH); UV (MeOH) $\lambda_{max}$: 202.2 nm; IR ($\nu_{max}$ $cm^{-1}$): 3391.4, 2947.8, 2868.3, 1748.0, 1722.0, 1698.9, 1641.4, 1065.5, 1028.0, and 892.3. HR-ESI-MS: *m/z* 661.3597 $[M-H]^-$ ($C_{36}H_{53}O_{11}$, calcd. for 661.3582). 1D NMR see Table 1 and Table 2.

## Acid hydrolysis and GC analysis

Acid hydrolysis and GC analysis of the glycoside were carried out according to Cai, et al. (2021). First, Compound **4** (2.1 mg) was hydrolyzed in HCl solution (2 M, 10 mL) in an oven (90°C, 4 h), and then evaporated to dryness. $H_2O$ was added to the residue and $CHCl_3$ was used for extraction twice, then sugar residue was obtained from the $H_2O$ layer. The sugar fraction was reacted with L-cysteine methyl ester hydrochloride (in pyridine, 1 mL) in an oven (60°C, 2 h).

After concentration and drying, the residue was reacted with 1-(trimethylsilyl) imidazole (0.2 mL) in an oven (60°C, 1 h) and then extracted with n-hexane. The n-hexane fraction was acquired for GC analysis. The sugar was identified as D-glucose ($t_R$/min) 25.170, reference D-glucose ($t_R$/min) 25.172.

## Computational section

All calculations and processing were conducted using ORCA 5.0.4 and Python 3.10.6. The optimization of the structures used for CD and NMR calculations was performed in pyridine solvents and B3LYP-D3BJ/6–31 g (d, p) levels in the CPCM model, using tight criteria and checking for the absence of virtual frequencies. NMR calculations were performed using the SMD model and at the revTPSS/PCSSEG −1 level (10.1021/ACS.JCTC. 1C00604 indicates that this is a good level, and ECD calculations were performed using TDDFT under the SMD model. We calculated 90 excited states at the ωb97x-d4/def2-TZVP level to cover the excited levels as much as possible, and the rotor intensity and excitation wavelength were expanded using the Gauss function. The FWHM was set at 10 nm to draw the spectrum.

## Bioactivity assays

### Luciferase reporter gene assay

The cells used in this experiment were MDA-MB-231 stable reporter cell lines transfected with ARE-luciferase plasmid in the previous study (Chen, et al., 2016). The cells were cultured in medium containing puromycin (1.5 mg $mL^{-1}$) in 48 well plates for 24 h. The isolated constituents **1**–**4** (1–10 $\mu$M) were added to the cells for 24 h. The luciferase activities were tested using the manufacturer's protocol after the digestion of the cells. TBHQ was used as positive control.

### Cytotoxic activity assay

The CCK8 method was applied in a cell viability assay in human MDA-MB-231 cells and human A549 cells. Compounds **1**–**4**

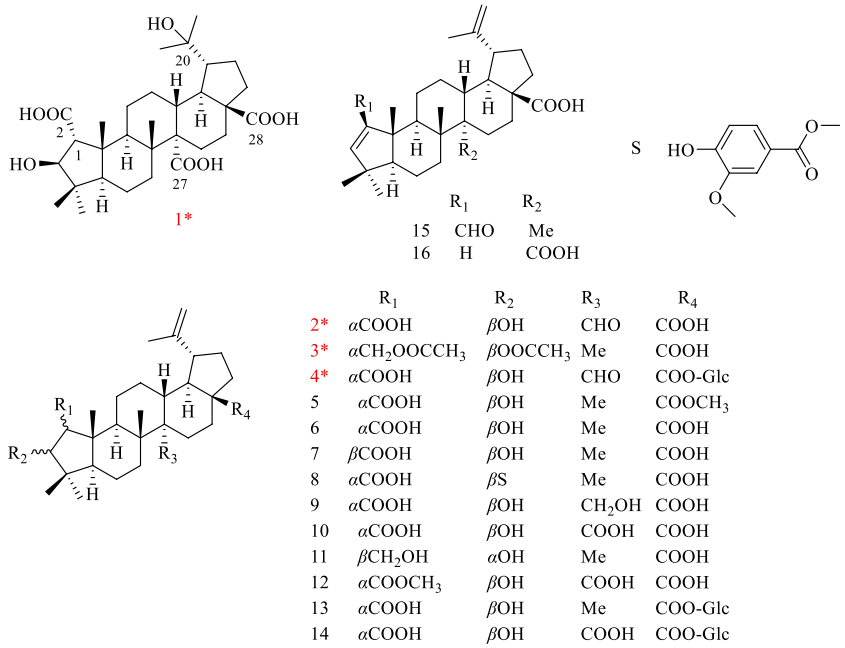


FIGURE 1
Structures of compounds **1**–**4**.

(10–80 $\mu$M) were added to the cells for 24 h. The medium was discarded, and CCK8 solution was added and then cultured for 90 min. Absorbance at 450 nm was recorded and used to calculate cell viability.

# Results and discussion

## Structure elucidation

The stems of *H. dulcis* were extracted with 70% EtOH, and EtOAc extraction fraction was further isolated by multi-separation methods, acquiring four novel ceanothane-type triterpenoid hovendulcisic acids A-D (**1**–**4**) and twelve known: methylceanothate (**5**) (Leal, et al., 2010), ceanothic acid (**6**) (Ganapaty, et al., 2006), epiceanothic acid (**7**) (Li, et al., 2007), 3-O-vanillylceanothic acid (**8**) (Ganapaty, et al., 2006), 27-hydroxyceanothic acid (**9**) (Li, et al., 1997), ceanothetric acid (**10**) (Li, et al., 1997), ceanothanolic acid (**11**) (Lee, et al., 1997), ceanothetric acid 2-methyl ester (**12**) (Lee, et al., 1997), ceanothic acid 28β-glucosylester (**13**) (Lee, et al., 1991), hovetrichoside H (**14**) (Yoshikawa, et al., 1998), zizyberenalic acid (**15**) (Zhang, et al., 2012), and ceanothenic acid (**16**) (Jou, et al., 2004) (Figure 1).

Compound **1** was a white amorphous powder, and its formula of $C_{30}H_{45}O_8$ was deduced by HR-ESI-MS peaks $[M-H]^-$ at *m/z* 533.3124 (calcd. for $C_{30}H_{45}O_8$, 533.3109). IR data showed absorption bands for OH (3330.0 $cm^{-1}$), C=O (1715.6, 1682.6 $cm^{-1}$), and C=C (1644.6 $cm^{-1}$). $^1H$ NMR spectrum (Table 1) exhibited six methyl groups [$\delta_H$ 1.48(3H, s, $H_3$-25), 1.30 (3H, s, $H_3$-23), 1.30 (3H, s, $H_3$-26), 1.25 (3H, s, $H_3$-24), 1.47 (3H, s, $H_3$-29), and 1.39 (3H, s, $H_3$-30)]. $^{13}C$ NMR and DEPT-135 data (Table 2) exhibited 30 carbon signals, including six methyls, eight methylenes, seven methines, and nine quaternary carbons (including three carboxylic acid carbons at $\delta_C$ 180.1, 179.2, 178.4). The hydrogen signals and relevant carbon atoms were assigned by HSQC spectrum, and the above information suggested that **1** possessed a triterpenoid skeleton. The NMR data of **1** was similar to those of the known compound ceanothetric acid but without the isoallyl signals (Yoshikawa et al., 1998b). Compared with ceanothetric acid, the molecular weight of **1** added 18 Da and the unsaturation degree decreased by 1, indicating that the double bond between C-20 and C-30 of ceanothetric acid was oxidized and a hydroxyl group was added. The correlations in the HMBC spectrum between C-20 (72.9) and H-29 ($\delta_H$ 1.47), H-30 ($\delta_H$ 1.39) revealed that **1** lost a double bond between C-20 and C-30, which was distinct from the typical ceanothane-type triterpenoid. The HMBC correlations between C-20 ($\delta_C$ 72.9) and H-18 ($\delta_H$ 2.89), H-19 ($\delta_H$ 2.25) also confirmed the position of quaternary carbon (Figure 2). Three carboxylic acid signals ($\delta_C$ 180.1, 179.2, 178.4) were attributed to C-28, C-27, and C-2 according to the HMBC spectra and literature data (Kang et al., 2017).

NOESY correlations between H−1 ($\delta_H$ 3.30) and $\delta_H$ H-25 (1.48), H-3 ($\delta_H$ 4.87) and H-5 ($\delta_H$ 2.22) suggested the $\alpha$-configuration of C-2 and $\beta$-configuration of C-3 (Li et al., 1997). NOESY correlations between $\delta_H$ 2.25 (H-19) and $\delta_H$ 3.13 (H-13) indicated $\alpha$-configuration at C-20 (Figure 3). The $^{13}C$ NMR chemical shift calculations for the 1*S*, 5*R*, 7*R*, and 23*R* of **1** agreed well with the experimental data, and the correlation coefficient $R^2$ was 99.64% (Figure 4A). Finally, the absolute configuration of **1** (1*S*, 5*R*, 7*R*, and 23*R*) was determined according to the comparison experimental data with calculated ECD spectra (Figure 5A).

Taken together, compound **1** was novel and was identified as 2$\alpha$-carboxy-3$\beta$, 20-dihydroxy-A (1)-norlup-27, 28-dioic acid and named "hovendulcisic acid A".

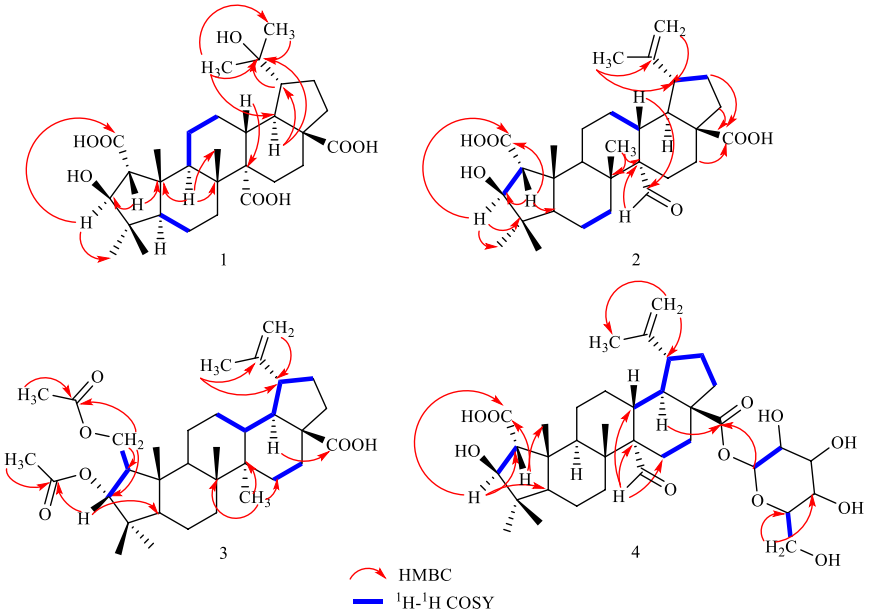


FIGURE 2
Key $^1$H–$^1$H COSY and HMBC correlations in compounds **1**–**4**.

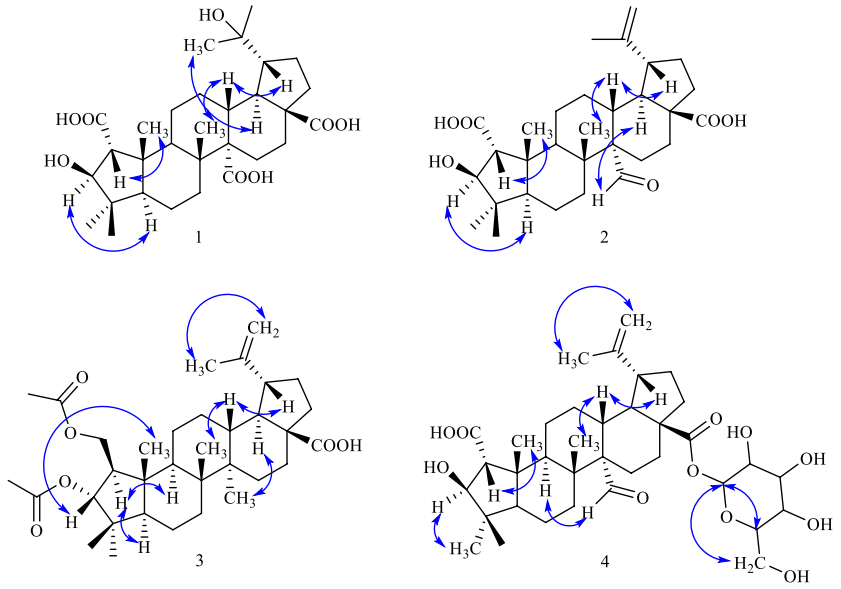

FIGURE 3
Key NOESY correlations in compounds **1**–**4**.

Compound **2** was obtained as a white amorphous powder, and the formula was observed to be $C_{30}H_{44}O_6$ according to HR-ESI-MS data $[M-H]^-$ at *m/z* 499.3060 (calcd for $C_{30}H_{43}O_6$, 499.3054). The IR absorption bands exhibited OH (3475.3 $cm^{-1}$), C=O (1722.0, 1718.9, 1688.0 $cm^{-1}$), C=C (1644.6 $cm^{-1}$), and C-O (1235.4 $cm^{-1}$). The $^1$H and $^{13}$C NMR spectral data of **2** are similar to those of ceanothetric acid, but added a aldehyde group instead of carboxylic acid carbons (Yoshikawa et al., 1998). The correlations in the HMBC spectrum between C-2 ($\delta_C$ 178.2) and H–1 ($\delta_H$ 2.50), H-3 ($\delta_H$ 4.08), C-28 ($\delta_C$ 179.4), and H-16 ($\delta_H$ 1.59), H-21 ($\delta_H$ 1.38), H-22 ($\delta_H$ 1.90) confirmed the position of the carboxylic acid groups. The HMBC correlations between C-2 ($\delta_C$ 178.2), C-4 ($\delta_C$ 44.2), and H-3 ($\delta_H$ 4.08) also indicated that the hydroxy was located at C-3. The HMBC correlations between the C-14 ($\delta_C$ 59.0) and aldehyde proton signal H-27 ($\delta_H$ 10.13), C-27 ($\delta_C$ 211.3) and H-13 ($\delta_H$ 2.53), H-15 (1.92) indicated that the aldehyde group was located at C-27 (Figure 2). NOESY correlations between $\delta_H$ 1.55 (H-18) and $\delta_H$ 10.13 (H-27) suggested that the $\alpha$-configuration was at C-27 (Figure 3). The $^{13}$C

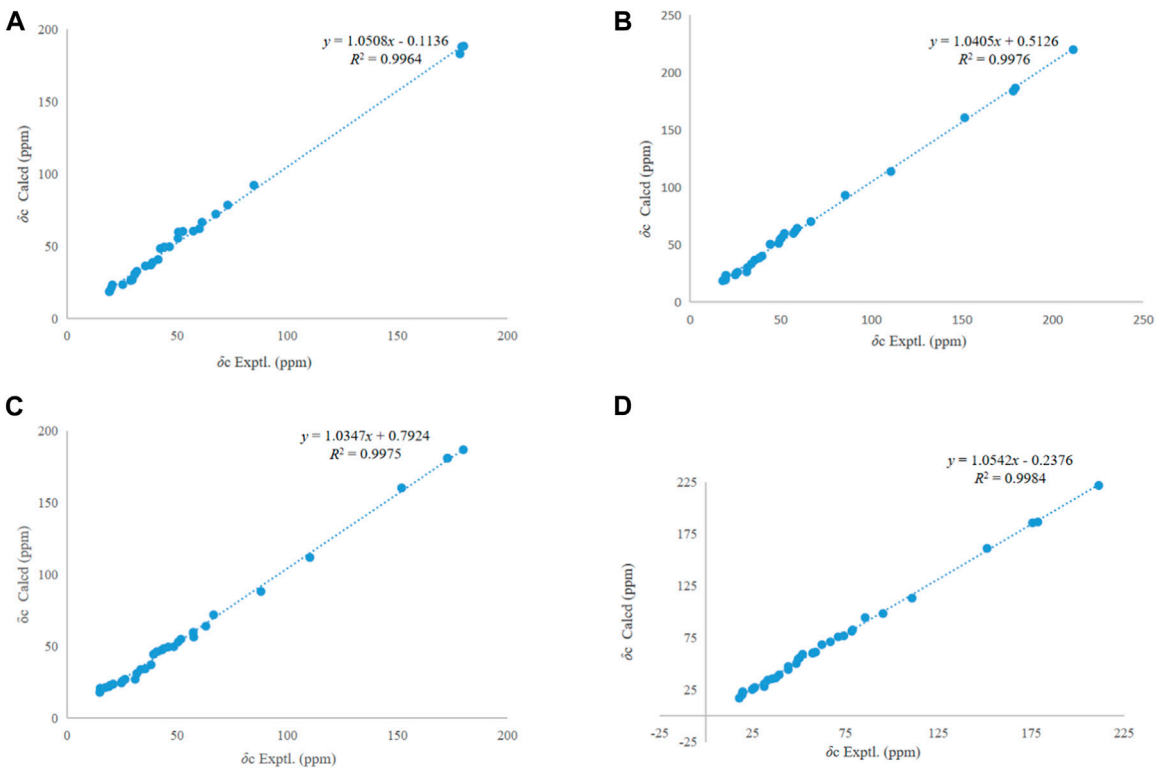


FIGURE 4
Regression analysis of experimental and calculated $^{13}$C NMR chemical shifts of **1**–**4 (A–D)**.

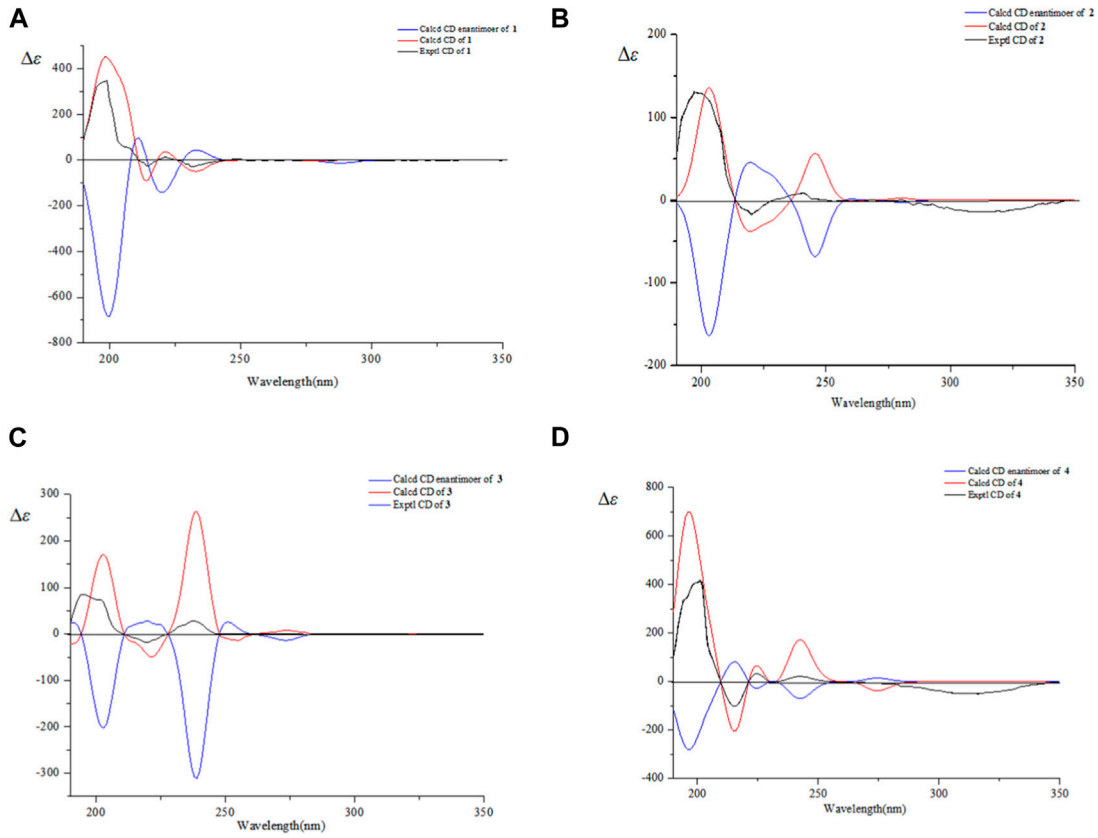


FIGURE 5
Experimental and calculated ECD spectra of **1**–**4 (A–D)**.

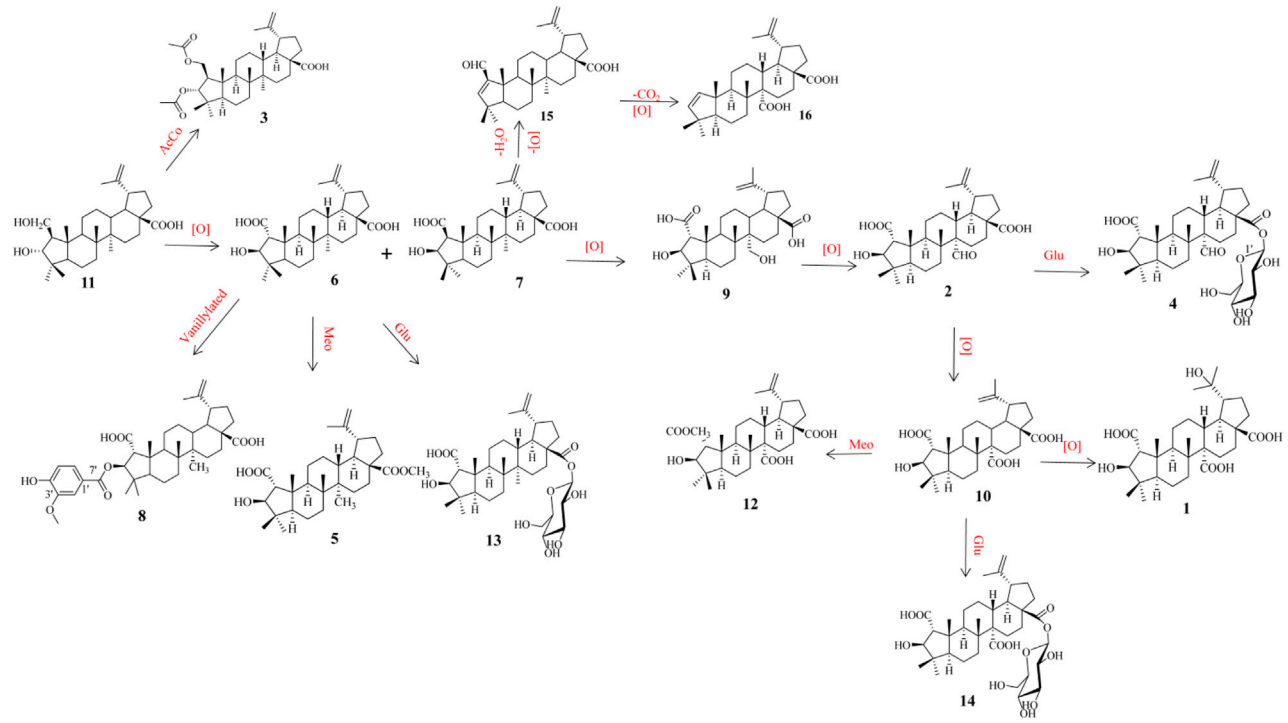


SCHEME 1
Putative biosynthetic pathways to **1**–**16**.

NMR chemical shift calculations for the 1*S*, 5*R*, 7*R*, and 23*R* of **2** correlated well with the experimental result, and the correlation coefficient $R^2$ was 99.76% (Figure 4B). The absolute configuration of **2** was determined by ECD method (Figure 5B). Taken together, compound **2** was identified as 2*α*-carboxy-3*β*-hydroxy-A (1)-norlup-20 (29)-en-27-aldehydo-28-oic acid and named "hovendulcisic acid B".

Compound **3** was obtained as a white amorphous powder, and its formula was $C_{34}H_{52}O_6$ though HR-ESI-MS data $[M-H]^-$ at *m/z* 555.3699 (calcd for $C_{34}H_{51}O_6$, 555.3680). The IR data exhibited the existence of OH (3397.0 $cm^{-1}$), C=O (1739.6, 1701.3 $cm^{-1}$), C=C (1644.6 $cm^{-1}$), and C-O (1186.2, 1029.0 $cm^{-1}$). The $^{13}C$ NMR and DEPT spectra exhibited 34 carbon resonances, including eight methyls, ten methylenes (including an oxygenated methylene group at $\delta_C$ 66.56), seven methines (including an oxygenated methine group at $\delta_C$ 88.07), and nine quaternary carbons (including a carboxylic acid carbons at $\delta_C$ 179.91 and two ester groups at $\delta_C$ 172.82, 172.70). The 1D NMR data of **3** were similar to those of **2** but different from the existence of two oxygenated methylene protons [$\delta_H$ 4.47 (1H, dd, *J* = 11.5, 4.5 Hz, H-2*α*), 4.04 (1H, dd, *J* = 11.5, 7.8 Hz, H-2*β*)] and one oxygenated methine proton [$\delta_H$ 4.94(1H, d, *J* = 8.7 Hz, H-3)] (Tables 1 and 2). The above data indicated that **3** was a ceanothane-type triterpenoid with two acetyl groups. HMBC correlation of oxygenated methylene proton [$\delta_H$ 4.47, 4.04 (H-2)] with $\delta_C$ 172.8 (C-1′) indicated that one acetyl group was linked at the C-2. HMBC correlation between oxygenated methine proton $\delta_H$ 4.94 (H-3) and $\delta_C$ 172.7 (C-3′), suggesting that another acetyl group was located at C-3 (Figure 2). According to the correlations in the HMBC spectrum between C-1' ($\delta_C$ 172.8) and H-2 ′ ($\delta_H$ 2.05), C-3' ($\delta_C$ 172.7) and H-4' ($\delta_H$ 1.98), the position of the methyl proton can be assigned. The position of the isopropenyl group can be determined according to the HMBC correlations between C-19 ($\delta_C$ 48.6), C-20 ($\delta_C$ 151.9), and [$\delta_H$ 4.73, 4.61 (H-29)], H-30 ($\delta_H$ 1.71). NOESY correlations between $\delta_H$ 1.86 (H–1) and $\delta_H$ 1.22 (H-5), $\delta_H$ 1.69 (H-9), between $\delta_H$ 4.94 (H-3) and $\delta_H$ 0.89 (H-25) indicated the *β*-configuration of C-2 and *α*-configuration of C-3' (Figure 3).

The $^{13}C$ NMR chemical shift calculations confirmed the relative configuration of **3** (Figure 4C) while the experimental and calculated ECD data confirmed its absolute configuration (Figure 5C). Therefore, compound **3** was identified as 2*β*, 3*α*-diacetyl-A (1)-norlup-20 (29)-en-28- oic acid and named "hovendulcisic acid C".

Compound **4** was isolated as a white amorphous powder with formula $C_{36}H_{54}O_{11}$ according to HR-ESI-MS data $[M-H]^-$ at *m/z* 661.3597 (calcd for $C_{36}H_{53}O_{11}$, 661.3582). IR absorption bands exhibited the existence of OH (3391.4 $cm^{-1}$), C=O (1748.0, 1722.0, 1699.0 $cm^{-1}$), C=C (1641.4 $cm^{-1}$) ,and C-O (1065.5, 1028.0 $cm^{-1}$). The NMR data of **4** were similar to those of **2** but added a sugar residue [$\delta_H$ 5.50 (1H, d, *J* = 8.0 Hz, H-1′ in Glu), proton signals at $\delta_H$ 3.32–3.82] (Tables 1 and 2). The sugar residue was finally identified as D-glucose according to acid hydrolysis and GC analysis. HMBC correlations between C-28 ($\delta_C$ 175.7) and H-1′ in Glu ($\delta_H$ 5.50) indicated that the glycosidic bonds were located at C-28. The HMBC correlations between the aldehyde proton signal H-27 ($\delta_H$ 10.12) and C-14 ($\delta_C$ 58.9), C-13 ($\delta_C$ 39.3), C-15 ($\delta_C$ 25.4) indicated that the aldehyde group was located at C-27. The position of the isopropenyl group can be determined according

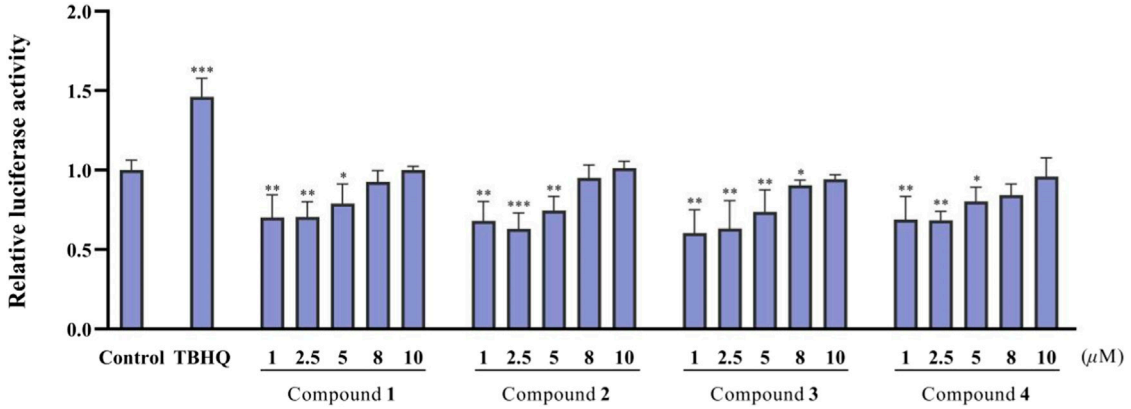


FIGURE 6
ARE-dependent luciferase activity of the isolated compounds **1**–**4** (n = 3).

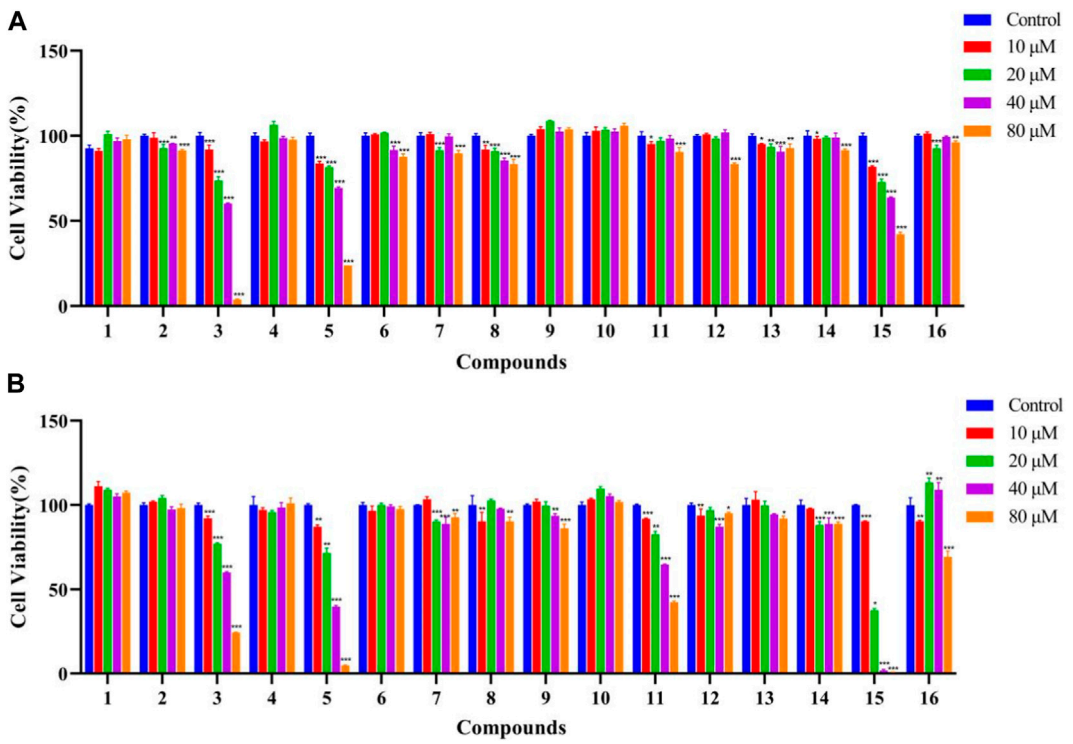


FIGURE 7
Effects of compounds **1**–**16** against A549 cells **(A)** and MDA-MB-231 cells **(B)** ($n$ = 3). The data represent the mean ± SD of three experiments. *$p$ < 0.05 and **$p$ < 0.01 vs. the control group.

to the HMBC correlations between [$\delta_H$ 4.74, 4.62 (H-29)] and C-19 ($\delta_C$ 48.6), C-30 ($\delta_C$ 19.3).

The relative configuration of **4** was deduced by the experimental and calculated $^{13}$C NMR method, while the absolute configuration of **4** was approved by experimental and calculated ECD data (Figures 4D, 5D). Therefore, **4** was elucidated as 2$\alpha$-carboxy-3$\beta$-hydroxy-A (1)-norlup-20 (29)-en-27-aldehydo-28-oic acid (hovendulcisic acid B) 28-$\beta$-D-glucopyranoside and named "hovendulcisic acid D".

## Putative biosynthetic pathways analysis

The plausible biosynthetic pathway of compounds **1**–**16** is shown in Scheme 1. The precursor ceanothanolic acid (**11**), which was first obtained from *Paliurus hemsleyanus* (Lee, et al., 1997), was oxidated at C-2 to give ceanothic acid (**6**) and epiceanothic acid (**7**), diacetylated at C-2 and C-3 to afford hovendulcisic acid C (**3**). Then ceanothic acid (**6**) was vanillylated with OH at C-3 to give 3-*O*-vanillylceanothic acid

(**8**), while ceanothic acid (**6**) was methyl esterificated and glycosylated of C-28 to afford methylceanothate (**5**) and ceanothic acid 28$\beta$-glucosylester (**13**), respectively. Epiceanothic acid (**7**) was oxidated to 27-hydroxyceanothic acid (**9**), hovendulcisic acid B (**2**), ceanothetric acid (**10**), and hovendulcisic acids A (**1**) with different levels. Hovendulcisic acid B (**2**) and ceanothetric acid (**10**) were further glycosylated to hovendulcisic acids D (**4**) and hovetrichoside H (**14**), respectively. Epiceanothic acid (**7**) was dehydrated and reduced to zizyberenalic acid (**15**), which was further decarboxylated and oxygenated to ceanothenic acid (**16**).

## Bioactivity results

The antitumor effects of isolated compounds **1**–**16** were investigated. The results of the ARE luciferase reporter gene showed that **1**–**4** showed strong inhibitory effect at low concentrations of 1 to 5 μM (Figure 6). Generally, MDA-MB-231 cells appeared to be more sensitive than A549 cells. Compounds **3**, **5,** and **15** exhibited significant inhibitory activity against A549 cells (Figure 7A), and **3**, **5**, **12,** and **15** exhibited significant inhibitory activity against MDA-MB-231 cells (Figure 7B). The structure–activity relationships analysis revealed that the acetyl and aldehyde groups played an important role in anti-tumor activity. The above results indicated that **3** suppressed tumor activity by inhibiting Nrf2 expression.

# Data availability statement

The raw data supporting the conclusion of this article will be made available by the authors, without undue reservation.

# Author contributions

JY: methodology and writing–original draft. WC: writing–original draft. FW: investigation, methodology, and writing–original draft. SX: investigation, methodology, supervision, and writing–review and editing. XZ: conceptualization and writing–review and editing. BL: writing–review and editing. FX: writing–original draft and writing–review and editing.

# Funding

The author(s) declare that financial support was received for the research, authorship, and/or publication of this article. This work was supported by the National Natural Science Foundation of China (Nos 82173700 and U1801287), the Science and Technology Planning Project of Guangdong Province (Nos 2022A1515010103 and 2023B1212060063; 2023B1212060062), The Special Foundation of Guangzhou Key Laboratory (Nos 2024A04J9997, 202201020488), the Research Fund for Bajian Talents of Guangdong Provincial Hospital of Chinese Medicine (No. BJ2022KY08), and the Special Funds for State Key Laboratory of Dampness Syndrome of Chinese Medicine (No. SZ2023ZZ13).

# Conflict of interest

The authors declare that the research was conducted in the absence of any commercial or financial relationships that could be construed as a potential conflict of interest.

# Publisher's note

All claims expressed in this article are solely those of the authors and do not necessarily represent those of their affiliated organizations, or those of the publisher, the editors, and the reviewers. Any product that may be evaluated in this article, or claim that may be made by its manufacturer, is not guaranteed or endorsed by the publisher.

# Supplementary material

The Supplementary Material for this article can be found online at: https://www.frontiersin.org/articles/10.3389/fchem.2024.1383886/full#supplementary-material

# References

Cai, W. N., Xu, S. M., Ma, T., Zhang, X. Q., Liu, Bo., and Xu, F. F. (2021). Five novel triterpenoid saponins from *Hovenia dulcis* and their Nrf2 inhibitory activities. *Arab J Chem* 14 (8), 103292. doi:10.1016/j.arabjc.2021.103292

Chen, W., Li, S., Li, J., Zhou, W., Wu, S. H., Xu, S. M., et al. (2016). Artemisitene activates the Nrf2-dependent antioxidant response and protects against bleomycin-induced lung injury. *FASEB J.* 30 (7), 2500–2510. doi:10.1096/fj.201500109R

Chinese materia medica editorial board (1999). *Chinese herbs*. Shanghai: Shanghai Scientific and Technical Publishers, 238.

Flora of China Editorial Committee (1982). *Flora of China[M]*. Beijing: Science Press.

Ganapaty, S., Thomas, P., Ramana, K., and KaragianisWaterman, G. P. G. (2006). Dammarane and ceanothane triterpenes from *Zizyphus glabrata*. *Z Naturforsch B* 61 (1), 87–92. doi:10.1515/znb-2006-0118

Ji, Y. (2003). The study of cytotoxic effect and antitumor effect by *Hovenia dulcis* Thunb. *Chin. Arch. Tradit. Chin. Med.* (04), 538–543. doi:10.13193/j.archtcm.2003.04.58.jiy.030

Ji, Y., Di, Y. M., Tao, S. Y., and Zhang, K. R. (2003). Experimental study on toxicity and antitumor effect of *Hovenia acerba*. *Chin. J. Tradit. Med. Sci. Technol.* (02), 98–99.

Jou, S., Chen, C., Guh, J., Lee, C. N., and Lee, S. S. (2004). Flavonol glycosides and cytotoxic triterpenoids from *Alphitonia Philippinensis*. *J. Chin. Chem. Soc.* 51, 827–834. doi:10.1002/jccs.200400124

Kang, K. B., Jun, J. B., Kim, J. W., Kim, H. W., and Sung, S. H. (2017). Ceanothane- and lupane-type triterpene esters from the roots of *Hovenia dulcis* and their antiproliferative activity on HSC-T6 cells. *Phytochemistry* 142, 60–67. doi:10.1016/j.phytochem.2017.06.014

Leal, I. C., dos Santos, K. R., Júnior, I. I., Porzel, O. A. C., and Wessjohann, A. (2010). Ceanothane and lupane type triterpenes from *Zizyphus joazeiro*, an anti-staphylococcal evaluation. *Planta Med.* 76, 47–52. doi:10.1055/s-0029-1185947

Lee, S., Shy, S., and Liu, K. C. (1997). Triterpenes from *Paliurus hemsleyanus*. *Phytochemistry* 46, 549–554. doi:10.1016/s0031-9422(97)00313-0

Lee, S., Su, W., Liu, K., and Liu, K. C. (1991). Two new triterpene glucosides from *Paliurus ramosissimus*. *J. Nat. Prod.* 54 (2), 615–618. doi:10.1021/np50074a047

Li, W. H., Zhang, X. M., Tian, R. R., Zheng, Y. T., Zhao, W. M., and Qiu, M. H. (2007). A new anti-HIV lupane acid from *Gleditsia sinensis* Lam. *J. Asian Nat. Prod. Res.* 9 (6-8), 551–555. doi:10.1080/10286020600883419

Li, X. C., Cai, L., and Wu, C. D. (1997). Antimicrobial compounds from *Ceanothus americanus* against oral pathogens. *Phytochemistry* 46 (1), 97–102. doi:10.1016/S0031-9422(97)00222-7

Lin, H., Qiao, Y., Yang, H., Nan, Q., Qu, W., Feng, F., et al. (2020). Small molecular Nrf2 inhibitors as chemosensitizers for cancer therapy. *Future Med. Chem.* 12, 243–267. doi:10.4155/fmc-2019-0285

Su, J. (1985). *New herbs [M]*. Shanghai: Shanghai Ancient Books Publishing House, 143.

Wang, H. Y. (1958). *The benediction of the peace [M]*. First edition. Beijing: People's Medical Publishing House, 1196.

Wu, Y. L. (2000). *Herbal medicine renews [M]*. First edition. Shanghai: Shanghai Scientific and Technical Publishers, 308.

Xu, F. F., Gao, M. H., Li, H., Han, X. D., Zhang, X. Q., Li, Y. L., et al. (2020). Three new bisflavonols from the seeds of *Hovenia dulcis* Thunb. and their anti-RSV activities. *Fitoterapia* 143, 104587. doi:10.1016/j.fitote.2020.104587

Xu, F. F., Liu, B., and Zhang, X. Q. (2020). Research progress on chemical constituents and pharmacological activities of *Hovenia*. *China J. Chin. Mater Med.* 45 (20), 4827–4835. doi:10.19540/j.cnki.cjcmm.20200706.602

Yoshikawa, K., Eiko, K., Mimura, N., Kondo, Y., and Arihara, S. (1998). Hovetrichosides C-G, Five new glycosides of two auronols, two neolignans, and a pheylpropanoid from the bark of *Hovenia trichocrea*. *J. Nat. Prod.* 61, 78–79.

Yoshikawa, K., Kondo, Y., Kimura, S., and Arihara, S. (1998). A lupane-triterpene and a 3(2→1) abeolupane glucoside from *Hoveina trichocarea*. *Phtochemistry* 49 (7), 2057–2060. doi:10.1016/s0031-9422(98)00409-9

Yoshikawa, K., Shinichi, T., Kazuko, Y., and Arihara, S. (1992). Antisweet natural products VII. Hodulosides I, II, III, IV, and V from the leaves of *Hovenia dulcis* Thunb. *Chem. Pharm. Bull.* 40 (9), 2287–2291. doi:10.1248/cpb.40.2287

Zhang, Q. (2017). *Isolation and purification of anti-tumor active compound SIPI-ZQ2 from* Hovenia dulcis *Thunb and its* in vitro *and* in vivo *antitumor activity evaluation and acute toxicity [D]*. Shanghai: Shanghai institute of pharmaceutical industry.

Zhang, X. Y., Cai, X. H., and Luo, X. D. (2012). Chemical constituents of *Allophylus longipes*. *Chin. J. Nat. Med.* 10 (01), 36–39. doi:10.1016/S1875-5364(12)60008-9

frontiers | Frontiers in Chemistry

TYPE Original Research
PUBLISHED 28 May 2024
DOI 10.3389/fchem.2024.1397634

Check for updates

OPEN ACCESS

EDITED BY
Xuetao Xu,
Wuyi University, China

REVIEWED BY
Mozaniel Oliveira,
Emílio Goeldi Paraense Museum, Brazil
Vijai Agnihotri,
Institute of Himalayan Bioresource Technology (CSIR), India

*CORRESPONDENCE
Pablo Luis B. Figueiredo,
pablo.figueiredo@uepa.br

RECEIVED 07 March 2024
ACCEPTED 09 May 2024
PUBLISHED 28 May 2024

CITATION
de Lima MNN, Santos PVL, Jerônimo LB, Viana RM, da Silva JK, Setzer WN, Maia JGS and Figueiredo PLB (2024), Seasonal influence on the essential oil chemical composition of *Hyptis crenata* Pohl ex Benth.: a valuable plant from Marajó, Brazil.
*Front. Chem.* 12:1397634.
doi: 10.3389/fchem.2024.1397634

COPYRIGHT
© 2024 de Lima, Santos, Jerônimo, Viana, da Silva, Setzer, Maia and Figueiredo. This is an open-access article distributed under the terms of the Creative Commons Attribution License (CC BY). The use, distribution or reproduction in other forums is permitted, provided the original author(s) and the copyright owner(s) are credited and that the original publication in this journal is cited, in accordance with accepted academic practice. No use, distribution or reproduction is permitted which does not comply with these terms.

# Seasonal influence on the essential oil chemical composition of *Hyptis crenata* Pohl ex Benth.: a valuable plant from Marajó, Brazil

Maria Nancy Norat de Lima[1,2], Paulo Vinicius Lima Santos[2,3], Lucas Botelho Jerônimo[2,4], Rian Martins Viana[2], Joyce Kelly da Silva[1], William N. Setzer[5], José Guilherme S. Maia[1,3] and Pablo Luis B. Figueiredo[2,3]*

[1]Programa de Pós-Graduação em Química, Instituto de Ciências Exatas e Naturais, Universidade Federal do Pará, Belém, Brazil, [2]Laboratório de Química dos Produtos Naturais, Universidade do Estado Pará, Belém, Brazil, [3]Programa de Pós-Graduação em Ciências Farmacêuticas, Instituto de Ciências da Saúde, Universidade Federal do Pará, Belém, Brazil, [4]Programa de Pós-Graduação em Ciências Ambientais, Centro de Ciências Naturais e Tecnologias, Universidade do Estado do Pará, Belém, Brazil, [5]Aromatic Plant Research Center, Lehi, UT, United States, [6]Laboratório de Bioprospecção e Biologia Experimental, Universidade Federal do Oeste do Pará, Santarém, Brazil

**Introduction:** Essential oils (EOs) from the *Hyptis* genus have been reported as bactericides and fungicides. However, the properties of these oils can be affected by climatic factors, as well as the collection period, which promotes changes in the chemical composition of the oil. In this context, this study aimed to evaluate the climatological influences on the chemical composition of the essential oil from the leaves of *Hyptis crenata*.

**Methods:** The leaves were collected in Marajó island (Brazil) monthly for a year. The EOs were obtained by hydrodistillation and analyzed by Gas Chromatography coupled to Mass Spectrometry (GC-MS). Pearson's correlation was used to evaluate the relationship between climatic parameters, content, and chemical composition of essential oil; multivariate analysis was used to evaluate the interrelationship between samples and their chemical constituents.

**Results and Discussion:** The constituents with the highest contents (>2.0%) in essential oils during the studied period were 1,8-cineole (28.48% ± 4.32%), α-pinene (19.58% ± 2.29%), camphor (11.98% ± 2.54%), β-pinene (9.19% ± 1.47%), limonene (6.12% ± 3.15%), α-terpineol (2.42% ± 0.25%) and borneol (2.34% ± 0.48%). β-Pinene significantly correlated ($p < 0.05$) with precipitation and humidity. According to the chemometric tools, two groups were formed: chemical profile I, marked by 1,8 cineole, α-pinene, β-pinene, borneol, α-terpineol, and limonene, while group II (July) presented a chemical type characterized by camphor. It is understood that the species in question can be a reliable source of biologically active components during different climatic periods in the Amazon. The chemical variability could have significant implications for the pharmaceutical industry and traditional medicine.

KEYWORDS

**salva-do-Marajó, volatiles, monoterpenes, medicinal plant, seasonality**

# 1 Introduction

*Hyptis crenata* Pohl ex Benth. (Lamiaceae) is an aromatic herb (Campos et al., 2021) that grows spontaneously in sandy and stony soils. In Brazil, this species occurs along the Amazon River, near streams on Marajó Island, Pará, Brazil, where it is popularly known among the local inhabitants as a salva-do-Marajó (Zoghbi et al., 2002).

In the Marajoara region, the *H. crenata* fresh or dried leaves are used to treat liver diseases, stomach pains, and headaches (Rebelo et al., 2009); another constant use is as a flavoring for drinks, scent baths, and incense due to the aromas released by the essential oils contained in the plant (BEZERRA, 2020).

Previous research reported that *Hyptis* species present in their extracts and essential oils bioactive compounds with antibacterial (Jesus et al., 2009; Feitosa-Alcântara et al., 2018) and antifungal (Oliveira et al., 2004), gastroprotective (Diniz et al., 2013), antinociceptive, and anti-inflammatory (de Lima et al., 2023).

Despite the biological effects of *H. crenata* described in the literature, the chemical composition of medicinal species can vary depending on several environmental and physiological factors of the plant, such as growth phase, geographic location, period of the year, climatic season, and solar index, which may change the bioactive properties of natural products such as essential oils (Gobbo-Neto and Lopes, 2007).

According to the main chemical constituents of *H. crenata* essential oil, ten chemical profiles (chemotypes) may occur due to genetic and collection site variation, giving an intraspecific chemical variability (Lima et al., 2023).

Moreover, there is a need to study how climatic parameters alter the chemical composition and consequently the biological activities of essential oils, since these factors appear to be associated with the quality control of natural products such as essential oils (Costa et al., 2022).

*Hyptis crenata* essential oil has a perspective on developing a phytotherapeutic product against pain and inflammation (de Lima et al., 2023). This study aims to evaluate the influence of climatic factors in the Brazilian Amazon on the chemical composition of *H. crenata* essential oil occurring in the Marajó Archipelago.

# 2 Methodology

## 2.1 Plant material and climate data

*H. crenata* was collected in Vila de Chiquita (rural area, Figure 1) in the city of Salvaterra, Marajó, Pará state, Brazil (Lat. 0°51′43.71″S, Long. 48°37′23.33″W), in accordance with biodiversity protection laws, and the registration of access to genetic heritage under number AEC4B1F (SISGEN).

For the seasonal study, 12 monthly collections were carried out, with approximately 150 g of botanical material, on the first day of each month, starting in September 2021 and ending in August 2022, at 3:00 p.m.

The botanical identification was made by morphological comparison with authentic samples, and a voucher was incorporated into the collection of the Herbario of Museu Paraense Emílio Goeldi in Belém, Pará, under registration number MG-243648.

Climatic data such as atmospheric humidity, rainfall, average temperature, and solar radiation were collected on the website of the National Institute of Meteorology (INMET) of the Brazilian Government. The seasonal parameters were recorded through the automatic station located in Belém, State of Pará, Brazil, which is approximately 78 km as the straight line from the collection site.

## 2.2 Essential oil extraction and yield calculation

The extraction of leaves essential oil from a single specimen of *H. crenata* was carried out using the hydrodistillation technique with a Clevenger-type device over a 3-h period, in triplicate. In this process, 50 g of dried and crushed leaves were added to a 2000-mL glass flask with 100 mL of distilled water. This system was coupled to the condenser, which was cooled at 10°C.

The extracted oils were centrifugated at 3,000 rpm for 5 min to allow total water separation and further dehydrated with anhydrous sodium sulfate ($Na_2SO_4$) under the same conditions. After this dehydration, the masses of the oils were determined using an analytical balance with an accuracy of 0.0001 g, stored in amber glass vials, and kept refrigerated at 5°C (Jerônimo et al., 2024). The essential oil yields were calculated from the moisture-free biomass, relating the plant mass, oil, and residual moisture, according to the Equation below.

$$\%EO = \left( \frac{\textbf{obtained oil volume (g)}}{\textbf{plant material mass (g)} - \left( \frac{\textbf{plat material mass (g) x humidity (\%)}}{100} \right)} \right) \textbf{x 100\%}$$

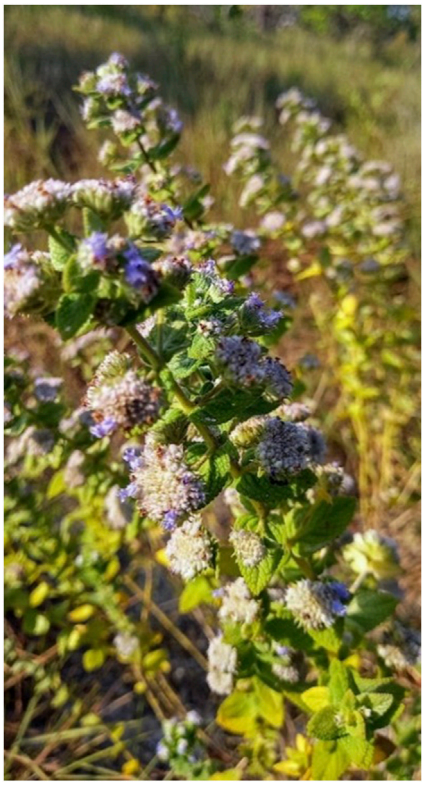

FIGURE 1
*Hyptis crenata* Pohl ex Benth aerial parts.

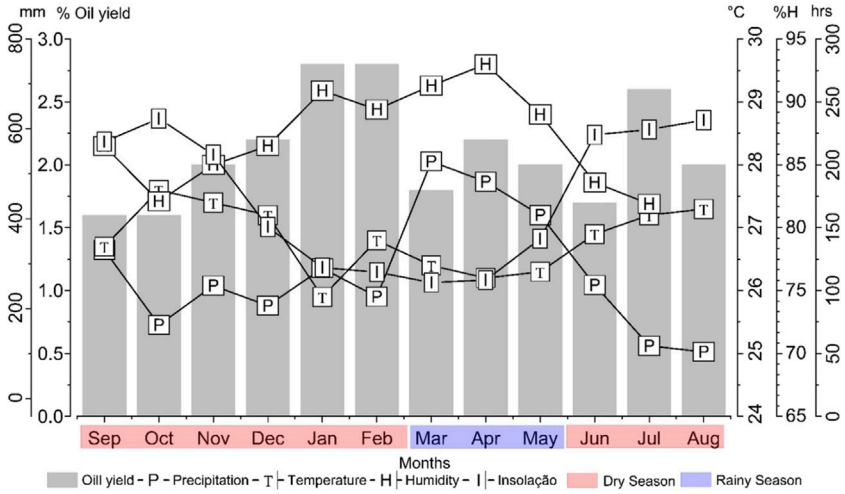


FIGURE 2
Relationship between climatic parameters and *Hyptis crenata* essential oil yield.

The residual moisture content of the leaves was calculated by water loss in an oven at 110°C until the material reached a constant weight.

## 2.3 Analysis of chemical composition

The obtained essential oils were diluted in *n*-hexane in a ratio of 2 μL of oil to 500 μL of solvent and analyzed simultaneously in these two systems: gas chromatography with a flame ionization detector (GC-FID, Shimadzu Corporation, Tokyo, Japan) and gas chromatography with a mass spectrometer (GC-MS, Shimadzu Corporation, Tokyo, Japan) as stabilized protocol (Jerônimo et al., 2024). The system was equipped with an auto-injector: AOC-20i, and an Rtx-5MS silica capillary column (30 m; 0.25 mm; 0.25 μm film thickness) under the following operating conditions: temperature program: 60°C–240°C (3°C/min); injector temperature: 250°C; carrier gas: helium (1 mL/min); injection: split type 1:20 (solution of 5 μL of essential oil: 500 μL of hexane); mass spectra: were obtained by electronic ionization at 70 eV; ion source temperature: 200°C.

To determine the chemical composition, the retention times of each peak (constituents) were converted in retention indices using a homologous series of $C_8$–$C_{40}$ *n*-alkanes (Sigma-Aldrich, Milwaukee, WI, United States) according to the linear method of van Den Dool and Kratz (Van Den Dool and Kratz, 1963). Each mass spectrum and retention index were compared with Adams and FFNSC-2 libraries (Adams, 2007; Mondello, 2011). The Relative amounts of individual components were calculated by peak area normalization using the flame ionization detector (GC-FID).

## 2.4 Statistical analysis

Principal component analysis (PCA) was applied to the essential oil components of *H. crenata* leaves (>1.5%) (OriginPro Learning Edition, OriginLab Corporation, Northampton, MA, United States).

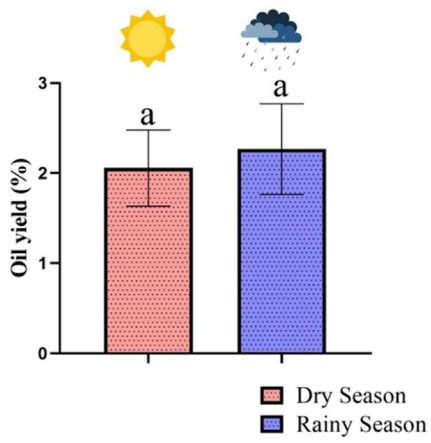


FIGURE 3
Relationship between seasons and oil production of *Hyptis crenata* during the seasonal study.

Hierarchical cluster analysis (HCA) was performed considering the unique distance and Ward linkage. Statistical significance was assessed using the Tukey test ($p < 0.05$) and Pearson correlation coefficients (r) were calculated to determine the relationship between the analyzed climatic parameters (sunlight, relative humidity, temperature, and precipitation), using the GraphPad Prism software, version 8.0.

# 3 Results and discussion

## 3.1 Relationship between essential oil yield and climatic parameters

The climatic parameters: temperature, solar radiation, precipitation, and relative humidity were monitored over the 12 months (September/2021 to August/2022) to evaluate the

TABLE 1 Seasonality of essential oils from *Hyptis crenata*.

| No. | $RI_C$ | $RI_L$ | Period | Dry | | | | | Rainy | | | Dry | | | |
|---|---|---|---|---|---|---|---|---|---|---|---|---|---|---|---|
| | | | Collection months | Sep | Oct | Nov | Dec | Jan | Feb | Mar | Apr | May | Jun | Jul | Aug |
| | | | Oil yield | 1.6 | 1.6 | 2.0 | 2.2 | 2.8 | 2.8 | 1.8 | 2.2 | 2.0 | 1.7 | 2.6 | 2.0 |
| | | | Constituintes | % | | | | | | | | | | | |
| 1 | 927 | 924[a] | α-thujene | 0.18 | 0.14 | 0.09 | 0.15 | 0.19 | 0.10 | 0.12 | 0.16 | 0.10 | | | |
| 2 | **934** | **932[a]** | **α-pinene** | **19.34** | **20.98** | **21.69** | **20.01** | **17.14** | **18.80** | **19.73** | **17.93** | **22.17** | **19.43** | **13.55** | **20.20** |
| 3 | 947 | 945[a] | α-fenchene | 0.70 | 0.61 | 0.45 | 0.39 | 0.42 | 0.44 | 0.49 | 0.36 | 0.40 | 0.42 | | |
| 4 | **949** | **946[a]** | **camphene** | **3.79** | **3.48** | **2.75** | **3.14** | **3.30** | **3.40** | **3.11** | **2.65** | **2.97** | **2.94** | **3.22** | **2.93** |
| 5 | 954 | 955[b] | thuja-2,4(10)-diene | 0.05 | 0.06 | | 0.06 | 0.02 | | | 0.01 | | | | |
| 6 | 973 | 969[a] | Sabinene | 0.02 | 0.02 | 0.03 | 0.04 | 0.07 | 0.11 | 0.08 | 0.07 | 0.04 | 0.75 | 0.43 | 0.49 |
| 7 | **978** | **974[a]** | **β-pinene** | **8.00** | **7.18** | **11.20** | **8.11** | **9.76** | **8.40** | **9.39** | **11.20** | **9.65** | **9.78** | **8.99** | **6.35** |
| 8 | 991 | 988[a] | myrcene | 1.69 | 1.58 | 1.62 | 1.72 | 1.94 | 1.79 | 1.72 | 1.43 | 1.46 | 1.52 | 1.69 | 1.59 |
| 9 | 1,006 | 1,002[a] | α-phellandrene | 0.51 | 0.44 | 0.42 | 0.47 | 0.46 | 0.51 | 0.52 | 0.38 | 0.43 | | 0.44 | 0.46 |
| 10 | 1,012 | 1,012[a] | δ-3-carene | 0.05 | 0.02 | | 0.01 | 0.04 | 0.05 | | 0.04 | 0.04 | | 0.04 | |
| 11 | 1,017 | 1,014[a] | α-terpinene | 0.65 | 0.54 | 0.61 | 0.67 | 0.68 | 0.70 | 0.70 | 0.61 | 0.65 | | 0.61 | 0.67 |
| 12 | 1,024 | 1,020[a] | *p*-cymene | 2.49 | 1.77 | | 1.23 | 1.32 | | | 1.07 | 1.08 | 1.00 | 1.35 | 1.49 |
| 13 | **1,030** | **1,024[a]** | **limonene** | | | **6.28** | | | **6.75** | **6.60** | **5.32** | **6.30** | **5.95** | **6.45** | **7.14** |
| 14 | **1,033** | **1,026[a]** | **1,8-cineole** | **32.47** | **36.90** | **31.18** | **32.47** | **30.87** | **24.15** | **24.29** | **29.70** | **22.76** | **26.90** | **22.48** | **26.38** |
| 15 | 1,058 | 1,054[a] | γ-terpinene | 0.84 | 0.72 | 1.01 | 0.96 | 1.03 | 1.05 | 1.05 | 1.12 | 1.07 | 0.87 | 0.99 | 0.85 |
| 16 | 1,066 | 1,065[a] | *cis*-sabinene hydrate | | | | 0.06 | 0.06 | | | 0.09 | 0.03 | | 0.11 | |
| 17 | 1,089 | 1,086[a] | terpinolene | 0.97 | 0.83 | 0.86 | 1.01 | 1.04 | 1.03 | 0.94 | 0.97 | 0.93 | 0.80 | 1.15 | 0.86 |
| 18 | 1,099 | 1,098[a] | *trans*-sabinene hydrate | 0.02 | 0.03 | | 0.07 | 0.07 | | | 0.09 | 0.03 | | 0.10 | |
| 19 | 1,114 | 1,114[a] | *endo*-fenchol | 0.32 | 0.26 | 0.18 | 0.18 | 0.24 | 0.20 | 0.21 | 0.21 | 0.18 | 0.16 | 0.24 | 0.21 |
| 20 | 1,121 | 1,119[a] | *trans*-pinene hydrate | | | | | | 0.11 | 0.12 | 0.16 | 0.11 | 0.09 | | |
| 21 | 1,122 | 1,122[a] | *cis-p*-menth-2-en-1-ol | 0.11 | 0.11 | 0.09 | 0.13 | 0.15 | | | | | — | 0.02 | 0.06 |
| 22 | 1,126 | 1,127[a] | α-campholenal | 0.02 | 0.02 | | | | | | | | — | | |
| 23 | 1,140 | 1,136[a] | *trans-p*-menth-2-en-1ol | | | | 0.02 | 0.04 | | | 0.05 | | — | | |
| 24 | **1,144** | **1,141[a]** | **camphor** | **11.11** | **9.39** | **8.86** | **13.56** | **15.22** | **14.34** | **10.12** | **14.79** | **10.76** | **12.84** | **15.90** | **9.30** |
| 25 | 1,148 | 1,145[a] | camphene hydrate | 0.61 | 0.63 | 0.49 | 0.44 | 0.45 | 0.46 | 0.39 | 0.41 | 0.35 | 0.46 | 0.46 | 0.46 |
| 26 | 1,157 | 1,155[a] | *iso*-borneol | 0.06 | 0.04 | | 0.02 | 0.04 | | | | | | 0.04 | |
| 27 | 1,163 | 1,163[a] | pinocarvone | 0.08 | 0.08 | 0.07 | 0.07 | 0.09 | 0.08 | 0.08 | 0.09 | 0.06 | 0.05 | 0.09 | 0.07 |
| 28 | **1,167** | **1,168[a]** | **borneol** | **2.57** | **2.36** | **1.74** | **2.11** | **3.03** | **1.74** | **2.46** | **1.98** | **3.38** | **2.43** | **2.31** | **2.07** |
| 29 | 1,177 | 1,174[a] | terpinen-4-ol | 0.81 | 0.70 | 0.73 | 0.61 | 0.74 | 0.73 | 0.67 | 0.81 | 0.62 | 0.61 | 0.69 | 0.63 |
| 30 | 1,175 | 1,175[a] | *cis*-pinocamphone | 0.04 | 0.02 | | | | | | | | | | |
| 31 | 1185 | 1,186[b] | *p*-cymen-8-ol | 0.09 | 0.08 | 0.04 | 0.03 | 0.05 | | | | | | 0.03 | |
| 32 | 1,191 | 1,186[a] | α-terpineol | 2.66 | 2.57 | 2.77 | 2.26 | 2.46 | 2.48 | 2.24 | 2.16 | 1.89 | 2.38 | 2.35 | 2.71 |
| 33 | 1,197 | 1,194[a] | myrtenol | 0.21 | 0.19 | 0.17 | 0.18 | 0.29 | 0.18 | 0.24 | 0.18 | 0.12 | 0.19 | 0.33 | 0.18 |
| 34 | 1,208 | 1,209[a] | *trans*-piperitol | 0.02 | 0.01 | | | 0.02 | | | | | | | |
| 35 | 1,220 | 1,220[a] | *trans*-carveol | 0.02 | | | | | | | | | | | |

(Continued on following page)

TABLE 1 (*Continued*) Seasonality of essential oils from *Hyptis crenata*.

| No. | $RI_C$ | $RI_L$ | Period | Dry | | | | | Rainy | | | Dry | | | |
|---|---|---|---|---|---|---|---|---|---|---|---|---|---|---|---|
| | | | Collection months | Sep | Oct | Nov | Dec | Jan | Feb | Mar | Apr | May | Jun | Jul | Aug |
| | | | Oil yield | 1.6 | 1.6 | 2.0 | 2.2 | 2.8 | 2.8 | 1.8 | 2.2 | 2.0 | 1.7 | 2.6 | 2.0 |
| | | | Constituintes | % | | | | | | | | | | | |
| 36 | 1,244 | 1,244[a] | carvacryl methyl ether | 0.03 | 0.03 | | | | | | | | | 0.03 | |
| 37 | 1,296 | 1,296[b] | thymol | 0.04 | 0.03 | | | | | | 0.04 | 0.04 | | | |
| 38 | 1,302 | 1,302[a] | carvacrol | 0.03 | 0.02 | | | | | | | | | | |
| 39 | 1,352 | 1,350[a] | α-longipinene | 0.95 | 1.30 | 0.91 | 1.12 | 1.26 | 0.74 | 1.11 | 0.70 | 0.76 | 1.08 | 1.51 | 1.99 |
| 40 | 1,357 | 1,357[b] | eugenol | 0.34 | 0.20 | 0.08 | 0.03 | 0.15 | 0.09 | | 0.04 | 0.05 | | 0.03 | 0.11 |
| 41 | 1,374 | 1,374[a] | isoledene | 0.03 | 0.02 | | 0.03 | | | | | | | 0.04 | |
| 42 | 1,377 | 1,374[a] | α-copaene | 0.02 | | | | | | | | | | 0.04 | |
| 43 | 1,411 | 1,412[a] | α-gurjunene | 0.05 | 0.04 | | 0.06 | | | | | | | 0.10 | |
| 44 | 1,421 | 1,417[a] | *E*-caryophyllene | 1.92 | 1.25 | 1.34 | 2.43 | 1.60 | 1.68 | 2.32 | 1.46 | 1.70 | 2.24 | 3.01 | 3.04 |
| 45 | 1,429 | 1,430[b] | γ-maaliene | 0.07 | 0.06 | | 0.09 | 0.07 | | 0.09 | 0.05 | 0.07 | | 0.13 | 0.08 |
| 46 | 1,434 | 1,434[b] | β-gurjunene | 0.02 | | | | | | | | | | 0.03 | |
| 47 | 1,435 | 1,436[b] | α-maaliene | 0.08 | 0.07 | 0.04 | 0.10 | 0.08 | 0.09 | 0.10 | 0.06 | 0.08 | | 0.15 | 0.10 |
| 48 | 1,441 | 1,439[a] | aromadendrene | 0.70 | 0.65 | 0.56 | 1.00 | 0.75 | 0.94 | 1.03 | 0.68 | 0.92 | 0.84 | 1.34 | 1.17 |
| 49 | 1,445 | 1,445[a] | selin-5,11-diene | 0.09 | 0.07 | 0.04 | 0.11 | 0.09 | | 0.13 | | 0.09 | 0.07 | 0.16 | 0.11 |
| 50 | 1,450 | 1,449[a] | α-himachalene | 0.16 | 0.18 | 0.01 | 0.17 | 0.18 | 0.10 | 0.17 | 0.08 | 0.10 | 0.14 | 0.22 | 0.29 |
| 51 | 1,454 | 1,452[a] | α-humulene | 0.10 | 0.05 | 0.04 | 0.11 | 0.07 | 0.07 | 0.11 | 0.05 | 0.06 | 0.07 | 0.14 | 0.12 |
| 52 | 1,462 | 1,464[a] | 9-*epi*-*E*-caryophyllene | 0.13 | 0.10 | 0.06 | 0.16 | 0.10 | 0.14 | 0.16 | 0.10 | 0.14 | 0.11 | 0.21 | 0.17 |
| 53 | 1,473 | 1,475[a] | γ-gurjunene | 0.03 | 0.01 | | 0.02 | | | | | | | 0.04 | |
| 54 | 1,479 | 1,481[a] | γ-himachalene | 0.20 | 0.24 | 0.14 | 0.22 | 0.22 | 0.12 | 0.21 | 0.11 | 0.13 | | 0.28 | 0.42 |
| 55 | 1,490 | 1,490[a] | β-selinene | 0.04 | 0.03 | | 0.04 | 0.03 | | | | | | 0.06 | |
| 56 | 1,496 | 1,496[a] | viridiflorene | 0.25 | 0.20 | 0.17 | 0.37 | 0.25 | 0.33 | 0.38 | 0.25 | 0.33 | 0.28 | 0.49 | 0.39 |
| 57 | 1,502 | 1,500[a] | β-himachalene | 0.44 | 0.49 | 0.34 | 0.49 | 0.55 | 0.32 | 0.48 | 0.30 | 0.38 | 0.58 | 0.67 | 1.12 |
| 58 | 1,514 | 1,516[a] | α-dehydro-*ar*-himachalene | | 0.07 | | | 0.06 | | | | | | 0.07 | |
| 59 | 1,529 | 1,530[a] | γ-dehydro-*ar*-himachalene | 0.07 | 0.07 | | 0.05 | 0.06 | | | | | | 0.08 | 0.07 |
| 60 | 1,543 | 1,544[a] | α-calacorene | 0.06 | 0.05 | | 0.05 | 0.05 | | | | | | 0.06 | 0.09 |
| 61 | 1,567 | 1566[a] | maaliol | 0.05 | 0.03 | | 0.05 | 0.04 | | | | | | 0.12 | |
| 62 | 1,570 | 1,570[a] | caryophyllenol | 0.07 | 0.01 | | | | | | | | | 0.12 | |
| 63 | 1,578 | 1,577[a] | spathulenol | 0.17 | 0.14 | 0.10 | 0.17 | 0.16 | 0.21 | 0.22 | 0.13 | 0.17 | | 0.37 | 0.17 |
| 64 | 1,584 | 1,585[a] | caryophyllene oxide | 0.64 | 0.48 | 0.46 | 0.81 | 0.62 | | | 0.76 | 0.87 | 0.91 | 1.64 | |
| 65 | 1,592 | 1,592[a] | viridiflorol | 0.13 | 0.25 | 0.04 | 0.08 | 0.06 | 0.17 | 0.95 | 0.09 | 0.08 | 0.05 | 0.06 | 0.21 |
| 66 | 1,602 | 1,600[a] | rosifoliol | 0.09 | 0.06 | | 0.10 | 0.07 | 0.10 | 0.12 | 0.04 | 0.09 | 0.09 | 0.20 | 0.13 |
| 67 | 1,611 | 1,611[b] | humulene epoxide II | 0.02 | 0.01 | | | | | | | | | 0.05 | |
| 68 | 1,613 | 1,615[a] | β-himachalene oxide | 0.05 | 0.08 | 0.02 | 0.08 | 0.09 | | 0.09 | 0.03 | 0.04 | 0.09 | 0.18 | 0.08 |
| 69 | 1,633 | 1,627[a] | 1-*epi*-cubenol | | | | | | | | 0.20 | 0.07 | | 0.16 | 0.15 |
| 70 | 1,634 | 1,634[b] | *cis*-cadin-4-en-7-ol | 0.07 | 0.08 | | | 0.08 | | | | | | | |

(Continued on following page)

TABLE 1 (*Continued*) Seasonality of essential oils from *Hyptis crenata*.

| No. | $RI_C$ | $RI_L$ | Period | Dry | | | | | Rainy | | | Dry | | | |
|---|---|---|---|---|---|---|---|---|---|---|---|---|---|---|---|
| | | | Collection months | Sep | Oct | Nov | Dec | Jan | Feb | Mar | Apr | May | Jun | Jul | Aug |
| | | | Oil yield | 1.6 | 1.6 | 2.0 | 2.2 | 2.8 | 2.8 | 1.8 | 2.2 | 2.0 | 1.7 | 2.6 | 2.0 |
| | | | Constituintes | % | | | | | | | | | | | |
| 71 | 1,637 | 1,639[a] | caryophylla-4(12),8(13)-dien-5β-ol | 0.13 | 0.07 | 0.04 | 0.11 | 0.06 | 0.11 | 0.12 | 0.04 | | 0.08 | 0.25 | |
| 72 | 1,652 | 1,648 | himachalol | | | 0.13 | 0.18 | 0.20 | 0.14 | 0.26 | 0.09 | 0.19 | 1.06 | 0.36 | 0.40 |
| 73 | 1,662 | 1,661[a] | *allo*-himachalol | 0.02 | 0.24 | 0.21 | 0.31 | 0.17 | | 0.42 | | 0.43 | | 0.05 | 0.68 |
| 74 | 1,666 | 1,668[a] | 14-hydroxy-9-*epi*-*E*-caryophyllene | | | | | | | | | | | | 0.14 |
| | Monoterpene hydrocarbons | | | 39.28 | 38.37 | 47.00 | 37.82 | 37.22 | 43.13 | 44.45 | 43.32 | 47.29 | 43.46 | 38.91 | 43.03 |
| | Oxygenated monoterpenoids | | | 51.32 | 53.47 | 46.32 | 52.21 | 53.82 | 44.47 | 40.82 | 50.76 | 44.83 | 46.11 | 45.18 | 42.07 |
| | Sesquiterpene hydrocarbons | | | 5.50 | 5.00 | 3.64 | 6.66 | 5.47 | 4.53 | 6.29 | 3.84 | 4.76 | 5.41 | 8.92 | 9.26 |
| | Oxygenated sesquiterpenoids | | | 1.44 | 1.45 | 1.00 | 1.89 | 1.55 | 0.73 | 2.09 | 1.20 | 1.94 | 2.28 | 3.56 | 1.96 |
| | Others | | | 0.34 | 0.20 | 0.08 | 0.03 | 0.15 | 0.09 | 0.00 | 0.04 | 0.05 | 0.00 | 0.03 | 0.11 |
| | Total identified | | | 97.88 | 98.49 | 98.04 | 98.61 | 98.21 | 92.95 | 93.65 | 99.16 | 98.87 | 97.26 | 96.60 | 96.43 |

$RI_C$, calculated retention index; $RI_L$, literature retention index.
[a]Adams (2007).
[b](Mondello, 2011); Main constituents in bold; Standard deviation was less than 2.0 ($n$ = 3).

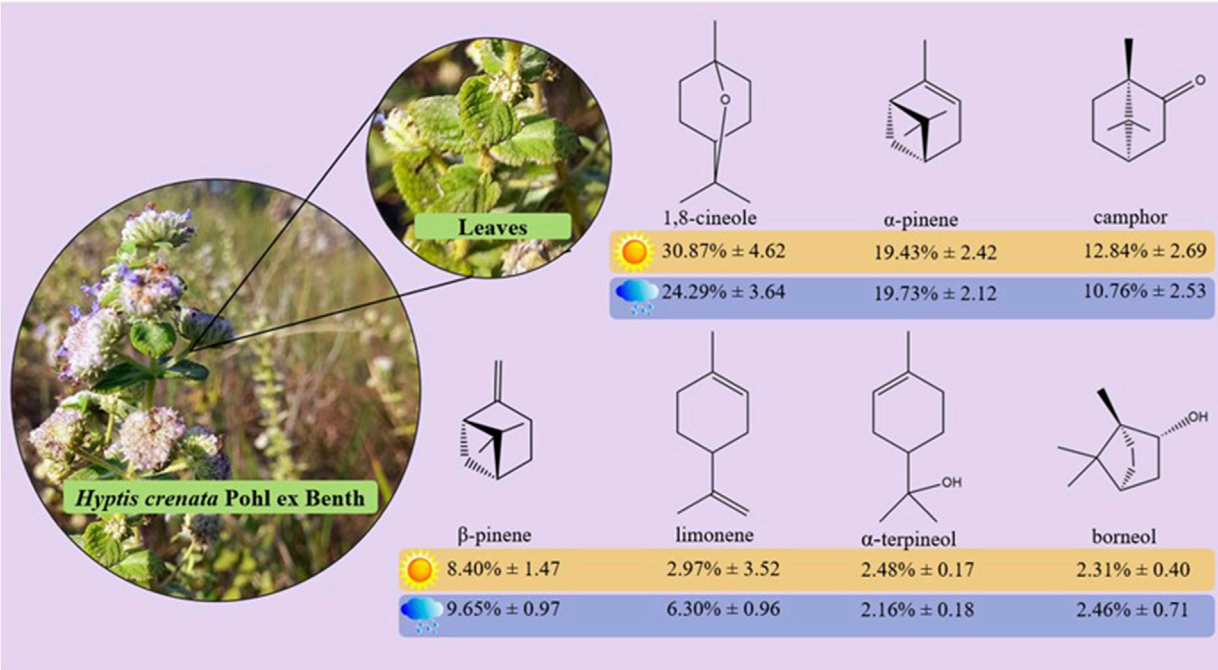


FIGURE 4
Chemical structures of the main compounds identified in *Hyptis crenata* essential oils leaves during the year.

influence of seasonality on the yield and composition of *H. crenata* leaves essential oil. During the study periods, insolation values ranged from 106.4 h (March) to 253.4 h (August), monthly precipitation from 103.9 mm (August) to 527.4 mm (March), temperature from 25.9°C (January) to 27.6°C (October) and relative humidity from 79.7% (August) to 93.0% (April).

According to precipitation data, the dry period in the region comprised the months of September to February and June to

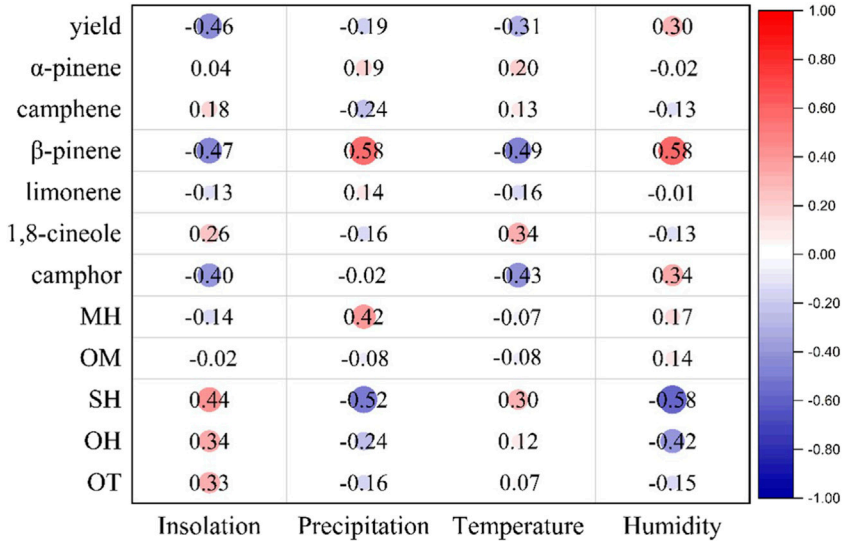


FIGURE 5
Correlations of *Hyptis crenata* essential oils and climatic parameters monitored during the seasonal study.

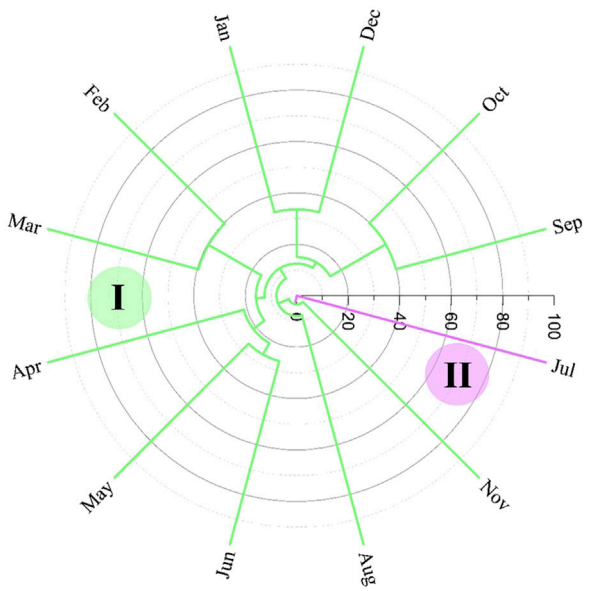


FIGURE 6
Hierarchical cluster analysis of *Hyptis crenata* essential oils.

August, with an average precipitation of 215.58 ± 76.26 mm, and the rainy period from March to May, with an average precipitation of 472.53 mm ± 60.22 mm (Figure 2).

In the seasonal study, *H. crenata* leaves essential oil yields varied from 1.6% (September) to 2.8% (January), averaging 2.05% ± 0.39% during the studied year. Statistical Tukey test showed no significant difference in essential oil production during the dry (1.97% ± 0.2%) and rainy (2.07% ± 0.44%) seasons (Figure 3). Furthermore, no significant correlations ($p > 0.05$) were observed between essential oil yield and precipitation ($r = -0.23$), temperature ($r = -0.12$), humidity ($r = -0.20$), and insolation ($r = -0.36$) indicating that *H. crenata* specimen presents the same essential oil production regardless of the climatic conditions. Variations in oil yield may be linked to other abiotic factors, edaphic and/or genetic.

Essential oils (extracted by hydrodistillation) from the dry and fresh aerial part of *H. crenata* collected in Marajó Island (Brazilian Amazon) presented yields between 0.6% and 0.9%, respectively, in samples from Melgaço and São Sebastião da Boa Vista (Zoghbi et al., 2002); in Salvaterra a yield of 1.4% was described (Rebelo et al., 2009). Other reported samples showed yields of 0.2%, 0.6%, and 1.4% in Tocantins (Zoghbi et al., 2002), Cuiabá (Violante et al., 2012), and Mato Grosso do Sul respectively. None of these specimens showed a higher yield than the present study. However, little information has been found regarding phytochemical studies of this species. Moreover, *Hyptis marrubioides* showed high variability in the concentration of the essential oil components due to seasonality variability probably related mainly to the rainfall regime (Botrel et al., 2010a).

## 3.2 Relationship between essential oil composition and climatic parameters

The chromatographic analysis identified 74 constituents in *H. crenata* leaf essential oils, representing an average of 97.96% (92.95%–99.16%) of the total chemical composition of the oils analyzed during the 12 months. The constituents are listed below in ascending order of their respective retention indexes (RI) in Table 1.

Oxygenated monoterpenoids (40.82%–53.82%, 46.21% ± 4.49) and monoterpene hydrocarbons (37.22%–47.29%, 43.08% ± 3.5) were the predominant in the essential oil, followed by sesquiterpene hydrocarbons (3.64%–9.26%, 5.44% ± 1.78) and oxygenated sesquiterpenoids (0.73%–3.56%, 1.72% ± 0.73).

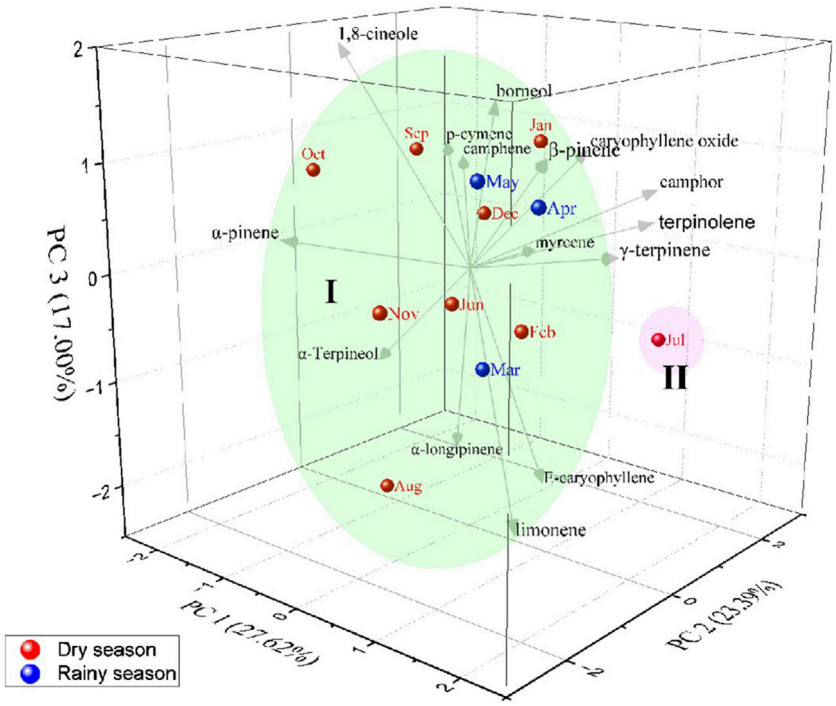


FIGURE 7
Principal components analysis of *Hyptis crenata* essential oil during the seasonal study.

The oxygenated monoterpenoid 1,8-cineole (eucalyptol) was the main constituent throughout the study, ranging from 22.48% (July/2022) to 36.90% (October/2021), presenting an annual average of 28.48 ± 4. 32%; followed by α-pinene, whose levels varied from 13.55% (July/2022) to 22.17% (May/2022), with an annual average of 19.58% ± 2.29%; the camphor content varied from 8.86% (November/2021) to 15.90% (July/2022), with an annual average of 11.98% ± 2.54%; β-pinene ranged from 6.35% (August/2022) to 11.20% (April/November/2021), with an annual average of 9.19% ± 1.47%; limonene, despite not occurring in the months of September, October, December (2021), and January (2022), presented an average annual content of 6.12% ± 3.15% with variations of 5.32% (April/2022) at 7.14% (August/2022); α-terpineol presented amounts ranging from 1.89% (May/2022) to 2.77% (November/2021) with an annual average of 2.42% ± 0.25% and borneol concentrations ranging from 1.74% (November/2021, February/2022) to 3.38% (May/2022) with an average concentration of 2.34% ± 0.48%. The chemical structures of these compounds are shown in Figure 4.

The chemical composition of *H. crenata* essential oil varies depending on the time of year and the location where the leaves are collected (Santos et al., 2023). Several studies report different chemical characteristics among essential oils of the *Hyptis* genus. A study on *H. marrubioides* showed that the composition of the essential oil varied significantly due to seasonal factors, with no qualitative variation in the composition of the oil throughout the seasons (Botrel et al., 2010b). Furthermore, it was found that the chemical composition of *H. crenata* essential oils presents notable variability, with different main constituents identified in the oils obtained from different samples (Lima et al., 2023).

Intraspecific variability in chemical composition was also noted in other *Hyptis* species, indicating the presence of several chemical compounds. Studies report the existence of different chemical characteristics among the essential oils of *H. crenata*, which generally has the constituents 1,8-cineole, borneol, camphor, limonene, α- and β-pinene, *E*-caryophyllene, *p*-cymene, all of which vary according to the time of year and place of collection (Scramin et al., 2000).

## 3.3 Correlation between climatic parameters and chemical composition

Based on Pearson's correlation data between the climatic parameters and the *H. crenata* chemical composition, it was possible to identify only a statistically significant correlation ($p < 0.05$) between the amounts of β-pinene and sesquiterpene hydrocarbons with the data of precipitation and humidity, the other constituents such as α-pinene, camphene, limonene, 1,8-cineole, and camphor, as well as the classes of hydrocarbon/oxygenated monoterpenes and oxygenated sesquiterpenes showed statistically insignificant correlations.

β-pinene showed a moderate negative correlation between insolation ($r = -0.47$) and temperature ($r = -0.49$) but without statistical significance ($p > 0.05$); however, this constituent showed a moderate correlation positive correlation with precipitation ($r = 0.58$) and humidity ($r = 0.58$) with statistical significance ($p < 0.05$), in the same way the class of sesquiterpene hydrocarbons showed a moderate and negative correlation ($r = -0.58$) with humidity as displayed in Figure 5.

These data suggest that, despite the four climatic parameters analyzed, the production of the main constituents and classes of terpenoids remains with few qualitative and considerable quantitative variations. However, correlations with β-pinene suggest increasing precipitation and humidity, producing higher monoterpene concentrations in this *H. crenata* specimen. Likewise, humidity influences the class of sesquiterpene hydrocarbons; that is, the increase in this climatic parameter leads to a decrease in the concentration of this terpene class.

α-Pinene and β-pinene are constituents of several essential oils. They have a broad pharmacological action spectrum, described in several studies, with effects such as anti-inflammatory, antitumor and antimicrobial, antibacterial (Leite et al., 2007; Silva et al., 2012), anxiolytic (Santos et al., 2022), antidepressant, anticonvulsant, hypotensive, myorelaxant, antispasmodic (Nikitina et al., 2009; Silva et al., 2012; Felipe et al., 2019; Salehi et al., 2019). β-Pinene, with a woody aroma, occurs in several plants of the Lamiaceae and naturally plays an indirect role in the defense of the plant, attracting natural enemies (predators and/or parasitoids) that help control the population of herbivores (Kutty and Mishra, 2023).

Furthermore, this *H. crenata* specimen displayed low acute toxicity and significant anti-inflammatory activity, with peripheral and no central antinociceptive action (de Lima et al., 2023). However, the chemical composition variation due to seasonality may change the pharmacological activity of *H. crenata* essential oil.

In this way, it is understood that some abiotic or biotic factors that the plant is exposed to favor the significant biosynthesis of α-pinene and, consequently, the decline of camphor since these constituents come from the same formation pathway. In the present study, it was possible to identify that there was no significant correlation between the four climatic parameters analyzed and the α-pinene and camphor amounts.

Furthermore, α-pinene is found in the essential oils of many plants, such as conifers, has a distinct pine aroma, and is known for its various biological properties. In medicinal and/or aromatic plants, α-pinene is involved in various actions, including plant defense mechanisms and repelling insects with its distinct aroma (Kutty and Mishra, 2023).

Furthermore, the chemical composition of essential oils can vary depending on the time and place of harvest. Furthermore, the chemical composition of these oils can undergo biotransformation processes to produce other compounds, such as verbenone, which complements the antibacterial activity of α-pinene (Dewick, 2009).

### 3.4 Multivariate analysis

Using hierarchical cluster analysis (HCA), a dendrogram was obtained showing two groups formed with the essential oils of *H. crenata* (see Figure 6). Group I comprised all months of study except July (2022), which formed group II.

Principal Component Analysis (PCA, Figure 7) confirmed the formation of two distinct groups and elucidated 68.01% of the data variability. PC1 explained 27.62% of the data and showed negative correlations with α-pinene ($r$ = −0.96), camphene ($r$ = −1.12), myrcene ($r$ = −0.10), *p*-cymene ($r$ = −1.25), 1,8-cineole ($r$ = −1.49), borneol ($r$ = −0.03), α-terpineol ($r$ = −1.33), and α-longipinene ($r$ = −0.89). The second component (PC2) explained 23.39% of the data and showed negative correlations α-pinene ($r$ = −2.01), β-pinene ($r$ = −0.92), limonene ($r$ = −1.00), 1,8-cineole ($r$ = −0.36), and γ-terpinene (r = −0.33). The third component (PC3) explained 17.00% of the data, presenting positive correlations with α-pinene ($r$ = 0.39), camphene ($r$ = 0.73), β-pinene ($r$ = 1.27), *p*-cymene ($r$ = 0.88), 1,8-cineole ($r$ = 1.94), γ-terpinene ($r$ = 0.43), terpinolene ($r$ = 0.32), camphor (r = 0.69), borneol ($r$ = 1.48), and caryophyllene oxide ($r$ = 1.03).

Group I is represented by oils from all months except July, this group was characterized by the chemical type of 1,8-cineole (24.15%–36.90%), α-pinene (17.14%–22.17%), α-terpineol (1.89%–2.77%), α-longipinene (0.70%–1.99%), limonene (5.32%–7.14%), *E*-caryophyllene (1.25%–3.04%), myrcene (1.43%–1.79%), camphene (2.65%–3.79%), caryophyllene oxide (0.46%–0.91%), β-pinene (6.35%–11.20%), and borneol (1.74%–3.38%). However, group II was characterized by the highest camphor levels (15.90%); that is, July was the only month that formed a distinct group, marked by the high occurrence of camphor compared to the other months. Moreover, in July *H. crenata* presented the lowest content of α-pinene (13.55%).

## 4 Conclusion

The *H. crenata* studied specimen showed constancy in essential oil production throughout the year, regardless of seasonal influences, with a chemical profile marked by 1,8-cineole, borneol, α-terpinene, β-pinene, and *E*-caryophyllene. The chemical composition in the dry period was similar to that of the rainy season. There was an occurrence of the same constituents but with a more marked presence of α-pinene and an inevitable decline in camphor.

These results imply that the biological activities presented by the plant and described in previous literature remain constant during the seasonal period due to its unchanged chemical profile. In this way, it is understood that this specimen can be an alternative source of biologically active compounds during different climatic periods in the Amazon. This could have significant implications for obtaining bioactive molecules for the pharmaceutical industry and reaffirms the importance of this medicinal herb for traditional medicine in the Amazon.

## Data availability statement

The original contributions presented in the study are included in the article/Supplementary material, further inquiries can be directed to the corresponding author.

## Author contributions

MdL: Formal Analysis, Methodology, Writing–original draft. PS: Formal Analysis, Writing–original draft. LJ: Formal Analysis, Writing–original draft. RV: Formal Analysis, Writing–original draft. JdS: Formal Analysis, Writing–original draft. WS: Writing–review and editing. JM: Formal Analysis, Methodology, Writing–original draft. PF: Conceptualization, Data curation, Funding acquisition,

Investigation, Methodology, Project administration, Supervision, Validation, Writing–original draft, Writing–review and editing.

## Funding

The author(s) declare that financial support was received for the research, authorship, and/or publication of this article. This research was funded by the PAPQ (Programa de Apoio à Publicação Qualificada), Propesp, UFPA.

## Acknowledgments

The authors are grateful to the Coordenação de Aperfeiçoamento de Pessoal de Nível Superior (CAPES) for providing scholarships to MdL, PS, and LJ; Conselho Nacional de Desenvolvimento Científico e Tecnológico (CNPq) for providing scholarships to RV; and Universidade do Estado do Pará (UEPA) for providing Postdoctoral scholarships to PF.

## Conflict of interest

The authors declare that the research was conducted in the absence of any commercial or financial relationships that could be construed as a potential conflict of interest.

## Publisher's note

All claims expressed in this article are solely those of the authors and do not necessarily represent those of their affiliated organizations, or those of the publisher, the editors and the reviewers. Any product that may be evaluated in this article, or claim that may be made by its manufacturer, is not guaranteed or endorsed by the publisher.

## References

Adams, R. P. (2007) *Identification of essential oil components by gas chromatography/mass spectrometry*. Carol Stream, Ilinois, EUA: Allured Publishing Corporation.

Bezerra, S. M. (2020). Agrobiodiversidade e conhecimentos locais das plantas alimentícias no quilombo de Deus Ajude, Arquipélago do Marajó – Pará. Universidade Federal do Pará e Empresa Brasileira de Pesquisa Agropecuária. Available at: https://repositorio.ufpa.br/jspui/handle/2011/14487.

Botrel, P. P., Pinto, J. E. B. P., Araújo, A. C. C. de, Bertolucci, S. K. V., Figueiredo, F. C., Ferri, P. H., et al. (2010a). Variações no teor e na composição volátil de Hyptis marrubioides EPL: cultivada no campo e em casa de vegetação. *Quim. Nova* 33, 33–37. doi:10.1590/S0100-40422010000100007

Botrel, P. P., Pinto, J. E. B. P., Ferraz, V., Bertolucci, S. K. V., and Figueiredo, F. C. (2010b). Teor e composição química do óleo essencial de Hyptis marrubioides Epl., Lamiaceae em função da sazonalidade. *Acta Sci. Agron.* 32. doi:10.4025/actasciagron.v32i3.3415

Campos, A. C. de S., Costa Neto, S. V., and Jardim, M. A. G. (2021). Floristica, estrutura e formas de vida da regeneração de uma savana amazônica, Pará, Brasil. *Rev. Bras. Geogr. Física* 14, 2550–2572. doi:10.26848/rbgf.v14.5.p2550-2572

Costa, W. K., de Oliveira, A. M., da Silva Santos, I. B., Silva, V. B. G., de Aguiar, J. C. R., de, O. F., et al. (2022). Influence of seasonal variation on the chemical composition and biological activities of essential oil from eugenia pohliana DC leaves. *Chem. Biodivers.* 19, e202200034. doi:10.1002/cbdv.202200034

de Lima, M. N. N., Guimarães, B. A., de Castro, A. L. S., Ribeiro, K. B., Miller, D. C., da Silva, P. I. C., et al. (2023). Chemical composition and antinociceptive and anti-inflammatory activity of the essential oil of Hyptis crenata Pohl ex Benth. from the Brazilian Amazon. *J. Ethnopharmacol.* 300, 115720. doi:10.1016/j.jep.2022.115720

Dewick, P. M. (2009) *Medicinal natural products: a biosynthetic approach*. Chichester: John Wiley and Sons Ltd. doi:10.1002/9780470742761

Diniz, L. R. L., Vieira, C. F. X., Santos, E. C. dos, Lima, G. C., Aragão, K. K. V., Vasconcelos, R. P., et al. (2013). Gastroprotective effects of the essential oil of Hyptis crenata Pohl ex Benth. on gastric ulcer models. *J. Ethnopharmacol.* 149, 694–700. doi:10.1016/j.jep.2013.07.026

Feitosa-Alcantara, R. B., Arrigoni-Blank, M. de F., Blank, A. F., Nogueira, P. C. de L., Sampaio, T. S., Nizio, D. A. de C., et al. (2018). Chemical diversity of essential oils from Hyptis pectinata (L.) Poit. *Biosci. J.*, 875–887. doi:10.14393/BJ-v34n1a2018-39382

Felipe, C. F. B., Albuquerque, A. M. S., de Pontes, J. L. X., de Melo, J. Í. V., Rodrigues, T. C. M. L., de Sousa, A. M. P., et al. (2019). Comparative study of alpha- and beta-pinene effect on PTZ-induced convulsions in mice. *Fundam. Clin. Pharmacol.* 33, 181–190. doi:10.1111/fcp.12416

Gobbo-Neto, L., and Lopes, N. P. (2007). Plantas medicinais: fatores de influência no conteúdo de metabólitos secundários. *Quim. Nova* 30, 374–381. doi:10.1590/S0100-40422007000200026

Jerônimo, L. B., Lima Santos, P. V., Pinto, L. C., da Costa, J. S., Andrade, E. H. de A., Setzer, W. N., et al. (2024). Acmella oleracea (L.) R.K. Jansen essential oils: chemical composition, antioxidant, and cytotoxic activities. *Biochem. Syst. Ecol.* 112, 104775. doi:10.1016/j.bse.2023.104775

Jesus, N. Z. T. de, Lima, J. C. da S., Silva, R. M. da, Espinosa, M. M., and Martins, D. T. de O. (2009). Levantamento etnobotânico de plantas popularmente utilizadas como antiúlceras e antiinflamatórias pela comunidade de Pirizal, Nossa Senhora do Livramento-MT, Brasil. *Rev. Bras. Farmacogn.* 19, 130–139. doi:10.1590/S0102-695X2009000100023

Kutty, N. N., and Mishra, M. (2023). Dynamic distress calls: volatile info chemicals induce and regulate defense responses during herbivory. *Front. Plant Sci.* 14, 1135000. doi:10.3389/fpls.2023.1135000

Leite, A. M., Lima, E. de O., Souza, E. L. de, Diniz, M., de, F. F. M., Trajano, V. N., et al. (2007). Inhibitory effect of beta-pinene, alpha-pinene and eugenol on the growth of potential infectious endocarditis causing Gram-positive bacteria. *Rev. Bras. Ciências Farm.* 43, 121–126. doi:10.1590/S1516-93322007000100015

Lima, M. N. N. de, Costa, J. S. da, Guimarães, B. A., Freitas, J. J. S., Setzer, W. N., Silva, J. K. R. da, et al. (2023). Chemometrics of the composition and antioxidant capacity of Hyptis crenata essential oils from Brazil. *Molecules* 28, 3371. doi:10.3390/molecules28083371

Mondello, L. (2011) *FFNSC 2: flavors and fragrances of natural and synthetic compounds, mass spectral database*. Chichester: John Wiley and Sons Inc.

Nikitina, L. E., Startseva, V. A., Vakulenko, I. A., Khismatulina, I. M., Lisovskaya, S. A., Glushko, N. P., et al. (2009). Synthesis and antifungal activity of compounds of the pinane series. *Pharm. Chem. J.* 43, 251. doi:10.1007/s11094-009-0282-3

Oliveira, C. M. A. de, Silva, M. do R. R., Kato, L., Silva, C. C. da, Ferreira, H. D., and Souza, L. K. H. (2004). Chemical composition and antifungal activity of the essential oil of Hyptis ovalifolia Benth. (Lamiaceae). *J. Braz. Chem. Soc.* 15, 756–759. doi:10.1590/S0103-50532004000500023

Rebelo, M. M., Silva, J. K. R. da, Andrade, E. H. A., and Maia, J. G. S. (2009). Antioxidant capacity and biological activity of essential oil and methanol extract of Hyptis crenata Pohl ex Benth. *Rev. Bras. Farmacogn.* 19, 230–235. doi:10.1590/S0102-695X2009000200009

Salehi, B., Upadhyay, S., Erdogan Orhan, I., Kumar Jugran, A. L. D., Jayaweera, S., A. Dias, D., et al. (2019). Therapeutic potential of α- and β-pinene: a miracle gift of nature. *Biomolecules* 9, 738. doi:10.3390/biom9110738

Santos, E. S., Abrantes Coelho, G. L., Saraiva Fontes Loula, Y. K., Saraiva Landim, B. L., Fernandes Lima, C. N., Tavares de Sousa Machado, S., et al. (2022). Hypoglycemic, hypolipidemic, and anti-inflammatory effects of beta-pinene in diabetic rats. *Evidence-Based Complement. Altern. Med.* 2022, 1–8. doi:10.1155/2022/8173307

Santos, P. V. L., da Cruz, E. de N. S., Nunes, J. de A., Mourão, R. H. V., do Nascimento, W. M. O., Maia, J. G. S., et al. (2023). Seasonal influence on volatile composition of psidium friedrichsthalianum leaves, sampled in the Brazilian Amazon. *Horticulturae* 9, 768. doi:10.3390/horticulturae9070768

Scramin, S., Saito, M. L., Pott, A., and Marques, M. O. M. (2000). Volatile constituents of Hyptis crenata Pohl (labiatae) native in Brazilian pantanal. *J. Essent. Oil Res.* 12, 99–101. doi:10.1080/10412905.2000.9712052

Silva, A. C. R. da, Lopes, P. M., Azevedo, M. M. B. de, Costa, D. C. M., Alviano, C. S., and Alviano, D. S. (2012). Biological activities of a-pinene and β-pinene enantiomers. *Molecules* 17, 6305–6316. doi:10.3390/molecules17066305

Van Den Dool, H., and Kratz, P. D. (1963). A generalization of the retention index system including linear temperature programmed gas—liquid partition chromatography. *J. Chromatogr. A* 11, 463–471. doi:10.1016/s0021-9673(01)80947-x

Violante, I. M. P., Garcez, W. S., da Silva Barbosa, C., and Garcez, F. R. (2012). Chemical composition and biological activities of essential oil from ***Hyptis crenata*** growing in the Brazilian cerrado. *Nat. Prod. Commun.* 7, 1934578X1200701. doi:10.1177/1934578X1200701037

Zoghbi, M., das, G. B., Andrade, E. H. A., da Silva, M. H. L., Maia, J. G. S., Luz, A. I. R., et al. (2002). Chemical variation in the essential oils of Hyptis crenata Pohl ex Benth. *Flavour Fragr. J.* 17, 5–8. doi:10.1002/ffj.1031

frontiers | Frontiers in Chemistry

TYPE Original Research
PUBLISHED 03 June 2024
DOI 10.3389/fchem.2024.1411801

Check for updates

OPEN ACCESS

EDITED BY
Xuetao Xu,
Wuyi University, China

REVIEWED BY
Guanghao Zhu,
Shanghai University of Traditional Chinese Medicine, China
Danying Huang,
Guangdong University of Petrochemical Technology, China
Haoxing Zhang,
Shenzhen University, China

*CORRESPONDENCE
Faliang Liang,
faliang2024@163.com

RECEIVED 03 April 2024
ACCEPTED 16 May 2024
PUBLISHED 03 June 2024

CITATION
Liang F (2024), Inhibition mechanism investigation of quercetagetin as a potential tyrosinase inhibitor.
*Front. Chem.* 12:1411801.
doi: 10.3389/fchem.2024.1411801

COPYRIGHT
© 2024 Liang. This is an open-access article distributed under the terms of the Creative Commons Attribution License (CC BY). The use, distribution or reproduction in other forums is permitted, provided the original author(s) and the copyright owner(s) are credited and that the original publication in this journal is cited, in accordance with accepted academic practice. No use, distribution or reproduction is permitted which does not comply with these terms.

# Inhibition mechanism investigation of quercetagetin as a potential tyrosinase inhibitor

Faliang Liang*

Pharmacy Department, Jiang Men Maternity and Child Healthcare Hospital, Jiangmen, China

Tyrosinase is one important rate limiting enzyme in melanin synthesis, directly affecting the melanin synthesis. Quercetagetin is one active ingredient from marigold. Thence, the inhibition effects of quercetagetin against tyrosinase were investigated. The results showed quercetagetin could inhibit tyrosinase activity with $IC_{50}$ value of 0.19 ± 0.01 mM and the inhibition type was a reversible mixed-type. Results of fluorescence quenching showed quercetagetin could quench tyrosinase fluorescence in static process. CD and 3D fluorescence results showed the interaction of quercetagetin to tyrosinase could change tyrosinase conformation to inhibit activity. Moreover, docking revealed details of quercetagetin's interactions with tyrosinase.

KEYWORDS

**nature product, quercetagetin, tyrosinase, inhibition effects, inhibitor**

## 1 Introduction

As we all know, various diseases affect people's health (Zhang et al., 2020; Zhang X. et al., 2021; Shi et al., 2023; Zhou S. et al., 2022). As a therapeutic target, tyrosinase is one important metal enzyme containing two copper, which widely presents in the organism (Min et al., 2023; Fan et al., 2017). Tyrosinase has been confirmed to be involved in the synthesis of melanin (Li et al., 2023; Hassan et al., 2023; Li J. et al., 2021). The first reaction process is monophenolase activity, in which L-tyrosine is hydroxylated into L-dopa and the second reaction process is diphenolase activity, in which L-dopa is subsequently oxidized into dopaquinone (Djafarou et al., 2023; Lee et al., 2023; Zargaham et al., 2023). In the organism, melanin acts crucial roles to protect the skin from UV radiation (Lu et al., 2023a; Znajafi et al., 2023). But, excessive elevated melanin content leads to lots of pigmentation disorders, including age spots and melanoma (Broulier et al., 2023; De Barros et al., 2023; Xue et al., 2023). Inhibition of tyrosinase activity would reduce melanin generation, thence, the finding on novel tyrosinase inhibitors is attracting more attention due to their potential application in medicine and cosmetics fields (Wang and Mu, 2021). Although kojic acid and arbutin (Figure 1) are applied as tyrosinase inhibitors in the medical and industrial fields, they still have been found to lots of adverse side effects (Wang et al., 2021; Esma et al., 2023). Now, to find novel tyrosinase inhibitors is essential for treatment of melanin synthesis (Romagnoli et al., 2022; Nasab et al., 2023).

Natural products have been the vital sources for clinical drugs (Li Y. et al., 2021; Wu et al., 2021; Chen et al., 2022; Zang et al., 2022). Many natural products display widely biological activities, such as antioxidant (Zhang Y. et al., 2021; Tao et al., 2022; Tang et al., 2023), anti-tumor (Liu et al., 2022; Chen et al., 2023; Song et al., 2023), anti-inflammatory (Wang et al., 2020; Wang X. et al., 2022; Zhou Y. et al., 2022), and so on (Wang Y. et al., 2022; Qi et al., 2022; Ma et al., 2023). In particular, natural products show low toxicity (Shao et al., 2020; Jiang et al., 2021;

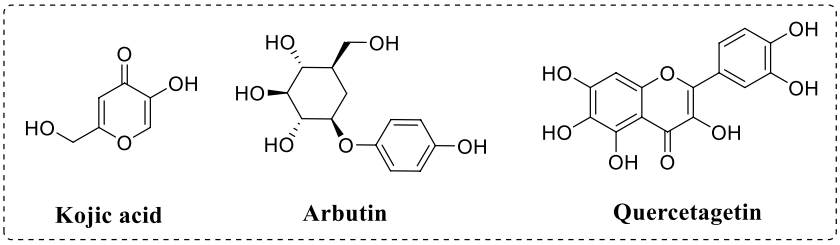


FIGURE 1
Chemical structure of kojic acid, arbutin and quercetagetin.

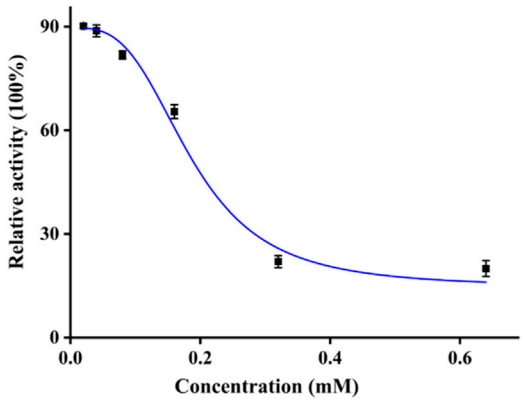


FIGURE 2
Tyrosinase inhibitory activity of quercetagetin.

Pei et al., 2021). Thence the development of natural products as tyrosinase inhibitors attracts much attention.

Quercetagetin (Figure 1) is one active ingredient from marigold and has a chemical structure of 3,3′,4′,5,6,7-hexahydroxyflavone (Bulut and Yilmaz, 2021; Wang X. et al., 2022). As one polyhydroxyphenol molecule with multiple hydrogen donor substituents, quercetagetin represents rich biological activities (Wu F. et al., 2023). For example, quercetagetin shows strong antioxidant activity and can effectively scavenge DPPH and ABTS (Fuentes et al., 2021). Quercetagetin also enhances the antioxidant enzymatic activities in broilers tissue by Nrf2/ARE signal pathway (Wu et al., 2022). In addition, quercetagetin displays immunomodulatory and anti-inflammatory to inhibit the release of macrophage-derived chemokine (Rufino et al., 2021). Besides, quercetagetin display other beneficial functions, including anti-virus and anti-diabetes (Seyedi et al., 2016). However, to our knowledge, the inhibition effects of quercetagetin against tyrosinase have not been reported yet.

Hence, in this study, we investigated the inhibition effects of quercetagetin against tyrosinase by the multispectral method, followed by the molecular docking.

# 2 Results and discussion

## 2.1 Inhibitory activity

The tyrosinase inhibitory activity of quercetagetin was examined on mushroom tyrosinase. The tyrosinase activity was measured under different concentrations of quercetagetin (Figure 2). It could be observed that tyrosinase relative activity gradually reduced with quercetagetin concentration (0–0.64 mM), meaning that quercetagetin could inhibit the tyrosinase activity with quercetagetin concentration. Its $IC_{50}$ value was calculated to be 0.19 ± 0.01 mM, which was lower than that of kojic acid. This result showed that quercetagetin could be used as a natural tyrosinase inhibitor.

## 2.2 Kinetic study

There are two kinds of inhibitors, reversible and non-reversible inhibitors. For a reversible inhibitor, it can reduce the enzyme activity by the binding to enzyme, which can restore the enzyme activity through the remove of inhibitor. There are three reversible inhibitors, including competitive, non-competitive and mixed-type inhibitors. The inhibition type of quercetagetin on tyrosinase was subsequently investigated. With different concentration of quercetagetin and tyrosinase, the absorbance changes were measured (Figure 3A) and found that the lines of quercetagetin with different concentration passed origin and slopes reduced with quercetagetin concentration. The results suggested quercetagetin as a reversible inhibitor. With different concentration of quercetagetin and substrate, the absorbance changes were analyzed using Lineweaver-Burk plots (Figure 3B). The lines of quercetagetin intersected in the third quadrant and their slops increased with quercetagetin concentrations. The results indicated that quercetagetin inhibited tyrosinase in a mixed-type, meaning that quercetagetin bound to tyrosinase and tyrosinase-substrate complex to inhibit its activity. Similar phenomena were obtained in inhibition type of indole-carbohydrazides (Iraji et al., 2022).

Moreover, as shown in Figures 4A, B, the inhibition constants $K_i$ and $K_{is}$ were obtained from the secondary curves of inhibitory kinetics to be 0.24 and 0.12 mM. Smaller $K_{is}$ value than $K_i$ meant that binding force of quercetagetin with tyrosinase-substrate complex was stronger than with tyrosinase. That was to say that quercetagetin preferred to bind with tyrosinase-substrate complex.

## 2.3 Fluorescence quenching

The fluorescence quenching process of tyrosinase by quercetagetin was investigated. For fluorescence spectra of tyrosinase, they all showed characteristic peaks at 344 nm at 295,

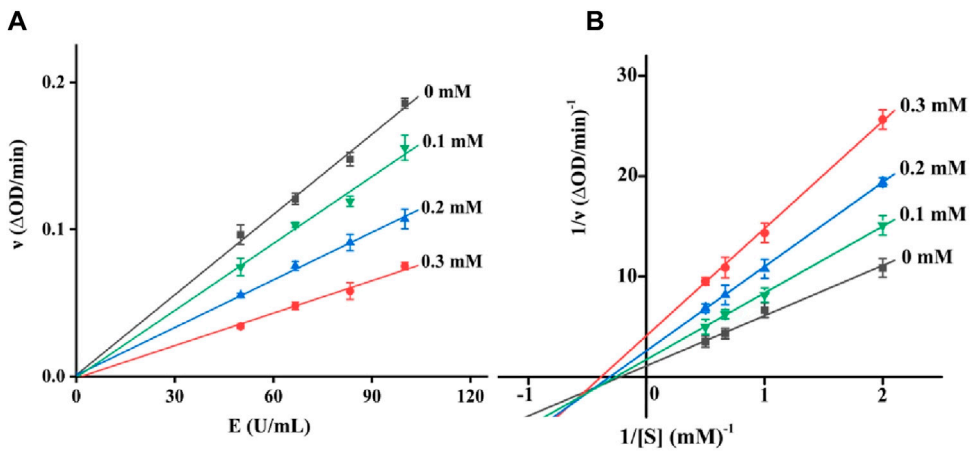


FIGURE 3
**(A)** Reversible assay of quercetagetin; **(B)** Lineweaver-Burk plots of quercetagetin.

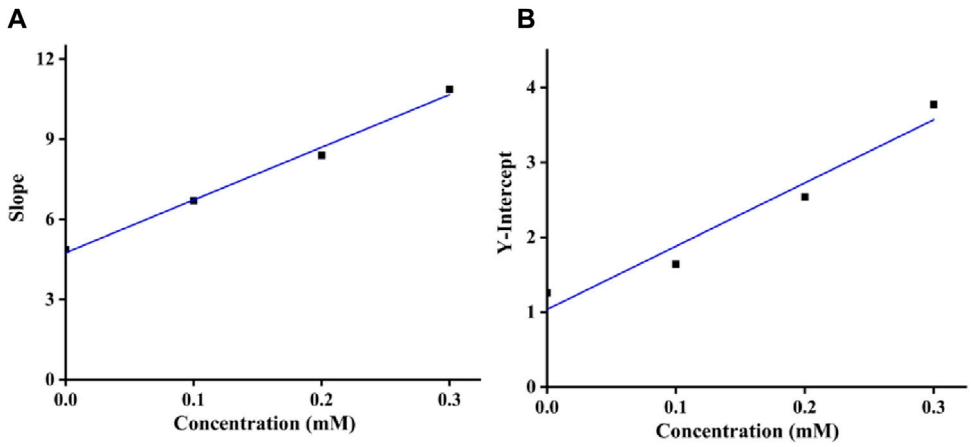


FIGURE 4
**(A)** $K_i$ assay of quercetagetin; **(B)** $K_{is}$ assay of quercetagetin.

298, and 305 K, respectively (Figures 5A–C). But, quercetagetin did not show effective fluorescence spectra. Moreover, when treated by quercetagetin, tyrosinase presented the gradually decreasing peak intensity (Figures 5A–C), which indicated that quercetagetin bound to tyrosinase.

The fluorescence quenching data at 295, 298, and 305 K were future analyzed by Stern-Volmer plots. As is shown in Figure 5D the Stern-Volmer plots of quercetagetin, lines with different temperature presented good linearity, meaning that there was only one quenching type of static or dynamic in quenching process. Then the quenching constant ($K_{sv}$) the bimolecular quench rate constant ($K_q$) were obtained (Table 1). The $K_{sv}$ results found that $K_{sv}$ values decreased with the temperature. And $K_q$ values at 295, 298, and 305 K were higher than $2 \times 10^{10}$ L mol$^{-1}$ S$^{-1}$. Above results suggested the quenching process of quercetagetin against tyrosinase was a static process. This quenching type presented in the quenching of indole derivatives on α-glucosidase (Hu et al., 2024). The quenching process also was the process of thermodynamic changes. Thence, the thermodynamic parameters were calculated (Table 1). The negative ΔG value unlocked one spontaneous process of quercetagetin binding to tyrosinase. The positive ΔH and ΔS values suggested hydrophobic interactions as the important forces between quercetagetin and tyrosinase.

## 2.4 CD spectra

The effect of quercetagetin on conformation change of tyrosinase was investigated using CD spectra. Figure 6 showed CD spectra of tyrosinase, the characteristic peaks around 210–220 nm stood for the peptide chains of tyrosinase. When treated with quercetagetin, the CD spectra of tyrosinase appeared some changes, meaning its conformation change. Then its secondary structure contents were calculated (Table 2) and found that quercetagetin treatment (molar ratio: 2:1) caused reduction of

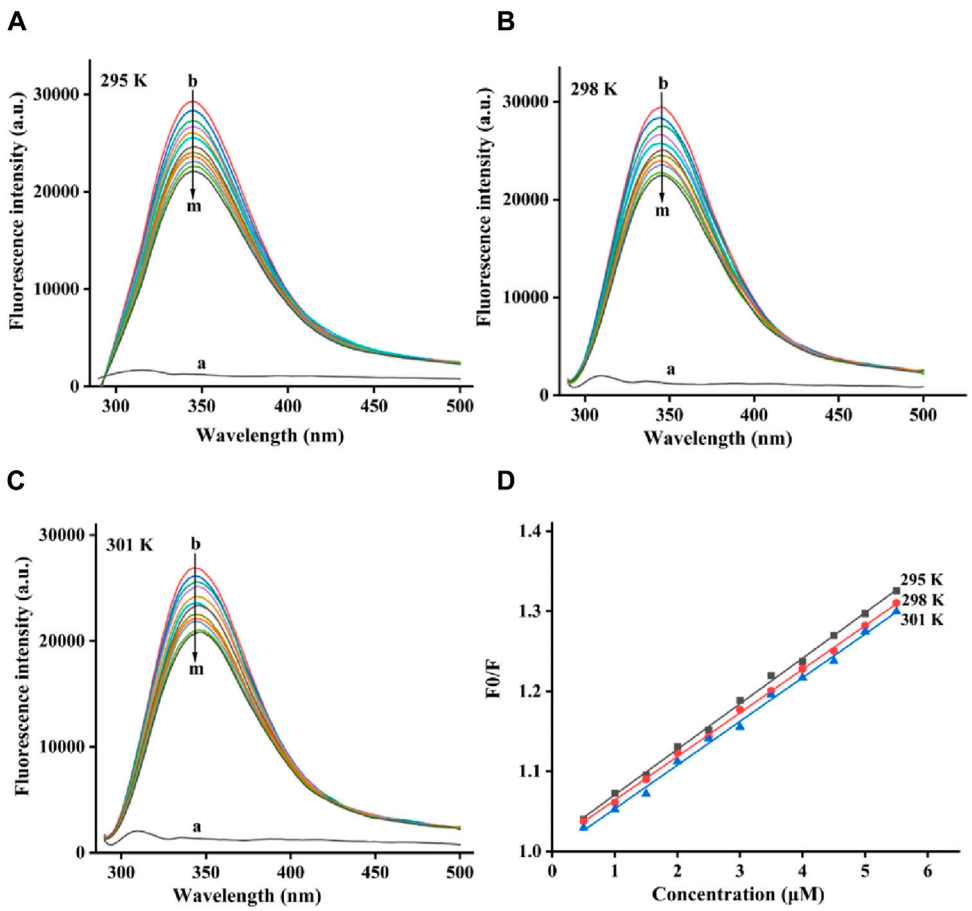


FIGURE 5
**(A–C)** Fluorescence quenching spectra of quercetagetin on tyrosinase at 295, 298, and 305 K, respectively; **(D)** Stern-Volmer plots of quercetagetin.

TABLE 1 Parameters of quercetagetin with tyrosinase.

| T (K) | $K_q$ (x$10^{12}$ $Lmol^{-1}S^{-1}$) | $K_{sv}$ (x$10^4 Lmol^{-1}$) | △H (KJ/moL) | △G (KJ/moL) | △S (J/(mol·K) |
|---|---|---|---|---|---|
| 295 | 5.69 | 5.69 | 25.34 | −23.27 | 164.78 |
| 298 | 5.45 | 5.45 | | −23.76 | |
| 301 | 5.40 | 5.40 | | −24.26 | |

α-helix and random coils and increase of β-sheet and β-turn. These results indicated that quercetagetin treatment could lead to conformation changes of tyrosinase.

## 2.5 3D fluorescence spectra

3D fluorescence spectra were monitored to further investigate the effect on conformation of tyrosinase by quercetagetin. As shown in Figure 7A the 3D fluorescence spectra tyrosinase, two characteristic peaks appeared, including Peak A for Tyr and Trp residues and Peak B for peptide backbone. When treated with quercetagetin, Peak A and Peak B were reduced the intensity by 35.4% and 13.3%, respectively (Figure 7B), which suggested that quercetagetin treatment would cause the changes of Tyr and Trp residues, and peptide backbone. That was to say that quercetagetin treatment would cause the conformation change of tyrosinase.

## 2.6 Molecular docking

The interaction of quercetagetin to tyrosinase was simulated by molecular docking method. As shown in Figure 8A the docking results, quercetagetin bound to the active pocket of tyrosinase with trihydroxychromone section in the active catalytic zone of active pocket. From Figure 8B the docking results in detail, it could be observed that quercetagetin made one hydrogen bond with His259 and hydrophobic interaction with Val248, His263, Val283, and Ala286. The results indicated that the interactions

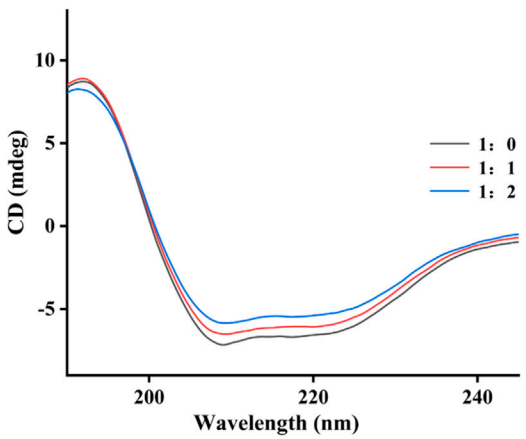


FIGURE 6
CD spectra of tyrosinase with quercetagetin.

between quercetagetin and tyrosinase resulted in the reduction of tyrosinase activity.

## 2.7 Copper-chelating activity

The copper-chelating activity of quercetagetin was finally assayed using copper sulfate. Figure 9A showed the quercetagetin-copper sulfate mixture. Quercetagetin showed its UV spectra with characteristic peak at 370 nm. While, after added copper sulfate, the UV characteristic peak of quercetagetin was gradually decreased. These results indicated that copper might complex with quercetagetin to change its UV characteristic peak. The peak intensity at different molar ratios of quercetagetin to copper sulfate was analyzed (Figure 9B) and found that the decreasing trend of quercetagetin peak intensity become equilibrium, meaning that the binding molar ratio of quercetagetin with copper sulfate was 1. The copper-chelating activity of quercetagetin also might be one reason of the reduction of tyrosinase activity.

# 3 Conclusion

Tyrosinase is one important rate limiting enzyme in melanin synthesis, directly affecting the melanin synthesis. Quercetagetin is one active ingredient from marigold. In this study, the inhibition effects of quercetagetin against tyrosinase were investigated. The results showed that quercetagetin could inhibit the tyrosinase activity with $IC_{50}$ value of 0.19 ± 0.01 mM and the inhibition type was a reversible mixed-type. Results of fluorescence quenching showed that quercetagetin could quench tyrosinase fluorescence in static process. CD and 3D fluorescence results showed interaction of quercetagetin to tyrosinase could change tyrosinase conformation to inhibit activity. Moreover, docking revealed details of quercetagetin's interactions with tyrosinase.

# 4 Materials and methods

## 4.1 Tyrosinase activity assay

Tyrosinase inhibitory activity of quercetagetin was measured (Lu et al., 2023b). 10 μL of quercetagetin in DMSO solutions was added into 140 μL of tyrosinase in PBS solution and incubated for

TABLE 2 The secondary structure contents of tyrosinase with quercetagetin.

| Molar ratio | α-Helix (%) | β-Sheet (%) | β-Turn (%) | Random coils (%) |
|---|---|---|---|---|
| 1:0 | 27.0 | 23.1 | 15.6 | 44.7 |
| 1:1 | 22.2 | 27.6 | 16.9 | 41.1 |
| 1:2 | 19.2 | 31.4 | 17.9 | 38.8 |

Note: Molar ratio means [tyrosinase]: [quercetagetin].

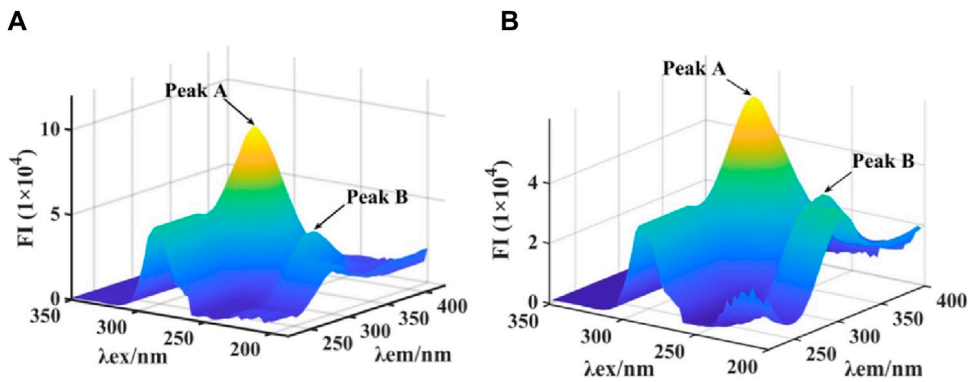


FIGURE 7
**(A,B)** 3D fluorescence of tyrosinase and quercetagetin-tyrosinase, respectively.

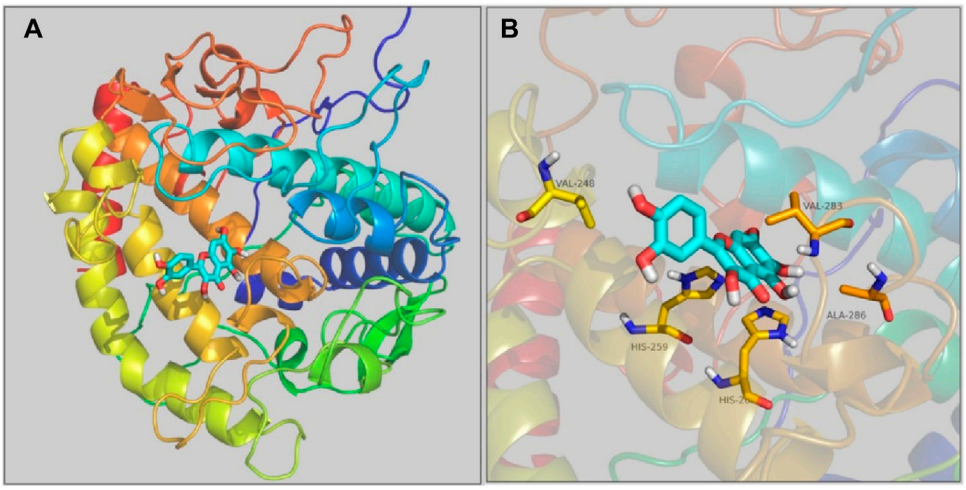


FIGURE 8
**(A,B)** The molecular docking of quercetagetin to tyrosinase.

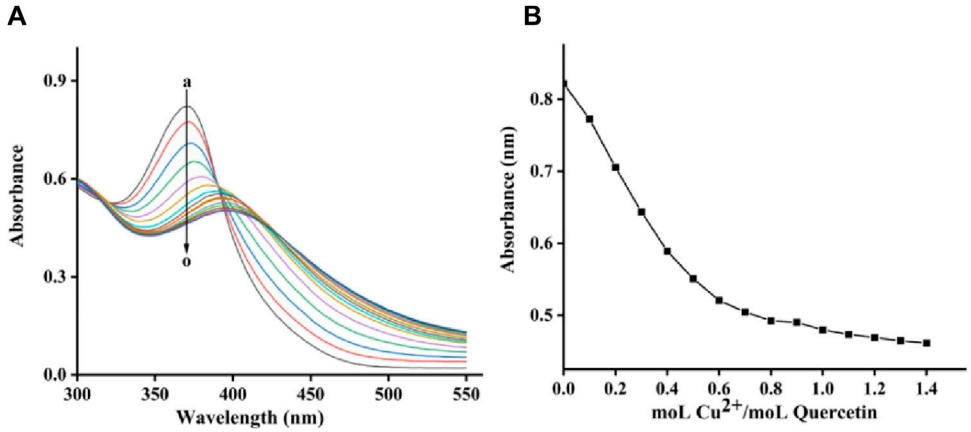


FIGURE 9
**(A)** UV spectra of quercetagetin-copper sulfate mixture; **(B)** UV peak of quercetagetin versus molar ratios of quercetagetin to copper sulfate.

10 min. 50 μL of L-dopa (in PBS) was added as the substrates. Then, the absorbance was measured at 475 nm on a microplate reader. Kojic acid was selected as the positive control. All experiments were tested in triplicate. Inhibition rate (%) = $[(OD_1\text{-}OD_0)/OD_0]\times100\%$. $OD_0$ and $OD_1$ were the absorbance of tyrosinase and tyrosinase-quercetagetin mixture.

## 4.2 Inhibitory kinetics

The reversibility of quercetagetin against tyrosinase was analyzed at different concentration of quercetagetin with tyrosinase or L-dopa. And the inhibitory kinetics of quercetagetin against tyrosinase was analyzed at different concentration of quercetagetin with tyrosinase or L-dopa. The inhibition constants $K_i$ and $K_{is}$ were obtained from the secondary curves of inhibitory kinetics (Xu et al., 2020; Deng et al., 2022; Lin et al., 2023).

## 4.3 Fluorescence quenching

To the 3.0 mL of tyrosinase solution, 1 μL of quercetagetin was added by titration method (Li et al., 2024a; Min et al., 2024). The mixture was measured fluorescence spectra at excitation of 280 nm. The experiments were conducted at temperatures of 295, 298, and 305 K, respectively. The Stern-Volmer equation and the van't Hoff equation were employed to obtained parameters.

## 4.4 CD spectra

To the 100 μL of tyrosinase solution, 1 μL of quercetagetin was added. CD spectra were measured at room temperature (Xiao et al., 2023; Li et al., 2024b). Tyrosinase solution without quercetagetin was also measured its CD spectra.

### 4.5 3D fluorescence spectra

To the 3.0 mL of tyrosinase solution, 1 μL of quercetagetin was added. 3D fluorescence spectra were measured (Wu X. et al., 2023).

### 4.6 Copper-chelating activity

To the 2 mL of quercetagetin solution, 5 μL of copper sulfate solution was gradually added. UV absorption spectra were detected. The molar ratios of quercetagetin to copper sulfate ranged from 10: 0 to 10: 14.

### 4.7 Molecular docking

Docking of quercetagetin with tyrosinase was simulated using the SYBYL software (Zhang et al., 2022; Feng et al., 2024). The tyrosinase crystal structure (PDB: 2Y9X) was optimized by removing water, adding hydrogen, and generation of active pocket. Quercetagetin structure was performed energy minimization. Thence, docking procedure was run in the default format.

## Data availability statement

The raw data supporting the conclusion of this article will be made available by the authors, without undue reservation.

## Author contributions

FL: Conceptualization, Investigation, Methodology, Project administration, Writing–original draft, Writing–review and editing.

## Funding

The author(s) declare that no financial support was received for the research, authorship, and/or publication of this article.

## Conflict of interest

The author declares that the research was conducted in the absence of any commercial or financial relationships that could be construed as a potential conflict of interest.

## Publisher's note

All claims expressed in this article are solely those of the authors and do not necessarily represent those of their affiliated organizations, or those of the publisher, the editors and the reviewers. Any product that may be evaluated in this article, or claim that may be made by its manufacturer, is not guaranteed or endorsed by the publisher.

## References

Broulier, R. I., Lazinski, L. M., Pérès, B., Olleik, H., Royal, G., Fishman, A., et al. (2023). Resorcinol-based hemiindigoid derivatives as human tyrosinase inhibitors and melanogenesis suppressors in human melanoma cells. *Eur. J. Med. Chem.* 246, 114972. doi:10.1016/j.ejmech.2022.114972

Bulut, O., and Yilmaz, M. D. (2021). Concise synthesis of quercetagetin (3,3',4',5,6,7-hexahydroxyflavone) with antioxidant and antibacterial activities. *Results Chem.* 3, 100255. doi:10.1016/j.rechem.2021.100255

Chen, J., Cao, D., Jiang, S., Liu, X., Pan, W., Cui, H., et al. (2022). Triterpenoid saponins from Ilex pubescens promote blood circulation in blood stasis syndrome by regulating sphingolipid metabolism and the PI3K/AKT/eNOS signaling pathway. *Phytomedicine* 104, 154242. doi:10.1016/j.phymed.2022.154242

Chen, Y., Yin, S., Liu, R., Yang, Y., Wu, Q., Lin, W., et al. (2023). β-Sitosterol activates autophagy to inhibit the development of hepatocellular carcinoma by regulating the complement C5a receptor 1/alpha fetoprotein axis. *Eur. J. Pharmacol.* 957, 175983. doi:10.1016/j.ejphar.2023.175983

De Barros, M. R., Menezes, T. M., Garcia, Y. S., and Neves, J. L. (2023). Inhibitory effects of iron-based carbonaceous nanocomposites on mushroom tyrosinase activity: molecular aspects and mechanistic insights. *New J. Chem.* 47, 9134–9142. doi:10.1039/d3nj00882g

Deng, X., Ke, J., Zheng, Y., Li, D., Zhang, K., Zheng, X., et al. (2022). Synthesis and bioactivities evaluation of oleanolic acid oxime ester derivatives as α-glucosidase and a-amylase inhibitors. *J. Enzyme Inhib.* 37, 451–461. doi:10.1080/14756366.2021.2018682

Djafarou, S., Mermer, A., Barut, B., Yılmaz, G. T., Khodja, I. A., and Boulebd, H. (2023). Synthesis and evaluation of the antioxidant and anti-tyrosinase activities of thiazolyl hydrazone derivatives and their application in the anti-browning of fresh-cut potato. *Food Chem.* 414, 135745. doi:10.1016/j.foodchem.2023.135745

Esma, A. T. K., Abd, E. H. K., Rabah, A., Djamila, B., Mohamed, S. B., Chawki, B., et al. (2023). *In vitro* assessment of antioxidant, neuroprotective, anti-urease and anti-tyrosinase capacities of Tamarix africana leaves extracts. *J. Tradit. Chin. Med.* 43, 252–264. doi:10.19852/j.cnki.jtcm.20230105.003

Fan, M., Zhang, G. W., Pan, J., and Gong, D. (2017). An inhibition mechanism of dihydromyricetin on tyrosinase and the joint effects of vitamins B6, D3 or E. *Food Funct.* 8, 2601–2610. doi:10.1039/c7fo00236j

Feng, M., Liang, B., Sun, J., Min, X., Wang, S., Lu, Y., et al. (2024). Synthesis, anti-α-glucosidase activity, inhibition interaction, and anti-diabetic activity of novel cryptolepine derivatives. *J. Mol. Struct.* 1310, 138311. doi:10.1016/j.molstruc.2024.138311

Fuentes, J., de Camargo, A. C., Atala, E., Gotteland, M., Olea-Azar, C., and Speisky, H. (2021). Quercetin oxidation metabolite present in onion peel protects caco-2 cells against the oxidative stress, NF-kB activation, and loss of epithelial barrier function induced by NSAIDs. *J. Agric. Food Chem.* 69, 2157–2167. doi:10.1021/acs.jafc.0c07085

Hassan, M., Shahzadi, S., and Kloczkowski, A. (2023). Tyrosinase inhibitors naturally present in plants and synthetic modifications of these natural products as anti-melanogenic agents: a review. *Molecules* 28, 378. doi:10.3390/molecules28010378

Hu, C., Liang, B., Sun, J., Li, J., Xiong, Z., Wang, S., et al. (2024). Synthesis and biological evaluation of indole derivatives containing thiazolidine-2,4-dione as α-glucosidase inhibitors with antidiabetic activity. *Eur. J. Med. Chem.* 264, 115957. doi:10.1016/j.ejmech.2023.115957

Iraji, A., Sheikhi, N., Attarroshan, M., Ardani, G. R. S., Kabiri, M., Bafghi, A. N., et al. (2022). Design, synthesis, spectroscopic characterization, *in vitro* tyrosinase inhibition, antioxidant evaluation, *in silico* and kinetic studies of substituted indole-carbohydrazides. *Bioorg. Chem.* 129, 106140–140. doi:10.1016/j.bioorg.2022.106140

Jiang, T., Ji, C., Cheng, X., Gu, S., Wang, R., Li, Y., et al. (2021). α-Mangostin alleviated HIF-1α-mediated angiogenesis in rats with adjuvant-induced arthritis by suppressing aerobic glycolysis. *Front. Pharmacol.* 12, 785586. doi:10.3389/fphar.2021.785586

Lee, J., Park, Y. J., Jung, H. J., Ullah, S., Yoon, D., Jeong, Y., et al. (2023). Design and synthesis of (Z)-2-(benzylamino)-5-benzylidenethiazol-4(5H)-one derivatives as tyrosinase inhibitors and their anti-melanogenic and antioxidant effects. *Molecules* 28, 848. doi:10.3390/molecules28020848

Li, J., Feng, L., Liu, L., Wang, F., Ouyang, L., Zhang, L., et al. (2021a). Recent advances in the design and discovery of synthetic tyrosinase inhibitors. *Eur. J. Med. Chem.* 224, 113744. doi:10.1016/j.ejmech.2021.113744

Li, J., Min, X., Zheng, X., Wang, S., Xu, X., and Peng, J. (2023). Synthesis, anti-tyrosinase activity, and spectroscopic inhibition mechanism of cinnamic acid-eugenol esters. *Molecules* 28, 5969. doi:10.3390/molecules28165969

Li, M., Li, H., Min, X., Sun, J., Liang, B., Xu, L., et al. (2024a). Identification of 1,3,4-thiadiazolyl-containing thiazolidine-2,4-dione derivatives as novel PTP1B inhibitors with anti-diabetic activity. *J. Med. Chem.* doi:10.1021/acs.jmedchem.4c00676

Li, M., Sun, J., Liang, B., Min, X., Hu, J., Wu, R., et al. (2024b). Thiazolidine-2,4-dione derivatives as potential α-glucosidase inhibitors: synthesis, inhibitory activity, binding

interaction and hypoglycemic activity. *Bioorg. Chem.* 144, 107177. doi:10.1016/j.bioorg.2024.107177

Li, Y., Dai, M., Wang, L., and Wang, G. (2021b). Polysaccharides and glycosides from Aralia echinocaulis protect rats from arthritis by modulating the gut microbiota composition. *J. Ethnopharmacol.* 269, 113749. doi:10.1016/j.jep.2020.113749

Lin, J., Xiao, D., Lu, L., Liang, B., Xiong, Z., and Xu, X. (2023). New β-carboline derivatives as potential α-glucosidase inhibitor: synthesis and biological activity evaluation. *J. Mol. Struct.* 1283, 135279. doi:10.1016/j.molstruc.2023.135279

Liu, J., Zhao, X., Qin, F., Zhou, J., Ding, F., Zhou, G., et al. (2022). Isoliquiritigenin mitigates oxidative damage after subarachnoid hemorrhage *in vivo* and *in vitro* by regulating Nrf2-dependent Signaling Pathway via Targeting of SIRT1. *Phytomedicine* 105, 154262. doi:10.1016/j.phymed.2022.154262

Lu, L., Hu, C., Min, X., Liu, Z., Xu, X., and Gan, L. (2023a). *In vitro* and *in vivo* biological evaluation of indole-thiazolidine-2,4-dione derivatives as tyrosinase inhibitors. *Molecules* 28, 7470. doi:10.3390/molecules28227470

Lu, L., Zhang, X., Kang, Y., Xiong, Z., Zhang, K., Xu, X., et al. (2023b). Novel coumarin derivatives as potential tyrosinase inhibitors: synthesis, binding analysis and biological evaluation. *Arab. J. Chem.* 16, 104724. doi:10.1016/j.arabjc.2023.104724

Ma, M., Wei, N., Yang, J., Ding, T., Song, A., Chen, L., et al. (2023). Schisandrin B promotes senescence of activated hepatic stellate cell *via* NCOA4-mediated ferritinophagy. *Pharm. Biol.* 61, 621–629. doi:10.1080/13880209.2023.2189908

Min, X., Guo, S., Lu, Y., and Xu, X. (2024). Investigation on the inhibition mechanism and binding behavior of cryptolepine to α-glucosidase and its hypoglycemic activity by multi-spectroscopic method. *J. Lumin.* 269, 120437. doi:10.1016/j.jlumin.2024.120437

Min, X., Lu, L., Xu, X. T., Wen, Y., and Zheng, X. (2023). Investigation on the inhibition mechanism and binding behavior of paeonol to tyrosinase and its anti-browning property by multi-spectroscopic and molecular docking methods. *Int. J. Biol. Macromol.* 253, 126962. doi:10.1016/j.ijbiomac.2023.126962

Nasab, N., Raza, H., Eom, Y., Hassan, M., Kloczkowski, A., and Kim, S. (2023). Synthesis and discovery of potential tyrosinase inhibitor of new coumarin-based thiophenyl-pyrazolylthiazole nuclei: in-vitro evaluation, cytotoxicity, kinetic and computational studies. *Chem. Biol. Drug. Des.* 101, 13–88. doi:10.1111/cbdd.14209

Pei, Y. Q., Zheng, Y. Q., Ding, Y. D., Xu, Q. X., Cao, D., Wu, Y. N., et al. (2021). Triptolide attenuates vascular calcification by upregulating expression of miRNA-204. *Front. Pharmacol.* 11, 581230. doi:10.3389/fphar.2020.581230

Qi, X., Zheng, S., Ma, M., Lian, N., Wang, H., Chen, L., et al. (2022). Curcumol suppresses CCF-mediated hepatocyte senescence through blocking LC3B-Lamin B1 interaction in alcoholic fatty liver disease. *Front. Pharmacol.* 13, 912825. doi:10.3389/fphar.2022.912825

Romagnoli, R., Oliva, P., Prencipe, F., Manfredini, S., Germanò, M., De Luca, L., et al. (2022). Cinnamic acid derivatives linked to arylpiperazines as novel potent inhibitors of tyrosinase activity and melanin synthesis. *Eur. J. Med. Chem.* 231, 114147. doi:10.1016/j.ejmech.2022.114147

Rufino, A. T., Ramalho, A., Sousa, A., de Oliveira, J. M. P. F., Freitas, P., Gómez, M. A. G., et al. (2021). Protective role of flavonoids against intestinal pro-inflammatory effects of silver nanoparticles. *Molecules* 26, 6610. doi:10.3390/molecules26216610

Seyedi, S. S., Shukri, M., Hassandarvish, P., Oo, A., Shankar, E. M., Abubakar, S., et al. (2016). Computational approach towards exploring potential anti-chikungunya activity of selected flavonoids. *Sci. Rep.* 6, 24027. doi:10.1038/srep24027

Shao, X., Li, B., Shen, J., Wang, Q., Chen, S., Jiang, X., et al. (2020). Ghrelin alleviates traumatic brain injury-induced acute lung injury through pyroptosis/NF-κB pathway. *Int. Immunopharmacol.* 79, 106175. doi:10.1016/j.intimp.2019.106175

Shi, L., Jiang, C., Xu, H., Wu, J., Lu, J., He, Y., et al. (2023). Hyperoside ameliorates cerebral ischaemic–reperfusion injury by opening the TRPV4 channel *in vivo* through the IP 3-PKC signalling pathway. *Pharm. Biol.* 61, 1000–1012. doi:10.1080/13880209.2023.2228379

Song, A., Ding, T., Wei, N., Yang, J., Ma, M., Zheng, S., et al. (2023). Schisandrin B induces HepG2 cells pyroptosis by activating NK cells mediated anti-tumor immunity. *Toxicol. Appl. Pharmacol.* 472, 116574. doi:10.1016/j.taap.2023.116574

Tang, Z., Zhang, M., Gao, L., Bao, Y., Li, P., Wang, M., et al. (2023). Optimal extraction of polysaccharides from Stevia rebaudiana roots for protection against hydrogen peroxide-induced oxidative damage in RAW264.7 cells. *Nat. Prod. Res.* 2023, 2263905. doi:10.1080/14786419.2023.2263905

Tao, Z. S., Li, T. L., and Wei, S. (2022). Silymarin prevents iron overload induced bone loss by inhibiting oxidative stress in an ovariectomized animal model. *Chem. Biol. Interact.* 366, 110168. doi:10.1016/j.cbi.2022.110168

Wang, D., Li, Y., Wu, Y., Wu, Y., Han, J., Olatunji, O., et al. (2021). Xanthones from Securidaca inappendiculata antagonized the antirheumatic effects of methotrexate *in vivo* by promoting its secretion into urine. *Expert Opin. Drug Metab. toxico.* 17, 241–250. doi:10.1080/17425255.2021.1843634

Wang, L., Wang, P., Wang, D., Tao, M., Xu, W., and Olatunji, O. J. (2020). Anti-inflammatory activities of kukoamine A from the root bark of lycium chinense miller. *Nat. Prod. Commun.* 15, 1934578X2091208. doi:10.1177/1934578x20912088

Wang, R., and Mu, J. (2021). Arbutin attenuates ethanol-induced acute hepatic injury by the modulation of oxidative stress and Nrf-2/HO-1 signaling pathway. *J. Biochem. Mol. Toxicol.* 35, 22872. doi:10.1002/jbt.22872

Wang, X., Zhou, D., Zhou, W., Liu, J., Xue, Q., Huang, Y., et al. (2022a). Clematichinenoside AR inhibits the pathology of rheumatoid arthritis by blocking the circPTN/miR-145-5p/FZD4 signal axis. *Int. Immunopharm.* 113, 109376. doi:10.1016/j.intimp.2022.109376

Wang, Y., Wu, H., Han, Z., Sheng, H., Wu, Y., Wang, Y., et al. (2022b). Guhong injection promotes post-stroke functional recovery via attenuating cortical inflammation and apoptosis in subacute stage of ischemic stroke. *Phytomedicine* 99, 154034. doi:10.1016/j.phymed.2022.154034

Wu, F., Wang, F., Tang, Z., Yang, X., Liu, Y., Zhao, M., et al. (2023a). Quercetagetin alleviates zearalenone-induced liver injury in rabbits through Keap1/Nrf2/ARE signaling pathway. *Front. Pharmacol.* 14, 1271384. doi:10.3389/fphar.2023.1271384

Wu, F., Wang, H., Li, S., Wei, Z., Han, S., and Chen, B. (2022). Effects of dietary supplementation with quercetagetin on nutrient digestibility, intestinal morphology, immunity, and antioxidant capacity of broilers. *Front. Vet. Sci.* 9, 1060140. doi:10.3389/fvets.2022.1060140

Wu, X., Zhu, W., Lu, L., Hu, C., Zheng, Y., Zhang, X., et al. (2023b). Synthesis and anti-α-glucosidase activity evaluation of betulinic acid derivatives. *Arab. J. Chem.* 16, 104659. doi:10.1016/j.arabjc.2023.104659

Wu, Z., Liang, D., Xu, M., Liu, Y., and Xie, H. (2021). A comparative pharmacokinetic study of schisandrol B after oral administration of schisandrol b monomer and schisandra chinensis extract. *Curr. Pharm. Anal.* 17, 273–284. doi:10.2174/1573412916666191114122101

Xiao, D., Lu, L., Liang, B., Xiong, Z., Xu, X., and Chen, W. (2023). Identification of 1,3,4-oxadiazolyl-containing β-carboline derivatives as novel α-glucosidase inhibitors with antidiabetic activity. *Eur. J. Med. Chem.* 261, 115795. doi:10.1016/j.ejmech.2023.115795

Xu, X., Deng, X., Chen, J., Liang, Q., Zhang, K., Li, D., et al. (2020). Synthesis and biological evaluation of coumarin derivatives as aglucosidase Inhibitors. *Eur. J. Med. Chem.* 112, 112013. doi:10.1016/j.ejmech.2019.112013

Xue, S., Li, Z., Ze, X., Wu, X., He, C., Shuai, W., et al. (2023). Design, synthesis, and biological evaluation of novel hybrids containing dihydrochalcone as tyrosinase inhibitors to treat skin hyperpigmentation. *J. Med. Chem.* 66, 5099–5117. doi:10.1021/acs.jmedchem.3c00012

Zang, L., Xu, H., Huanh, C., Wang, C., Wang, R., Chen, R., et al. (2022). A link between chemical structure and biological activity in triterpenoids. *Recent Pat. Anti-Canc* 17, 145–161. doi:10.2174/1574892816666210512031635

Zargaham, M. K., Ahmed, M., Akhtar, N., Ashraf, Z., Abdel-Maksoud, M. A., Aufy, M., et al. (2023). Synthesis, *in silico* studies, and antioxidant and tyrosinase inhibitory potential of 2-(substituted phenyl) thiazolidine-4-carboxamide derivatives. *Pharmaceuticals* 16, 835. doi:10.3390/ph16060835

Zhang, X., Lu, Y., Li, W., Tao, T., Peng, L., Wang, W., et al. (2021a). Astaxanthin ameliorates oxidative stress and neuronal apoptosis via SIRT1/NRF2/Prx2/ASK1/p38 after traumatic brain injury in mice. *Brit. J. Pharmacol.* 178, 1114–1132. doi:10.1111/bph.15346

Zhang, X., Peng, L., Zhang, J., Dong, Y. P., Wang, C. J., Liu, C., et al. (2020). Berberine ameliorates subarachnoid hemorrhage injury via induction of sirtuin 1 and inhibiting HMGB1/Nf-κB pathway. *Front. Pharmacol.* 11, 1073. doi:10.3389/fphar.2020.01073

Zhang, X., Zheng, Y., Hu, C., Wu, X., Lin, J., Xiong, Z., et al. (2022). Synthesis and biological evaluation of coumarin derivatives containing oxime ester as α-glucosidase inhibitors. *Arab. J. Chem.* 15, 104072. doi:10.1016/j.arabjc.2022.104072

Zhang, Y., Zhang, X., Li, H. J., Zhou, T. F., Zhou, A. C., Zhong, Z. L., et al. (2021b). Antidepressant-like effects of helicid on a chronic unpredictable mild stress-induced depression rat model: inhibiting the IKK/IκBα/NF-κB pathway through NCALD to reduce inflammation. *Int. Immunopharm.* 93, 107165. doi:10.1016/j.intimp.2020.107165

Zhou, S., Sun, Y., Xing, Y., Wang, Z., Wan, S., Yao, X., et al. (2022a). Exenatide ameliorates hydrogen peroxide-induced pancreatic β-cell apoptosis through regulation of METTL3-mediated m6A methylation. *Eur. J. Pharmacol.* 924, 174960. doi:10.1016/j.ejphar.2022.174960

Zhou, Y., Xiang, R., Qin, G., Ji, B., Yang, S., Wang, G., et al. (2022b). Xanthones from *Securidaca inappendiculata Hassk.* attenuate collagen-induced arthritis in rats by inhibiting the nicotinamide phosphoribosyltransferase/glycolysis pathway and macrophage polarization. *Int. Immunopharm.* 111, 109137. doi:10.1016/j.intimp.2022.109137

Znajafi, E. A., Chehardoli, G., Ziaei, M., Akbarzadeh, T., Saeedi, M., Gholamhoseini, P., et al. (2023). Design, synthesis, *in vitro*, and *in silico* studies of novel benzylidene 6-methoxy-1-tetralone linked to benzyloxy and benzyl-1, 2, 3-triazole rings as potential tyrosinase inhibitors. *J. Mol. Struct.* 1271, 134018. doi:10.1016/j.molstruc.2022.134018

frontiers | Frontiers in Pharmacology

TYPE Original Research
PUBLISHED 05 June 2024
DOI 10.3389/fphar.2024.1411230

Check for updates

OPEN ACCESS

EDITED BY
Xi Zheng,
Rutgers, The State University of New Jersey, United States

REVIEWED BY
Yiqiang Zhang,
University of Hawaii at Manoa, United States
Sofia Viana,
University of Coimbra, Portugal
Xiaoli Tang,
Brown University, United States

*CORRESPONDENCE
Donghui Xu,
donghuixu007@163.com,
lssxdh@mail.sysu.edu.cn

†These authors have contributed equally to this work

RECEIVED 02 April 2024
ACCEPTED 13 May 2024
PUBLISHED 05 June 2024

CITATION
Sun W, Mei X, Wang J, Mai Z and Xu D (2024), Zn(II)–curcumin prevents cadmium-aggravated diabetic nephropathy by regulating gut microbiota and zinc homeostasis. *Front. Pharmacol.* 15:1411230. doi: 10.3389/fphar.2024.1411230

COPYRIGHT
© 2024 Sun, Mei, Wang, Mai and Xu. This is an open-access article distributed under the terms of the Creative Commons Attribution License (CC BY). The use, distribution or reproduction in other forums is permitted, provided the original author(s) and the copyright owner(s) are credited and that the original publication in this journal is cited, in accordance with accepted academic practice. No use, distribution or reproduction is permitted which does not comply with these terms.

# Zn(II)–curcumin prevents cadmium-aggravated diabetic nephropathy by regulating gut microbiota and zinc homeostasis

Wenjia Sun[1†], Xueting Mei[2†], Jiasheng Wang[1], Zhicong Mai[1] and Donghui Xu[1*]

[1]Laboratory of Traditional Chinese Medicine and Marine Drugs, Institute of Aquatic Economic Animals and Guangdong Provincial Key Laboratory for Aquatic Economic Animals, School of Life Sciences, Sun Yat-sen University, Guangzhou, China, [2]Laboratory Animal Center, Sun Yat-sen University, Guangzhou, China

**Background:** Diabetic nephropathy (DN) is known as the most common complication of diabetes, resulting from a complex inheritance-environment interaction without effective clinical treatments. Herein, we revealed the protective effects and mechanisms of Zn(II)-curcumin, a curcumin derivative, against streptozotocin-induced DN in rats in the presence or absence of cadmium exposure.

**Methods:** The present study focused on investigating the therapy of Zn(II)-curcumin against cadmium-aggravated DN by regulating gut microbiota, metabolism, inflammation and zinc homeostasis based on pathological changes, TLR4/NF-κB signaling pathway, inductively coupled plasma-mass spectrometry (ICP-MS), 16S rRNA gene sequencing and gas chromatography-mass spectrometer (GC-MS).

**Results:** We found Zn(II)-curcumin significantly mitigated the cadmium-aggravated phenotypes of diabetic nephropathy, as indicated by the remission of renal dysfunction, pathological changes, inflammation and zinc dyshomeostasis in streptozotocin-treated rats exposed to cadmium. Administration of Zn(II)-curcumin significantly alleviated the dysbiosis of gut microbiota and the changes of serum metabolite profiles in rats treated with streptozotocin in combination with cadmium. Notably, fecal microbial transplantation identified the ability of Zn(II)-curcumin to regulate renal function, inflammation and zinc homeostasis was partly dependent on the gut microbiota.

**Conclusion:** These findings revealed that Zn(II)-curcumin alleviated cadmium-aggravated diabetic nephropathy by reshaping the gut microbiota and zinc homeostasis, which provided unique insights into the mechanisms of the treatment and prevention of diabetic nephropathy.

KEYWORDS

**cadmium, diabetic nephropathy, Zn(II)–curcumin, gut microbiota, zinc homeostasis, metabolism**

**Abbreviations:** BUN, blood urea nitrogen; Cd, cadmium; CM, curcumin; DN, diabetic nephropathy; FMT, fecal microbiota transplantation; Met, metformin; NF-κB p65, nuclear factor-κB p65; PVP-30, polyvinylpyrrolidone K30; SD, standard deviation; STZ, streptozotocin; Scr, serum creatinine; TLR4, toll-like receptor 4; ZIP14, Zrt, Irt-related protein 14; Zn, zinc; ZnCM, Zn(II)–curcumin.

# 1 Introduction

Diabetic nephropathy is a major complication of diabetes with the incidence of approximately 30%–47% in all diabetic patients and represents a major cause of the increased risks of developing renal failure, cardiovascular events, and death (Jiang et al., 2020; Defronzo et al., 2021; Xing et al., 2021). Structural changes in diabetic nephropathy in type 1 and type 2 diabetes are mainly in the glomerulus with mesangial expansion and thickening of the glomerular basement membrane (GBM), and they also include arteriolar, tubular, and interstitial lesions (Navarro-Gonzalez et al., 2011). Diabetic nephropathy is characterized by hyperglycemia, hyperlipidemia, and progressive deterioration of renal function, which are the main phenotype bases for the clinical treatment (Song et al., 2022). Currently, clinical strategies to alleviate the progression of diabetic nephropathy are limited. The treatment options such as angiotensin II receptor blockers (ARB), sodium–glucose cotransporter-2 (SGLT-2) inhibitors, and angiotensin-converting enzyme (ACE) inhibitors have received much attention for their anti-inflammatory and cardio-protective activities, but their risks and benefits need to be clarified (Fineberg et al., 2013; Hu et al., 2020; Huang et al., 2022; He et al., 2023; Shen et al., 2023). The development and progression of diabetic nephropathy involve multiple factors, including inheritance and environment, resulting in the underlying pathogenesis that is still not fully understood. Thus, it is very necessary to further discover the mechanisms and develop new drugs for the treatment of diabetic nephropathy.

Gut dysbiosis has been identified as an important cause of the development of diabetes and its complications (Fan and Pedersen, 2021). The disturbance in intestinal microbiota increases the leakage of pro-inflammatory bacterial products into the circulation (Cao et al., 2021a; Cao et al., 2021b). These harmful substances can cause insulin resistance and accelerate the progression of diabetes and its complications in patients. For instance, Gram-negative bacteria-produced endotoxin lipopolysaccharides (LPS) and peptidoglycans can stimulate the toll-like receptor 4 (TLR4)- and NF-κB-involved inflammatory response, leading to systemic and renal inflammation, which further worsen kidney dysfunction (Sun et al., 2020a; Yang et al., 2020; Zhou et al., 2023). The dsybiosis of the gut microbiota can be sensitively caused by western diet and environmental factors (Amato et al., 2015). For example, cadmium (Cd) exposure has been found to induce a remarkable alteration in the microbial community structure and composition, along with the activation of intestinal inflammatory response and intestinal barrier disruption (Tinkov et al., 2018). Furthermore, an environmental dose of Cd at early stages of life induces the alterations in gut microbiota, which accelerates hepatic lipid accumulation and results in lifelong metabolic syndrome, such as fat accumulation and hyperglycemia (Ba et al., 2017). Notably, Cd exposure has been positively linked to increased diabetes risk in several previous studies (Xing et al., 2018; He et al., 2024). However, the potential pathogenic mechanism of Cd exposure affecting diabetic nephropathy is still unclear, which prevents the development of new drugs for the prevention and treatment of diabetic nephropathy.

Plant-derived natural products and their derivatives represent effective potential treatment for type 2 diabetes and related metabolic diseases in the past decades (Qi et al., 2022; Wu et al., 2023; Hu et al., 2024). Curcumin, a natural small-molecule compound, is extracted from *Curcuma longa* Linn. (turmeric) and used as an anti-diabetic, anti-inflammatory, anticancer, and anti-aging agent in preclinical and clinical trials (Kotha and Luthria, 2019; Ghosh et al., 2015). However, the therapeutic usage of curcumin is limited due to the poor aqueous solubility and bioavailability (Prasad and Lall, 2022). To address these disadvantages, several curcumin formulations, including curcumin–metal complexes and solid dispersion, have been developed in our previous studies. Zn(II)–curcumin (ZnCM) not only exerts stronger anti-cancer, anti-cardiotoxic, and anti-diabetic effects than curcumin alone but also significantly attenuates gut dysbiosis and zinc dyshomeostasis in animals (Wu et al., 2019a; Wu et al., 2019b). Therefore, we hypothesize that oral consumption of ZnCM could alleviate the dysregulation of the gut microbiota and prevent the development of diabetic nephropathy.

In the present study, we first assessed the impact of Cd exposure on streptozotocin (STZ)-induced diabetic nephropathy by determining the renal function, inflammation, and zinc homeostasis in rats. Next, the efficacy of ZnCM on Cd-aggravated diabetic nephropathy was evaluated in STZ-treated rats. 16S rRNA gene sequences and gas chromatography–mass spectrometry (GC-MS) were performed to analyze the gut microbiota composition and serum metabolite profiling, respectively. The role of gut microbiota in the mitigation of ZnCM on diabetic nephropathy was confirmed by fecal microbiota transplantation.

# 2 Methods

## 2.1 Materials and chemicals

Zn(II)–curcumin (ZnCM) was synthesized from curcumin (Guangdong Zhongda Greenfield Biotech. Co., Guangzhou, China) and zinc acetate, and prepared as solid dispersion using PVP-30 (BASF Chemical Ltd., Atlantic City, NJ, United States), according to our previous descriptions (the mass ratio for ZnCM: PVP-30 = 1 : 6) (Mei et al., 2011). Streptozotocin (STZ; S0130) was purchased from Sigma-Aldrich Corporation (Sigma-Aldrich, St. Louis, MaO, United States). Other reagents were of analytical grade and were purchased from local chemical suppliers.

## 2.2 Animal experimental design

All animal experiments were approved by the Experimental Animal Care and Use Committee of Sun Yat-sen University (number IACUC-20221030002) and strictly conducted in line with the Guidelines for Care and Use of Laboratory Animals of this organization. Healthy adult female Sprague–Dawley rats (body weight 240–260 g) were provided by the Laboratory Animal Center of Sun Yat-sen University. They were housed under specific pathogen-free standard conditions with a 12-h light/dark cycle and free access to diet and water. After acclimation for 1 week, animals were treated in the presence or absence of 1 mg/kg $CdCl_2$ in drinking water in the initial 8 weeks, subsequently, treated with or without a single intraperitoneal injection of STZ (60 mg/kg) (Xu et al., 2020), and orally administered with or without 100 mg/kg/d ZnCM, 700 mg/kg/d PVP, or 135 mg/kg/d Met (metformin, positive drug) for 8 weeks ($n$ = 8 per group). The schematic diagram of the experimental design is shown in Figure 1A. The animals were

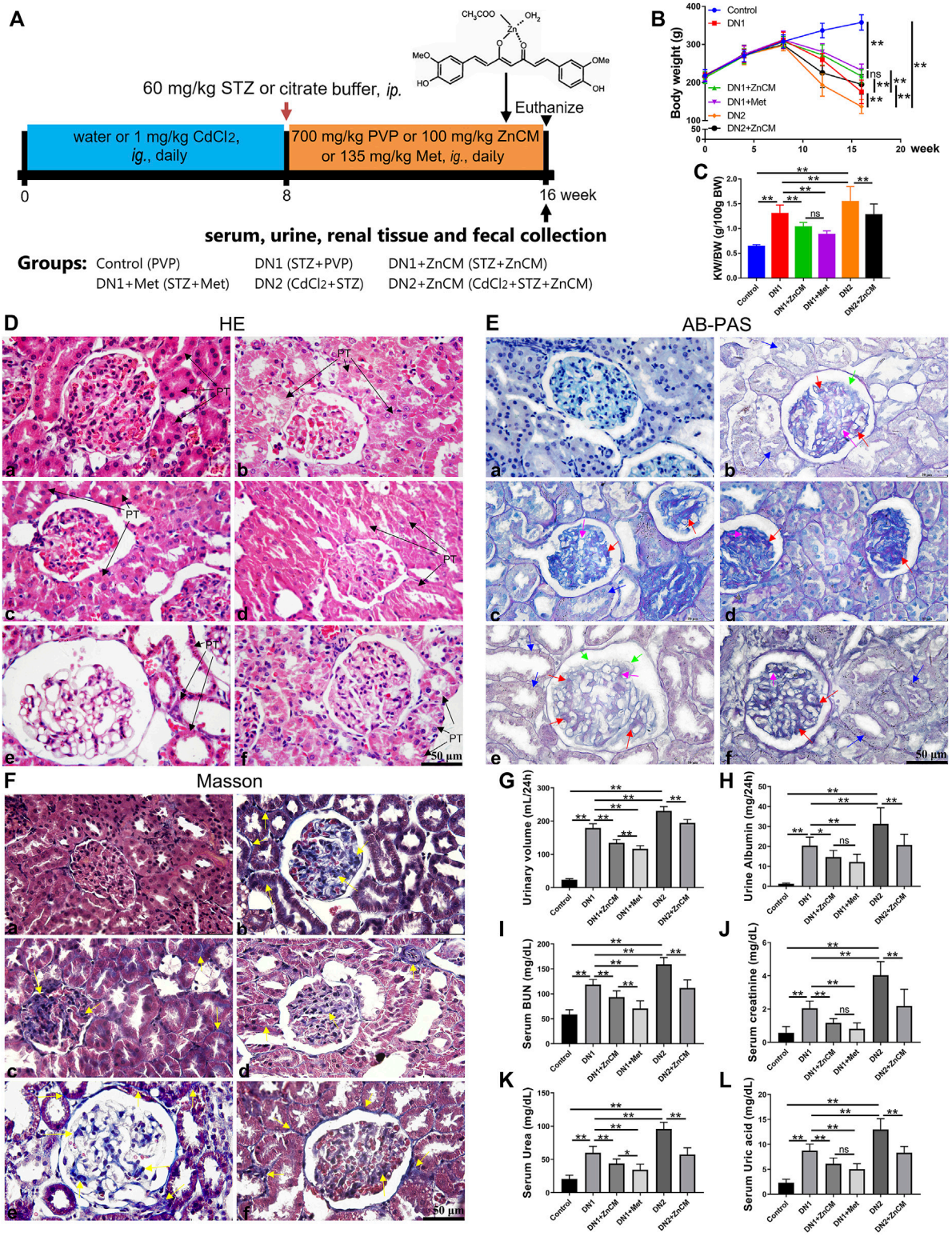


FIGURE 1
ZnCM attenuated renal pathological deterioration and dysfunction in STZ-induced rats exposed to Cd. **(A)** Schematic diagram of the experimental design. **(B)** Body weight throughout the experiment. **(C)** The ratio of kidney weight to body weight (KW/BW). **(D–F)** Representative images of H&E staining, AB-PAS staining, and Masson's trichrome staining of the kidney (scale bar, 50 μm). PT: proximal tubule; proximal tubule epithelial cell edema and hypertrophy (black arrowheads); tubular epithelial damage (blue arrowheads); thickening of the glomerular basement membrane (light purple arrowheads); mesangial regions proliferative and expansion (red arrowheads); podocyte apoptosis and necrosis (green arrowheads); fibroblasts proliferation (yellow arrowheads). **(G, H)** Levels of urinary volume and albumin of 24 h. **(I)** Levels of blood urea nitrogen (BUN). **(J–L)** Levels of creatinine, urea, and uric acid in the serum. Data are represented by mean ± SD ($n$ = 8) and were analyzed by one-way ANOVA followed by the original FDR method of the Benjamini and Hochberg test. *$p$ < 0.05 and **$p$ < 0.01; ns indicates no significance.

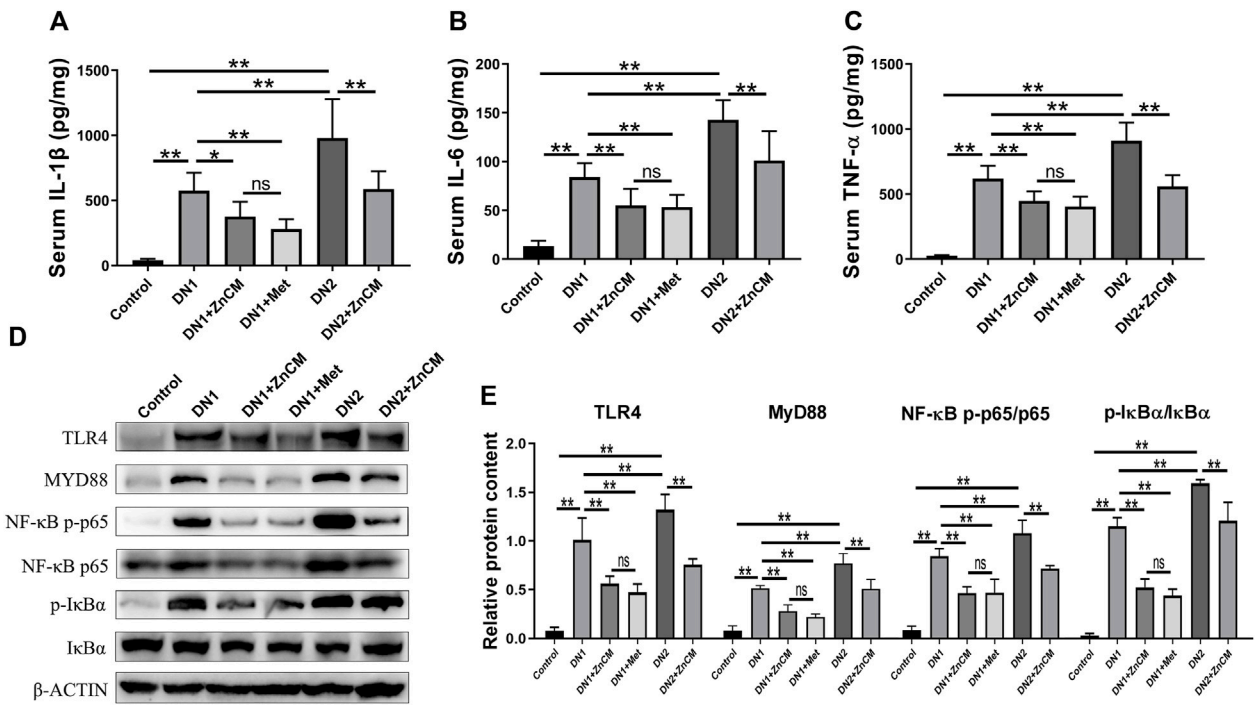


FIGURE 2
ZnCM relieved the inflammation in Cd-exposed rats with diabetic nephropathy. **(A–C)** The concentrations of IL-1β, IL-6, and TNF-α in the serum determined by ELISA ($n$ = 8). **(D)** Representative blots of renal TLR4, MYD88, NF-κB p-p65, NF-κB p65, p-IκBα, and IκBα. **(E)** Relative expressions of TLR4, MYD88, NF-κB p-p65, NF-κB p65, p-IκBα, and IκBα quantified from (d) ($n$ = 3). Data are represented by mean ± SD and analyzed by one-way ANOVA followed by the original FDR method of the Benjamini and Hochberg test. *$p$ < 0.05 and **$p$ < 0.01; ns indicates no significance.

weighed weekly in the course of the experiments. In addition, the stool samples were collected at week 16 for gene analysis. At the end of the experiment, rats were fasted for approximately 12 h and humanely euthanized by the administration of $CO_2$. Afterward, serum, urine, and kidney samples were collected for biochemical, histopathological, and metabolic analyses, respectively.

## 2.3 Fecal microbiota transplantation (FMT)

Recipient rats were pretreated with a cocktail of antibiotics (ABX containing 1 g/L ampicillin, 0.5 g/L neomycin, 0.5 g/L vancomycin, and 1 g/L metronidazole) in drinking water for 1 week. Fresh feces from donor rats were daily collected, pooled (100 mg feces/mL), and vigorously mixed for 30 s, and then centrifuged at 800 g for 3 min. A measure of 100 μL of fecal supernatants of each rat was orally transferred to STZ-treated recipient rats once a day for 8 weeks. Kidney, blood, and urine samples from the recipient rats were collected for subsequent experiments.

## 2.4 Biochemical analysis

The levels of creatinine, uric acid, urea, and urea nitrogen (BUN) in the serum or urine were tested using commercial kits (Nanjing Jiancheng Bioengineering Institute, Nanjing, China) (Xu et al., 2020). The contents of serum TNF-α, IL-1β, and IL-6 were quantified using ELISA kits (Nanjing Jiancheng Bioengineering Institute, Nanjing, China), according to the instructions of reagents and previous methods (Zhang et al., 2020; Li W. et al., 2021; Zhang et al., 2021).

## 2.5 Histopathological analysis

Renal tissue was analyzed histologically as previous methods with minor modifications (Wang et al., 2021; Hao et al., 2022). Briefly, renal tissues were fixed in 4% paraformaldehyde and embedded in paraffin. A measure of 3-μm sections were stained with hematoxylin and eosin (H&E), Alcian blue-periodic acid–schiff (AB-PAS), or Masson's trichrome staining by using standard methods (Zhou et al., 2021; Tao et al., 2022; Zhang et al., 2023). Images were captured under a Leica DM6B microscope (Leica, Weltzar, Germany).

## 2.6 Western blotting

The expressions of proteins were determined by Western blot as described before (Ding et al., 2021; Chen et al., 2022; Zhou et al., 2022). In brief, the total protein of renal tissue was extracted by using RIPA extraction buffer, and the concentrations were quantified using BCA protein assay kits. 10% SDS polyacrylamide gel was used to separate proteins, transferred onto PVDF membranes, and then blocked with 5% skimmed milk for 1 h at room temperature. The primary antibodies (showed in Supplementary Table S1) were immunoblotted with the membranes at 4°C overnight and followed by the incubation with the

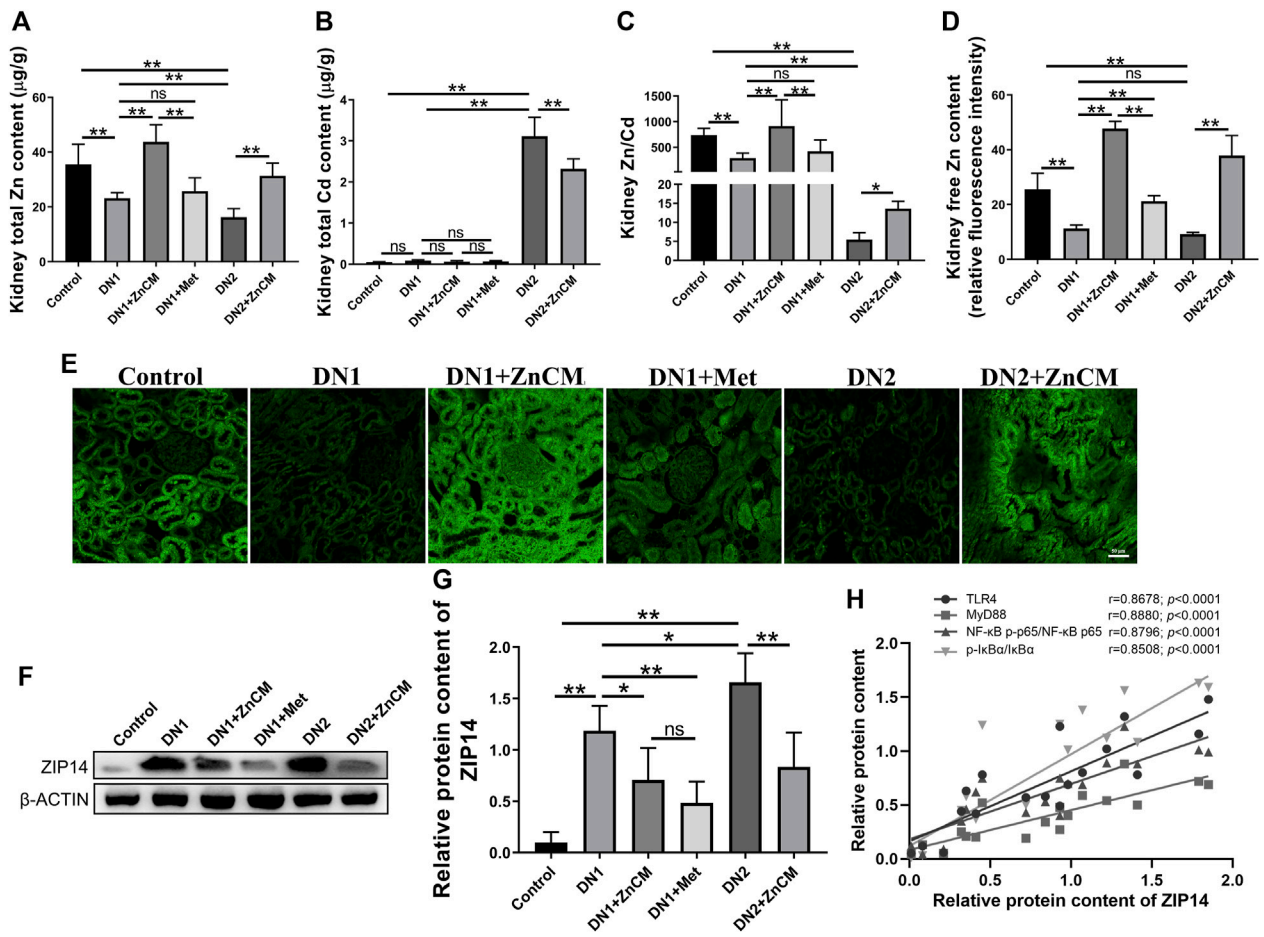


FIGURE 3
ZnCM relieved zinc dyshomeostasis in Cd-induced rats treated by STZ. **(A)** Renal Zn and **(B)** Cd levels were detected by ICP-MS ($n$ = 8). **(C)** Zn/Cd ratio in the kidney ($n$ = 8). **(D, E)** The level of free Zn quantified from fluorescence intensity. ($n$ = 4). **(E)** Representative images of renal-free zinc level were determined by TSQ (scale bar, 50 μm). **(F, G)** Representative blots of renal ZIP14 and relative expressions ($n$ = 3). **(H)** Relationships between the relative protein expression of ZIP14 and the relative expressions of TLR4, MYD88, NF-κBp-p65/NF-κBp65, and p-IκBα/IκBα. Data are represented by mean ± SD and analyzed by one-way ANOVA followed by the original FDR method of the Benjamini and Hochberg test or Spearman's rank correlation. *$p$ < 0.05 and **$p$ < 0.01; ns indicates no significance.

respective secondary antibodies for 1 h at room temperature. The bands were visualized using ECL kits (Applygen, Beijing, China) on the Tanon5200 chemiluminescence imaging system (Shanghai Tianneng Technology Co., Ltd., Shanghai, China). The relative expressions of proteins were calculated against β-actin.

## 2.7 Zn and Cd measurements

For the quantification of Zn and Cd, 0.1–0.5 g of renal tissue was digested by concentrated nitric acid in a microwave digestion system (MARS-6, CEM Co. Ltd., Matthews, NC, United States). The obtention was subjected to determine the contents of Zn and Cd by using inductively coupled plasma-mass spectrometry (ICP-MS; Thermo Fisher Scientific, Waltham, MA, United States) (Wu et al., 2019a; Wu et al., 2019b). The following formula can be used to calculate the Zn or Cd content per gram of tissue:

Zn or Cd content (μg/g) = (Zn or Cd concentration of tissue suspension) × liquid volume (mL)/wet weight of tissue.

For the imaging of Zn ions in renal tissue, the sections were deparaffinized, rehydrated, and incubated with fluorescent Zn ion probe TSQ (AAT Bioquest, Inc., United States) for 30 min at room temperature (Wu et al., 2019a; Wu et al., 2019b). Images were captured using a confocal laser scanning microscope (LSM880, Zeiss, Germany).

## 2.8 16S rRNA gene amplicon sequencing analysis

The composition of fecal microbiota was analyzed by 16S rRNA-sequencing, as previously described (Li Y. et al., 2021; Wang et al., 2023). In brief, genomic DNA of bacteria was extracted from feces using the QIAamp DNA Stool Mini Kit (QIAGEN, Hilden, Germany) according to the manufacturer's instructions. DNA concentration and purification were determined by using a NanoDrop instrument (Thermo Fisher Scientific, Waltham, MA, United States). The V3–V4 regions of genes were amplified with the following primers: 338F (5′-ACTCCTACGGGAGGCAGCAG-3′)

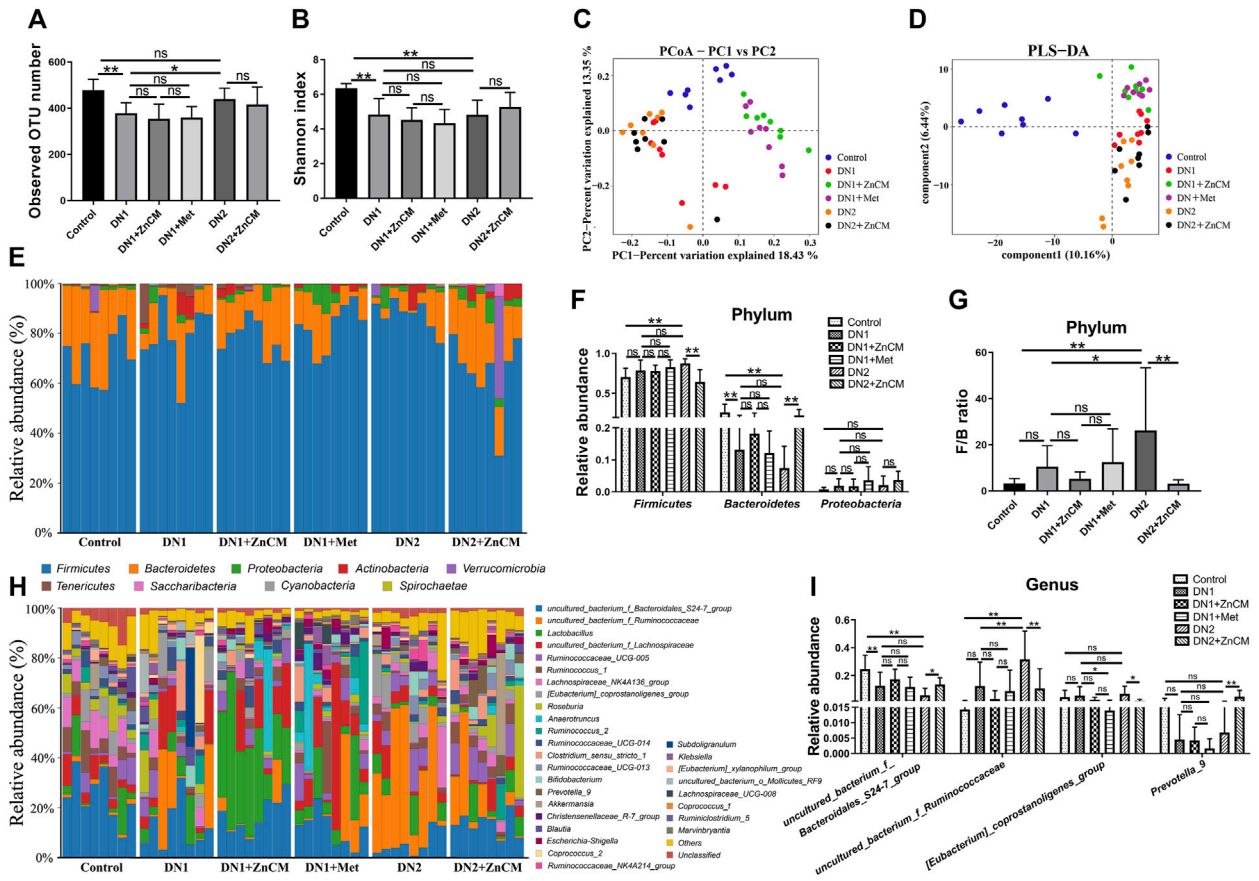


FIGURE 4
Oral administration of ZnCM regulated the composition of gut microbiota in Cd-induced diabetic nephropathy rats. **(A)** The number of observed OTU. **(B)** α-diversity of gut microbiota determined by the Shannon index. **(C)** PCoA and **(D)** PLS-DA of gut microbiota composition by weighted UniFrac distance (ANOSIM test). **(E)** The composition of the gut bacteria at the phylum level. **(F)** The relative abundance of *Firmicutes*, *Bacteroides*, and *Proteobacteria*. **(G)** The ratio of *Firmicutes*/*Bacteroides*. **(H)** The relative abundance of top 30 abundant bacteria at the genus level. **(I)** The relative abundance of major altered bacteria at the genus level. Data are shown as means ± SD ($n$ = 8) and analyzed by one-way ANOVA followed by the original FDR method of the Benjamini and Hochberg test. *$p$ < 0.05 and **$p$ < 0.01; ns indicates no significance.

and 806R (5′-GGACTACHVGGGTWTCTAAT-3′) using the thermocycler PCR system (thermal cycling condition: 95°C for 5 min (1 cycle), 95°C for 30 s, 50°C for 30 s, 72°C for 40 s (25 cycles), and a final extension at 72°C for 7 min). After purification and quantification, the amplicons were subjected to sequence on a HiSeq 2500 platform (Illumina, San Diego, United States) with the standard protocols by Biomarker Technologies Co., Ltd. (Beijing, China) (Li et al., 2023). The alpha diversity, beta diversity, and differential types of bacteria were analyzed with an online platform at BMKCloud (www.biocloud.net).

## 2.9 Metabolite analysis

The serum metabolites were extracted and measured by gas chromatography–mass spectrometry (GC-MS), as previously described with minor modifications (Chen et al., 2019; Jiang et al., 2021). A measure of 80 μL of 20 mg/mL methoxyamine hydrochloride (Sigma-Aldrich, St Louis, MO, United States) in pyridine was added in 100 μL of serum. The mixture was vigorously vortexed for 5 min and incubated at 37°C for 90 min. A measure of 80 μL of N-methyl-N-trimethylsilyltrifluoroacetamide (Sigma-Aldrich, St Louis, MO, United States) was added and derivatized at 37°C for 30 min. The mixture was centrifuged at 30,000 × g at 4°C for 15 min, and the supernatant was filtered through a 0.2-μM filter. The filtrates were lyophilized and then resuspended in ultrapure water. The metabolites were detected by using an Agilent GC7890A-MS5975C gas chromatography–mass spectrometer (Agilent Technologies, Santa Clara, CA, United States) equipped with the experienced instrument settings (described in Supplementary Table S2) and coupled to an LCMS-8050 triple-quadrupole mass spectrometer (Shimadzu Corporation, Kyoto, Japan). The data were analyzed using SIMCA 14.1 software (Umetrics, Umea, Sweden). Spearman's correlation between differential metabolites and microbiota was analyzed by using GraphPad Prism software 9.0 or MetaboAnalyst 5.0 (https://www.metaboanalyst.ca/).

## 2.10 Statistics

GraphPad Prism software 9.0.0 (GraphPad Software, La Jolla, CA, United States) was used for the statistical analyses.

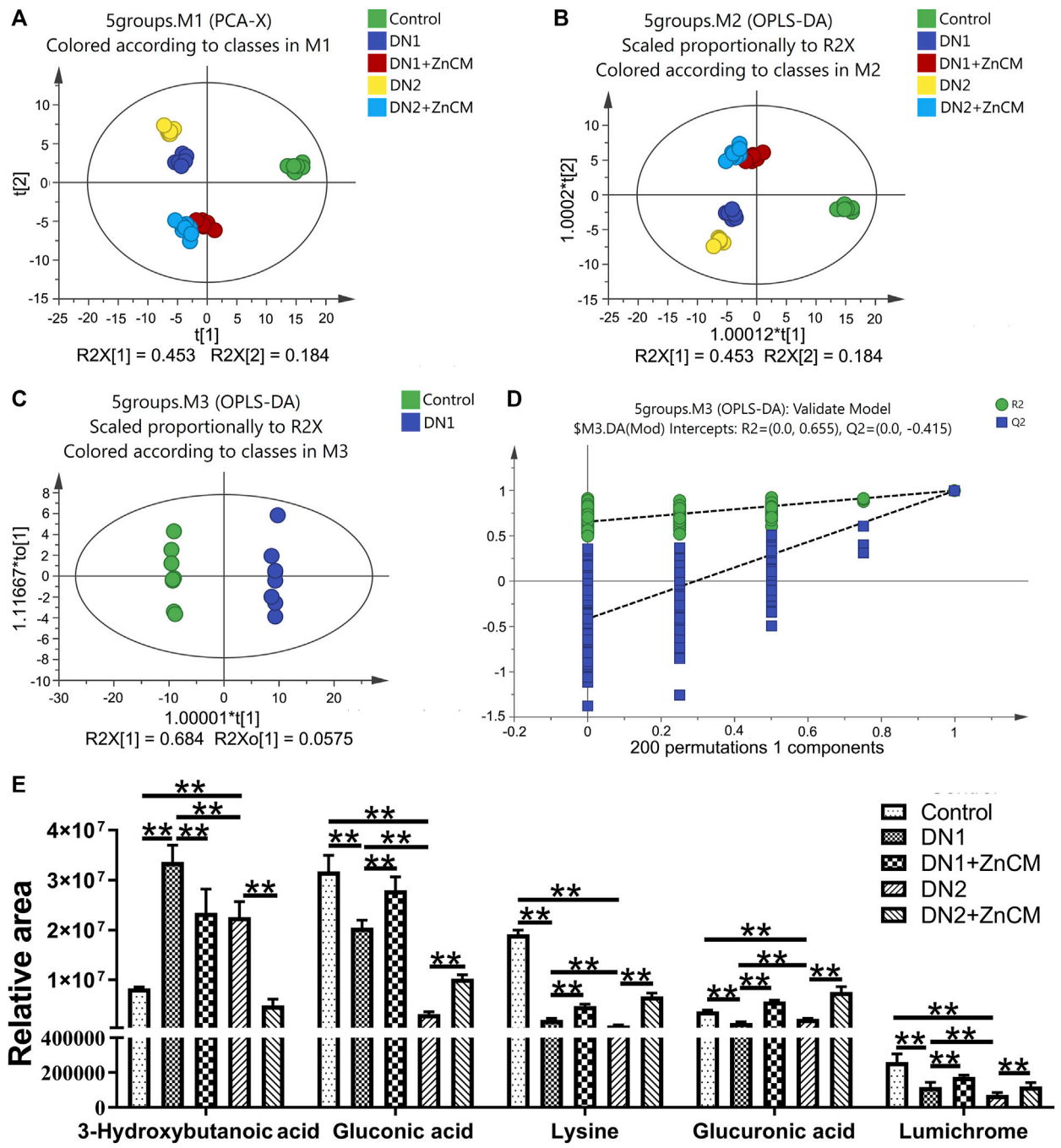


FIGURE 5
ZnCM altered the metabolite profiling in serum in Cd-induced diabetic nephropathy rats. **(A, B)** The composition of metabolite profiling analyzed by PCA and OPLS-DA. **(C)** OPLS-DA score plot and **(D)** corresponding permutation plot (200 times) between the control rats and the STZ-induced rats obtained from GC–MS. **(E)** The relative intensities of selected metabolites in the serum. Data are shown as means ± SD ($n$ = 8) and analyzed by two-way ANOVA followed by Tukey's multiple comparison tests. *$p$ < 0.05 and **$p$ < 0.01; ns indicates no significance.

Unpaired two-tailed t-tests were used to determine the significance of the differences between two groups. One-way ANOVA or two-way ANOVA was used to compare the statistical significance among more than two groups followed by the original false discovery rate (FDR) method of Benjamini and Hochberg or Tukey's multiple comparison tests. Data are expressed as means ± standard deviation (SD). $p$-values <0.05 were statistically significant.

# 3 Results

## 3.1 ZnCM improves the renal function in STZ-induced rats exposed to Cd

To test whether ZnCM could protect the renal function of diabetic rats, STZ-induced rats were orally gavaged with 100 mg/kg ZnCM for 8 weeks in the presence or absence of Cd

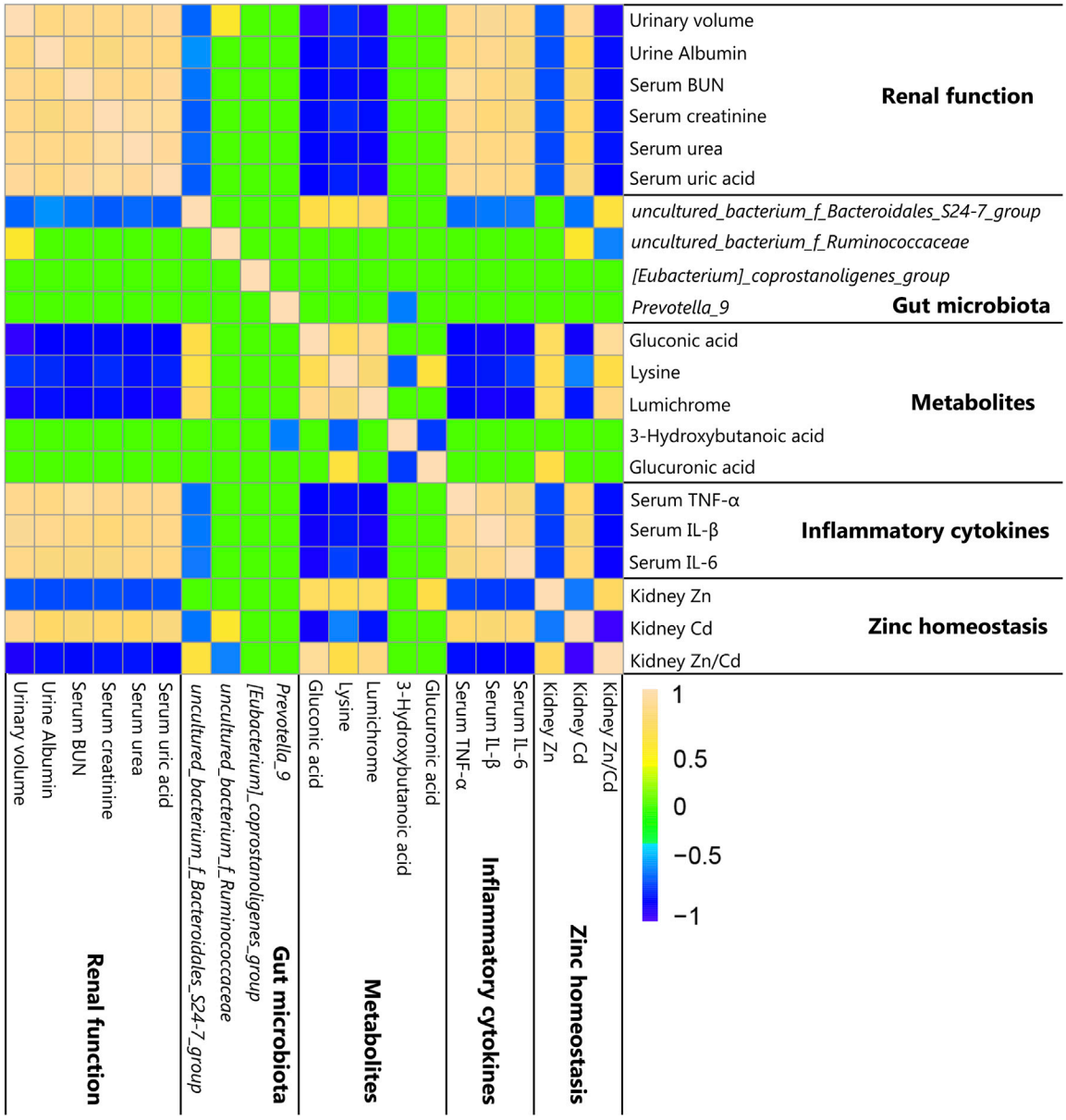


FIGURE 6
Correlation among clinical symptoms, zinc homeostasis, metabolites, and gut microbiota shown by heat map ($n$ = 8). Yellow, green, and blue squares indicate significant positive correlations, non-significant correlations, and significant negative correlations, respectively. Spearman's and $p$ values' correlation coefficients ($|r| > 0.5$ and $p < 0.05$) were considered statistically significant.

exposure (Figure 1A). Compared with control rats, STZ treatment induced a significant decrease in the body weight of rats. Cd exposure decreased body weights of STZ rats, and this could be significantly prevented by the administration of ZnCM (Figure 1B). Furthermore, compared with STZ-treated rats, the ratios of kidney weight/body weight (KW/BW) were significantly increased in rats exposed to Cd, which could be significantly reduced after ZnCM treatment (Figure 1C). Following this discovery, pathobiology and renal function parameters were analyzed. Compared with control rats, STZ treatment induced significant pathological changes in glomeruli, as evidenced by proximal tubule edema and hypertrophy with tubular epithelial cell damage, thickening of the glomerular basement membrane, mesangial region proliferation and expansion, podocyte apoptosis and necrosis, and the proliferation of the glomerular and glomeruli interstitial fibroblasts in rats (Figures 1D–F). Obviously, these changes in the kidney induced by STZ rats exposed to Cd were more serious than those by STZ alone. Notably, the administration of ZnCM dramatically ameliorated nephrotic phenotype in STZ-treated rats exposed to Cd, indicating that ZnCM effectively delayed the progression of diabetic nephropathy. Moreover, oral consumption of ZnCM not only significantly reduced the urinary volume and urine albumin but also remarkably decreased the levels of serum BUN, creatinine, urea, and uric acid in Cd-exposed rats with diabetic nephropathy induced by STZ (Figures 1G–L). These results indicate that ZnCM could effectively alleviate renal

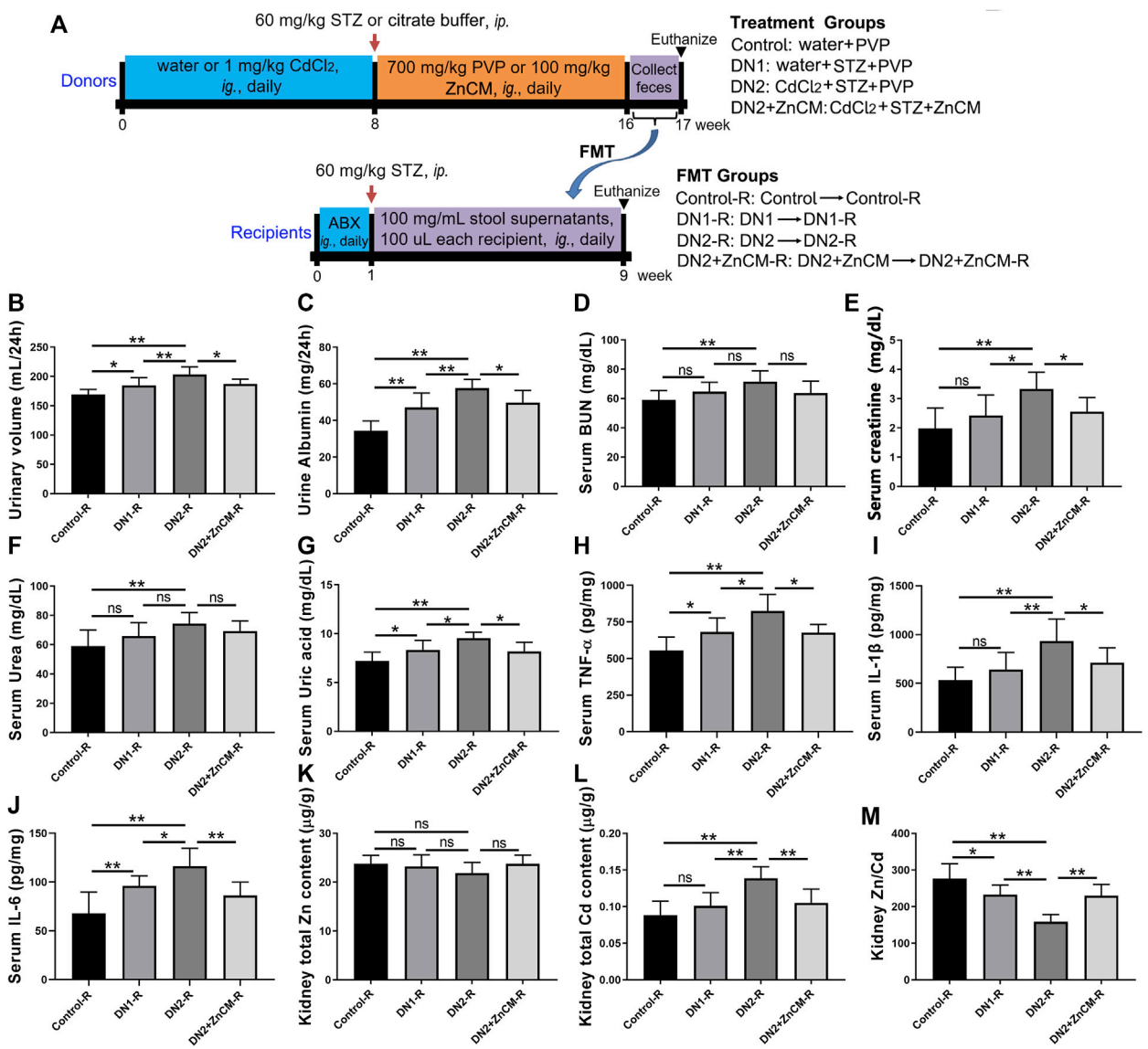


FIGURE 7
Effects of fecal microbiota transplantation (FMT) on renal function, inflammation, and zinc homeostasis in STZ-treated rats exposed to Cd. Recipient rats daily received fecal microbiota from donor rats by oral gavage for 8 weeks. **(A)** The experimental scheme of FMT. Fecal microbiota from control, DN1, DN2, and DN2 + ZnCM rats were transplanted to antibiotics (ABX)-pretreated rats treated by STZ and Cd ($n$ = 6). **(B, C)** The levels of urinary volume and urine albumin of recipient rats. **(D–G)** The levels of BUN, creatinine, urea and uric acid in the serum. **(H–J)** The serum levels of inflammatory cytokines TNF-α, IL-1β, and IL-6. **(K–M)** The contents of the Zn, Cd, and Zn/Cd ratio in the kidney. Data are shown as means ± SD ($n$ = 6) and analyzed by one-way ANOVA followed by the original FDR method of the Benjamini and Hochberg test. *$p$ < 0.05 and **$p$ < 0.01; ns indicates no significance.

pathological deterioration and dysfunction in Cd-exposed rats with diabetic nephropathy.

## 3.2 ZnCM attenuates inflammatory response in Cd-exposed rats induced by STZ

As the pathology of diabetic nephropathy is associated with the overproduction of early response pro-inflammatory cytokines (He et al., 2022), we determined the inflammatory biomarkers (Sun et al., 2020b; Wang et al., 2020b). STZ treatment induced a significant increase in the levels of IL-1β, IL-6, and TNF-α (Figures 2A–C) in rats exposed to Cd when compared to those of control rats. ZnCM treatment significantly attenuated inflammatory response by decreasing those levels of response pro-inflammatory cytokines in STZ-treated rats exposed to Cd. STZ-treated rats exposed to Cd display significant increase in the protein expressions of TLR4, MYD88, NF-κB p-p65/NF-κBp65, and p-IκBα/IκBα in the kidney when compared with control rats. Interestingly, the administration of ZnCM clearly downregulated those increased protein expressions in STZ-treated rats exposed to Cd (Figures 2D, E). These findings provide evidence that treatment with ZnCM could attenuate inflammatory response and may be related to the inactivation of the TLR4/NF-κB pathway in Cd-exposed rats with diabetic nephropathy.

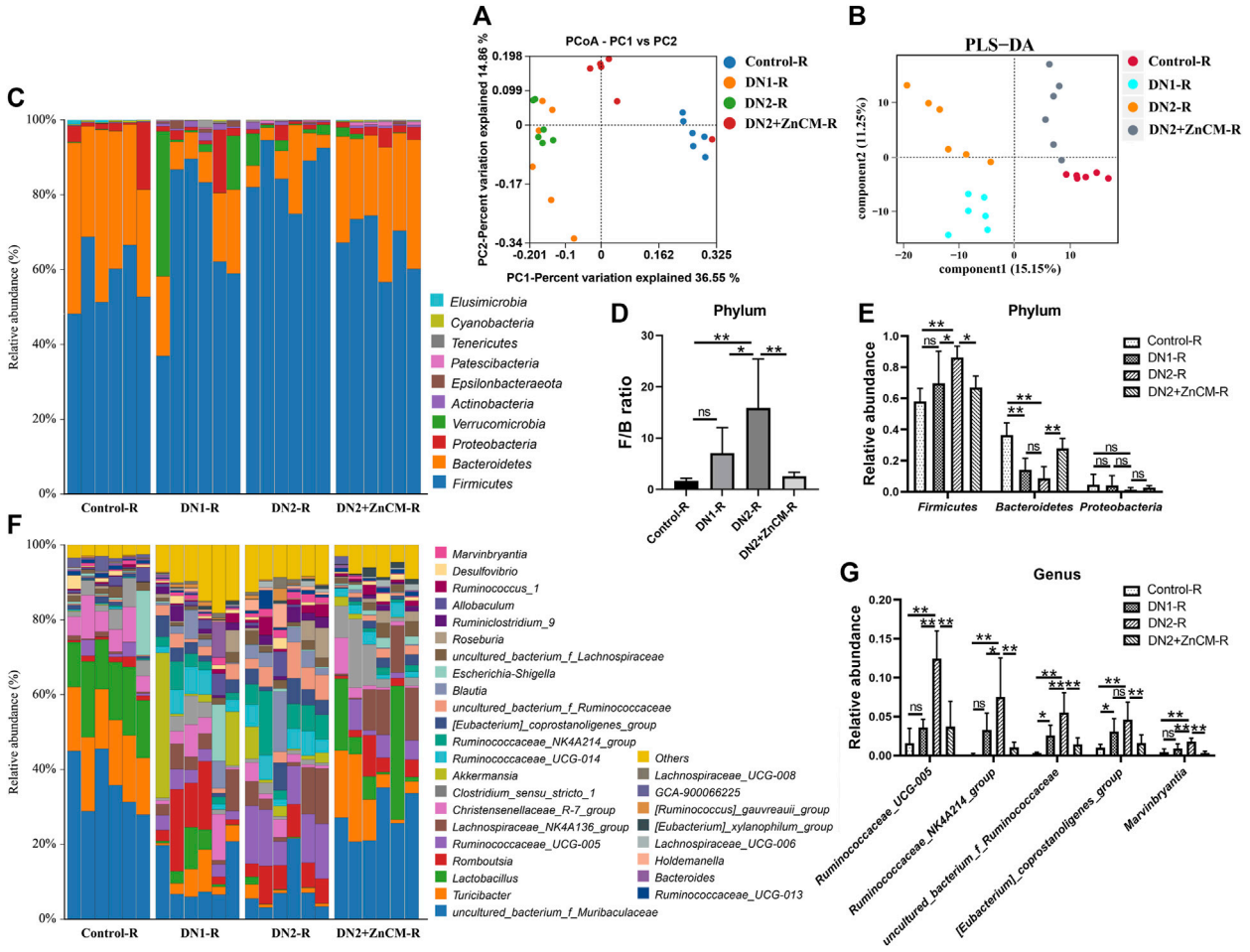


FIGURE 8
Fecal microbiota transplantation reproduced the ZnCM-induced structure of the gut microbiota in recipient rats. **(A, B)** The composition of the gut microbiota analyzed by PCoA and PLS-DA. **(C)** The relative abundance of the top nine abundant bacteria at the phylum level. **(D)** The ratio of *Firmicutes*/*Bacteroides*. **(E)** The relative abundance of *Firmicutes*, *Bacteroides*, and *Proteobacteria*. **(F)** The relative abundance of top 30 abundant bacteria at the genus level. **(G)** The relative abundance of major altered bacteria at the genus level. Data are shown as means ± SD ($n = 6$) and analyzed by one-way ANOVA followed by the original FDR method of the Benjamini and Hochberg test. *$p < 0.05$ and **$p < 0.01$; ns indicates no significance.

## 3.3 ZnCM attenuated Zn dyshomeostasis in Cd-exposed rats with diabetic nephropathy

Zinc homeostasis is often impaired in diabetic nephropathy (Al-Timimi et al., 2014). We were interested to test the changes of zinc in the kidney. A significant decrease in the level of total Zn and Zn/Cd ratio and a remarkable elevation of total Cd levels were observed in the kidneys of STZ-treated rats when compared with controls. Compared with STZ-treated rats, those changes in zinc homeostasis were significantly aggravated in those rats exposed to Cd, which could be effectively reversed after ZnCM treatment (Figures 3A–C). Compared to control rats, STZ-treated rats with or without Cd all had a lower level of renal-free Zn, which was significantly increased after ZnCM treatment (Figures 3D, E). Moreover, a remarkable increase in zinc transporter ZIP14 expression in STZ-treated rats exposed to Cd was observed when compared with either control rats or rats treated with STZ alone. Notably, treatment with ZnCM significantly reduced the expression of ZIP14 in Cd-exposed rats with diabetic nephropathy (Figures 3F, G). Furthermore, a significant positive correlation was presented between ZIP14 content and relative expressions of inflammation-related proteins, namely, TLR4, MYD88, NF-κBp-p65/NF-κBp65, and p-IκBα/IκBα (Figure 3H). Overall, these results suggest that Cd exposure significantly deteriorated Zn dyshomeostasis in diabetic rats, which could be effectively reversed by ZnCM supplementation.

## 3.4 ZnCM modulates gut microbiota dysbiosis in Cd-exposed diabetic nephropathy rats

To further explore the effects of ZnCM on the gut microbiota in Cd-exposed rats with diabetic nephropathy, we performed microbial 16S rRNA gene sequencing for feces. Compared to controls, the observed OTU number and α-diversity (Shannon index) (Figures 4A, B) were significantly decreased in the rats with diabetic nephropathy independent of Cd exposure; β-diversity determined

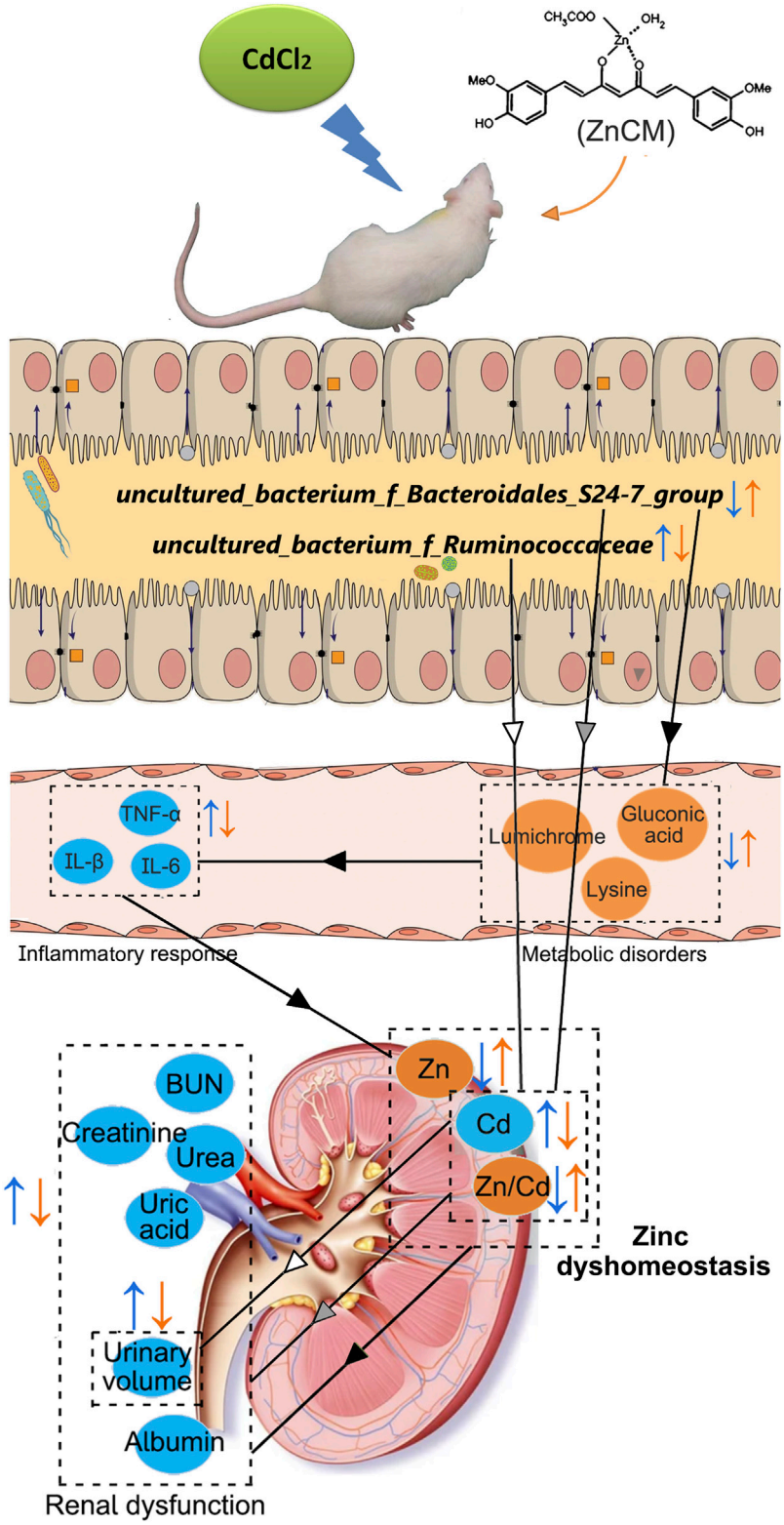


FIGURE 9
Possible mechanisms involved in the prevention of ZnCM on Cd-aggravated diabetic nephropathy. Oral administration of ZnCM regulated the composition of the gut microbiota and derived metabolites, which are conducive to alleviate inflammatory response and zinc dyshomeostasis, resulting in the mitigation of diabetic nephropathy aggravated by Cd.

by principal coordinate analyses (PCoA) and partial least-squares discriminant analysis (PLS-DA) (Figures 4C, D) revealed that the gut microbial compositions of diabetic nephropathy rats were significantly different from those of control rats. In addition, ZnCM treatment significantly altered the composition of the gut microbiota in STZ-treated rats exposed to Cd or not (Figures 4C, D). At the phylum level, *Firmicutes*, *Bacteroidetes*, and *Proteobacteria* are the dominated phylum in the microbial community structure (Figures 4E–G). Compared with controls, STZ-treated rats exposed to Cd induced a significant increase in the relative abundance of *Firmicutes* and decrease in the relative abundance of *Bacteroidetes*, which were dramatically reversed by ZnCM supplementation. In addition, we found that STZ-induced rats had a highly increased *Firmicutes*-to-*Bacteroidetes* (F/B) ratio, a biomarker of gut dysbiosis, which was markedly reduced by ZnCM treatment (Figures 4F, G). At the genus level, compared with the control group, the relative abundance of *uncultured_bacterium_f_Bacteroidales_S24-7_group* (*S24-7_group*) and *Prevotella_9* were significantly decreased, and the relative abundance of *uncultured_bacterium_f_Ruminococcaceae*, and *[Eubacterium]_coprostanoligenes_group* were increased in STZ-treated rats exposed to Cd. These altered genera in Cd-exposed rats with diabetic nephropathy were markedly reversed by ZnCM supplementation. However, there is no significant difference in these microbiota between Met and ZnCM in both phylum and genus levels in rats with diabetic nephropathy (Figures 4H, I). These results show that Cd exposure destructed the composition of the gut microbiota in rats with diabetic nephropathy, which could considerably be reversed by ZnCM supplementation.

## 3.5 ZnCM altered metabolite profiles in Cd-induced diabetic nephropathy rats

Because ZnCM could regulate the gut microbiota composition that affects serum metabolites, we next performed GC–MS to examine the metabolite profiles in the serum of Cd-induced rats with diabetic nephropathy. Principal component analysis (PCA) and orthogonal projection to latent structures-discriminant analysis (OPLS-DA) represent a clear separation of metabolite profiles among different groups, indicating significant changes in metabolites in rats with diabetic nephropathy, which could be remoulded by ZnCM supplementation (Figures 5A, B). The representative total ion chromatograms (TICs) are shown in Supplementary Figure S1. Subsequently, the serum samples were clearly separated into two blocks according to their metabolic profiles of different groups by the score plot of OPLS-DA in both positive and negative ion modes (Supplementary Figure S2). For example, as shown in Figures 5C, D, the results suggested that these metabolites were significantly altered in the control group compared with the STZ-treated group. A total of 135 differential metabolites in the serum were identified in rats with diabetic nephropathy (Supplementary Tables S3–S8). Notably, five differential metabolites, including gluconic acid, lysine, lumichrome, 3-hydroxybutanoic acid, and glucuronic acid, were significantly changed in different groups. Among them, the contents of 3-hydroxybutanoic acid in the serum were clearly increased, and the contents of gluconic acid, lysine, lumichrome, and glucuronic acid were significantly decreased in STZ-treated rats when compared to controls (Figure 5E). Importantly, the serum contents of these five differential metabolites in STZ-treated rats were significantly restored by ZnCM treatment to a certain extent. These findings suggest that oral treatment with ZnCM could reshape the metabolite profiles and improve metabolic disorders in rats with diabetic nephropathy.

## 3.6 Correlations among clinical symptoms, zinc homeostasis, metabolites, and gut microbiota

To explore the relationships among metabolites, cytokines, zinc homeostasis, clinical symptoms, and gut microbiota, Spearman's correlation analysis was adopted in our study ($|r| > 0.5$, $p < 0.05$). Spearman's and $p$ values' correlation coefficient datasets are shown in Supplementary Tables S9, S10. The relative abundance of ZnCM-enriched *uncultured_bacterium_f_Bacteroidales_S24-7_group* (*S24-7_group*) was positively associated with serum levels of gluconic acid, lysine, and lumichrome as well as the renal Zn/Cd ratio, and was negatively correlated with clinical symptoms and serum levels of inflammatory cytokines and renal Cd contents (Figure 6). The relative abundance of ZnCM-decreased *uncultured_bacterium_f_Ruminococcaceae* was found to be negatively correlated with the kidney Zn/Cd ratio and positively correlated with the kidney Cd ratio (Figure 6). Furthermore, the levels of renal Zn and Zn/Cd were positively correlated with metabolites (gluconic acid, lysine, and lumichrome), whereas they were negatively correlated with the serum levels of inflammatory cytokines (Figure 6). Taken together, these findings suggest that the homeostasis of renal zinc and the production of beneficial metabolites such as gluconic acid, lysine, and lumichrome might be at least in part related to the regulation of gut microbiota such as *Bacteroidales_S24-7_group* and *Ruminococcaceae*, which may be in charge of protective effects of ZnCM against the development of diabetic nephropathy in rats exposed by Cd.

## 3.7 Fecal microbial transplantation mitigated renal dysfunction, inflammation, and zinc dyshomeostasis in Cd-exposed rats with diabetic nephropathy

In order to investigate the role of gut microbiota in the mitigation of ZnCM on diabetic nephropathy fecal microbiota from the control, DN1, DN2, and DN2+ZnCM-treated rats were collected and transplanted to the corresponding groups of recipient rats (Figure 7A). Compared to the control-R group, a significant decrease in the renal Zn/Cd ratio and an increase in the urinary volume and the contents of urine albumin and serum creatinine were observed in DN1-R and DN2-R groups. In addition, higher levels of uric acid, TNF-α, IL-1β, and IL-6 in the serum were found in both DN1-R and DN2-R groups than those in the control-R group. Nevertheless, there are no significant differences in the levels of BUN, serum urea, and renal total Zn between the DN1-R group and DN2-R group (Figure 7B-m). Notably, the DN2 + ZnCM-R group not only displayed lower levels of urinary volume and urine

albumin but also showed a remarkable decrease in the serum levels of creatinine, uric acid, TNF-α, IL-1β, and IL-6, as well as total Cd and Zn/Cd when compared to the DN2-R group (Figures 7B–M). These results indicate that the ability of ZnCM to regulate zinc homeostasis and exert renal protective effects in Cd-exposed rats with diabetic nephropathy may be mediated by the gut microbiota.

### 3.8 Fecal microbial transplantation reshaped the composition of gut microbiota in diabetic nephropathy rats exposed to Cd

To further confirm the ability of ZnCM to modulate the gut microbiota, we analyzed the gut microbiota composition in recipients. PCoA and PLS-DA revealed that the DN2 + ZnCM-R group had a dramatically different microbial landscape from the DN1-R group and DN2-R group (Figures 8A, B). Compared to the DN1-R group, a higher relative abundance of *Firmicutes* and a lower F/B ratio and relative abundance of *Bacteroidetes* were observed in the DN2-R group at the phylum level (Figures 8C–E). The relative abundance of *Ruminococcaceae_UCG-005*, *Ruminococcaceae_NK4A214_group*, *uncultured_bacterium_f_Ruminococcaceae* [*Eubacterium*] *_coprostanoligenes_group*, and *Marvinbryantia* were significantly increased in the DN2-R group at the genus level compared to the DN1-R group (Figures 8F, G). Notably, these changes in the gut microbiota caused by the transplantation of fecal microbiota from Cd-exposed diabetic nephropathy rats were significantly attenuated in the DN2 + ZnCM-R groups (Figures 8F, G). These alterations in the structure and composition of the gut microbiota in the recipient rats were similar to those in the donor rats (Figure 4). These results indicate that gut microbiota may be responsible for the protective effects of ZnCM against diabetic nephropathy.

## 4 Discussion

Acute or chronic Cd exposure has been found to initiate multi-system injuries such as insulin-producing β-cell damage, immune disorder, diabetes, and diabetic retinopathy (El et al., 2012; Filippini et al., 2022). The kidney acts as the major accumulative and vulnerable target organ of Cd exposure, but the unclear mechanism of Cd-aggravated diabetic nephropathy restricts the development of preventive and therapeutic strategies. In the present study, we found that ZnCM treatment effectively improved clinical symptoms, inflammation, and zinc dyshomeostasis in diabetic nephropathy rats exposed to Cd. The administration of ZnCM significantly ameliorated the dysbiosis of fecal microbiota and serum metabolite profiling in Cd-exposed rats with diabetic nephropathy. Transferring of fecal microbiota from ZnCM-treated rats significantly improved clinical symptoms, inflammation, and zinc dyshomeostasis in diabetic nephropathy rats. These findings reveal that the protective effects of ZnCM on diabetic nephropathy may be dependent on the gut microbiota. The ZnCM might be a prospective therapeutic agent for diabetic nephropathy in terms of its strong efficacy.

Diabetic nephropathy is characterized by increased microalbuminuria and macroalbuminuria, and changes in renal morphology such as nodular glomerulosclerosis formation, interstitial fibrosis, and the decrease in glomerular thickness and endothelial cell fenestration (Fineberg et al., 2013). The progression of diabetic nephropathy can be induced by a complex inheritance–environment interaction. For instance, a positive correlation between the environmental pollutant Cd exposure and the incidence and severity of diabetes and its complications has been established in recent epidemiological studies (Edwards and Prozialeck, 2009; Fevrier-Paul et al., 2021). Cd exposure can activate inflammatory response, disturb renin–angiotensin–aldosterone system, and produce mutagenic effect, which may be conducive to the development of diabetes and its complications. Drugs targeted to inflammatory cytokines, adrenocorticotropic hormone receptor (ACTH), TLR4/NF-κB, and TGF-β1 receptors partly prevent the occurrence and development of diabetic nephropathy in clinical trials (Rao et al., 2019). In line with these findings, we found that Cd exposure significantly aggravated clinical symptoms of diabetic nephropathy, renal inflammation, and zinc dyshomeostasis in STZ-treated rats, demonstrating the destructive effect of Cd exposure on renal dysfunction. Cd-induced changes in STZ-treated rats could be improved by ZnCM supplementation. Furthermore, the administration of ZnCM clearly reduces the Cd-loaded local and systemic inflammation that is considered the critical reason for the progression of diabetic nephropathy. Meanwhile, ZnCM inhibited the activation of the inflammation-related TLR4/NF-κB signaling pathway, which is helpful in the alleviation of the progression of diseases (Sun et al., 2021; Sun et al., 2023). The development of inflammation is related to zinc deficiency, which induces a decrease in the innate and adaptive immune response (Bonaventura et al., 2015). Zinc homeostasis is tightly modulated by several transporters and regulators. Changes in zinc status are particularly susceptible to the survival, proliferation, and differentiation of different cells in organs. Fortunately, in addition to the modulation of nephrotoxicity and inflammation of diabetes, ZnCM treatment significantly reduced Cd-induced zinc dyshomeostasis, as indicated by increased renal zinc levels and Zn/Cd ratio and decreased Cd contents in the kidney. Furthermore, ZnCM significantly downregulated the Cd-increased ZIP14, whose high expression increases the accumulation of Cd and leads to zinc deficiency (Min et al., 2013). These profitable effects of ZnCM may be attributed to the success of zinc supplementation because zinc may replace Cd by competitively binding to ZIP14 and alleviating the inflammatory response and zinc dyshomeostasis.

Zinc utilization is vitally regulated by the gut. Zinc deficiency impairs intestinal permeability and induces alterations in the gut microbial ecology (Reed et al., 2015). Gut microbiota dysbiosis has been linked with the process of inflammatory bowel disease, diabetes mellitus, and diabetic complications such as diabetic nephropathy (Zhang et al., 2022). A significant alteration in the composition of the gut microbiota and an increased ratio of *Firmicutes* and *Bacteroidetes* (F/B), the biomarker of gut dysbiosis, were observed in diabetic nephropathy people or animals, which is associated positively with blood glucose concentration (Zhao et al., 2019). Consistent with these findings, we observed that the F/B ratio was noticeably higher in either diabetic nephropathy rats or those exposed to Cd than that of controls. Notably, ZnCM treatment markedly reshaped the composition of the gut microbiota and decreased the F/B ratio in rats with diabetic nephropathy, suggesting that ZnCM effectively maintained or rebalanced intestinal microflora disorder to a healthy status in STZ-treated rats exposed to Cd. In addition, we discovered several useful bacteria, such as *Bacteroidales_S24-7_group*, *[Eubacterium]*

_*Coprostanogenes_group*, and *Prevotella_9*, that were significantly changed after ZnCM administration in diabetic nephropathy rats treated by Cd. Among them, the *Bacteroidales_S24-7_group* has been considered as a gut probiotic that negatively correlated with the lipopolysaccharide, blood glucose, HOMA-IR, and inflammatory response, and positively correlated with the SCFAs content and zinc transporter 2 in mice (Liu et al., 2018; Xiao et al., 2020). Moreover, oral treatment with ZnCM remarkably reduced the relative abundance of pathogenic bacteria such as *Ruminococcaceae* that were significantly enriched in both diabetes mellitus and inflammatory disease animals (Ma et al., 2020; Kunasegaran et al., 2021). In addition, ZnCM significantly decreased the relative abundance of the [*Eubacterium*]_*Coprostanogenes_group*, which is significantly enriched in T2DM patients with diabetes-associated chronic kidney disease patients and associated with dyslipidemia and plasma concentrations of interleukin-12 and miR-142-5p (Huang et al., 2023). These findings suggest that ZnCM improves inflammation, renal dysfunction, and zinc dyshomeostasis, which may be related to the regulation of the gut microbiota in Cd-induced diabetic nephropathy rats.

Alterations in gut microbiota often affect the host metabolism, especially metabolites that are involved in intestinal barrier function, glucose regulation, energy homeostasis, insulin sensitivity, and inflammation (Tremaroli and Backhed, 2012). In the present study, the serum metabolite profile of control animals is significantly different from that of the rats with diabetic nephropathy or those exposed to Cd. Importantly, oral administration of ZnCM dramatically reshaped the composition of metabolite profiles in diabetic nephropathy rats exposed to Cd. Notably, ZnCM treatment significantly increased five metabolites (gluconic acid, lysine, lumichrome, glucuronic acid, and 3-hydroxybutanoic) that were negatively correlated with clinical phenotypes of diabetic nephropathy and positively correlated with the *Bacteroidales_S24-7_group*. These five metabolites have been documented to exert anti-inflammatory and anti-metabolic disease effects. For example, gluconic acid has been found to inhibit NF-κB activity along with its downstream inflammation signaling cascade (Hsieh et al., 2024). Supplementation with lysine upregulates anti-inflammation cytokines and downregulates pro-inflammation cytokines in fish (Hu et al., 2021). Lumichrome functions as one of the photodegradation products of riboflavin which exerts a critical role in cell oxidation and energy metabolism in rats (Remucal and Mcneill, 2011). These observations together indicate that treatment with ZnCM could improve the metabolites, which are beneficial for the remission of diabetic nephropathy and related to the regulation of the gut microbiota. According to the results of the correlation analysis, the imbalance in gut microbiota, metabolites, cytokines, and zinc homeostasis might be the underlying pathological mechanism of DN injury, and ZnCM might be involved in the regulation of the microbiota–metabolism–inflammation–zinc homeostasis axis and the microbiota–zinc homeostasis axis to ameliorate renal dysfunction in Cd-induced DN (Figure 9). The beneficial effect induced by ZnCM-regulated gut microbiota on the improvement of renal dysfunction, inflammation, and zinc homeostasis was further confirmed by the FMT. Transfering fecal microbiota from diabetic nephropathy rats treated by ZnCM partially recapitulated the composition of the gut microbiota and significantly reduced renal dysfunction, inflammation, and zinc dyshomeostasis in Cd-exposed rats with diabetic nephropathy. These observations further support the concept that the gut bacteria are involved in diabetic nephropathy in Cd-induced rats. However, one of the major open questions is that do fecal suspensions contain negligible amounts of ZnCM, which may directly influence the determination of the effect of the gut microbiota? Further research is needed to explore the role of specific bacteria in the prevention of diabetic nephropathy in the future.

## 5 Conclusion

In conclusion, oral consumption of ZnCM effectively mitigated clinical phenotypes, inflammatory response, and zinc dyshomeostasis in Cd-exposed rats with diabetic nephropathy. Simultaneously, ZnCM treatment not only reversed the composition of fecal microbiota but also changed the serum metabolite profiling in diabetic nephropathy rats exposed to Cd. Fecal microbiota from rats orally treated by ZnCM could reduce clinical phenotypes and zinc dyshomeostasis in Cd-exposed rats with diabetic nephropathy, suggesting that the prevention of ZnCM on Cd-aggravated diabetic nephropathy was partly dependent on the gut microbiota. These findings indicate that ZnCM supplementation may be a promising candidate to mitigate diabetic nephropathy. However, more detailed mechanisms are needed to be investigated in further studies.

## Data availability statement

The data presented in the study are deposited in the NCBI Sequence Read Archive repository, accession numbers PRJNA864569 and PRJNA1015156.

## Ethics statement

The animal study was approved by the International Animal Care and Use Committee (IACUC) and strictly performed according to the guidelines of Sun Yat-sen University (Guangzhou, China) for the Care and Use of Laboratory Animals (IACUC approval no. 171208). The study was conducted in accordance with the local legislation and institutional requirements.

## Author contributions

WS: Conceptualization, Data curation, Formal Analysis, Investigation, Methodology, Project administration, Software, Writing–original draft, Writing–review and editing. XM: Conceptualization, Writing–review and editing. JW: Resources, Writing–review and editing. ZM: Resources, Writing–review and editing. DX: Conceptualization, Funding acquisition, Investigation, Supervision, Writing–review and editing.

## Funding

The author(s) declare that financial support was received for the research, authorship, and/or publication of this article. This work was supported by the Guangzhou Science and Technology Research Fund (202201011656).

## Conflict of interest

The authors declare that the research was conducted in the absence of any commercial or financial relationships that could be construed as a potential conflict of interest.

## Publisher's note

All claims expressed in this article are solely those of the authors and do not necessarily represent those of their affiliated organizations, or those of the publisher, the editors, and the reviewers. Any product that may be evaluated in this article, or claim that may be made by its manufacturer, is not guaranteed or endorsed by the publisher.

## Supplementary material

The Supplementary Material for this article can be found online at: https://www.frontiersin.org/articles/10.3389/fphar.2024.1411230/full#supplementary-material

## References


Al-Timimi, D. J., Sulieman, D. M., and Hussen, K. R. (2014). Zinc status in type 2 diabetic patients: relation to the progression of diabetic nephropathy. *J. Clin. Diagn. Res.* 8 (11), CC04–8. doi:10.7860/JCDR/2014/10090.5082

Amato, K. R., Yeoman, C. J., Cerda, G., Schmitt, C. A., Cramer, J. D., Miller, M. E., et al. (2015). Variable responses of human and non-human primate gut microbiomes to a Western diet. *Microbiome* 3, 53. doi:10.1186/s40168-015-0120-7

Ba, Q., Li, M., Chen, P., Huang, C., Duan, X., Lu, L., et al. (2017). Sex-dependent effects of cadmium exposure in early life on gut microbiota and fat accumulation in mice. *Environ. Health Perspect.* 125 (3), 437–446. doi:10.1289/EHP360

Bonaventura, P., Benedetti, G., Albarede, F., and Miossec, P. (2015). Zinc and its role in immunity and inflammation. *Autoimmun. Rev.* 14 (4), 277–285. doi:10.1016/j.autrev.2014.11.008

Cao, Y. Y., Wang, Z., Wang, Z. H., Jiang, X. G., and Lu, W. H. (2021b). Inhibition of miR-155 alleviates sepsis-induced inflammation and intestinal barrier dysfunction by inactivating NF-κB signaling. *Int. Immunopharmacol.* 90, 107218. doi:10.1016/j.intimp.2020.107218

Cao, Y. Y., Wang, Z. H., Xu, Q. C., Chen, Q., Wang, Z., and Lu, W. H. (2021a). Sepsis induces variation of intestinal barrier function in different phase through nuclear factor kappa B signaling. *Korean J. Physiol. Pharmacol.* 25 (4), 375–383. doi:10.4196/kjpp.2021.25.4.375

Chen, J., Cao, D., Jiang, S., Liu, X., Pan, W., Cui, H., et al. (2022). Triterpenoid saponins from Ilex pubescens promote blood circulation in blood stasis syndrome by regulating sphingolipid metabolism and the PI3K/AKT/eNOS signaling pathway. *Phytomedicine* 104, 154242. doi:10.1016/j.phymed.2022.154242

Chen, Y. Y., Chen, D. Q., Chen, L., Liu, J. R., Vaziri, N. D., Guo, Y., et al. (2019). Microbiome-metabolome reveals the contribution of gut-kidney axis on kidney disease. *J. Transl. Med.* 17 (1), 5. doi:10.1186/s12967-018-1756-4

Defronzo, R. A., Reeves, W. B., and Awad, A. S. (2021). Pathophysiology of diabetic kidney disease: impact of SGLT2 inhibitors. *Nat. Rev. Nephrol.* 17 (5), 319–334. doi:10.1038/s41581-021-00393-8

Ding, M., Tang, Z., Liu, W., Shao, T., Yuan, P., Chen, K., et al. (2021). Burdock fructooligosaccharide attenuates high glucose-induced apoptosis and oxidative stress injury in renal tubular epithelial cells. *Front. Pharmacol.* 12, 784187. doi:10.3389/fphar.2021.784187

Edwards, J. R., and Prozialeck, W. C. (2009). Cadmium, diabetes and chronic kidney disease. *Toxicol. Appl. Pharmacol.* 238 (3), 289–293. doi:10.1016/j.taap.2009.03.007

El, M. M., Raja, M. R., Zhang, X., Macrenaris, K. W., Bhatt, S., Chen, X., et al. (2012). Accumulation of cadmium in insulin-producing β cells. *Islets* 4 (6), 405–416. doi:10.4161/isl.23101

Fan, Y., and Pedersen, O. (2021). Gut microbiota in human metabolic health and disease. *Nat. Rev. Microbiol.* 19 (1), 55–71. doi:10.1038/s41579-020-0433-9

Fevrier-Paul, A., Soyibo, A. K., De Silva, N., Mitchell, S., Nwokocha, C., and Voutchkov, M. (2021). Addressing the challenge of potentially hazardous elements in the reduction of hypertension, diabetes and chronic kidney disease in the caribbean. *J. Health Pollut.* 11 (30), 210613. doi:10.5696/2156-9614-11.30.210613

Filippini, T., Wise, L. A., and Vinceti, M. (2022). Cadmium exposure and risk of diabetes and prediabetes: a systematic review and dose-response meta-analysis. *Environ. Int.* 158, 106920. doi:10.1016/j.envint.2021.106920

Fineberg, D., Jandeleit-Dahm, K. A., and Cooper, M. E. (2013). Diabetic nephropathy: diagnosis and treatment. *Nat. Rev. Endocrinol.* 9 (12), 713–723. doi:10.1038/nrendo.2013.184

Hao, J., Bei, J., Li, Z., Han, M., Ma, B., Ma, P., et al. (2022). Qing`e Pill Inhibits Osteoblast Ferroptosis *via* ATM Serine/Threonine Kinase (ATM) and the PI3K/AKT Pathway in Primary Osteoporosis. *Front. Pharmacol.* 13, 902102. doi:10.3389/fphar.2022.902102

He, C., Wang, D., Wang, R., Huang, Y., Huang, X., Shen, S., et al. (2022). Epigallocatechin gallate induces the demethylation of actinin alpha 4 to inhibit diabetic nephropathy renal fibrosis via the NF-KB signaling pathway *in vitro*. *Dose-Response* 20 (2), 15593258221105704. doi:10.1177/15593258221105704

He, S., Jiang, T., Zhang, D., Li, M., Yu, T., Zhai, M., et al. (2024). Association of exposure to multiple heavy metals during pregnancy with the risk of gestational diabetes mellitus and insulin secretion phase after glucose stimulation. *Environ. Res.* 248, 118237. doi:10.1016/j.envres.2024.118237

He, X., Liu, G., Chen, X., Wang, Y., Liu, R., Wang, C., et al. (2023). Pharmacokinetic and pharmacodynamic interactions between henagliflozin, a novel selective SGLT-2 inhibitor, and warfarin in healthy Chinese subjects. *Clin. Ther.* 45 (7), 655–661. doi:10.1016/j.clinthera.2023.06.002

Hsieh, C. C., Yu, S. H., Kuo, H. C., Cheng, K. W., Hsu, C. C., Lin, Y. P., et al. (2024). Alleviation of PM2.5-induced alveolar macrophage inflammation using extract of fermented Chenopodium formosanum Koidz sprouts via regulation of NF-κB pathway. *J. Ethnopharmacol.* 318 (Pt B), 116980. doi:10.1016/j.jep.2023.116980

Hu, C., Liang, B., Sun, J., Li, J., Xiong, Z., Wang, S. H., et al. (2024). Synthesis and biological evaluation of indole derivatives containing thiazolidine-2,4-dione as α-glucosidase inhibitors with antidiabetic activity. *Eur. J. Med. Chem.* 264, 115957. doi:10.1016/j.ejmech.2023.115957

Hu, C. L., Wang, Y. C., Xi, Y., and Yao, X. M. (2020). Dapagliflozin therapy curative effect observation on nonalcoholic fatty liver disease in patients with type 2 diabetes mellitus. *Indian J. Pharm. Sci.* 82, 122–129. doi:10.36468/pharmaceutical-sciences.spl.155

Hu, Y., Feng, L., Jiang, W., Wu, P., Liu, Y., Kuang, S., et al. (2021). Lysine deficiency impaired growth performance and immune response and aggravated inflammatory response of the skin, spleen and head kidney in grown-up grass carp (Ctenopharyngodon idella). *Anim. Nutr.* 7 (2), 556–568. doi:10.1016/j.aninu.2020.07.009

Huang, H., Zhao, T., Li, J., Shen, J., Xiao, R., and Ma, W. (2023). Gut microbiota regulation of inflammatory cytokines and microRNAs in diabetes-associated cognitive dysfunction. *Appl. Microbiol. Biotechnol.* 107 (23), 7251–7267. doi:10.1007/s00253-023-12754-3

Huang, Y., Liu, R., Wang, Y., Liu, G., Wang, C., Chen, X., et al. (2022). Evaluation of pharmacokinetic interactions between the new SGLT2 inhibitor SHR3824 and valsartan in healthy Chinese volunteers. *Clin. Ther.* 44 (7), 945–956. doi:10.1016/j.clinthera.2022.06.001

Jiang, T. T., Ji, C. F., Cheng, X. P., Gu, S. F., Wang, R., Li, Y., et al. (2021). α-Mangostin alleviated HIF-1α-Mediated angiogenesis in rats with adjuvant-induced arthritis by suppressing aerobic glycolysis. *Front. Pharmacol.* 12, 785586. doi:10.3389/fphar.2021.785586

Jiang, Y. X., Li, W., Wang, J., and Wang, G. G. (2020). Cardiac dysfunction is attenuated by ginkgolide B via reducing oxidative stress and fibrosis in diabetic rats. *J. Basic Med. Sci.* 23 (8), 1078–1084. doi:10.22038/ijbms.2020.44210.10358

Kotha, R. R., and Luthria, D. L. (2019). Curcumin: biological, pharmaceutical, nutraceutical, and analytical aspects. *Molecules* 24 (16), 2930. doi:10.3390/molecules24162930

Kunasegaran, T., Balasubramaniam, V., Arasoo, V., Palanisamy, U. D., and Ramadas, A. (2021). The modulation of gut microbiota composition in the pathophysiology of gestational diabetes mellitus: a systematic review. *Biology-Basel.* 10 (10), 1027. doi:10.3390/biology10101027

Li, W., Zhao, X., Yu, T. T., Hao, W., and Wang, G. G. (2021a). Knockout of PKC theta gene attenuates oleic acid-induced acute lung injury via reduction of inflammation and oxidative stress. *Iran. J. Basic Med. Sci.* 24 (7), 986–991. doi:10.22038/ijbms.2021.56908.12695

Li, Y., Dai, M., Wang, L., and Wang, G. (2021b). Polysaccharides and glycosides from Aralia echinocaulis protect rats from arthritis by modulating the gut microbiota composition. *J. Ethnopharmacol.* 269, 113749. doi:10.1016/j.jep.2020.113749

Li, Y., Li, Z., Chen, B., Hou, Y., Wen, Y., Gan, L., et al. (2023). Ultrasonic assisted extraction, characterization and gut microbiota-dependent anti-obesity effect of polysaccharide from Pericarpium Citri Reticulatae 'Chachiensis. *Ultrason. Sonochem.* 95, 106383. doi:10.1016/j.ultsonch.2023.106383

Liu, G., Bei, J., Liang, L., Yu, G., Li, L., and Li, Q. (2018). Stachyose improves inflammation through modulating gut microbiota of high-fat diet/streptozotocin-induced type 2 diabetes in rats. *Mol. Nutr. Food Res.* 62 (6), e1700954. doi:10.1002/mnfr.201700954

Ma, Q., Li, Y., Wang, J., Li, P., Duan, Y., Dai, H., et al. (2020). Investigation of gut microbiome changes in type 1 diabetic mellitus rats based on high-throughput sequencing. *Biomed. Pharmacother.* 124, 109873. doi:10.1016/j.biopha.2020.109873

Mei, X., Xu, D., Xu, S., Zheng, Y., and Xu, S. (2011). Gastroprotective and antidepressant effects of a new zinc(II)-curcumin complex in rodent models of gastric ulcer and depression induced by stresses. *Pharmacol. Biochem. Behav.* 99 (1), 66–74. doi:10.1016/j.pbb.2011.04.002

Min, K. S., Takano, M., Amako, K., Ueda, H., and Tanaka, K. (2013). Involvement of the essential metal transporter Zip14 in hepatic Cd accumulation during inflammation. *Toxicol. Lett.* 218 (1), 91–96. doi:10.1016/j.toxlet.2013.01.010

Navarro-Gonzalez, J. F., Mora-Fernandez, C., Muros, D. F. M., and Garcia-Perez, J. (2011). Inflammatory molecules and pathways in the pathogenesis of diabetic nephropathy. *Nat. Rev. Nephrol.* 7 (6), 327–340. doi:10.1038/nrneph.2011.51

Prasad, S., and Lall, R. (2022). Zinc-curcumin based complexes in health and diseases: an approach in chemopreventive and therapeutic improvement. *J. Trace Elem. Med. Biol.* 73, 127023. doi:10.1016/j.jtemb.2022.127023

Qi, X., Zheng, S., Ma, M., Lian, N., Wang, H., Chen, L., et al. (2022). Curcumol suppresses CCF-mediated hepatocyte senescence through blocking LC3B-lamin B1 interaction in alcoholic fatty liver disease. *Front. Pharmacol.* 13, 912825. doi:10.3389/fphar.2022.912825

Rao, V. A., Tan, S. H., Candasamy, M., and Bhattamisra, S. K. (2019). Diabetic nephropathy: an update on pathogenesis and drug development. *Diabetes Metab. syndr.-clin. Res. Rev.* 13 (1), 754–762. doi:10.1016/j.dsx.2018.11.054

Reed, S., Neuman, H., Moscovich, S., Glahn, R. P., Koren, O., and Tako, E. (2015). Chronic zinc deficiency alters chick gut microbiota composition and function. *Nutrients* 7 (12), 9768–9784. doi:10.3390/nu7125497

Remucal, C. K., and Mcneill, K. (2011). Photosensitized amino acid degradation in the presence of riboflavin and its derivatives. *Environ. Sci. Technol.* 45 (12), 5230–5237. doi:10.1021/es200411a

Shen, C., Shao, W., Wang, W., Sun, H., Wang, X., Geng, K., et al. (2023). Physiologically based pharmacokinetic modeling of levetiracetam to predict the exposure in hepatic and renal impairment and elderly populations. *Syst. Pharmacol.* 12 (7), 1001–1015. doi:10.1002/psp4.12971

Song, J., Xu, H., Zhang, W., Yang, C., Li, L., and Luan, J. (2022). Impact of solute carrier family 47 member 1 gene polymorphism detection on therapeutic effect of diabetes. *Int. J. Pharmacol.* 18 (3), 398–406. doi:10.3923/ijp.2022.398.406

Sun, S., Li, S., Du, Y., Wu, C., Zhang, M., Li, J., et al. (2020a). Anti-inflammatory effects of the root, stem and leaf extracts of Chloranthus serratus on adjuvant-induced arthritis in rats. *Pharm. Biol.* 58 (1), 528–537. doi:10.1080/13880209.2020.1767159

Sun, S., Wang, Y., Du, Y., Sun, Q., He, L., Zhu, E., et al. (2020b). Oxidative stress-mediated hepatotoxicity in rats induced by ethanol extracts of different parts of Chloranthus serratus. *Pharm. Biol.* 58 (1), 1277–1289. doi:10.1080/13880209.2020.1859552

Sun, S., Zhang, J., Li, H., Du, Y., Li, S., Li, A., et al. (2021). Anti-inflammatory activity of the water extract of Chloranthus serratus roots in LPS-stimulated RAW264.7 cells mediated by the Nrf2/HO-1, MAPK and NF-κB signaling pathways. *J. Ethnopharmacol.* 271, 113880. doi:10.1016/j.jep.2021.113880

Sun, X., Zheng, Y., Tian, Y., Xu, Q., Liu, S., Li, H., et al. (2023). Astragalus polysaccharide alleviates alcoholic-induced hepatic fibrosis by inhibiting polymerase I and transcript release factor and the TLR4/JNK/NF-κB/MyD88 pathway. *J. Ethnopharmacol.* 314, 116662. doi:10.1016/j.jep.2023.116662

Tao, Z., Li, T., and Wei, S. (2022). Silymarin prevents iron overload induced bone loss by inhibiting oxidative stress in an ovariectomized animal model. *Chem.-Biol. Interact.* 366, 110168. doi:10.1016/j.cbi.2022.110168

Tinkov, A. A., Gritsenko, V. A., Skalnaya, M. G., Cherkasov, S. V., Aaseth, J., and Skalny, A. V. (2018). Gut as a target for cadmium toxicity. *Environ. Pollut.* 235, 429–434. doi:10.1016/j.envpol.2017.12.114

Tremaroli, V., and Backhed, F. (2012). Functional interactions between the gut microbiota and host metabolism. *Nature* 489 (7415), 242–249. doi:10.1038/nature11552

Ghosh, S., Banerjee, S., and Sil, P. C. (2015). The beneficial role of curcumin on inflammation, diabetes and neurodegenerative disease: A recent update. *Food. Chem. Toxicol.* 83, 111–124. doi:10.1016/j.fct.2015.05.022

Wang, L., Wang, P., Wang, D., Tao, M., Xu, W., and Olatunji, O. J. (2020). Anti-inflammatory activities of kukoamine A from the root bark of Lycium chinense Miller. *Nat. Prod. Commun.* 15 (3), 1934578X2091208. doi:10.1177/1934578X20912088

Wang, Q. H., Li, Y., Dou, D. Y., Wang, R., Jiang, T. T., Wang, L., et al. (2021). Nicotinamide mononucleotide-elicited NAMPT signaling activation aggravated adjuvant-induced arthritis in rats by affecting peripheral immune cells differentiation. *Int. Immunopharmacol.* 98, 107856. doi:10.1016/j.intimp.2021.107856

Wang, X., Shen, C., Wang, X., Tang, J., Wu, Z., Huang, Y., et al. (2023). Schisandrin protects against ulcerative colitis by inhibiting the SGK1/NLRP3 signaling pathway and reshaping gut microbiota in mice. *Chin. Med.* 18 (1), 112. doi:10.1186/s13020-023-00815-8

Wu, R., Mei, X., Wang, J., Sun, W., Xue, T., Lin, C., et al. (2019a). Zn(ii)-Curcumin supplementation alleviates gut dysbiosis and zinc dyshomeostasis during doxorubicin-induced cardiotoxicity in rats. *Food Funct.* 10 (9), 5587–5604. doi:10.1039/c9fo01034c

Wu, R., Mei, X., Ye, Y., Xue, T., Wang, J., Sun, W., et al. (2019b). Zn(II)-curcumin solid dispersion impairs hepatocellular carcinoma growth and enhances chemotherapy by modulating gut microbiota-mediated zinc homeostasis. *Pharmacol. Res.* 150, 104454. doi:10.1016/j.phrs.2019.104454

Wu, X., Zhu, W., Lu, L., Hu, C., Zheng, Y., Zhang, X., et al. (2023). Synthesis and anti-α-glucosidase activity evaluation of betulinic acid derivatives. *Arab. J. Chem.* 16 (5), 104659. doi:10.1016/j.arabjc.2023.104659

Xiao, S., Liu, C., Chen, M., Zou, J., Zhang, Z., Cui, X., et al. (2020). Scutellariae radix and coptidis rhizoma ameliorate glycolipid metabolism of type 2 diabetic rats by modulating gut microbiota and its metabolites. *Appl. Microbiol. Biotechnol.* 104 (1), 303–317. doi:10.1007/s00253-019-10174-w

Xing, Y., Xia, W., Zhang, B., Zhou, A., Huang, Z., Zhang, H., et al. (2018). Relation between cadmium exposure and gestational diabetes mellitus. *Environ. Int.* 113, 300–305. doi:10.1016/j.envint.2018.01.001

Xing, Y. J., Liu, B. H., Wan, S. J., Cheng, Y., Zhou, S. M., Sun, Y., et al. (2021). A SGLT2 inhibitor dapagliflozin alleviates diabetic cardiomyopathy by suppressing high glucose-induced oxidative stress *in vivo* and *in vitro*. *Front. Pharmacol.* 12, 708177. doi:10.3389/fphar.2021.708177

Xu, S., He, L., Ding, K., Zhang, L., Xu, X., Wang, S., et al. (2020). Tanshinone IIA ameliorates streptozotocin-induced diabetic nephropathy, partly by attenuating PERK pathway-induced fibrosis. *Drug Des. Devel Ther.* 14, 5773–5782. doi:10.2147/DDDT.S257734

Yang, Z., Yin, Q., Olatunji, O. J., Li, Y., Pan, S., Wang, D., et al. (2020). Activation of cholinergic anti-inflammatory pathway involved in therapeutic actions of α-mangostin on lipopolysaccharide-induced acute lung injury in rats. *Int. J. Immunopathol. Pharmacol.* 34, 2058738420954941. doi:10.1177/2058738420954941

Zhang, L., Wang, Z., Zhang, X., Zhao, L., Chu, J., Li, H., et al. (2022). Alterations of the gut microbiota in patients with diabetic nephropathy. *Microbiol. Spectr.* 10 (4), e0032422. doi:10.1128/spectrum.00324-22

Zhang, S., Zhu, P., Yuan, J., Cheng, K., Xu, Q., Chen, W., et al. (2023). Non-alcoholic fatty liver disease combined with rheumatoid arthritis exacerbates liver fibrosis by stimulating co-localization of PTRF and TLR4 in rats. *Front. Pharmacol.* 14, 1149665. doi:10.3389/fphar.2023.1149665

Zhang, X., Peng, L., Zhang, J., Dong, Y., Wang, C., Liu, C., et al. (2020). Berberine ameliorates subarachnoid hemorrhage injury via induction of sirtuin 1 and inhibiting HMGB1/Nf-κB Pathway. *Front. Pharmacol.* 11, 1073. doi:10.3389/fphar.2020.01073

Zhang, Y. X., Zhang, X. T., Li, H. J., Zhou, T. F., Zhou, A. C., Zhong, Z. L., et al. (2021). Antidepressant-like effects of helicid on a chronic unpredictable mild stress-induced depression rat model: inhibiting the IKK/IκBα/NF-κB pathway through NCALD to reduce inflammation. *Int. Immunopharmacol.* 93, 107165. doi:10.1016/j.intimp.2020.107165

Zhao, L., Lou, H., Peng, Y., Chen, S., Zhang, Y., and Li, X. (2019). Comprehensive relationships between gut microbiome and faecal metabolome in individuals with type 2 diabetes and its complications. *Endocrine* 66 (3), 526–537. doi:10.1007/s12020-019-02103-8

Zhou, H. H., Zhang, Y. M., Zhang, S. P., Xu, Q. X., Tian, Y. Q., Li, P., et al. (2021). Suppression of PTRF alleviates post-infectious irritable bowel syndrome via downregulation of the TLR4 pathway in rats. *Front. Pharmacol.* 12, 724410. doi:10.3389/fphar.2021.724410

Zhou, Y., Liu, L., Xiang, R., Bu, X., Qin, G., Dai, J., et al. (2023). Arctigenin mitigates insulin resistance by modulating the IRS2/GLUT4 pathway via TLR4 in type 2 diabetes mellitus mice. *Int. Immunopharmacol.* 114, 109529. doi:10.1016/j.intimp.2022.109529

Zhou, Y., Xiang, R., Qin, G., Ji, B., Yang, S., Wang, G., et al. (2022). Xanthones from Securidaca inappendiculata Hassk. attenuate collagen-induced arthritis in rats by inhibiting the nicotinamide phosphoribosyltransferase/glycolysis pathway and macrophage polarization. *Int. Immunopharmacol.* 111, 109137. doi:10.1016/j.intimp.2022.109137

frontiers | Frontiers in Pharmacology

TYPE Original Research
PUBLISHED 19 June 2024
DOI 10.3389/fphar.2024.1425832

Check for updates

OPEN ACCESS

EDITED BY
Xuetao Xu,
Wuyi University, China

REVIEWED BY
Shao-Hua Wang,
Lanzhou University, China
Haoxing Zhang,
Shenzhen University, China

*CORRESPONDENCE
Xin Zhong,
344100489@qq.com

RECEIVED 30 April 2024
ACCEPTED 04 June 2024
PUBLISHED 19 June 2024

CITATION
Zhu H and Zhong X (2024), Honokiol as an α-glucosidase inhibitor.
*Front. Pharmacol.* 15:1425832.
doi: 10.3389/fphar.2024.1425832

COPYRIGHT
© 2024 Zhu and Zhong. This is an open-access article distributed under the terms of the Creative Commons Attribution License (CC BY). The use, distribution or reproduction in other forums is permitted, provided the original author(s) and the copyright owner(s) are credited and that the original publication in this journal is cited, in accordance with accepted academic practice. No use, distribution or reproduction is permitted which does not comply with these terms.

# Honokiol as an α-glucosidase inhibitor

Hua Zhu[1] and Xin Zhong[2]*

[1]School of Chemistry and Chemical Engineering, Mianyang Teacher's College, Mianyang, China, [2]Dean's Office, Mianyang Teacher's College, Mianyang, China

Honokiol, a naturally occurring compound from *Magnolia obovata Thunb.*, has many biological activities, but its anti-α-glucosidase activity is still unclear. Therefore, we determined its inhibitory effects against α-glucosidase. Activity assays showed that honokiol was a reversible mixed-type inhibitor of α-glucosidase, and its $IC_{50}$ value was 317.11 ± 12.86 μM. Fluorescence results indicated that the binding of honokiol to α-glucosidase caused a reduction in α-glucosidase activity. 3D fluorescence and CD spectra results indicated that the binding of honokiol to α-glucosidase caused conformational change in α-glucosidase. Docking simulated the detailed interactions between honokiol and α-glucosidase, including hydrogen and hydrophobic bonds. All findings showed that honokiol could be used as a natural inhibitor to develop α-glucosidase agents.

KEYWORDS

**nature product, honokiol, α-glucosidase, inhibition mechanism, inhibitor**

## 1 Introduction

Type 2 diabetes mellitus (T2DM) is a growing health concern with increased prevalence (Xu et al., 2020; ElSayed et al., 2023; Zhou et al., 2023). Now, T2DM has become a significant global health issue (Hu et al., 2024; Li et al., 2024). Epidemiological trends indicate that the prevalence of diabetes could reach an alarming 643 million individuals worldwide by 2030 (Song et al., 2022; Lin et al., 2023). The hallmark clinical feature of T2DM is elevated blood glucose levels, or hyperglycemia, which can result in a spectrum of debilitating complications (Jiang et al., 2020; Ding et al., 2021; Xing et al., 2021). Therefore, management of hyperglycemia is a critical aspect for T2DM patients (Hu et al., 2020).

One key characteristic of T2DM is postprandial hyperglycemia, which is intricately linked to the breakdown of carbohydrates (Hameed et al., 2019; Davies et al., 2022). α-Glucosidase, an enzyme present in enterocytes of the small intestine, facilitates the hydrolysis of glycosidic bonds to liberate glucose (Basri et al., 2023; Xiao et al., 2023). The suppression of α-glucosidase activity can thus delay carbohydrate digestion and absorption, leading to a reduction in the postprandial glucose spike (Basri et al., 2023; Wu et al., 2023). This rationale has made the inhibition of α-glucosidase a strategic target for therapeutic interventions to manage postprandial hyperglycemia (Khan et al., 2022; Zhang et al., 2022). Clinically, a number of α-glucosidase inhibitors, including acarbose and voglibose, have been employed to mitigate T2DM (Feng et al., 2024). However, chronic administration of these pharmaceuticals has its drawbacks, which urges people to seek safer and more effective α-glucosidase inhibitors (Lambrinoudaki et al., 2022; Min et al., 2024). Exploration of natural products as a repository for novel therapeutic agents has been a promising avenue (Zhang et al., 2021; Chen et al., 2022; Wang et al., 2022; Zhou et al., 2022). The active constituents

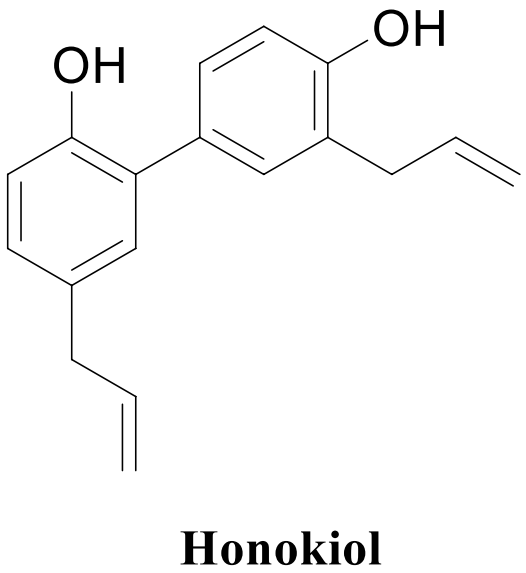


FIGURE 1
Structure of honokiol.

have demonstrated a diverse array of pharmacological effects, including anti-oxidant (Sun et al., 2020; Tao et al., 2022; Tang et al., 2023), anti-tumor (Chen et al., 2023; Liang et al., 2023; Song et al., 2023), anti-inflammatory (Sun et al., 2020; Wang et al., 2021; Wang et al., 2022), and anti-tissue damage (Shao et al., 2020; Qi et al., 2022; Ding et al., 2023) properties (Wang et al., 2020; Chen et al., 2022; Zang et al., 2022; He et al., 2023). Moreover, a notable advantage of natural products is their generally lower toxicity profiles (Hao et al., 2022; Mao et al., 2022; Wang et al., 2023), which makes them a preferable source for development of α-glucosidase inhibitors.

Honokiol (Figure 1), a naturally occurring compound from *Magnolia obovata* Thunb., has been recognized for its diverse medicinal properties (Zengin et al., 2017; Ma et al., 2023). As a bioactive neolignan, honokiol has demonstrated a range of activities, including anti-cancer, anti-inflammation, and anti-oxidant effects (He et al., 2015; Guo et al., 2021; Niu et al., 2021). In recent research studies, honokiol has garnered significant interest due to its ability to mitigate hyperglycemic conditions, enhance glucose uptake, and inhibit α-glucosidase activity (Bekircan et al., 2015; Pulvirenti et al., 2017; Ahmad et al., 2018). This shows the potential of honokiol as a natural α-glucosidase and hypoglycemic agent.

As far as we know, the detailed inhibitory effects of honokiol on α-glucosidase are still unclear. Hence, the biological activity of honokiol as an α-glucosidase inhibitor was investigated by spectroscopic methods and molecular docking.

## 2 Results and discussion

### 2.1 Inhibitory activity of honokiol on α-glucosidase

First, we assessed the inhibitory activity of honokiol on α-glucosidase, as shown in Figure 2. With an increase in the honokiol concentration, the inhibition rate gradually increased, and its $IC_{50}$ value was calculated to be 317.11 ± 12.86 μM, which was lower than that of acarbose ($IC_{50}$ =

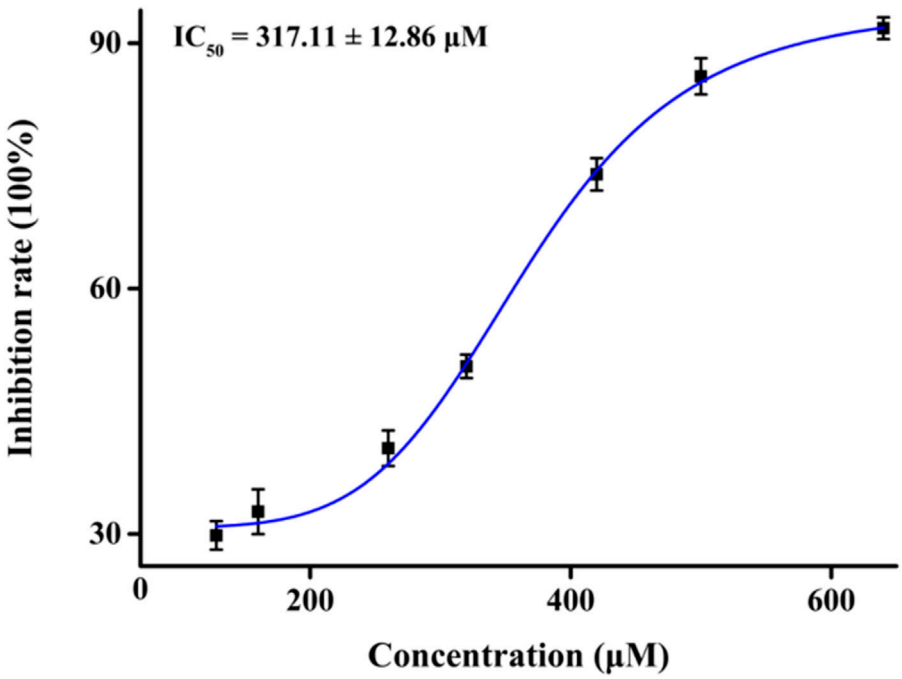


FIGURE 2
Inhibition of honokiol on α-glucosidase.

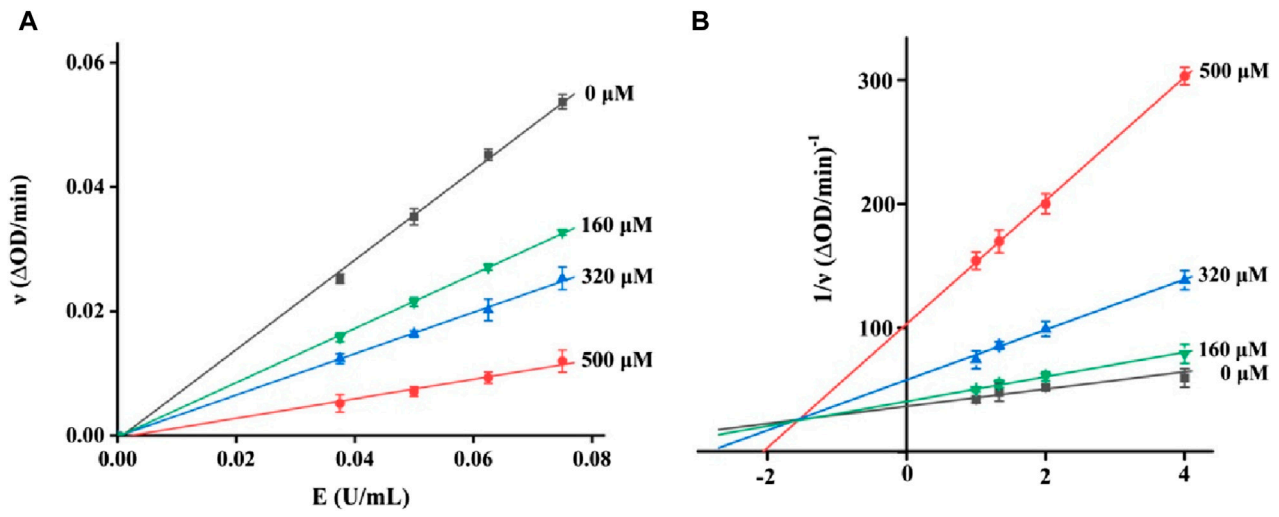


FIGURE 3
**(A)** Plots of the enzyme reaction rate to enzyme concentration **(B)** Lineweaver–Burk plots of the enzyme reaction rate to the substrate concentration.

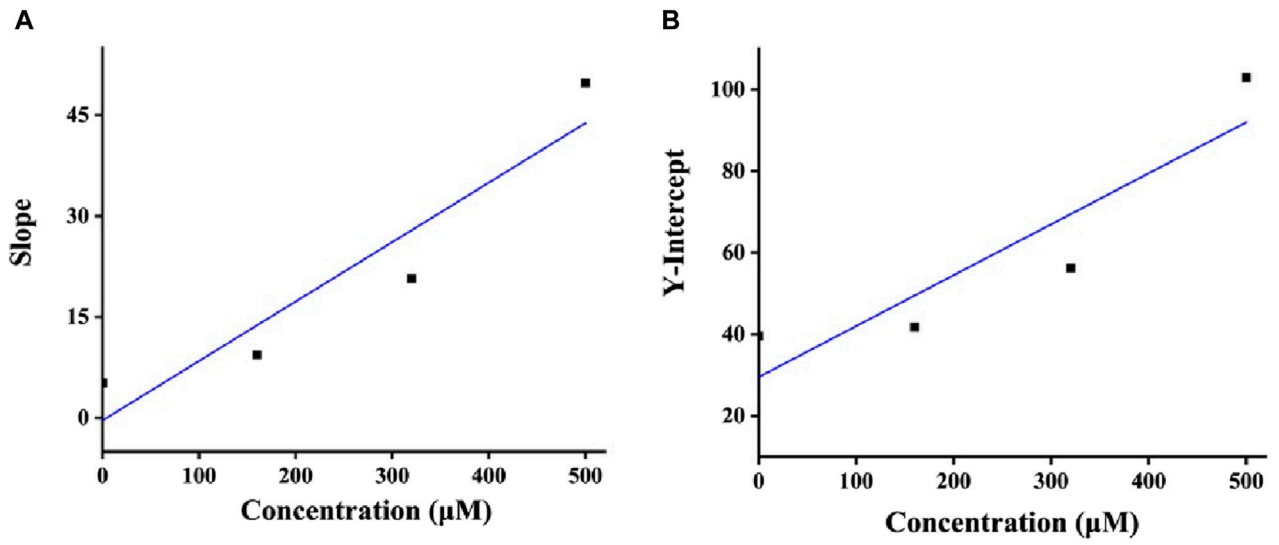


FIGURE 4
**(A,B)** Ki and Kis plots of honokiol.

584.51 ± 8.56 μM). The potential inhibitory activity of honokiol on α-glucosidase might make it a natural hypoglycemic agent.

## 2.2 Kinetic study

It is very important to clarify the inhibition mode of inhibitors against enzymes for understanding the performance of inhibitors. Hence, the kinetics of honokiol on α-glucosidase were studied. In the plots of the enzyme reaction rate to the enzyme concentration under honokiol (Figure 3A), all lines passed the origin point. This indicated honokiol as a reversible α-glucosidase inhibitor. In the Lineweaver–Burk plots of the enzyme reaction rate to substrate concentration under honokiol (Figure 3B), all lines intersected at the second quadrant. Their slope and *Y*-intercept were both changed with honokiol concentration. Therefore, it is evident that honokiol was a mixed-type inhibitor.

As a mixed-type inhibitor, honokiol was determined to have an inhibition constant. The fitting plot of slope and *Y*-intercept *versus* honokiol (Figures 4A,B) yielded Ki and Kis values of 16.03 and 285.22 μM, respectively. The lower Ki indicated that honokiol tended to bind to substrates.

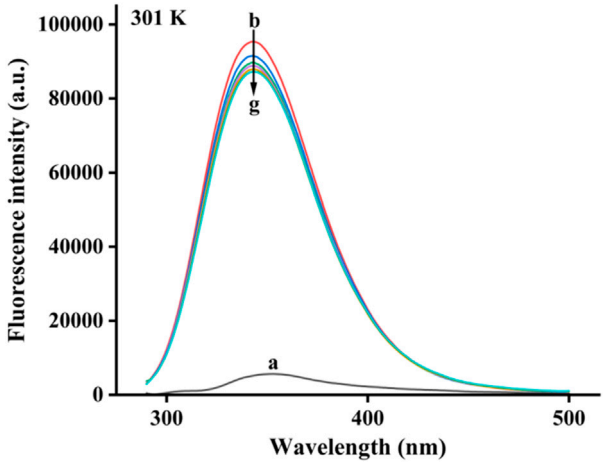


FIGURE 5
Fluorescence spectra of α-glucosidase binding by honokiol.

## 2.3 Fluorescence assay

Based on the fluorescence characteristics of α-glucosidase, the binding of honokiol to α-glucosidase was studied by fluorescence spectroscopy at 298K. In Figure 5, α-glucosidase presented fluorescence with a characteristic peak at 340 nm, while honokiol had very weak fluorescence at 340 nm. With continuous addition of honokiol, α-glucosidase fluorescence gradually decreased. This phenomenon indicated that there were binding interactions between honokiol and α-glucosidase, which could quench the endogenous fluorescence of α-glucosidase.

Subsequently, the binding of honokiol to α-glucosidase was further described by 3D fluorescence (Figures 6A,B). The 3D fluorescence spectra of α-glucosidase had two characteristic peaks due to intrinsic fluorophores and the backbone, which could be reduced by the addition of honokiol. This result was consistent with that of the fluorescence assay.

## 2.4 CD spectra

CD spectra were investigated to evaluate the specific effects of honokiol on α-glucosidase structure. α-Glucosidase showed its own unique CD spectra at 210–222 nm (Figure 7). Honokiol treatment changed the CD spectra of α-glucosidase (Figure 7), which further indicated the binding of honokiol to α-glucosidase. The conformational changes in α-glucosidase were obtained from CD spectral data and showed that honokiol treatment resulted in changes in the α-glucosidase secondary structure content (Table 1). This might be the reason for the inhibition of honokiol on α-glucosidase.

## 2.5 Molecular docking

The docking interaction of honokiol with α-glucosidase was simulated. In a 3D view of docking (Figure 8A), honokiol was bound into the α-glucosidase active pocket, with a binding energy of −4.9 kcal/mol, presumably binding to amino acid residues in the pocket. Further analysis (Figure 8B) found that honokiol formed hydrogen bonds with GLU-276 (2.5 Å), ASP-349 (2.0 Å), and ASP214 (1.9 Å). Moreover, honokiol formed hydrophobic bonds with TYR-71, TYR-313, LEU-437, ARG-312, and PHE300. These main interactions between honokiol and α-glucosidase might be the reason for honokiol's inhibitory effect on α-glucosidase activity.

# 3 Materials and methods

## 3.1 α-Glucosidase inhibitory activity

α-Glucosidase was dissolved in PBS (pH 6.8), and honokiol was dissolved in DMSO. Honokiol solution and α-glucosidase solution were mixed and incubated for an appropriate time, and then a certain amount of substrate p-nitrophenyl-α-D-galactopyranoside

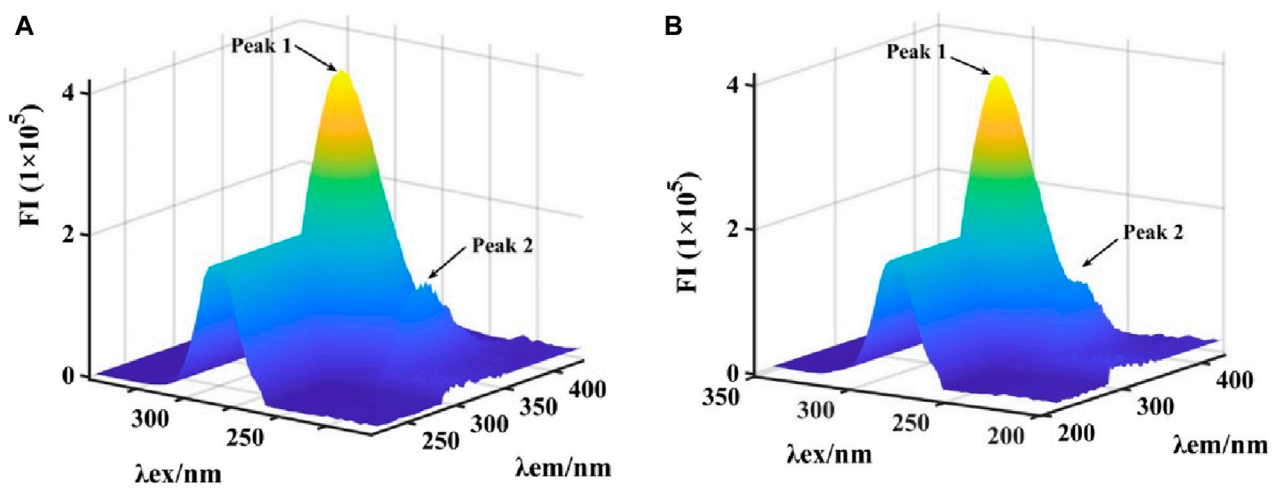


FIGURE 6
**(A,B)** 3D fluorescence spectra of α-glucosidase binding by honokiol.

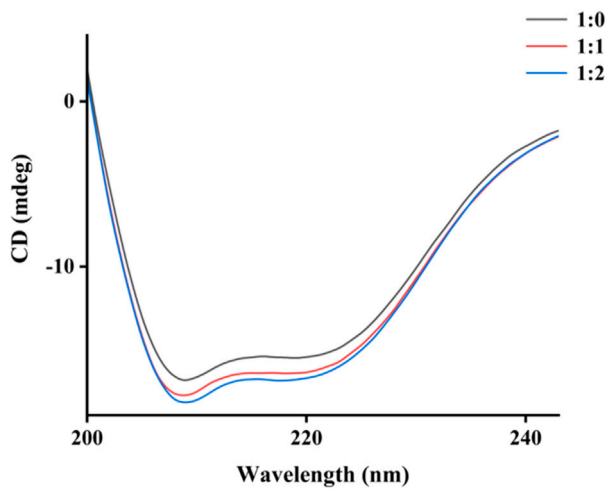


FIGURE 7
CD spectra of α-glucosidase binding by honokiol.

(pNPG) was added. Then, the absorbance of the solution at 405 nm was determined. Then, the α-glucosidase inhibitory effect of honokiol was obtained (Xu et al., 2020; Ali et al., 2023).

## 3.2 Inhibition kinetics

The test procedure for inhibition kinetics followed the same protocol as the α-glucosidase inhibition assay. For enzyme kinetics, the absorbance of a mixture with different concentrations of honokiol and α-glucosidase was recorded. For substrate kinetics, the absorbance of the mixture with different concentrations of honokiol and substrate was recorded (Kaur et al., 2021).

## 3.3 Fluorescence

Fluorescence measurements of α-glucosidase were conducted at an excitation wavelength of 280 nm (Wu et al., 2024). Then, honokiol was added step by step, and the corresponding fluorescence of the mixture was recorded.

## 3.4 3D fluorescence

3D fluorescence spectra of α-glucosidase with/without honokiol were recorded. The concentration of α-glucosidase was 0.1 mg/mL. Honokiol (0.25 μM) was added to α-glucosidase to prepare their mixture.

TABLE 1 Conformational changes in α-glucosidase by honokiol.

| [Enzyme]: [Honokiol] | α-Helix (%) | β-Sheet (%) | β-Turn (%) | Random coil (%) |
|---|---|---|---|---|
| 1: 0 | 16.7 | 37.6 | 20.0 | 56.2 |
| 1: 1 | 17.0 | 36.5 | 19.9 | 59.4 |
| 1: 2 | 17.2 | 36.1 | 19.8 | 61.5 |

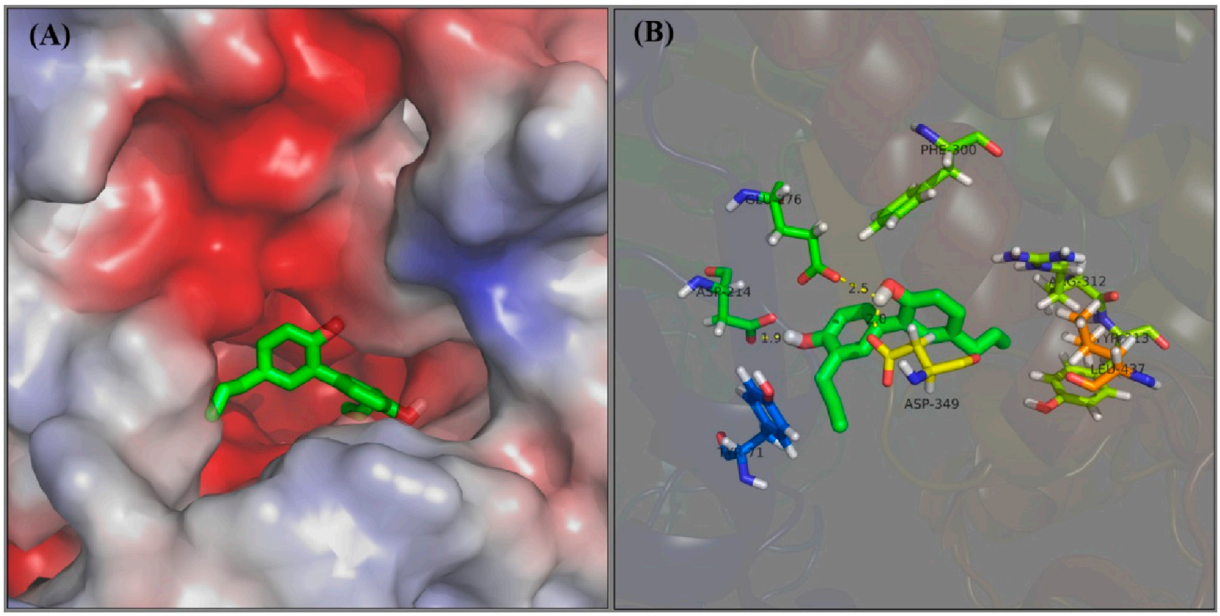


FIGURE 8
**(A,B)** Docking of honokiol with α-glucosidase in 3D and 2D view.

### 3.5 CD spectra

CD spectra of α-glucosidase with/without honokiol were also recorded. The concentration of α-glucosidase was 0.1 mg/mL. Honokiol was added to α-glucosidase to prepare their mixture. The data were analyzed using CDNN software (Li et al., 2024).

### 3.6 Molecular docking

The docking of honokiol with α-glucosidase was conducted using SYBYL (Deng et al., 2022; Patil et al., 2022). After being imported into the software, the honokiol structure was hydro-treated and charge-treated. Then, the homology model of α-glucosidase was also prepared by hydro-treating and charge-treating. Due to the absence of ligands in the protein, the active pocket of α-glucosidase was produced. Then, the docking of honokiol with α-glucosidase was performed in the default mode.

### 3.7 Statistical analysis

All data were presented as mean ± SD. One-way ANOVA was performed to evaluate the differences between the groups (Zhao et al., 2017; Zhang et al., 2021; Zheng et al., 2021; Sheng et al., 2023). $p < 0.05$ was considered significant.

## 4 Conclusion

As a naturally occurring compound from *Magnolia obovata Thunb.*, honokiol was ascertained for its anti-α-glucosidase activity and inhibition mechanism. So we designed experiments to clarify these properties. Activity assays showed that honokiol was a reversible mixed-type inhibitor of α-glucosidase, and its $IC_{50}$ value was 317.11 ± 12.86 μM. Fluorescence, 3D fluorescence, and CD spectra investigations indicated that the binding of honokiol to α-glucosidase caused a reduction in α-glucosidase activity. Docking simulated the detailed interactions between honokiol and α-glucosidase.

## Data availability statement

The raw data supporting the conclusion of this article will be made available by the authors, without undue reservation.

## Author contributions

HZ: investigation, project administration, writing–original draft, and writing–review and editing. XZ: investigation, project administration, and writing–original draft.

## Funding

The author(s) declare that no financial support was received for the research, authorship, and/or publication of this article.

## Conflict of interest

The authors declare that the research was conducted in the absence of any commercial or financial relationships that could be construed as a potential conflict of interest.

## Publisher's note

All claims expressed in this article are solely those of the authors and do not necessarily represent those of their affiliated organizations, or those of the publisher, the editors, and the reviewers. Any product that may be evaluated in this article, or claim that may be made by its manufacturer, is not guaranteed or endorsed by the publisher.

## References

Ahmad, S., Nadeem, H., Muhammad, S. A., Naz, S., Imran, M., and Saeed, A. (2018). Synthesis, antimicrobial and α-glucosidase inhibitory potential of Mannich bases of mercapto oxadiazoles and their molecular docking studies. *Farmacia* 66, 708–717. doi:10.31925/farmacia.2018.4.22

Ali, A., Ali, A., Asati, V., Kaya, S., and Ahsan, M. J. (2023). Design, synthesis and anti-hyperglycemic assessments of novel 5-benzylidenethiazolidine-2,4-dione derivatives as PPAR-γ agonist. *J. Indian Chem. Soc.* 100, 101100. doi:10.1016/j.jics.2023.101100

Basri, R., Ullah, S., Khan, A., Mali, S. N., Abchir, O., Chtita, S., et al. (2023). Synthesis, biological evaluation and molecular modelling of 3-Formyl-6-isopropylchromone derived thiosemicarbazones as α-glucosidase inhibitors. *Bioorg. Chem.* 139, 106739. doi:10.1016/j.bioorg.2023.106739

Bekircan, O., Ülker, S., and Menteşe, E. (2015). Synthesis of some novel heterocylic compounds derived from 2-[3-(4-chlorophenyl)-5-(4-methoxybenzyl)-4H-1, 2, 4-triazol-4-yl] acetohydrazide and investigation of their lipase and α-glucosidase inhibition. *J. Enzyme Inhib. Med. Chem.* 30, 1002–1009. doi:10.3109/14756366.2014.1003213

Chen, J., Cao, D., Jiang, S., Liu, X., Pan, W., Cui, H., et al. (2022). Triterpenoid saponins from Ilex pubescens promote blood circulation in blood stasis syndrome by regulating sphingolipid metabolism and the PI3K/AKT/eNOS signaling pathway. *Phytomedicine* 104, 154242. doi:10.1016/j.phymed.2022.154242

Chen, W., Zhang, S., Pan, S., Wang, Z., Xu, J., Sheng, X., et al. (2022). α-Mangostin treats early-stage adjuvant-induced arthritis of rat by regulating the CAP-SIRT1 pathway in macrophages. *Drug Des. Dev. Ther.* 16, 509–520. doi:10.2147/DDDT.S348836

Chen, Y., Yin, S., Liu, R., Yang, Y., Wu, Q., Lin, W., et al. (2023). β-Sitosterol activates autophagy to inhibit the development of hepatocellular carcinoma by regulating the complement C5a receptor 1/alpha fetoprotein axis. *Eur. J. Pharmacol.* 957, 175983. doi:10.1016/j.ejphar.2023.175983

Davies, M. J., Aroda, V. R., Collins, B. S., Gabbay, R. A., Green, J., Maruthur, N. M., et al. (2022). Management of hyperglycaemia in type 2 diabetes, 2022. A consensus report by the American diabetes association (ADA) and the European association for the study of diabetes (EASD). *Diabetologia* 65, 1925–1966. doi:10.1007/s00125-022-05787-2

Deng, X., Ke, J., Zheng, Y., Li, D., Zhang, K., Zheng, X., et al. (2022). Synthesis and bioactivities evaluation of oleanolic acid oxime ester derivatives as α-glucosidase and a-amylase inhibitors. *J. Enzyme Inhib.* 37, 451–461. doi:10.1080/14756366.2021.2018682

Ding, D., Shen, X., Yu, L., Zheng, Y., Liu, Y., Wang, W., et al. (2023). Timosaponin BII inhibits TGF-β mediated epithelial-mesenchymal transition through Smad-dependent pathway during pulmonary fibrosis. *Phytother. Res.* 37, 2787–2799. doi:10.1002/ptr.7774

Ding, M., Tang, Z., Liu, W., Shao, T., Yuan, P., Chen, K., et al. (2021). Burdock fructooligosaccharide attenuates high glucose-induced apoptosis and oxidative stress injury in renal tubular epithelial cells. *Front. Pharmacol.* 12, 784187. doi:10.3389/fphar.2021.784187

ElSayed, N. A., Aleppo, G., Aroda, V. R., Bannuru, R. R., Brown, F. M., Bruemmer, D., et al. (2023). 2. Classification and diagnosis of diabetes: standards of care in diabetes-2023. *Diabetes Care* 46, S19–S40. doi:10.2337/dc23-S002

Feng, M., Liang, B., Sun, J., Min, X., Wang, S., Lu, Y., et al. (2024). Synthesis, anti-α-glucosidase activity, inhibition interaction, and anti-diabetic activity of novel cryptolepine derivatives. *J. Mol. Struct.* 1310, 138311. doi:10.1016/j.molstruc.2024.138311

Guo, Y., Hou, E., Wen, T., Yan, X., Han, M., Bai, L., et al. (2021). Development of membrane-active honokiol/magnolol amphiphiles as potent antibacterial agents against methicillin-resistant *Staphylococcus aureus* (MRSA). *J. Med. Chem.* 64, 12903–12916. doi:10.1021/acs.jmedchem.1c01073

Hameed, S., Seraj, F., Rafique, R., Chigurupati, S., Wadood, A., Ur Rehman, A., et al. (2019). Synthesis of benzotria-zoles derivatives and their dual potential as α-amylase and α-glucosidase inhibitors *in vitro*: structure-activity relationship, molecular docking, and kinetic studies. *Eur. J. Med. Chem.* 183, 111677. doi:10.1016/j.ejmech.2019.111677

Hao, J., Bei, J., Li, Z., Han, M., Ma, B., Ma, P., et al. (2022). Qing`e pill inhibits osteoblast ferroptosis via ATM serine/threonine kinase (ATM) and the PI3K/AKT pathway in primary osteoporosis. *Front. Pharmacol.* 13, 902102. doi:10.3389/fphar.2022.902102

He, L., Fan, T., Hu, J., and Zhang, L. (2015). Polyethylene glycol-based ultrasound-assisted extraction of magnolol and honokiol from Cortex Magnoliae Officinalis. *Nat. Prod. Res.* 29, 31–36. doi:10.1080/14786419.2014.955800

He, X., Liu, G., Chen, X., Wang, Y., Liu, R., Wang, C., et al. (2023). Pharmacokinetic and pharmacodynamic interactions between henagliflozin, a novel selective SGLT-2 inhibitor, and warfarin in healthy Chinese subjects. *Clin. Ther.* 45, 655–661. doi:10.1016/j.clinthera.2023.06.002

Hu, C., Liang, B., Sun, J., Li, J., Xiong, Z., Wang, S., et al. (2024). Synthesis and biological evaluation of indole derivatives containing thiazolidine-2,4-dione as α-glucosidase inhibitors with antidiabetic activity. *Eur. J. Med. Chem.* 264, 115957. doi:10.1016/j.ejmech.2023.115957

Hu, C., Wang, Y., Xi, Y., and Yao, X. (2020). Dapagliflozin therapy curative effect observation on nonalcoholic fatty liver disease in patients with type 2 diabetes mellitus. *Indian J. Pharm. Sci.* 82, 122–129. doi:10.36468/pharmaceutical-sciences.spl.155

Jiang, Y., Li, W., Wang, J., and Wang, G. (2020). Cardiac dysfunction is attenuated by ginkgolide B *via* reducing oxidative stress and fibrosis in diabetic rats. Iran. *J. Basic Med. Sci.* 23, 1078–1084. doi:10.22038/ijbms.2020.44210.10358

Kaur, R., Kumar, R., Dogra, N., Kumar, A., Yadav, A. K., and Kumar, M. (2021). Synthesis and studies of thiazolidinedione-isatin hybrids as α-glucosidase inhibitors for management of diabetes. *Future Med. Chem.* 13, 457–485. doi:10.4155/fmc-2020-0022

Khan, S., Ullah, H., Rahim, F., Nawaz, M., Hussain, R., and Rasheed, L. (2022). Synthesis, *in vitro* α-amylase, α-glucosidase activities and molecular docking study of new benzimidazole bearing thiazolidinone derivatives. *J. Mol. Struct.* 1269, 133812. doi:10.1016/j.molstruc.2022.133812

Lambrinoudaki, I., Paschou, S. A., Armeni, E., and Goulis, D. G. (2022). The interplay between diabetes mellitus and menopause: clinical implications. *Nat. Rev. Endocrinol.* 18, 608–622. doi:10.1038/s41574-022-00708-0

Li, M., Li, H., Min, X., Sun, J., Liang, B., Xu, L., et al. (2024). Identification of 1,3,4-thiadiazolyl-containing thiazolidine-2,4-dione derivatives as novel PTP1B inhibitors with antidiabetic activity. *J. Med. Chem.* 67, 8406–8419. doi:10.1021/acs.jmedchem.4c00676

Li, M., Sun, J., Liang, B., Min, X., Hu, J., Wu, R., et al. (2024). Thiazolidine-2,4-dione derivatives as potential α-glucosidase inhibitors: synthesis, inhibitory activity, binding interaction and hypoglycemic activity. *Bioorg. Chem.* 144, 107177. doi:10.1016/j.bioorg.2024.107177

Liang, T., Wang, F., Elhassan, R., Cheng, Y., Tang, X., Chen, W., et al. (2023). Targeting histone deacetylases for cancer therapy: trends and challenges. *Acta Pharm. Sin. B* 13, 2425–2463. doi:10.1016/j.apsb.2023.02.007

Lin, J., Xiao, D., Lu, L., Liang, B., Xiong, Z., and Xu, X. (2023). New β-carboline derivatives as potential α-glucosidase inhibitor: synthesis and biological activity evaluation. *J. Mol. Struct.* 1283, 135279. doi:10.1016/j.molstruc.2023.135279

Ma, M., Wei, N., Yang, J., Ding, T., Song, A., Chen, L., et al. (2023). Schisandrin B promotes senescence of activated hepatic stellate cell via NCOA4-mediated ferritinophagy. *Pharm. Biol.* 61, 621–629. doi:10.1080/13880209.2023.2189908

Mao, Y., Xu, R., Li, Y., and Jiang, F. (2022). Baicalin ameliorates preeclampsia *in vitro* by regulating the miRNA-19a/PTEN axis. *Lat. Am. J. Pharm.* 41, 2254–2265.

Min, X., Guo, S., Lu, Y., and Xu, X. (2024). Investigation on the inhibition mechanism and binding behavior of cryptolepine to α-glucosidase and its hypoglycemic activity by multi-spectroscopic method. *J. Lumin.* 269, 120437. doi:10.1016/j.jlumin.2024.120437

Niu, L., Hou, Y., Jiang, M., and Bai, G. (2021). The rich pharmacological activities of Magnolia officinalis and secondary effects based on significant intestinal contributions. *J. Ethnopharmacol.* 281, 114524. doi:10.1016/j.jep.2021.114524

Patil, V. M., Tilekar, K. N., Upadhyay, N. M., and Ramaa, C. S. (2022). Synthesis, *in-vitro* evaluation and molecular docking study of N-substituted thiazolidinediones as α-glucosidase inhibitors. *ChemistrySelect* 7, e202103848. doi:10.1002/slct.202103848

Pulvirenti, L., Muccilli, V., Cardullo, N., Spatafora, C., and Tringali, C. (2017). Chemoenzymatic synthesis and α-glucosidase inhibitory activity of dimeric neolignans inspired by magnolol. *J. Nat. Prod.* 80, 1648–1657. doi:10.1021/acs.jnatprod.7b00250

Qi, X., Zheng, S., Ma, M., Lian, N., Wang, H., Chen, L., et al. (2022). Curcumol suppresses CCF-mediated hepatocyte senescence through blocking LC3B-Lamin B1 interaction in alcoholic fatty liver disease. *Front. Pharmacol.* 13, 912825. doi:10.3389/fphar.2022.912825

Shao, X., Li, B., Shen, J., Wang, Q., Chen, S., Jiang, X., et al. (2020). Ghrelin alleviates traumatic brain injury-induced acute lung injury through pyroptosis/NF-κB pathway. *Int. Immunopharmacol.* 79, 106175. doi:10.1016/j.intimp.2019.106175

Sheng, B., Lai, N., Tao, T., Chen, X., Gao, S., Zhu, Q., et al. (2023). Diagnosis potential of subarachnoid hemorrhage using miRNA signatures isolated from plasma-derived extracellular vesicles. *Front. Pharmacol.* 14, 1090389. doi:10.3389/fphar.2023.1090389

Song, A., Ding, T., Wei, N., Yang, J., Ma, M., Zheng, S., et al. (2023). Schisandrin B induces HepG2 cells pyroptosis by activating NK cells mediated anti-tumor immunity. *Toxicol. Appl. Pharmacol.* 472, 116574. doi:10.1016/j.taap.2023.116574

Song, J., Xu, H., Zhang, W., Yang, C., Li, L., and Luan, J. (2022). Impact of solute carrier family 47 member 1 gene polymorphism detection on therapeutic effect of diabetes. *Int. J. Pharmacol.* 18, 398–406. doi:10.3923/ijp.2022.398.406

Sun, S., Li, S., Du, Y., Wu, C., Zhang, M., Li, J., et al. (2020a). Anti-inflammatory effects of the root, stem and leaf extracts of *Chloranthus serratus* on adjuvant-induced arthritis in rats. *Pharm. Biol.* 58, 528–537. doi:10.1080/13880209.2020.1767159

Sun, S., Wang, Y., Du, Y., Sun, Q., He, L., Zhu, E., et al. (2020b). Oxidative stress-mediated hepatotoxicity in rats induced by ethanol extracts of different parts of Chloranthus serratus. *Pharm. Biol.* 58, 1277–1289. doi:10.1080/13880209.2020.1859552

Tang, Z., Zhang, M., Gao, L., Bao, Y., Li, P., Wang, M., et al. (2023). Optimal extraction of polysaccharides from Stevia rebaudiana roots for protection against hydrogen peroxide-induced oxidative damage in RAW264.7 cells. *Nat. Prod. Res.*, 2263905. doi:10.1080/14786419.2023.2263905

Tao, Z., Li, T., and Wei, S. (2022). Silymarin prevents iron overload induced bone loss by inhibiting oxidative stress in an ovariectomized animal model. *Chem. Biol. Interact.* 366, 110168. doi:10.1016/j.cbi.2022.110168

Wang, H., Chen, Y., Wang, L., Liu, Q., Yang, S., and Wang, C. (2023). Advancing herbal medicine: enhancing product quality and safety through robust quality control practices. *Front. Pharmacol.* 14, 1265178. doi:10.3389/fphar.2023.1265178

Wang, J., Li, D., Ni, W., Qin, X., Liu, H., Yu, L. L., et al. (2020). Molecular networking uncovers steroidal saponins of Paris tengchongensis. *Fitoterapia* 145, 104629. doi:10.1016/j.fitote.2020.104629

Wang, R., Li, D., Hu, Y., Liao, Q., Jiang, T., Olatunji, O. J., et al. (2021). Qing-Luo-Yin alleviated monocytes/macrophages-mediated inflammation in rats with adjuvant-induced arthritis by disrupting their interaction with (Pre)-Adipocytes through PPAR-γ signaling. *Drug. Des. Dev. Ther.* 15, 3105–3118. doi:10.2147/DDDT.S320599

Wang, X., Zhou, D., Zhou, W., Liu, J., Xue, Q., Huang, Y., et al. (2022). Clematichinenoside AR inhibits the pathology of rheumatoid arthritis by blocking the circPTN/miR-145-5p/FZD4 signal axis. *Int. Immunopharmacol.* 113, 109376. doi:10.1016/j.intimp.2022.109376

Wang, Y., Wu, H., Han, Z., Sheng, H., Wu, Y., Wang, Y., et al. (2022). Guhong injection promotes post-stroke functional recovery via attenuating cortical inflammation and apoptosis in subacute stage of ischemic stroke. *Phytomedicine* 99, 154034. doi:10.1016/j.phymed.2022.154034

Wu, S., Tang, J., Zhou, Y., Xu, X., Zhang, H., and Wang, S. (2024). α-Glucosidase inhibition research of derivatives based on 2β-acetoxyferruginol scaffold excluding acetic acid group. *Chin. J. Org. Chem.* 44, 613–621. doi:10.6023/cjoc202307027

Wu, X., Zhu, W., Lu, L., Hu, C., Zheng, Y., Zhang, X., et al. (2023). Synthesis and anti-a-glucosidase activity evaluation of betulinic acid derivatives. *Arab. J. Chem.* 16, 104659. doi:10.1016/j.arabjc.2023.104659

Xiao, D., Lu, L., Liang, B., Xiong, Z., Xu, X., and Chen, W. (2023). Identification of 1,3,4-oxadiazolyl-containing β-carboline derivatives as novel α-glucosidase inhibitors with antidiabetic activity. *Eur. J. Med. Chem.* 261, 115795. doi:10.1016/j.ejmech.2023.115795

Xing, Y., Liu, B., Wan, S., Cheng, Y., Zhou, S., Sun, Y., et al. (2021). A SGLT2 inhibitor dapagliflozin alleviates diabetic cardiomyopathy by suppressing high glucose-induced oxidative stress *in vivo* and *in vitro*. *Front. Pharmacol.* 12, 708177. doi:10.3389/fphar.2021.708177

Xu, S., He, L., Ding, K., Zhang, L., Xu, X., Wang, S., et al. (2020). Tanshinone IIA ameliorates streptozotocin-induced diabetic nephropathy, partly by attenuating PERK pathway-induced fibrosis. *Drug Des. Dev. Ther.* 14, 5773–5782. doi:10.2147/DDDT.S257734

Xu, X., Deng, X., Chen, J., Liang, Q., Zhang, K., Li, D., et al. (2020). Synthesis and biological evaluation of coumarin derivatives as aglucosidase Inhibitors. *Eur. J. Med. Chem.* 189, 112013. doi:10.1016/j.ejmech.2019.112013

Zang, L., Xu, H., Huanh, C., Wang, C., Wang, R., Chen, R., et al. (2022). A link between chemical structure and biological activity in triterpenoids. *Recent Pat. Anti-Canc* 17, 145–161. doi:10.2174/1574892816666210512031635

Zengin, G., Locatelli, M., Stefanucci, A., Macedonio, G., Mollica, A., Mirzaie, S., et al. (2017). Chemical characterization, antioxidant properties, anti-inflammatory activity, and enzyme inhibition of Ipomoea batatas L. leaf extracts. *Int. J. Food Prop.* 20, 1–13. doi:10.1080/10942912.2017.1357127

Zhang, X., Lu, Y., Li, W., Tao, T., Peng, L., Wang, W., et al. (2021). Astaxanthin ameliorates oxidative stress and neuronal apoptosis via SIRT1/NRF2/Prx2/ASK1/p38 after traumatic brain injury in mice. *Brit. J. Pharmacol.* 178, 1114–1132. doi:10.1111/bph.15346

Zhang, X., Zheng, Y., Hu, C., Wu, X., Lin, J., Xiong, Z., et al. (2022). Synthesis and biological evaluation of coumarin derivatives containing oxime ester as a-glucosidase inhibitors. *Arab. J. Chem.* 15, 104072. doi:10.1016/j.arabjc.2022.104072

Zhang, Y., Zhang, X., Li, H., Zhou, T., Zhou, A., Zhong, Z., et al. (2021). Antidepressant-like effects of helicid on a chronic unpredictable mild stress-induced depression rat model: inhibiting the IKK/IκBα/NF-κB pathway through NCALD to reduce inflammation. *Int. Immunopharmacol.* 93, 107165. doi:10.1016/j.intimp.2020.107165

Zhao, S., Ma, L., Chu, Z., Xu, H., Wu, W., and Liu, F. (2017). Regulation of microglial activation in stroke. *Acta Pharmacol. Sin.* 38, 445–458. doi:10.1038/aps.2016.162

Zheng, Y., Ding, W., Zhang, T., Zhao, Z., Wang, R., Li, Z., et al. (2021). Antimony-induced astrocyte activation via mitogen-activated protein kinase activation-dependent CREB phosphorylation. *Toxicol. Lett.* 352, 9–16. doi:10.1016/j.toxlet.2021.09.006

Zhou, Y., Liu, L., Xiang, R., Bu, X., Qin, G., Dai, J., et al. (2023). Arctigenin mitigates insulin resistance by modulating the IRS2/GLUT4 pathway via TLR4 in type 2 diabetes mellitus mice. *Int. Immunopharmacol.* 114, 109529. doi:10.1016/j.intimp.2022.109529

Zhou, Y., Xiang, R., Qin, G., Ji, B., Yang, S., Wang, G., et al. (2022). Xanthones from *Securidaca inappendiculata Hassk.* attenuate collagen-induced arthritis in rats by inhibiting the nicotinamide phosphoribosyltransferase/glycolysis pathway and macrophage polarization. *Int. Immunopharmacol.* 111, 109137. doi:10.1016/j.intimp.2022.109137

frontiers | Frontiers in Pharmacology

TYPE Original Research
PUBLISHED 20 June 2024
DOI 10.3389/fphar.2024.1392338

Check for updates

OPEN ACCESS

EDITED BY
Xiping Cui,
Guangdong University of Technology, China

REVIEWED BY
Palash Mandal,
Charotar University of Science and Technology, India
Giovanni Tarantino,
University of Naples Federico II, Italy

*CORRESPONDENCE
Ri-Hui Wu,
wyuchemwrh@126.com
Chen Li,
chenli@wyu.edu.cn

†These authors have contributed equally to this work

RECEIVED 27 February 2024
ACCEPTED 15 May 2024
PUBLISHED 20 June 2024

CITATION
Zhang X-M, Huang Y-C, Chen B-Z, Li Q, Wu P-P, Chen W-H, Wu R-H and Li C (2024), Water decoction of *Pericarpium citri reticulatae* and *Amomi fructus* ameliorates alcohol-induced liver disease involved in the modulation of gut microbiota and TLR4/NF-κB pathway. *Front. Pharmacol.* 15:1392338.
doi: 10.3389/fphar.2024.1392338

COPYRIGHT
© 2024 Zhang, Huang, Chen, Li, Wu, Chen, Wu and Li. This is an open-access article distributed under the terms of the Creative Commons Attribution License (CC BY). The use, distribution or reproduction in other forums is permitted, provided the original author(s) and the copyright owner(s) are credited and that the original publication in this journal is cited, in accordance with accepted academic practice. No use, distribution or reproduction is permitted which does not comply with these terms.

# Water decoction of *Pericarpium citri reticulatae* and *Amomi fructus* ameliorates alcohol-induced liver disease involved in the modulation of gut microbiota and TLR4/NF-κB pathway

Xing-Min Zhang[1,2,3†], Yue-Chang Huang[1,2,3†], Bai-Zhong Chen[4], Qian Li[1,2,3], Pan-Pan Wu[1,2,3], Wen-Hua Chen[1,2,3], Ri-Hui Wu[1,2,3]* and Chen Li[1,2,3]*

[1]School of Pharmacy and Food Engineering, Wuyi University, Jiangmen, China, [2]International Healthcare Innovation Institute (Jiangmen), Jiangmen, China, [3]Guangdong Provincial Key Laboratory of Large Animal Models for Biomedicine, Wuyi University, Jiangmen, China, [4]Guangdong Xinbaotang Biotechnology Co., Ltd., Jiangmen, China

**Introduction:** Alcohol consumption alters the diversity and metabolic activities of gut microbiota, leading to intestinal barrier dysfunction and contributing to the development of alcoholic liver disease (ALD), which is the most prevalent cause of advanced liver diseases. In this study, we investigated the protective effects and action mechanism of an aqueous extraction of *Pericarpium citri reticulatae* and *Amomi fructus* (PFE) on alcoholic liver injury.

**Methods:** C57BL/6 mice were used to establish the mouse model of alcoholic liver injury and orally administered 500 and 1,000 mg/kg/d of PFE for 2 weeks. Histopathology, immunohistochemistry, immunofluorescence, Western blotting, qRT-PCR, and 16S rDNA amplicon sequencing were used to analyze the mechanism of action of PFE in the treatment of alcohol-induced liver injury.

**Results:** Treatment with PFE significantly improved alcohol-induced liver injury, as illustrated by the normalization of serum alanine aminotransferase, aspartate aminotransferase, total triglyceride, and cholesterol levels in ALD mice in a dose-dependent manner. Administration of PFE not only maintained the intestinal barrier integrity prominently by upregulating mucous production and tight junction protein expressions but also sensibly reversed the dysregulation of intestinal microecology in alcohol-treated mice. Furthermore, PFE treatment significantly reduced hepatic lipopolysaccharide (LPS) and attenuated oxidative stress as well as inflammation related to the TLR4/NF-κB signaling pathway. The PFE supplementation also significantly promoted the production of short-chain fatty acids (SCFAs) in the ALD mice.

**Conclusion:** Administration of PFE effectively prevents alcohol-induced liver injury and may also regulate the LPS-involved gut–liver axis; this could provide valuable insights for the development of drugs to prevent and treat ALD.

KEYWORDS

***Pericarpium citri reticulatae*, *Amomi fructus*, alcoholic liver disease, gut microbiota, oxidative stress, inflammatory response**

# 1 Introduction

Alcohol use has been reported to cause approximately 3.3 million deaths annually, accounting for about 5.9% of all deaths globally (Thursz et al., 2018). Excessive consumption of alcohol induces alcoholic liver disease (ALD), which has become a major health concern in recent times, and its incidence has increased mainly among the youth (Tarantino et al., 2022). ALD can cause liver fibrosis, cirrhosis, and even liver cancer if appropriate interventions are not implemented (Zhou et al., 2020). Currently, the primary drugs used in the clinical treatment of liver diseases comprise corticosteroids, N-acetylcysteine (NAC), pentoxifylline, and silybin, etc (Ohashi et al., 2018). Among these, silybin is a natural compound known for its potent antioxidant activity and acts as one of the most effective agents in the clinical treatment of ALD with favorable tolerability. However, the limited solubility of silybin hampers its intestinal absorption efficiency and oral bioavailability, resulting in a series of side effects including gastrointestinal discomfort, headache, and pruritus (Bijak, 2017; Federico et al., 2017; Soleimani et al., 2019; Horowitz, 2022). Therefore, development of safer and more effective strategies to prevent and treat ALD holds critical importance.

The gut microbiota play central roles in the regulation of human physiology, metabolism, and nutrition. Alterations in the gut microbial community have been linked with the development of liver diseases induced by heavy drinking (Stärkel et al., 2018; Bajaj, 2019). Numerous studies have shown that alcohol intake can lead to intestinal dysbiosis and increase intestinal permeability (Konturek et al., 2018). Gut dysbiosis has been demonstrated to increase gut-derived endotoxins, such as lipopolysaccharide (LPS), and cause hepatic inflammation in alcohol-induced liver injuries (An et al., 2022). LPS can activate the toll-like receptor-4 (TLR4) and initiate a signaling cascade that results in the activation of the transcription factor nuclear factor-κB (NF-κB) and production of inflammatory cytokines (Wang et al., 2020a). The release of proinflammatory cytokines, such as tumor necrosis factor-α (TNF-α), interleukin-1β (IL-1β), and interleukin-6 (IL-6), can also be aggravated by excess reactive oxygen species (ROS) induced by alcohol exposure (O'Shannessy et al., 2015). Moreover, the consumption of alcohol disrupts fat metabolism by shifting the primary fuel source from fatty acids to ethanol, resulting in reduced oxidation of fatty acids and increased hepatic accumulation of fat (You and Arteel, 2019; Jeon and Carr, 2020). Controlling the origins of inflammation and regulating fat metabolism may therefore present viable strategies for ALD treatment.

Over the past few decades, numerous natural products and their derivatives have been shown to exhibit excellent biological activities against diabetes and liver diseases (Hu et al., 2024; Li et al., 2024). In particular, several natural products have been used in various traditional practices to prevent and treat ALD (Zhang et al., 2021a; Sun et al., 2023) owing to their minimal toxicity and comprehensive efficacy. Notably, different kinds of traditional Chinese medicines (TCMs), including the Jianpi Liqi Huoxue decoction, *Pueraria lobata*, and semen hoveniae extract, as well as some natural products like costunolide, *Coprinus comatus* polysaccharide, and Antarctic krill oil have been reviewed and demonstrated to improve alcohol-induced liver injury and steatosis. These effects have been shown to be closely associated with modulation of gut microbiota, suggesting that targeted modulation of gut microbiota by TCMs and natural products may be beneficial for ALD therapy (Zhu et al., 2023). *Pericarpium citri reticulatae* (PCR) and *Amomi fructus* (FA) are two commonly known medicinal and food homologous plants that are abundant in active ingredients, such as polyphenols, polysaccharides, and flavones. These main active ingredients have shown various excellent hepatoprotective properties in different environments. For instance, flavonoid-enriched PCR extracts have been found to inhibit liver injuries induced by different factors like cyclophoshamide (CTX) and $CCl_4$ (Gao et al., 2023). Another recent study has systematically explored the mechanism of *Citri Reticulatae Pericarpium* as anti-liver injury approach, independently from the damage origin (Wu et al., 2021). Our previous study also revealed that polysaccharides from PCR could effectively improve high-fat-diet-induced liver steatosis by reshaping the gut microbiota in mice (Li et al., 2023). FA is widely used as an anti-inflammatory TCM in the treatment of gastrointestinal diseases owing to its capacity for heat clearing (Cai et al., 2021). Volatile oils from FA have been found to not only prevent 5-fluorouracil-induced intestinal mucositis by reducing the abundance of pathogenic bacteria and increasing the amount of probiotics (Zhang et al., 2017) but also inhibit non-alcoholic fatty liver disease (NAFLD) via the gut–liver axis (Lu et al., 2018). These studies have expanded the applications of PCR and FA in the study of TCMs. Importantly, PCR and FA act as a classical herb pair in TCM and have been used for thousands of years to clinically reinforce "qi," invigorate the spleen, dry dampness, eliminate phlegm, and promote urination. There is increasing evidence supporting the fact that there may be various common mechanisms underlying both ALD and NAFLD (Tarantino and Citro, 2024). The hepatoprotective effects of PCR and FA on non-alcoholic liver injury have been demonstrated individually; however, the potentially synergistic effects of these two food-homologous plants against alcoholic liver injury remain unclear.

In the present study, *in vitro* enzyme experimental models were established to optimize the combination of PCR and FA (PFE). The synergistic effects of PCR and FA against alcoholic liver injury were then investigated in alcohol-treated mice. Classical molecular biology techniques were used to reveal the hepatoprotective potential mechanisms of PFE. These findings are expected to provide novel insights into the prevention and treatment of ALD.

# 2 Materials and methods

## 2.1 PFE extraction

PCR (collected in the year 2019) was provided by Guangdong Xinbaotang Biotechnology Co., Ltd. (Jiangmen, China). FA was obtained from Guangdong Huiqun Traditional Chinese Medicine Slices Co., Ltd. (Shantou, China). The PCR and FA samples were identified by Prof. Li-She Gan of Wuyi University for authenticity. Extractions of different ratios of PCR and FA were prepared (1:1, 1:2, and 2:1 by weight) in a 1:20 ratio of material to liquid. The mixture was soaked in water for 1 h and decocted for another 1 h. The obtained filtrates were diluted with 10 times the volume of water and decocted for another 30 min before filtering to obtain another

filtrate. These diluted filtrates were combined and dehydrated using a rotary evaporator (R-210, Buchi Labortechnik AG, Switzerland), followed by drying in a lyophilizer (Jiangsu Saifei Medical Device Co., Ltd., Jiangsu, China).

## 2.2 Determination of *in vitro* enzymatic and antioxidant activities

Alpha-diphenyl-β-picrylhydrazyl (DPPH) and 2,2-azino-bis (3-ethylbenzothiazoline-6-sulfonic acid) (ABTS) were used to evaluate the antioxidant capacity of PFE according to the methods reported in literature with slight modifications (Liu et al., 2022a). Vitamin C (VC) was used as the positive control. The activities of alcohol dehydrogenase (ADH) and acetaldehyde dehydrogenase (ALDH) were determined using commercially available kits according to the manufacturer's instructions, for which HaiWangJinZunPian (HWJZP) was used as the positive control.

## 2.3 Experimental design and drug administration

Seven-week-old male C57BL/6 mice (18–20 g bodyweight) were purchased from Zhuhai BesTest Bio-Tech Co., Ltd. (Zhuhai, China). The mice were housed in a specific-pathogen-free (SPF) facility under controlled conditions at a temperature of 25°C ± 2°C, light/dark cycle of 12/12 h, and relative humidity of 50% ± 10%. The mice were allowed free access to water and a standard diet *ad libitum*. After 1 week of adaptation, all animals were randomly assigned into five groups as follows: normal control group (NC), model group (Alcohol), silybin group (Sly), low-dose group (PFE-L, 500 mg/kg/d), and high-dose group (PFE-H, 1,000 mg/kg/d). Intragastric administration was performed once daily with sterile water or silybin at a dosage of 100 mg/kg or PFE at dosages of 500 mg/kg or 1,000 mg/kg for 14 days. For the alcohol exposure, from day 8, the mice were orally administered 20% alcohol (3 days), 40% alcohol (2 days), and 50% alcohol (2 days). Twelve hours after the last alcohol administration, the mice were humanely euthanized with $CO_2$, and the serum, liver, and ileum were collected for further analyses. All animal-related experiments were ethically approved by the Committee on the Ethics of Animal Experiments of the International Healthcare Innovation Institute (Jiangmen, China) and consistently conducted in accordance with the institutional Guidelines for the Care and Use of Laboratory Animals.

## 2.4 Biochemical analysis

The blood samples were centrifuged at 3,500 rpm for 10 min at 4°C to collect the sera. The liver tissues were homogenated with saline in a ratio of 1:9 and centrifuged at 3,500 rpm for 10 min to obtain the supernatant. The levels of alanine aminotransferase (ALT) and aspartate aminotransferase (AST) (Mindray Bio-Medical Electronics Co., Ltd., Shenzhen, China) were determined as per previous methods with slight adjustments (Wang et al., 2021a). The total triglyceride (TG), total cholesterol (TC), high-density lipoprotein cholesterol (HDL-C), and low-density lipoprotein cholesterol (LDL-C) levels (Mindray Bio-Medical Electronics Co., Ltd., Shenzhen, China) in the serum or liver were tested as per previously described methods (Shuai et al., 2021; Zhang et al., 2023b). The malondialdehyde (MDA), glutathione (GSH), superoxide dismutase (SOD), and glutathione peroxidase (GSH-Px) levels were determined using commercially available kits (Nanjing Jiancheng Bioengineering Institute, Nanjing, China) according to reported methods with slight modifications (Xing et al., 2021; Liu et al., 2023). The LPS, TNF-α, IL-6, and IL-1β levels in the liver samples were analyzed with ELISA kits (Ruida Henghui Technology Development Co., Ltd., Beijing, China) as per previously reported methods with slight modifications (Yang et al., 2020; Li et al., 2021a).

## 2.5 Histopathological analysis

The histopathological examinations were performed according to previous reports (Jiang et al., 2020; Tao et al., 2022). In brief, the liver and ileum tissues were fixed in 4% paraformaldehyde for 24 h and prepared for paraffin sectioning and cryosectioning. Then, the 5-μm paraffin sections were deparaffinized with xylene and rehydrated with gradient alcohol, and 10-μm-thick cryosections were prepared by embedding in Tissue-Tek O.C.T. compound. The paraffin sections and cryosections of the liver and ileum were stained with hematoxylin and eosin (H&E), oil red O, or alcian blue (Servicebio, Wuhan, China), and images were captured with an orthographic biomicroscope (Olympus Corporation, Tokyo, Japan).

## 2.6 Quantitative real-time PCR (qRT-PCR)

The mRNA expressions of the genes were analyzed by qRT-PCR as reported before (Ding et al., 2021; Liu et al., 2022b; Hao et al., 2022). Briefly, the total RNA was extracted from the liver and ileum tissues using TRIzol® Reagent (Life Technology, CA, United States). Then, cDNA synthesis was performed using a cDNA reverse transcription kit (Kailian Biotechnology Co., Ltd., Shengzhen, China) following the manufacturer's instructions. Quantitative real-time PCR (qRT-PCR) analysis was performed using the 2× SYBR Green qPCR Master Mix (Saiweier Biotechnology Co., Ltd., Wuhan, China) with the target primers. The primer sequences of the relevant genes are listed in Table 1. The relative expressions of the target genes were normalized with that of β-actin.

## 2.7 Immunofluorescence (IF) staining

Immunofluorescence staining was performed to detect the expressions of ileal ZO-1 and occludin following previously described methods with slight modifications (Zhang et al., 2020; Zhang et al., 2021b; Zhou et al., 2021). In brief, after deparaffinization of the paraffin sections, antigen retrieval was implemented using ethylenediamine tetraacetic acid (EDTA) buffer (10 mM Tris, 1 mM EDTA, pH 9.0) in a microwave. The antigen-repaired sections were then incubated with primary antibodies ZO-1 and occludin (1:2000; Servicebio, Wuhan,

TABLE 1 Primer sequences of the target genes used for qRT-PCR.

| Primers | Forward primer | Reverse primer |
|---|---|---|
| TNF-α | TAGCCAGGAGGGAGAACAGA | CCAGTGAGTGAAAGGGACAGA |
| IL-1β | GCCCATCCTCTGTGACTCAT | AGGCCACAGGTATTTTGTCG |
| IL-6 | TTCTTGGGACTGATGCTGGTG | CACAACTCTTTTCTCATTTCCACGA |
| IL-10 | AAGAAGGCATGCACAGCTCA | AAGTGGGTGCAGCTGTTCTC |
| IL-18 | ACTGTAGAGATAATGCACCCCG | AGTTACAGCCATACCTCTAGGC |
| Caspase-1 | AGACATCCCACAATGGGCTC | TGAAAATCGAACCTTGCGGAAA |
| NLRP3 | CTCCAACCATTCTCTGACCAG | ACAGATTGAAGTAAGGCCGG |
| iNOS | CGCTTGGGTCTTGTTCACT | TCTTTCAGGTCACTTTGGTA |
| Arginase-1 | GCTTGCTTCGGAACTCAAC | CGCATTCACAGTCACTTAGG |
| Occludin | GCGGAAGAGGTTGACAGTCC | ACTCCCCACCTGTCGTGTAG |
| ZO-1 | CAGCCGCATCTTCTTGTG | AGGAGCGAGACCCCACTAA |
| β-Actin | GGCTGTATTCCCTCCATCG | CCAGTTGGTAACAATGCCATG |

China) overnight at 4°C. After thorough washing steps, secondary horseradish peroxidase (HRP)-conjugated anti-rabbit antibody (Servicebio, Wuhan, China) was incubated at room temperature for 50 min under dark conditions. Following three washes with tris-buffered saline with 0.1% Tween (TBST), the samples were restained with DAPI (Servicebio, Wuhan, China) for 10 min. The slides were viewed under an orthotopic biomicroscope and quantified using ImageJ software (National Institutes of Health, Bethesda, MD, United States).

## 2.8 Immunohistochemical (IHC) staining

Immunohistochemical (IHC) staining of the tissues was performed as per previous studies (Pei et al., 2021; Chen et al., 2022). Briefly, the deparaffinized sections were incubated in 3% hydrogen peroxide solution at room temperature for 25 min. Subsequently, the sections were washed three times with phosphate-buffered saline (PBS) for 5 min each time and blocked with 3% bovine serum albumin and 0.5% Triton X-100 in PBS. Then, the primary antibodies against TNF-α, IL-1β, and IL-6 (Servicebio, Wuhan, China) were incubated overnight at 4°C. Thereafter, secondary HRP-conjugated anti-rabbit antibody (1: 300, Servicebio, Wuhan, China) was incubated for 50 min at room temperature followed by counterstaining with DAB (Servicebio, Wuhan, China) and hematoxylin. The sections were observed with an orthographic biomicroscope and quantified using ImageJ software (National Institutes of Health, Bethesda, MD, United States).

## 2.9 Western blot analysis

Western blot analysis was performed to determine the expressions of the proteins, as described in previous reports (Wang et al., 2021a; Zhang et al., 2021c; Ding et al., 2023). In brief, 200 mg of the liver tissue was lysed with 1 mL RIPA buffer (Beyotime, Shanghai, China) and centrifuged at 10,000 r/min and 4°C for 10 min. The supernatant was then collected, and the protein concentration was determined using the BCA kit (Aidlab, Beijing, China). Each sample was next mixed with a loading buffer in the volume ratio of 4:1 and denatured at 100°C for 5 min. Subsequently, the samples were resolved on 12% or 10% SDS-PAGE gels before being transferred onto nitrocellulose membranes. The membranes were then blocked using 5% skim milk in TBST at room temperature for 2 h. The primary antibodies TLR4, IκB, and NF-κB (1:1,000, Abcam, Cambridge, MA, United States) were incubated overnight at 4°C, followed by incubation of the secondary HRP-conjugated anti-rabbit antibody (1:1,000, Abcam, Cambridge, MA, United States) for 2 h. The GeIView 1,500 system was used to image the membranes, and ImageJ software was utilized to quantitatively analyze the protein bands with β-actin protein as the internal standard.

## 2.10 Gut microbiota analysis

The total fecal DNA was extracted using the QIAamp-DNA Stool Mini Kit (Qiagen, Hilden, Germany). The integrity, quantity, and quality of the extracted DNA were examined by electrophoresis in 1% (wt/vol) agarose gels with an Agilent Bioanalyzer 2100 system (Agilent Technologies, San Diego, CA, United States). The 16S rRNA gene amplicon was sequenced as described previously (Li et al., 2021b; Wang et al., 2023). The V3–V4 regions of the bacterial 16S rRNA genes were amplified using the 338F/806R primers on the ABI GeneAmp®9700 PCR System (Applied Biosystems, Foster City, CA, United States). The PCR amplification products were then purified using Agencourt AMPure XP magnetic beads and eluted in an elution buffer before being quantified by a QuantiFluorTM-ST Handheld Fluorometer with UV/blue channels (Promega Corporation, Madison, WI, United States). A Nextera kit set A (Illumina, San Diego, CA, United States) was used to prepare the DNA library, and the qualified libraries were selected for sequencing on an Illumina HiSeq platform at HuaDa Gene Technology Co., Ltd. (Shenzhen, China) in accordance with the manufacturer's

instructions. The filtered and trimmed sequencing data were classified into operational taxonomic units (OTUs) based on sequence similarity (>97%) by using UCLUST software. The generated valid sequences were assigned taxonomy using the SILVA database (Release115 http://www.arb-silva.de). The Quantitative Insights Into Microbial Ecology (QIIME) software package was then used to analyze the sequencing results in line with a previous study, with slight modifications (Li et al., 2023). The MOTHUR program was next used to analyze the rarefaction curves and calculate the richness estimators and diversity indices. The linear discriminant analysis effect size (LEfSe) was performed to identify the significantly difference species.

## 2.11 Determination of short-chain fatty acids (SCFAs) by gas chromatography mass spectrometry (GC-MS)

The metabonomics was performed according to a previous method with slight modifications (Jiang et al., 2021). In brief, about 200 mg/mL of the cecal content was homogenized, vortexed, mixed, and incubated on ice for 30 min. After centrifugation at 10000 *g*/min for 10 min, 0.5 mL of the supernatant was removed and mixed with 0.1 mL of metaphosphoric acid solution (25%) and 11.65 μL crotonic acid solution (210 mmol/L) at 4°C for 30 min. The mixture was then centrifuged at 8,000 *g*/min for 10 min to obtain the purified filtrate and injected into a GC-MS apparatus for analysis. The chromatographic conditions included a temperature of 260°C, volume of 1 μL, and rate of 0.5 mL/min. The time-setting program started with an initial temperature of 100°C maintained for 5 min, followed by increasing to 190°C at 20°C/min and maintaining for 1 min, and finally increased to 260°C at 20°C/min. The entire program required about 13.5 min for execution.

## 2.12 Statistical analysis

The quantitative data were expressed as means ± standard deviations (SDs). The significance between multiple groups with only one dependent variable was analyzed using one-way analysis of variance (ANOVA) followed by Dunnett's multiple-comparison test in SPSS 26.0 software (IBM, New York, NY, United States). The results were visualized with Origin 2022 software (OriginLab, Massachusetts, United States). The significance level was set at $p < 0.05$.

# 3 Results

## 3.1 *In vitro* enzymatic activity and antioxidant assays of PFE

As the ratio of PCR to FA in the PFE might affect the pharmacological evaluations, we first screened for the optimal ratio of PCR to FA. The extractions of PCR and FA (PFE) were prepared with ratios of 1:1, 1:2, and 2:1 by weight. The DPPH and ABTS radical scavenging activities of PCR and FA were sequentially enhanced in the ratio order of 1:1, 2:1, and 1:2 (Figures 1A, B), indicating that PFE has strong antioxidant activity. However, the activities of ethanol dehydrogenase and acetaldehyde dehydrogenase *in vitro* for PCR and FA were sequentially enhanced in the ratio order of 1:2, 1:1, and 2:1 (Figures 1C, D), suggesting that PFE could promote alcohol metabolism. By taking into account the results of both antioxidant and enzymatic activities, PFE in the ratio of 2:1 was selected for *in vivo* evaluations in the subsequent experiments.

## 3.2 PFE improves lipid metabolism disorders in alcohol-fed mice

To test whether PFE could improve liver injuries induced by excess alcohol intake, the experimental mice were orally treated with or without alcohol in combination with or without PFE for 3 weeks (Figure 2A). Compared with the controls, the mice subjected to alcohol feeding exhibited downward trends in their bodyweights (Figure 2B). The bodyweights of mice exposed to alcohol were maintained to a certain extent when compared to those not exposed to alcohol. Compared to NC mice, the alcohol-fed mice showed significantly increased levels of TG, TC, and LDL-C, as well as a clearly decreased level of HDL-C in serum (Figures 2C–F). Accordingly, the PFE treatment not only effectively reduces serum levels of TG, TC, and LDL-C but also elevates the serum HDL-C level in mice exposed to alcohol in a dose-dependent manner (Figures 2C–F). The TC and TG levels in the mice liver tissues were determined to be consistent with the changes obtained from serum measurements (Figures 2G, H). Furthermore, an increase in the oil red O positive area of the liver was observed in the alcohol-fed mice, indicating that alcohol exposure induced lipid accumulation in the liver in mice. The alcohol-exposure-induced hepatic lipid accumulation was significantly reduced after treatment with PFE in the mice (Figures 2I, J). These results suggest that PFE can effectively regulate lipid metabolism disorders induced by alcohol, which could help ameliorate alcoholic fatty liver disease.

## 3.3 PFE alleviates liver injury and oxidative stress in alcohol-fed mice

To investigate the protective effects of PFE against alcohol-induced liver injury, we conducted histopathological examination of the liver tissues. The hepatocytes in the liver of the control mice exhibited well-preserved structural integrity around the central vein in a highly organized manner, with homogeneous cytoplasmic staining and clear nuclei (Figure 3A). In contrast, the hepatocytes in the liver of the alcohol-fed mice displayed enlarged sizes, cellular swelling, blurred cell boundaries, formation of aggregates (indicated by circles), and inflammatory cell infiltration (Figure 3A). Notably, the PFE treatment significantly revised these pathological changes induced by alcohol exposure, resulting in clearer demarcation between cells in the liver (Figure 3A). Furthermore, the ratio of liver weight to bodyweight was lower in the PFE-treated mice exposed to alcohol than in mice fed with alcohol alone (Figure 3B). Compared to the control mice, the key markers of liver injury, including serum AST and ALT, in the alcohol-fed mice were significantly increased by 1.5-fold and 2.0-fold, respectively

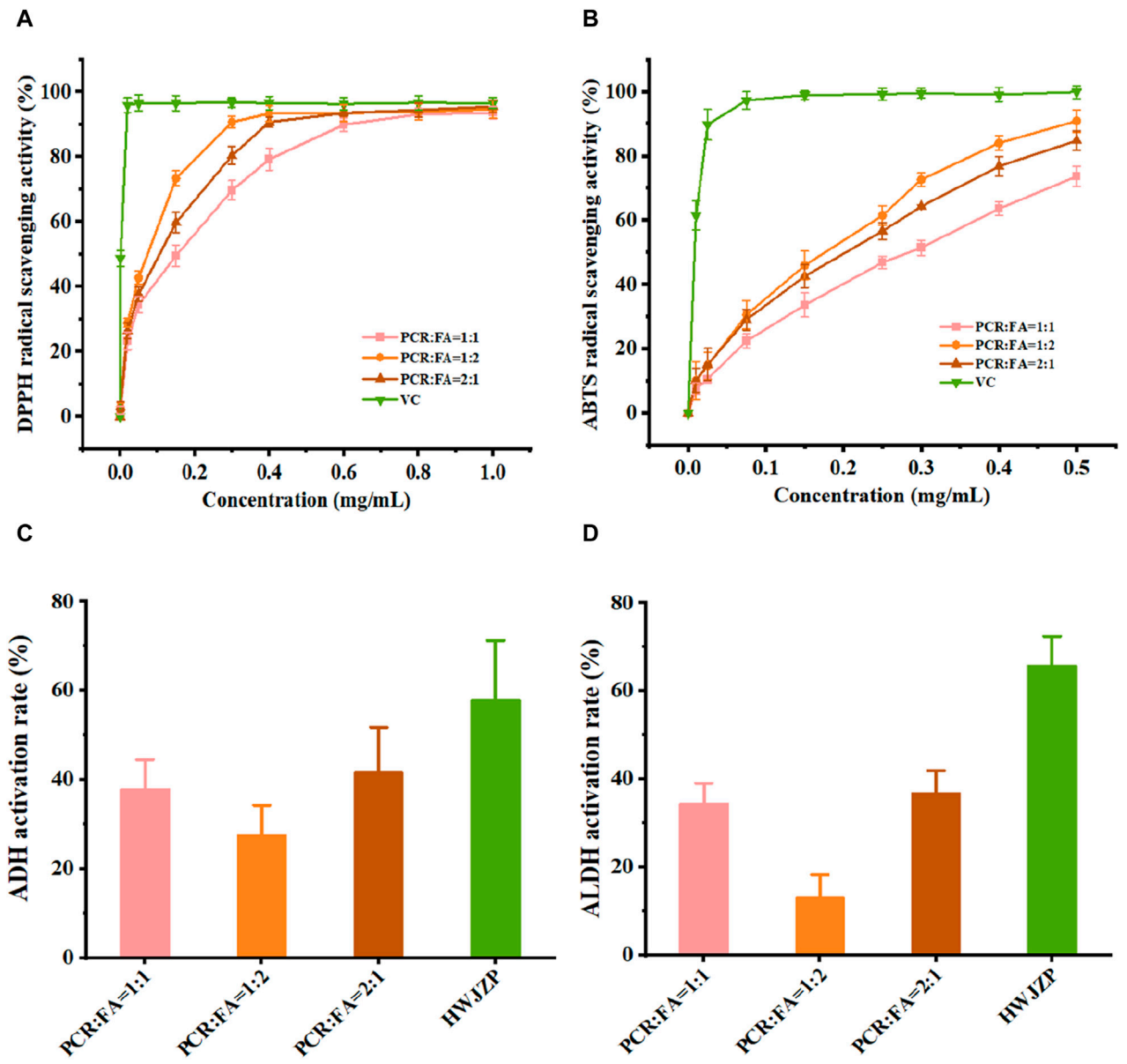


FIGURE 1
PFE differentially enhances the *in vitro* activities of enzymes and antioxidants. **(A)** DPPH radical scavenging activity. **(B)** ABTS radical scavenging activity. **(C)** Alcohol dehydrogenase (ADH) activity. **(D)** Acetaldehyde dehydrogenase (ALDH) activity. ABTS: 2,2-azino-bis (3-ethylbenzothiazoline-6-sulfonic acid), DPPH: alpha-diphenyl-β-picrylhydrazyl, PCR: *Pericarpium citri reticulatae*, FA: *Amomi fructus*, VC: vitamin C, HWJZP: HaiWangJinZunPian.

(Figures 3C, D). Importantly, treatment with PFE significantly decreased the activities of serum AST and ALT in the alcohol-fed mice. Furthermore, mice exposed to alcohol showed significantly decreased activities of the antioxidant enzymes, including SOD, GSH, and GSH-Px in the liver, which were significantly reversed after PFE treatment in the livers of the alcohol-fed mice (Figures 3F–H). Meanwhile, MDA, a marker of lipid peroxidation, was significantly increased in the liver tissues of alcohol-fed mice relative to the control mice, which was also effectively reversed by PFE intervention (Figure 3E), indicating that PFE could enhance of the liver in alcohol-fed mice. The above results suggest that PFE alleviates alcohol-induced liver injury, which could be related to the strong antioxidant capacity against liver oxidative stress in mice.

## 3.4 PFE reduces LPS and inhibits TLR4/NF-κb-related inflammatory response

As severe injuries always evoke systemic inflammatory response, we next tested whether PFE showed anti-inflammatory activity against alcoholic liver injury by measuring the inflammatory cytokines. Compared to the controls, the TNF-α, IL-1β, and IL-6 levels were found to be elevated by approximately 1.6-fold, 1.5-fold, and 1.8-fold, respectively, in the livers of the alcohol-fed mice (Figures 4A–C). Interestingly, administration of PFE effectively reduced the hepatic contents of TNF-α, IL-1β, and IL-6 in the alcohol-induced mice in a dose-dependent manner (Figures 4A–C). These changes caused by PFE treatment in the alcohol-exposed mice

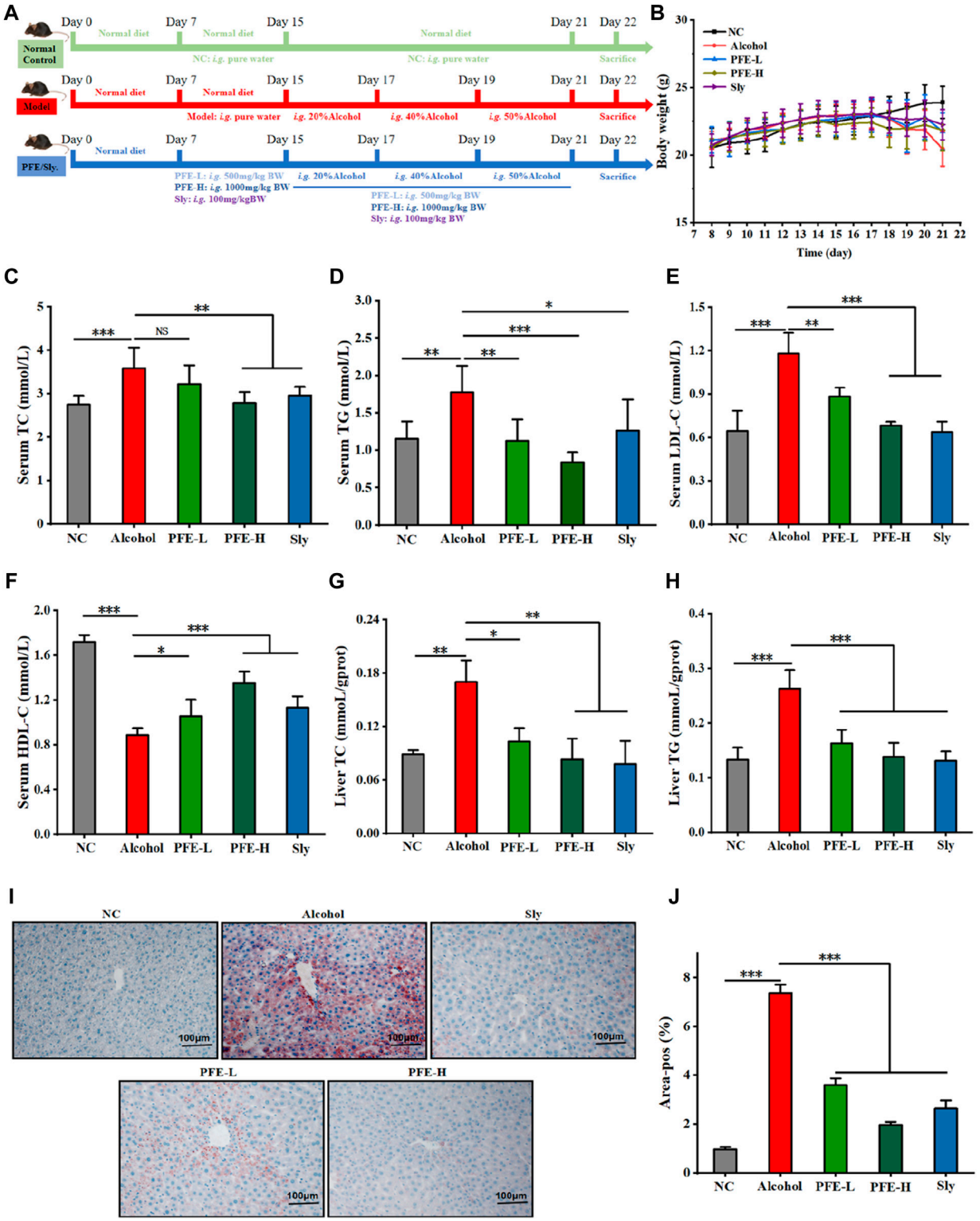


FIGURE 2
Treatment with PFE improves lipid metabolism disorders induced by alcohol feeding in mice. **(A)** Schematic representation of the intervention schedules for the different experimental groups. **(B)** Bodyweights of the mice. **(C,D)** Serum concentrations of total cholesterol (TC) and total triglyceride (TG). **(E,F)** Serum levels of low-density lipoprotein cholesterol (LDL-C) and high-density lipoprotein cholesterol (HDL-C). **(G,H)** Liver TC and TG levels. **(I,J)** Representative images of oil red O staining for liver tissues and their quantification. The data are expressed as means ± SD ($n$ = 6–8). Statistical significance was determined by comparison with the alcohol group; *$p < 0.05$, **$p < 0.01$, and ***$p < 0.001$. NS denotes non-significant. NC: normal control group, Alcohol: model group, Sly: silybin group, PFE-L: low-dose group, PFE-H: high-dose group.

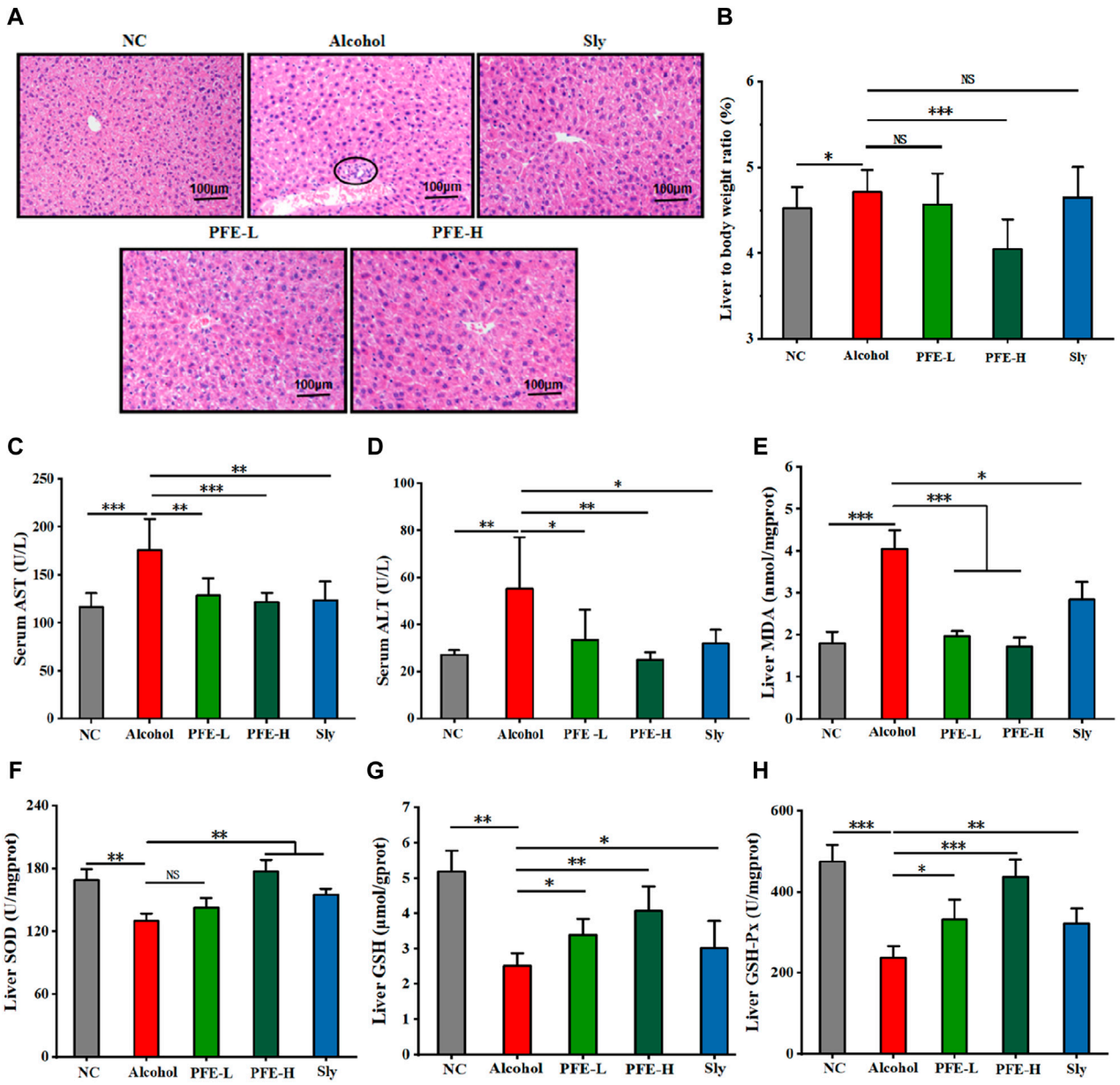


FIGURE 3
Supplementation with PFE mitigates liver injury and oxidative stress induced by alcohol exposure in mice. **(A)** Representative images of H&E staining for liver tissues. **(B)** Liver weight/bodyweight ratio. **(C,D)** Levels of serum aspartate aminotransferase (AST) and alanine aminotransferase (ALT). **(E)** Liver content of malondialdehyde (MDA). **(F–H)** Liver contents of superoxide dismutase (SOD), glutathione (GSH), and glutathione peroxidase (GSH-Px). The data are expressed as means ± SD. ($n$ = 6–8). Statistical significance was determined by comparison with the alcohol group; *$p < 0.05$, **$p < 0.01$, and ***$p < 0.001$. NS denotes non-significant. NC: normal control group, Alcohol: model group, Sly: silybin group, PFE-L: low-dose group, PFE-H: high-dose group.

were further confirmed by IHC results (Figures 4D–G). In line with the changes to the liver proteins, the mRNA expressions of TNF-α, IL-1β, and IL-6 were also significantly decreased in the alcohol-exposed mice treated with PFE compared to mice exposed to alcohol alone (Figure 4H). We also tested the hepatic LPS level, a well-characterized pathogen-associated molecular pattern that induces an inflammatory response via stimulation of the TLRs. Notably, the alcohol-fed mice showed high concentrations of LPS in their livers, but this was effectively reduced after PFE administration (Figure 4I).

As the synthesis and release of proinflammatory cytokines and chemokines are induced by activation of the TLR4/NF-κB signaling pathway, we tested the mechanistic path by which PFE modulates the gut–liver axis. Compared to the controls, alcohol exposure significantly upregulated the expressions of TLR4 and NF-κB p65 proteins as well as mRNA expressions of the NOD-like receptor thermal protein domain associated protein 3 (NLRP3) and caspase-1 while downregulating IκB protein expression in the liver (Figures 4J–N). Conversely, treatment with PFE-H resulted in substantial reductions in the hepatic TLR4, NF-κB,

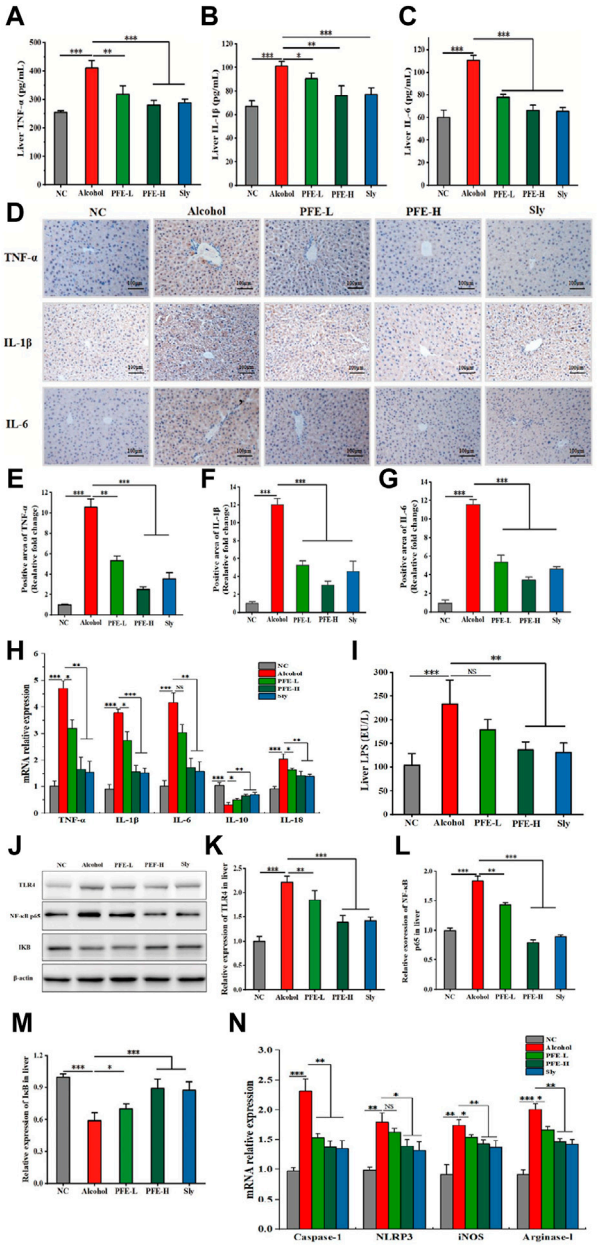


FIGURE 4
Administration of PFE inhibits inflammatory responses and the TLR4/NF-κB signaling pathway in mice with alcohol-induced liver injury. **(A–C)** Levels of tumor necrosis factor-α (TNF-α), interleukin-1β (IL-1β), and interleukin-6 (IL-6) in mice liver tissues. **(D)** Representative immunohistochemical images of inflammatory cytokines TNF-α, IL-1β, and IL-6 in mice liver tissues. **(E–G)** Quantitative analysis of the immunohistochemical staining for TNF-α, IL-1β, and IL-6 ($n$ = 3). **(H)** mRNA relative expressions of TNF-α, IL-1β, IL-6, interleukin-10 (IL-10), and interleukin-18 (IL-18) in mouse liver determined by qRT-PCR. **(I)** Content of hepatic lipopolysaccharides (LPS) in mice. **(J–M)** Representative images of Western blot analysis for toll-like receptor 4 (TLR4), nuclear factor-κBp65 (NF-κBp65), and inhibitor of NF-κB (IκB) protein expressions in mouse liver and its relative quantitative analysis. **(N)** mRNA relative expressions of caspase-1, NOD-like receptor thermal protein domain associated protein 3 (NLRP3), inducible nitric oxide synthase (iNOS), and arginase-1 in mouse liver determined by qRT-PCR. The data are expressed as means ± SD ($n$ = 6–8). Statistical significance was determined by comparison with the alcohol

*(Continued)*

FIGURE 4 (Continued)
group; $*p < 0.05$, $**p < 0.01$, and $***p < 0.001$. NS denotes non-significant. NC: normal control group, Alcohol: model group, Sly: silybin group, PFE-L: low-dose group, PFE-H: high-dose group.

NLRP3, and caspase-1 expressions along with increased IκB protein expression in the alcohol-fed mice (Figures 4J–N), indicating that PFE amelioration of inflammation in ALD could be related to the suppression of the LPS-TLR4-NF-κB/NLRP3 axis. Because the microbial component of LPS can drive macrophage polarization toward the M1 phenotype macrophages that are mainly involved in proinflammatory responses (Chen et al., 2020), we wanted to determine whether PFE affected macrophage polarization. Compared with the controls, the mRNA expressions of IL-10 in the alcohol-exposed mice were significantly decreased, while the mRNA expressions of IL-18, inducible nitric oxide synthase (iNOS), and arginase-1 were significantly increased (Figures 4H, N). Interestingly, PFE administration dramatically increased hepatic mRNA expression of IL-10 and decreased hepatic mRNA expressions of IL-18, iNOS, and arginase-1 in the alcohol-fed mice (Figures 4H, N), indicating that PFE could inhibit macrophage polarization. Taken together, these findings suggest that PFE mitigates alcohol-induced liver inflammation by regulating macrophage polarization and suppressing the LPS-TLR4-NF-κB/NLRP3 axis.

## 3.5 PFE repairs intestinal barrier in alcohol-fed mice

Because LPS accumulation in the liver is closely associated with intestinal integrity (Cao et al., 2021a), we conducted a histopathological assessment and IF analysis to evaluate the ileum barrier function. Compared to the control mice, the alcohol-exposed mice exhibited significant loosening and disordering of the intestinal villi in the ileum (Figure 5A). These destructive changes were significantly attenuated after PFE intervention in the alcohol-fed mice. Furthermore, compared with the controls, the alcohol-fed mice showed notable histological changes, including detachment between crypts from the intestinal wall and reductions in both the villus height and crypt depth (Figures 5A–E), indicating that alcohol consumption altered the intestinal morphology. Fortunately, PFE administration significantly ameliorated these alcohol-induced morphological changes (Figures 5A–E). Compared to the control mice, lower expression levels of the tight junction proteins, including occludin and ZO-1 were found in the alcohol-fed mice (Figures 5F–H), which were mitigated by PFE intervention at a higher level than that achieved by positive drug treatment (Figures 5F–H). Furthermore, the qRT-PCR results showed significantly reduced mRNA expression levels of occludin and ZO-1 in response to alcohol induction when compared to those observed in the control mice (Figures 5I, J). Administration of PFE significantly upregulated the mRNA expressions of occludin and ZO-1 that were earlier diminished by alcohol exposure. The aforementioned results

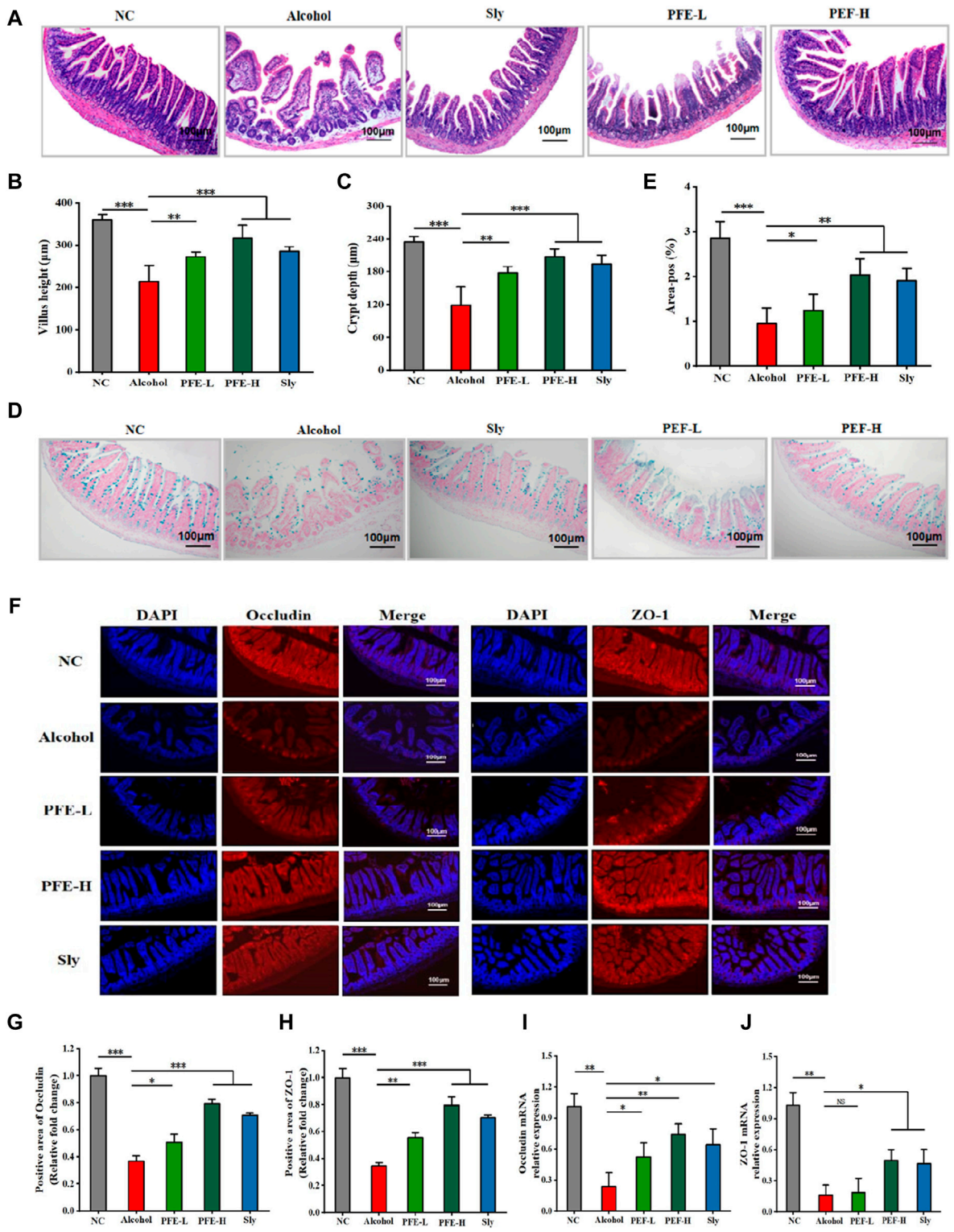


FIGURE 5
PFE preserves the integrity of the intestinal barrier in mice with alcoholic liver injury. **(A)** H&E staining of the ileum. **(B)** Quantification of ileal villus length. **(C)** Depth of the ileal crypt. **(D,E)** Representative images and quantitative analysis of Alcian blue staining for the ileum. **(F)** Representative images of ileal occludin and zonula occludens-1 (ZO-1) immunofluorescence staining of the ileum. **(G,H)** Quantitative analysis of occludin and ZO-1 proteins. **(I,J)** Relative gene expressions of occludin and ZO-1 in the ileum determined by qRT-PCR. The data are expressed as means ± SD. ($n$ = 3–6). Statistical significance was determined by comparison with the alcohol group; *$p$ < 0.05, **$p$ < 0.01, and ***$p$ < 0.001. NS denotes non-significant. DAPI: 4′,6-diamidino-2-phenylindole, NC: normal control group, Alcohol: model group, Sly: silybin group, PFE-L: low-dose group, PFE-H: high-dose group.

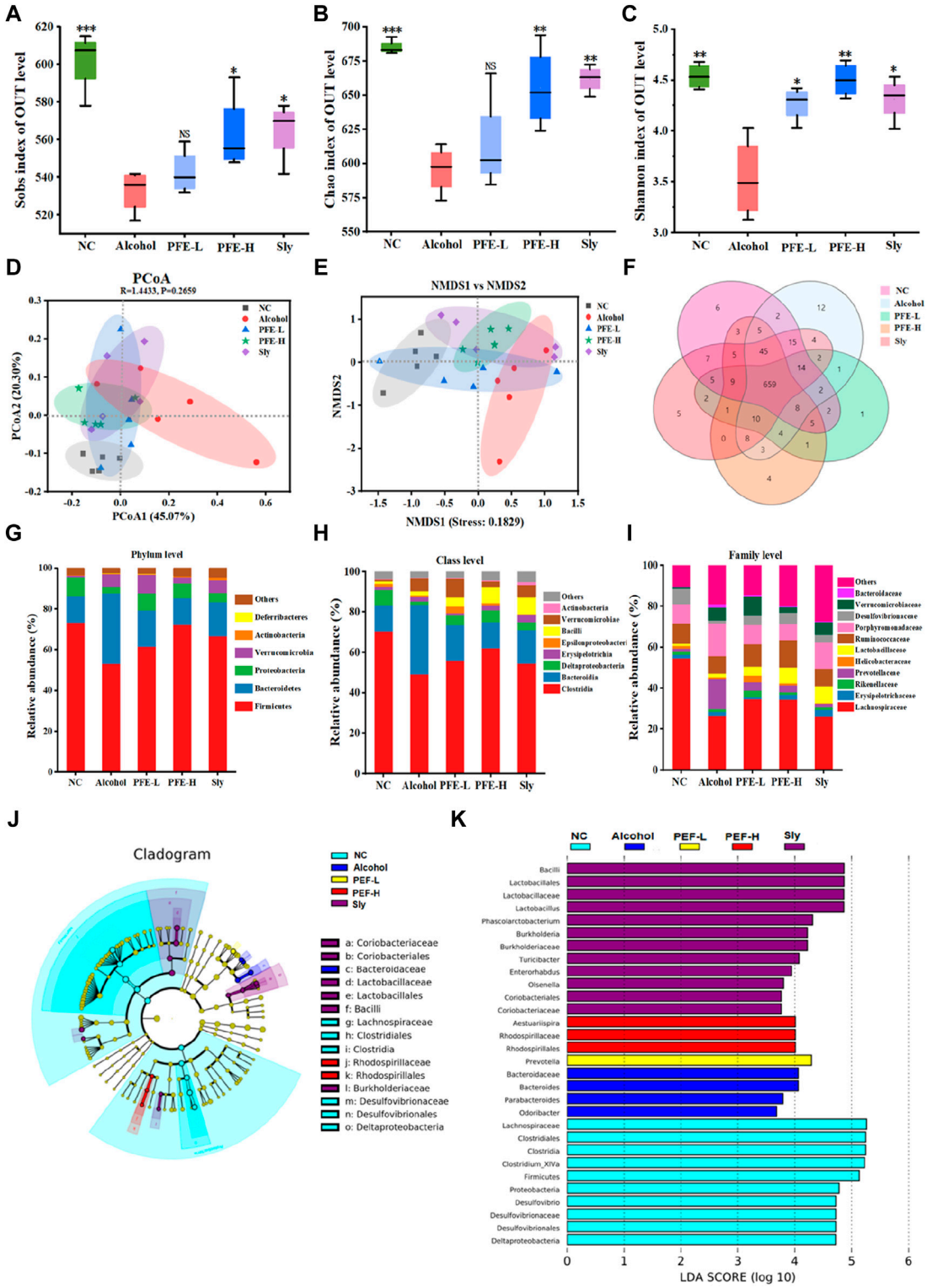


FIGURE 6
PFE alleviates alcohol-induced gut microbiota disorders in mice. **(A–C)** α-diversity assessed by Sobs index, Chao index, and Shannon index. **(D,E)** Principal coordinate analysis (PCoA) and non-metric multidimensional scaling (NMDS) analysis for β-diversity. **(F)** Venn diagram of the different groups. **(G–I)** Relative abundances of the bacteria at phylum, class, and family levels. **(J,K)** LEfSe analysis of the microbiota and its linear discriminant analysis (LDA). The data are expressed as means ± SD. ($n$ = 5). Statistical significance was determined by comparison with the alcohol group; *$p < 0.05$, **$p < 0.01$, and ***$p < 0.001$. NS denotes non-significant. OUT: operational taxonomic unit, NC: normal control group, Alcohol: model group, Sly: silybin group, PFE-L: low-dose group, PFE-H: high-dose group.

suggest that alcohol feeding impaired the intestinal barrier function, while PFE could effectively alleviate these injuries to maintain intestinal barrier integrity.

## 3.6 PFE alleviates alcohol-induced disturbance of the gut microbiota

As intestinal dysbiosis may play a pivotal role in ALD pathogenesis, we performed 16S rDNA gene sequencing on the mouse fecal samples to analyze their microbial composition. Alpha diversity was evaluated using the Sobs, Chao, and Shannon indexes. Compared to the control mice, the alcohol-fed mice exhibited significantly decreased values of the Sobs, Chao, and Shannon indexes, indicating reduced alpha diversity induced by alcohol exposure (Figures 6A–C). PFE treatment prevented reductions of these indices induced by alcohol consumption, with better efficacy observed in the mice treated with PFE-H compared to those receiving silybin treatment. Furthermore, we employed principal coordinate analysis (PCoA) and non-metric multidimensional scaling (NMDS) analysis to identify differences in the microbial communities among the five different groups of treated mice. The results revealed that the samples from the different subjects were significantly separated, showing that the five different mice groups had significant differences in the compositions of their microbial communities (Figures 6D, E). Venn diagrams depicting the overlaps between the groups (Figure 6F) were utilized to comprehend the shared richness among these groups, with the treated groups showing similarity to the control group.

To further evaluate the effects of PFE on intestinal composition in mice with alcoholic liver injury, the bacterial compositions were analyzed at the phylum, class, and family levels. At the phylum level, *Firmicutes* and *Bacteroidetes* were dominant in each group. Compared to the control mice, the relative abundance of *Firmicutes* decreased from 73.33% to 53.24%, but the relative abundance of *Bacteroidetes* increased from 13.01% to 34.45% in the alcohol-fed mice (Figure 6G). Notably, after treatment, the relative abundances of *Firmicutes* and *Bacteroidetes* increased to 61.50% and 17.77% in mice administered PFE-L as well as 72.30% and 13.05% in mice administered PFE-H, respectively (Figure 6G). Furthermore, alcohol intake increased *Verrucomicrobia* abundance but decreased *Proteobacteria* and *Actinobacteria* relative abundances when compared to the control mice. However, PFE-H-treated mice showed significantly reduced *Verrucomicrobia* abundance as well as significantly increased relative abundances of *Proteobacteria* and *Actinobacteria* compared to the alcohol-exposed mice (Figure 6G). At the class level, compared to the controls, the relative abundances of *Bacteroidia*, *Erysipelotrichia*, *Bacilli,* and *Verrucomicrobiae* were clearly higher; however, the relative abundances of *Clostridia*, *Deltaproteobacteria*, *Epsilonproteobacteria,* and *Actinobacteria* exhibited decreases in the alcohol-treated mice. The relative abundances of these bacteria altered by alcohol exposure were restored by PFE treatment to some extent (Figure 6H). At the family level, compared to the control mice, the relative abundances of *Lachnospiraceae, Rikenellaceae, Prevotellaceae, Helicobacteraceae, Ruminococcaceae,* and *Desulfovibrionaceae* were lower, and the relative abundances of *Erysipelotrichaceae, Lactobacillaceae, Porphyromonadaceae, Verrucomicrobiaceae,* and *Bacteroidaceae* were higher in the alcohol-fed mice (Figure 6I). In turn, the relative abundances of *Lachnospiraceae, Rikenellaceae, Helicobacteraceae, Lactobacillaceae,* and *Ruminococcaceae* increased while the relative abundances of *Prevotellaceae, Porphyromonadaceae, Verrucomicrobiaceae,* and *Bacteroidaceae* decreased in the alcohol-fed mice treated with PFE when compared to mice fed with alcohol alone (Figure 6I).

To further identify the microbial and functional biomarkers from the alcohol-fed mice induced by PFE consumption, the LEfSe was performed (Figures 6J, K). The results showed that *Lactobacillus*, *Faecalibaculum,* and *Akkermansia* were the most dominant types in alcohol-fed mice treated with PFE. The administration of PFE partially restored alcohol-induced gut microbiota dysbiosis by recovering the abundance of *Lactobacillus, Faecalibaculum,* and *Akkermansia*. These findings indicate that PFE has the potential to regulate alcohol-induced dysbiosis of gut microbiota in mice.

## 3.7 PFE enriches the cecal concentrations of SCFAs in alcohol-fed mice

SCFAs are a group of saturated fatty acids that are produced by fermentation of non-digestible fibers, and they have been established as representative metabolites of the gut microbiota that can communicate from the microbiome to host tissues (Cait et al., 2018). In comparison to the control mice, the concentrations of acetic acid, propionic acid, and butyric acid in the ceca of the alcohol-fed mice were significantly lower (Figures 7A–C). Moreover, there was no significant difference in the valeric acid content between the control and alcohol-fed mice (Figure 7D). Notably, the concentrations of acetic acid, propionic acid, and butyric acid in the cecum were significantly higher in the alcohol-induced mice after PFE treatment (Figures 7A–C). These findings suggest that PFE exertion of an ameliorative effect on alcoholic liver injury could be related to the intestinal SCFAs.

# 4 Discussion

Excessive alcohol consumption exceeding the metabolic capacity could disrupt lipid metabolism and gut microbiota equilibrium, thereby promoting various forms of liver diseases (Wang et al., 2020b; Ren et al., 2020). Dietary interventions can effectively rectify imbalances in the intestinal microbiota, enhance the gastrointestinal physiological functions, mitigate oxidative stress, and consequently shield the liver (Gaundal et al., 2022). These interventions represent an effective strategy against ALD. PCR and FA are two well-known traditional Chinese herbal medicines having both food and medicinal functions for healthcare. However, the effects of PCR or FA treatments on alcohol-induced liver diseases and dysregulated lipid metabolism have not been reported. The present study demonstrates that an extract derived from a combination of PCR and FA (PFE) can effectively mitigate alcohol-induced liver injury and disturbance of lipid metabolism in mice. Furthermore, treatment with PFE significantly restores gut microbiota dysbiosis and maintains the integrity of the intestinal barrier, which are

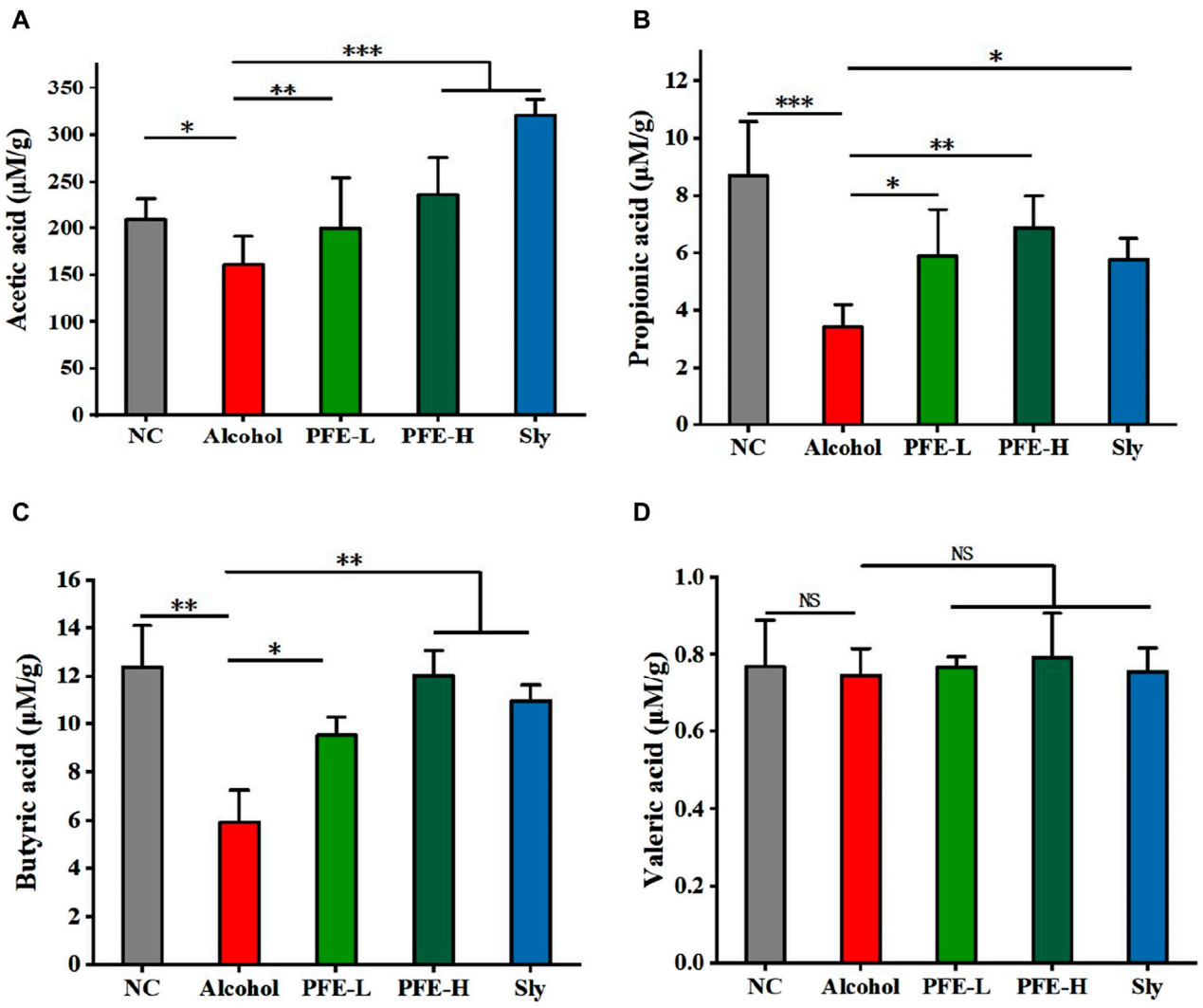


FIGURE 7
Administration of PFE facilitates production of SCFAs in mice exposed to alcohol. **(A)** Cecal levels of acetic acid. **(B)** Cecal levels of propionic acid. **(C)** Cecal levels of butyric acid. **(D)** Cecal levels of valeric acid. The data are expressed as means ± SD. ($n$ = 5). Statistical significance was determined by comparison with the alcohol group; *$p < 0.05$, **$p < 0.01$, and ***$p < 0.001$. NS denotes non-significant. NC: normal control group, Alcohol: model group, Sly: silybin group, PFE-L: low-dose group, PFE-H: high-dose group.

conducive for reducing hepatic LPS and increasing circulating SCFAs in mice exposed to alcohol. Administration of PFE was also found to sensibly suppress the TLR4/NF-κB signaling pathway while reducing hepatic inflammation induced by alcohol in mice. Our findings specifically identified that PFE could be used as a new dietary candidate for treating ALD.

ALD is characterized by liver inflammation, oxidative stress, hepatocyte metabolism dysfunction, bacterial product translocation from the gut microbiota into circulation, and regeneration process modifications (Qi et al., 2022). Numerous studies have shown that alcohol feeding induces liver injury with increased ALT and AST levels in both animals and humans (Du et al., 2022; Shen et al., 2024). Consistent with these studies, clear increases in the serum ALT and AST were observed in mice fed with alcohol. The serum levels of ALT and AST were significantly reduced after PFE treatment in the ALD mice in a dose-dependent manner, suggesting the hepatoprotective effect produced by PFE. The metabolism of ethanol directly triggers production of ROS and reactive nitrogen species, which create an environment favorable to oxidative stress (Wang and Mu, 2021b; Contreras-Zentella et al., 2022). Moreover, chronic alcohol consumption induces liver oxidative stress accompanied by depletion of GSH levels and decrease of antioxidant activity (Ge et al., 2023). In line with these findings, mice exposed to alcohol exhibited lower levels of hepatic GSH, GSH-Px, and SOD as well as higher hepatic MDA levels than the control mice. Fortunately, PFE administration significantly enhanced the hepatic levels of GSH, GSH-Px, and SOD, while also reducing hepatic MDA levels in the alcohol-fed mice, indicating that PFE has good antioxidant capacity. There is growing evidence that oxidative stress can activate fatty acid synthesis to trigger lipid droplet accumulation in the hepatocytes (Sun et al., 2020). Hepatocytes exposed to alcohol increase the NADH/$NAD^+$ ratio, which can enhance lipid synthesis and prevent β-oxidation of free fatty acids, leading to triglyceride accumulation in the liver (German et al., 2021; Kasper et al., 2023). Disturbance of the

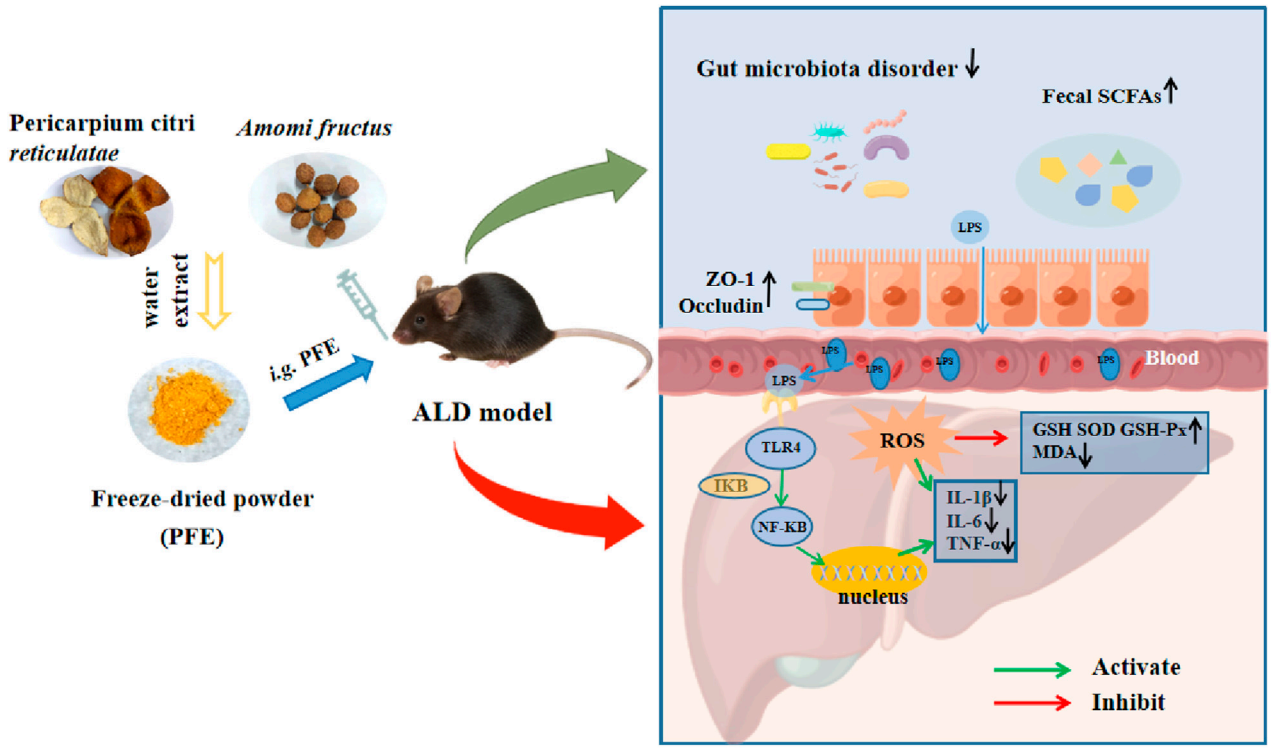


FIGURE 8
Possible protective mechanism of PFE against alcohol-induced liver injury.

lipid metabolism will result in progression of hepatic steatosis, which is the early stage of alcoholic liver injury (Jeon and Carr, 2020). The present study found significant accumulation of lipids in both the blood and liver in mice fed with alcohol. Notably, PFE administration significantly improved lipid accumulation in the alcohol-fed mice, as evidenced by the reductions in the TG and TC levels in both the liver and serum. These findings suggest that supplementation with PFE effectively prevents lipid droplet accumulation in the liver in ALD mice.

Lipid accumulation in the macrophages and other immune cells can promote inflammatory responses by augmenting TLR signaling and inflammasome activation (Tall and Yvan-Charvet, 2015; Hu, et al., 2021). NLRP3 inflammasomes can be activated by the TLR4-NF-κB axis to promote the maturation and release of downstream inflammatory cytokines while aggravating the progression of ALD (Seoane et al., 2020). In the present study, we found that the levels of LPS and inflammatory cytokines TNF-α, IL-6, and IL-1β were higher in the alcohol-exposed mice than the control mice, suggesting that alcohol-induced inflammatory responses may be triggered by excessive LPS. Exposure to LPS can induce tissue damage and organ failure (Dayang et al., 2021). Fortunately, treatment with PFE significantly reduces the levels of these inflammatory cytokines in alcohol-fed mice. Moreover, increased levels of bacterial LPS have been found to trigger a TLR4-mediated proinflammatory cascade in the immune cells (monocytes and macrophages), resulting in the activation of the NF-κB signaling pathway and leading to inflammation (Manco et al., 2010; Sun et al., 2021). Notably, in line with the changes in these inflammatory cytokines and LPS, PFE treatment also significantly inhibited activation of the hepatic TLR4/NF-κB/NLRP3 signaling pathway in mice fed with alcohol. TLR4 and NF-κB are widely recognized for their crucial roles in innate immunity and orchestration of inflammatory responses (Shao et al., 2020; Gudowska-Sawczuk and Mroczko, 2022; Zhou et al., 2023). Dysregulation of TLR4/NF-κB/NLRP3 signals have been implicated in various diseases that are primarily associated with dysfunction of the defense system and inflammation (He et al., 2022; Pu et al., 2023). It is known that activated macrophages are usually divided into M1-like and M2-like macrophages, which are individually involved in proinflammatory and anti-inflammatory responses. LPS can drive macrophage polarization to the M1 phenotype and are involved in the proinflammatory responses (Chen et al., 2020). Interestingly, PFE administration significantly regulates macrophage polarization, as indicated by the increased hepatic mRNA expression of IL-10 and decreased hepatic mRNA expressions of IL-18, iNOS, and arginase-1 in the alcohol-fed mice. This finding is supported by previous findings that the control of macrophage activation and polarization is conducive to regulating chronic inflammation (Pei et al., 2020; Zhou et al., 2022; Wu et al., 2023). Together, these findings suggest that PFE alleviates alcohol-induced hepatic inflammation possibly through inhibition of the LPS-TLR4-NF-κB/NLRP3 axis as well as modulation of macrophage activation and polarization.

Numerous studies have demonstrated that LPS are mainly produced by the gut microbiota and translocated to the portal blood stream. The composition and functions of the gut microbiota could be altered by alcohol exposure (Jung et al., 2022; Jew and Hsu, 2023). In the present study, there were significant decreases in the relative abundances of *Firmicutes*, *Proteobacteria*, and *Actinobacteria* at the phylum level in the alcohol-fed mice compared with the control mice. This finding is consistent with a previous report on the increase in relative

abundance of *Proteobacteria* following alcohol consumption (Zogona et al., 2023). These bacterial changes were well reversed by PFE treatment. It has been reported that *Lachnospiraceae, Lactobacillaceae,* and *Akkermansiaceae* (the major family of *Verrucomicobiota*) can produce SCFAs. The significant absence of butyric-acid-producing bacteria and butyric acid genes in the gut causes alcohol-induced intestinal microecological dysbiosis, which plays a crucial pathogenic role in the development of alcoholic liver injury (Singhal et al., 2021). As expected, PFE treatment significantly enriches the content of SCFAs in mice exposed to alcohol. SCFAs have been considered to play important roles in modulating the integrity of the epithelial barrier by coordinated regulation of the tight junction proteins (Morrison and Preston, 2016). These proteins modulate the intracellular molecular highway between the lumen and hepatic portal system. The intestinal barrier integrity is strongly correlated with the accumulation of endotoxin LPS in the body. Increased permeability is related to translocation of the harmful bacteria and their metabolites that trigger an inflammatory cascade (Cao, et al., 2021b). In the present study, we observed that alcohol-fed mice exhibited impaired integrity of the ileum, as indicated by reduced intestinal villi and crypts than the control mice. Furthermore, the expressions of occludin and ZO-1 proteins in the ileum in the ALD mice were significantly lower than those in the control mice, suggesting a dysfunction of the intestinal barrier induced by alcohol exposure in these mice. This may also be attributed to alcohol and its major oxidative metabolite acetaldehyde, which can disrupt epithelial tight junctions (Hyland et al., 2022). Fortunately, PFE administration improved alcohol-induced impairment of the intestinal functions in mice by increasing the levels of tight junction proteins ZO-1 and occludin, which are crucial components for maintaining selective permeability against bacterial invasion and antigens. These findings indicate that PFE exerts substantial protective effects on both ALD and intestinal barrier integrity, which might at least be partly related to regulation of the gut microbiota and circulating SCFAs.

## 5 Conclusion

PFE administration exerts strong hepatoprotective effects against metabolic disorders, oxidative damage, and inflammation induced by alcohol exposure. The amelioration of alcohol-induced hepatic inflammation by PFE treatment could be related to the decrease in bacteria-derived LPS and inactivation of the TLR4/NF-κB signaling pathway. Notably, supplementation with PFE effectively reshaped the gut microbiota and strengthened the intestinal barrier in ALD mice, which helped prevent the translocation of LPS into the blood and liver (Figure 8). These findings offer novel insights into the underlying mechanisms by which PFE prevents ALD. PFE can thus serve as an effective clinical candidate for minimizing the risks of various ALD. However, the detailed mechanisms by which PFE improves ALD will need more work in the future. For instance, fecal microbial transplantation may be used to identify the roles of both gut microbiota and specific strains in the anti-ALD of PFE. Furthermore, the anti-ALD of specific strains alone or in combination with PFE can also be explored using germ-free animals.

## Data availability statement

All data included in this study are available upon request by contacting the corresponding authors. The 16S rRNA data generated in this study were deposited in the NCBI (SRA) database; accession number PRJNA1123434, available at: http://www.ncbi.nlm.nih.gov/bioproject/1123434.

## Ethics statement

The animal study was approved by the Committee on the Ethics of Animal Experiments (N2023002) of the International Healthcare Innovation Institute (Jiangmen), Jiangmen, China. The study was conducted in accordance with the local legislation and institutional requirements.

## Author contributions

X-MZ: writing–original draft, validation, methodology, data curation, and conceptualization. Y-CH: writing–original draft, methodology, investigation, and formal analysis. B-ZC: writing–review and editing, supervision, resources, and project administration. QL: writing–review and editing, formal analysis, and data curation. P-PW: writing–review and editing, supervision, and conceptualization. W-HC: writing–review and editing, supervision, and conceptualization. R-HW: writing–review and editing, supervision, methodology, and conceptualization. CL: writing–review and editing, supervision, project administration, funding acquisition, and conceptualization.

## Funding

The author(s) declare that financial support was received for the research, authorship, and/or publication of this article. This work was financially supported by the National Natural Science Foundation of China (Nos. 81803390 and 22077020), Natural Science Foundation of Guangdong Province, China (No. 2021A1515010221), Guangdong and Macao Cooperation Project from the Department of Science and Technology of Guangdong Province and Jiangmen Science and Technology Bureau (No. 2022A0505020026), Department of Education of Guangdong Province, China (Nos. 2021ZDZX4041 and 2020KZDZX1202), Jiangmen Science and Technology Plan Project Fund (No. 2021030102620004497), and Science and Technology Planning Project of Guangdong Province, China (No. 2021B1212040016).

## Conflict of interest

Author B-ZC was employed by Guangdong Xinbaotang Biotechnology Co. Ltd.

The remaining authors declare that the research was conducted in the absence of any commercial or financial relationships that could be construed as a potential conflict of interest.

## Publisher's note

All claims expressed in this article are solely those of the authors and do not necessarily represent those of their affiliated organizations or those of the publisher, editors, and reviewers. Any product that may be evaluated in this article or claim that may be made by its manufacturer is not guaranteed or endorsed by the publisher.

## References

An, L., Wirth, U., Koch, D., Schirren, M., Drefs, M., Koliogiannis, D., et al. (2022). The role of gut-derived lipopolysaccharides and the intestinal barrier in fatty liver diseases. *J. Gastrointest. Surg.* 26 (3), 671–683. doi:10.1007/s11605-021-05188-7

Bajaj, J. S. (2019). Alcohol, liver disease and the gut microbiota. *Nat. Rev. Gastroenterol. Hepatol.* 16 (4), 235–246. doi:10.1038/s41575-018-0099-1

Bijak, M. (2017). Silybin, a major bioactive component of Milk Thistle (Silybum marianum L. Gaernt.)-chemistry, bioavailability, and metabolism. *Molecules* 22 (11), 1942. doi:10.3390/molecules22111942

Cai, R., Yue, X. Y., Wang, Y. L., Yang, Y. Y., Sun, D. J., Li, H., et al. (2021). Chemistry and bioactivity of plants from the genus Amomum. *J. Ethnopharmacol.* 281, 114563. doi:10.1016/j.jep.2021.114563

Cait, A., Hughes, M. R., Antignano, F., Cait, J., Dimitriu, P. A., Maas, K. R., et al. (2018). Microbiome-driven allergic lung inflammation is ameliorated by short-chain fatty acids. *Mucosal. Immunol.* 11 (3), 785–795. doi:10.1038/mi.2017.75

Cao, Y. Y., Wang, Z., Wang, Z. H., Jiang, X. G., and Lu, W. H. (2021a). Inhibition of miR-155 alleviates sepsis-induced inflammation and intestinal barrier dysfunction by inactivating NF-κB signaling. *Int. Immunopharmacol.* 90, 107218. doi:10.1016/j.intimp.2020.107218

Cao, Y. Y., Wang, Z. H., Xu, Q. C., Chen, Q., Wang, Z., and Lu, W. H. (2021b). Sepsis induces variation of intestinal barrier function in different phase through nuclear factor kappa B signaling. *Korean J. Physiol. Pharmacol.* 25 (4), 375–383. doi:10.4196/kjpp.2021.25.4.375

Chen, J., Cao, D., Jiang, S. Q., Liu, X., Pan, W. C., Cui, H., et al. (2022). Triterpenoid saponins from Ilex pubescens promote blood circulation in blood stasis syndrome by regulating sphingolipid metabolism and the PI3K/AKT/eNOS signaling pathway. *Phytomedicine* 104, 154242. doi:10.1016/j.phymed.2022.154242

Chen, Y. N., Hu, M. R., Wang, L., and Chen, W. D. (2020). Macrophage M1/M2 polarization. *Eur. J. Pharmacol.* 877, 173090. doi:10.1016/j.ejphar.2020.173090

Contreras-Zentella, M. L., Villalobos-García, D., and Hernández-Muñoz, R. (2022). Ethanol metabolism in the liver, the induction of oxidant stress, and the antioxidant defense system. *Antioxidants* 11, 1258. doi:10.3390/antiox11071258

Dayang, E. Z., Luxen, M., Kuiper, T., Yan, R., Rangarajan, S., Meurs, M. V., et al. (2021). Pharmacological inhibition of focal adhesion kinase 1 (FAK1) and anaplastic lymphoma kinase (ALK) identified via kinome profile analysis attenuates lipopolysaccharide-induced endothelial inflammatory activation. *Biomed. Pharmacother.* 133, 111073. doi:10.1016/j.biopha.2020.111073

Ding, D., Shen, X. B., Yu, L. Z., Zheng, Y. Y., Liu, Y., Wang, W., et al. (2023). Timosaponin BII inhibits TGF-β mediated epithelial-mesenchymal transition through Smad-dependent pathway during pulmonary fibrosis. *Phytother. Res.* 37 (7), 2787–2799. doi:10.1002/ptr.7774

Ding, M. R., Tang, Z. Y., Liu, W., Shao, T. L., Yuan, P. C., Chen, K. S., et al. (2021). Burdock fructooligosaccharide attenuates high glucose-induced apoptosis and oxidative stress injury in renal tubular epithelial cells. *Front. Pharmacol.* 12, 784187. doi:10.3389/fphar.2021.784187

Du, Y., Yang, C. C., Ren, D. Y., Shao, H. J., Zhao, Y., and Yang, X. B. (2022). Fu brick tea alleviates alcoholic liver injury by modulating the gut microbiota-liver axis and inhibiting the hepatic TLR4/NF-κB signaling pathway. *Food Funct.* 13 (18), 9391–9406. doi:10.1039/d2fo01547a

Federico, A., Dallio, M., and Loguercio, C. (2017). Silymarin/silybin and chronic liver disease: a marriage of many years. *Molecules* 22 (2), 191. doi:10.3390/molecules22020191

Gao, S. H., Chen, X. J., Yu, Z. Q., Du, R., Chen, B. Z., Wang, Y. X., et al. (2023). Progress of research on the role of active ingredients of Citri Reticulatae Pericarpium in liver injury. *Phytomedicine* 115, 154836. doi:10.1016/j.phymed.2023.154836

Gaundal, L., Myhrstad, M. C. W., Rud, I., Gjøvaag, T., Byfuglien, M. G., Retterstøl, K., et al. (2022). Gut microbiota is associated with dietary intake and metabolic markers in healthy individuals. *Food Nutr. Res.* 66, 8580. doi:10.29219/fnr.v66.8580

Ge, J., Li, G. M., Chen, Z. W., Xu, W. J., Lei, X. H., and Zhu, S. G. (2023). Kaempferol and nicotiflorin ameliorated alcohol-induced liver injury in mice by miR-138-5p/SIRT1/FXR and gut microbiota. *Heliyon* 10, e23336. doi:10.1016/j.heliyon.2023.e23336

German, M. N., Musto, J., and Lucey, M. R. (2021). Novel treatments for alcoholic hepatitis. *Curr. Opin. Gastroenterol.* 37, 179–186. doi:10.1097/MOG.0000000000000725

Gudowska-Sawczuk, M., and Mroczko, B. (2022). The role of nuclear factor kappa B (NF-κB) in development and treatment of COVID-19: review. *Int. J. Mol. Sci.* 23 (9), 5283. doi:10.3390/ijms23095283

Hao, J., Bei, J., Li, Z., Han, M., Ma, B., Ma, P., et al. (2022). Qing`e pill inhibits osteoblast ferroptosis via ATM serine/threonine kinase (ATM) and the PI3K/AKT pathway in primary osteoporosis. *Front. Pharmacol.* 13, 902102. doi:10.3389/fphar.2022.902102

He, C., Wang, D., Wang, R., Huang, Y., Huang, X., Shen, S., et al. (2022). Epigallocatechin gallate induces the demethylation of actinin alpha 4 to inhibit diabetic nephropathy renal fibrosis via the NF-κB signaling pathway *in vitro*. *Dose-Response* 2022, 20. doi:10.1177/15593258221105704

Horowitz, B. Z. (2022). Silibinin: a toxicologist's herbal medicine? *Clin. Toxicol.* 60 (11), 1194–1197. doi:10.1080/15563650.2022.2128815

Hu, C., Liang, B., Sun, J., Li, J., Xiong, Z., Wang, S., et al. (2024). Synthesis and biological evaluation of indole derivatives containing thiazolidine-2,4-dione as α-glucosidase inhibitors with antidiabetic activity. *Eur. J. Med. Chem.* 264, 115957. doi:10.1016/j.ejmech.2023.115957

Hu, Y. H., Han, J., Wang, L., Shi, C., Li, Y., Olatunji, O. J., et al. (2021). α-Mangostin alleviated inflammation in rats with adjuvant-induced arthritis by disrupting adipocytes-mediated metabolism-immune feedback. *Front. Pharmacol.* 12, 692806. doi:10.3389/fphar.2021.692806

Hyland, N. P., Cavanaugh, C. R., and Hornby, P. J. (2022). Emerging effects of tryptophan pathway metabolites and intestinal microbiota on metabolism and intestinal function. *Amino Acids* 54 (1), 57–70. doi:10.1007/s00726-022-03123-x

Jeon, S., and Carr, R. (2020). Alcohol effects on hepatic lipid metabolism. *J. Lipid Res.* 61 (4), 470–479. doi:10.1194/jlr.R119000547

Jew, M. H., and Hsu, C. L. (2023). Alcohol, the gut microbiome, and liver disease. *J. Gastroenterol. Hepatol.* 38 (8), 1205–1210. doi:10.1111/jgh.16199

Jiang, T. T., Ji, C. F., Cheng, X. P., Gu, S. F., Wang, R., Li, Y., et al. (2021). α-mangostin alleviated HIF-1α-mediated angiogenesis in rats with adjuvant-induced arthritis by suppressing aerobic glycolysis. *Front. Pharmacol.* 12, 785586. doi:10.3389/fphar.2021.785586

Jiang, Y. X., Li, W., Wang, J., and Wang, G. G. (2020). Cardiac dysfunction is attenuated by ginkgolide B via reducing oxidative stress and fibrosis in diabetic rats. *Iran. J. Basic Med. Sci.* 23 (8), 1078–1084. doi:10.22038/ijbms.2020.44210.10358

Jung, J. H., Kim, S. E., Suk, K. T., and Kim, D. J. (2022). Gut microbiota-modulating agents in alcoholic liver disease: links between host metabolism and gut microbiota. *Front. Med.* 9, 913842. doi:10.3389/fmed.2022.913842

Kasper, P., Lang, S., Steffen, H. M., and Demir, M. (2023). Management of alcoholic hepatitis: a clinical perspective. *Liver Int.* 43, 2078–2095. doi:10.1111/liv.15701

Konturek, P. C., Harsch, I. A., Konturek, K., Schink, M., Konturek, T., Neurath, M. F., et al. (2018). Gut-liver axis: how do gut bacteria influence the liver? *Med. Sci.* 6 (3), 79. doi:10.3390/medsci6030079

Li, M. Y., Li, H., Min, X., Sun, J., Liang, B., Xu, L., et al. (2024). Identification of 1,3,4-thiadiazolyl-containing thiazolidine-2,4-dione derivatives as novel PTP1B inhibitors with anti-diabetic activity. *J. Med. Chem.* doi:10.1021/acs.jmedchem.4c00676

Li, W., Zhao, X., Yu, T. T., Hao, W., and Wang, G. G. (2021a). Knockout of PKC θ gene attenuates oleic acid-induced acute lung injury via reduction of inflammation and oxidative stress. *Basic Med. Sci.* 24 (7), 986–991. doi:10.22038/ijbms.2021.56908.12695

Li, Y. P., Li, Z., Chen, B. Z., Hou, Y. J., Wen, Y. L., Gan, L. S., et al. (2023). Ultrasonic assisted extraction, characterization and gut microbiota-dependent anti-obesity effect of polysaccharide from Pericarpium Citri Reticulatae 'Chachiensis. *Ultrason. Sonochem.* 95, 106383. doi:10.1016/j.ultsonch.2023.106383

Li, Y. Z., Dai, M. X., Wang, L. L., and Wang, G. D. (2021b). Polysaccharides and glycosides from Aralia echinocaulis protect rats from arthritis by modulating the gut microbiota composition. *J. Ethnopharmacol.* 269, 113749. doi:10.1016/j.jep.2020.113749

Liu, H. X., Kang, X., Yang, X. D., Yang, H., Kuang, X. Y., Ren, P., et al. (2023). Compound probiotic ameliorates acute alcoholic liver disease in mice by modulating gut microbiota and maintaining intestinal barrier. *Probiotics Antimicrob. Proteins* 15 (1), 185–201. doi:10.1007/s12602-022-10005-x

Liu, J. Q., Zhao, X. T., Qin, F. Y., Zhou, J. W., Ding, F., Zhou, G., et al. (2022a). Isoliquiritigenin mitigates oxidative damage after subarachnoid hemorrhage *in vivo* and *in vitro* by regulating Nrf2-dependent Signaling Pathway via

Targeting of SIRT1. *Phytomedicine* 105, 154262. doi:10.1016/j.phymed.2022.154262

Liu, W. B., Wang, H. L., Chen, L., Tang, B., Ke, G., Wang, S., et al. (2022b). Cucurbitacin E inhibits cellular proliferation and induces apoptosis in melanoma by suppressing HSDL2 expression. *Chin. Med.* 17 (1), 28. doi:10.1186/s13020-022-00582-y

Lu, S. H., Zhang, T., Gu, W., Yang, X. X., Lu, J. M., Zhao, R. H., et al. (2018). Volatile oil of amomum villosum inhibits nonalcoholic fatty liver disease via the gut-liver axis. *Biomed. Res. Int.* 2018, 3589874. doi:10.1155/2018/3589874

Manco, M., Putignani, L., and Bottazzo, G. F. (2010). Gut microbiota, lipopolysaccharides, and innate immunity in the pathogenesis of obesity and cardiovascular risk. *Endocr. Rev.* 31, 817–844. doi:10.1210/er.2009-0030

Morrison, D. J., and Preston, T. (2016). Formation of short chain fatty acids by the gut microbiota and their impact on human metabolism. *Gut Microbes* 7 (3), 189–200. doi:10.1080/19490976.2015.1134082

Ohashi, K., Pimienta, M., and Seki, E. (2018). Alcoholic liver disease: a current molecular and clinical perspective. *Liver Res.* 2 (4), 161–172. doi:10.1016/j.livres.2018.11.002

O'Shannessy, D. J., Somers, E. B., Wang, L. C., Wang, H. W., and Hsu, R. (2015). Expression of folate receptors alpha and beta in normal and cancerous gynecologic tissues: correlation of expression of the beta isoform with macrophage markers. *J. Ovarian Res.* 8, 29. doi:10.1186/s13048-015-0156-0

Pei, W., Zhang, Y., Li, X., Luo, M., Chen, T., Zhang, M., et al. (2020). LncRNA AK085865 depletion ameliorates asthmatic airway inflammation by modulating macrophage polarization. *Int. Immunopharmacol.* 83, 106450. doi:10.1016/j.intimp.2020.106450

Pei, Y. Q., Zheng, Y. Q., Ding, Y. D., Xu, Q. X., Cao, D., Wu, Y. N., et al. (2021). Triptolide attenuates vascular calcification by upregulating expression of miRNA-204. *Front. Pharmacol.* 11, 581230. doi:10.3389/fphar.2020.581230

Pu, Z., Sui, B., Wang, X., Wang, W., Li, L., and Xie, H. (2023). The effects and mechanisms of the anti-COVID-19 traditional Chinese medicine, dehydroandrographolide from andrographis paniculata (Burm.f.) wall, on acute lung injury by the inhibition of NLRP3-mediated pyroptosis. *Phytomedicine* 114, 154753. doi:10.1016/j.phymed.2023.154753

Qi, X. Y., Zheng, S. G., Ma, M. Y., Lian, N. Q., Wang, H. T., Chen, L. R., et al. (2022). Curcumol suppresses CCF-mediated hepatocyte senescence through blocking LC3B-Lamin B1 interaction in alcoholic fatty liver disease. *Front. Pharmacol.* 13, 912825. doi:10.3389/fphar.2022.912825

Ren, D. X., Wang, Z. M., Wu, M. M., and Wang, H. (2020). Emerging roles of SIRT1 in alcoholic liver disease. *Int. J. Biol. Sci.* 16 (16), 3174–3183. doi:10.7150/ijbs.49535

Seoane, P. I., Lee, B., Hoyle, C., Yu, S., Lopez-Castejon, G., Lowe, M., et al. (2020). The NLRP3-inflammasome as a sensor of organelle dysfunction. *J. Cell Biol.* 219 (12), e202006194. doi:10.1083/jcb.202006194

Shao, X. F., Li, B., Shen, J., Wang, Q. F., Chen, S. S., Jiang, X. C., et al. (2020). Ghrelin alleviates traumatic brain injury-induced acute lung injury through pyroptosis/NF-κB pathway. *Int. Immunopharmacol.* 79, 106175. doi:10.1016/j.intimp.2019.106175

Shen, Y. Y., Zhao, Y. X., Zhong, C. X., Huang, H. M., Yang, Z. Q., Wu, M. X., et al. (2024). Primary study on the effects and mechanisms of separate and combined decoctions of Scutellaria baicalensis Georgi - coptis chinensis Franch extracts in relieving acute alcoholic liver injury in rats. *J. Ethnopharmacol.* 324, 117790. doi:10.1016/j.jep.2024.117790

Shuai, C., Xia, G. Q., Yuan, F., Wang, S., and Lv, X. W. (2021). CD39-mediated ATP-adenosine signalling promotes hepatic stellate cell activation and alcoholic liver disease. *Eur. J. Pharmacol.* 905, 174198. doi:10.1016/j.ejphar.2021.174198

Singhal, R., Donde, H., Ghare, S., Stocke, K., Zhang, J. W., Vadhanam, M., et al. (2021). Decrease in acetyl-CoA pathway utilizing butyrate-producing bacteria is a key pathogenic feature of alcohol-induced functional gut microbial dysbiosis and development of liver disease in mice. *Gut Microbes* 13 (1), 1946367. doi:10.1080/19490976.2021.1946367

Soleimani, V., Delghandi, P. S., Moallem, S. A., and Karimi, G. (2019). Safety and toxicity of silymarin, the major constituent of milk thistle extract: an updated review. *Phytother. Res.* 33 (6), 1627–1638. doi:10.1002/ptr.6361

Stärkel, P., Leclercq, S., Timary, P. D., and Schnabl, B. (2018). Intestinal dysbiosis and permeability: the yin and yang in alcohol dependence and alcoholic liver disease. *Clin. Sci.* 132 (2), 199–212. doi:10.1042/CS20171055

Sun, S., Zhang, J., Li, H., Du, Y., Li, S., Li, A., et al. (2021). Anti-inflammatory activity of the water extract of Chloranthus serratus roots in LPS-stimulated RAW264.7 cells mediated by the Nrf2/HO-1, MAPK and NF-κB signaling pathways. *J. Ethnopharmacol.* 271, 113880. doi:10.1016/j.jep.2021.113880

Sun, S. P., Wang, Y., Du, Y. Y., Sun, Q., He, L. J., Zhu, E. Z., et al. (2020). Oxidative stress-mediated hepatotoxicity in rats induced by ethanol extracts of different parts of Chloranthus serratus. *Pharm. Biol.* 58 (1), 1277–1289. doi:10.1080/13880209.2020.1859552

Sun, X., Zheng, Y. Q., Tian, Y. Q., Xu, Q. X., Liu, S. C., Li, H. H., et al. (2023). Astragalus polysaccharide alleviates alcoholic-induced hepatic fibrosis by inhibiting polymerase I and transcript release factor and the TLR4/JNK/NF-κB/MyD88 pathway. *J. Ethnopharmacol.* 314, 116662. doi:10.1016/j.jep.2023.116662

Tall, A. R., and Yvan-Charvet, L. (2015). Cholesterol, inflammation and innate immunity. *Nat. Rev. Immunol.* 15 (2), 104–116. doi:10.1038/nri3793

Tao, Z. S., Li, T. L., and Wei, S. (2022). Silymarin prevents iron overload induced bone loss by inhibiting oxidative stress in an ovariectomized animal model. *Chem. Biol. Interact.* 366, 110168. doi:10.1016/j.cbi.2022.110168

Tarantino, G., Cataldi, M., and Citro, V. (2022). Could alcohol abuse and dependence on junk foods inducing obesity and/or illicit drug use represent danger to liver in young people with altered psychological/relational spheres or emotional problems? *Int. J. Mol. Sci.* 23 (18), 10406. doi:10.3390/ijms231810406

Tarantino, G., and Citro, V. (2024). What are the common downstream molecular events between alcoholic and nonalcoholic fatty liver? *Lipids Health Dis.* 23 (1), 41. doi:10.1186/s12944-024-02031-1

Thursz, M., Gual, A., Lackner, C., Mathurin, P., Morenno, C., Spahr, L., et al. (2018). EASL clinical practice guidelines: management of alcohol-related liver disease. *J. Hepatol.* 69 (1), 154–181. doi:10.1016/j.jhep.2018.03.018

Wang, L., Wang, P., Wang, D., Tao, M., Xu, W., and Olatunji, O. J. (2020a). Anti-inflammatory activities of kukoamine A from the root bark of lycium chinense Miller. *Nat. Prod. Comm.* 15, 1934578X2091208. doi:10.1177/1934578x20912088

Wang, Q. H., Li, Y., Dou, D. Y., Wang, R., Jiang, T. T., Wang, L., et al. (2021a). Nicotinamide mononucleotide-elicited NAMPT signaling activation aggravated adjuvant-induced arthritis in rats by affecting peripheral immune cells differentiation. *Int. Immunopharmacol.* 98, 107856. doi:10.1016/j.intimp.2021.107856

Wang, R. S., and Mu, J. J. (2021b). Arbutin attenuates ethanol-induced acute hepatic injury by the modulation of oxidative stress and Nrf-2/HO-1 signaling pathway. *J. Biochem. Mol. Toxicol.* 35 (10), e22872. doi:10.1002/jbt.22872

Wang, X. H., Shen, C. Z., Wang, X. W., Tang, J., Wu, Z. J., Huang, Y. Z., et al. (2023). Schisandrin protects against ulcerative colitis by inhibiting the SGK1/NLRP3 signaling pathway and reshaping gut microbiota in mice. *Chin. Med.* 18 (1), 112. doi:10.1186/s13020-023-00815-8

Wang, Z., Zhang, X. X., Zhu, L. L., Yang, X. L., He, F., Wang, T., et al. (2020b). Inulin alleviates inflammation of alcoholic liver disease via SCFAs-inducing suppression of M1 and facilitation of M2 macrophages in mice. *Int. Immunopharmacol.* 78, 106062. doi:10.1016/j.intimp.2019.106062

Wu, J. X., Ye, X. T., Yang, S. H., Yu, H., Zhong, L. Y., and Gong, Q. F. (2021). Systems pharmacology study of the anti-liver injury mechanism of *Citri Reticulatae Pericarpium*. *Front. Pharmacol.* 12, 618846. doi:10.3389/fphar.2021.618846

Wu, Y. J., Zhang, S. S., Yin, Q., Lei, M., Wang, Q. H., Chen, W. G., et al. (2023). α-mangostin inhibited M1 polarization of macrophages/monocytes in antigeni nduced Arthritis mice by up-regulating silent information regulator 1 and peroxisome proliferators-activated receptor γ simultaneously. *Drug Des. Dev. Ther.* 17, 563–577. doi:10.2147/DDDT.S397914

Xing, Y. J., Liu, B. H., Wan, S. J., Cheng, Y., Zhou, S. M., Sun, Y., et al. (2021). A SGLT2 inhibitor dapagliflozin alleviates diabetic cardiomyopathy by suppressing high glucose-induced oxidative stress *in vivo* and *in vitro*. *Front. Pharmacol.* 12, 708177. doi:10.3389/fphar.2021.708177

Yang, Z., Yin, Q., Olatunji, O. J., Li, Y., Pan, S., Wang, D. D., et al. (2020). Activation of cholinergic anti-inflammatory pathway involved in therapeutic actions of α-mangostin on lipopolysaccharide-induced acute lung injury in rats. *Int. J. Immunopathol. Pharmacol.* 34, 2058738420954941. doi:10.1177/2058738420954941

You, M., and Arteel, G. E. (2019). Effect of ethanol on lipid metabolism. *J. Hepatol.* 70 (2), 237–248. doi:10.1016/j.jhep.2018.10.037

Zhang, L., Ren, X. H., He, J., Li, W. N., Hao, J. W., Jing, Y. R., et al. (2021a). Protective effect of Phaeoporus obliquus polysaccharide against acute liver injury induced by carbon tetrachloride and alcohol in mice. *Pak. J. Pharm. Sci.* 34 (2), 649–656. doi:10.36721/PJPS.2021.34.2.REG.649-656.1

Zhang, S. P., Zhu, P., Yuan, J. N., Cheng, K. M., Xu, Q. X., Chen, W., et al. (2023b). Non-alcoholic fatty liver disease combined with rheumatoid arthritis exacerbates liver fibrosis by stimulating co-localization of PTRF and TLR4 in rats. *Front. Pharmacol.* 14, 1149665. doi:10.3389/fphar.2023.1149665

Zhang, T., Lu, S. H., Bi, Q., Liang, L., Wang, Y. F., Yang, X. X., et al. (2017). Volatile oil from amomi fructus attenuates 5-fluorouracil-induced intestinal mucositis. *Front. Pharmacol.* 8, 786. doi:10.3389/fphar.2017.00786

Zhang, X. H., Peng, L., Zhang, J., Dong, Y. P., Wang, C. J., Liu, C., et al. (2020). Berberine ameliorates subarachnoid hemorrhage injury via induction of sirtuin 1 and inhibiting HMGB1/Nf-κB pathway. *Front. Pharmacol.* 11, 1073. doi:10.3389/fphar.2020.01073

Zhang, X. S., Lu, Y., Li, W., Tao, T., Peng, L., Wang, W. H., et al. (2021b). Astaxanthin ameliorates oxidative stress and neuronal apoptosis via SIRT1/NRF2/Prx2/ASK1/p38 after traumatic brain injury in mice. *Br. J. Pharmacol.* 178 (5), 1114–1132. doi:10.1111/bph.15346

Zhang, Y. X., Zhang, X. T., Li, H. J., Zhou, T. F., Zhou, A. C., Zhong, Z. L., et al. (2021c). Antidepressant-like effects of helicid on a chronic unpredictable mild stress-

induced depression rat model: inhibiting the IKK/IκBα/NF-κB pathway through NCALD to reduce inflammation. *Int. Immunopharmacol.* 93, 107165. doi:10.1016/j.intimp.2020.107165

Zhou, H. H., Zhang, Y. M., Zhang, S. P., Xu, Q. X., Tian, Y. Q., Li, P., et al. (2021). Suppression of PTRF alleviates post-infectious irritable bowel syndrome via downregulation of the TLR4 pathway in rats. *Front. Pharmacol.* 12, 724410. doi:10.3389/fphar.2021.724410

Zhou, Y., Liu, L., Xiang, R., Bu, X., Qin, G., Dai, J., et al. (2023). Arctigenin mitigates insulin resistance by modulating the IRS2/GLUT4 pathway via TLR4 in type 2 diabetes mellitus mice. *Int. Immunopharmacol.* 114, 109529. doi:10.1016/j.intimp.2022.109529

Zhou, Y., Xiang, R., Qin, G., Ji, B., Yang, S., Wang, G., et al. (2022). Xanthones from Securidaca inappendiculata Hassk. attenuate collagen-induced arthritis in rats by inhibiting the nicotinamide phosphoribosyltransferase/glycolysis pathway and macrophage polarization. *Int. Immunopharmacol.* 111, 109137. doi:10.1016/j.intimp.2022.109137

Zhou, Y., Yuan, G. D., Zhong, F. D., and He, S. Q. (2020). Roles of the complement system in alcohol-induced liver disease. *Clin. Mol. Hepatol.* 26 (4), 677–685. doi:10.3350/cmh.2020.0094

Zhu, L. R., Li, S. S., Zheng, W. Q., Ni, W. J., Cai, M., and Liu, H. P. (2023). Targeted modulation of gut microbiota by traditional Chinese medicine and natural products for liver disease therapy. *Front. Immunol.* 14, 1086078. doi:10.3389/fimmu.2023.1086078

Zogona, D., Zongo, A. W. S., Elkhedir, A. E., Salah, M., Tao, M. F., Li, R., et al. (2023). Red raspberry supplementation mitigates alcohol-induced liver injury associated with gut microbiota alteration and intestinal barrier dysfunction in mice. *Food. Funct.* 14 (2), 1209–1226. doi:10.1039/d2fo03245g

frontiers | Frontiers in Pharmacology

TYPE Original Research
PUBLISHED 10 July 2024
DOI 10.3389/fphar.2024.1422310

Check for updates

OPEN ACCESS

EDITED BY
Xi Zheng,
Rutgers, The State University of New Jersey, United States

REVIEWED BY
Xian Wu,
Miami University, United States
Nai-Yun Ji,
Chinese Academy of Sciences (CAS), China
Yi Zhang,
Guangdong Ocean University, China

*CORRESPONDENCE
Hang Ma,
hang_ma@uri.edu
Dongli Li,
wyuchemldl@wyu.edu.cn

RECEIVED 23 April 2024
ACCEPTED 20 June 2024
PUBLISHED 10 July 2024

CITATION
Fan F, Chen L, Chen C, Ang S, Gutkowski J, Seeram NP, Ma H and Li D (2024), Prenylated flavonoids from *Sophora flavescens* inhibit mushroom tyrosinase activity and modulate melanogenesis in murine melanoma cells and zebrafish.
*Front. Pharmacol.* 15:1422310.
doi: 10.3389/fphar.2024.1422310

COPYRIGHT
© 2024 Fan, Chen, Chen, Ang, Gutkowski, Seeram, Ma and Li. This is an open-access article distributed under the terms of the Creative Commons Attribution License (CC BY). The use, distribution or reproduction in other forums is permitted, provided the original author(s) and the copyright owner(s) are credited and that the original publication in this journal is cited, in accordance with accepted academic practice. No use, distribution or reproduction is permitted which does not comply with these terms.

# Prenylated flavonoids from *Sophora flavescens* inhibit mushroom tyrosinase activity and modulate melanogenesis in murine melanoma cells and zebrafish

Fenling Fan[1], Lanqing Chen[1], Caihong Chen[1], Song Ang[1], Justin Gutkowski[2], Navindra P. Seeram[2], Hang Ma[2]* and Dongli Li[1,3]*

[1]School of Pharmacy and Food Engineering, Wuyi University, Jiangmen, Guangdong, China, [2]Bioactive Botanical Research Laboratory, Biomedical and Pharmaceutical Sciences, College of Pharmacy, University of Rhode Island, Kingston, RI, United States, [3]Guangdong Provincial Key Laboratory of Large Animal Models for Biomedicine, Wuyi University, Jiangmen, Guangdong, China

**Background:** *Sophora flavescens*, a traditional Chinese medicine for treating conditions associated with abnormal skin pigmentation, contains flavonoids with inhibitory effects on tyrosinase. However, their mechanisms of action and their modulatory effects on melanogenesis remain unclear.

**Methods:** Herein, a group of prenylated flavonoids was identified from *S. flavescens* extracts and their inhibitory activities on mushroom tyrosinase were evaluated. The anti-melanogenesis effects of these prenylated flavonoids were investigated in cellular (with murine melanoma cells) and animal (with zebrafish) models.

**Results:** Prenylated flavonoids including isoanhydroicaritin (IAI), kurarinone (KR), and sophoraflavanone G (SG) were the major active constituents in *S. flavescens* extracts with anti-tyrosinase activity ($IC_{50}$ = 0.7, 7.1, and 6.7 μM, respectively). Enzyme kinetic assays showed that IAI, KR, and SG had a mixed type of tyrosinase inhibition, supported by data from computational docking. Notably, KR at concentrations of 5 and 10 μM enhanced intracellular tyrosinase activity and stimulated melanin production in B16F10 cells, whereas SG and IAI did not exhibit significant activity. Further studies with the zebrafish model showed that IAI (80 and 160 μM) inhibited melanin biosynthesis by about 30.0% while KR (20 μM) stimulated melanogenesis by 36.9%. Furthermore, a zebrafish depigmentation model supported the anti-melanogenesis effect of IAI (80 and 160 μM) by 33.0% and 34.4%, respectively.

**Conclusion:** In summary, IAI was identified as a tyrosinase inhibitor with an anti-melanogenic effect and KR was an enhancer for melanin production in B16F10 cells and zebrafish. Findings from the current study suggest that IAI

and KR from *S. flavescens* may exert contrasting effects in the modulation of melanin production, providing important insights into the development of *S. flavescens* as a cosmeceutical or medicinal ingredient.

KEYWORDS

***Sophora flavescens*, prenylated flavonoid, isoanhydroicaritin, kurarinone, tyrosinase, melanogenesis, zebrafish**

# 1 Introduction

Melanins are biological pigments responsible for the skin, hair, and eye color generated by specialized epidermal cells (Mort et al., 2015; Karunarathne et al., 2019). Under normal physiological conditions, melanins confer protective effects against ultraviolet (UV) radiation (Jang et al., 2020; Rai et al., 2020). Defective melanin production is associated with skin hypopigmentation, which increases the risk of various disorders including skin cancers (Ahmed et al., 2021). However, excessive or frequent UV exposure can result in abnormal melanin production, leading to hyperpigmentation conditions such as melasma and age spots (Grimes et al., 2006; Choi et al., 2022). The production of melanin is a complex biological process. Tyrosinase (EC 1.14.18.1) is the main rate-limiting enzyme in biosynthesis of melanin. It catalyzes the conversion of tyrosine to dihydroxyphenylalanine (DOPA) and further oxidizes DOPA to dopaquinone. Subsequent steps involve additional enzymes, such as tyrosinase-related protein 1 (TRP-1) and dopachrome tautomerase (DCT), to produce eumelanin (Del Marmol and Beermann, 1999). Melanin production can be induced by $\alpha$-melanocyte-stimulating hormone ($\alpha$-MSH) and 3-isobutyl-1-methylxanthine (IBMX) (Park et al., 2011; Han et al., 2020). The activity of tyrosinase is stimulated by $\alpha$-MSH and IBMX via the cyclic adenosine phosphate (cAMP) pathway (Kim et al., 2018). $\alpha$-MSH binds to the melanocortin-1 receptor (MC1R) on the cell surface, activates the protein kinase A (PKA) pathway, and phosphorylates CREB transcription factors, which collectively induce the expression of microphthalmia-associated transcription factor (MITF) (D'Mello et al., 2016). MITF can regulate the expression of TRP1 and DCT by binding to the M-box of the distal tyrosinase element (TDEs) (Yasumoto et al., 1994; Yasumoto et al., 1997).

Numerous natural product-based tyrosinase inhibitors (e.g., arbutin and kojic acid) have been widely used for anti-melanogenesis (Slominski et al., 2004; Pillaiyar et al., 2017). However, several anti-melanogenic agents are reported to cause side effects such as albinism (Niu and Aisa, 2017). Natural products with the opposite effect, i.e., compounds that can enhance tyrosinase activity, may restore pigmentation as a management for pathological conditions such as vitiligo (Heriniaina et al., 2018). Thus, compounds that can modulate the production of melanins by either inhibiting tyrosinase activity or increasing melanogenesis are of interest to the biomedical and cosmetic industries (Lajis and Ariff, 2019). *Sophora flavescens* Aiton (Kushen in Chinese), belonging to the Fabaceae family, has been used in traditional Chinese medicine (TCM) for the treatment of dysentery, hematochezia, jaundice, eczema, and ulcers (He et al., 2015; Kim et al., 2018). Notably, published studies support that *S. flavescens* extracts can exert various modulatory effects on melanin-related skin conditions including hyperpigmentation (Shin et al., 2013) and vitiligo (Sun and Bao, 2008; Cai et al., 2011; Zhang and Zhang, 2020). The phytochemical investigations reported that the main active metabolites of *S. flavescens* are alkaloids and flavonoids (He et al., 2015). Some of these flavonoids are tyrosinase inhibitors (Kim et al., 2003; Son et al., 2003; Hyun et al., 2008; Kim et al., 2018). For instance, prenylated flavonoids including sophoraflavanone G (SG), kuraridin, and kurarinone (KR) from *S. flavescens* exert a strong inhibitory effect on tyrosinase activity (Kim et al., 2003). However, the tyrosinase inhibition mechanism of these prenylated flavonoids remains unclear. Moreover, the modulatory effects of *S. flavescens* prenylated flavonoids on melanogenesis in cells- or animal-based models are unknown. As a continuous effort to study the bioactive constituents of medicinal plants from the Lingnan regions in China (Li et al., 2015; Zhou et al., 2019; Xu et al., 2021; Zhang et al., 2021), we aimed to evaluate the modulatory effects of *S. flavescens* extract and its active constituents on tyrosinase activity and melanogenesis in the current study. Herein, we evaluated the inhibitory effect of *S. flavescens* extract and four prenylated flavonoids on mushroom tyrosinase *in vitro*, and the anti-tyrosinase and anti-melanogenesis effects of these flavonoids using cellular (murine melanoma cells) model. In addition, prenylated flavonoids were further evaluated for their effects on melanogenesis with a zebrafish model.

# 2 Materials and methods

## 2.1 Materials

Tyrosinase, 3,4-dihydroxy-L-phenylalanine (L-DOPA), 8-methoxypsoralen (8-MOP) (purity 98%), glabridin (purity 98%), $\alpha$-MSH, 1-phenyl-2-thiourea (PTU), and 3-(4,5-dimethylthiazol-2-yl)-2,5-diphenyltetrazolium bromide (MTT) were purchased from Sigma-Aldrich (St. Louis, MO, United States). Kushenol I (KI) (purity>98%), isoanhydroicaritin (IAI, purity > 98%), KR (purity > 98%), and SG (purity > 98%) were purchased from Shanghai Yuanye Bio-Technology Co., Ltd. Dulbecco's modified Eagle's medium (DMEM), fetal bovine serum (FBS), penicillin/streptomycin (P/S) and bicinchoninic acid assay (BCA) kit were purchased from Thermo Fisher Scientific (Waltham, MA, United States). TYR, TRP-1, MITF, DCT, and $\beta$-actin primary antibodies were acquired from Affinity Biosciences (Woburn, MA, United States). The anti-mouse IgG and anti-rabbit IgG secondary antibodies were bought from Cell Signaling Technology (Beverly, MA, United States). The roots of *S. flavescens* from Shanxi Province were purchased from Anguo Kangde Ruiqi Trading Co., LTD.

## 2.2 Preparation of extracts and principal component analysis

Dried roots of *S. flavescens* were powdered and weighed in five portions (5 g each). Ethyl acetate, dichloromethane, 70%

methanol, 70% ethanol, and dichloromethane/methanol (1:1; v/v) were used for their respective extractions. The extracts were filtered after being sonicated for 30 min at 40 kHz (500 W, 40°C) and concentrated under reduced pressure, then weighed at room temperature for use. All samples were dissolved with methanol and filtered through a membrane filter (0.22 μm). The contents of major flavonoids in them were determined by a chromatographic method performed on a waters ACQUITY UPLC H-class PLUS system coupled with a DAD detector. The separation of flavonoids was achieved on an ACQUITY-UPLC-BEH-C18 column (100 mm × 2.1 mm; 1.7 μm) at a flow rate of 0.3 mL/min with detection wavelengths of 280 nm and 295 nm. The gradient elution system consisting of solvent A (water) and solvent B (methanol) was set as follows: 0–2 min, 50%–65% B; 2–4 min, 65%–70% B; 4–6 min, 70%–75% B; 6–8 min, 75%–80% B; 8–10 min, 80% B; 10–12 min, 80%–90% B; 12–14 min, 90%–100% B; 14–18 min, 100% B; 18–20 min, 100%–50% B. The injection volume for each analysis was 2 μL and the column temperature was kept at 35°C. The peak area corresponding to different concentrations of each standard was measured and recorded. Standard curves were constructed with the concentration as the X-axis and the peak area response value as the Y-axis. The content of each compound was determined by substituting the standard curve into the test sample.

## 2.3 Cell line and cell culture

B16F10 cells were purchased from Procell Life Science and Technology Co., Ltd. (Wuhan, China). The cells were cultured in DMEM supplemented with 10% FBS and 1% penicillin and streptomycin at 37°C under an atmosphere of 5% $CO_2$. To control the pH value of the culture medium to be suitable for cell growth, two equal volumes of DMEM with 3.7 g/L $NaHCO_3$ or 1.5 g/L $NaHCO_3$ were mixed for use.

## 2.4 Cell viability assay

B16F10 cells were seeded into 96-well plates at the density of $5 \times 10^4$ cells/mL, and incubated at 37°C for 24 h. Then, the cells were treated with different concentrations of test samples for 48 h. After incubation, 20 μL MTT (5 mg/mL) was added to each well, and incubated for another 4 h at 37°C. The reaction was stopped by adding 150 μL DMSO per well. The optical density at 490 nm was measured using a microplate reader. Cell viability was calculated as the percentage of viable cells relative to the control group.

## 2.5 *In vitro* tyrosinase inhibition assay

Tyrosinase inhibition assay was measured by using L-tyrosine as a substrate according to a previously described method with minor modifications (Kim et al., 2018). Briefly, a mixture of phosphate buffer (130 μL, 50 mM, pH 6.8), tyrosinase solution (10 μL, 666.67 U/mL) and different concentrations of test samples (10 μL) was incubated in 96-well plates for 5 min. After adding substrate L-tyrosine solution (50 μL, 2 mM) to each well and incubating at 37°C for another 20 min, the absorbance was measured at the wavelength of 475 nm using a microplate reader. The inhibitory rate was calculated using the following formula:

$$\text{Inhibitory rate (\%)} = \left(1 - \frac{A - B}{C - D}\right) \times 100\%$$

where A is the absorbance of the sample group, B is the absorbance of the background group, C is the absorbance of the control group, and D is the absorbance of the blank group. The test sample concentration that inhibits 50% of tyrosinase activity ($IC_{50}$) was calculated. All tests were performed in triplicate.

## 2.6 Tyrosinase inhibition kinetic analysis

Based on $IC_{50}$ values, test samples that showed better inhibitory activity were selected for kinetic analysis. The enzyme reaction kinetics of these compounds were measured by constructing Lineweaver-Burk plots of inverse velocities (1/[V]), contrary to the inverse of substrate concentration (1/[S]) (Yoshino and Murakami, 2009; Butt et al., 2019). Preincubations and measurement times were performed using the same protocol as described above. The substrate tyrosine concentration was kept between 0.5 and 8 mM in all kinetic studies, test sample concentrations were set as follows: glabridin (0–0.625 μM), KR (0–5 μM), SG (0–10 μM), IAI (0–2 μM). The values of the kinetic constants were calculated using Lineweaver-Burk plot analysis, and the maximum velocity ($V_{max}$) and Michaelis constant ($K_m$) were also calculated by the Lineweaver-Burk plots with the various concentrations of substrate.

## 2.7 Molecular docking

To anticipate the ligand-receptor interactions, molecular docking experiments were conducted using AutoDock Tools software. The three-dimensional structures of compounds were downloaded from https://pubchem.ncbi.nlm.nih.gov/ in SDF format, which was converted to PDB format using the Discovery Studio 4.5 software (Accelrys, San Diego, CA). A crystal structure of tyrosinase (PDB ID: 2Y9X, resolution: 2.78Å) was retrieved in PDB format from the RCSB protein data bank (https://www.rcsb.org/). Water molecules, ions, and other known ligands were removed. Then, the grid map was set to the dimensions of 60 × 60 × 60 with a spacing of 0.375 Å in the process of docking. The lowest energy docking conformation at the binding site for each compound was selected and further analyzed using Discovery Studio 4.5 software.

## 2.8 Measurement of tyrosinase activity in B16F10 cells

Intracellular tyrosinase activity was determined by measuring the rate of oxidation of L-DOPA to dopachrome according to a previously described method with a slight modification (Maack and Pegard, 2016). The tyrosinase inhibitor glabridin (Zhang et al., 2023) and tyrosinase

activator 8-MOP (Yin et al., 2018) were both utilized as controls to ensure the accuracy of tyrosinase activity assay in living cells. B16F10 cells were cultured in 24-well plates at the density of $5 \times 10^4$ cells/mL overnight and then treated with different concentrations of test samples for 48 h. After treatments, cells were washed twice with PBS, lysed with PBS containing 1% Triton X-100, and frozen at −80°C for 1 h. The lysates were then clarified by centrifugation for 20 min at 4°C, 12,000 r/min. The protein content in the supernatants was measured using the Pierce BCA protein assay kit. After protein quantification and the adjustment of the protein concentrations, 100 μL of each lysate was mixed with 100 μL of 4 mM L-DOPA in a 96-well plate, and then incubated at 37°C for 1 h, the optical density at 475 nm was measured using a microplate reader. Tyrosinase activity was expressed as a percentage of the control. All experiments were carried out at least three times.

## 2.9 Measurement of melanin content in B16F10 cells

Measurement of melanin content was carried out according to a previously described method with a slight modification (Karunarathne et al., 2019). B16F10 cells were cultured in 6-well plates at the density of $2 \times 10^5$ cells/mL overnight before being treated with different concentrations of test samples for 48 h. After the treatments, the medium was discarded and the cells were washed twice with PBS and were collected, then 200 μL of RIPA lysis buffer was added to each well, and left standing in an ice bath for 40 min. The lysates were then clarified by centrifugation for 20 min at 4°C, 12,000 r/min. The protein content in the supernatants was measured using the Pierce BCA protein assay kit. Then the harvested cell pellets were photographed and dissolved in 100 μL of 1 M NaOH (containing 10% DMSO) at 100°C for 1 h. Melanin content was determined by measuring absorption at 405 nm. For the accurate calculation of melanin content, absorbance values were normalized to total protein absorbance values.

## 2.10 Western blotting

Equal amounts of proteins from the preceding step were loaded and separated by using the 10% SDS-PAGE gels before being electro-transferred onto polyvinylidene fluoride membranes. The membrane was then blocked with 5% skim milk in TBST (Tris-buffered saline containing 0.1% Tween 20) at room temperature for 2 h. The blots were incubated overnight with primary antibodies against TYR, TRP-1, MITF, DCT, and $\beta$-actin at 4°C. After washing thrice with TBST (5 min), the membrane was incubated with the secondary antibody for 1 h at room temperature. The protein bands were detected using the ECL detection kit and imaged using a chemiluminescence gel imaging system, and the band intensities were analyzed by the Image J software.

## 2.11 Origin and maintenance of zebrafish

AB strain zebrafish were purchased from Guangdong Perfect Life Health Science and Technology Research Institute Co., LTD, and maintained at 28°C in a temperature-controlled room with a 14/10 h day/night cycle. Zebrafish embryos were produced by natural mating and raised in 2,000 mL of embryo media, which included 7.0 g NaCl, 0.4 g $NaHCO_3$, 0.1 g KCl, and 0.2 g $CaCl_2$ in distilled water. The day before the experiment was performed, female and male zebrafish were placed in the breeding tank at a ratio of 1:1 and embryos were collected the next morning for subsequent experiments.

## 2.12 Determination of the maximum tolerated concentration (MTC)

Zebrafish embryos that were developing normally at 24 h were chosen at random, five zebrafish embryos per well were seeded in 48 well plates, and each group was set up with three duplicates. The embryo culture medium in the 48-well plate was removed except the blank group, and 1 mL of culture medium containing different concentrations of test samples was added to treatment groups for 24 h. The vehicle control group was added to the embryo culture medium containing 0.1% of DMSO. MTC was defined as the concentration group that did not show any embryonic death after 24 h of treatments.

## 2.13 Melanogenesis in zebrafish larvae *in vivo*

To assess the effects of these compounds on melanogenesis *in vivo*, the total melanin content of whole zebrafish extracts was measured according to a previously described method with minor modification (Karunarathne et al., 2019; Ding et al., 2021). Briefly, zebrafish larvae of 24 h post-fertilized (hpf) were seeded in 24-well plates with ten embryos per well, each group was set up with four replicates and pretreated with 200 μM PTU for 24 h. Then, the culture medium was replaced with different concentrations of test samples and treated for another 48 h. 8-MOP (50 μM) was used as a positive control, blank controls were not treated and were cultured normally. In addition, to further verify the whitening effect of the compounds, ten zebrafish larvae (24 hpf) per well were seeded in a 24-well plate and cultured for another 24 h using fresh culture media, and each group was set up with four duplicates. Then, the culture medium was replaced with different concentrations of test samples, and the zebrafish larvae were incubated for another 48 h. 8-MOP (50 μM) and arbutin (100 mM) were used as positive controls. Spontaneous melanin content was measured from zebrafish larvae at 96 hpf. The fish embryos were fixed upright with sodium carboxymethylcellulose fixative. Five fish embryos from each experiment were randomly selected for photography under a stereomicroscope. The densitometric analysis was performed using Image J software.

## 2.14 Statistical analyses

All data are presented as the mean ± SD of at least three independent experiments. Student t-tests were used to compare the two groups and one-way analysis of variance (ANOVA) was used to determine any statistical differences between multiple groups. When the $p$-value was less than 0.05, the difference between groups was considered statistically significant.

TABLE 1 Yield and tyrosinase inhibitory activity of *Sophora flavescens* extract.

| Solvent | Weight of extract (mg) | Rate of yield (%) | $IC_{50}$ (μg/mL) |
|---|---|---|---|
| 70% ethanol | 1518.7 | 30.4 | 6.9 |
| 70% methanol | 1377.7 | 27.6 | 90.0 |
| ethylacetate | 92.5 | 1.9 | 0.7 |
| dichloromethane | 81.0 | 1.6 | 0.4 |
| dichloromethane:methanol (1:1) | 806.3 | 16.1 | 5.0 |

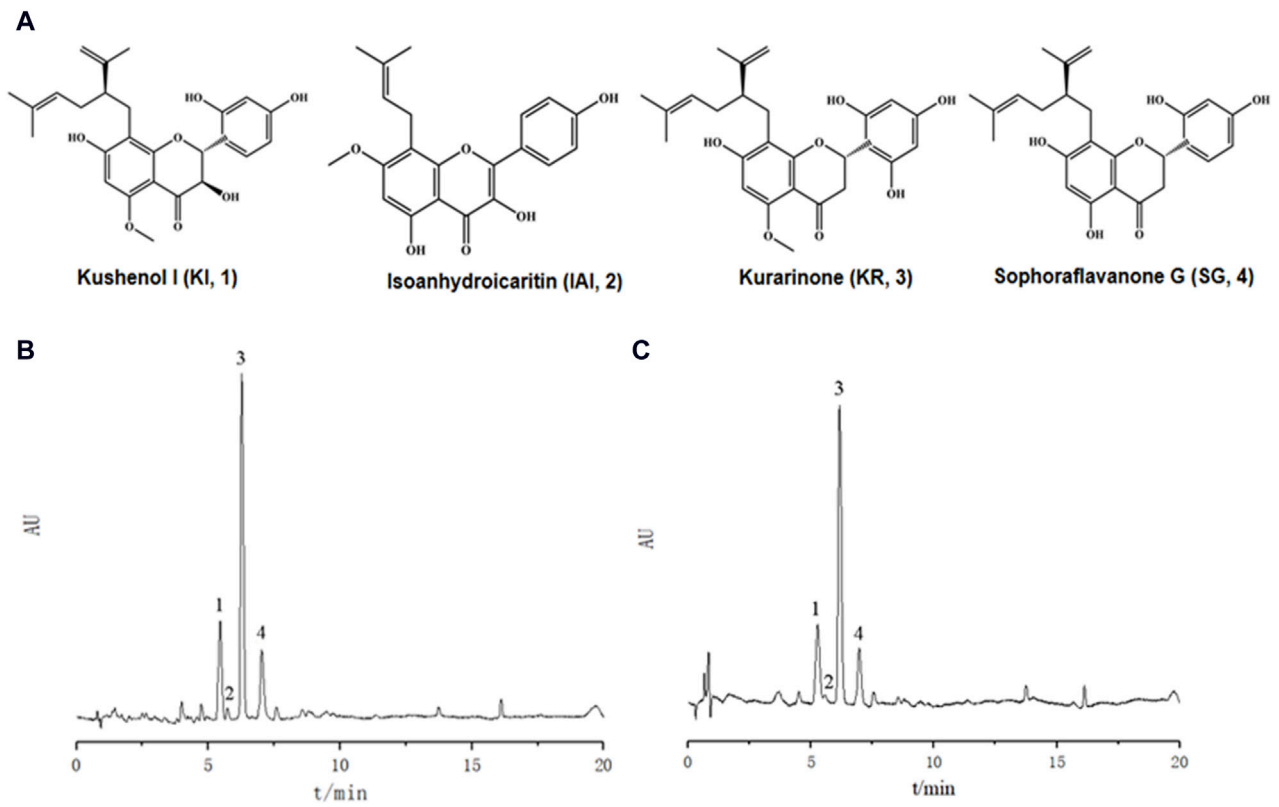


FIGURE 1
UPLC chromatograms of *Sophora flavescens* extract. **(A)** Chemical structures of the four major chemical components. **(B)** SF-EA, **(C)** SF-DM. Peak 1: KI, peak 2: IAI, peak 3: KR, peak 4: SG.

# 3 Results

## 3.1 Tyrosinase inhibition activity and chemical components of *Sophora flavescens* extracts

Ultrasonic-assisted extraction with five solvents yielded a 70% aqueous ethanol extract (1,518.7 mg), a 70% aqueous methanol extract (1,377.7 mg), an ethyl acetate extract (92.5 mg), a dichloromethane extract (81.0 mg) and a dichloromethane/methanol (1:1; v/v) extract (806.3 mg), respectively. Then, the inhibitory activity of each extract against tyrosinase was evaluated separately (Table 1). The extracts of ethyl-acetate (SF-EA) and dichloromethane (SF-DM) showed stronger inhibitory activity with $IC_{50}$ values of 0.7 μg/mL and 0.4 μg/mL, respectively. Therefore, SF-EA and SF-DM extracts were selected for further qualitative and quantitative analyses of their main chemical components by UPLC (Figure 1). The peaks were assigned by comparing their retention times ($t_R$) with that of each reference compound. Peaks 1–4 were determined as prenylated flavonoids KI ($t_R$ = 5.3 min), IAI ($t_R$ = 5.8 min), KR ($t_R$ = 6.2 min), and SG ($t_R$ = 7.0 min), respectively, and their content in SF-EA and SF-DM extracts were shown in Tables 2, 3.

In addition, we purchased the standard of the four main compounds and measured the tyrosinase activity. IAI and the positive control glabridin (a prenylated flavonoids from licorice) (Yoshioka et al., 2020) had the strongest inhibitory effect on

TABLE 2 Contents of the four major components in SF-EA extract.

| References | Regression equation | $r^2$ | Linearity range μg/mL | Content/% |
|---|---|---|---|---|
| KI (1) | y = 9130.2x+399.6 | 0.9990 | 1.5–59.0 | 2.3 |
| IAI (2) | y = 903.8x-699.6 | 0.9999 | 1.0–8.0 | 3.0 |
| KR (3) | y = 15437.0x-8480.5 | 0.9992 | 1.1–56.0 | 6.4 |
| SG (4) | y = 9829.4x-6972.1 | 0.9994 | 1.2–62.0 | 2.8 |

TABLE 3 Contents of the four main components in SF-DM extract.

| References | Regression equation | $r^2$ | Linearity range μg/mL | Content/% |
|---|---|---|---|---|
| KI (1) | y = 9130.2x+399.6 | 0.9990 | 1.5–59.0 | 2.1 |
| IAI (2) | y = 903.8x-699.6 | 0.9999 | 1.0–8.0 | 2.8 |
| KR (3) | y = 15437.0x-8480.5 | 0.9992 | 1.1–56.0 | 4.7 |
| SG (4) | y = 9829.4x-6972.1 | 0.9994 | 1.2–62.0 | 2.1 |

TABLE 4 Tyrosinase inhibitory activity of the four major chemical components.

| Compound | $IC_{50}$ values (μM) |
|---|---|
| KI | >80 |
| IAI | 0.7 |
| KR | 7.1 |
| SG | 6.7 |
| Glabridin | 0.1 |
| Kojic acid | 25.9 |

tyrosinase with an $IC_{50}$ value of 0.7 and 0.1 μM, respectively. KR and SG also exhibited inhibition against tyrosinase with an $IC_{50}$ value of 7.1 and 6.7 μM, respectively. The activities of these three compounds were much higher than the other positive control kojic acid ($IC_{50}$ = 25.9 μM), whilst KI showed weaker inhibitory activity with the $IC_{50}$ value >80 μM (Table 4).

## 3.2 Kinetic analysis of tyrosinase inhibition

Next, the inhibitory mechanisms of the three most active compounds were studied by kinetic assays using L-tyrosine as a substrate. Figure 2 showed the Lineweaver-Burk double reciprocal plots (1/[V] vs. 1/[S]) for glabridin and the prenylated flavonoids. The intersection of the curves was outside the X and Y-axes, suggesting that the inhibition type of IAI, KR, and SG was a mixed type. This is characterized by the intersection of the double reciprocal lines at different concentrations above the X-axis. As the concentration increased, there was a gradual reduction in $V_{max}$ and an increase in $K_m$, resulting in a steeper slope. Table 5 showed the relevant enzyme kinetic parameters, which suggested that IAI, KR, and SG may bind to the enzyme and the substrate-enzyme complexes.

## 3.3 Molecular docking

Computational docking experiments were used to further understand the inhibition mechanism of prenylated flavonoids on tyrosinase. Among the tested flavonoids, SG had the strongest binding affinity with a binding free energy of −8.19 kcal/mol. KR, glabridin, and IAI also exhibited comparable binding affinities with binding free energies of −7.86, −7.04, and −7.03 kcal/mol, respectively. These compounds were able to form two or three hydrogen bonds with the amino acid residues located within this specific pocket. Upon binding, the phenolic hydroxyl group of IAI could create hydrogen bonds with the amino acid residues His244 and Arg268. This was further stabilized by $\pi$-$\pi$ and $\pi$-$\sigma$ stacking. The primary contact between SG and tyrosinase was hydrogen bonding. Specifically, the phenolic hydroxyl group of SG could create hydrogen bonds with residues of amino acids including Arg268, Gly281, and Asn260, as well as different non-covalent interactions involving van der Waals forces. When bound to amino acid residues such as Gly281, Arg268, and Asn260, the phenolic hydroxyl group of KR could establish hydrogen bonds with them. It could also engage non-covalently with tyrosinase proteins in a variety of ways, such as $\pi$-$\sigma$ stacking and $\pi$-alkyl interaction (Figure 3).

## 3.4 Cytotoxicity in B16F10 cells

To further evaluate the cellular anti-tyrosinase activity of IAI, KR, and SG, the cytotoxicity of these flavonoids and two positive controls (glabridin and 8-MOP) in B16F10 cells were assessed. As shown in Figure 4, after treatment with different concentrations of IAI (0–5 μM), KR (0–20 μM), and SG (0–10 μM), along with the positive controls glabridin (0–2 μM) and 8-MOP (0–100 μM) for 48 h, the cell viability was maintained above 80%. This indicates these compounds were non-toxic at the indicated concentration range.

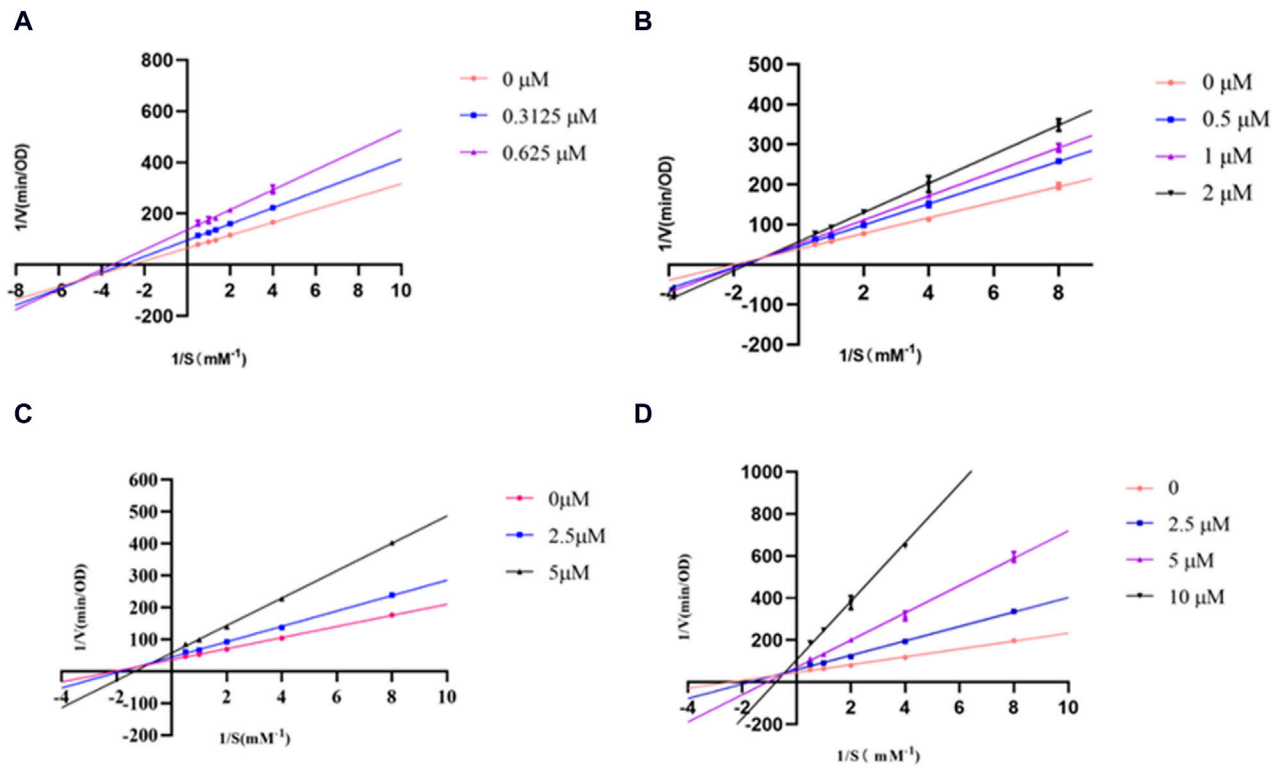


FIGURE 2
Lineweaver-Burk plots for inhibition of tyrosinase in the presence of compounds: **(A)** Glabridin, **(B)** IAI, **(C)** KR, **(D)** SG.

TABLE 5 Kinetic analysis of active compounds on tyrosinase.

| Concentration (μM) | Intercept | Slope | $K_m$ | $V_{max}$ | Relevancy |
|---|---|---|---|---|---|
| (Glabridin) 0 | 65.42 | 25.90 | 0.396 | 0.015 | 0.9978 |
| (Glabridin) 0.3125 | 95.97 | 31.66 | 0.330 | 0.010 | 0.9977 |
| (Glabridin) 0.625 | 136.9 | 38.95 | 0.285 | 0.007 | 0.9916 |
| (IAI) 0 | 38.74 | 19.46 | 0.502 | 0.026 | 0.9984 |
| (IAI) 0.5 | 45.68 | 26.48 | 0.580 | 0.022 | 0.9991 |
| (IAI) 1.0 | 50.84 | 30.07 | 0.591 | 0.020 | 0.9998 |
| (IAI) 2.0 | 57.21 | 36.35 | 0.635 | 0.017 | 0.9998 |
| (KR) 0 | 35.99 | 17.41 | 0.484 | 0.028 | 0.9988 |
| (KR) 2.5 | 44.31 | 24.13 | 0.545 | 0.023 | 0.9980 |
| (KR) 5.0 | 57.70 | 42.93 | 0.744 | 0.017 | 0.9991 |
| (SG) 0 | 45.78 | 18.69 | 0.408 | 0.022 | 0.9962 |
| (SG) 2.5 | 59.22 | 34.29 | 0.579 | 0.017 | 0.9973 |
| (SG) 5.0 | 70.13 | 64.87 | 0.925 | 0.014 | 0.9976 |
| (SG) 10.0 | 106.00 | 139.40 | 1.315 | 0.009 | 0.9992 |

## 3.5 Melanin content in B16F10 cells

To identify the effect of IAI, KR, and SG on melanogenesis, B16F10 cells were treated with various concentrations of test samples for 48 h to measure the melanin content. As shown in Figure 5A, cells treated with test compounds were slender and darkened when compared to untreated control cells. The appearance of the collected cell pellets from B16F1 cells was visibly darkened,

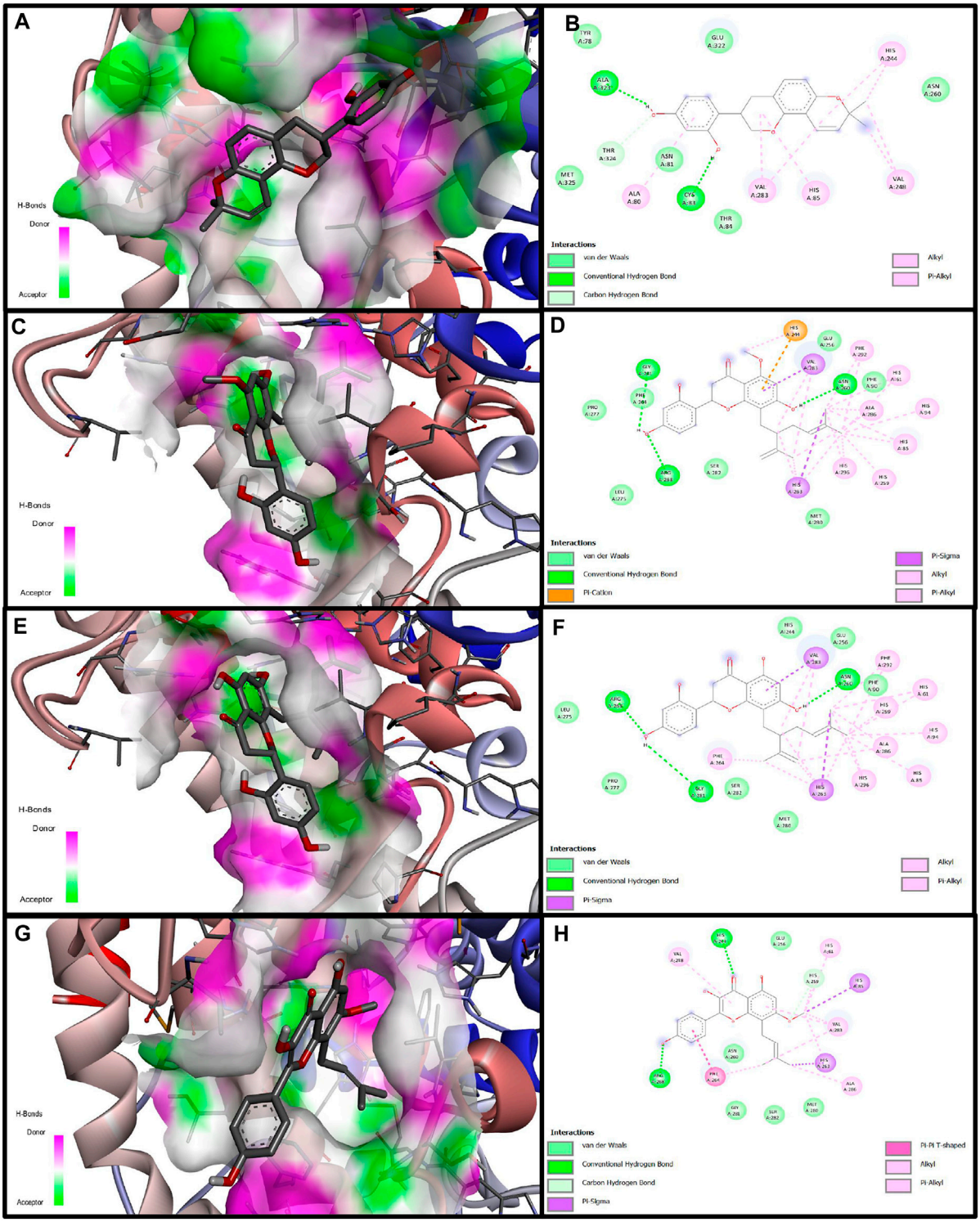


FIGURE 3
Molecular docking simulation of glabridin, IAI, KR, and SG with tyrosinase. 3D diagram of the docking of compounds with tyrosinase protein molecules, **(A)** Glabridin, **(C)** IAI, **(E)** KR, **(G)** SG. 2D diagram of the interaction between compounds and amino acid residues of tyrosinase proteins, **(B)** Glabridin, **(D)** IAI, **(F)** KR, **(H)** SG.

indicating the accumulation of melanin in the cells (Figure 5B). In addition, the relative melanin content produced in the cells was measured (Figures 5C–E). As expected, glabridin exhibited a strong anti-melanogenic effect and 8-MOP promoted melanin biosynthesis. Among the tested flavonoids, KR increased the intracellular melanin content in B16F10 cells by 61.6% and 85.5% at concentrations of 5 and 10 μM, respectively. SG and IAI did not exert any significant effects on melanin production in B16F10 cells.

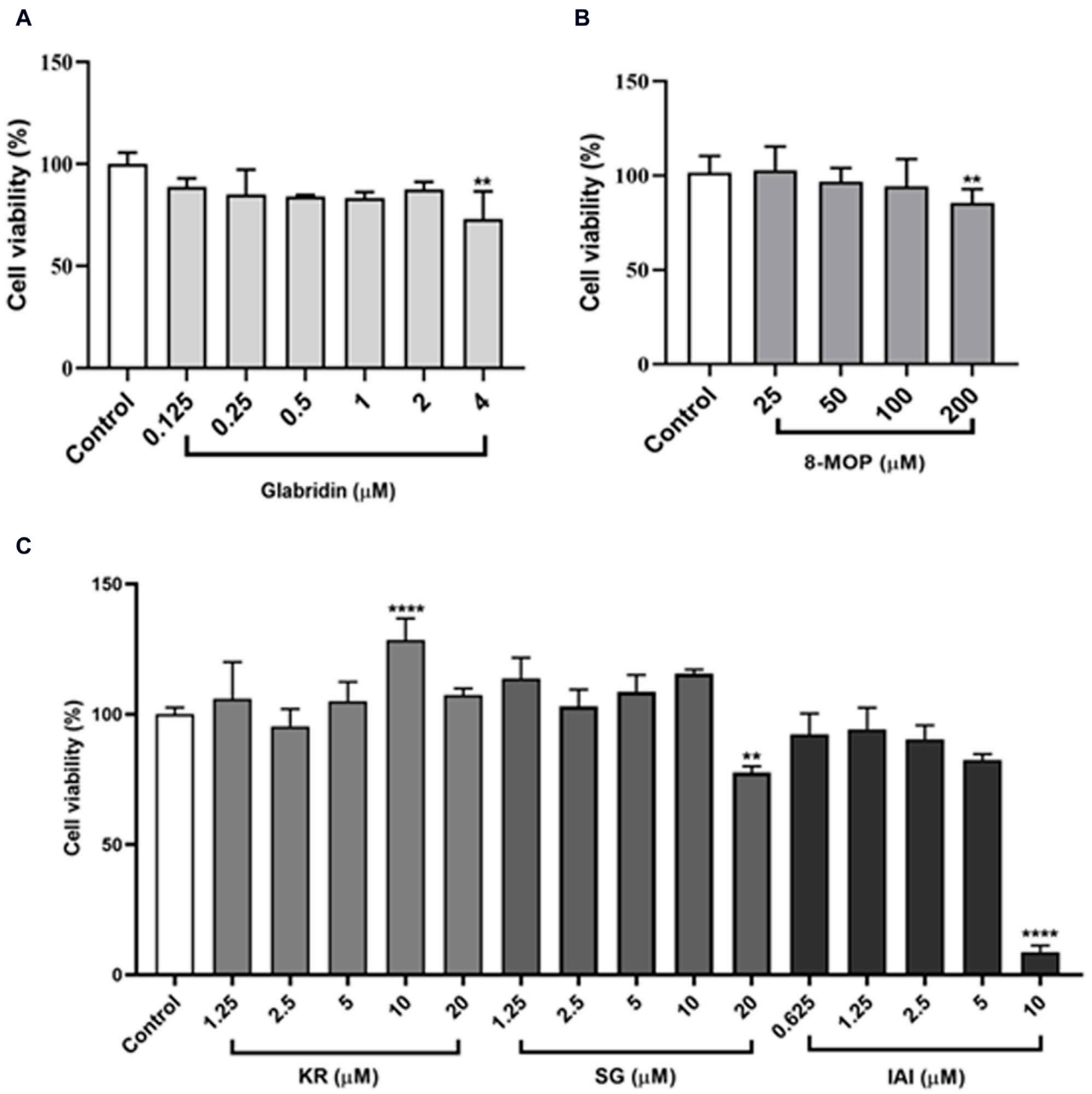


FIGURE 4
B16F10 cell viability after treatment with various concentrations of test samples. Cells exposed to varying concentrations of test samples for 48 h, cell viability was assessed by MTT assay. **(A)** Glabridin, **(B)** 8-MOP, **(C)** IAI, KR, and SG. The results were expressed as mean ± SD and represent three independent tests. *$p < 0.05$, **$p < 0.01$, ***$p < 0.001$, and ****$p < 0.0001$ vs. control.

## 3.6 Tyrosinase activity in B16F10 cells

As tyrosinase is the key enzyme for melanin biosynthesis, we measured the tyrosinase activity in B16F10 cells that were treated with IAI, KR, and SG, along with glabridin and 8-MOP as control groups. As shown in Figures 6A, B, consistent with our findings on melanin production, glabridin inhibited tyrosinase activity and 8-MOP was able to enhance cellular tyrosinase activity. KR enhanced tyrosinase activity in a concentration-dependent manner (increasing 25.1%, 42.1%, and 77.2% enzyme activity by 2.5, 5, and 10 μM). Cells treated with SG and IAI only slightly increased tyrosinase activity at the highest concentration (SG 10 μM and IAI 5 μM) by 45.7% and 25.2%, respectively (Figure 6C).

## 3.7 Effects on melanogenesis signaling pathways

Melanin synthesis was mainly catalyzed by three melanocyte-specific enzymes, namely, tyrosinase (TYR), tyrosinase-related protein 1 (TRP-1), and dopachrome tautomerase (DCT) (Yin et al., 2018). The expression of these proteins was transcriptionally regulated by the

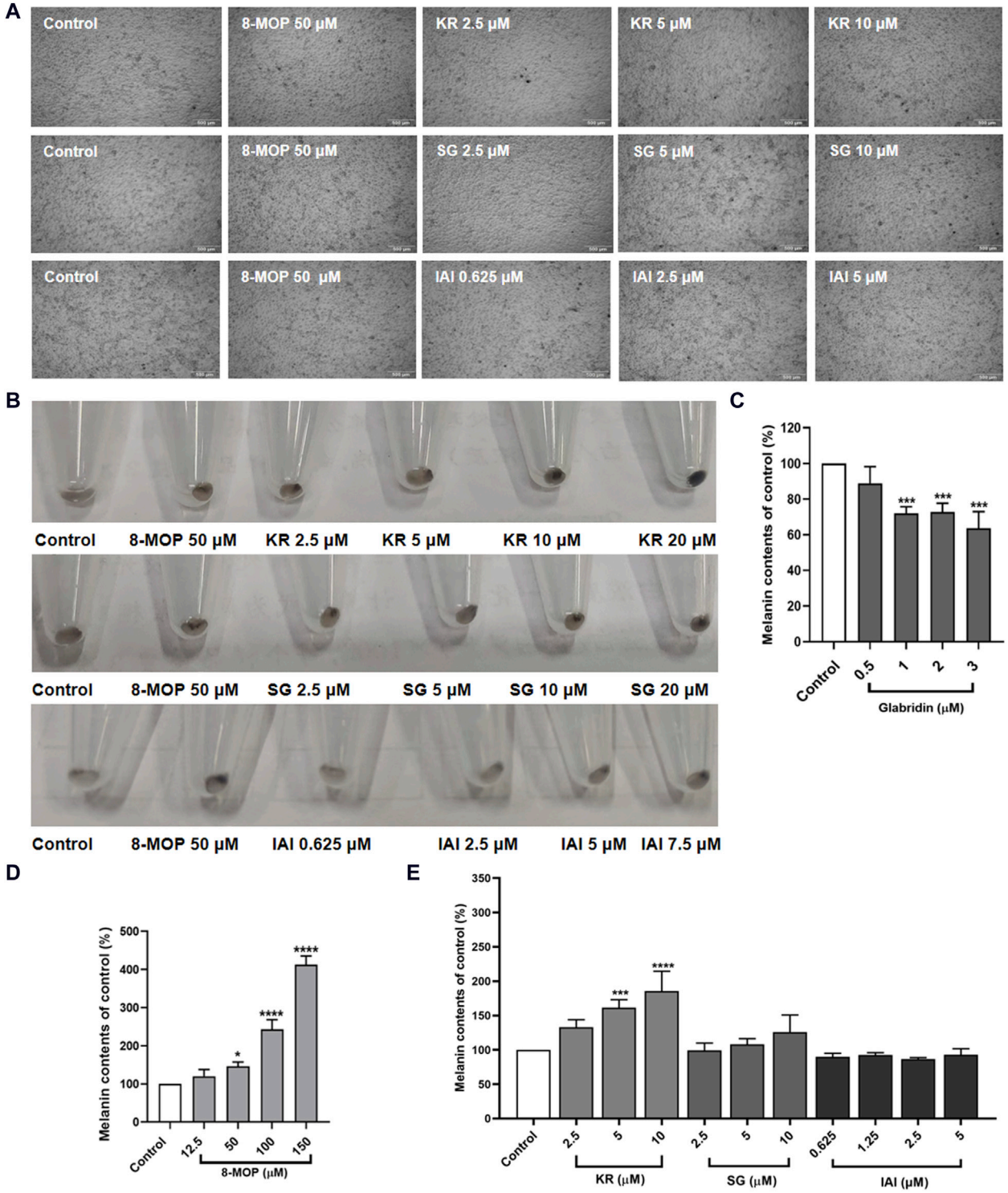


FIGURE 5
Effects of test samples on melanin production in B16F10 melanoma cells. Cells were treated with test samples at the indicated concentrations for 48 h, glabridin and 8-MOP were used as positive control, respectively. The melanin content was expressed as percentages relative to untreated cells. **(A)** Cell morphology of micrograph, **(B)** Appearance of the recovered cell pellets in test tubes. Contents of extracellular melanin in B16F10 cells treated with samples for 48 h, **(C)** glabridin, **(D)** 8-MOP, **(E)** IAI, KR, and SG. The results were expressed as mean ± SD and represent three independent tests. *$p < 0.05$, **$p < 0.01$, ***$p < 0.001$, and ****$p < 0.0001$ vs. control.

microphthalmia-associated transcription factor (MITF) (Rai et al., 2020). To further explore the mechanisms of IAI, KR, and SG in melanogenesis, the expression of melanogenesis-related proteins such as TRP-1, DCT, MITF, and TYR were evaluated by Western blotting analysis in B16F10 cells (Yin et al., 2018). As shown in Figures 7A–C, the expression of MITF and TRP-1 were increased after the treatment with

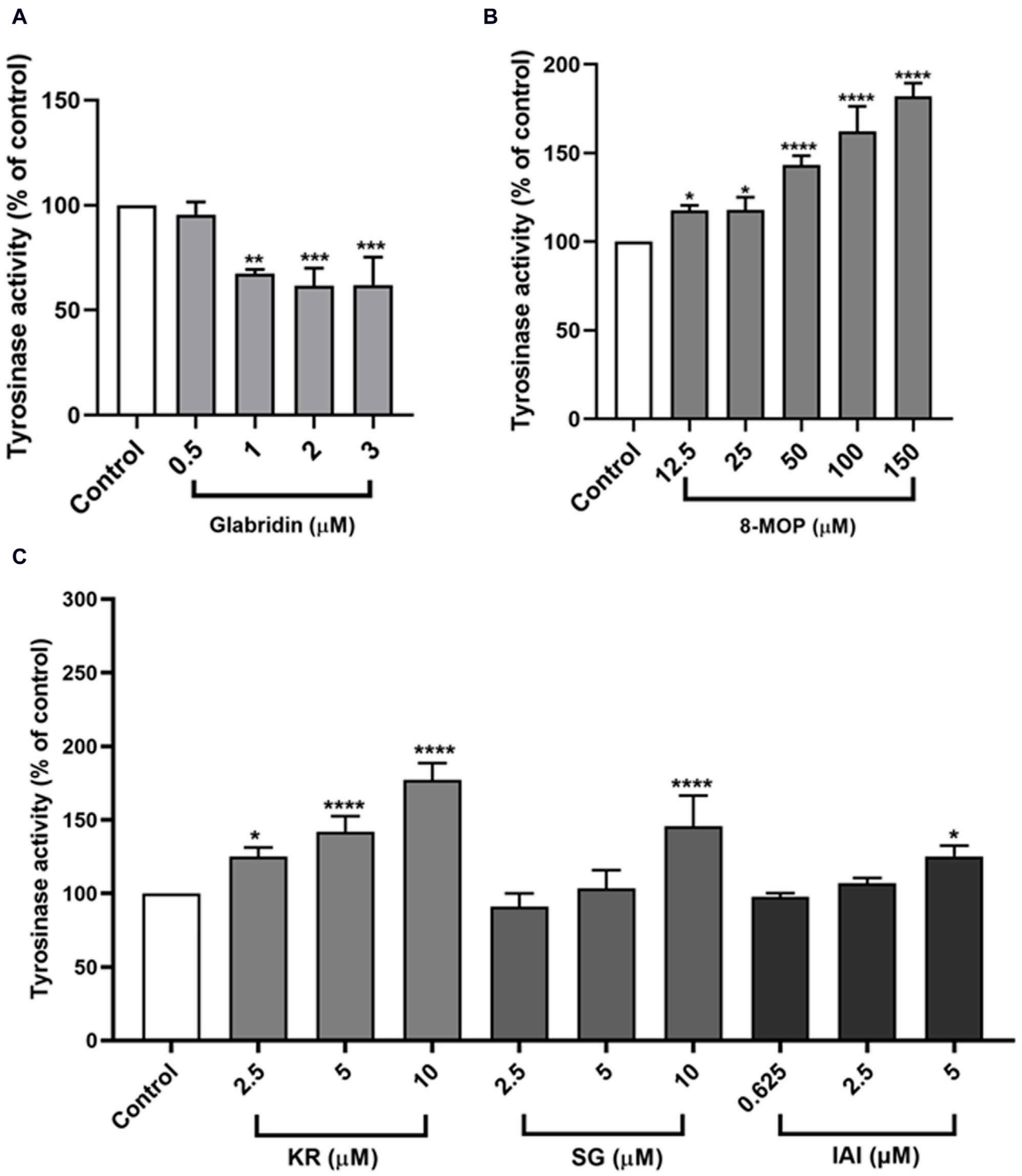


FIGURE 6
Effects of test samples on tyrosinase activity in B16F10 melanoma cells. Cells were treated with test samples at the indicated concentrations for 48 h, glabridin and 8-MOP were used as positive control, respectively. The tyrosinase activity was expressed as percentages relative to untreated cells. **(A)** Glabridin, **(B)** 8-MOP, **(C)** IAI, KR, and SG. The results were expressed as mean ± SD and represent three independent tests. *$p < 0.05$, **$p < 0.01$, ***$p < 0.001$, and ****$p < 0.0001$ vs. control.

8-MOP. After the treatment of IAI at a concentration of 5 μM, the relative expression of TRP-1 and DCT proteins was upregulated by 240.0% and 83.4%, respectively. KR (10 μM) significantly upregulated the relative expression of MITF, TRP-1, and DCT proteins by 84.0%, 79.2%, and 127.8%, respectively. SG (10 μM) increased the expression of TYR, TRP-1, and DCT by 78.4%, 229.3%, and 70.0%, respectively. These findings suggest that IAI, KR, and SG may increase melanogenesis by inducing the expression of relative proteins.

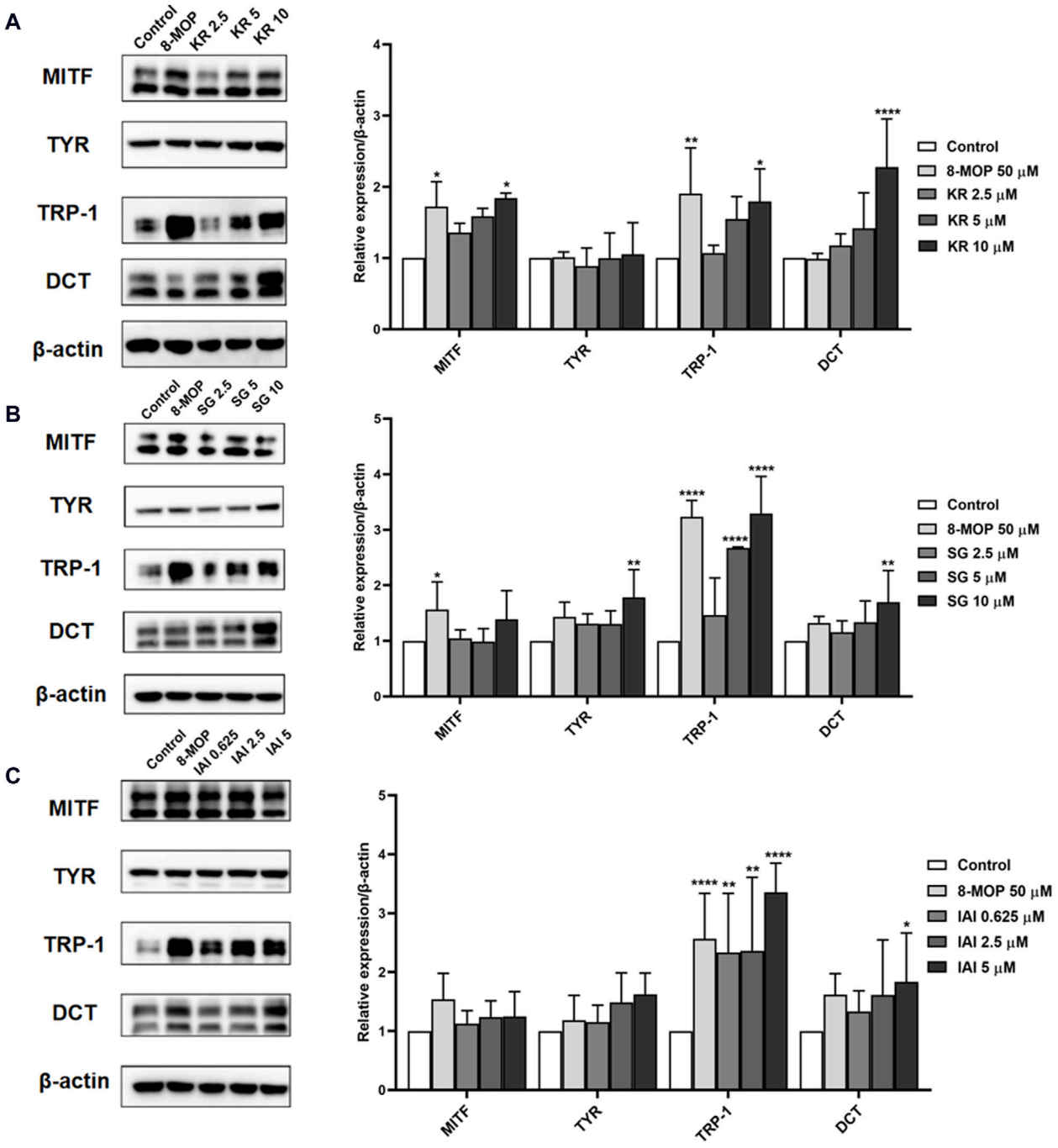


FIGURE 7
Effects of IAI, KR, and IAI on the protein expression levels of MITF, TYR, TRP-1, and DCT in B16F10 cells. Cells were treated with the indicated concentrations of test samples for 48 h, and 8-MOP was used as a positive control. Protein levels were examined by Western blotting, actin was used as the control, and results were expressed as percentages of untreated cells. **(A)** KR, **(B)** SG, **(C)** IAI. The results were expressed as mean ± SD and represent three independent tests. *$p < 0.05$, **$p < 0.01$, ***$p < 0.001$, and ****$p < 0.0001$ vs. control.

## 3.8 Effects on melanin pigmentation in zebrafish embryos

To further assess if prenylated flavonoids in *S. flavescens* extract can affect melanogenesis *in vivo*, a zebrafish model was used. The similarity of drug binding regions between human and zebrafish proteins provides a basis for using zebrafish as an *in vivo* suitable model for the evaluation of melanogenesis (Love et al., 2004). First, KR, SG, and IAI were evaluated for their toxicity in zebrafish by the MTC assay. As a result, IAI (40, 80, and 160 μM), KR (5, 10, and 20 μM), and SG (10 μM) were nontoxic to zebrafish and these concentrations were used for subsequent experiments. A small molecule named PTU is a known tyrosinase inhibitor commonly used to block pigmentation and aid visualization of zebrafish development (Escriva et al., 2011). As shown in Figures 8A,

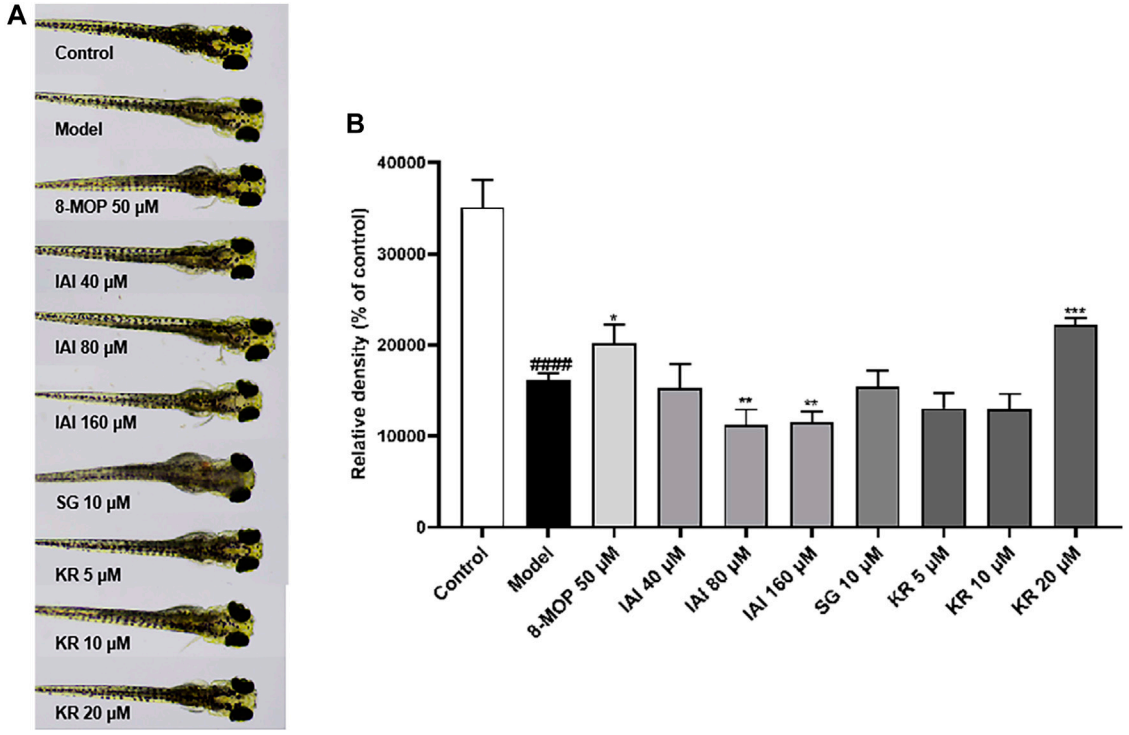


FIGURE 8
KR upregulates melanin pigmentation in zebrafish larvae. **(A)** The zebrafish larvae ($n$ = 40) were collected at 24 hpf and they were treated with PTU (200 μM) for another 24 h. Then, zebrafish larvae were treated with test samples for 48 h (96 hpf), and images were captured at 96 hpf under a microscope, 8-MOP (50 μM) was used as a positive control, and blank control was not treated and was cultured normally. **(B)** Relative density was calculated using Image J software. The results were expressed as mean ± SD and represent three independent tests. $^{\#\#\#\#}p < 0.0001$ vs. control, $^{*}p < 0.05$, $^{**}p < 0.01$ and $^{***}p < 0.001$ vs. model.

B, when compared with the model (PTU) group, the positive controls 8-MOP (50 μM) and KR (20 μM) increased melanin production by 25.0% and 36.9%, respectively. However, SG at 10 μM showed no effect and IAI significantly inhibited melanin production (by 30.8%, and 29.2% at 80 and 160 μM, respectively). In addition, zebrafish without PTU pretreatment were further employed to evaluate the depigmentation effect. As results shown in Figures 9A, B, when compared to the control group, the positive control arbutin (100 mM) reduced pigmentation by 51.4%. IAI also reduced pigmentation by 33.0% and 34.4% at 80 and 160 μM, respectively, whilst 8-MOP and KR did not affect melanin production in this zebrafish model.

## 4 Discussion

Prenylated flavonoids derived from *S. flavescens* are reported as potent tyrosinase inhibitors. However, most of these studies concentrated on the assessment of prenylated flavonoids' inhibition of tyrosinase (Kim et al., 2003; Son et al., 2003; Ryu et al., 2008). The current study further explored the mechanism of inhibition with enzyme kinetic assays. In addition, several models at the molecular, cellular, and animal levels were used to characterize the modulatory effects of *S. flavescens* prenylated flavonoids on melanin biosynthesis. Notably, SG, kuraridin, and KR had a greater inhibition on tyrosinase activity than the positive control kojic acid ($IC_{50}$ = 6.6 μM, 0.6 μM, and 6.2 μM vs. 20.5 μM, respectively) (Kim et al., 2003). Given that IAI, KR, and SG were the main active compounds in the *S. flavescens* extracts, our findings support the reported overall anti-tyrosinase activity of *S. flavescens*. Moreover, the enzyme kinetics and molecular docking simulation showed that the inhibition type of IAI, KR, and SG on tyrosinase was a mixed type. Among these prenylated flavonoids, KR significantly increased intracellular tyrosinase activity and promoted melanin production in B16F10 cells by activating MITF and its downstream proteins TRP-1 and DCT. This is the first study showing that KR enhances the biosynthesis of melanin. This was further supported by the *in vivo* zebrafish model assessing the effects of IAI, KR, and SG on melanogenesis. With the pretreatment with PTU, IAI substantially inhibited melanin production in zebrafish larvae at nontoxic concentrations. Furthermore, data from the zebrafish whitening model supported the observed inhibition of melanogenesis by IAI. In comparison, KR can stimulate melanin production but SG had no significant effect on melanin formation. These contrasting effects of prenylated flavonoids from *S. flavescens* may partially account for the uses of this medicinal plant for skin lightening and darkening. However, the molecular mechanism of these prenylated flavonoids exerting contrasting effects in melanogenesis is not clear. Further studies are needed to clarify the specific structure-activity relationships (SARs). This is critical as further studies would provide insight into the development of *S. flavescens* based ingredients for cosmeceutical applications or potential medicinal management for vitiligo.

Our study also highlights the importance of using multiple models to evaluate the effects of natural products on melanin biosynthesis and skin

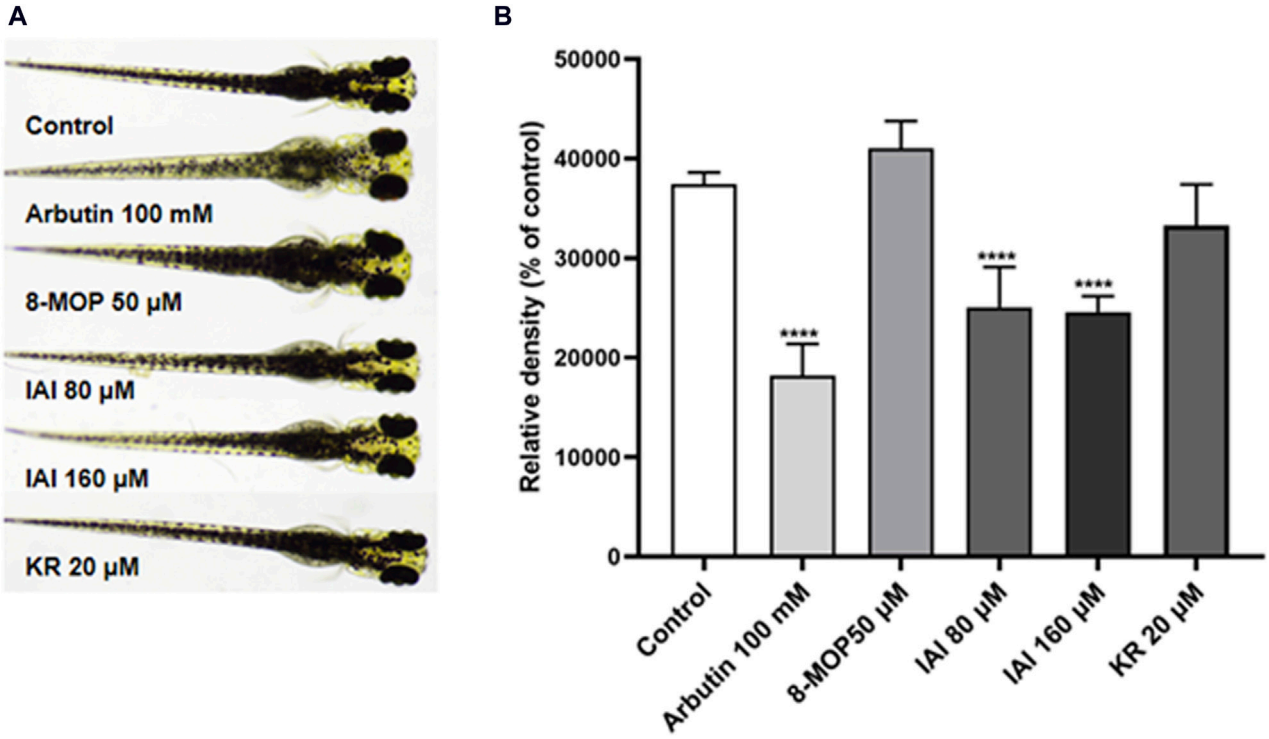


FIGURE 9
IAI downregulates melanin pigmentation in zebrafish larvae. **(A)** The zebrafish larvae ($n$ = 40) were collected at 24 hpf and they were treated with fresh culture media for another 24 h. Then, zebrafish larvae were treated with test samples for 48 h (96 hpf), and images were captured at 96 hpf under a microscope, 8-MOP (50 μM) and arbutin (100 mM) were used as positive controls, blank control was not treated and was cultured normally. **(B)** Relative density was calculated using Image J software. The results were expressed as mean ± SD and represent three independent tests. ****$p$ < 0.0001 vs. control.

pigmentation. This is attributed to bioassays with different models (i.e., enzymatic assays, cell-and animal-based models) that may generate contrasting findings. For instance, IAI showed an anti-tyrosinase effect in the biochemical enzyme assay but was not an inhibitor of tyrosinase in the cellular assay. However, it reduced melanin production in the zebrafish model. This suggests that it is not suitable to evaluate the anti-melanogenic effect solely relying on a single assay. A similar trend was observed where KR demonstrated consistent effects in the cellular and animal models but was inconsistent with the *in vitro* enzyme inhibition assay. This is in agreement with some previously reported studies. Glycyrrhizin acid was reported to stimulate the activity of mushroom tyrosinase but suppress tyrosinase activity in B16F10 cells. In the cell-based model, glycyrrhizin acid was found to increase intracellular melanin content, which was contradictory to the effect in zebrafish showing an anti-melanogenic activity. A human clinical study supported that glycyrrhizin acid indeed can reduce melanin generation (Sun, 2022). Another example is that an Oolong tea extract showed weak inhibition of tyrosinase but reduced melanogenesis in the cellular assay (with B16F10 cells) and *in vivo* guinea pig models (Aoki et al., 2014). Kaempferide, a weak inhibitor of tyrosinase, inhibited melanogenesis in theophylline-stimulated B16 melanoma 4A5 cells (Matsuda et al., 2009), whereas other studies showed that kaempferide dose-dependently enhanced melanin production in both B16F10 cells and C57BL/6 mice (Wang et al., 2017Wang et al., 2018). Human clinical studies can provide the most relevant and convincing evidence for the evaluation of the modulation of melanogenesis. However, it is not a practical approach to screen natural products as modulators of melanin biosynthesis. Thus, research efforts should be directed to using rigorous models with data from molecular assays to provide profound information.

In summary, we evaluated the anti-tyrosinase activity and melanogenesis effects of four prenylated flavonoids from *S. flavescens* extracts. Among these flavonoids, IAI showed promising tyrosinase inhibitory activity and anti-melanogenic effect in the zebrafish model. KR promoted melanin production in B16F10 cells and the zebrafish model. Although IAI and KR from *S. flavescens* may have contrasting effects on melanogenesis, they might both be promising candidates as modulators for melanin production with different cosmeceutical or medicinal purposes.

## Data availability statement

The original contributions presented in the study are included in the article/Supplementary Material, further inquiries can be directed to the corresponding authors.

## Author contributions

FF: Investigation, Validation, Writing–original draft. LC: Investigation, Validation, Visualization, Writing–original draft.

CC: Data curation, Visualization, Writing–original draft. SA: Writing–review and editing. JG: Data curation, Visualization, Writing–original draft. NS: Writing–review and editing. HM: Conceptualization, Methodology, Writing–review and editing. DL: Conceptualization, Funding acquisition, Project administration, Supervision, Writing–review and editing.

## Funding

The authors declare that financial support was received for the research, authorship, and/or publication of this article. This work was supported by the Science and Technology Planning Project of Guangdong Province (2021B1212040016).

## Conflict of interest

The authors declare that the research was conducted in the absence of any commercial or financial relationships that could be construed as a potential conflict of interest.

## Publisher's note

All claims expressed in this article are solely those of the authors and do not necessarily represent those of their affiliated organizations, or those of the publisher, the editors and the reviewers. Any product that may be evaluated in this article, or claim that may be made by its manufacturer, is not guaranteed or endorsed by the publisher.

## References

Ahmed, M. B., Islam, S. U., and Lee, Y. S. (2021). PRP4 promotes skin cancer by inhibiting production of melanin, blocking influx of extracellular calcium, and remodeling cell actin cytoskeleton. *Int. J. Mol. Sci.* 22 (13), 6992. doi:10.3390/ijms22136992

Aoki, Y., Tanigawa, T., Abe, H., and Fujiwara, Y. (2014). Melanogenesis inhibition by an oolong tea extract in B16 mouse melanoma cells and UV-induced skin pigmentation in brownish Guinea pigs. *Biosci. Biotechnol. Biochem.* 71 (8), 1879–1885. doi:10.1271/bbb.70099

Butt, A. R. S., Abbasi, M. A., Aziz ur, R., Siddiqui, S. Z., Raza, H., Hassan, M., et al. (2019). Synthesis and structure-activity relationship of tyrosinase inhibiting novel bi-heterocyclic acetamides: mechanistic insights through enzyme inhibition, kinetics and computational studies. *Bioorg. Chem.* 86, 459–472. doi:10.1016/j.bioorg.2019.01.036

Cai, Y., Cai, Q., Liu, Z., Huang, P., and Han, H. (2011). Chinese medicine preparation for treating vitiligo. *Hebei China Natl. Intellect. Prop. Adm. C. N. Pat. No* 102, 228–522.

Choi, H., Yoon, J.-H., Youn, K., and Jun, M. (2022). Decursin prevents melanogenesis by suppressing MITF expression through the regulation of PKA/CREB, MAPKs, and PI3K/Akt/GSK-3β cascades. *Biomed. Pharmacother.* 147, 112651. doi:10.1016/j.biopha.2022.112651

Del Marmol, V., and Beermann, F. (1999). Tyrosinase and related proteins in mammalian pigmentation. *FEBS Lett.* 381 (3), 165–168. doi:10.1016/0014-5793(96)00109-3

Ding, Q., Luo, L., Yu, L., Huang, S.-l., Wang, X.-q., and Zhang, B. (2021). The critical role of glutathione redox homeostasis towards oxidation in ermanin-induced melanogenesis. *Free Radic. Biol. Med.* 176, 392–405. doi:10.1016/j.freeradbiomed.2021.09.017

D'Mello, S., Finlay, G., Baguley, B., and Askarian-Amiri, M. (2016). Signaling pathways in melanogenesis. *Int. J. Mol. Sci.* 17 (7), 1144. doi:10.3390/ijms17071144

Escriva, H., Bohnsack, B. L., Gallina, D., and Kahana, A. (2011). Phenothiourea sensitizes zebrafish cranial neural crest and extraocular muscle development to changes in retinoic acid and IGF signaling. *PLoS ONE* 6 (8), e22991. doi:10.1371/journal.pone.0022991

Grimes, P., Nordlund, J. J., Pandya, A. G., Taylor, S., Rendon, M., and Ortonne, J.-P. (2006). Increasing our understanding of pigmentary disorders. *J. Am. Acad. Dermatol.* 54 (5), S255–S261. doi:10.1016/j.jaad.2005.12.042

Han, H. J., Park, S. K., Kang, J. Y., Kim, J. M., Yoo, S. K., and Heo, H. J. (2020). Anti-melanogenic effect of ethanolic extract of sorghum bicolor on IBMX-induced melanogenesis in B16/F10 melanoma cells. *Nutrients* 12 (3), 832. doi:10.3390/nu12030832

He, X., Fang, J., Huang, L., Wang, J., and Huang, X. (2015). *Sophora flavescens* Ait.: traditional usage, phytochemistry and pharmacology of an important traditional Chinese medicine. *J. Ethnopharmacol.* 172, 10–29. doi:10.1016/j.jep.2015.06.010

Heriniaina, R. M., Dong, J., Kalavagunta, P. K., Wu, H.-L., Yan, D.-S., and Shang, J. (2018). Effects of six compounds with different chemical structures on melanogenesis. *Chin. J. Nat. Med.* 16 (10), 766–773. doi:10.1016/s1875-5364(18)30116-x

Hyun, S. K., Lee, W.-H., Jeong, D. M., Kim, Y., and Choi, J. S. (2008). Inhibitory effects of kurarinol, kuraridinol, and trifolirhizin from *Sophora flavescens* on tyrosinase and melanin synthesis. *Biol. Pharm. Bull.* 31 (1), 154–158. doi:10.1248/bpb.31.154

Jang, D. K., Pham, C. H., Lee, I. S., Jung, S.-H., Jeong, J. H., Shin, H.-S., et al. (2020). Anti-melanogenesis activity of 6-o-isobutyrylbritannilactone from *Inula britannica* on B16F10 melanocytes and *in vivo* zebrafish models. *Molecules* 25 (17), 3887. doi:10.3390/molecules25173887

Karunarathne, W. A. H. M., Molagoda, I. M. N., Kim, M. S., Choi, Y. H., Oren, M., Park, E. K., et al. (2019). Flumequine-mediated upregulation of p38 MAPK and JNK results in melanogenesis in B16F10 cells and zebrafish larvae. *Biomolecules* 9 (10), 596. doi:10.3390/biom9100596

Kim, C., Noh, S., Park, Y., Kang, D., Chun, P., Chung, H., et al. (2018a). A potent tyrosinase inhibitor, (E)-3-(2,4-Dihydroxyphenyl)-1-(thiophen-2-yl)prop-2-en-1-one, with anti-melanogenesis properties in α-MSH and IBMX-induced B16F10 melanoma cells. *Molecules* 23 (10), 2725. doi:10.3390/molecules23102725

Kim, J. H., Cho, I. S., So, Y. K., Kim, H.-H., and Kim, Y. H. (2018b). Kushenol A and 8-prenylkaempferol, tyrosinase inhibitors, derived from *Sophora flavescens*. *J. Enzyme Inhib. Med. Chem.* 33 (1), 1048–1054. doi:10.1080/14756366.2018.1477776

Kim, S. J., Son, K. H., Chang, H. W., Kang, S. S., and Kim, H. P. (2003). Tyrosinase inhibitory prenylated flavonoids from *Sophora flavescens*. *Biol. Pharm. Bull.* 26 (9), 1348–1350. doi:10.1248/bpb.26.1348

Lajis, A. F. B., and Ariff, A. B. (2019). Discovery of new depigmenting compounds and their efficacy to treat hyperpigmentation: evidence from *in vitro* study. *J. Cosmet. Dermatol.* 18 (3), 703–727. doi:10.1111/jocd.12900

Li, D.-L., Zheng, X., Chen, Y.-C., Jiang, S., Zhang, Y., Zhang, W.-M., et al. (2015). Terpenoid composition and the anticancer activity of *Acanthopanax trifoliatus*. *Arch. Pharm. Res.* 39 (1), 51–58. doi:10.1007/s12272-015-0655-y

Love, D. R., Pichler, F. B., Dodd, A., Copp, B. R., and Greenwood, D. R. (2004). Technology for high-throughput screens: the present and future using zebrafish. *Curr. Opin. Biotechnol.* 15 (6), 564–571. doi:10.1016/j.copbio.2004.09.004

Maack, A., and Pegard, A. (2016). *Populus nigra* (Salicaceae) absolute rich in phenolic acids, phenylpropanoids and flavonoids as a new potent tyrosinase inhibitor. *Fitoterapia* 111, 95–101. doi:10.1016/j.fitote.2016.04.001

Matsuda, H., Nakashima, S., Oda, Y., Nakamura, S., and Yoshikawa, M. (2009). Melanogenesis inhibitors from the rhizomes of *Alpinia officinarum* in B16 melanoma cells. *Bioorg. Med. Chem.* 17 (16), 6048–6053. doi:10.1016/j.bmc.2009.06.057

Mort, R. L., Jackson, I. J., and Patton, E. E. (2015). The melanocyte lineage in development and disease. *Development* 142 (4), 620–632. doi:10.1242/dev.106567

Niu, C., and Aisa, H. A. (2017). Upregulation of melanogenesis and tyrosinase activity: potential agents for vitiligo. *Molecules* 22 (8), 1303. doi:10.3390/molecules22081303

Park, S. Y., Jin, M. L., Kim, Y. H., Kim, Y., and Lee, S.-J. (2011). Aromatic-turmerone inhibits α-MSH and IBMX-induced melanogenesis by inactivating CREB and MITF signaling pathways. *Arch. Dermatol. Res.* 303 (10), 737–744. doi:10.1007/s00403-011-1155-7

Pillaiyar, T., Manickam, M., and Namasivayam, V. (2017). Skin whitening agents: medicinal chemistry perspective of tyrosinase inhibitors. *J. Enzyme Inhib. Med. Chem.* 32 (1), 403–425. doi:10.1080/14756366.2016.1256882

Rai, A., Chatterjee, B., Bhowmick, S., Sagar, S., and Roy, S. S. (2020). Beclin 1 controls pigmentation by changing the nuclear localization of melanogenic factor MITF. *Biochem. Biophys. Res. Commun.* 528 (4), 719–725. doi:10.1016/j.bbrc.2020.05.118

Ryu, Y. B., Westwood, I. M., Kang, N. S., Kim, H. Y., Kim, J. H., Moon, Y. H., et al. (2008). Kurarinol, tyrosinase inhibitor isolated from the root of *Sophora flavescens*. *Phytomed* 15 (8), 612–618. doi:10.1016/j.phymed.2007.09.022

Shin, D. H., Cha, Y. J., Joe, G. J., Yang, K. E., Jang, I.-S., Kim, B. H., et al. (2013). Whitening effect of *Sophora flavescensextract*. *Pharm. Biol.* 51 (11), 1467–1476. doi:10.3109/13880209.2013.799708

Slominski, A., Tobin, D. J., Shibahara, S., and Wortsman, J. (2004). Melanin pigmentation in mammalian skin and its hormonal regulation. *Physiol. Rev.* 84 (4), 1155–1228. doi:10.1152/physrev.00044.2003

Son, J. K., Park, J. S., Kim, J. A., Kim, Y., Chung, S. R., and Lee, S. H. (2003). Prenylated flavonoids from the roots of *Sophora flavescens* with tyrosinase inhibitory activity. *Planta Med.* 69 (6), 559–561. doi:10.1055/s-2003-40643

Sun, R., and Bao, G. (2008). *Chinese medicinal tincture for treating facial vitiligo*. Zhejiang: China National Intellectual Property Administration. C. N. Patent No 101.

Sun, T. (2022). *Efficacy evaluation and comparative study of four whitening efficacy evaluation models on several whitening ingredients*. [Guangdong]: Guangdong University of Technology. [MA thesis].

Wang, J., Wang, X., Tang, Y., and Zhang, B. (2018). The network pharmacological mechanisms of four anti-vitiligo Uyghur medicines based on Phlegmatic temperament theory. *China J. Chin. Materia Medica* 43 (09), 1780–1788. doi:10.19540/j.cnki.cjcmm.2018.0061

Wang, J. Y., Chen, H., Wang, Y. Y., Wang, X. Q., Chen, H. Y., Zhang, M., et al. (2017). Network pharmacological mechanisms of *Vernonia anthelmintica (L.)* in the treatment of vitiligo: isorhamnetin induction of melanogenesis via up-regulation of melanin-biosynthetic genes. *BMC Syst. Biol.* 11 (1), 103. doi:10.1186/s12918-017-0486-1

Xu, W., Li, J., Li, D., Tan, J., Ma, H., Mu, Y., et al. (2021). Chemical characterization, antiproliferative and antifungal activities of *Clinacanthus nutans*. *Fitoterapia* 155, 105061. doi:10.1016/j.fitote.2021.105061

Yasumoto, K.-I., Yokoyama, K., Shibata, K., Tomita, Y., and Shibahara, S. (1994). Microphthalmia-associated transcription factor as a regulator for melanocyte-specific transcription of the human tyrosinase gene. *Mol. Cell. Biol.* 14 (12), 8058–8070. doi:10.1128/mcb.14.12.8058

Yasumoto, K.-I., Yokoyama, K., Takahashi, K., Tomita, Y., and Shibahara, S. (1997). Functional analysis of microphthalmia-associated transcription factor in pigment cell-specific transcription of the human tyrosinase family Genes. *J. Biol. Chem.* 272 (1), 503–509. doi:10.1074/jbc.272.1.503

Yin, L., Pang, G., Niu, C., Habasi, M., Dou, J., and Aisa, H. (2018). A novel psoralen derivative-MPFC enhances melanogenesis via activation of p38 MAPK and PKA signaling pathways in B16 cells. *Int. J. Mol. Med.* 41 (6), 3727–3735. doi:10.3892/ijmm.2018.3529

Yoshino, M., and Murakami, K. (2009). A graphical method for determining inhibition constants. *J. Enzyme Inhib. Med. Chem.* 24 (6), 1288–1290. doi:10.3109/14756360902829766

Yoshioka, Y., Samukawa, Y., Yamashita, Y., and Ashida, H. (2020). 4-Hydroxyderricin and xanthoangelol isolated from Angelica keiskeiprevent dexamethasone-induced muscle loss. *Food Funct.* 11 (6), 5498–5512. doi:10.1039/d0fo00720j

Zhang, J., Wu, X., Zhong, B., Liao, Q., Wang, X., Xie, Y., et al. (2023). Review on the diverse biological effects of glabridin. *Drug Des. Devel Ther.* 17, 15–37. doi:10.2147/DDDT.S385981

Zhang, Q., and Zhang, Q. (2020). Method for preparation of traditional Chinese medicine for treating vitiligo. *Shanxi China Natl. Intellect. Prop. Adm. C. N. Pat. No* 111 (494).

Zhang, Y., Sun, L., Lai, X., Peng, X., Wen, S., Zhang, Z., et al. (2021). Gastroprotective effects of extract of *Jasminum grandiflorum* L. flower in HCl/EtOH-induced gastric mucosal ulceration mice. *Biomed. Pharmacother.* 144, 112268. doi:10.1016/j.biopha.2021.112268

Zhou, X., Fouda, S., Zeng, X.-Y., Li, D., Zhang, K., Xu, J., et al. (2019). Characterization of the therapeutic profile of albiflorin for the metabolic syndrome. *Front. Pharmacol.* 10, 1151. doi:10.3389/fphar.2019.01151

frontiers | Frontiers in Pharmacology

TYPE Original Research
PUBLISHED 09 August 2024
DOI 10.3389/fphar.2024.1396001

Check for updates

OPEN ACCESS

EDITED BY
Xuetao Xu,
Wuyi University, China

REVIEWED BY
Klaus Peter Latté,
Independent Researcher, Berlin, Germany
Chu Chu,
Zhejiang University of Technology, China
Huaiyou Wang,
Henan University, China

*CORRESPONDENCE
Dan Zhang,
zhangdanid@163.com
Yunsheng Zhao,
zwhjzs@126.com
Long Guo,
guo_long11@163.com

†These authors have contributed equally to this work and share first authorship

RECEIVED 05 March 2024
ACCEPTED 26 July 2024
PUBLISHED 09 August 2024

CITATION
Shi H, Wang Q, Chang Y, Zheng Y, Zhang D, Zhao Y and Guo L (2024) Screening of anti-inflammatory activities components of *Angelica dahurica* root based on spectrum-effect relationship analysis and NF-κB pathway. *Front. Pharmacol.* 15:1396001.
doi: 10.3389/fphar.2024.1396001

COPYRIGHT
© 2024 Shi, Wang, Chang, Zheng, Zhang, Zhao and Guo. This is an open-access article distributed under the terms of the Creative Commons Attribution License (CC BY). The use, distribution or reproduction in other forums is permitted, provided the original author(s) and the copyright owner(s) are credited and that the original publication in this journal is cited, in accordance with accepted academic practice. No use, distribution or reproduction is permitted which does not comply with these terms.

# Screening of anti-inflammatory activities components of *Angelica dahurica* root based on spectrum-effect relationship analysis and NF-κB pathway

Huan Shi[1†], Qianqian Wang[1†], Yaqing Chang[1], Yuguang Zheng[2], Dan Zhang[1]*, Yunsheng Zhao[1]* and Long Guo[1]*

[1]Traditional Chinese Medicine Processing Technology Innovation Center of Hebei Province, Hebei University of Chinese Medicine, Shijiazhuang, China, [2]Hebei Chemical and Pharmaceutical College, Shijiazhuang, China

*Angelica dahurica* root (ADR), a commonly utilized herbal medicine in China and other Asian nations, which has anti-inflammatory effects on diverse inflammatory ailments. However, the bioactive components and underlying mechanism responsible for the anti-inflammatory effect of ADR are still unclear. This work attempted to discover the anti-inflammatory bioactive compounds and explore their underlying mechanism in ADR based on spectrum-effect relationship analysis and NF-κB signaling pathway. Chromatographic fingerprints of ADR samples were established by high performance liquid chromatography with diode array detection (HPLC-DAD), and a total of eleven common peaks were selected. Then, high performance liquid chromatography coupled with quadrupole time-of-flight mass spectrometry (HPLC-Q/TOF-MS) was employed for identification of eleven common peaks in ADR Meanwhile, the anti-inflammatory activities of ADR samples were assessed by inhibition of NO, interleukin-1β (IL-1β), interleukin-6 (IL-6) and tumor necrosis factor-α (TNF-α) production in LPS-induced RAW264.7 cells. The spectrum-effect relationships between the eleven common peaks in HPLC fingerprints and anti-inflammatory effects of ADR samples were investigated to identify the potential anti-inflammatory bioactive compounds by grey relational analysis (GRA) and partial least squares regression (PLSR). The spectrum-effect relationship analysis results indicated that six coumarin compounds, including bergapten, xanthotoxin, phellopterin, isoimperatorin, xanthotoxol and imperatorin could be potential anti-inflammatory bioactive compounds in ADR. The further validation experiments also showed that these six coumarins demonstrated significant inhibition of NO, IL-1β, IL-6, and TNF-α production in LPS-induced RAW264.7 cells. In addition, western blot analysis was conducted to explore the mechanisms of two potential anti-inflammatory bioactive compounds (phellopterin and isoimperatorin) by assessing the protein levels in the NF-κB signaling pathway. The western blot results illustrated that phellopterin and isoimperatorin could significantly down-regulate the phosphorylated NF-κB p65 (p-p65), phosphorylated IκBα (p-IκBα) and iNOS,

and depress the pro-portion of p-p65/p65 and p-IκBα/IκBα, which indicated that these two coumarins in ADR could potentially exert anti-inflammatory effects by suppressing of NF-κB pathway.

KEYWORDS

*Angelica dahurica* root, anti-inflammatory, HPLC-Q/TOF-MS, spectrum-effect relationships, NF-κB

## 1 Introduction

*Angelica dahurica* root (ADR), the dried roots of *A. dahurica* (Fisch. ex Hoffm.) Benth. et Hook.f. and *A. dahurica* (Fisch. ex Hoffm.) Benth. et Hook.f. var. formosana (Boiss.) Shan et Yuan, is a popular used herbal medicine to treat pain, cold fever, abscesses, rhinitis, toothache, furunculosis, acne and cold-damp pain in China, Korea and Japan (Zhao et al., 2022). Except as an important herbal medicine, ADR is also commonly used in foods as a spice to increase their fragrance and eliminate unpleasant odors. Previous researches demonstrated that ADR contains various bioactive constitutes, such as coumarins, essential oils, flavonoids and polysaccharides (Wang et al., 2023). Among the bioactive compounds, coumarins are the primary bioactive ingredients in ADR, which play a crucial role in herbal remedy (Shi et al., 2022). Multiple pharmacological studies have shown that coumarins contained in ADR has anti-inflammatory, anticancer, antidepressant, antiviral, vasodilation, antibacterial and antidiabetic effects (Lee et al., 2020; Luo et al., 2020; Banikazemi et al., 2021). Although the utilization of ADR as herbal medicine has a long history, there is still a limited amount of research on the phytochemicals and bioactive compounds. Several studies have demonstrated that some coumarins isolated from ADR had significant anti-inflammatory effects (Yang et al., 2015). However, the coumarins constituents responsible for the anti-inflammatory activities of ADR and their mechanism is still not fully clear (Kang SW et al., 2010). It is necessary to investigate and screen out main coumarins components that represent the anti-inflammatory properties of ADR.

It is commonly recognized that the therapeutic effects of herbal remedies are achieved through a comprehensive approach involving various components. Therefore, it is time-consuming and inefficient to screen bioactive compounds from herbal medicines by conventional methods of extraction, purification, structure identification and bioactive study of the compounds (Gong et al., 2020). The chemical fingerprint serves as a convenient and efficient method to assess the consistency and quality of herbal medicines, and also providing insights into their chemical characteristics to some extent (Chen et al., 2019). The spectrum-effect relationship analysis is a credible technique to associate the chemical fingerprints with biological activities of herbal medicines and to screen for bioactive components (Li et al., 2023). By merging pharmacodynamics research with chemical fingerprints data, the analysis of spectrum-effect relationships can effectively link the chemical components in fingerprints with their respective biological activities, and clarify the correlation between fingerprint characteristics and biological activity. Therefore, the spectrum–effect relationship analysis has been extensively utilized in the assessment and selection of active components from medicinal herbs.

Inflammation is a natural and protective immune response activated in response to external factors such as infections, injury, or chemical irritants. A properly functioning inflammatory response safeguards our body from internal injury and external invaders. However, dysregulation of inflammatory mediators may contribute to the progression of inflammatory disease pathogenesis (Fang et al., 2021). Therefore, controlling inflammation is a crucial focus for preventing and treating inflammatory disorders. Macrophages are the primary inflammatory and immune cells, which have a crucial function in the inflammatory process through the release of various pro-inflammatory mediators including interleukin-1β (IL-1β), interleukin-6 (IL-6), and tumor necrosis factor-α (TNF-α). Suppression of pro-inflammatory mediators and cytokines has been explored as a crucial strategy in the treatment of inflammatory disorders (Tian et al., 2021). Lipopolysaccharide (LPS) is derived from Gram-negative bacteria and serves as an endotoxin component. The RAW 264.7 macrophages stimulated by LPS are commonly utilized as a crucial cellular model for screening anti-inflammatory bioactive compounds and investigating the underlying mechanisms. Hence, this study evaluated the anti-inflammatory activities of ADR samples by inhibiting the production of NO, IL-1β, IL-6, and TNF-α in LPS-stimulated RAW264.7 macrophages. Furthermore, the spectrum-effect analysis methods, including grey relational analysis (GRA) and partial least squares regression (PLSR) were establish to explore the relationships between the phytochemical fingerprints and anti-inflammatory activities of ADR samples, and screen out the potential anti-inflammatory compounds in ADR. GRA is frequently utilized to effectively compare quantitative trends in dynamically changing systems (Li et al., 2024). PLSR is a powerful method of regression modeling handle multiple dependent variables in relation to multiple independent variables effectively, which can effectively decompose and filter the data to accurately predict outcomes (Chang et al., 2021).

Nuclear factor kappa-B (NF-κB) plays an important role in the occurrence and development of inflammatory diseases and is a classic and central transcription factor in the secretion of inflammatory mediators and cytokines in LPS-stimulated RAW 264.7 macrophages (Wang et al., 2022). In addition, NF-κB is composed of p50 and p65 subunits, which reside in the cytoplasm and interact with the IκB protein in inactive cells. Upon activation by LPS or other inflammatory triggers, IκB kinase rapidly phosphorylates and breaks down IκB within the IκB/NF-κB complex (Fang et al., 2021). Consequently, inhibition of the NF-κB signaling pathway is viewed as a pivotal target and an efficient treatment approach for inflammatory diseases. Meanwhile, NO is an inflammatory mediator produced by the catalytic action of the enzyme of inducible nitroxide synthase (iNOS) enzyme (Ke

et al., 2021). Numerous researches have shown that an overabundance of iNOS could cause the excessive creation of the inflammatory factor NO. Based on the evidence presented, the protein expression of iNOS and NF-κB including IκBα, phosphorylated IκBα (p-IκBα), p65 and phosphorylated p65 (p-p65) pathways were evaluated using western blot analysis to investigate the underlying mechanism of potential anti-inflammatory compounds screened out in ADR.

In general, the primary objective of this study was to identify the anti-inflammatory bioactive components in ADR using a comprehensive approach. Firstly, HPLC-DAD method was developed to establish the chemical fingerprints of ADR samples. HPLC-Q/TOF-MS method was then utilized to specifically identify and characterize the coumarins present in the chemical fingerprints of ADR. The anti-inflammatory effects of different batches of ADR samples were assessed by measuring the suppression of NO, IL-1β, IL-6, and TNF-α production in LPS-induced RAW 264.7 macrophages. Furthermore, the spectrum-effect relationships between chemical fingerprints and anti-inflammatory activities of ADR samples were investigated by GRA and PLSR to determine the specific coumarins responsible for the observed anti-inflammatory activities. In addition, the potential anti-inflammatory coumarins screen out in ADR were further verified by the inhibitory effects on NO, IL-1β, IL-6, and TNF-α production in LPS-stimulated RAW 264.7 macrophages. The underlying mechanism of potential anti-inflammatory coumarins in ADR were also explored through NF-κB signaling pathways.

# 2 Materials and methods

## 2.1 Materials and reagents

A total of twenty batches of ADR samples were obtained from various regions in China. After fibrous roots removed, the ADR samples were dried in a constant temperature oven at 50°C. The sources of the samples detailed were shown in Supplementary Table S1. The voucher specimens, identified by Associate Professor Long Guo have been stored at Traditional Chinese Medicine Processing Technology Innovation Center of Hebei Province, Hebei University of Chinese Medicine.

Reference standards of xanthotoxol, xanthotoxin, bergapten, imperatorin and isoimperatorin and phellopterin were purchased from Chengdu Must Bio-Technoligy Co., Ltd. (Chengdu, China). Their purities were confirmed to be over 98% by HPLC-DAD analysis. Methanol, acetonitrile and formic acid of HPLC grade were obtained from Fisher Scientific (Pittsburgh, United States). Ultrapure water was generated using a Synergy water purification system (Millipore, United States). All other chemicals and reagents utilized were of analytical grade.

RAW264.7 mouse macrophages were purchased from the Cell Bank of the Chinese Academy of Sciences (Kunming, China). Fetal bovine serum and Dulbecco's Modified Eagle's Medium (DMEM) were purchased from GIBCO (New York, United States). Penicillin-streptomycin solution, pancreatic enzymes, LPS, cell counting kit-8 (CCK-8), IL-1β detection kit, IL-6 detection kit and TNF-α detection kit were purchased from Solarbio (Beijing, China). Sulfanilamide and N-(1-naphthyl) ethylenediamine dihydrochloride were purchased from Rhnwa (Shanghai, China). Dexamethasone (DEX) were purchased from Macklin Biochemcial (Shanghai, China). Sodium nitrite ($NaNO_2$) was purchased from Tianjin Oubokai Chemical Co., Ltd. (Tianjin, China). Antibodies for β-actin, iNOS, p65, p-p65 (Ser536), IκBα, p-IκBα and secondary antibodies were purchased from Cell Signaling Technology (Boston, United States).

## 2.2 Sample preparation

The ADR samples were crushed into powders and sieved through a 0.30-mm mesh sieve. 0.5 g of the ADR powder was subjected to extraction in 15 mL of 80% (v/v) methanol using an ultrasonic extractor operating at 40 kHz and 300 W at room temperature for a duration of 50 min. Subsequent to the extraction, the mixed suspension was centrifuged at 13,000 rpm for 10 min, and the supernatant was then passed through a 0.22 μm membrane filter anterior to HPLC-DAD and HPLC-Q/TOF-MS analysis.

Standard solutions of xanthotoxol (0.85 mg/mL), xanthotoxin (1.20 mg/mL), bergapten (0.60 mg/mL), imperatorin (2.20 mg/mL), phellopterin (2.55 mg/mL) and isoimperatorin (2.60 mg/mL) were prepared by accurately weighing and dissolving in methanol. Then, the standard solutions were diluted with methanol to a series of accurate concentrations for the establishment of linearity. All the solutions were stored at 4°C until use.

For anti-inflammatory experiments, 0.5 g of the ADR powder was subjected to extraction in 15 mL of 80% (v/v) methanol using an ultrasonic extractor operating at 40 kHz and 300 W at room temperature for a duration of 50 min. Subsequent to the extraction, the mixed suspension was centrifuged at 13,000 rpm for 10 min, and 150 μL of the supernatant was dried in a Termovap Sample Concentrator (Hangzhou Miulab Instruments Co., Ltd.) at 30°C. Subsequently, the remaining residue was redissolved in 25 mL DMEM. Preceding the cell experiment, the solution was sieved through a 0.22 μm membrane. The concentrations of ADR sample solutions were determined based on the quantity of crude herbal medicine, resulting in a final concentration of 50 μg/mL.

## 2.3 HPLC-DAD and HPLC-Q/TOF-MS conditions

The HPLC-DAD analysis was carried on a Shimadzu LC-2030 HPLC system comprised a solvent delivery unit, autosampler, binary pump, column oven and photodiode array detector (Shimadzu, Kyoto, Japan). The column (Agilent ZORBAX SB C18, 4.6 mm × 250 mm, and 1.8 μm) was utilized for analysis. The mobile phases consisted of 0.1% formic acid in water (A) and acetonitrile (B). The gradient elution protocol as follows: 0–5 min, 10%–20% B; 5–15 min, 20%–35% B; 15–30 min, 35%–60% B; 30–35 min, 60%–70% B; and 35–36 min, 70%–100% B. The flow rate remained constant at 0.5 mL/min with the column temperature set at 25°C. Detection occurred at 250 nm wavelength, and a 5 μL sample injection volume was used. Data acquisition was carried out using Shimadzu Labsolutions.

The HPLC-Q/TOF-MS analysis was conducted using an Agilent 1290 HPLC system coupled with an Agilent 6545 quadrupole time-

of-flight mass spectrometer system (Agilent Technologies, Santa Clara, CA, United States). Chromatographic separation was also performed on an Agilent ZORBAX SB C18 column (4.6 mm × 50 mm, 1.8 μm) and the HPLC chromatographic conditions were the same as HPLC-DAD analysis, the sample volume was set at 1 μL. The MS acquisition parameters were as follows: sheath gas temperature, 350°C; drying gas ($N_2$) temperature, 320°C; drying gas ($N_2$) flow rate, 10.0 L/min; sheath gas flow ($N_2$) rate, 11 L/min; nebulizer gas pressure, 35 psi; capillary voltage, 3,500 V; fragmentor voltage, 135 V; collision energy, 40 eV. The analysis was performed in positive ion mode ($ESI^+$) with the mass range of *m/z* 100–1,000 Da, and data acquisition was carried out using MassHunter Workstation.

## 2.4 HPLC fingerprints

### 2.4.1 Method validation

The reliability of the HPLC-DAD method employed in the analysis of ADR samples was ensured by verifying its precision, repeatability, stability and linearity. The precision of the analysis was evaluated through injecting and analyzing the same sample for six consecutive times. Repeatability was assessed by the preparation and parallel analysis of six ADR samples. Meanwhile, the stability was determined by analyzing the same sample at 0, 4, 8, 12, 24 and 48 h at room temperature. The precision, stability, and repeatability of the established HPLC-DAD method were determined by calculating the relative standard deviations (RSDs) of peak areas corresponding to common peaks. Six level concentrations of working standard solutions were analysed to evaluate the linearity of the HPLC-DAD method. The calibration curves were calculated by plotting the peak areas of each analyte.

### 2.4.2 Establishment and evaluation of HPLC fingerprints

The established HPLC-DAD method was used to analyze twenty batches of samples of ADR to gain chromatograms that included peak areas and retention times, and the data from the chromatograms was saved in CDF format. The HPLC fingerprints of the ADR samples were automatically matched by the Similarity Evaluation System for Chromatographic Fingerprint of Traditional Chinese Medicine (version 2012 A). The reference fingerprint chromatogram was created using the median method by comparing the chromatograms of the twenty batches of ADR samples. The software also calculated the similarity between the reference fingerprint chromatogram and the chromatographic profiles of the ADR samples.

## 2.5 Anti-inflammatory activities of ADR samples

### 2.5.1 Determination of NO production

The concentration of nitrite in the medium was quantified to assess NO production through the Griess reaction. RAW264.7 macrophage cells were cultured in DMEM with 10% fetal bovine serum and 1% penicillin-streptomycin. The cells were incubated at 37°C in a humidified atmosphere containing 5% $CO_2$. Briefly, cells were seeded in a 96-well plate at a density of $5 \times 10^5$ cells per well. Following a 24-h incubation period, the cells were treated with ADR extract for 1 h, then stimulated with LPS (1 μg/mL) for 24 h. Subsequently, 100 μL of culture supernatant was combined with an equal volume of Griess reagent (1% sulfanilamide in water and 0.1% naphthylethylenedi-amine dihydrochloride in 5% phosphoric acid) and allowed to react at room temperature in the dark for 15 min before measuring absorbance at a wavelength of 540 nm with a microplate reader. Standard curve was generated using $NaNO_2$, and nitrite concentrations in the media were determined. DEX (10 μg/mL) was utilized as a positive control. The inhibition rate of NO production was calculated using a specific formula:

$$\textbf{Inhibition ratio of NO production } (\%) = 1 - \frac{Cs - Cn}{Cm - Cn} \times 100$$

$C_m$ is the NO concentration of model group, $C_s$ is the NO concentration of sample group and $C_n$ is the NO concentration of normal control group.

The viability of cells was assessed through the CCK-8 assay. Cells were plated on 96-well plates at a density of $2 \times 10^5$ cells/well, and cultured in serum-deprived medium with the concentrations of ADR samples (100 μg/mL) for 24 h. Following a 3 h incubation period, the CCK-8 reagent was introduced, and the absorbance (OD) was quantified at 450 nm using a microplate reader. CCK-8 reagent was then added and the absorbance (OD) at 450 nm was measured using a microplate reader. Cell viability was determined by comparing the results to those of the control group. All experiments were performed in triplicate.

### 2.5.2 Determination of IL-1β, IL-6, and TNF-α production

After the incubation of cells with LPS, DEX, or ADR extract for 24 h, the RAW 264.7 cell culture supernatants were collected and processed. The supernatant was obtained by centrifuging the medium at 1,000 rpm at 4°C for 10 min. Cell culture supernatants were added to ELISA plates to measure the levels of IL-1β, IL-6, and TNF-α as the respective instructions. Each sample was tested in triplicate.

## 2.6 Spectrum-effect relationship analysis

### 2.6.1 Gray relational analysis

GRA could express the interconnections among different factors, which is commonly used in spectrum-effect relationship analysis of herbal medicines (Chen et al., 2021; Wu et al., 2024). The areas of eleven common peaks in HPLC fingerprints of ADR samples were considered as the sub-sequence, and the anti-inflammatory effects were considered as the parent sub-sequence. Then, the gray correlation degree (GRD) was calculated to determine the contribution of these common peaks on the anti-inflammatory effects of ADR samples with a distinguishing coefficient set as 0.8. The higher the value of GRD was, the stronger activities of the common peaks could be.

### 2.6.2 Partial least squares regression analysis

PLSR is a regression model in statistics that can effectively address the issue of multicollinearity between a group of independent variables and a set of dependent variables (Jiang

et al., 2024). In this study, PLSR was utilized to analyze the relationship between the common peaks and anti-inflammatory effects of ADR samples. The eleven common peak areas were considered as the independent variable (X), while the anti-inflammatory activities were determined by assessing the levels of NO, IL-1β, IL-6, and TNF-α was considered as the dependent variable (Y). The PLSR model was established using Simca-P14.1 (Umetrics, Umea, Sweden) software and the regression coefficient was utilized to demonstrate the impact of the independent variables on the dependent variables.

## 2.7 Verification of the anti-inflammatory activity

### 2.7.1 Determination of NO, IL-1β, IL-6, and TNF-α production

To further verify the anti-inflammatory activities of the potential anti-inflammatory compounds in LPS-induced macrophages, secretion of NO and IL-1β, IL-6, and TNF-α were assessed by Griess reaction and ELISA kits, respectively.

### 2.7.2 Western blot analysis

The western blot assay was utilized to determine protein expression. Briefly, RAW 264.7 macrophages were first seeded culturing for 24 h and pretreated with different concentrations of potential anti-inflammatory compounds for 1 h, then LPS (1 μg/mL) was added for 24 h of treatment. Subsequently, the collected cells were lysed in RIPA lysis buffer to extract the total protein, and the quantification of the protein concentration was measured using the BCA protein kit. The concentration of the protein was measured using the BCA protein kit. Following electrophoresis of protein on 10% SDS-PAGE gels and transfer onto PVDF membranes. The membranes were blocking for 3 h at room temperature with 5% nonfat dry milk and then incubated overnight at 4°C with the following primary antibodies: β-actin (1:10,000), iNOS (1:1,000), p65 (1:1,000), p-p65 (Ser536) (1:1,000), IκBα (1:1,500) and p-IκBα (1:1,500). After washing the membranes thrice for 10 min with 1 × TBST, the secondary antibodies were (1:20,000) incubated for 1 h. Finally, chemiluminescence was used to visualize the immunoreactive bands, which were quantified using Alpha Analysis Software through densitometry. Data were normalized to the level of β-action.

# 3 Results and discussions

## 3.1 HPLC fingerprints

### 3.1.1 Optimization of HPLC-DAD condition

To efficiently separate ADR samples using HPLC-DAD, various conditions such as mobile phases, column temperatures, flow rates, and detective wavelengths were compared and optimized. Among the different mobile phases tested, formic acid water-acetonitrile with gradient elution proved to be the most effective for separating the analytes. The column temperature was maintained at 25°C, and a flow rate of 0.50 mL/min was chosen for optimal results. By setting the detective wavelength at 310 nm, the majority of common peaks showed stable and strong absorption intensity, leading to the best response signal for the determined compounds. These optimized HPLC-DAD conditions led to rapid and efficient separation of the ADR samples.

### 3.1.2 Method validation

The precision, repeatability and stability of the established HPLC-DAD method were validated. The results in Supplementary Table S2 demonstrated that the precision presented as RSDs of peak areas for the eleven common peaks were less than 1.29%. The repeatability presented as RSDs was less 1.97%, and the stability was less than 1.72%. As shown in Supplementary Table S3, the correlation coefficient values ($R^2 \geq 0.9990$) showed satisfactory linearity between the concentration and peak area of six analytes within the linearity range. The method validation results clearly indicate that the established HPLC-DAD method is reliable and appropriate for conducting fingerprint analysis of ADR samples.

### 3.1.3 HPLC fingerprints establishment and similarity analysis

Twenty batches of ADR samples obtained from diverse regions were subjected to the validated HPLC-DAD analysis under optimized condition, and the chromatogram of ADR samples were shown in Figure 1A. Subsequently, the HPLC fingerprints were constructed based on the chromatograms of ADR samples, and the median method were used to generate reference fingerprints after multi-point calibration and data alignment using the similarity evaluation software (Similarity Evaluation System for Chromatographic Fingerprints of Traditional Chinese Medicines). As shown in Figure 1B, eleven distinctive peaks present in all the ADR samples with clear segregation and resolution were identified as the common peaks, which illustrated the similarity between the different samples.

The comparison of the HPLC chromatograms of ADR samples with the reference fingerprint was conducted, and similarity values were determined using the correlative coefficient and cosine value of vectorial angle through the evaluation software for similarity. As shown in Table 1, the similarity values ranged from 0.930 to 0.984 between HPLC fingerprint of each ADR sample and the reference fingerprint. The analysis of similarity results suggested that there were similar chemical compositions among different batches of ADR samples.

## 3.2 Characterization of common peaks in ADR by HPLC-Q/TOF-MS

According to the results of HPLC fingerprint, eleven peaks (1–11) were selected as the common peaks of ADR samples. An HPLC-Q/TOF-MS method was also utilized to quickly identify the eleven common peaks in HPLC fingerprints. The total ion chromatogram (TIC) of ADR sample in positive ion mode is shown in Figure 2. Based on previous literature, fragmentation behaviors, retention time, major fragment ions, retention time and reference standards, a total of eleven coumarins were

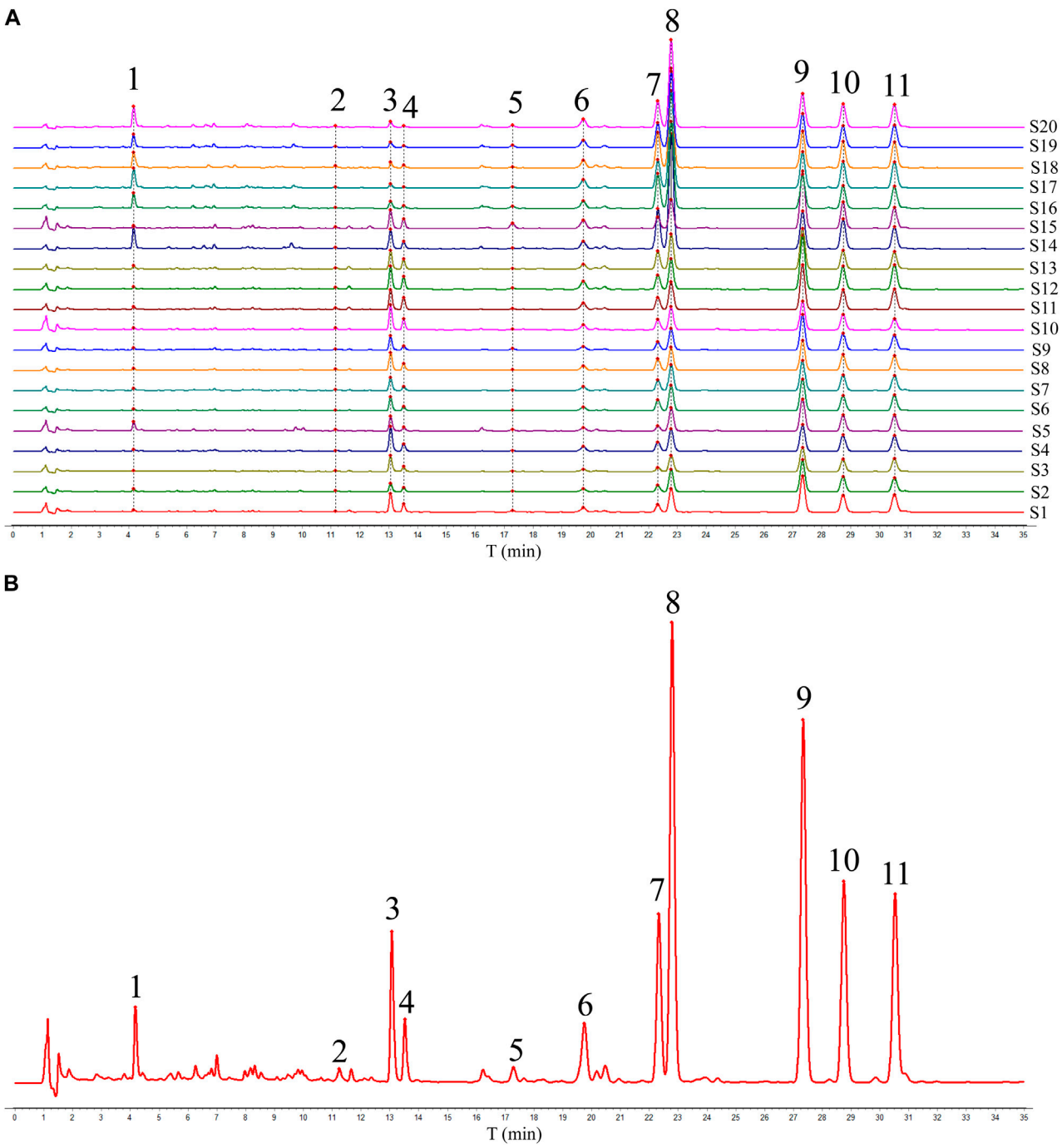


FIGURE 1
HPLC fingerprints **(A)** and reference fingerprint **(B)** of twenty batches of ADR samples.

identified, including scopolin, xanthotoxol, oxypeucedanin hydrate, byakangelicin, xanthotoxin, bergapten, byakangelicol, oxypeucedanin, imperatorin, phellopterin, and isoimperatorin (Zheng et al., 2010; Li et al., 2014). The information of identification, including retention time, chemical formula, and fragment ions was shown in Table 2. The chemical structures of the recognized elven coumarins are displayed in Supplementary Figure S1, and the MS and MS/MS spectrums of the eleven coumarin compounds was shown in Supplementary Figure S2.

## 3.3 Anti-inflammatory activities of ADR samples

### 3.3.1 Inhibition of NO production

To assess the cytotoxic impact of ADR extract on RAW 264.7 cells, the viability cells was firstly evaluated by the CCK-8 assay. RAW 264.7 macrophages were processed with different concentrations (0, 12.5, 25, 50, 100, and 200 μg/mL) of ADR extract for 24 h. The CCK-8 assay results (Supplementary Figure

TABLE 1 Similarity of 20 batches of ADR samples.

| Sample number | Similarity | Sample number | Similarity |
|---|---|---|---|
| S1 | 0.956 | S11 | 0.952 |
| S2 | 0.963 | S12 | 0.951 |
| S3 | 0.940 | S13 | 0.983 |
| S4 | 0.956 | S14 | 0.939 |
| S5 | 0.959 | S15 | 0.930 |
| S6 | 0.979 | S16 | 0.952 |
| S7 | 0.984 | S17 | 0.952 |
| S8 | 0.970 | S18 | 0.950 |
| S9 | 0.949 | S19 | 0.970 |
| S10 | 0.955 | S20 | 0.955 |

S3) indicated that there was no notable variance in viability levels between the control group and the group treated with all concentrations of ADR extract. The results suggests that the ADR extract did not cytotoxic effects on RAW264.7 cells within the specified test concentrations ranges, which were equivalent to 0–200 μg/mL of the raw herbal medicine.

The depression of NO production serves as a direct indicator of the anti-inflammatory effect due to close relationship between excessive NO production and the triggering of pro-inflammatory cytokines. The current investigation first evaluated the anti-inflammatory activities of ADR samples by determining the inhibition rate of NO production in LPS-induced RAW264.7 cells using the Griess assay reaction. The effects of ADR samples extract (50 μg/mL) on NO production in LPS-stimulated RAW264.7 cells were shown in Supplementary Figure S4. As presented in Figure 3A, all the twenty batches of ADR samples exhibited considerable inhibition of NO production with the rate of 42.39%–79.54% at the concentration 50 μg/mL raw herbal medicine. It could be noted that different batches of ADR samples showed significantly differences in the inhibition of NO production, potentially resulting from differences in bioactive constituents present in ADR samples. Previous studies reported that ADR samples extracted with different solvents (70% ethanol, ethanol, 70% methanol, methanol, and water) at 400 μg/mL concentration could significantly suppressed NO production in LPS-stimulated RAW 264.7 cells, but the inhibitory effects were inconsistent with the present experiment (Wang et al., 2016). The reason for the difference might be due to the different extraction solvents for the ADR samples.

### 3.3.2 Inhibition of pro-inflammatory cytokines production

The potential anti-inflammatory activities of ADR samples were assessed by studying their inhibition on the release of pro-inflammatory cytokines such as TNF-α, IL-1β, and IL-6. The RAW264.7 cells were treated with LPS in presence or absence of ADR extract (50 μg/mL raw herbal medicine), and the concentrations of IL-1β, IL-6, and TNF-α were assessed using ELISA kits. The effects of ADR samples extract (50 μg/mL) on IL-1β, IL-6, and TNF-α production in LPS-stimulated RAW264.7 cells were presented in Supplementary Figure S4. As shown in Figures 3B–D, the ADR extract treatment significantly suppressed the productions of IL-1β, IL-6, and TNF-α in LPS-stimulated RAW264.7 cells ($p < 0.05$), which indicated that ADR might exhibit anti-inflammatory activities by reducing the release of pro-inflammatory cytokines releases.

To sum up, the results of the anti-inflammatory experiments indicated a significant reduction in NO, IL-1β, IL-6, and TNF-α levels in LPS-induced RAW264.7 cells treated with ADR samples. It was clear that the variability of anti-inflammatory among different batches of ADR samples was evident, which demonstrated that differences in the bioactive ingredient content across different

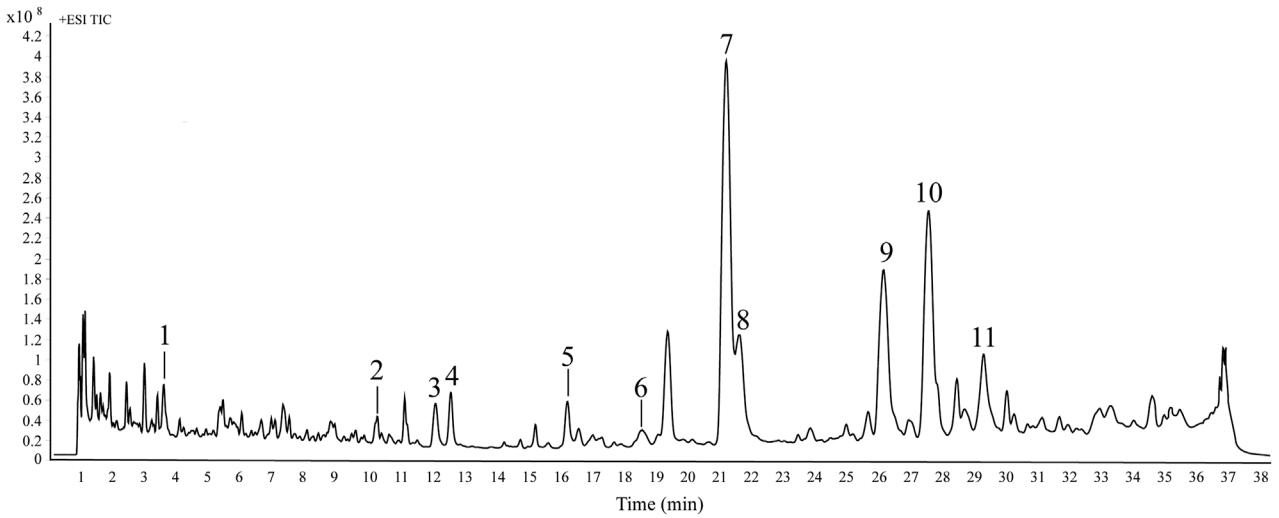


FIGURE 2
The typical total ion chromatograms of ADR samples in positive ion mode by HPLC-Q/TOF-MS. The peak numbers are consistent with the compound numbers presented in Table 2.

TABLE 2 HPLC-Q/TOF-MS information for identification of coumarin compounds in ADR samples.

| No | $T_R$ (min) | Formula | Theoretical mass (*m/z*) | Measured mass $[M + H]^+$ | (+) ESI-MS/MS (*m/z*) | Error (ppm) | Identification | Reference |
|---|---|---|---|---|---|---|---|---|
| 1 | 3.42 | $C_{16}H_{18}O_9$ | 354.0951 | 355.1039 | 193.0498 (100), 178.0261 (42.62), 163.0392 (50.64), 133.0282 (67.98), 117.0333 (31.67) | 1.69 | Scopolin | Zheng et al. (2010) |
| 2 | 10.22 | $C_{11}H_6O_4$ | 202.0266 | 203.0342 | 175.0391 (31.15), 147.0443 (100), 131.0489 (28.32) | 0.54 | Xanthotoxol | Zheng et al. (2010) |
| 3 | 12.05 | $C_{16}H_{16}O_6$ | 304.0947 | 305.1041 | 203.0346 (50.17), 175.0392 (4.95), 159.0443 (16.21), 147.0446 (100), 131.0494 (30.23), 119.0492 (8.94) | −0.93 | Oxypeucedanin hydrate | Li et al. (2014) |
| 4 | 12.53 | $C_{17}H_{18}O_7$ | 334.1053 | 335.114 | 233.0451 (36.82), 218.0215 (94.03), 203.0342 (6.14), 190.0265 (14.86), 173.0235 (100), 162.0308 (24.41) | 1.56 | Byakangelicin | Li et al. (2014) |
| 5 | 16.22 | $C_{12}H_8O_4$ | 216.0423 | 217.0503 | 202.0263 (100), 185.0234 (11.74), 174.0311 (30.29), 161.0597 (35.57), 146.0363 (3.87) | 0.77 | Xanthotoxin[a] | [a] |
| 6 | 18.60 | $C_{12}H_8O_4$ | 216.0423 | 217.0503 | 202.0261 (27.89), 174.0312 (85.95), 146.0362 (45.48), 131.0490 (9.61), 118.0415 (100), 90.0465 (95.98) | 0.74 | Bergapten[a] | [a] |
| 7 | 21.19 | $C_{17}H_{16}O_6$ | 316.0947 | 317.1035 | 231.0290 (11.64), 218.0217 (84.84), 188.0110 (55.16), 175.0394 (100), 160.0158 (29.25), 145.0284 (14.44) | 1.68 | Byakangelicol | Li et al. (2014) |
| 8 | 21.67 | $C_{16}H_{14}O_5$ | 286.0841 | 287.0922 | 203.0342 (13.5), 175.0390 (1.84), 159.0439 (6.22), 147.0445 (46.69), 59.0496 (100) | 1.40 | Oxypeucedanin | Zheng et al. (2010) |
| 9 | 26.17 | $C_{16}H_{14}O_4$ | 270.0892 | 271.0975 | 203.0342 (100), 185.0236 (3.14), 175.0390 (8.99), 147.0442 (13.55), 131.0489 (3.64) | 1.14 | Imperatorin[a] | [a] |
| 10 | 27.52 | $C_{17}H_{16}O_5$ | 300.0998 | 301.1083 | 218.0217 (100), 202.0261 (6.73), 190.0263 (11.19), 173.0233 (13.96), 162.0312 (27.5), 134.0363 (25.28) | 1.78 | Phellopterin[a] | [a] |
| 11 | 29.34 | $C_{16}H_{14}O_4$ | 270.0892 | 271.0975 | 203.0344 (100), 175.0390 (2.04), 159.0440 (5.07), 147.0444 (9.99), 131.0490 (3.34) | 1.44 | Isoimperatorin[a] | [a] |

[a]Compounds identified with reference standards.

batches of ADR samples to a certain extent. Variations in the anti-inflammatory effects might be attributed to the variation of bioactive components present in different samples of ADR samples. It is necessary to investigate the latent relevance between the bioactive compounds and anti-inflammatory effects, and screen out the potential anti-inflammatory constituents in ADR samples based on spectrum-effect relationship analysis.

## 3.4 Spectrum-effect relationship analysis

### 3.4.1 Grey relational analysis

GRA is a versatile and efficient multi-variable statistical method capable of revealing correlations between multiple objects with limited information, which is widely used to solve problems involving multiple factors and complex relationships between variables (Chang et al., 2022).

In this present work, GRA was conducted to evaluate the connection between the peak areas of eleven common peaks (Supplementary Table S4) in HPLC fingerprints and anti-inflammatory activities of ADR samples. We obtained the information sequences of the peak areas of eleven common peaks in HPLC fingerprints of different batches of ADR samples as subsequences, and the four inflammatory indicators (inhibition rates of NO, IL-1β, IL-6, and TNF-α) of different batches of ADR samples as parent sub-sequence. The GRD was used to explain the relationship between common peaks and anti-inflammatory effects, and the GRD of the eleven common peaks

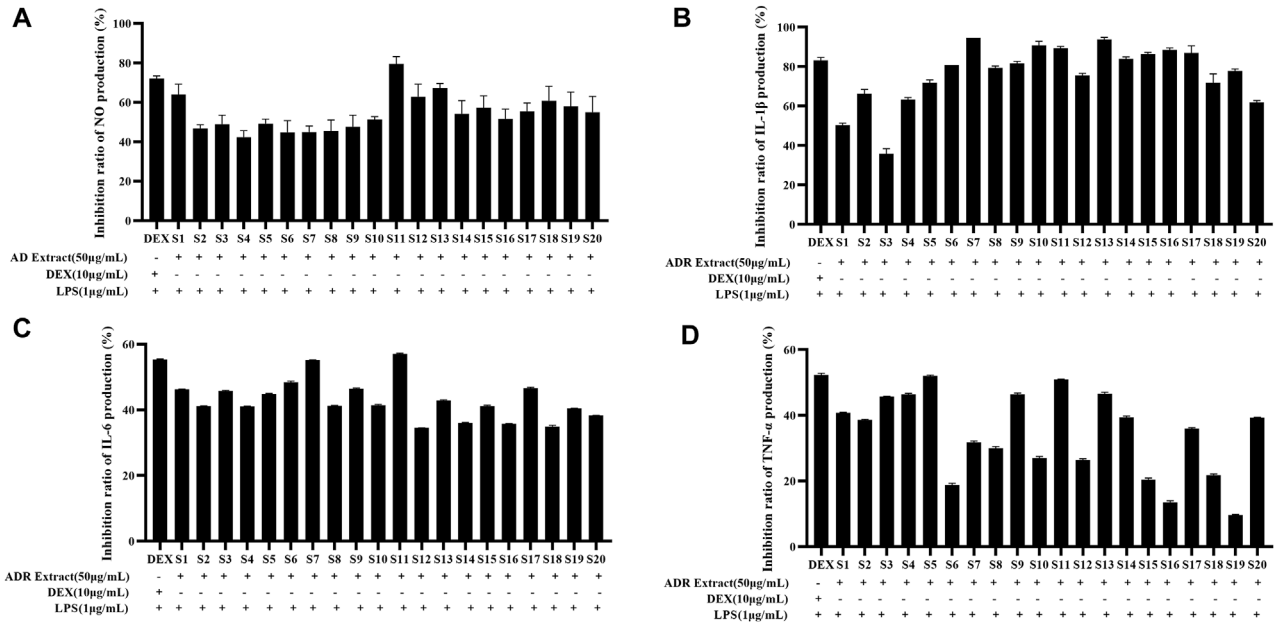


FIGURE 3
Inhibition ratio of NO **(A)**, IL-1β **(B)**, IL-6 **(C)**, and TNF-α **(D)** production in LPS-stimulated RAW264.7 cells treated with ADR samples extract (50 μg/mL).

in ADR fingerprints were calculated. The results (Figure 4) showed that the GRD of eight common peaks including xanthotoxol, oxypeucedanin hydrate, byakangelicin, xanthotoxin, bergapten, imperatorin, phellopterin, and isoimperatorin were more than 0.8, which demonstrated that these eight coumarin compounds contributed strongly to the anti-inflammatory effects of ADR. Furthermore, the higher the values of GRD were, the stronger anti-inflammation activities the coumarin compounds had.

### 3.4.2 Partial least squares regression analysis

PLSR is a powerful regression modeling method for exploring and understanding the intricate connections among various factors in a systematic and comprehensive manner, which addresses the issue of multiple dependent variables and multiple independent variables through the integration of multiple linear regression, canonical correlation analysis, and principal component analysis (Aghdamifar et al., 2023). The independent variable X was defined as the peak areas of the eleven common peaks, while the dependent variable Y was the anti-inflammatory activities (inhibition rates of NO, IL-1β, IL-6, and TNF-α). PLSR models were established, the regression coefficients and the variable importance in projection (VIP) values were determined. As shown in Figure 5, scopolin, xanthotoxol, byakangelicin, xanthotoxin, bergapten, byakangelicol, oxypeucedanin, imperatorin, phellopterin, and isoimperatorin were positively related to anti-inflammatory activities of ADR samples. As the regression coefficients values increased, the coumarin compounds exhibited stronger anti-inflammatory effects. The ranking of the regression coefficients for the coumarin compounds was as follows: bergapten > xanthotoxin > phellopterin > isoimperatorin > xanthotoxol > imperatorin > byakangelicin > oxypeucedanin > scopolin > byakangelicin > oxypeucedanin hydrate.

The VIP values serve as indicators of the significance of the variables, and peaks that correspond to variables with VIP values exceeding 1.0 could be considered to be responsible for anti-inflammatory activities of ADR samples. Six coumarin compounds, including bergapten, xanthotoxin, phellopterin, isoimperatorin, xanthotoxol, and imperatorin were selected with the VIP values greater than 1.0.

According to the results of GRA and PLSR analysis, some certain constituents contained in ADR samples had significant contribution to the anti-inflammatory activities. The spectrum-effect relationship analysis results indicated that bergapten, xanthotoxin, phellopterin, isoimperatorin, xanthotoxol, and imperatorin were considered as potential anti-inflammatory ingredients of ADR.

## 3.5 Verification of the anti-inflammatory activity

### 3.5.1 Inhibition of NO, IL-1β, IL-6, and TNF-α production

The above spectrum-effect relationship analysis illustrated that bergapten, xanthotoxin, phellopterin, isoimperatorin, xanthotoxol, and imperatorin could be the potential anti-inflammatory compounds in ADR. In order to confirm the accuracy of the results, the effects of the six coumarins on reducing inflammation were tested by assessing their ability to inhibit the production of NO, IL-1β, IL-6, and TNF-α in LPS-induced RAW264.7 macrophage cells. The CCK-8 assay results (Supplementary Table S5) indicated that there was no significant difference in cell viability between the control group and the group treated with six coumarins at different concentrations. Then, the inhibition of the six selected coumarins on NO, IL-1β, IL-6, and

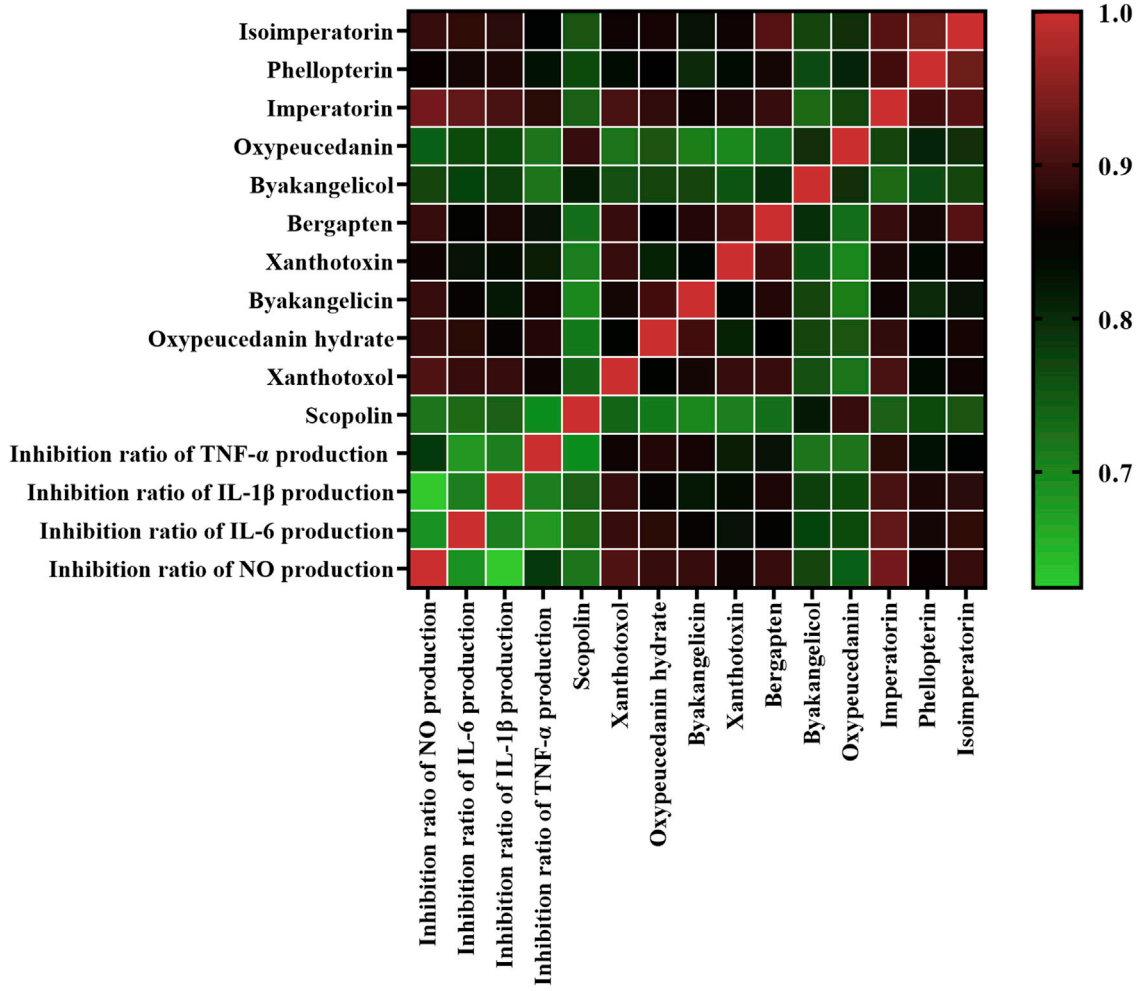


FIGURE 4
Heatmap analysis of grey relational analysis of eleven common peak areas and anti-inflammation activities. Red represents high correlated and green indicates low correlated.

TNF-α production in LPS-induced RAW264.7 macrophage cells were investigated. The results (Figure 6) showed that all the six coumarins certain and dose-dependent inhibitory effects on NO, IL-1β, IL-6, and TNF-α production. The IC50 values of bergapten, xanthotoxin, phellopterin, isoimperatorin, xanthotoxol, and imperatorin for the release of NO, IL-1β, IL-6, and TNF-α in LPS-induced RAW264.7 macrophage cells were also calculated. As shown in Table 3, phellopterin and isoimperatorin exhibited the relatively lower IC50 values on NO, IL-1β, IL-6, and TNF-α production among the six potential anti-inflammatory constituents in ADR, which indicated that phellopterin and isoimperatorin have relatively strong anti-inflammatory effects. Previous investigation has reported that isoimperatorin showed anti-inflammatory activity by decreasing the production of TNF-α, IL-6, and IL-1β in LPS-activated RAW264.7 cells, which was in basic consistence with the results of this study (Wu et al., 2024). Meanwhile, there is evidence that phellopterin displayed inhibitory activity against NO production in LPS-activated RAW 264.7 macrophage cells (Deng et al., 2015). Therefore, phellopterin and isoimperatorin were selected for further verification of underlying mechanism of the potential anti-inflammatory compounds in ADR.

### 3.5.2 Suppression on LPS-stimulated iNOS and NF-κB activation in RAW 264.7 macrophages

In the current research, we have selected the potential anti-inflammatory components in ADR, but the underlying mechanism remained uncertain. In general, iNOS play a vital role in the inflammatory process through the production of NO. Based on the significant suppression of NO by phellopterin and isoimperatorin, western blot analysis was used to measure the protein levels of iNOS. As shown in Figure 7, iNOS protein expression was remarkably up-regulated with LPS treatment, whereas the ratios decreased in phellopterin and isoimperatorin treatment groups dose-dependently manner in LPS-induced RAW 264.7 macrophages.

NF-κB is a key factor for the transcription of various inflammatory mediators, chemokines and other genes in the inflammatory response. When NF-κB is activated, it moves into

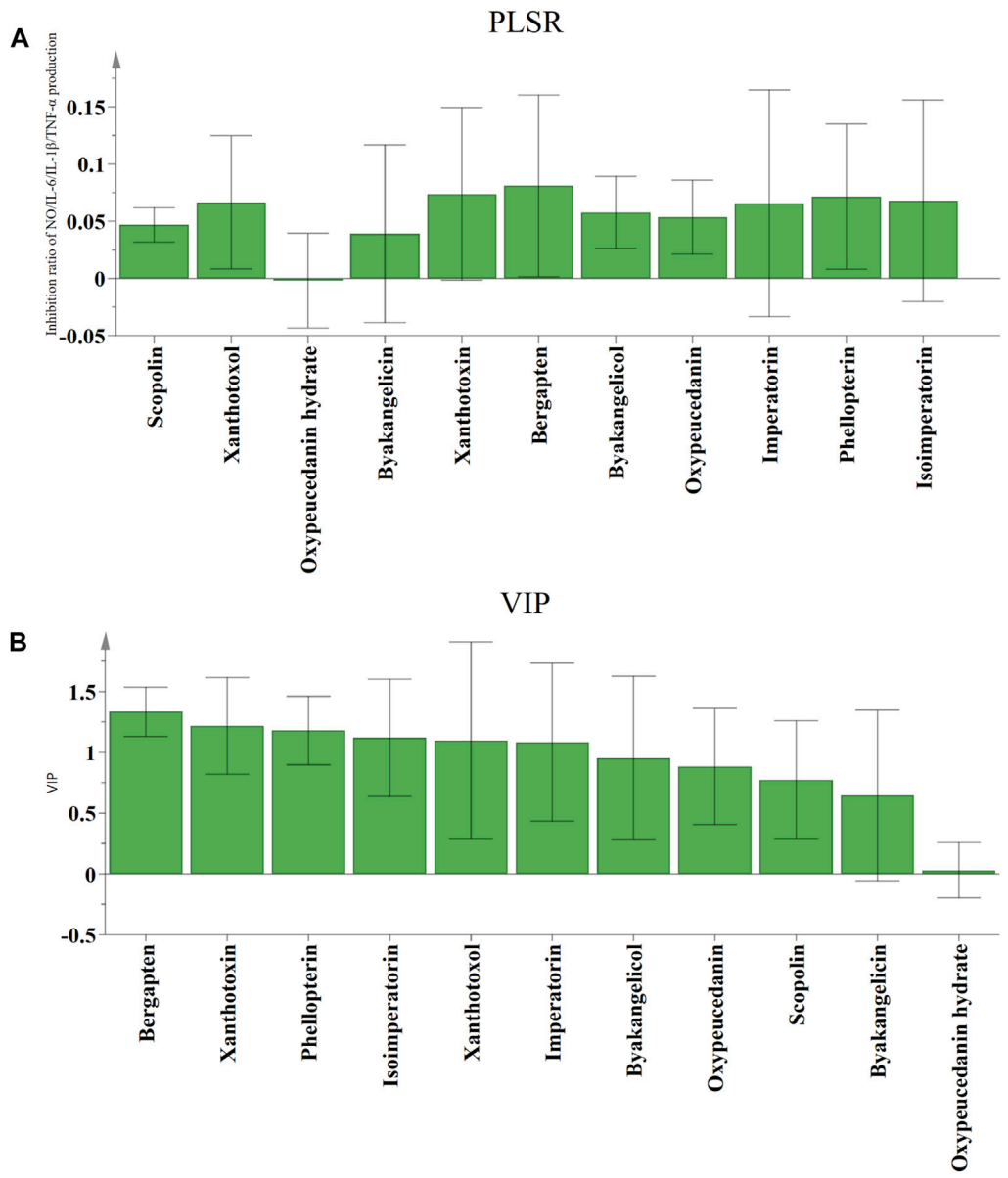


FIGURE 5
The correlation analysis by PLSR. Regression coefficients **(A)** and VIP values **(B)** between eleven common peaks and anti-inflammation activities.

the nucleus to initiate the transcription of inflammatory factors and further enhancing the production of pro-inflammatory cytokines. To further explore the underlying anti-inflammatory mechanism of the potential anti-inflammatory components phellopterin and isoimperatorin in ADR, western blot assays were used to analyze the protein expression of the NF-κB signaling pathway. As shown in Figure 7, western blot analysis demonstrated that the levels of p-p65 and p-IκBα protein induced by LPS was significantly higher than that of the control group. Phellopterin and isoimperatorin did not impact total p65 and IκBα protein levels, but they effectively inhibited the expression of both p-p65 and p-IκBα. Moreover, the ratio of p-p65/p65 and p-IκBα/IκBα was markedly down-regulated by phellopterin and isoimperatorin dose-dependently. Phellopterin and isoimperatorin demonstrated the ability to block NF-κB activation NF-κB activation by inhibiting phosphorylation levels of p65 and IκBα, thereby inhibiting the production of pro-inflammatory cytokines, thus achieving the purpose of treatment and prevention of inflammatory diseases.

## 4 Conclusion

This study looked at screening of the anti-inflammatory bioactive compounds in ADR and investigating their underlying anti-inflammatory mechanism. Firstly, the HPLC fingerprints were established based on the chromatograms of different batches of ADR samples, and eleven commons peaks were selected. Then, the eleven common peaks in HPLC fingerprints were characterized by HPLC-Q/TOF-MS. The anti-inflammatory activities of different batches of ADR samples were assessed by inhibiting the production of NO, IL-

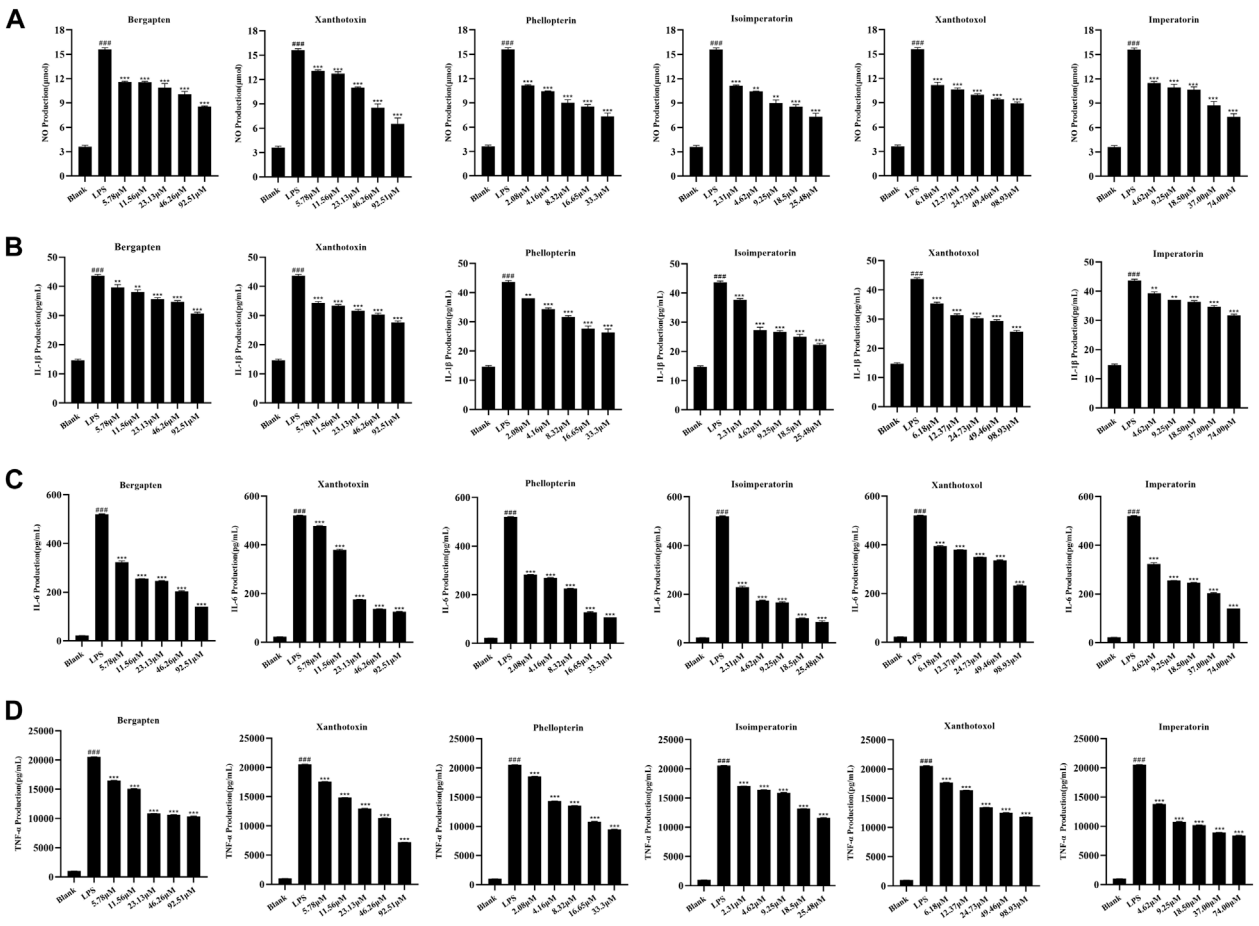


FIGURE 6
Effects of bergapten, xanthotoxin, phellopterin, isoimperatorin, xanthotoxol, and imperatorin on NO **(A)**, IL-1β **(B)**, IL-6 **(C)**, and TNF-α **(D)** production in LPS-stimulated RAW264.7 cells.$^{###}p < 0.001$, $^{***}p < 0.001$.

**TABLE 3** The inhibitory effects of six coumarins on NO, IL-1β, IL-6, and TNF-α production in LPS-induced RAW264.7 cells (IC50 values, μM).

| | Bergapten | Xanthotoxin | Phellopterin | Isoimperatorin | Xanthotoxol | Imperatorin |
|---|---|---|---|---|---|---|
| NO | 53.79 | 41.51 | 8.03 | 4.31 | 32.69 | 21.90 |
| IL-1β | 149.00 | 37.21 | 15.60 | 6.48 | 60.92 | 175.50 |
| IL-6 | 12.29 | 91.79 | 3.20 | 1.38 | 18.99 | 3.46 |
| TNF-α | 51.50 | 114.20 | 19.09 | 40.65 | 42.10 | 15.06 |

1β, IL-6, and TNF-α in LPS-induced RAW264.7 macrophage cells. The connections between chemical constituents and anti-inflammatory effects were investigated by spectrum-effect relationship analysis, and the results illustrated that bergapten, xanthotoxin, phellopterin, isoimperatorin, xanthotoxol, and imperatorin were potential anti-inflammatory constituents in ADR.

The anti-inflammatory activities of the six coumarins were validated by repression of NO, IL-1β, IL-6 and TNF-α production, and phellopterin and isoimperatorin exhibited the most significant anti-inflammatory activities among the six coumarin components. Moreover, the western blot results demonstrated that phellopterin and isoimperatorin could diminish the expression of iNOS and the phosphorylation of p65 and IκBα, which indicated that these two coumarins in ADR might exert anti-inflammatory by inhibiting of iNOS and NF-κB. The current study developed a comprehensive method utilizing HPLC fingerprints, HPLC-Q/TOF-MS and spectrum-effect relationship analysis to investigate the bioactive ingredients in herbal medicines, and also provided experimental data about the bioactive compositions and underlying mechanism for the anti-inflammatory activity of ADR.

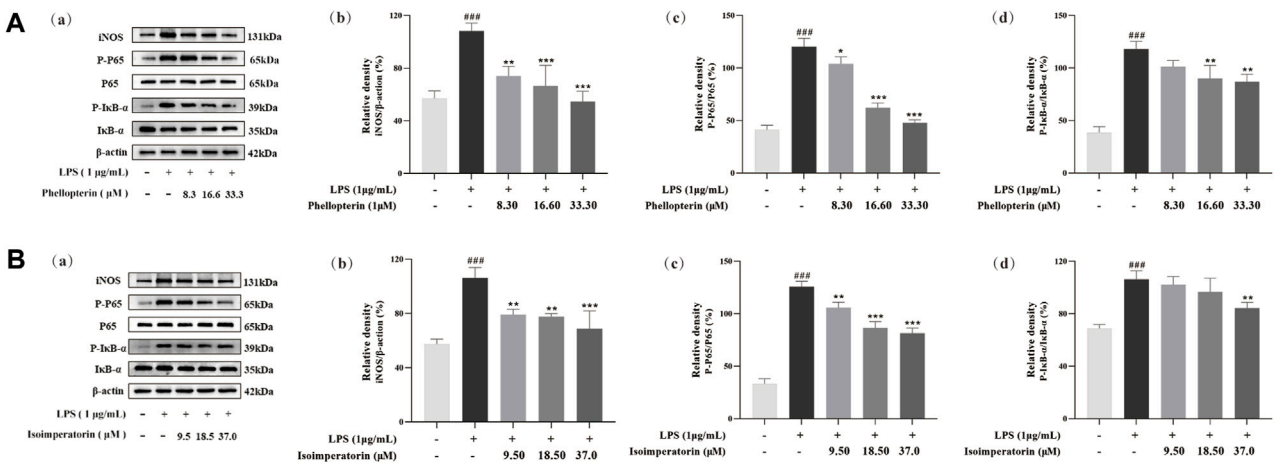


FIGURE 7
Effect of phellopterin **(A)** and isoimperatorin **(B)** on iNOS and NF-κB signaling pathway in LPS-induced RAW 264.7 macrophages. (a) Pictures of the protein levels of iNOS, p65, p-p65, IκBα, and p-IκBα analyzed by Western blot. (b) Relative density of iNOS. (c) Statistical analysis for ratios of p-p65/p65. (d) Statistical analysis for ratios of p-IκBα/IκBα. Each bar represents the mean ± SD (n = 3). $^{###}p < 0.001$ compared to the un-stimulated control cells; $^{*}p < 0.05$ compared to the LPS-stimulated cells; $^{**}p < 0.01$ compared to the LPS-stimulated cells; $^{***}p < 0.001$ compared to the LPS-stimulated cells.

## Data availability statement

The original contributions presented in the study are included in the article/Supplementary Material, further inquiries can be directed to the corresponding authors.

## Author contributions

HS: Data curation, Methodology, Visualization, Writing–original draft. QW: Validation, Visualization, Writing–review and editing. YC: Data curation, Validation, Writing–review and editing. YZ: Investigation, Validation, Writing–review and editing. DZ: Methodology, Visualization, Writing–review and editing. YZ: Conceptualization, Project administration, Writing–review and editing. LG: Funding acquisition, Methodology, Project administration, Resources, Writing–review and editing.

## Funding

The author(s) declare that financial support was received for the research, authorship, and/or publication of this article. This research was funded by Natural Science Foundation of Hebei Province (H2022418001, H2024423015), S&T Program of Hebei Province (223777127D, 22372503D), The Central Guidance on Local Science and Technology Development Fund of Hebei Province (226Z7714G), Key project of Hebei Natural Science Foundation Chinese Medicine Joint Fund (H2023423019), Hebei Province "333 Talents Project" Funded project (C20231013), Research Foundation of Hebei Provincial Administration of Traditional Chinese Medicine (Z2022019, 2022100), The Innovation Team of Hebei Province Modern Agricultural Industry Technology System (HBCT2023080201, HBCT2023080205), Key Research and Development Project of Hebei Province: Scientific and Technological Innovation Team of Modern Seed Industry of Traditional Chinese Medicine (21326312D).

## Conflict of interest

The authors declare that the research was conducted in the absence of any commercial or financial relationships that could be construed as a potential conflict of interest.

## Publisher's note

All claims expressed in this article are solely those of the authors and do not necessarily represent those of their affiliated organizations, or those of the publisher, the editors and the reviewers. Any product that may be evaluated in this article, or claim that may be made by its manufacturer, is not guaranteed or endorsed by the publisher.

## Supplementary material

The Supplementary Material for this article can be found online at: https://www.frontiersin.org/articles/10.3389/fphar.2024.1396001/full#supplementary-material

# References


Aghdamifar, E., Sharabiani, V. R., Taghinezhad, E., Szymanek, M., and Dziwulska-Hunek, A. (2023). E-nose as a non-destructive and fast method for identification and classification of coffee beans based on soft computing models. *Sensors and Actuators B. Chem.* 393, 134229. doi:10.1016/j.snb.2023.134229

Banikazemi, Z., Mirazimi, S. M., Dashti, F., Mazandaranian, M. R., Akbari, M., Morshedi, K., et al. (2021). Coumarins and gastrointestinal cancer: a new therapeutic option? *Front. Oncol.* 11, 752784. doi:10.3389/fonc.2021.752784

Chang, Y., Fan, W., Shi, H., Feng, X., Zhang, D., Wang, L., et al. (2022). Characterization of phenolics and discovery of α-glucosidase inhibitors in *Artemisia argyi* leaves based on ultra-performance liquid chromatography-tandem mass spectrometry and relevance analysis. *J. Pharm. Biomed. Anal.* 220, 114982. doi:10.1016/j.jpba.2022.114982

Chang, Y., Zhang, D., Yang, G., Zheng, Y., and Guo, L. (2021). Screening of anti-lipase components of *Artemisia argyi* leaves based on spectrum-effect relationships and HPLC-MS/MS. *Front. Pharmacol.* 12, 675396. doi:10.3389/fphar.2021.675396

Chen, G., Liu, Y., Xu, Y., Zhang, M., Guo, S., and Zhang, G. (2021). Isoimperatorin exerts anti-inflammatory activity by targeting the LPS-TLR4/MD-2-NF-κB pathway. *Eur. J. Inflamm.* 19, 205873922110005–205873922110010. doi:10.1177/20587392211000573

Chen, X. Y., Gou, S. H., Shi, Z. Q., Xue, Z. Y., and Feng, S. L. (2019). Spectrum-effect relationship between HPLC fingerprints and bioactive components of *Radix Hedysari* on increasing the peak bone mass of rat. *J. Pharm. Anal.* 9 (4), 266–273. doi:10.1016/j.jpha.2018.10.004

Deng, G. G., Wei, W., Yang, X. W., Zhang, Y. B., Xu, W., Gong, N. B., et al. (2015). New coumarins from the roots of *Angelica dahurica* var. formosana cv. chuanbaizhi and their inhibition on NO production in LPS-activated RAW264.7 cells. *Fitoterapia* 101, 194–200. doi:10.1016/j.fitote.2015.01.016

Fang, Y., Yang, L., and He, J. (2021). Plantanone C attenuates LPS-stimulated inflammation by inhibiting NF-κB/iNOS/COX-2/MAPKs/Akt pathways in RAW 264.7 macrophages. *Biomed. Pharmacother.* 143, 112104. doi:10.1016/j.biopha.2021.112104

Gong, X., Wang, J., Zhang, M., Wang, P., Wang, C., Shi, R., et al. (2020). Bioactivity, compounds isolated, chemical qualitative, and quantitative analysis of *cymbaria daurica* extracts. *Front. Pharmacol.* 11, 48. doi:10.3389/fphar.2020.00048

Jiang, M., Yang, L., Zou, L., Zhang, L., Wang, S., Zhong, Z., et al. (2024). A comprehensive quality evaluation for huangqi guizhi wuwu decoction by integrating UPLC-DAD/MS chemical profile and pharmacodynamics combined with chemometric analysis. *J. Ethnopharmacol.* 319 (Pt 3), 117325. doi:10.1016/j.jep.2023.117325

Kang, S. W., Kim, C. Y., Song, D. G., Pan, C. H., Cha, K. H., Lee, D. U., et al. (2010). Rapid identification of furanocoumarins in *Angelica dahurica* using the online LC-MMR-MS and their nitric oxide inhibitory activity in RAW 264.7 cells. *Phytochem. Anal.* 21 (4), 322–327. doi:10.1002/pca.1202

Ke, Y. Y., Shyu, Y. T., and Wu, S. J. (2021). Evaluating the anti-inflammatory and antioxidant effects of broccoli treated with high hydrostatic pressure in cell models. *Foods* 10 (1), 167. doi:10.3390/foods10010167

Lee, B. W., Ha, T. K. Q., Cho, H. M., An, J. P., Kim, S. K., Kim, C. S., et al. (2020). Antiviral activity of furanocoumarins isolated from *Angelica dahurica* against influenza a viruses H1N1 and H9N2. *J. Ethnopharmacol.* 259, 112945. doi:10.1016/j.jep.2020.112945

Li, B., Zhang, X., Wang, J., Zhang, L., Gao, B., Shi, S., et al. (2014). Simultaneous characterisation of fifty coumarins from the roots of *Angelica dahurica* by off-line two-dimensional high-performance liquid chromatography coupled with electrospray ionisation tandem mass spectrometry. *Phytochem. Anal.* 25 (3), 229–240. doi:10.1002/pca.2496

Li, C. J., Zhai, R. R., Zhu, X. Y., Guo, Z. F., and Yang, H. (2023). Discovery of effective combination from renshen-fuzi herbal pair against heart failure by spectrum-effect relationship analysis and zebrafish models. *J. Ethnopharmacol.* 317, 116832. doi:10.1016/j.jep.2023.116832

Li, J., Sun, M., Xu, C., Zhou, C., Jing, S. J., Jiang, Y. Y., et al. (2024). An integrated strategy for rapid discovery and identification of the potential effective fragments of polysaccharides from Saposhnikoviae Radix. *J. Ethnopharmacol.* 319 (Pt 1), 117099. doi:10.1016/j.jep.2023.117099

Luo, L., Sun, T., Yang, L., Liu, A., Liu, Q. Q., Tian, Q. Q., et al. (2020). Scopoletin ameliorates anxiety-like behaviors in complete freund's adjuvant-induced mouse model. *Mol. Brain* 13 (1), 15. doi:10.1186/s13041-020-0560-2

Shi, H., Chang, Y. Q., Feng, X., Yang, G. Y., Zheng, Y. G., Zheng, Q., et al. (2022). Chemical comparison and discrimination of two plant sources of angelicae dahuricae radix, *Angelica dahurica* and *Angelica dahurica* var. *formosana*, by HPLC-Q/TOF-MS and quantitative analysis of multiple components by a single marker. *Phytochem. Anal.* 33 (5), 776–791. doi:10.1002/pca.3129

Tian, Y., Zhou, S., Takeda, R., Okazaki, K., Sekita, M., Sakamoto, K., et al. (2021). Anti-inflammatory activities of amber extract in lipopolysaccharide-induced RAW 264.7 macrophages. *Biomed. Pharmacother.* 141, 111854. doi:10.1016/j.biopha.2021.111854

Wang, L., Cui, Y. R., Wang, K., Fu, X., Xu, J., Gao, X., et al. (2022). Anti-inflammatory effect of fucoidan isolated from fermented *Sargassum fusiforme* in *in vitro* and *in vivo* models. *Int. J. Biol. Macromol.* 222 (Pt B), 2065–2071. doi:10.1016/j.ijbiomac.2022.10.005

Wang, M. H., Jeong, S. H., Guo, H., and Park, J. B. (2016). Anti-inflammatory and cytotoxic effects of methanol, ethanol, and water extracts of *Angelicae Dahuricae* Radix. *J. Oral Sci.* 58 (1), 125–131. doi:10.2334/josnusd.58.125

Wang, Q. Q., Li, Y., Wang, S. G., Xiang, Z. D., Dong, W. C., Li, X. Y., et al. (2023). A review of the historical records, chemistry, pharmacology, pharmacokinetics and edibility of *Angelica dahurica*. *Arab. J. Chem.* 16, 104877. doi:10.1016/j.arabjc.2023.104877

Wu, H., Lv, Y., Zhao, M., Tang, R., Li, Y., Fang, K., et al. (2024). Study on the substance basis of the efficacy of eucommiae cortex before and after salt processing for the treatment of kidney-yang deficiency syndrome based on the spectrum-effect relationship. *J. Ethnopharmacol.* 318 (Pt A), 116926. doi:10.1016/j.jep.2023.116926

Yang, W. Q., Song, Y. L., Zhu, Z. X., Su, C., Zhang, X., Wang, J., et al. (2015). Anti-inflammatory dimeric furanocoumarins from the roots of *Angelica dahurica*. *Fitoterapia* 105, 187–193. doi:10.1016/j.fitote.2015.07.006

Zhao, H., Feng, Y. L., Wang, M., Wang, J. J., Liu, T., Yu, J., et al. (2022). The *Angelica dahurica*: a review of traditional uses, phytochemistry and pharmacology. *Front. Pharmacol.* 13, 896637. doi:10.3389/fphar.2022.896637

Zheng, X., Zhang, X., Sheng, X., Yuan, Z., Yang, W., Wang, Q., et al. (2010). Simultaneous characterization and quantitation of 11 coumarins in *Radix Angelicae Dahuricae* by high performance liquid chromatography with electrospray tandem mass spectrometry. *J. Pharm. Biomed. Anal.* 51 (3), 599–605. doi:10.1016/j.jpba.2009.09.030

frontiers | Frontiers in Pharmacology

TYPE Original Research
PUBLISHED 06 December 2024
DOI 10.3389/fphar.2024.1480626

Check for updates

OPEN ACCESS

EDITED BY
Ochuko Lucky Erukainure,
University of the Free State, South Africa

REVIEWED BY
Gloria O. Izu,
Central University of Technology, South Africa
Akingbolabo Daniel Ogunlakin,
Bowen University, Nigeria

*CORRESPONDENCE
Shicui Jiang,
shicuijiang@wmu.edu.cn
Chi Zhang,
zhangchi515@wmu.edu.cn

†These authors have contributed equally to this work

RECEIVED 14 August 2024
ACCEPTED 25 November 2024
PUBLISHED 06 December 2024

CITATION
Li J, Zhuang Y, Fan G, Wang S, Yan E, Guo J, Zhang C and Jiang S (2024) Impact of baicalin and components of Scutellaria baicalensis on renal fibrosis of diabetic kidney disease. *Front. Pharmacol.* 15:1480626. doi: 10.3389/fphar.2024.1480626

COPYRIGHT
© 2024 Li, Zhuang, Fan, Wang, Yan, Guo, Zhang and Jiang. This is an open-access article distributed under the terms of the Creative Commons Attribution License (CC BY). The use, distribution or reproduction in other forums is permitted, provided the original author(s) and the copyright owner(s) are credited and that the original publication in this journal is cited, in accordance with accepted academic practice. No use, distribution or reproduction is permitted which does not comply with these terms.

# Impact of baicalin and components of Scutellaria baicalensis on renal fibrosis of diabetic kidney disease

Jiarui Li[1,2†], Yuan Zhuang[1,2†], Guoyong Fan[1,3], Simeng Wang[1], Enhui Yan[1,3], Jianpeng Guo[2], Chi Zhang[1,3]* and Shicui Jiang[1,2,3]*

[1]Wenzhou Key Laboratory for the Diagnosis and Prevention of Diabetic Complications, The Third Affiliated Hospital of Wenzhou Medical University (Ruian People's Hospital), Ruian, China, [2]College of Pharmacy, Yanbian University, Yanji, Jilin, China, [3]Liji Medical Research Academy, The Third Affiliated Hospital of Wenzhou Medical University (Ruian People's Hospital), Ruian, China

**Background:** Fibrosis is key in the development and progression of diabetic kidney disease (DKD). Baicalin (BA), wogonin (WGN), and wogonoside (WGS) have renoprotective effects. The mechanism of alleviation of DKD progression, by improving renal fibrosis, is unclear. This study aimed to investigate the mechanisms and effects of a *Scutellaria baicalensis* Georgi. (Lamiaceae) mixture (MIX, WGN:BA:WGS = 4:2:1) on DKD in a spontaneous DKD model.

**Methods:** Male *db/m* mice were controls, and *db/db* mice were diabetes models. Both groups received daily oral gavage of normal saline. Treatment groups received daily oral gavage of BA or MIX (20 mg/kg) for 10 weeks. Biochemical indicators and kidney lesions were assessed. Fibrosis-related proteins were detected by immunoblotting, immunohistochemistry, and real-time fluorescence quantitative PCR.

**Results:** MIX significantly reduced body weight (40.97 ± 1.43 vs. 42.26 ± 1.60), improved insulin sensitivity (63.70 ± 8.98 vs. 109.48 ± 0.69), lowered the renal hypertrophy index (19.81 ± 2.86 vs. 28.94 ± 0.256), and decreased blood urea nitrogen levels (7.57 ± 0.79 vs. 9.57 ± 0.38) and the urine protein/creatinine ratio (0.50 ± 0.06 vs. 0.80 ± 0.18). MIX also enhanced lipid profiles and renal function by improving renal tubular dilation, restoring renal structures, and reducing glomerulosclerosis, basal membrane thickening, and glycogen deposition. These effects were achieved by reducing the protein and gene expression of collagen II (Col-II), connective tissue growth factor, and collagen I (Col-I).

**Conclusion:** MIX inhibits the transforming growth factor-β/Smads signaling pathway, thus alleviating renal fibrosis, and can be used to develop a treatment for DKD.

KEYWORDS

**flavonoids, traditional Chinese medicine, diabetic nephropathy, baicalin, renal fibrosis, insulin sensitivity**

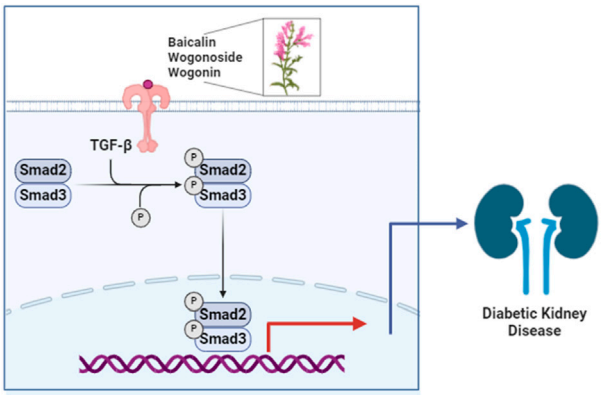


GRAPHICAL ABSTRACT

## Highlights

- MIX outperformed BA in reducing renal fibrosis markers.
- MIX significantly lowered the renal hypertrophy index in DKD mice.
- BA and MIX improved insulin sensitivity and reduced blood urea nitrogen.
- MIX inhibited TGF-β/Smad signaling, alleviating renal fibrosis.
- MIX shows potential as a natural treatment for diabetic nephropathy.

## Introduction

Diabetic kidney disease (DKD) is the main cause of end-stage lesions in diabetic patients (Aschner et al., 2021; Du et al., 2017). It is one of the most serious complications, affecting 10%–40% of patients (Adeshara et al., 2016). In China, the incidence of DKD is expected to increase in the coming decades as the prevalence of diabetes rises (Guo et al., 2016; Tang et al., 2017).

The pathogenesis of DKD involves many factors including metabolic disorders, immune-inflammatory mechanisms, oxidative stress, and genetic factors (Li et al., 2017; Lavoz et al., 2020; Meshkani and Vakili, 2016). Renal fibrosis is considered a complex and irreversible process occurring in the DKD lesions at later stages, further exacerbating disease progression. Renal fibrosis is a multifactorial dynamic process, with studies indicating the involvement of numerous factors in DKD fibrosis development including transforming growth factor-ß (TGF-ß), interleukin (IL)-1, IL-6, tumor necrosis factor-α, and oxidative stress. Research has found that NAD(P)H quinone oxidoreductase 1 mitigates diabetes-induced renal inflammation and fibrosis by modulating the Toll-like receptor 4 (TLR4)/NF-κB and TGF-ß/Smads signaling pathways (Qiu et al., 2023). Under the influence of multiple factors leading to inflammation and damage, excessive extracellular matrix deposition and the epithelial-mesenchymal transition occur, resulting in a loss of differentiated epithelial cells and their capillaries, and the accumulation of myofibroblasts and inflammatory cells, ultimately leading to structural and functional damage of the kidney (Hu et al., 2021; Yamashita and Kramann, 2024).

*Scutellaria baicalensis* Georgi. (Lamiaceae), a plant with a medicinal history spanning at least 2000 years, was first recorded around 200 AD in *Shennong's Classic of Materia Medica* (Liao et al., 2021; Zhao et al., 2019). The roots of *S. baicalensis* are known to promote wound healing, remove heat and dampness, clear fires, detoxify and reconcile toxins, and regulate immunity. It is used for the prevention and treatment of diabetes, have the effects of improving the renal function, insulin resistance and retinopathy of type 2 diabetic patients (Lai and Li, 2024). And exhibits various pharmacological properties, including antitumor, free-radical-scavenging, antioxidant, anti-inflammatory, and antiviral activity (Shang et al., 2023). Baicalin (BA), wogonin (WGN), and wogonoside (WGS) are bioactive flavonoids found in *S. baicalensis* (Wu et al., 2014). BA has numerous health benefits, including anti-inflammatory, antibacterial, antitumor, and antioxidant activity (Liao et al., 2021; Shang et al., 2023). BA has been proposed as a potential drug for the treatment of DKD (Hu et al., 2024), alleviate podocyte damage (Ou et al., 2021), diminish renal fibrosis [ (Zhang et al., 2020; Wang H. et al., 2022)], enhance renal functionality (Yang et al., 2019), oxidative stress and inflammation (Ma et al., 2021) and provide relief in DKD scenarios. WGN mitigates glomerulopathy and podocyte injury by regulating Bcl-2-mediated crosstalk between autophagy and apoptosis (Liu et al., 2022). WGS and WGN can reduce the expression levels of TLR4 mRNA and NF-κBp65 mRNA in renal tissue. Consequently, the proteins TLR4 and NF-κBp65 are decreased, inhibiting the TLR/NF-κB signaling pathway and playing a protective role in renal tissue (Wang YR. et al., 2022).

*Scutellaria baicalensis* Georgi. (Lamiaceae) mixture (MIX, WGN: BA:WGS = 4:2:1), that using multi-chamber electrophoresis screening technology, three components that bind to the target protein were selected from a multi-component mixture of *S. baicalensis*. These components, qualitatively identified as WGN, BA, and WGS through LC-MS/MS in the multiple reaction monitoring mode, were subsequently quantified. The molar ratio of the components was 4:2:1 (v/v). Using a high glucose-induced human renal tubular epithelial cell (HK-2) model, we demonstrated that these components suppress inflammatory responses and mitigate apoptosis in high glucose-induced HK-2 cells (Suo, 2022). There is insufficient *in vivo* evidence validating the therapeutic efficacy and safety of MIX in

animal models of DKD and inadequate understanding of the molecular pathways modulated by these combined components, specifically through the TGF-β/Smads signaling pathway.

In this study, we investigated the impact of multiple components of *S. baicalensis* on the TGF-β/Smads signaling pathway in the renal tissues of DKD *db/db* mice. We aimed to explore the mechanisms by which BA and MIX ameliorate DKD and provide an experimental foundation for the potential clinical applications of BA and MIX.

# Methods

## Ethics statement

All animal experiments were conducted in accordance with internationally recognized animal welfare guidelines and were approved by the Medical Ethics Committee of Experimental Animal Ethics at Ruian People's Hospital (SYSQ-2023-008, 30 April 2023).

## Drugs

BA (>98.0% purity, catalog no. MB6698), WGN (>98.0% purity; catalog no. MB6662), and WGS (>98.0% purity; catalog no. MB6663) were purchased from Meilunbio (Dalian, China). A MIX of *S. baicalensis* was prepared using WGN, BA, and WGS in a molar ratio of 4:2:1. Isoflurane was obtained from RWD Life Science Co. Ltd. (Shenzhen, China).

## Experimental animals and treatment

*db/db* mice (males, 7 weeks, weighing 36 ± 2 g, n = 18), and *db/m* mice (males, 7 weeks, weighing 22 ± 2 g, n = 6) which were non-diabetic mice born in the same litter as the *db/db* mice, were obtained from Jiangsu Changzhou Kavins Laboratory Animal Co., Ltd. (license number: SCXK (Su) 2021-0013). They were housed in separate individually ventilated cages (temperature: 23°C ± 3°C, humidity 40%–70%, light/dark cycle 12 h). The mice had *ad libitum* access to a standard diet and water.

The *db/db* mice were divided randomly into three groups based on fasting blood glucose levels and body weight (n = 6): the *db/db* group (model of diabetes), the *db/db* mice treated with MIX group, and the BA group. The *db/m* mice (n = 6) served as the normal control group of non-diabetic mice (Jin et al., 2023). Mice in the *db/m* and *db/db* groups received normal saline, while those in the BA group received a daily dose of 20 mg/kg BA, and those in the MIX group received 20 mg/kg MIX. The three components were calculated according to a WGN: BA: WGS ratio of 4:2:1. All treatments were administered by oral gavage once daily at 10:00 a.m. for 10 weeks.

## Metabolic and biochemical parameters

The fasting blood glucose levels of the mice were assessed using a blood glucose meter and test strips once a week throughout the treatment period, with blood samples obtained from the tail tip. At 18 weeks old, the mice were weighed and placed in metabolic cages for 24 h for urine collection. The mice were anesthetized using an anesthesia machine with 1.5%–2% isoflurane. After anesthesia, blood samples were collected from the orbital venous plexus, and both kidneys were carefully removed, washed with phosphate-buffered saline, and weighed. The following parameters were measured using an automated biochemical analyzer (IDEXX Laboratories, Shanghai, China): urine protein, urine creatinine, blood urea nitrogen (BUN), cholesterol, and triglycerides.

## Intraperitoneal glucose tolerance

The mice were fasted for 12 h. An intraperitoneal injection of a glucose solution (2 g/kg, 50%) was administered. Blood samples were collected from the tail vein 0, 30, 60, and 120 min after the injection, and the corresponding blood glucose values were recorded. The area under the curve (AUC) for the glucose tolerance test was calculated (Huang et al., 2024).

## Kidney histology

The kidney tissues were fixed in 4% paraformaldehyde buffer (P1110, Beijing Solaibao Technology Co., Ltd.), embedded in paraffin, and sectioned. These sections were further processed for histological staining using hematoxylin and eosin (HE) (G1120, Beijing Solaibao Technology Co., Ltd.), Masson's modified trichrome (G1340, Beijing Solaibao Technology Co., Ltd.), or periodic acid-Schiff (PAS) (C0142S, Beijing Solaibao Technology Co., Ltd.) and viewed under a 400× power lens.

## Immunohistochemistry staining

Following the standard deparaffinization and hydration protocol. Antigen repair was performed by microwaving 10 mM sodium citrate (pH 6.0) buffer solution for 10 min. To block endogenous peroxidase activity, the slides were incubated with 3% hydrogen peroxide ($H_2O_2$) at room temperature for 30 min. The slides were blocked with 20% normal goat serum for 1 h. The sections were incubated overnight with the appropriate primary antibody TGF-β (25 kDa, 1:500, #ab92486, Abcam, Cambridge, United Kingdom) and Smad2/3 (60 kDa, 1:500, #3700, CST, Danvers, MA, United States) were applied to the slides and left overnight at 4°C. (Negative control: no primary antibody was added during the staining process). DAB color development (DAB chromogenic reagent for histochemical kit; G1212; Wuhan servicebio technology CO.,LTD.) and counterstained with hematoxylin (G1004; G1039; G1040; Wuhan servicebio technology CO.,LTD.). Images were captured at a magnification of ×400 and analyzed Immunohistochemistry positive area using ImagePro Plus 6.0 quantitative software (NIH, Bethesda, MD, United States).

## RT-qPCR

Total RNA was extracted from mouse kidney tissues using the RNAiso Plus reagent following the standard protocol (MF846, Mei5 Biotechnology, Beijing, China). The cDNA was

TABLE 1 Primer sequences.

| Gene | Primer sequence |
|---|---|
| Collagen I (Forward) | CTGACGCATGGCCAAGAAGA |
| Collagen I (Reverse) | TACCTCGGGTTTCCACGTCT |
| β-Actin (Forward) | ATCACTATTGGCAACGAGCGGTTC |
| β-Actin (Reverse) | CAGCACTGTGTTGGCATAGAGGTC |

reverse-transcribed (MF012, Mei5 Biotechnology, Beijing, China). RT-qPCR (MF049, Mei5 Biotechnology, Beijing, China) was performed on the QuantStudio™ 3 system (Thermo Fisher Scientific, Waltham, MA, United States). The mRNA levels of the target genes were normalized and analyzed using the $2^{-\Delta\Delta CT}$ method. The primer sequences are listed in Table 1.

## Western blot assays

Renal tissues (approximately 100 mg) were collected and lysed in radioimmunoprecipitation assay buffer (P0013B, Beyotime Biotechnology Co., Ltd.). The lysates were centrifuged at 4°C and 12,000 g for 15 min, and the resulting supernatants were collected. Total protein was extracted from the supernatant, and the protein concentration was ascertained using a bicinchoninic acid assay (BCA, P0010 Beyotime Biotechnology Co., Ltd.). Equivalent amounts of protein (35 μg/lane) were separated by sodium dodecyl sulfate-polyacrylamide gel electrophoresis (SDS-PAGE, P0010, Beyotime Biotechnology Co., Ltd.) and transferred to polyvinylidene difluoride membranes by electroblotting.

The membranes were blocked in 5% (w/v) nonfat milk at room temperature for 1 h. They were then incubated overnight at 4°C with specific primary antibodies against TGF-β (25kDa, 1:1,000 dilution; #ab92486, Abcam, Cambridge, United Kingdom), Smad2/3 (60 kDa, 1:1,000 dilution; #12470, CST, Danvers, MA, United States), collagen I (Col-I) (220 kDa1:1,000 dilution, #72026 CST, Danvers, MA, United States), collagen II (Col-II) (200 kDa, 1:1,000 dilution, #43306S, CST, Danvers, MA, United States), and connective tissue growth factor (CTGF) (35 kDa, 1:1,000 dilution, #86641S, CST, Danvers, MA, United States). The internal control β-actin/GAPDH calibration was used to correct the errors in the quantification and loading of protein samples to ensure the accuracy of the experimental results. After washing with tris-buffered saline/0.1% Tween 20 (TBST), the membranes were incubated with the appropriate secondary antibody at room temperature for 1 h. Following washing with TBST, the membranes were stained with an enhanced chemiluminescence reagent and visualized using a gel imaging system. ImagePro Plus 6.0 was used to analyze the gray scale of the obtained strips.

## Statistical analyses

Data analysis was conducted using SPSS version 22.0. Results are presented as mean ± standard deviation. Differences among multiple sample groups were assessed using one-way analysis of variance. Pairwise comparisons between groups with homogeneous variances were performed using the Bonferroni method, while Tamhane's T2 test was employed for groups with heterogeneous variances. $p < 0.05$ was considered statistically significant.

# Results

## Effect of baicalin and MIX on weight, blood sugar, and glucose tolerance of db/db mice

During the experiment, both the *db/m* and *db/db* groups exhibited significant increases in average body weight. However, after 4 weeks of treatment, the *db/db* MIX treatment group showed a marked decrease in body weight, surpassing the decrease observed in the *db/db* BA group. The *db/db* group demonstrated a notable elevation in blood glucose levels compared to the *db/m* group. Neither BA nor MIX administration in the *db/db* group reduced the blood glucose level. This indicates that both BA and MIX were ineffective in mitigating the onset and progression of DKD by lowering blood glucose levels.

In the *db/m* group, blood glucose levels gradually decreased after intraperitoneal insulin injections and reached their lowest value 30 min after injection. In contrast, blood glucose levels in the *db/db* group did not change significantly after insulin injection, indicating a marked decrease in insulin sensitivity and the presence of insulin resistance. The AUC of the insulin tolerance test also increased significantly in the *db/db* group compared to the control group. In the BA and MIX treatment groups, blood glucose levels decreased after intraperitoneal insulin injection, reaching their lowest values at 60 min. This indicates that BA and MIX restored insulin sensitivity in mice. Among the treatment groups, the MIX group demonstrated the greatest improvement in glucose and insulin tolerance, as indicated by the insulin tolerance test AUC values shown in Figure 1.

## Effect of baicalin and MIX on renal function and serum biochemical indicators in db/db mice

The ratio of kidney weight to tibial length in mice serves as an indicator of renal hypertrophy. Compared to the *db/m* group, the *db/db* group exhibited a significant increase in the renal hypertrophy index. However, the BA and MIX treatment groups significantly reduced the renal hypertrophy index compared with the *db/db* group. In particular, the MIX treatment group showed a more substantial decrease in the renal hypertrophy index than the BA treatment group did, as shown in Figure 2A.

The *db/db* group showed a substantial increase in BUN levels compared with the *db/m* group. In contrast, the BA and MIX treatment groups exhibited varying degrees of reduction in BUN levels compared with the *db/db* group, suggesting improved renal function. Among the treatment groups, the MIX treatment group showed a significant decrease in BUN levels compared with the BA treatment group (Figure 2B).

The urinary protein-to-creatinine ratio was significantly higher in the *db/db* group than in the *db/m* group. However, the treatment groups demonstrated varying degrees of reduction in this ratio, indicative of improved renal function. The MIX treatment group

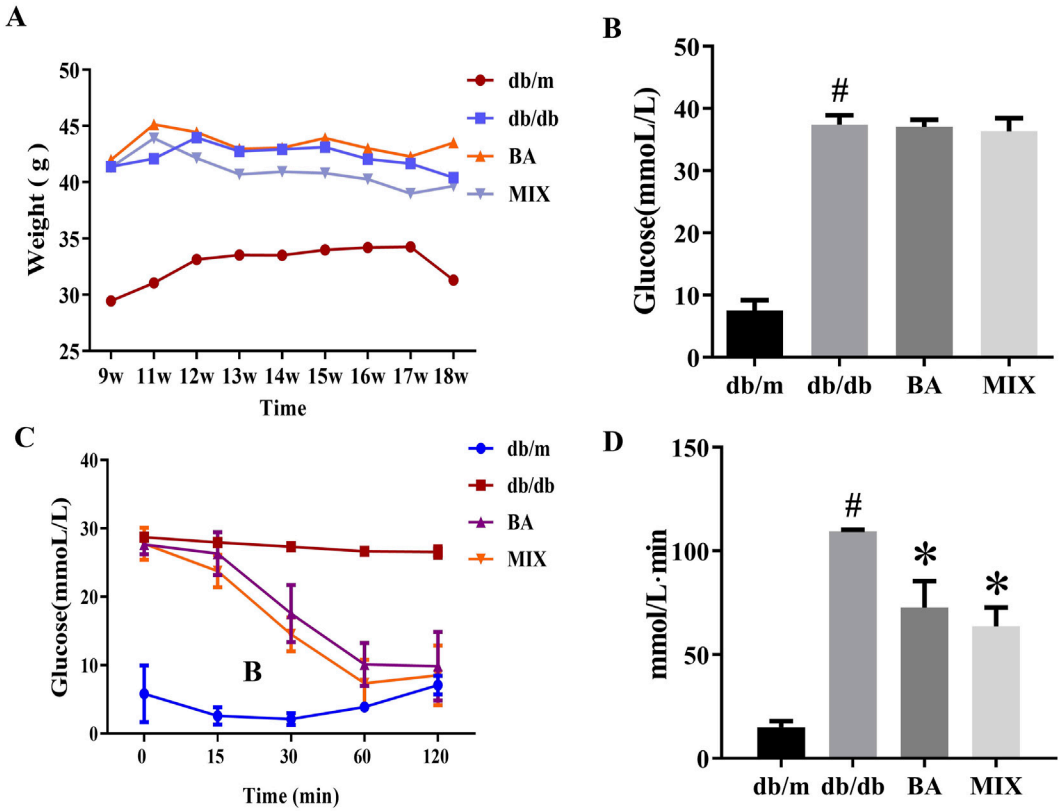


FIGURE 1
Changes in body weight, blood glucose, and glucose tolerance in each group **(A)** The weight change (g) of each group over the study period. **(B)** The blood glucose levels (mmol/L) measured at the end of the study. **(C)** The time trend of blood glucose levels (mmol/L) after insulin injection. **(D)** The area under the curve of the insulin tolerance test for each group (n = 6, compared to the *db/m* group, #$p < 0.05$; compared to the *db/db* group, *$p < 0.05$). Abbreviations: db/m: normal control group of non-diabetic mice, db/db: model of diabetes, BA: baicalin, MIX: multi-component mixture.

exhibited the most pronounced reduction in the urinary protein-to-creatinine ratio, especially when compared to the BA treatment group (Figure 2C). These findings suggest that MIX enhanced renal filtration and alleviated the progression of DKD.

The *db/db* group demonstrated a significant increase in cholesterol (CHOL) and triglyceride (TRIG) levels compared with the control group. However, the treatment groups showed varying degrees of reduction in TRIG and CHOL levels compared with the *db/db* group, indicating a beneficial effect. In particular, the MIX treatment group exhibited a significant decrease in TRIG levels compared with the *db/db* group. The results are shown in Figure 2E.

## Effect of baicalin and MIX on renal pathological morphology of db/db mice

HE and PAS staining revealed a well-preserved renal tissue structure in the *db/m* group, with normal glomerular size and morphology and healthy interstitial space without mesangial proliferation. The nuclear membrane boundaries were clear and showed no abnormalities and the renal tubules maintained their integrity and compact arrangement, with no anomalies detected in the interstitium. In contrast, the *db/db* group exhibited substantial abnormalities, including extensive strip-shaped blank areas, significant reduction in nuclei, loss of renal tubular shape, noticeable tubular dilation, epithelial cell apoptosis and necrosis, cell loss, and abnormal changes in the renal interstitium. Following the administration of various doses of BA and MIX, pathological improvements were observed to varying degrees, with a reduction in interstitial fibrosis. The BA treatment group showed more pronounced improvement than the MIX treatment group did, indicating greater efficacy in mitigating these pathological changes.

In the *db/m* group, the boundaries of the kidney cells remained distinct. The glomeruli showed no significant signs of sclerosis, with no collagen production or minimal filamentous deposition. In contrast, in the *db/db* group, the glomeruli exhibited marked fibrosis, intercellular congestion, substantial accumulation of collagen fibers around the renal tubules, widening of the renal interstitium, a significant increase in collagen fibers, the presence of protein casts, and diffuse distribution throughout the renal interstitium. The areas of collagen deposition and fibrosis were significantly reduced in each treatment group compared to the model group. Only a small number of filamentous fibers were observed in the BA and MIX treatment groups, with the most substantial improvement seen in these groups, as shown in Figure 3.

Compared to the *db/m* group, the glomeruli in the *db/db* group showed noticeable swelling, evident glycogen deposition, prominent extracellular matrix deposition by glomerular mesangial cells, and thickening of the basement membrane. Various degrees of improvement were observed in each treatment group. The BA

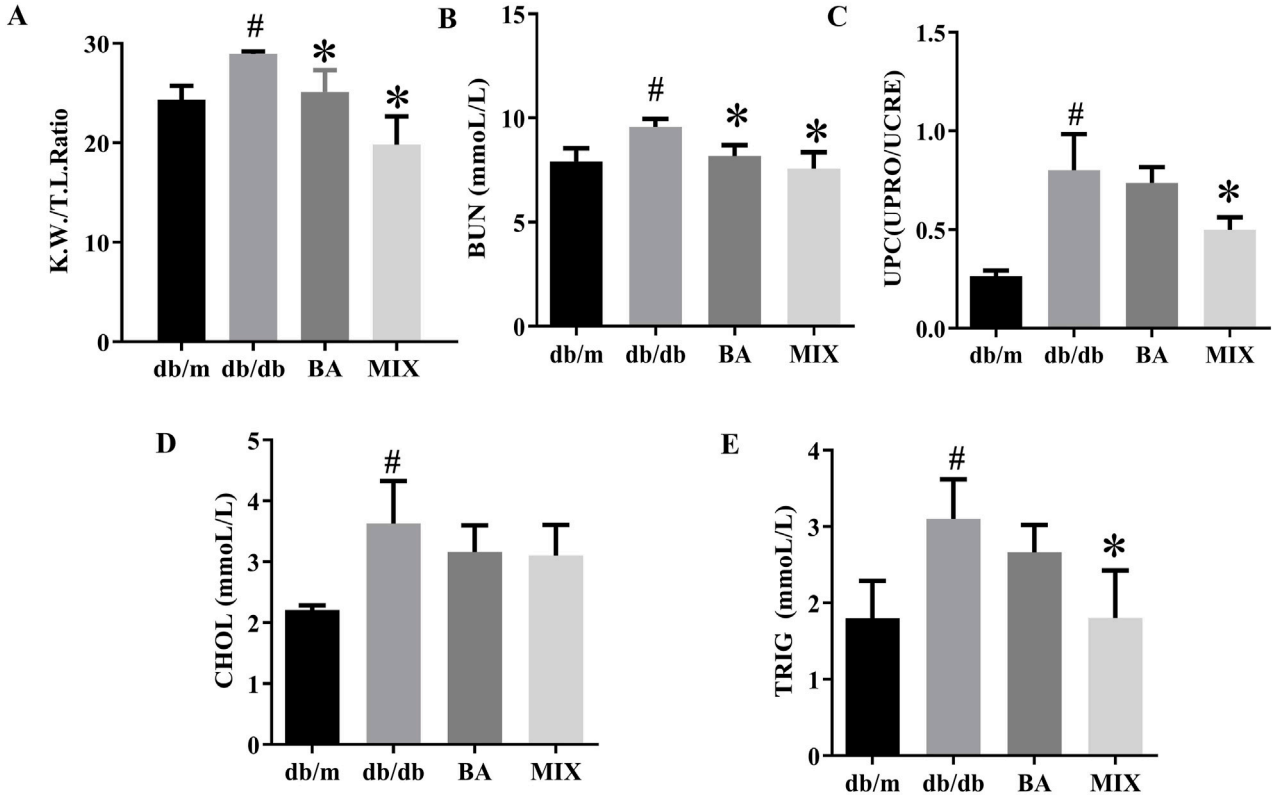


FIGURE 2
Effect on renal function, and serum biochemical indicators, in each group of type 2 diabetic mice **(A)** The ratio of renal weight to tibial length. **(B)** Urea nitrogen. **(C)** Ratio of urinary protein to urinary creatinine. **(D)** Cholesterol level. **(E)** Triglyceride level (n = 6, compared to the db/m group, #$p < 0.05$; compared to the db/db group, *$p < 0.05$). Abbreviations: K.W: renal weight, T. I: tibial length, BUN: blood urea nitrogen, UPRO: urinary protein, UCRE: urinary creatinine, CHOL: cholesterol, TRIG: triglyceride, db/m: normal control group of non-diabetic mice, db/db: model of diabetes, BA: baicalin, MIX: multi-component mixture, UPC: ratio of urinary protein to urinary creatinine.

and MIX treatment groups exhibited reduced glomerular volume, a significant reduction in extracellular matrix deposition by glomerular mesangial cells, decreased thickness of the glomerular mesangial basement membrane, and decreased glycogen deposition. However, these changes were not significant, as shown in Figure 3.

## Effect of baicalin and MIX on fibrosis in db/db mice

The Western blot results and data analysis are presented in Figure 4. These results demonstrate that, compared to the *db/m* group, the model group exhibited a significant increase in the protein expression levels of CTGF, Col-I, and Col-II. In the treatment groups, both BA and MIX demonstrated varying degrees of improvement in CTGF, Col-I, and Col-II levels. Specifically, the BA treatment group showed significantly reduced expression of Col-I protein compared to that of the *db/db* group. Simultaneously, the MIX treatment group also exhibited a reduction in the expression of Col-I protein, although the difference was not statistically significant. The BA and MIX treatment groups showed significantly decreased expression of Col-I protein compared with that of the model group. Regarding CTGF protein expression, the BA group showed significantly reduced levels compared to those in the *db/db* group, and the MIX treatment group also showed a reduction, although this was not statistically significant. These results indicated that BA and MIX could effectively ameliorate renal fibrosis in diabetic mice, with BA demonstrating a slightly more pronounced effect.

RT-PCR revealed that, compared to the *db/m* group, Col-I mRNA expression levels were markedly elevated in the *db/db* group, indicating severe fibrosis in the *db/db* group. In contrast, the BA and MIX treatment groups showed varying degrees of improvement in Col-I gene levels. The BA treatment group exhibited the most pronounced reduction in gene expression. Simultaneously, the MIX treatment group demonstrated a decrease in fibrosis, although not as extensively as that in the BA treatment group.

The findings from the transcriptional to translational levels of fibrotic factors clearly demonstrate a substantial increase in these factors in diabetic organisms. BA emerged as an effective agent for improving diabetes-induced renal fibrosis, thereby slowing the progression of diabetic kidney sclerosis.

## Baicalin and MIX inhibited the TGF-β/Smads signaling pathway in the renal tissues of db/db mice

Our study evaluated the expression of TGF-β, Smad2/3, and p-Smad2/3 by Western blots and immunohistochemistry staining

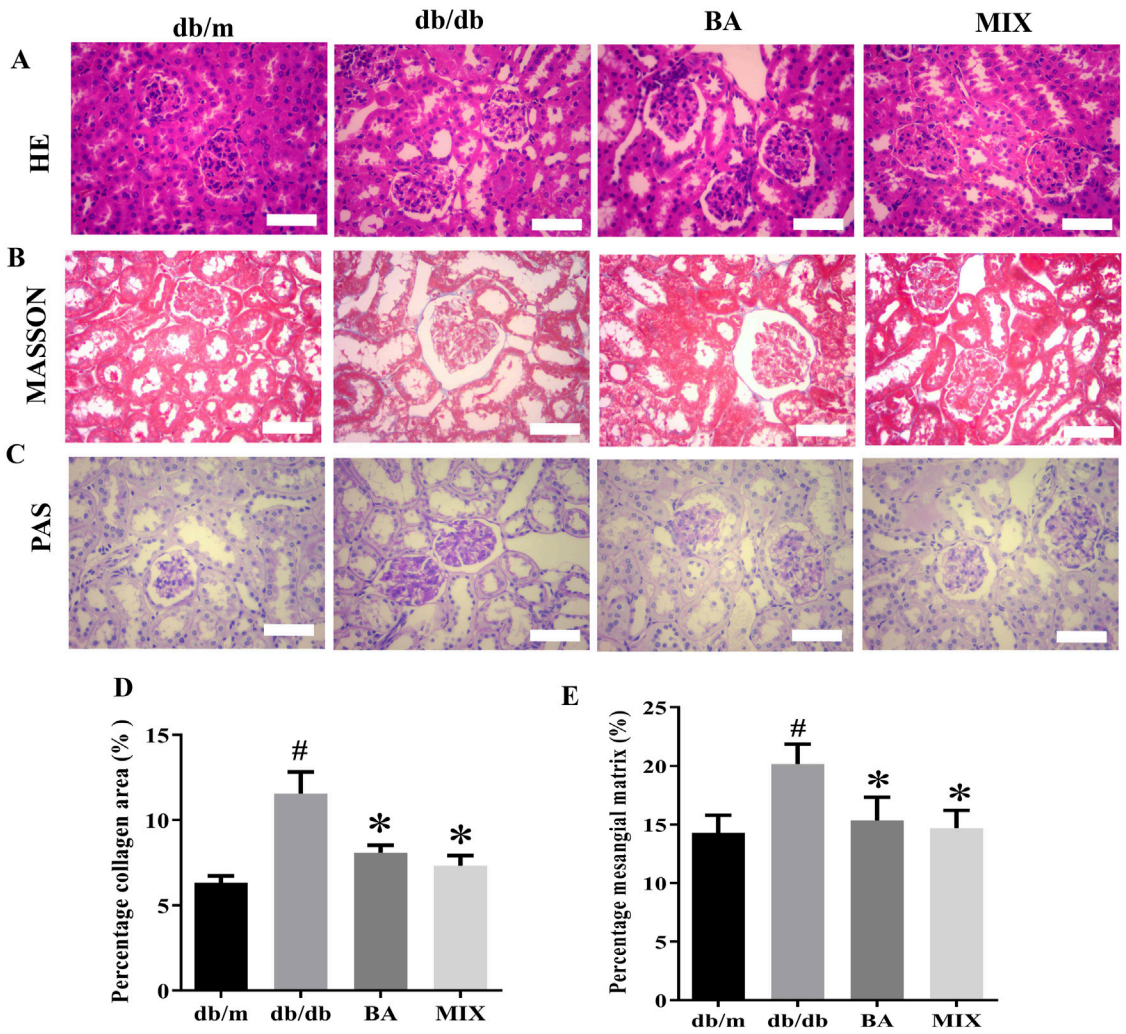


FIGURE 3
Photomicrographs of kidney sections from each group of mice, stained with hematoxylin and eosin **(A)** Masson's trichome **(B)** and periodic acid-Schiff **(C)** observed under a light microscope (×400). **(D)** Changes in the glomerular area are seen with Masson's trichome staining. **(E)** The percentage of the mesangial matrix observed with PAS staining (n = 6, compared to the *db/m* group, #$p < 0.05$; compared to the *db/db* group, *$p < 0.05$). Abbreviations: HE: hematoxylin and eosin, PAS: periodic acid-Schiff, db/m: normal control group of non-diabetic mice, db/db: model of diabetes, BA: baicalin, MIX: multi-component mixture.

(Figure 5). Western blot results and data analysis are presented in Figures 5A–D. These results demonstrate that, compared to the *db/m* group, the *db/db* group exhibited a significant increase in protein expression levels of TGF-β, Smad2/3, and p-Smad2/3. In the administration groups, BA and MIX demonstrated varying degrees of improvement in TGF-β, Smad2/3 and p-Smad2/3 protein levels. Specifically, the MIX treatment group significantly reduced the expression of TGF-β, Smad2/3, and p-Smad2/3 proteins compared to that of the *db/db* group. Concurrently, the BA treatment group also showed a reduction in the expression of TGF-β, Smad2/3, and p-Smad2/3 proteins, although it was not statistically significant. These results indicate that BA and MIX can inhibit the TGF-β/Smads signaling pathway in the renal tissues of *db/db* mice, with MIX demonstrating a slightly more pronounced effect.

TGF-ß and Smad2/3 were weakly expressed in the kidneys of *db/m* mice but showed strong expression in the kidneys of *db/db* mice, with brown staining detected predominantly in glomerular epithelial cells and renal tubules. The levels of TGF-ß and Smad2/3 were significantly reduced in both treatment groups compared to the *db/db* group, although they remained higher than those in the *db/m* group (Figures 5E–G). Meanwhile, no significant differences were observed between the BA and MIX treatment groups, indicating that both BA and MIX reduced the abundance of TGF-β and Smad2/3 proteins in the renal tissues of *db/db* mice.

## Discussion

DKD is a chronic microvascular disease caused by sustained hyperglycemia. The incidence of DKD in patients with diabetes exceeds 40% and is a key factor in the development of end-stage renal disease (Chen et al., 2022). Without timely treatment, it can lead to kidney failure, significantly increasing patient disability and mortality

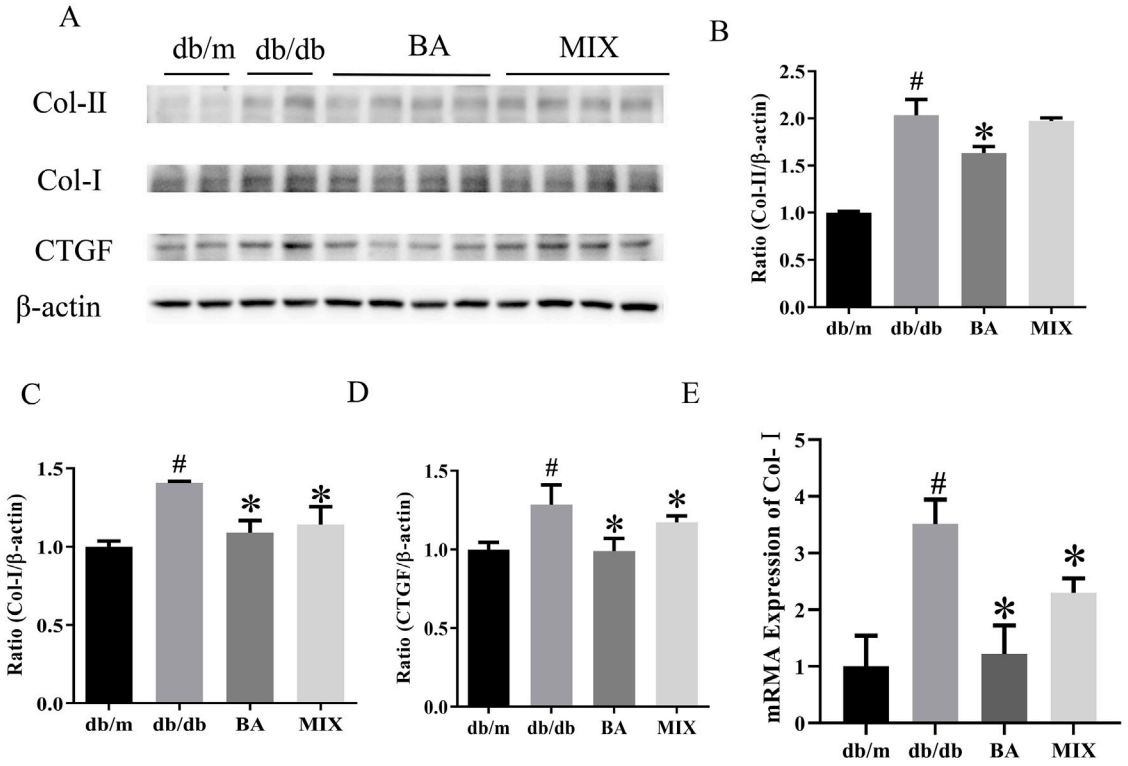


FIGURE 4
Effects on the expression of fibrotic protein in type 2 diabetic mice **(A)** Immunoblotting bands depicting collagen-II, collagen-I, and CTGF protein levels in mice in each group. **(B)** Expression of collagen-II protein in the mice of each group. **(C)** Expression of collagen-I protein in the mice of each group. **(D)** Expression of the CTGF protein in the mice of each group. **(E)** Relative expression of collagen-I mRNA in each group (n = 6, compared to the db/m group, #$p < 0.05$; compared to the db/db group, *$p < 0.05$). Abbreviations: HE: hematoxylin and eosin, PAS: periodic acid-Schiff, db/m: normal control group of non-diabetic mice, db/db: model of diabetes, BA: baicalin, MIX: multi-component mixture, Col- (I) collagen I, Col-II: collagen II, CTGF: connective tissue growth factor.

rates. With the improvement of living standards in recent years, the incidence and mortality of DKD have been on the rise. Currently, the treatment of DKD mainly involves comprehensive therapies, such as glycemic control, lipid regulation, anti-inflammatory drugs, and calcium channel blockers. However, the treatment outcomes are not entirely satisfactory. Therefore, actively exploring new therapeutic drugs for DKD holds significant importance. DKD in traditional Chinese medicine belongs to diabetes syndrome, the main pathogenesis of which is Qi-yin deficiency, stasis, and turbidity-poison stopping. *Scutellaria baicalensis* is known for its high content of active components. These components have been shown to reduce mouse body weight, regulate blood lipid metabolism, and significantly improve insulin sensitivity (Miao et al., 2023).

Renal tissue fibrosis is a pathological, morphological, and structural change that occurs in the early stage of DKD and progressively aggravates, which is an important reason for the continuous deterioration of renal function. In studies of the pathogenesis of DKD, researchers have found alterations in cytokine levels in such patients, which can exacerbate renal function loss. Examples include the activation of signaling pathways such as TGF-β, Smad, and p38MAPK.

To investigate the effects of BA and MIX (WGN, BA, and WGS), we used a spontaneous mouse model of type 2 diabetes (db/db) to assess how these interventions impact diabetic kidney disease (DKD) in mice. These components improve glomerular filtration function, reduce the kidney enlargement index, and improve kidney function. They alleviate interstitial fibrosis, reduce glomerular volume, and inhibit the formation of the glomerular mesangial matrix (Hu et al., 2024). Reduces the synthesis of Col-I at both the gene and protein levels. Decreases the production of CTGF, an early marker of fibrosis. TGF-β1 is a universal cytokine in mammalian cells; it can induce the transcription expression and deposition of extracellular matrix genes and accelerate tissue fibrosis. Col-I and Col-II are essential components of the extracellular matrix (Hu et al., 2018; Chen et al., 2021). Multiple signaling pathways regulate the transformation of renal tubular epithelial cells into fibroblasts, with the TGF-β1/Smads pathway playing an important role (Gewin, 2020). The expression of Smads is regulated by TGF-β1, with Smad2 and Smad3 being most closely related to renal fibrosis. TGF-β1 can induce their polymerization (Smad2/3), which shifts to the nucleus and induces excessive expression of the extracellular matrix to promote tissue fibrosis (Budi et al., 2021; Walton et al., 2017).

This study showed that MIX enhanced lipid profiles and renal function by improving renal tubular dilation, restoring the tight arrangement of renal structures, and reducing glomerulosclerosis, basal membrane thickening, and glycogen deposition. These effects were achieved by reducing the protein and gene expressions of Col-II, Col-I, and CTGF. This indicates that inhibiting the TGF-β1/Smad2/3 pathway may be an important molecular mechanism by which MIX inhibits renal fibrosis in *db/db* mice. The results suggest

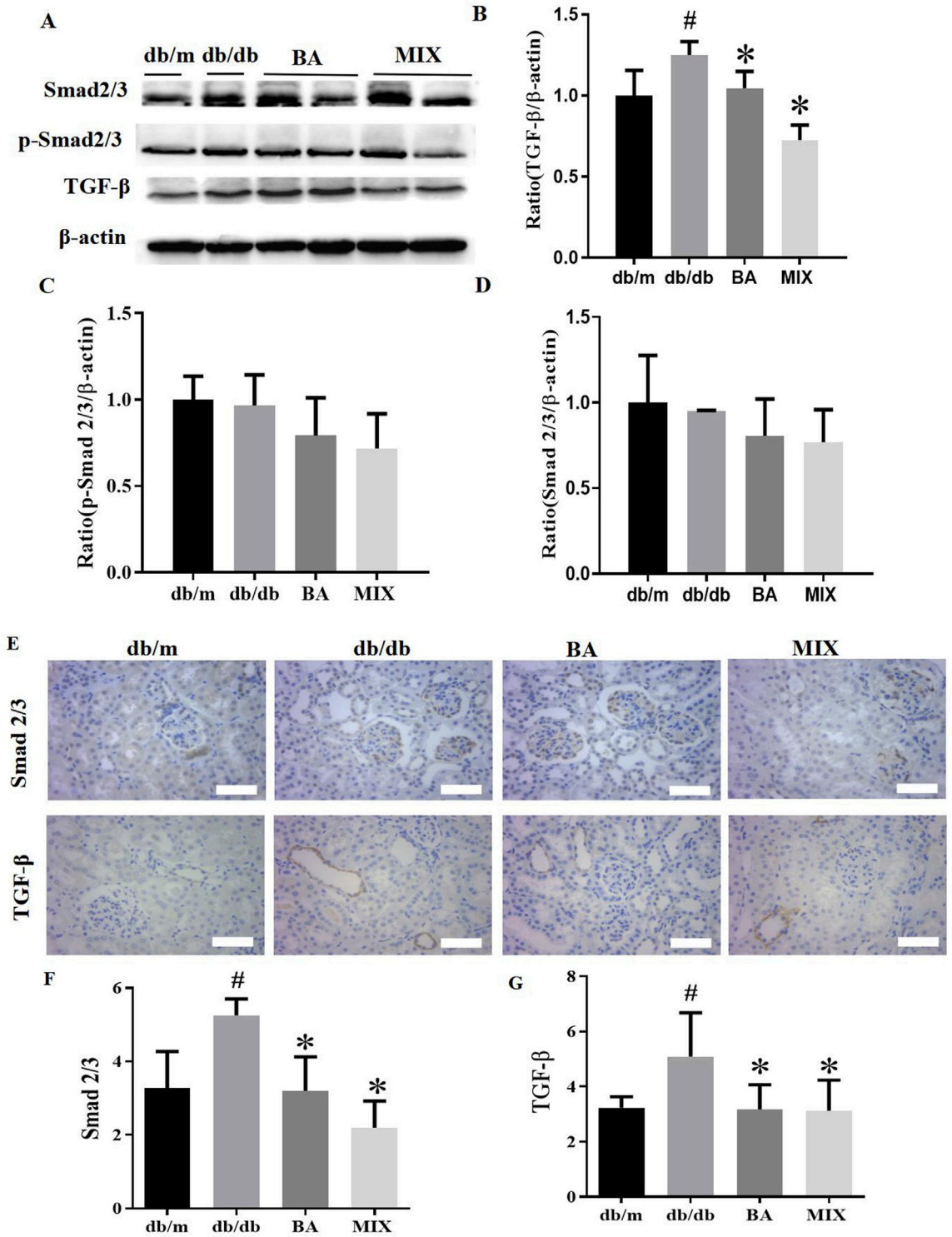


FIGURE 5
Effects indicating that baicalin and *Scutellaria baicalensis* mixture can inhibit the TGF-β/Smads signaling pathway in the renal tissues of HG mice **(A)** Immunoblotting bands depicting TGF-β, Smad2/3, and p- Smad2/3 protein levels in the mice from each group. **(B)** Expression levels of TGF-β protein in mice from each group. **(C)** Expression levels of p-Smad2/3 protein in mice from each group. **(D)** Expression levels of Smad2/3 protein in the mice from each group. **(E)** Photomicrographs of Smad2/3 and TGF-β staining of the kidney sections from each group, observed under a light microscope (×400). **(F)** Quantitative statistical plot of Smad2/3 in kidney sections. **(G)** Quantitative statistical plot of TGF-β in kidney sections (n = 6, compared to the *db/m* group, #$p < 0.05$; compared to the *db/db* group, *$p < 0.05$). Abbreviations: HE: hematoxylin and eosin, PAS: periodic acid-Schiff, db/m: normal control group of non-diabetic mice, db/db: model of diabetes, BA: baicalin, MIX: multi-component mixture, Col- (I) collagen, I Col-II: collagen II, TGF-β: transforming growth factor-β.

that BA and MIX play protective roles against DKD. The therapeutic effect of MIX was superior to that of BA. MIX significantly reduced body weight, improved insulin sensitivity, lowered the renal hypertrophy index, and reduced BUN levels and the urine protein/creatinine ratio. MIX inhibited the TGF-β/Smads signaling pathway, thus alleviating renal fibrosis.

In the study, we focused on investigating the effects of BA and MIX, specifically examining the potential of MIX in alleviating fibrosis associated with DKD. BA is one of the primary active flavonoid compounds in S. *baicalensis* and has demonstrated beneficial effects in reducing fibrosis, inflammation, and oxidative stress in DKD, making it a promising candidate for further development and application. WGN and WGS were a kind of flavonoids, which have many pharmacological effects, such as anti-oxidation, antiinflammatory and anti-fibrosis. WGN treats DKD by in mitigating tubulointerstitial fibrosis and renal tubular cell injury via regulating PI3K/Akt/NF-κB signaling pathway-mediated autophagy and inflammation (Lei et al., 2021), glomerulopathy and podocyte injury by regulating Bcl-2-mediated crosstalk between autophagy and apoptosis (Liu et al., 2022). WGS can inhibit inflammation, oxidative stress regulates renal endothelial injury (Wang YR. et al., 2022). Although the results of the study suggest that WGN and WGS have a certain application in the treatment of DKD. However, the main purpose of this study was to evaluate the effect of MIX combination therapy. And focused on investigating the effects of BA and MIX, specifically examining the potential of MIX in alleviating fibrosis associated with DKD with the aim of advancing the development of MIX.

The value of comparing the individual effects of WGN and WGS with MIX is also recognized (Liu et al., 2022; Wang YR. et al., 2022; Lei et al., 2021), as this would provide insights into potential synergistic effects. Future studies will explore the interactions among BA, WGN, and WGS in more detail. To this end, additional experiments will be conducted to compare WGN and WGS with MIX, in order to better understand each component's contribution and the overall effectiveness of MIX. It remains unclear how MIX regulates downstream genes and proteins in the TGF-β1/Smad2/3 pathway. Additionally, the impact of MIX on fibrosis in DKD mice involves multiple pathways, requiring further investigation.

## Data availability statement

The original contributions presented in the study are included in the article/supplementary material, further inquiries can be directed to the corresponding authors.

## Ethics statement

The animal study was approved by Medical Ethics Committee of Experimental Animal Ethics at Ruian People's Hospital. The study was conducted in accordance with the local legislation and institutional requirements.

## Author contributions

JL: Writing–review and editing, Methodology, Validation. YZ: Formal Analysis, Methodology, Validation, Writing–original draft. GF: Formal Analysis, Visualization, Writing–original draft. SW: Data curation, Methodology, Validation, Writing–original draft. EY: Formal Analysis, Methodology, Validation, Writing–original draft. JG: Writing–review and editing. CZ: Funding acquisition, Writing–review and editing. SJ: Funding acquisition, Writing–original draft, Writing–review and editing.

## Funding

The author(s) declare that financial support was received for the research, authorship, and/or publication of this article. This study was supported by a grant from the Wenzhou Bureau of Science and Technology (grant number: Y2023936), the Ruian Bureau of Science and Technology (MS2022017), and the National Science Foundation of China (82370368; 82073843).

## Conflict of interest

The authors declare that the research was conducted in the absence of any commercial or financial relationships that could be construed as a potential conflict of interest.

## Publisher's note

All claims expressed in this article are solely those of the authors and do not necessarily represent those of their affiliated organizations, or those of the publisher, the editors and the reviewers. Any product that may be evaluated in this article, or claim that may be made by its manufacturer, is not guaranteed or endorsed by the publisher.

## References

Adeshara, K. A., Diwan, A. G., and Tupe, R. S. (2016). Diabetes and complications: cellular signaling pathways, current understanding and targeted therapies. *Curr. Drug Targets* 17, 1309–1328. doi:10.2174/1389450117666151209124007

Aschner, P., Karuranga, S., James, S., Simmons, D., Basit, A., Shaw, J. E., et al. (2021). The International Diabetes Federation's guide for diabetes epidemiological studies. *Diabetes Res. Clin. Pract.* 172, 108630. doi:10.1016/j.diabres.2020.108630

Budi, E. H., Schaub, J. R., Decaris, M., Turner, S., and Derynck, R. (2021). TGF-β as a driver of fibrosis: physiological roles and therapeutic opportunities. *J. Pathol.* 254, 358–373. doi:10.1002/path.5680

Chen, X., Sun, L., Li, D., Lai, X., Wen, S., Chen, R., et al. (2022). Green tea peptides ameliorate diabetic nephropathy by inhibiting the TGF-β/Smad signaling pathway in mice. *Food Funct.* 13, 3258–3270. doi:10.1039/d1fo03615g

Chen, Y., Lin, X., Zheng, Y., Yu, W., Lin, F., and Zhang, J. (2021). *Dendrobium* mixture ameliorates diabetic nephropathy in db/db mice by regulating the TGF-*β*1/Smads signaling pathway. *Evid. Based Complement. Altern. Med.* 2021, 9931983. doi:10.1155/2021/9931983

Du, N., Liu, S., Cui, C., Zhang, M., Jia, J., and Cao, X. (2017). DMP-1 attenuates oxidative stress and inhibits TGF-β activation in rats with diabetic kidney disease. *Ren. Fail* 39, 229–235. doi:10.1080/0886022X.2016.1256319

Gewin, L. S. (2020). TGF-B and diabetic nephropathy: lessons learned over the past 20 years. *Am. J. Med. Sci.* 359, 70–72. doi:10.1016/j.amjms.2019.11.010

Guo, K., Zhang, L., Zhao, F., Lu, J., Pan, P., Yu, H., et al. (2016). Prevalence of chronic kidney disease and associated factors in Chinese individuals with type 2 diabetes: cross-sectional study. *J. Diabetes Complicat.* 30, 803–810. doi:10.1016/j.jdiacomp.2016.03.020

Hu, H., Li, W., Hao, Y., Peng, Z., Zou, Z., and Liang, W. (2024). Baicalin ameliorates renal fibrosis by upregulating CPT1α-mediated fatty acid oxidation in diabetic kidney disease. *Phytomedicine* 122, 155162. doi:10.1016/j.phymed.2023.155162

Hu, H. H., Chen, D. Q., Wang, Y. N., Feng, Y. L., Cao, G., Vaziri, N. D., et al. (2018). New insights into TGF-β/Smad signaling in tissue fibrosis. *Chem. Biol. Interact.* 292, 76–83. doi:10.1016/j.cbi.2018.07.008

Hu, L., Ding, M., and He, W. (2021). Emerging therapeutic strategies for attenuating tubular EMT and kidney fibrosis by targeting wnt/β-catenin signaling. *Front. Pharmacol.* 12:830340. doi:10.3389/fphar.2021.830340

Huang, W., Huang, G. P., Zhang, L. X., Yu, E., Yang, W. K., Ye, M., et al. (2024). Lignan-rich extract from Cinnamomum camphora leaf attenuates metabolic syndrome by modulating glycolipid metabolism and gut microbiota in T2DM mice. *Phytomedicine* 135, 156118. doi:10.1016/j.phymed.2024.156118

Jin, X., Zhu, L., Lu, S., Li, C., Bai, M., Xu, E., et al. (2023). Baicalin ameliorates CUMS-induced depression-like behaviors through activating AMPK/PGC-1α pathway and enhancing NIX-mediated mitophagy in mice. *Eur. J. Pharmacol.* 938, 175435. doi:10.1016/j.ejphar.2022.175435

Lai, J., and Li, C. X. (2024). Review on the pharmacological effects and pharmacokinetics of scutellarein. *Arch. Pharm. Weinh.* 357 (9), e2400053. doi:10.1002/ardp.202400053

Lavoz, C., Rodrigues-Diez, R. R., Plaza, A., Carpio, D., Egido, J., Ruiz-Ortega, M., et al. (2020). VEGFR2 blockade improves renal damage in an experimental model of type 2 diabetic nephropathy. *J. Clin. Med.* 9, 302. doi:10.3390/jcm9020302

Lei, L., Zhao, J., Liu, X. Q., Chen, J., Qi, X. M., Xia, L. L., et al. (2021). Wogonin alleviates kidney tubular epithelial injury in diabetic nephropathy by Inhibiting PI3K/Akt/NF-κB signaling pathways. *Drug Des. Devel Ther.* 15, 3131–3150. doi:10.2147/DDDT.S310882

Li, L., Zhang, X., Li, Z., Zhang, R., Guo, R., Yin, Q., et al. (2017). Renal pathological implications in type 2 diabetes mellitus patients with renal involvement. *J. Diabetes Complicat.* 31, 114–121. doi:10.1016/j.jdiacomp.2016.10.024

Liao, H., Ye, J., Gao, L., and Liu, Y. (2021). The main bioactive compounds of *Scutellaria baicalensis* Georgi. for alleviation of inflammatory cytokines: a comprehensive review. for alleviation of inflammatory cytokines: a comprehensive review. *Biomed. Pharmacother.* 133, 110917. doi:10.1016/j.biopha.2020.110917

Liu, X. Q., Jiang, L., Li, Y. Y., Huang, Y. B., Hu, X. R., Zhu, W., et al. (2022). Wogonin protects glomerular podocytes by targeting Bcl-2-mediated autophagy and apoptosis in diabetic kidney disease. *Acta Pharmacol. Sin.* 43, 96–110. doi:10.1038/s41401-021-00721-5

Ma, L., Wu, F., Shao, Q., Chen, G., Xu, L., and Lu, F. (2021). Baicalin alleviates oxidative stress and inflammation in diabetic nephropathy via Nrf2 and MAPK signaling pathway. *Drug Des. Devel Ther.* 15, 3207–3221. doi:10.2147/DDDT.S319260

Meshkani, R., and Vakili, S. (2016). Tissue resident macrophages: key players in the pathogenesisof type 2 diabetes and its complications. *Clin. Chim. Acta* 462, 77–89. doi:10.1016/j.cca.2016.08.015

Miao, L., Liu, C., Cheong, M. S., Zhong, R., Tan, Y., Rengasamy, K. R. R., et al. (2023). Exploration of natural flavones' bioactivity and bioavailability in chronic inflammation induced-type-2 diabetes mellitus. *Crit. Rev. Food Sci. Nutr.* 63, 11640–11667. doi:10.1080/10408398.2022.2095349

Ou, Y., Zhang, W., Chen, S., and Deng, H. (2021). Baicalin improves podocyte injury in rats with diabetic nephropathy by inhibiting PI3K/Akt/mTOR signaling pathway. *Open Med. (Wars)* 16, 1286–1298. doi:10.1515/med-2021-0335

Qiu, D., Song, S., Chen, N., Bian, Y. W., Zhang, W., Wei, Z., et al. (2023). NQO1 alleviates renal fibrosis by inhibiting the TLR4/NF-κB and TGF-β/Smad signaling pathways in diabetic nephropathy. *Cell Signal* 108, 110712. doi:10.1016/j.cellsig.2023.110712

Shang, L. Y., Zhou, M. H., Cao, S. Y., Zhang, M., Wang, P. J., Zhang, S., et al. (2023). Effect of polyethylene glycol 400 on the pharmacokinetics and tissue distribution of baicalin by intravenous injection based on the enzyme activity of UGT1A8/1A9. *Eur. J. Pharm. Sci.* 180, 106328. doi:10.1016/j.ejps.2022.106328

Suo, J. Y. (2022). *Screening of anti-inflammatory active ingredients combined with myd88 in qian-jin-wen-Wu decoction and its synergistic effect*. Master's Thesis. Yanbian University.

Tang, F., Hao, Y., Zhang, X., and Qin, J. (2017). Effect of echinacoside on kidney fibrosis by inhibition of TGF-β1/Smads signaling pathway in the db/db mice model of diabetic nephropathy. *Drug Des. Devel Ther.* 11, 2813–2826. doi:10.2147/DDDT.S143805

Walton, K. L., Johnson, K. E., and Harrison, C. A. (2017). Targeting TGF-β mediated SMAD signaling for the prevention of fibrosis. *Front. Pharmacol.* 8, 461. doi:10.3389/fphar.2017.00461

Wang, H., Jiang, Q., and Zhang, L. (2022a). Baicalin protects against renal interstitial fibrosis in mice by inhibiting the TGF-β/Smad signalling pathway. *Pharm. Biol.* 60, 1407–1416. doi:10.1080/13880209.2022.2097700

Wang, Y. R., Liu, Z., Liu, G. Y., and Wang, H. J. (2022b). Research progress of active ingredients of Scutellaria baicalensis in the treatment of type 2 diabetes and its complications. *Biomed. Pharmacother.* 148, 112690. doi:10.1016/j.biopha.2022.112690

Wu, H., Long, X., Yuan, F., Chen, L., Pan, S., Liu, Y., et al. (2014). Combined use of phospholipid complexes and self-emulsifying microemulsions for improving the oral absorption of a BCS class IV compound, baicalin. *Acta Pharm. Sin. B* 4, 217–226. doi:10.1016/j.apsb.2014.03.002

Yamashita, N., and Kramann, R. (2024). Mechanisms of kidney fibrosis and routes towards therapy. *Trends Endocrinol. Metab.* 35 (1), 31–48. doi:10.1016/j.tem.2023.09.001

Yang, M., Kan, L., Wu, L., Zhu, Y., and Wang, Q. (2019). Effect of baicalin on renal function in patients with diabetic nephropathy and its therapeutic mechanism. *Exp. Ther. Med.* 3, 2071–2076. doi:10.3892/etm.2019.7181

Zhang, S., Xu, L., Liang, R., Yang, C., and Wang, P. (2020). Baicalin suppresses renal fibrosis through microRNA-124/TLR4/NF-κB axis in streptozotocin-induced diabetic nephropathy mice and high glucose-treated human proximal tubule epithelial cells. *J. Physiol. Biochem.* 3, 407–416. doi:10.1007/s13105-020-00747-z

Zhao, T., Tang, H., Xie, L., Zheng, Y., Ma, Z., Sun, Q., et al. (2019). *Scutellaria baicalensis* Georgi. (Lamiaceae): a review of its traditional uses, botany, phytochemistry, pharmacology and toxicology. *J. Pharm. Pharmacol.* 71, 1353–1369. doi:10.1111/jphp.13129

frontiers | Frontiers in Pharmacology

TYPE Original Research
PUBLISHED 06 December 2024
DOI 10.3389/fphar.2024.1474768

Check for updates

OPEN ACCESS

EDITED BY
Michael Heinrich,
University College London, United Kingdom

REVIEWED BY
Xie-an Yu,
Shenzhen Institute For Drug Control, China
Mahmood Oppong,
University of Ghana, Ghana

*CORRESPONDENCE
Yanfei Huang,
huangyf@bjmu.edu.cn

†These authors have contributed equally to this work

RECEIVED 02 August 2024
ACCEPTED 11 November 2024
PUBLISHED 06 December 2024

CITATION
Tian Y, Liu Y, Kong Y, Li L, Yang Z, Li W, Li Q, Ren C, Sun W and Huang Y (2024) Discovery of quality markers of *Meconopsis quintuplinervia* based on an absorption-based metabolite approach and rapid quantification using polarity-switching UPLC-QQQ-MS/MS. *Front. Pharmacol.* 15:1474768. doi: 10.3389/fphar.2024.1474768

COPYRIGHT
© 2024 Tian, Liu, Kong, Li, Yang, Li, Li, Ren, Sun and Huang. This is an open-access article distributed under the terms of the Creative Commons Attribution License (CC BY). The use, distribution or reproduction in other forums is permitted, provided the original author(s) and the copyright owner(s) are credited and that the original publication in this journal is cited, in accordance with accepted academic practice. No use, distribution or reproduction is permitted which does not comply with these terms.

# Discovery of quality markers of *Meconopsis quintuplinervia* based on an absorption-based metabolite approach and rapid quantification using polarity-switching UPLC-QQQ-MS/MS

Yifan Tian[1†], Yuan Liu[1†], Yuanlin Kong[1], Limin Li[2], Zhengming Yang[1], Wenbin Li[1], Qiang Li[3], Chaoqin Ren[4], Wenxia Sun[5] and Yanfei Huang[1]*

[1]Qinghai-Tibetan Plateau Ethnic Medicinal Resources Protection and Utilization Key Laboratory of National Ethnic Affairs Commission of the People's Republic of China, Southwest Minzu University, Chengdu, China, [2]Institute of Chinese Materia Medica Pharmacology and Toxicology, Sichuan Academy of Chinese Medicine Sciences, Chengdu, China, [3]Shimadzu China Co. LTD., Chengdu, China, [4]College of Resources and Environment, Aba Teachers College, Wenchuan, China, [5]Engineering Research Center for Pharmaceuticals and Equipments of Sichuan Province, School of pharmacy, Sichuan Industrial Institute of Antibiotics, Chengdu University, Chengdu, China

**Background:** *Meconopsis quintuplinervia* Regel (MQ) is a traditional Chinese medicine (TCM) used for clearing liver and lung heat in Tibetan medicine for over a thousand years. However, the lack of quality markers that correlate with pharmacological actions and absorption *in vivo* limits the safety and efficacy in its clinical application and on the drug market. Furthermore, a universal and rapid method for simultaneously determining quality markers in the MQ crude drug is still lacking.

**Purpose:** An absorption-based metabolite approach was used to discover and identify the quality markers of MQ. An efficient method based on polarity-switching ultra-performance liquid chromatography triple quadrupole mass spectrometry (UPLC-QQQ-MS/MS) was then established to determine the quality markers.

**Methods:** The absorbed compounds and metabolites were first characterized using UPLC plus Q-Exactive Orbitrap tandem mass spectrometry (UPLC-Q-Exactive Orbitrap-MS) after giving oral MQ extract to rats. Subsequently, the absorbed compounds and precursors of metabolites correlating with the hepatocyte protection activity were screened as quality markers. Finally, a polarity-switching UPLC-QQQ-MS/MS method was developed for the quantitative analysis of the MQ crude drug, enabling the detection of quality markers in both negative and positive ion modes in a single run. The $MS^2$ characteristics of target compounds were investigated to select appropriate product ions.

**Results:** A total of 13 absorbed compounds and 30 metabolites were characterized. Among these, nine compounds, including five absorbed

compounds and four precursors of metabolites intimately correlated with hepatocyte protection activity and absorption *in vivo*, were considered the quality markers of MQ in the current study. The quantification of quality markers was conducted using an Acquity UPLC HSS T3 (2.1 × 100 mm, 1.8 μm) column, the mobile phase consisting of acetonitrile and 0.1% formic acid solution (containing 10 mmol/L ammonium acetate). The validated UPLC-QQQ-MS/MS method was successfully applied to quantify the quality markers in the MQ crude drug.

**Conclusion:** We defined the quality markers and established a universal and rapid method for simultaneously determining the quality markers of MQ, which will be helpful for further investigation of the quality evaluation of MQ in clinical application and the drug market.

KEYWORDS

**traditional Chinese medicine, *Meconopsis quintuplinervia* Regel, quality markers, metabolism, LC-MS, content determination**

## 1 Introduction

*Meconopsis quintuplinervia* Regel (MQ) is a valuable botanical drug belonging to the Papaveraceae family, distributed only in the Qinghai–Tibetan plateau (Luo et al., 1984). It has been used as a traditional Chinese medicine (TCM) named *Herba Meconopsis* with a long clinical history dating back to the eighth century in the Tibetan book *Yue Wang Yao Zhen* and recorded in the Tibetan masterpieces *The Four Medical Tantras* and the *Jing Zhu Materia Medica*. It has traditionally been used for clearing liver and lung heat (Guo et al., 2016). Given its significant and reliable biological activities, MQ is widely used in more than 100 prescriptions of Tibetan medicine and 31 marketed prescription drugs, such as *Ershiwuwei Luronghao Wan*, *Shiqiwei Hanshuishi Wan*, and *Shibawei Niuhuang San* (Luo et al., 1984; Wang and Ma, 2009; Guo et al., 2016). Previous studies have shown that the pharmacological effect of MQ may be attributed to its chemical compounds such as flavonoids (Shang et al., 2002; Shang et al., 2006b), alkaloids (Shang et al., 2003; Wu et al., 2007), and phenolics (Shang et al., 2006a). The total flavonoid and phenolic fraction extracted from MQ exhibit an obvious hepatoprotective effect on experimental liver damage and hepatic fibrosis, which significantly decreases alanine aminotransferase (ALT), aspartate aminotransferase (AST), and malondialdehyde (MDA) levels, while increasing superoxide dismutase (SOD), catalase (CAT), and reduced glutathione (GSH) levels in carbon tetrachloride ($CCl_4$)-induced liver damage mice. Additionally, these fractions reduce the levels of hydroxyproline and collagen in liver tissue, as well as liver fibrosis indicators such as hyaluronic acid, type III procollagen, type IV collagen, and laminin in rats with liver fibrosis (He et al., 2012; Wang et al., 2013a; Wang et al., 2013b). Total alkaloids extracted from MQ exhibit a strong anti-inflammatory effect on LPS-induced acute inflammation in mouse models. This is related to MQ's ability to inhibit the expression of the pro-inflammatory cytokines tumor necrosis factor-α (TNF-α) and Interleukin-6 (IL-6) and the production of nitric oxide (NO) and to reduce inducible nitric oxide synthase (iNOS) activity (Yu et al., 2021). Kong et al. (2022) employed ultra-performance liquid chromatography plus Q-Exactive Orbitrap tandem mass spectrometry (UPLC-Q-Exactive Orbitrap/MS) and network analysis to analyze the active compounds acting against liver fibrosis. They found that MQ presumably exerted an anti-liver fibrosis effect through luteolin, isorhamnetin, quercetin, apigenin, kaempferide, amurine, 2-methylflavinantine, and allocryptopine on RAC-alpha serine/threonine-protein kinase (AKT1), proto-oncogene tyrosine-protein kinase Src (SRC), transcription factor Jun (JUN), epidermal growth factor receptor (EGFR), and other core targets, and regulated the phosphatidylinositol 3-kinases/protein kinase B (PI3K/AKT), forkhead box protein O (FoxO) and other signaling pathways (Kong et al., 2022).

Traditionally, MQ has primarily been obtained from wild sources, and several species of *Meconopsis* with blue flower were used as *Herba Meconopsis* in clinics and the medical industry. It is difficult to guarantee the clinical efficacy and safety of MQ. Furthermore, the "Pharmaceutical Standards of the Ministry of Health of the People's Republic of China" for *Herba Meconopsis* uses only morphological and microscopic identification for the quality control of MQ (Chinese Pharmacopoeia Commission, 1995). However, these quality control methods do not reflect MQ's clinical efficacy or pharmacological activity (Li Y. Z. et al., 2019; Zhang et al., 2019). With the discovery of new compounds and deeper research into the pharmacological activity of MQ, its quality control in clinical application and the market has become more important. It is thus necessary to discover scientific and reasonable quality markers for the quality control of MQ. "Quality markers" are several specific chemical compounds of botanical drugs and their products that are closely related to therapeutic effects and absorption *in vivo* and could be used for qualitative and quantitative analysis (Liu et al., 2016; Liu et al., 2018; Li Y. Z. et al., 2019). In recent years, some studies of quality markers have focused on characterizing the chemical compound–bioactivity association (Wei et al., 2021; Li Y. L. et al., 2022; Li et al., 2024) and prototype-based pharmacokinetic *in vivo* absorption (Li et al., 2018; Duan et al., 2020). These have been the general approach for the analysis of quality markers. However, some studies have shown that TCM metabolism is a crucial link between pharmacological activity *in vivo* and phytochemistry *in vitro*. In brief, the absorbed compounds and metabolites of TCM *in vivo* are the ultimate material basis for the expression of the efficacy of TCM (Xu et al., 2022). Some of the precursors of the metabolites, which are the effective forms of TCM, can be used as quality markers for its quality control (Zhang et al., 2022). This strategy based on metabolites, including absorption compounds and metabolites *in vivo*, we term "absorption-based metabolite

strategy". Unfortunately, few studies have focused on absorption-based metabolite strategy for quality evaluation research into TCM; it may be a powerful approach, and this is the first study of the quality markers of MQ.

Moreover, many methods have been developed to quantify one or several compounds as quality indicators in the MQ raw material. For example, Yue et al. (2010) determined four major flavonoids in hydrolyzed MQ samples by high-performance liquid chromatography (HPLC) coupled with diode array detection. Shi et al. (2011) established an HPLC method for determining one alkaloid in MQ raw material by HPLC. However, for the complex chemical compounds in MQ, the established quantification methods developed by HPLC were limited in their application for the quality control of multiple compounds in varying polarity with long running times and low sensitivity (Jiao et al., 2019). It is thus necessary to establish a universal and rapid method for the simultaneous determination of quality markers in MQ crude drug.

Ultra-performance liquid chromatography triple quadrupole mass spectrometry (UPLC-QQQ-MS/MS) is a widely utilized technology with high separation capability and sensitivity for quantification quality markers in TCM (Li X. Y. et al., 2022). The multiple reaction monitoring (MRM) mode of UPLC-QQQ-MS/MS is a powerful technology for screening specified molecular ion-to-product transitions to quantify quality markers in a specified condition which can effectively avoid interference peak (Jiao et al., 2019; Sun et al., 2023). More importantly, the polarity-switching function in UPLC-QQQ-MS/MS can simultaneously detect different polarity compounds in negative and positive ion modes in a single run (Shen et al., 2022). Therefore, UPLC-QQQ-MS/MS enables the simultaneous determination of different polarity quality markers of MQ simultaneously, sensitively, and rapidly.

In the current study, we explored MQ to discover, identify, and quantify the quality markers by an absorption-based metabolite strategy. First, we explored the metabolism of MQ extract in rats using UPLC-Q-Exactive Orbitrap/MS technology and elucidated the absorbed compounds and metabolites and the metabolic pathways of MQ compounds. Second, we screened the absorbed compounds and the precursors of metabolites that correlated with hepatocyte protection activity, and we validated by reported experimentation these absorbed compounds and the precursors of metabolites *in vivo* that were used as quality markers. Finally, an efficient method based on polarity-switching UPLC-QQQ-MS/MS technology for determining quality markers in MQ was established to determine the quality marker in MQ crude drug. To our knowledge, this is the first study to discover the quality markers of MQ based on the metabolism of absorbed compounds *in vivo*. Our research will be helpful for screening the quality markers of MQ and providing a useful perspective for discovering the quality markers of other TCMs.

# 2 Materials and methods

## 2.1 Chemical reagents

Quercetin (Lot: MUST-22042012), luteolin (Lot: MUST-22072315), apigenin (Lot: MUST-22111214), taxifolin (Lot: MUST-22101411), isorhamnetin (Lot: MUST-22082703), caffeic acid (Lot: MUST-22062118), chlorogenic acid (Lot: MUST-22111711), allocryptopine (Lot: MUST-22031114), and protopine (Lot: MUST-22062118) with purity ≥98% were purchased from Chengdu MUST Bio-technology Co., Ltd (Chengdu, China). Their structures are shown in Figure 1. HPLC-grade acetonitrile and formic acid were sourced both from Thermo Fisher (Waltham, MA, United States). Ultrapure water was purified at 18.2 MΩ using PERSEE GWB-1E ultrapure water system (Beijing, China). Other reagents were of analytical grade and were purchased locally.

## 2.2 Plant materials

Ten batches of MQ crude drug samples were collected or purchased from Qinghai, Gansu, and Sichuan, China. They were identified by Professor Yuan Liu and Dr. Yanfei Huang as *M. quintuplinervia* Regel (Supplementary Table S1). The voucher specimens of these samples were deposited at the Tibetan, Qiang, and Yi medicinal resources herbarium, Qinghai–Tibetan Plateau Ethnic Medicinal Resources Protection and Utilization Key Laboratory of the National Ethnic Affairs Commission of the People's Republic of China, Southwest Minzu University.

MQ extract was prepared as per our previous study (Kong et al., 2022). MQ powders (1000 g) were mixed with 70% ethyl alcohol (*v*/*v*) (8 L) and extracted by heating reflux extraction for 1.5 h. This step was repeated three times. The extract was then filtered and dried in vacuum at 50°C and treated with D101 macroporous resins. Afterward, 30%, 50%, and 70% ethyl alcohol eluent was collected and mixed, and the extract was concentrated and freeze-dried into a powder.

## 2.3 Animals and metabolic study

Twelve male Sprague–Dawley rats (weighing 180–220 g) were obtained from the Experimental Animal Center of the Sichuan Academy of Chinese Medicine Sciences (animal production license number: SYXK (2018)-100, Chengdu, China). The rats were kept in an environmentally controlled animal room for 7 days, with water and food *ad libitum* twice daily. The rats were randomly divided into two groups—MQ and blank, with six rats per group—and were housed in metabolic cages for 3 days to acclimatize to the facilities prior to the experiments. MQ extract was suspended in 0.5% CMC-Na solution and orally administered to the MQ group at a daily dose of 50 mg/kg. The MQ extract administration lasted for 5 days, once a day at 9:00 a.m. The blank group was orally administered 0.5% CMC-Na solution at the same volume time. These animal experiments were conducted under the guidance of the *Care and Use of Laboratory Animals* published by the US National Institute of Health and were approved by the Biomedical Ethical Committee of Southwest Minzu University (approval no. SWU-202401160).

## 2.4 Biological sample collection and preparation

### 2.4.1 Urine and feces samples

Urine samples were collected after administration of MQ extract in the drug and blank groups at 0–24 h. The collection tubes for urine samples were pre-filled with a small volume of absolute ethanol as a

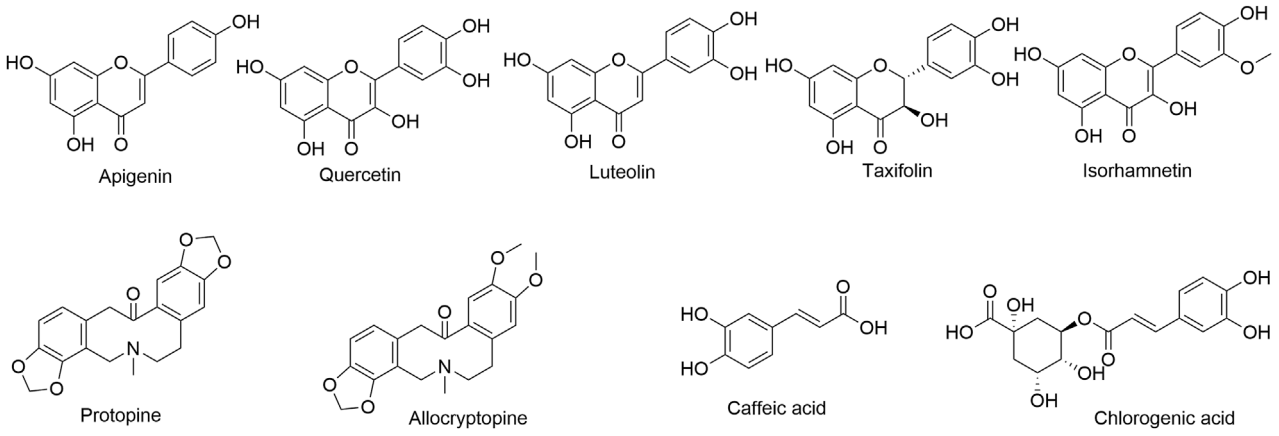


FIGURE 1
Chemical structures of the nine investigated compounds in MQ.

preservative. After collection in 1 day, the samples were merged and evaporated to dryness under reduced pressure at 50°C using an electro thermostatic blast oven (DS-30H, Shanghai Dengsheng Instrument Manufacturing Co., Ltd., Shanghai, China). The dried samples of the different groups were then extracted with four-fold methanol (*v*/*w*) in an ultrasonic cleaner for 30 min to precipitate the endogenous substances. These samples were centrifuged at 5,000 rpm, and the supernatant was dried in vacuum at 40°C. Subsequently, each 1.0 g residue of the MQ and blank groups was reconstituted in 5.0 mL methanol and filtered through a 0.22-μm nylon filter before UPLC-Q-Exactive Orbitrap/MS analysis.

Feces samples from the drug group and the blank group were collected twice daily from 8:00 am and 8:00 pm and dried immediately at 50°C using an electro-thermostatic blast oven. Thence, pulverized feces samples (1.0 g) of each group were mixed with 5.0 mL methanol and extracted using an ultrasonic bath for 30 min three times. The extracted samples were centrifuged at 5,000 rpm for 15 min, and the supernatant of the two groups was collected and dried in a rotary evaporator at 40°C. Subsequently, 100 mg of the resulting residue for each group was dissolved in 3 mL methanol and filtered through a 0.22-μm nylon filter before UPLC-Q-Exactive Orbitrap/MS analysis.

### 2.4.2 Plasma samples

On day 5, after 0.5, 1.0, and 1.5 h of the last administration of MQ extract, blood samples of the two groups were collected into heparinized tubes through heart puncture while the rats were anesthetized by pentobarbital sodium (i.p. 70 mg/kg body weight). Two rats were sacrificed at one time point, and blood samples collected at the same time point from each of the two groups were combined into one sample. These blood samples were centrifuged at 5,000 rpm and 4°C for 10 min to obtain plasma. Next, 6 mL of the two groups of plasma samples (mixed from the three time points, 2 mL per time point) was supplemented with 24 mL methanol and ultrasonically extracted for 30 min to precipitate the protein. The extraction mixture of the drug and blank groups was then centrifuged at 5,000 rpm for 15 min. After that, the supernatant was condensed in a vacuum at 40°C, and the residue was dissolved in 300 μL methanol. Finally, the prepared samples were centrifuged at 15,000 rpm using a Sorvall ST 16R centrifuge (Thermo Fisher Scientific Inc., United States) for 10 min before UPLC-Q-Exactive Orbitrap/MS analysis.

### 2.4.3 Organ samples

After collecting blood samples from the two groups, the main organs, including the brain, heart, lung, liver, kidney, intestine, and spleen, were rapidly removed from the rats, flushed with pre-cooled normal saline, and frozen at −80°C before further processing. Each of the organs was homogenized in fourfold (volume/wet weight) pre-cooled normal saline. Eightfold methanol was then added to 6 mL homogenate, and extraction was performed in an ultrasonic bath for 30 min. The extraction mixtures of the two groups were centrifuged at 5,000 rpm for 15 min. Next, the supernatant was condensed in a vacuum at 40°C, and the residue was dissolved in 1 mL methanol and filtered through a 0.22-μm nylon filter before UPLC-Q-Exactive Orbitrap/MS analysis.

## 2.5 MQ sample preparation and standard solution

The primary stock solutions of 1,000 μg/mL quercetin, luteolin, apigenin, taxifolin, isorhamnetin, caffeic acid, chlorogenic acid, allocryptopine, and protopine were dissolved in 70% methanol. A series of working standard solutions were prepared by diluting the primary stock solution with 70% methanol. All solutions were stored at 4°C before analysis.

The dried MQ crude drugs were finely powdered in a grinder. One gram of the powder was accurately weighed and then extracted in 70% methanol (75 mL) with the help of heating reflux in 30 min. Afterward, the supernatants were filtered through a 0.22-μm membrane filter before analysis.

## 2.6 UPLC-Q-Exactive Orbitrap/MS analysis conditions

The UPLC-Q-Exactive Orbitrap/MS analyses were performed on a Thermo Scientific Vanquish Flex UPLC coupled with a

Q-Exactive Orbitrap Mass analyzer (Thermo Fisher Scientific Inc., United States). The LC-HRMS data were processed by Xcalibur. Chromatography separation was performed on an ACQUITY HSS T3 column (100 × 2.1 mm, 1.8 μm) (Waters, United States) protected with an ACQUITY HSS T3 VanGuard pre-column (2.1 × 5 mm, 1.8 μm) (Waters, United States) at 30°C. The mobile phase consisted of 0.1% formic acid solution (A) and acetonitrile (B), and the gradient elution program was as follows: 5%–10% B at 0–10 min; 10%–20% B at 10–35 min; 20%–27% B at 35–40 min; 27%–33% B at 40–45 min; 33%–55% B at 45–50 min; 55%–90% B at 50–55 min. The flow rate was 0.2 mL/min, and the injection volume was 2 μL.

High-resolution mass spectra analysis conditions were as follows: the data were collected in electrospray ionization (ESI) mode with mass range of *m/z* 100–1000 Da of $MS^1$ and *m/z* 50–1000 Da of $MS^2$ in both positive and negative detection modes, with a mass resolution of 75,000. The capillary temperature was 320°C, interface voltage was 3.0 kV (−) and 3.5 kV (+), auxiliary gas heater temperature was 350°C, auxiliary gas flow rate was 3 L/min, and sheath gas flow rate was 12 L/min.

## 2.7 Metabolite characterization

Data analysis was conducted using Xcalibur software. The MQ metabolite extract in the rats was screened as per Li et al. (2017). The structural elucidation strategy of metabolites was conducted in accordance with Li et al. (2020), Zhang et al. (2022), and Su et al. (2023). First, the absorbed compounds were identified by comparison with the previously reported UPLC-Q-Exactive Orbitrap/MS analysis results of MQ (Kong et al., 2022). Second, the skeleton structure of the metabolites was identified by comparing the $MS^1$ and $MS^2$ data with references or elucidating the chemical structures from online databases, such as SciFinder, PubChem, and ChemSpider. Finally, the metabolic reaction type was confirmed by characteristic mass differences, such as 14.01 Da ($CH_2$), 2.01 Da ($H_2$), 176.03 Da ($C_6H_8O_6$), and 79.95 Da ($SO_3$), respectively denoting methylation, hydrogenation, glucuronidation, and sulfation metabolic reactions.

The absorbed compounds and metabolites were characterized through the analytical methods described above. Subsequently, the precursors of the MQ metabolites were obtained from the proposed metabolic pathways. Then, the quality markers were screened from the absorbed compounds and the precursors of metabolites were correlated with the hepatocyte protection activity, which was validated by reported experimental validation.

## 2.8 UPLC-QQQ-MS/MS analysis conditions

The UPLC-QQQ-MS/MS assay was performed on an LCMS 8050 triple quadrupole mass spectrometer coupled to the Nexera UPLC with data analysis software Labsolutions LC-MS (Shimadzu, Japan). The column used Acquity UPLC HSS T3 (2.1 × 100 mm, 1.8 μm, Waters) at a column temperature of 40°C. Mobile phase A was acetonitrile, and mobile phase B was 0.1% formic acid solution (containing 10 mmol/L ammonium acetate). The gradient elution procedure was: 5%–60% A at 0–6.5 min; 60%–95%A at 6.5–6.6 min; 95% A at 6.6–8 min; 95%–5%A at 8–8.01 min; 5% B at 8.01–10 min. The flow rate was 0.35 mL/min. Mass spectrometry data were obtained by MRM mode in both positive and negative modes with ESI source. The flow rate of the nebulizer was 3 L/min, drying gas flow rate was 10 L/min, interface temperature was set at 300°C, DL temperature was 250°C, and the heating block temperature was 300°C. The MRM analysis conditions of each target compound for simultaneous analysis are summarized in Table 1.

## 2.9 Method validation of the established UPLC-QQQ-MS/MS assay

In accordance with the guidelines for the analytical method verification of the Chinese Pharmacopoeia, 2020, Volume 4 (Pharmacopoeia Commission of PRC, 2020), various factors such as linear regression, precision, recovery, limit of detection (LOD), and limit of quantification (LOQ) were investigated. The calibration curve for each target compound was constructed by more than five different concentrations of mixed standard solutions. The sensitivity of the proposed method was evaluated by establishing LOD and LOQ, which were given by concentrations with signal-to-noise ratios (S/N) of 3:1 and 10:1, respectively. Recovery experiments were conducted through six samples of the same MQ sample and spiked authentic standards in MQ sample directly.

# 3 Results and discussion

## 3.1 Metabolite characterization of MQ extract *in vivo*

A total of 13 absorbed compounds (including seven alkaloids, three phenolic acids, two flavonoids, and one other constituent) and 30 metabolites were found in rat urine, feces, plasma, brain, heart, lung, liver, kidney, intestine, and spleen samples. The metabolites consisted of seven phase-I and 23 phase-II metabolites; the chemical structure of these metabolites included 13 alkaloids, 10 flavonoids, and 7 phenolic acids. According to the metabolic reactions, the 23 phase-II metabolites were divided into four groups: methylated metabolites (8), acetylated metabolites (2), sulfated metabolites (9), and glucuronidated metabolites (4). Detailed information of the identification of absorbed compounds, metabolites, and metabolic reactions and the MS data are summarized in Tables 2 and 3; the base peak chromatograms and the distribution of metabolites in main rat organs are shown in Supplementary Figures S1–S10 and Supplementary Tables S2, S3. The structural elucidation of a group of metabolites relevant to meconquintupline is presented below. **M5** and **M6** exhibited $[M + H]^+$ at *m/z* 330.17, their molecular formula was predicted to be $C_{19}H_{23}NO_4$, and the ring double bond (RDB) was 8. Compared with meconquintupline (MW: 318 Da, MF: $C_{19}H_{21}NO_4$, RDB: 9), the MW of **M5** and **M6** were increased by 2 Da, and the RDB decreased by 1. Therefore, **M5** and **M6** were identified as dihydromeconoquintupline. **M5** and **M6** displayed the same fragment ions of *m/z* 271.10, *m/z* 255.10, *m/z* 241.08, *m/z* 195.08, and *m/z* 192.10 in $MS^2$ spectra. Among these, *m/z* 192.10 ($C_{11}H_{14}NO_2$) is a characteristic fragment ion produced by the B ring

TABLE 1 UPLC-QQQ-MS/MS MRM conditions for nine quality markers.

| Name | Ion mode | Retention time (min) | Precursor ion (Q1, *m/z*) | Product ion (Q3, *m/z*) | Collision energy (eV) | Q1 pre bias | Q3 pre bias |
|---|---|---|---|---|---|---|---|
| Protopine | + | 4.20 | 354.1 | 188.1 | −31 | −13 | −12 |
| Allocryptopine | + | 4.45 | 370.1 | 188.1 | −31 | −19 | −21 |
| Caffeic acid | - | 3.37 | 179.0 | 135.1 | 25 | 20 | 24 |
| Taxifolin | - | 4.16 | 303.0 | 285.1 | 21 | 21 | 29 |
| Luteolin | - | 5.02 | 285.0 | 133.1 | 25 | 30 | 24 |
| Quercetin | - | 5.07 | 301.0 | 151.1 | 18 | 14 | 29 |
| Apigenin | - | 5.55 | 268.9 | 117.1 | 24 | 18 | 23 |
| Chlorogenic acid | - | 2.90 | 353.0 | 191.1 | 41 | 13 | 18 |
| Isorhamnetin | - | 5.73 | 315.0 | 299.9 | 28 | 22 | 18 |

TABLE 2 Characterization of absorbed compounds in rats after orally-administered MQ extract.

| No. | $t_R$/ min | ESI-MS/ (*m/z*) | Diff (ppm) | Formula | HR-MS/MS characteristic ion | Identification |
|---|---|---|---|---|---|---|
| F1 | 23.46 | 163.03891 $[M-H]^-$ | −0.061 | $C_9H_8O_3$ | 119.04887, 117.03339, 93.03315 | *p*-coumaric acid |
| F2 | 7.49 | 167.03375 $[M-H]^-$ | −0.809 | $C_8H_8O_4$ | 123.04378, 121.02814 | Homoprotocatechuic acid |
| F3 | 14.34 | 179.03377 $[M-H]^-$ | −0.644 | $C_9H_8O_4$ | 135.04387, 117.05267, 109.02795, 93.03318 | Caffeic acid |
| F4 | 47.56 | 269.04510 $[M-H]^-$ | 2.416 | $C_{15}H_{10}O_5$ | N | Apigenin |
| F5 | 44.95 | 315.05084 $[M-H]^-$ | 2.891 | $C_{16}H_{12}O_7$ | 300.02710, 272.03232, 243.02901, 151.00235, 107.01301 | Isorhamnetin |
| F6 | 49.04 | 329.06638 $[M-H]^-$ | −0.573 | $C_{17}H_{14}O_7$ | 243.02890, 227.03416, 215.03323, 203.03403, 199.03900 | Preussiafuran B |
| F7 | 21.44 | 326.13858 $[M + H]^+$ | −0.105 | $C_{19}H_{19}NO_4$ | 295.09607, 283.09607, 280.07281, 265.08530, 237.09061, 205.06464, 191.09442, 162.09116, 145.08817, 121.50990 | Reframoline |
| F8 | 13.15 | 328.15424 $[M + H]^+$ | −0.095 | $C_{19}H_{21}NO_4$ | N | Meconquintupline |
| F9 | 18.71 | 342.16986 $[M + H]^+$ | −0.125 | $C_{20}H_{23}NO_4$ | 297.11194, 282.08850, 265.08572, 250.06212, 237.09076, 222.06754, 191.08539, 166.07793 | *O*-methylflavinantine |
| F10 | 32.04 | 354.13312 $[M + H]^+$ | 2.629 | $C_{20}H_{19}NO_5$ | N | Protopine |
| F11 | 33.81 | 370.16498 $[M + H]^+$ | −0.998 | $C_{21}H_{23}NO_5$ | N | Allocryptopine |
| F12 | 29.77 | 372.14423 $[M + H]^+$ | 0.178 | $C_{20}H_{21}NO_6$ | N | Hydroxylated dihydroprotopine |
| F13 | 27.12 | 384.14383 $[M + H]^+$ | −0.869 | $C_{21}H_{21}NO_6$ | N | Hydroxylated oxypseudopalmatine |

Note: N, The $MS^2$ characteristic ion was not detected.

opening reaction for meconoquintupline (Kong et al., 2022). The loss of the whole bridge ring of **M5** and **M6** produces *m/z* 195.08. Furthermore, the dehydration of **M5** was identified, which demonstrated that hydrogenation could occur in the carbonyl at the C-7 position, where the carbonyl was reduced to oxhydryl. In addition, hydrogenation in **M6** may occur in the double bond of C-5 and C-6, given that the loss of carbonyl (C=O) occurred in **M6** but not in **M5**. In particular, the retention time of **M6** ($t_R$: 18.2 min) was longer than that of **M5** ($t_R$: 14.0 min), which was consistent with a larger Clog P value meaning a longer $t_R$ in UPLC. In the present study, the Clog P values of **M5** and **M6** were 1.4 and 1.7, respectively, which demonstrated that **M6** is more hydrophobic than **M5**. Therefore, **M5** and **M6** were identified as 7- dihydro meconoquintupline and dihydromeconoquintupline, respectively. The EICs and $MS^2$ data and characteristic fragment ions are shown in Figure 2.

TABLE 3 Characterization of identified metabolites in rats after orally administrated MQ extract.

| No. | $t_R$/ min | ESI-MS/ (*m/z*) | Formula | HR-MS/MS characteristic ion | Identification | Reference |
|---|---|---|---|---|---|---|
| M1 | 48.09 | 271.06091 [M-H]$^-$ | $C_{15}H_{12}O_5$ | 227.07085, 201.05508, 177.01820, 151.00240, 11 9.04883, 107.01244 | Hydrogenated apigenin | Li et al. (2019a) |
| M2 | 44.92 | 317.02969 [M-H]$^-$ | $C_{15}H_{10}O_8$ | 299.01920, 271.02444, 255.02942, 227.03430, 178.99741, 151.00237 | Hydroxylated quercetin | Qin et al. (2017) |
| M3 | 31.27 | 355.10318 [M-H]$^-$ | $C_{16}H_{20}O_9$ | 191.05623, 173.08076, 135.04387, 111.00742 | Hydrogenated chlorogenic acid | Liu et al. (2022) |
| M4 | 31.8 | 206.08102 [M + H]$^+$ | $C_{11}H_{11}NO_3$ | 185.06320, 162.95728, 160.07561, 145.05209, 133.06476, 117.05734, 103.05454 | Demethylated oleracein E | Kong et al. (2022) |
| M5 | 13.99 | 330.16974 [M + H]$^+$ | $C_{19}H_{23}NO_4$ | 312.16016, 281.11758, 271.09692, 269.11707, 266.09323, 255.10144, 249.09091, 242.11722, 241.08600, 223.07521, 218.07245, 195.08040, 192.10197, 162.09160 | 7- dihydro meconoquintupline | Kong et al. (2022) |
| M6 | 18.24 | 330.16965 [M + H]$^+$ | $C_{19}H_{23}NO_4$ | 285.11172, 282.12543, 271.09741, 269.11673, 255.10107, 240.07860, 227.10632, 215.10646, 195.08035, 192.10233, 181.06470, 165.06911, 136.06157, 107.04935 | Dihydromeconoquintupline | Kong et al. (2022) |
| M7 | 17.06 | 298.14334 [M + H]$^+$ | $C_{18}H_{19}NO_3$ | 298.14355, 281.11691, 269.11685, 237.09029, 223.07532, 210.10393, 192.10173, 176.07048, 161.08339, 146.05991, 134.09644 | Demethoxylated meconquintupline | Kong et al. (2022) |
| M8 | 12.98 | 193.04955 [M-H]$^-$ | $C_{10}H_{10}O_4$ | 178.02600, 137.02306, 121.02816 | Methylated caffeic acid | Shi et al. (2019) |
| M9 | 9.83 | 258.99130 [M-H]$^-$ | $C_9H_8O_7S$ | 135.04382 | Caffeic acid sulfate isomer 1 | Shi et al. (2019) |
| M10 | 11.52 | 258.99127 [M-H]$^-$ | $C_9H_8O_7S$ | 179.03387, 135.04382, 107.04877 | Caffeic acid sulfate isomer 2 | Shi et al. (2019) |
| M11 | 12.97 | 258.99133 [M-H]$^-$ | $C_9H_8O_7S$ | 135.04387, 107.04881 | Caffeic acid sulfate isomer 3 | Shi et al. (2019) |
| M12 | 4.34 | 277.00186 [M-H]$^-$ | $C_9H_{10}O_8S$ | 197.04460, 153.05457, 123.00743 | Hydrogenated and hydroxylated caffeic acid sulfate | Shi et al. (2019) |
| M13 | 12.41 | 355.06662 [M-H]$^-$ | $C_{15}H_{16}O_{10}$ | 179.03387, 135.04384, 113.02302 | Caffeic acid glucuronide | Shi et al. (2019) |
| M14 | 39.94 | 357.05829 [M-H]$^-$ | $C_{18}H_{14}O_8$ | 163.07518, 137.05927, 135.08078 | Acetylated isorhamnetin | Ni et al. (2023) |
| M15 | 45.69 | 379.01248 [M-H]$^-$ | $C_{16}H_{12}O_9S$ | 299.05566, 284.03220, 256.03726, 211.03970, 151.00250 | Methylated kaempferide sulfate | Yang et al. (2023) |
| M16 | 38.53 | 475.08737 [M-H]$^-$ | $C_{22}H_{20}O_{12}$ | 379.06506, 299.05563, 284.03217, 175.02367, 151.00195, 129.01758 | Methylated luteolin glucuronide isomer 1 | Yang et al. (2023) |
| M17 | 39.62 | 475.08737 [M-H]$^-$ | $C_{22}H_{20}O_{12}$ | 379.06821, 299.05566, 284.03223, 256.03720, 151.00269 | Methylated luteolin glucuronide isomer 2 | Yang et al. (2023) |
| M18 | 20.54 | 493.09821 [M-H]$^-$ | $C_{22}H_{22}O_{13}$ | 331.08292, 317.06628, 289.07147, 273.07654, 151.00243, 149.02274, 137.02321 | Methylated taxifolin glucuronide | Yang et al. (2016a) |
| M19 | 34.13 | 505.09833 [M-H]$^-$ | $C_{23}H_{22}O_{13}$ | 329.06631, 271.02472, 255.02992, 243.02899 | Acetylated isoquercetin | Lu et al. (2013) |
| M20 | 23.00 | 234.11227 [M + H]$^+$ | $C_{13}H_{15}NO_3$ | 219.08884, 206.11729, 190.08630, 175.07532, 163.06258, 151.07523, 136.05183, 119.04919, 109.21142 | Methylated oleracein E isomer 1 | Kong et al. (2022) |
| M21 | 13.20 | 234.11223 [M + H]$^+$ | $C_{13}H_{15}NO_3$ | 219.08878, 201.07809, 190.08549, 163.06262, 151.07518, 136.05162, 119.04922 | Methylated oleracein E isomer 2 | Kong et al. (2022) |
| M22 | 23.44 | 234.11226 [M + H]$^+$ | $C_{13}H_{15}NO_3$ | 219.08891, 200.07101, 190.08603, 175.07561, 163.06281, 151.07524, 136.05162, 119.04933 | Methylated oleracein E isomer 3 | Kong et al. (2022) |

(Continued on following page)

TABLE 3 (*Continued*) Characterization of identified metabolites in rats after orally administrated MQ extract.

| No. | $t_R$/ min | ESI-MS/ (*m/z*) | Formula | HR-MS/MS characteristic ion | Identification | Reference |
|---|---|---|---|---|---|---|
| M23 | 29.11 | 248.12794 [M + H]$^+$ | $C_{14}H_{17}NO_3$ | 233.10454, 220.09654, 205.07246, 202.13390, 189.09126, 175.07523, 163.06281, 151.07530, 145.06508, 134.02707, 119.04926, 105.06998 | Dimethylated oleracein E | Kong et al. (2022) |
| M24 | 11.64 | 300.05350 [M + H]$^+$ | $C_{12}H_{13}NO_6S$ | 220.09656, 202.08560, 190.08585, 161.05930, 137.05956, 119.04919 | Oleracein E sulfate | Kong et al. (2022) |
| M25 | 10.56 | 396.12808 [M + H]$^+$ | $C_{18}H_{21}NO_9$ | 202.08549, 192.10136, 175.07491, 137.05963 | Oleracein E glucuronide | Kong et al. (2022) |
| M26 | 20.02 | 342.16968 [M + H]$^+$ | $C_{20}H_{23}NO_4$ | 296.10410, 280.10910, 265.08557, 254.09366, 225.09076, 211.07457, 191.09404, 162.09105, 145.08904 | Methylated meconquintupline (or *O*-methylflavinantine isomer) | Kong et al. (2022) |
| M27 | 10.69 | 358.16461 [M + H]$^+$ | $C_{20}H_{23}NO_5$ | 281.08057, 265.08542, 251.07011, 197.05948, 192.10170, 177.07828, 162.09116, 147.04391, 119.04928 | Methoxylated meconquintupline | Kong et al. (2022) |
| M28 | 16.93 | 372.18045 [M + H]$^+$ | $C_{21}H_{25}NO_5$ | 326.13937, 285.07581, 257.08038, 242.05727, 211.07536, 192.10185, 177.07919, 153.05536, 125.06001 | Methoxylated *O*-methylflavinantine | Kong et al. (2022) |
| M29 | 13.31 | 532.18115 [M + H]$^+$ | $C_{26}H_{29}NO_{11}$ | 356.14877, 206.08105, 189.06909, 188.07025, 151.07523, 135.04384, 119.04931 | Hydrogenated protopine glucuronide isomer 1 | Huang et al. (2018) |
| M30 | 17.69 | 532.18109 [M + H]$^+$ | $C_{26}H_{29}NO_{11}$ | 189.07030, 188.07054, 165.05449, 151.07524, 135.04398 | Hydrogenated protopine glucuronide isomer 2 | Huang et al. (2018) |

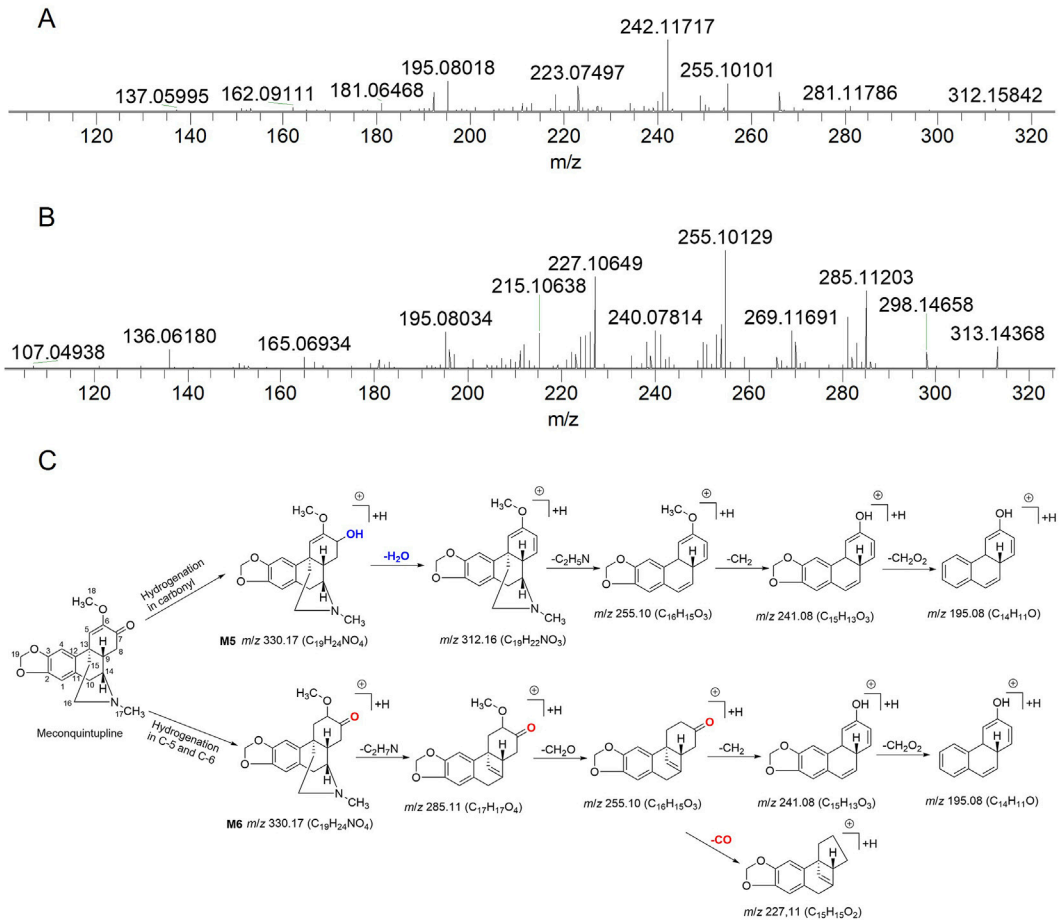


FIGURE 2
MS$^2$ spectra of **M5 (A)** and **M6 (B)** and proposed fragmentation pathway of **M5** and **M6 (C)**.

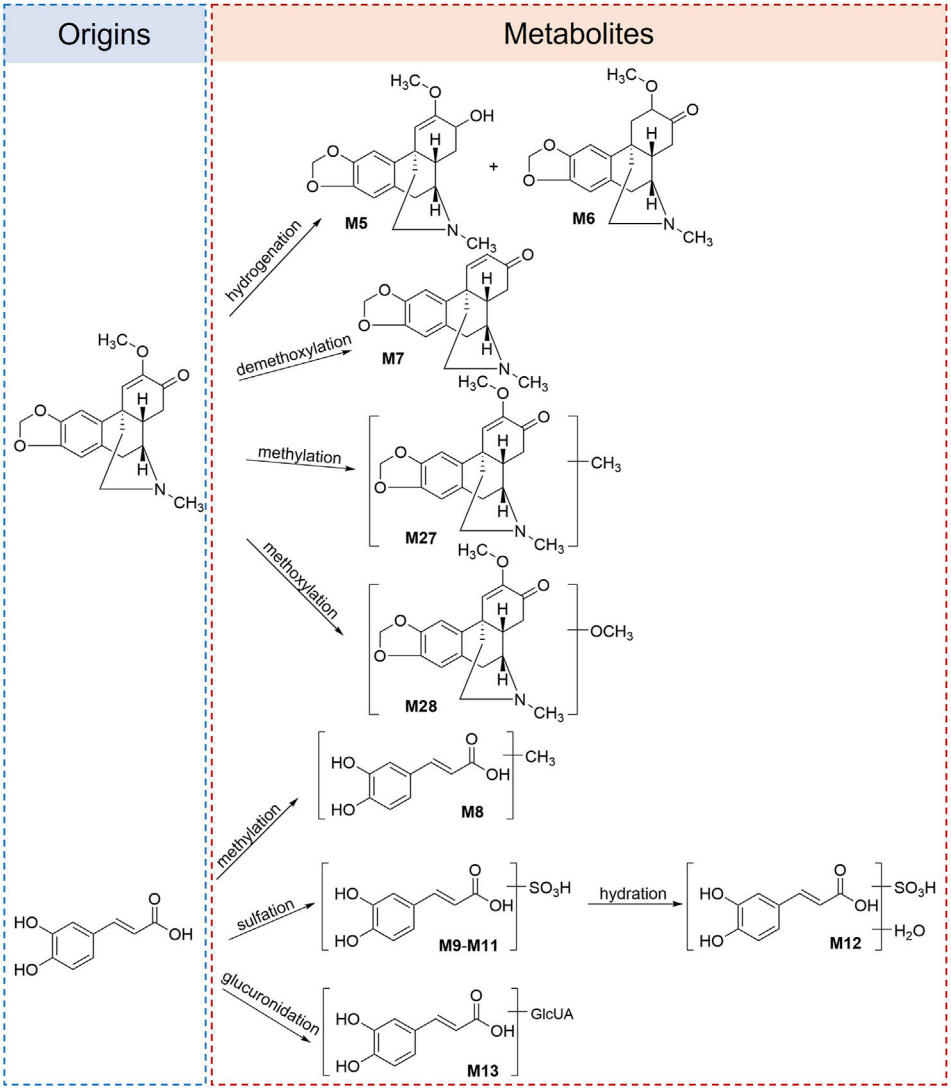


FIGURE 3
Metabolites and proposed metabolic pathways of meconquintupline and caffeic acid in rats.

## 3.2 Potential metabolic pathways and precursors of metabolites

In the present study, the proposed precursors of the metabolites were identified by the parent chemical structures and proposed metabolic pathways of the metabolites. As an example, the proposed metabolic pathways of meconquintupline and caffeic acid are presented in Figure 3. The metabolites of 16 MQ compounds were compared with the relevant literature and analyzed to determine their precursors. Finally, we identified seven metabolites derived from oleracein E (**M4**, **M20**, **M21**, **M22**, **M23**, **M24**, and **M25**), six derived from caffeic acid (**M8**, **M9**, **M10**, **M11**, **M12**, and **M13** five from meconquintupline (**M5**, **M6**, **M7**, **M26**, and **M27**), two from luteolin (**M16** and **M17**), two from protopine (**M29** and **M30**), and eight metabolites derived from eight MQ compounds—apigenin (**M1**), quercetin (**M2**), chlorogenic acid (**M3**), isorhamnetin (**M14**), kaempferide (**M15**), taxifolin (**M18**), isoquercetin (**M19**), and *O*-methylflavinantine (**M28**). Consequently, these absorbed compounds and the proposed metabolite precursors were selected as candidate quality markers.

## 3.3 Hepatocyte protection activity of screened candidate quality markers

In order to verify the reliability of the candidate quality markers screened from absorbed compounds and the precursors of metabolites, the references of experimental validation for hepatocyte protection activity were obtained and analyzed. Apigenin is a common natural flavonoid. Yang et al. (2018) have found that apigenin has the effect of improving hepatocellular carcinoma, one of the mechanisms being apigenin inhibiting cell proliferation and inducing autophagy by inhibiting the PI3K/AKT/mTOR pathway. The data obtained from Rashidi et al. (2023) revealed that isorhamnetin significantly decreases HSC-T6 activation *in vitro* and declines the expression of *COLA1* and *α-SMA* and the protein level of phosphorylated *AKT*, demonstrating

that isorhamnetin improves antifibrotic effect by suppressing the PI3K-AKT signaling pathway. Quercetin could ameliorate the lipid metabolism of nonalcoholic fatty liver disease (NAFLD) progression. The mechanism may be that quercetin treatment reduces gene expression, including AKT phosphorylation, inflammation, oxidative stress, and lipid metabolism, and regulates the PI3K/AKT pathway (Sandra et al., 2015). Luteolin also has similar activity. Ahmed et al. (2022) found that luteolin nanoparticles ameliorated NAFLD by regulating the PI3K/AKT/FoxO1 pathway. Taxifolin is an effective flavonoid for liver protection, possibly by inhibiting the activation of hepatic stellate cells and the production of the extracellular matrix (ECM) by regulating the PI3K/AKT/mTOR and TGF-β1/Smads pathways to play an anti-hepatic fibrosis role (Liu et al., 2021). Protopine can inhibit the viability of hepatocellular carcinoma cells and trigger apoptosis in a caspase-dependent manner. Additionally, it exerts an anti-hepatocellular carcinoma effect by inducing the accumulation of ROS in hepatocellular carcinoma cells, thereby inhibiting the PI3K/AKT signaling pathway (Nie et al., 2021). Studies have shown that caffeic acid can revert the imbalance of gut microbiota and ameliorate the inflammatory lipopolysaccharide-mediated responses in a NAFLD mouse model, inhibiting the dysregulation of the gene expression of lipid metabolism and improving NAFLD symptoms (Mu et al., 2021). Chlorogenic acid exhibited an effect of improving liver fibrosis in an NAFLD mice model, possibly by inhibiting HSC activation, which promotes mitochondrial biogenesis and reduces ECM production initiated by HMGB1 in hepatic vascular endothelial cells (Miao et al., 2022). Allocryptopine exhibits a significant hepatocyte protection effect, improvement of liver function, and anti-hepatic fibrosis effects in rats with $CCl_4$-induced liver fibrosis. It can significantly reduce the expression of liver index, spleen index, AST, ALT, and collagen (CoI, CoIII) in liver tissue (Xiao et al., 2011). Therefore, nine candidate quality markers possess hepatoprotective effects and are absorbable, and these can be detected using reference standards. Consequently, we deduced that apigenin, isorhamnetin, quercetin, luteolin, taxifolin, protopine, allocryptopine, caffeic acid, and chlorogenic acid could be the quality markers of MQ.

The quality markers we have identified in MQ are common compounds, and no specific constituents unique to MQ have been used as quality markers. This poses certain challenges in distinguishing MQ from other botanical drugs of the genus *Meconopsis* during the quality control processes. However, our previous study on *Blumea riparia* and *B. megacephala* found that, although the chemical compounds were similar, their proportions could differ between the two botanical drugs (Su et al., 2023). Other studies have also observed this phenomenon (Kong et al., 2017; Yang et al., 2017). Therefore, we speculate that quality control based on multiple quality markers can achieve differentiation among different botanical drugs of the genus *Meconopsis*.

## 3.4 Method development and quantification of nine quality markers by UPLC-QQQ-MS/MS

### 3.4.1 Optimization of extraction and UPLC-QQQ-MS/MS conditions

To ensure the extraction efficiency of the compounds being investigated, we investigated as extraction methods different proportions of methanol solvent, material–liquid ratios, and extraction times of MQ samples. The results showed that 70% methanol as the extraction solvent, a material–liquid ratio of 1:75, and heating reflux extraction for 30 min were the best extraction conditions (Supplementary Tables S4–S7). For the chromatographic conditions, according to our previous study (Kong et al., 2022), an acetonitrile–0.1% formic acid solution mobile phase system was preferred for the peak separation of flavonoids and phenolic acids. However, several studies have demonstrated that ammonium acetate could improve the ionization and chromatographic peak shape for alkaloids (Wang et al., 2017). Therefore, acetonitrile-0.1% formic acid solution (containing 10 mmol ammonium acetate) was optimized as the mobile phase system.

To fully understand the MS characteristics and select appropriate product ions of the nine quality markers, the fragmentation behavior of these compounds was investigated. Among the nine compounds investigated, the chemical structure of apigenin, luteolin, quercetin, and isorhamnetin was that of flavones and flavonols, and they were analyzed in the negative mode. In the $MS^2$ spectrogram after CID cracking, the products of Retro–Diels–Alder (RDA) cleavage were characteristic fragments, such as *m/z* 117 ($^{1,3}B^-$) from apigenin, *m/z* 133 ($^{1,3}B^-$) from luteolin, and *m/z* 151 ($^{1,3}A^-$) from quercetin and isorhamnetin. These fragments could be used as product ions in MRM analysis except for isorhamnetin, because the RDA product of isorhamnetin was not the dominant fragment ion. The dominant fragment ion of isorhamnetin was *m/z* 300 $[M\text{-}H\text{-}CH_3^{\bullet}]^{-\bullet}$, which was the product from the loss of $CH_3^{\bullet}$. Differently from these three compounds where C-2 and C-3 had a double bond, taxifolin is a flavanonol; for the saturated bond in C-2 and C-3, the dehydration product *m/z* 285 $[M\text{-}H\text{-}H_2O]^-$ was the dominant fragment ion, which could be used as product ion in MRM analysis (Figure 4). Protopine and allocryptopine are isoquinoline alkaloids, and they were analyzed in the positive ion mode. The chemical structure of allocryptopine is similar to that of protopine, and the fragmentation pathway is also similar. Protopine and allocryptopine displayed abundant fragment ions of *m/z* 336, *m/z* 306, *m/z* 206, *m/z* 188, and *m/z* 149 in $MS^2$ spectra. In particular, *m/z* 206 was a diagnostic fragment ion produced by RDA cleavage from the parent ion; the ion of *m/z* 188 was a dehydration product from *m/z* 206; *m/z* 188 was also the dominant fragment ion in $MS^2$ spectra. Therefore, *m/z* 188 could be used as product ion in MRM analysis (Figure 4).

Yang W. Y. et al. (2016) and Shen et al. (2022) have sought to simultaneously determine the content of different polarity compounds in TCM. The highly specific MRM technique can accurately quantify the analytes of interest with MS or $MS^2$ characteristics in the positive and negative ion modes. Hence, in the present study, polarity-switching used for MRM analysis was selected to analyze MQ samples in order to simultaneously determine flavonoids, phenolic acids, and alkaloids. In MRM analysis, it is crucial to determine the precursor ions of each compound and its product ions. Usually, the precursor ions were determined in Q1 MS mode, and then one to two product ions with higher abundance were selected according to the results of its product ion scanning. Finally, collision voltage (CE) was optimized to ensure the best MRM conditions. Under optimized conditions, nine quality markers were isolated and eluted in 10 min (Figure 4), with detailed parameters listed in Table 1.

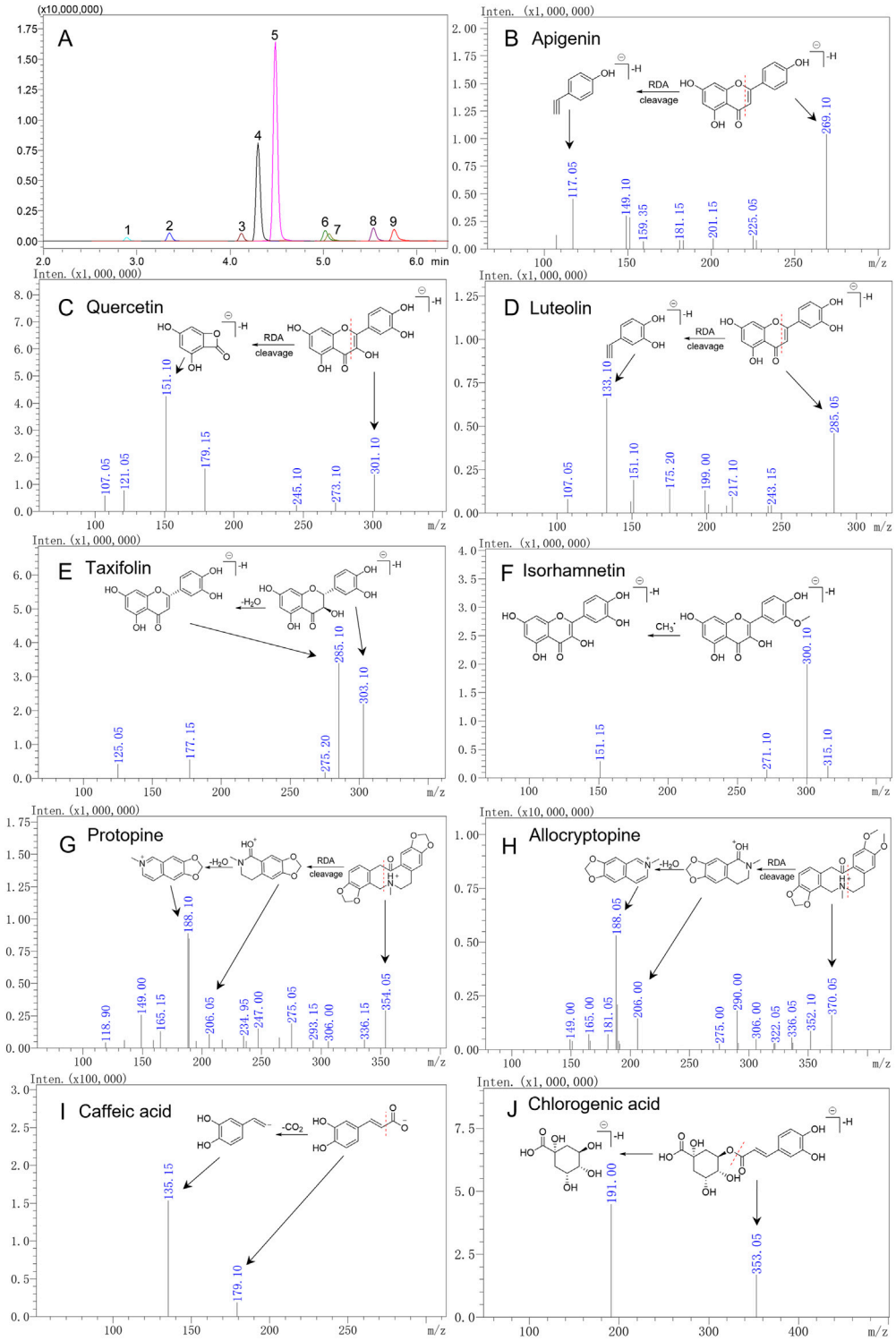


FIGURE 4
Extracted ion chromatogram of nine quality markers in the MRM mode **(A)** and secondary mass spectra of nine compounds **(B–J)**. 1. Chlorogenic acid, 2. caffeic acid, 3. taxifolin, 4. protopine, 5. allocryptopine, 6. luteolin, 7. quercetin, 8. apigenin, and 9. isorhamnetin.

### 3.4.2 Method validation of the developed UPLC-QQQ-MS/MS MRM assay

To evaluate the sensitivity and precision of the established UPLC-QQQ-MS/MS method, the linearity, LOD, LOQ, precision, stability, repeatability, and recovery of the nine target compounds were verified, with the results in Table 4 and Supplementary Tables S8–S10. The standard curves for all nine target compounds showed good linear fit in the range of 100–2000 ng/mL, and the correlation coefficients (*r*) were above 0.99. The LOD and LOQ values of the nine target compounds were 0.81–4.15 ng/mL and 2.47–12.59 ng/

TABLE 4 Calibration curves, linearity, LOD, and LOQ for nine quality markers.

| Name | Retention time (min) | Linear range (ng/mL) | Regression equation | *r* | LOD (ng/mL) | LOQ (ng/mL) | Recovery (%) | RSD (%) |
|---|---|---|---|---|---|---|---|---|
| Protopine | 4.20 | 100–2000 | $y = 22{,}471.0x\text{-}106242$ | 0.9995 | 0.81 | 2.47 | 97.82 | 1.03 |
| Allocryptopine | 4.45 | 100–2000 | $y = 20{,}711.8x+10{,}232.2$ | 0.9994 | 0.90 | 2.70 | 95.17 | 3.91 |
| Caffeic acid | 3.37 | 100–2000 | $y = 3{,}346.53x+138{,}348$ | 0.9900 | 2.86 | 8.67 | 85.71 | 1.46 |
| Taxifolin | 4.16 | 100–2000 | $y = 2{,}674.22x+29{,}478.6$ | 0.9997 | 1.80 | 5.42 | 90.73 | 1.50 |
| Luteolin | 5.02 | 100–2000 | $y = 4{,}120.01x+149{,}437$ | 0.9929 | 2.41 | 7.33 | 90.71 | 2.49 |
| Quercetin | 5.07 | 100–2000 | $y = 2{,}997.01x+74{,}321.8$ | 0.9940 | 3.38 | 10.23 | 102.45 | 3.55 |
| Apigenin | 5.55 | 100–2000 | $y = 4{,}641.91x+78{,}986.6$ | 0.9965 | 1.26 | 3.82 | 86.65 | 2.81 |
| Chlorogenic acid | 2.90 | 100–2000 | $y = 1941.8x+78{,}501.0$ | 0.9974 | 1.97 | 5.96 | 93.29 | 1.74 |
| Isorhamnetin | 5.73 | 100–2000 | $y = 7{,}363.41x\text{-}38408.6$ | 0.9957 | 4.15 | 12.59 | 103.77 | 4.28 |

TABLE 5 Content determination results of nine quality markers of MQ samples (μg/g crude drug).

| Name | MQ1 | MQ2 | MQ3 | MQ4 | MQ5 | MQ6 | MQ7 | MQ8 | MQ9 | MQ10 | Average |
|---|---|---|---|---|---|---|---|---|---|---|---|
| Protopine | 5.83 | 5.88 | 5.69 | 10.13 | 6.19 | 8.96 | 13.52 | 13.14 | 4.88 | 7.48 | 8.17 ± 3.00 |
| Allocryptopine | 0.55 | 0.46 | 2.15 | 1.92 | 1.85 | 1.84 | 0.48 | 0.27 | 0.1 | 0.58 | 1.02 ± 0.77 |
| Caffeic acid | 21.93 | 20.66 | 17.43 | 16.74 | 16.42 | 16.99 | 19.31 | 1.45 | 20.29 | 1.55 | 15.28 ± 7.11 |
| Taxifolin | 221.86 | 224.68 | 84.11 | 79.47 | 54.82 | 80.70 | 58.33 | 73.43 | 276.03 | 219.45 | 137.29 ± 82.02 |
| Luteolin | 69.83 | 67.48 | 19.74 | 47.28 | 29.91 | 48.49 | 66.97 | 66.03 | 105.61 | 102.93 | 62.43 ± 26.31 |
| Quercetin | 7.97 | 8.05 | 5.29 | 6.82 | 4.09 | 6.47 | 4.27 | 4.7 | 16.42 | 9.72 | 7.38 ± 3.48 |
| Apigenin | 8.70 | 8.77 | 2.18 | 7.03 | 4.44 | 6.77 | 10.33 | 6.57 | 14.85 | 5.26 | 7.49 ± 3.31 |
| Chlorogenic acid | 17.25 | 16.28 | 8.87 | 6.75 | 27.72 | 36.27 | 55.93 | 4.74 | 62.30 | 9.94 | 24.61 ± 19.61 |
| Isorhamnetin | 10.48 | 10.27 | 8.31 | 6.26 | 8.06 | 7.76 | 7.40 | 6.22 | 9.23 | 6.55 | 8.05 ± 1.47 |

mL, respectively, indicating high sensitivity under the optimized chromatographic conditions. Precision was evaluated by the spiked standard at a concentration of 1000 ng/mL. The results showed that the RSD value of each compound varied 0.78–2.97%, indicating good precision. In addition, repeatability was tested for the MQ1 sample in sextuplicate; the concentrations of the nine target compounds were calculated, and the mean repeatability expressed as RSD was 2.49–5.68%. Accuracy was assessed by the MQ1 sample in sextuplicate with a known amount of standard with 100% level that was compared with the concentration of the nine target compounds in the MQ1 sample. Recovery was calculated by the following formula: recovery (%) = (amount detected − original amount)/100%. In the present study, the mean RSD of the recovery test in our developed analytical method was 85.71–103.78%. Finally, stability was examined under the MQ1 sample at 0, 2, 4, 6, 10, and 24 h in triplicate; the results showed that the RSD of the peak area of the nine target compounds was 1.37%–4.79%. These results indicated that the UPLC-QQQ-MS/MS method that we developed was accurate, precise, sensitive, and reliable enough to quantitatively determine simultaneously the nine quality markers in the MQ samples.

### 3.4.3 Quantification of quality markers in MQ by UPLC-QQQ-MS/MS

The UPLC-QQQ-MS/MS method developed was successfully applied to the quantitative analysis of quality markers belonging to flavonoids, alkaloids, and phenolics in MQ samples collected from different areas at different altitudes of Gansu, Qinghai, and Sichuan provinces in China. All compounds investigated were eluted within 10 min in the polarity-switching positive and negative ion modes of the ESI source. The content of the nine quality markers was detected at the average range of 1.02–137.29 μg/g; among them, luteolin and taxifolin had relatively large amounts in the MQ samples (Table 5). A comparison between the sample collected at the highest altitude (MQ1) and the batches collected at the lowest altitudes (MQ8) revealed a decreasing trend in alkaloid content with increasing altitude; for example, the protopine content in MQ1 was 5.83 μg/g but was 13.14 μg/g in MQ8. In contrast, the flavonoid content exhibited an increasing trend with higher altitudes; for example, the isorhamnetin content in MQ1 was 10.48 μg/g but was 6.22 μg/g in MQ8. Zhang et al. 2010) also found a similar trend in MQ, with the content of quercetin and luteolin significant increasing with rising altitude in the Qinghai Dalijia area. However, in the Lajishan area,

there was a trend of first decrease and then increase. Pandey et al. (2018) also reported similar results in alkaloid and flavonoids. They found that the berberine content of *Thalictrum foliolosum* varied inversely with altitude, the flavonoid and phenolic content of *T. foliolosum* increased at higher altitudes, while the content of these compounds may still vary according to growth and season (Pandey et al., 2018).

## 4 Conclusion

In the present study, a total of 13 absorbed compounds (including seven alkaloids, three phenolic acids, two flavonoids, and one other compound) and 30 metabolites of MQ extract were found in rat urine, feces, plasma, brain, heart, lung, liver, kidney, intestine, and spleen samples. The nine absorbed compounds and the precursors of metabolites, luteolin, isorhamnetin, quercetin, apigenin, allocrytopine, taxifolin, protopine, caffeic acid, and chlorogenic acid were related to hepatocyte protection activity, which selected them as the quality markers.

The established UPLC-QQQ-MS/MS quantitative method presented reasonable linearity, precision, accuracy, repeatability, stability and recovery for the nine quality markers. These markers were all detected in MQ crude drug. Among them, luteolin and taxifolin had relatively large amounts in the MQ samples. There are variations in the quality of MQ samples sourced from different areas and altitudes, with the variations presenting a decreasing trend in alkaloids with increasing altitude and an increasing trend in flavonoids with increasing altitude.

This study used an absorption-based metabolite strategy to successfully explore, discover, and identify the quality markers of MQ, and a universal and rapid method based on the polarity-switching UPLC-QQQ-MS/MS technology was established for the simultaneous determination of quality markers in MQ. Our study provides a research strategy to optimize quality markers and more rigorous quality control of TCM.

## Data availability statement

The original contributions presented in the study are included in the article/Supplementary Material, further inquiries can be directed to the corresponding author.

## Ethics statement

The animal study was approved by the Biomedical Ethical Committee of Southwest Minzu University. The study was conducted in accordance with the local legislation and institutional requirements.

## Author contributions

YT: formal analysis, investigation, methodology, and writing–original draft. YL: writing–original draft, conceptualization, and funding acquisition. YK: writing–original draft, formal analysis, and investigation. LL: formal analysis, investigation, and writing–review and editing. ZY: investigation, methodology, and writing–review and editing. WL: methodology and writing–review and editing. QL: methodology and writing–review and editing. CR: investigation and writing–review and editing. WS: investigation and writing–review and editing. YH: writing–review and editing, conceptualization, funding acquisition, project administration, and supervision.

## Funding

The authors declare that financial support was received for the research, authorship, and/or publication of this article. This work was supported by the grants from the Natural Science Foundation of Sichuan Province (2022NSFSC1605), the Special Fund of Natural Science for the Central Universities (ZYN2023099), the Engineering Research Center for Pharmaceuticals and Equipment of Sichuan Province Fund (ERCPEF2201), and the First Batch of Scientific and Technological Innovation Team Projects for the Institute of the Qinghai–Tibet Plateau at Southwest Minzu University (2024CXTD04).

## Conflict of interest

Author QL was employed by Shimadzu China Co. LTD.

The remaining authors declare that the research was conducted in the absence of any commercial or financial relationships that could be construed as a potential conflict of interest.

## Publisher's note

All claims expressed in this article are solely those of the authors and do not necessarily represent those of their affiliated organizations, or those of the publisher, the editors, and the reviewers. Any product that may be evaluated in this article, or claim that may be made by its manufacturer, is not guaranteed or endorsed by the publisher.

## Supplementary material

The Supplementary Material for this article can be found online at: https://www.frontiersin.org/articles/10.3389/fphar.2024.1474768/full#supplementary-material

## References

Ahmed, E. S., Mohamed, H. E., and Farrag, M. A. (2022). Luteolin loaded on zinc oxide nanoparticles ameliorates non-alcoholic fatty liver disease associated with insulin resistance in diabetic rats via regulation of PI3K/AKT/FoxO1 pathway. *Int. J. Immunopathol. Pharmacol.* 36, 03946320221137435. doi:10.1177/03946320221137435

Chinese Pharmacopoeia Commission (1995). *Herba Meconopsis in: pharmaceutical standards of the Ministry of Health of the people's Republic of China*.

Duan, S., Niu, L., Yin, T., Li, L., Gao, S., Yuan, D., et al. (2020). A novel strategy for screening bioavailable quality markers of traditional Chinese medicine by integrating

intestinal absorption and network pharmacology: application to Wu Ji Bai Feng Pill. *Phytomedicine* 76, 153226. doi:10.1016/j.phymed.2020.153226

Guo, Q., Bai, R. F., Zhao, B. S., Feng, X., Zhao, Y. F., Tu, P. F., et al. (2016). An ethnopharmacological, phytochemical and pharmacological review of the genus Meconopsis. *Am. J. Chin. Med.* 44, 439–462. doi:10.1142/S0192415X16500257

He, J. S., Huang, B., Ban, X. Q., Tian, J., Zhu, L., and Wang, Y. W. (2012). *In vitro* and *in vivo* antioxidant activity of the ethanolic extract from Meconopsis quintuplinervia. *J. Ethnopharmacol.* 141, 104–110. doi:10.1016/j.jep.2012.02.006

Huang, Y. J., Cheng, P., Zhang, Z. Y., Tian, S. J., Sun, Z. L., Zeng, J. G., et al. (2018). Biotransformation and tissue distribution of protopine and allocryptopine and effects of Plume Poppy total alkaloid on liver drug-metabolizing enzymes. *Sci. Rep.* 8, 537. doi:10.1038/s41598-017-18816-7

Jiao, Y., Chen, D. L., Fan, M. T., and Young Quek, S. (2019). UPLC-QqQ-MS/MS-based phenolic quantification and antioxidant activity assessment for thinned young kiwifruits. *Food Chem.* 281, 97–105. doi:10.1016/j.foodchem.2018.12.062

Kong, Y., Wang, Q. H., Shang, M. Y., Xiao, J. J., Meng, S. C., and Cai, S. Q. (2017). Effects of active constituents of Sinopodophylli Fructus on cell proliferation, cell cycle and mitochondrial membrane potential of human breast cancer cell. *China Pharm.* 28, 1368–1371.

Kong, Y. L., Zhang, J. G., Su, H. N., La, M. J., Lan, J. L., Yang, Z. M., et al. (2022). Chemical constituents and anti-liver fibrosis mechanism of Meconopsis quintuplinervia based on UPLC-Q-Exactive-MS/MS and network pharmacology. *China J. Chin. Mat. Medica* 44, 6097–6116. doi:10.19540/j.cnki.cjcmm.20220917.201

Li, H. F., Li, T., Yang, P., Wang, Y., Tang, X. J., Liu, L. J., et al. (2020). Global profiling and structural characterization of metabolites of ononin using HPLC-ESI-IT-TOF-$MS^n$ after oral administration to rats. *J. Agric. Food Chem.* 68, 15164–15175. doi:10.1021/acs.jafc.0c04247

Li, H. F., Xu, F., Yang, P., Liu, G. X., Shang, M. Y., Wang, X., et al. (2017). Systematic screening and characterization of prototype constituents and metabolites of total astragalosides using HPLC-ESI-IT-TOF-MSn after oral administration to rats. *J. Pharm. Biomed. Anal.* 142, 102–112. doi:10.1016/j.jpba.2017.05.009

Li, M. R., Si, D. D., Fu, Z. F., Sang, M. M., Zhang, Z., Liu, E. W., et al. (2019a). Enhanced identification of the *in vivo* metabolites of Ecliptae Herba in rat plasma by integrating untargeted data-dependent MS2 and predictive multiple reaction monitoring-information dependent acquisition-enhanced product ion scan. *J. Chromatogr. B* 1109, 99–111. doi:10.1016/j.jchromb.2019.02.001

Li, W. J., Cai, Y. F., Ouyang, Y., Li, X. Y., Shi, X. L., Cao, S. X., et al. (2024). Quality evaluation of Angelica Sinensis Radix dispensing granules by integrating microvascular activity and chemical analysis. *J. Ethnopharmacol.* 319, 117236. doi:10.1016/j.jep.2023.117236

Li, X. Y., Fu, Y. J., Fu, Y. F., Wei, W., Xu, C., Yuan, X. H., et al. (2022a). Simultaneous quantification of fourteen characteristic active compounds in Eucommia ulmoides Oliver and its tea product by ultra-high performance liquid chromatography coupled with triple quadrupole mass spectrometry (UPLC-QqQ-MS/MS). *Food Chem.* 389, 133106. doi:10.1016/j.foodchem.2022.133106

Li, Y. L., Ju, S. S., Lin, Z. J., Wu, H., Wang, Y., Jin, H. Y., et al. (2022b). Bioactive-chemical quality markers revealed: an integrated strategy for quality control of chicory. *Front. Nutr.* 9, 934176. doi:10.3389/fnut.2022.934176

Li, Y. Z., Xie, Y., He, Y. F., Hou, W. B., Liao, M. L., and Liu, C. X. (2019b). Quality markers of traditional Chinese medicine: concept, progress, and perspective. *Engineering* 5, 888–894. doi:10.1016/j.eng.2019.01.015

Li, Z. Q., Liu, J., Li, Y. Z., Du, X., Li, Y. F., Wang, R. H., et al. (2018). Identify super quality markers from prototype-based pharmacokinetic markers of Tangzhiqing tablet (TZQ) based on *in vitro* dissolution/permeation and *in vivo* absorption correlations. *Phytomedicine* 45, 59–67. doi:10.1016/j.phymed.2018.04.001

Liu, C. X., Chen, S. L., Xiao, X. H., Zhang, T. J., Hou, W. B., and Liao, M. L. (2016). A new concept on quality marker of Chinese materia medica: quality control for Chinese medicinal products. *Chin. Tradit. Herb. Drugs* 47, 1443–1457.

Liu, C. X., Guo, D. A., and Liu, L. (2018). Quality transitivity and traceability system of herbal medicine products based on quality markers. *Phytomedicine* 44, 247–257. doi:10.1016/j.phymed.2018.03.006

Liu, W. J., Li, W., Zhang, P. J., Gong, X. C., Tu, P., Tang, L., et al. (2022). Quality structural annotation for the metabolites of chlorogenic acid in rat. *Food Chem.* 379, 132134. doi:10.1016/j.foodchem.2022.132134

Liu, X. L., Liu, W. C., Ding, C. B., Zhao, Y. C., Chen, X., Ling, D., et al. (2021). Taxifolin, extracted from waste larix olgensis roots, attenuates CCl4-induced liver fibrosis by regulating the PI3K/AKT/mTOR and TGF-β1/Smads signaling pathways. *Drug Des. devel. Ther.* 15, 871–887. doi:10.2147/DDDT.S281369

Lu, L. L., Qian, D. W., Yang, J., Jiang, S., Guo, J. M., Shang, E. X., et al. (2013). Identification of isoquercitrin metabolites produced by human intestinal bacteria using UPLC-Q-TOF/MS. *Biomed. Chromatogr.* 27, 509–514. doi:10.1002/bmc.2820

Luo, D. S., Sun, A. L., and Xia, G. C. (1984). Tibetan drug in Qingzang plateau, a preliminary investigation of resources Meconopsis. *Chin. Tradit. Herb. Drugs* 15, 23–24.

Miao, H., Ouyang, H., Guo, Q., Wei, M. J., Lu, B., Kai, G. Y., et al. (2022). Chlorogenic acid alleviated liver fibrosis in methionine and choline deficient diet-induced nonalcoholic steatohepatitis in mice and its mechanism. *J. Nutr. Biochem.* 106, 109020. doi:10.1016/j.jnutbio.2022.109020

Mu, H. N., Zhou, Q., Yang, R. Y., Tang, W. Q., Li, H.-X., Wang, S. M., et al. (2021). Caffeic acid prevents non-alcoholic fatty liver disease induced by a high-fat diet through gut microbiota modulation in mice. *Food Res. Int.* 143, 110240. doi:10.1016/j.foodres.2021.110240

Ni, L. Q., Lu, H., Gao, M., and Fan, X. P. (2023). *In vivo* metabolites of isorhamnetin in mice after oral administration based on UPLC-Q/TOF-MS/MS. *Mil. Med. Sci.* 47, 364–370. doi:10.7644/j.issn.1674-9960.2023.05.008

Nie, C. H., Wang, B., Wang, B. Q., Lv, N., Yu, R., and Zhang, E. F. (2021). Protopine triggers apoptosis via the intrinsic pathway and regulation of ROS/PI3K/Akt signalling pathway in liver carcinoma. *Cancer Cell Int.* 21, 396. doi:10.1186/s12935-021-02105-5

Pandey, G., Khatoon, S., Pandey, M. M., and Rawat, A. K. S. (2018). Altitudinal variation of berberine, total phenolics and flavonoid content in Thalictrum foliolosum and their correlation with antimicrobial and antioxidant activities. *J. Ayurveda Integr. Med.* 9, 169–176. doi:10.1016/j.jaim.2017.02.010

Pharmacopoeia Commission of PRC (2020). *Pharmacopoeia of the people's republicof China*.

Qin, X. L., Sun, H. Y., Yang, W., Li, Y. J., Zheng, L., Liu, T., et al. (2017). Analysis of metabolites of quercitrin in rat intestinal flora by using UPLC-ESI-Q-TOF-MS/MS. *China J. Chin. Mat. Medica* 42, 357–362. doi:10.19540/j.cnki.cjcmm.20161222.018

Rashidi, M., Matour, E., Beheshti Nasab, H., Cheraghzadeh, M., and Shakerian, E. (2023). Isorhamnetin exerts antifibrotic effects by attenuating platelet-derived growth factor-BB-induced HSC-T6 cells activation via suppressing PI3K-AKT signaling pathway. *Iran. Biomed. J.* 27, 199–204. doi:10.61186/ibj.3948

Sandra, P. V., Ángel, M. F., María, V. G. M., Susana, M. F., Anna, F., Marta, B., et al. (2015). Quercetin ameliorates dysregulation of lipid metabolism genes via the PI3K/AKT pathway in a diet-induced mouse model of nonalcoholic fatty liver disease. *Mol. Nutr. Food Res.* 59, 879–893. doi:10.1002/mnfr.201400913

Shang, X. Y., Li, C., Zhang, C. Z., Yang, Y. C., and Shi, J. G. (2006a). Non-alkaloid constituents from a Tibetan medicine Meconopsis quintuplinervia. *China J. Chin. Mat. Medica* 31, 468–471.

Shang, X. Y., Shi, J. G., Yang, Y. C., Liu, X., Li, C., and Zhang, C. Z. (2003). Alkaloids from a Tibetan medicine Meconopsis quintuplinervia Regel. *Acta Pharm. Sin.* 38, 276–278. doi:10.16438/j.0513-4870.2003.04.009

Shang, X. Y., Wang, Y. H., Li, C., Zhang, C. Z., Yang, Y. C., and Shi, J. G. (2006b). Acetylated flavonol diglucosides from Meconopsis quintuplinervia. *Phytochemistry* 67, 511–515. doi:10.1016/j.phytochem.2005.12.002

Shang, X. Y., Zhang, C. Z., Li, C., Yang, Y. C., and Shi, J. G. (2002). Studies on chemical constituents of Meconopsis quintuplinervia Regel. *J. Chin. Med. Mat.* 25, 250–252. doi:10.13863/j.issn1001-4454.2002.04.010

Shen, Q., Wang, H. X., Quan, B., Sun, X. H., Wu, G. H., Huang, D. R., et al. (2022). Rapid quantification of bioactive compounds in Salvia miltiorrhiza Bunge derived decoction pieces, dripping pill, injection, and tablets by polarity-switching UPLC-MS/MS. *Front. Chem.* 10, 964744. doi:10.3389/fchem.2022.964744

Shi, B. M., Yang, L. J., Gao, T., Ma, C., Li, Q., Nan, Y. F., et al. (2019). Pharmacokinetic profile and metabolite identification of bornyl caffeate and caffeic acid in rats by high performance liquid chromatography coupled with mass spectrometry. *RSC Adv.* 9, 4015–4027. doi:10.1039/c8ra07972b

Shi, X., Cheng, F., Guo, M., and Shao, J. (2011). Determination of O-methylflavinantine in a Tibetan medicine Meconopsis quintuplinervia by HPLC. *China J. Chin. Mat. Medica* 36, 3290–3292.

Su, H. N., Li, X. X., Li, Y., Kong, Y. L., Lan, J. L., Huang, Y. F., et al. (2023). Chemical profiling and rapid discrimination of Blumea riparia and Blumea megacephala by UPLC-Q-Exactive-MS/MS and HPLC. *Chin. Herb. Med.* 15, 317–328. doi:10.1016/j.chmed.2022.06.009

Sun, Z., Liu, X., Zuo, W., Fu, Q., Xu, T. T., Cui, L. Y., et al. (2023). Development of a robust UPLC-MS/MS method for the quantification of riluzole in human plasma and its application in pharmacokinetics. *Front. Pharmacol.* 14, 1227354. doi:10.3389/fphar.2023.1227354

Wang, H. Y., and Ma, W. Y. (2009). Fifty-six cases of chronic severe hepatitis treated by Tibetan Medicine Ershiwuwei Luronghao Wan. *Chin. Community Dr.* 11, 145.

Wang, J. L., Zheng, D. D., Wang, Y. Z., Zhang, C., and Sun, X. M. (2017). Pharmacokinetics study of Erhuang decoction extracts in rats by HPLC-MS/MS. *J. Chromatogr. B-Anal. Technol. Biomed. Life Sci.* 1059, 35–42. doi:10.1016/j.jchromb.2017.05.019

Wang, Z. W., Shao, J., Guo, M., Wang, R. Q., and Ren, Y. (2013a). Effect of total flavonoids and alkaloids from Meconopsis quintuplinervia on hepatic fibrosis in rat. *Chin. Tradit. Pat. Med.* 35, 1125–1128. doi:10.3969/j.issn.1001-1528.2013.06.004

Wang, Z. W., Wang, R. Q., Guo, M., Shao, J., and Ren, Y. (2013b). Study on liver protection of total flavones of Meconopsis quintuplinervia from Gansu province in mice. *Chin. J. Exp. Tradit. Med. Formulae* 19, 206–209.

Wei, X. Y., Guo, W. J., Chen, Z. Y., Qiu, Z. D., Guo, J., Cui, G. H., et al. (2021). Chemical-activity-based quality marker screening strategy for Viscum articulatum. *Biomed. Chromatogr.* 35, e5175. doi:10.1002/bmc.5175

Wu, H. F., Pan, L., Ding, L. S., and Zhang, X. F. (2007). Chemical constituents of a Tibetan medicine Meconopsis quintuplinervia Regel. *Nat. Prod. Res. Dev.* 19, 811–813. doi:10.16333/j.1001-6880.2007.05.022

Xiao, L., Zeng, J. G., Liu, L., Wang, Y. H., Zhong, M., He, X. H., et al. (2011). Effect of allocryptopine on antagonizing hepatic fibrosis. *Chin. Tradit. Herb. Drugs* 42, 1158–1163.

Xu, J. J., Xu, F., Wang, W., Zhang, Y. F., Hao, B.-Q., Shang, M. Y., et al. (2022). Elucidation of the mechanisms and effective substances of Paeoniae Radix Rubra against toxic heat and blood stasis syndrome with a stage-oriented strategy. *Front. Pharmacol.* 13, 842839. doi:10.3389/fphar.2022.842839

Yang, J. L., Pi, C. C., and Wang, G. H. (2018). Inhibition of PI3K/Akt/mTOR pathway by apigenin induces apoptosis and autophagy in hepatocellular carcinoma cells. *Biomed. Pharmacother.* 103, 699–707. doi:10.1016/j.biopha.2018.04.072

Yang, M. F., Li, H., Xu, X. R., Zhang, Q. Y., Wang, T. Y., Feng, L., et al. (2023). Comprehensive identification of metabolites and metabolic characteristics of luteolin and kaempferol in Simiao Yong′an Decoction in rats by UHPLC-LTQ-Orbitrap MS/MS. *China J. Chin. Mat. Medica* 48, 6191–6199. doi:10.19540/j.cnki.cjcmm.20230621.201

Yang, P., Xu, F., Li, H. F., Wang, Y., Li, F. C., Shang, M. Y., et al. (2016a). Detection of 191 taxifolin metabolites and their distribution in rats using HPLC-ESI-IT-TOF-MSn. *Molecules* 21, 1209. doi:10.3390/molecules21091209

Yang, W. Y., Han, Q. J., Guo, P. P., Wang, C. Y., and Zhang, Z. J. (2016b). Simultaneous detection of flavonoids, phenolic acids and alkaloids in Abri herba and Abri Mollis herba using liquid chromatography tandem mass spectrometry. *Phytochem. Anal.* 27, 50–56. doi:10.1002/pca.2598

Yang, Z. W., Xu, F., Liu, X., Cao, Y., Tang, Q., Chen, Q. Y., et al. (2017). An untargeted metabolomics approach to determine component differences and variation in their *in vivo* distribution between Kuqin and Ziqin, two commercial specifications of Scutellaria Radix. *RSC Adv.* 7, 54682–54695. doi:10.1039/C7RA10705F

Yu, R. X., Zhang, Y. P., Wu, N., Wang, X., Mei, L. J., and Yang, X. B. (2021). Study on anti-inflammatory effects of total alkaloids extracted from Meconopsis quintuplinervia Regel. *Tradit. Chin. Drug Res. Clin. Pharmacol.* 32, 461–466. doi:10.19378/j.issn.1003-9783.2021.04.002

Yue, P. P., Sun, J., Zhang, C. X., Ye, R. R., Lu, X. F., Zhou, Y. B., et al. (2010). HPLC-DAD separation and determination of major active constituents in an important Tibetan medicine Meconopsis quintuplinervia from different regions of Qinghai-Tibet Plateau. *J. Med. Plants Res.* 4, 1053–1058.

Zhang, C. X., Ye, R. R., Lu, X. F., Yue, P. P., Yang, S. B., Liu, W. H., et al. (2010). Variations on the contents of quercetin and luteolin of Meconopsis quintuplinervia Regel from different altitudes. *Nat. Prod. Res. Dev.* 22, 643–646.

Zhang, J., Lv, Y., Zhang, J., Shi, W. J., Guo, X. Y., Xu, J. J., et al. (2022). Metabolism of paeoniae radix rubra and its 14 constituents in mice. *Front. Pharmacol.* 13, 995641. doi:10.3389/fphar.2022.995641

Zhang, T. J., Bai, G., and Liu, C. X. (2019). The concept, core theory and research methods of Chinese medicine quality markers. *Acta Pharm. Sin.* 54, 187–196+186. doi:10.16438/j.0513-4870.2018-0912

frontiers | Frontiers in Pharmacology

TYPE Mini Review
PUBLISHED 09 December 2024
DOI 10.3389/fphar.2024.1477878

Check for updates

OPEN ACCESS

EDITED BY
Bin Wu,
Zhejiang University, China

REVIEWED BY
Javad Mottaghipisheh,
Swedish University of Agricultural Sciences, Sweden
MingZhong Wang,
Shenzhen Technology University, China
Xiaodong Xiong,
Nanchang University, China
Smith B. Babiaka,
University of Tuebingen, Germany

*CORRESPONDENCE
Junyang Liu,
liujy@wyu.edu.cn

RECEIVED 08 August 2024
ACCEPTED 26 November 2024
PUBLISHED 09 December 2024

CITATION
Yan J-L, Nan H, Fang X, Long X-E, Jiang Y and Liu J (2024) The isolation, bioactivity, and synthesis of natural products from *Litsea verticillate* with anti-HIV activities. *Front. Pharmacol.* 15:1477878. doi: 10.3389/fphar.2024.1477878

COPYRIGHT
© 2024 Yan, Nan, Fang, Long, Jiang and Liu. This is an open-access article distributed under the terms of the Creative Commons Attribution License (CC BY). The use, distribution or reproduction in other forums is permitted, provided the original author(s) and the copyright owner(s) are credited and that the original publication in this journal is cited, in accordance with accepted academic practice. No use, distribution or reproduction is permitted which does not comply with these terms.

# The isolation, bioactivity, and synthesis of natural products from *Litsea verticillate* with anti-HIV activities

Jia-Lei Yan, Huiru Nan, Xiaoyu Fang, Xiong-En Long, Yu Jiang and Junyang Liu*

School of Pharmacy and Food Engineering, Wuyi University, Jiangmen, China

Natural products isolated from *Litsea verticillata* have attracted considerable attention from the chemical community due to their unique structures and promising anti-HIV activities. Recent progresses in the isolation and bioactivity studies for these natural molecules were summarized comprehensively. From the 23 previously uncharacterized compounds isolated from the plant *Litsea verticillata*, litseaverticillol B demonstrated the most potent anti-HIV activity *in vitro*, with $IC_{50}$ ranging from 2 to 3 μg/mL. Meanwhile, litseaverticillol E displayed the highest selectivity index (SI = 3.1), indicating a favorable balance between antiviral potency and cellular toxicity. The plausible biosynthetic pathways and the total synthetic approaches for the representative members (litseaverticillols) were introduced in detail.

KEYWORDS

***litsea verticillate*, natural product, anti-HIV, total synthesis, bioactive**

## 1 Introduction

Acquired Immunodeficiency Syndrome (AIDS) is caused by infection with the Human Immunodeficiency Virus (HIV) (Fauci, 1988). HIV infection progressively destroys the host's immune system, leading to severe cellular immunodeficiency and ultimately resulting in serious complications such as wasting, neurological impairment, opportunistic infections, and malignancies (Richman, 2001). Moreover, the emergence of drug resistance mutations (DRMs) in HIV, typically induced by antiretroviral therapy (ART) pressure, can result in rapid virologic failure and limited treatment options (Larder and Kemp, 1989; Tantillo et al., 1994; Lepri et al., 2000), posing a significant public health threat. As a result, the discovery of novel drug candidates or the structural modification of existing drugs has become a critical and urgent priority. In this pursuit, the exploration of natural products has emerged as a prevalent and effective strategy employed by pharmacologists (Li et al., 2024).

Plant-derived natural products are extensively utilized in pharmaceuticals and nutraceuticals, serving as the basis for numerous drugs such as antimalarial artemisinin, analgesic morphine, anticancer paclitaxel, and tanshinones for cardiovascular and cerebrovascular diseases (Atanasov et al., 2015; Newman and Cragg, 2020; Chaachouay and Zidane, 2024). Owing to their broad pharmacological activities, potent efficacy, and significant clinical demand, these natural products have consistently attracted the attention of pharmaceutical chemists (Atanasov et al., 2021; Chopra and Dhingra, 2021; Hu et al., 2024). The *Litsea verticillata* Hance belongs to the genus *Litsea* in the Lauraceae family,

TABLE 1 Natural products isolated from *L. verticillata* Hance with anti-HIV activities.

| Isolated compound | Separation method | Active part | Anti-HIV to HOG.R5 $IC_{50}$ (μg/mL) | Cytotoxicity to HOG.R5 $CC_{50}$ (μg/mL) | Selectivity index ($CC_{50}$/$IC_{50}$) | References |
|---|---|---|---|---|---|---|
| 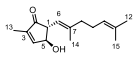 (±)-Litseaverticillol A (**1**) | PH | LF + TW | 5.0[a] | 13.2[a] | 2.6 | Zhang et al. (2001) |
| 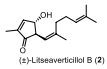 (±)-Litseaverticillol B (**2**) | PH | LF + TW | 2–3[a] | 5.7[a] | 2.8–1.9 | Zhang et al. (2003a) |
| 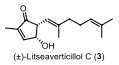 (±)-Litseaverticillol C (**3**) | PH | LF + TW | 7.1[a] | 17.5[a] | 2.4 | Zhang et al. (2003a) |
| 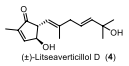 (±)-Litseaverticillol D (**4**) | PH | LF + TW | 14.4[a] | >20[a] | >1 | Zhang et al. (2003a) |
| 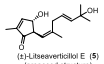 (±)-Litseaverticillol E (**5**) (proposed structure) | PH | LF + TW | 4.0[a] | 12.4[a] | 3.1 | Zhang et al. (2003a) |
| 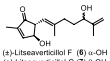 (±)-Litseaverticillol F (**6**) α-OH (±)-Litseaverticillol G (**7**) β-OH | PH | LF + TW | 11.3[a] | 20.0[a] | 1.7 | Zhang et al. (2003a) |
| 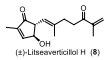 (±)-Litseaverticillol H (**8**) | PH | LF + TW | T[a] | 2.5–5.0[a] | — | Zhang et al. (2003a) |
| (-)-Verticillatol (**9**) | SC | LF + TW | 34.5[a] | NT[a] | — | Hoang et al. (2002) |
| 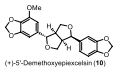 (+)-5′-Demethoxyepiexcelsin (**10**) | SC | LF + TW | 16.4[a] | 23.0[a] | 1.4 | Hoang et al. (2002) |
| 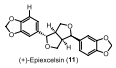 (+)-Epiexcelsin (**11**) | SC | LF + TW | I[a] | NT[a] | — | Hoang et al. (2002) |
| (+)-Litseagermacrane (**12**) | PH | LF + TW | 6.5[a] | 15.9[a] | 2.4 | Zhang et al. (2003b) |
| (–)-7-*epi*-Eudesm-4(15)-ene-1α,6α-diol (**13**) | PH | LF + TW | I[a] | NT[a] | — | Zhang et al. (2003b) |
| (+)-5-*epi*-Eudesm-4(15)-ene-1β,6β-diol (**14**) | PH | LF + TW | 17.4[a] | NT[a] | — | Zhang et al. (2003b) |
| (–)-Litseahumulane A (**15**) | PH | LF + TW | I[a] | NT[a] | — | Zhang et al. (2003b) |
| (–)-Litseahumulane B (**16**) | PH | LF + TW | I[a] | NT[a] | — | Zhang et al. (2003b) |
| (+)-Litseachromolaevane A (**17**) | PH | LF + TW | I[a] | NT[a] | — | Zhang et al. (2003b) |
| Litseachromolaevane B (**18**) | PH | LF + TW | 28.0[a] | NT[a] | — | Zhang et al. (2003b) |
| 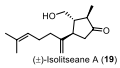 (±)-Isolitseane A (**19**) | PH | LF + TW | I[b] | NT[b] | — | Zhang et al. (2005) |
| 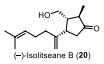 (–)-Isolitseane B (**20**) | PH | LF + TW | 9.0[b] | 26.5[b] | 2.9 | Zhang et al. (2005) |

(Continued on following page)

TABLE 1 (*Continued*) Natural products isolated from *L. verticillata* Hance with anti-HIV activities.

| Isolated compound | Separation method | Active part | Anti-HIV to HOG.R5 $IC_{50}$ (μg/mL) | Cytotoxicity to HOG.R5 $CC_{50}$ (μg/mL) | Selectivity index ($CC_{50}$/$IC_{50}$) | References |
|---|---|---|---|---|---|---|
| 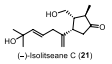 (−)-Isolitseane C (**21**) | PH | LF + TW | I[b] | NT[b] | — | Zhang et al. (2005) |
| 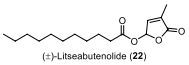 (±)-Litseabutenolide (**22**) | PH | LF + TW | 14.0[b] | NT[b] | >1 | Zhang et al. (2005) |
| 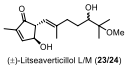 (±)-Litseaverticillol L/M (**23/24**) | PH | LF + TW + FB | 14.0[b] | NT[b] | — | Guan et al. (2016) |
| 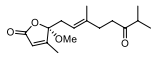 (−)-Litseasesquibutenolide (**25**) | PH | LF + TW + FB | I[b] | -[b] | — | Guan et al. (2016) |

*Note*: PH, preparative HPLC; SC, si gel column; LF, leaves; TW, twigs; FB, flower buds; I, inactive; NT, nontoxic at 20 μg/mL; T, toxic.
[a]Untreated cells served as controls.
[b]3TC (Lamivudine) was used as control compound with a $IC_{50}$ value of 1.2 μM in the same HOG.R5 system.

which comprises over 400 species that are distributed across southwestern China, Vietnam, Cambodia, Laos, and Thailand (Mabberley, 1997). Notably, *Litsea* species are used in traditional Chinese medicine in China for a variety of therapeutic purposes, such as dispelling wind, removing dampness, and promoting blood circulation (Kong et al., 2015), thereby showcasing considerable medicinal value. The pharmacological activities of *Litsea* species usually encompass antioxidant, antibacterial, anti-inflammatory, cytotoxic, neuroprotective, hepatoprotective, cytokine-modulatory, and analgesic effects (Wang et al., 2016). However, a series of novel compounds with anti-HIV activity were isolated from *L. verticillate* recently, and further investigations into their bioactive constituents are expected to lead to new anti-HIV drugs.

In this review, we focus on the anti-HIV active natural products isolated from *L. verticillata* Hance, discussing their isolation and bioactivities, along with hypotheses concerning their biosynthetic pathways and chemical total synthesis. This review aims to spark the interest of scientists in exploring the bioactive constituents of *L. verticillata*, as well as to encourage pharmacologists to investigate the structural modification of these anti-HIV active compounds that hold promise for clinical drug development.

## 2 Isolation and anti-HIV activities

In 1992, Fong initiated an International Cooperative Biodiversity Group (ICBG) project to investigate *L. verticillata* Hance, a perennial shrub or arbor found in the Cuc Phuong National Park, Vietnam (Soejarto et al., 1999). Initial bioassay-directed evaluation of the chloroform extract led to its fractionation through successive flash column chromatography on silica gel and RP-18, followed by preparative high-performance liquid chromatography (HPLC), which resulted in the isolation of a diverse array of active natural products with potent anti-HIV properties (Table 1).

Since 2001, Fong and co-workers isolated a series of active sesquiterpenes with a novel and unique skeleton from the leaves and twigs of *L. verticillata* and named these compounds litseanes (Zhang et al., 2001). The first sesquiterpene identified with anti-HIV-1 replication properties was named as litseaverticillol A (**1**). It was a racemic sesquiterpenoid with a unique structure that had not been reported previously. The inhibitory activity against HIV-1 was conducted using HOG.R5, a reporter cell line developed to quantify the replication of HIV-1. The results indicated that litseaverticillol A suppresses HIV-1 replication with an $IC_{50}$ value (the concentration that inhibits viral replication by 50%) of 5.0 μg/mL (21.4 μM). However, this compound also showed cytotoxic effects on HOG.R5 cells, with a $CC_{50}$ value (the concentration that reduces cell viability by 50%) of 13.2 μg/mL (56.4 μM).

In 2003, Fong and co-workers reported the isolation and structural elucidation of eight previously undescribed litseane sesquiterpenes, designated as litseaverticillols B-H (**2**-**8**), from the leaves and twigs of *L. verticillate* (Zhang et al., 2003a). The stereochemical configurations of these compounds were determined to be racemic mixtures, as confirmed by Mosher ester reactions and optical rotation analyses. The structures of litseaverticillols B–H were determined to be closely related to that of litseaverticillol A. These compounds exhibited $IC_{50}$ values ranging from 2 to 15 μg/mL (8–58 μM) in the HOG.R5 cell-based system. Primary studies on the structure-activity relationship of these compounds indicated that the *Z*,*E* geometrical configuration at $\Delta^{6,7}$, the chirality at the C1 position, and the position of the double bonds at C9–C10, C10–C11, and C11–C12, all influence the anti-HIV activity of the compounds. For instance, compared to **6**/**7**, compound **8** exhibited significantly enhanced anti-HIV activity, attributed to the presence of an α,β-conjugated structure at the C-10 position and the $\Delta^{11,12}$ ring system. However, compound **8** displayed noticeable cytotoxicity, making it unsuitable for evaluation as an anti-HIV drug. In Fong's study, litseaverticillols B-H (**2**-**8**) exhibited $CC_{50}$ values in HOG.R5 cells, that were 2–3 times higher than their corresponding $IC_{50}$ values, resulting in a selectivity index (SI = $CC_{50}/IC_{50}$) ranging from 2 to 3 for these compounds. While this selectivity index is not optimal for an ideal drug candidate, the valuable structure-activity relationships observed for the litseaverticillol series provide valuable insights for the exploration of new drug candidates.

Lignans possess a unique chemical architecture, often consisting of two phenylpropane units linked by a carbon-carbon bond. This

core framework frequently adopts diverse configurations, such as dibenzylbutanes, dibenzylbutyrolactones, and aryltetralin lignans. Additionally, lignans often contain multiple hydroxyl groups attached to the aromatic rings, which enhance their antioxidant potential. These structural elements endow lignans with a wide array of biological activities and considerable pharmacological promise (MacRae and Towers, 1984; Xiao et al., 2023; Liang et al., 2024).

In 2002, Fong and co-workers discovered a sesquiterpene and two lignans in *L. verticillata* Hance (Hoang et al., 2002). These compounds were identified as verticillatol (**9**), (+)-50-demethoxyepiexcelsin (**10**), and the known compound (+)-epiexcelsin (**11**), respectively. (+)-epiexcelsin (**11**) differs from verticillatol (**9**) only in the presence of a methoxy group at position 5'. Compounds **9**-**11** were evaluated for their *in vitro* inhibitory effects against HIV replication in HOG.R5 cells. Compound **10** exhibited strongest selective anti-HIV-1 activity, displaying an $IC_{50}$ value of 16.4 μg/mL (42.7 μM). However, its selectivity index (SI = 1.4) was deemed unsuitable for further development. Compound **11** exhibited no inhibitory activity against HIV-1 replication, potentially attributed to the presence of the 5′-methoxy group and its reduced solubility relative to Compound **10**. The eudesmane sesquiterpenoid (**9**) exhibited modest activity against HIV-1, with an $IC_{50}$ value of 34.5 μg/mL (144.7 μM). Notably, this compound showed no toxicity up to a concentration of 20 μg/mL. This represents the inaugural identification of sesquiterpenoids within this class demonstrating anti-HIV activity.

The mechanism underlying lignans's anti-HIV activity entails inhibiting viral replication by interfering with multiple stages of the viral life cycle, encompassing viral entry, reverse transcription, integration, and assembly (Rimando et al., 1994). Moreover, lignans can modulate host immune responses, inhibit key viral enzymes like reverse transcriptase and protease, or disrupt critical viral protein-protein interactions necessary for replication (Hara et al., 1997). These multifaceted mechanisms collectively enhance the antiviral efficacy of lignans against HIV.

In the same year, Fong and co-workers isolated seven new sesquiterpenes from *L. verticillata*, designated as litseagermacrane (**12**), 7-*epi*-eudesm-4 (15)-ene-1α,6α-diol (**13**), 5-*epi*-eudesm-4 (15)-ene-1β,6β-diol (**14**), litseahumulanes A (**15**) and B (**16**), and litseachromolaevanes A (**17**) and B (**18**) (Zhang et al., 2003b). Three compounds (**12**, **14**, **18**) demonstrated moderate to weak anti-HIV activity. litseagermacrane (**12**) exhibited the highest anti-HIV activity, with an $IC_{50}$ value of 6.5 μg/mL (27.5 μM), but it also displayed cytotoxicity to HOG.R5 cells with a $CC_{50}$ value of 15.9 μg/mL (63.4 μM). The $IC_{50}$ values of isolates **14** and **18** were 17.4 μg/mL (73.1 μM) and 28.0 μg/mL (119.7 μM), respectively, with no cytotoxicity observed up to a concentration of 20 μg/mL. However, the selectivity index (SI) values for isolates **12**, **14**, and **18** indicated low selectivity.

In 2005, the research team led by Tan and Zhang continued their phytochemical investigations on the leaves and twigs of *L. verticillata* Hance, leading to the isolation of eleven compounds (Zhang et al., 2005). The isolated compounds included three previously undescribed sesquiterpenes, isolitseanes A-C (**19**-**21**), in addition to a new butenolide derivative, litseabutenolide (**22**). The isolitseane sesquiterpenes A, B, and C exhibited subtle structural differences. Isolitseanes A and B differed only in the configuration of the C6 stereogenic center. In contrast, isolitseane C possessed the same pentacyclic ring system as isolitseane B, with minor structural variation at the position of double bond and oxidation state of the side chain. Litseabutenolide (**22**) was characterized as a furan-containing ester. Subsequent HIV-1 antiviral evaluation studies demonstrated that isolates **20** and **22** inhibited HIV-1 replication in HOG.R5, with $IC_{50}$ values of 38.1 and 40.3 μM, respectively.

In 2016, Zhang and co-workers discovered three additional novel sesquiterpenes from *L. verticillata*, namely, litseaverticillols L and M (**23**/**24**) and litseasesquibutenolide (**25**) (Guan et al., 2016). Litseaverticillols L and M (**23**/**24**) exhibited anti-HIV activity with an $IC_{50}$ value of 49.6 μM and no toxicity to host HOG.R5 cells at a concentration of 70 μM. These findings indicated that litseaverticillols L and M (**23**/**24**) possess potency comparable to that of litseaverticillol D (**25**) and other litseanes. However, litseasesquibutenolide (**25**) did not show inhibitory activity against HIV-1 replication at a concentration of 70 μM.

In summary, most natural products isolated from *Litsea verticillata* exhibit good anti-HIV effects, whereas litseaverticillols display exceptional inhibitory activity in both anti-HIV efficacy and selectivity indices. Of note, lignans are the most abundant compounds produced in this plant, and litseanes are considered minor components, with litseaverticillol A being the most abundant at a yield of 0.0016% (Guan et al., 2016). Among them, litseaverticillols B (**2**) and E (**5**) exhibited the best anti-HIV efficacy with $IC_{50}$ = 2-3 and 4.0 μg/mL, respectively, but their selectivity indices ($CC_{50}/IC_{50}$) remain inadequate for therapeutic applications. Moreover, both litseaverticillols B (**2**) and E (**5**) were isolated as racemic mixtures, and the activities of their optically pure forms have yet to be determined. Consequently, further investigations on the total synthesis, structure modification, and activity evaluation of these natural products are highly demanded.

## 3 Biosynthetic pathways

A plausible biosynthetic pathway for litseaverticillol A (**1**) was proposed by (Zhang et al., 2001). As displayed in Figure 1A, litseaverticillol A was probably formed through the mevalonate pathway characteristic of sesquiterpenes. Given that the side chain of litseaverticillol A (**1**) represents a geranyl unit, it was postulated that the condensation of an isopentenyl diphosphate (**26**) with a geranyl diphosphate derived cation **27** produced the farnesyl diphosphate (**28**). Intermediate **28** was then oxidized to **29**, followed by a sequential cyclization and oxidation to afford the litseaverticillol A (**1**). As far as we know, this remains the only reported example of biosynthetic investigation for natural products belonging to this family.

## 4 Total synthesis

Due to their notable bioactivity and unique chemical structure, natural products from *Litsea verticillate* have become attractive targets in the field of synthetic chemistry (Vassilikogiannakis and Stratakis, 2003). Thoroughly analyzed the structure of litseaverticillols, and concluded that litseaverticillols D-H (**4**-**8**) could arise from direct oxidation of the litseaverticillols A-C (**1**-**3**) via an ene reaction with $^1O_2$ at the side-chain double bond most

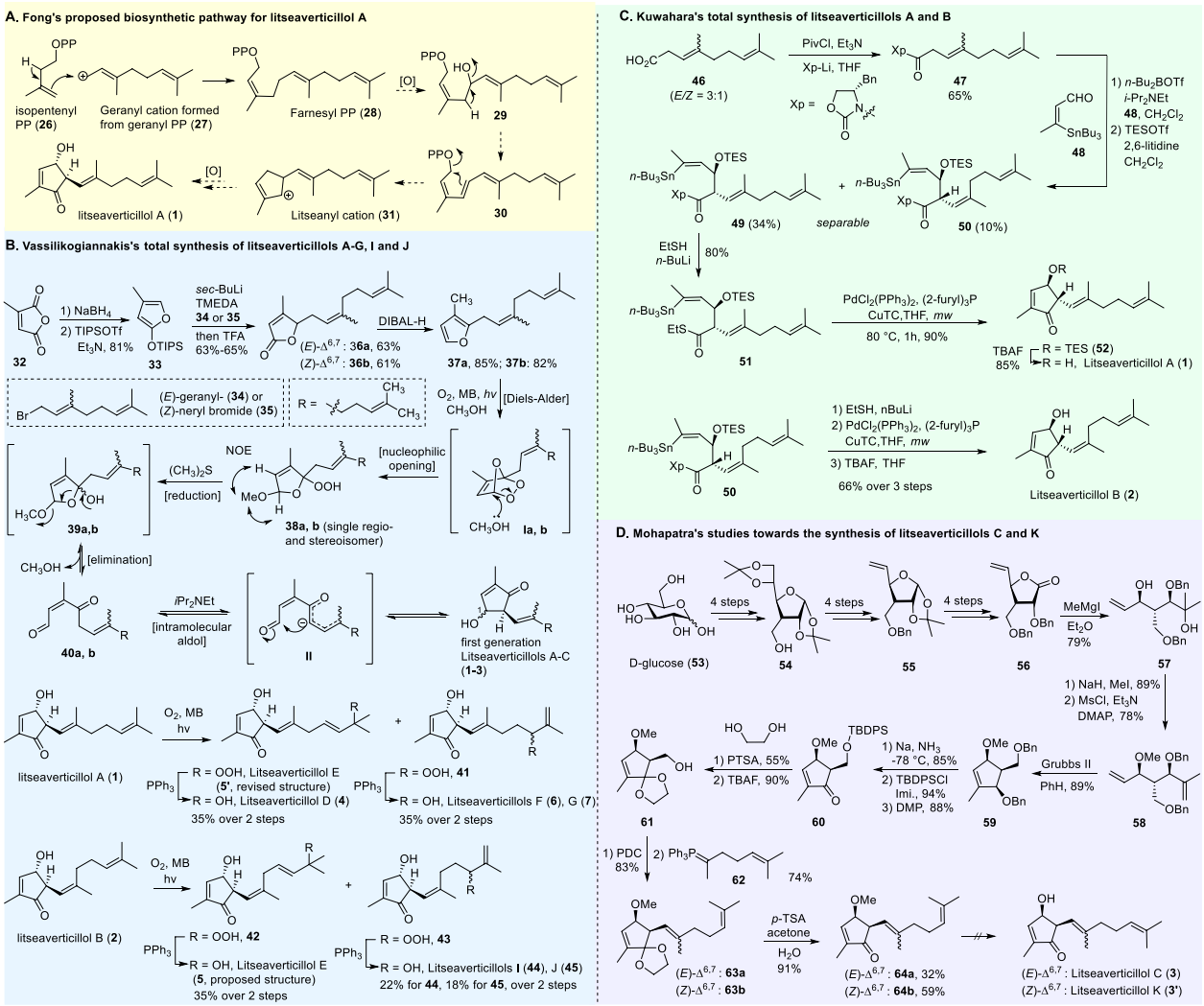


FIGURE 1
**(A)** The biosynthetic pathway for litseaverticillol A proposed by Fong; **(B)** The total synthesis of litseaverticillols A–G, I and J by Vassilikogiannakis's group; **(C)** The total synthesis of litseaverticillols A and B by Kuwahara's group; **(D)** Synthetic studies towards litseaverticillols C and K by Mohapatra's group.

distal to the cyclopentenone ring. Thus, a divergent synthetic strategy was employed in their synthetic work (Vassilikogiannakis and Stratakis, 2003; Vassilikogiannakis et al., 2004; Vassilikogiannakis et al., 2005; Margaros et al., 2006). As shown in Figure 1B, the synthesis started from commercially available citraconic anhydride (**32**), which was then transformed to 2-triisopropylsilyloxyfuran (**33**) in two steps. *Ortho*-lithiation at the 5-position of **33** with sec-butyllithium, followed alkylatioin of the resultant anion with either geranyl (**34**) or neryl bromide (**35**) and subsequent acidic hydrolysis of the triisopropylsilyl protection group, afforded lactones **36a** and **36b** in moderate yields, respectively. DIBAL reduction of lactones **36a** and **36b** furnished sesquirosefuran **37a** and **37b**, respectively. Subsequently, a key singlet oxygen ($^1O_2$) cascade sequence was employed to derive the complete litseaverticillol core. This cascade sequence was required to initiate at the furan moiety without concomitant side reaction at either of the two susceptible double bonds in the attached side chain. Under the optimized conditions, sesquirosefuran **37a/b** was irradiated for 1 min in a methanolic solution (containing $10^{-4}$ M methylene blue as a photosensitiser) with $O_2$ gently bubbled through it, resulting in the exclusive formation of hydroperoxides **38a/b** as the [4 + 2] adducts in quantitative yields. Afterward, hydroperoxide **38a/b** was reduced by dimethyl sulfide, followed by an elimination of methol and subsequential intramolecular aldol reaction, to produce the first generation litseaverticillols A-C (**1**-**3**). Then $^1O_2$-mediated oxidation of the distal double bond ($\triangle^{10,11}$) in the side chains of litseaverticillol A (**1**) provided litseaverticillol E (**5′**, revised structure) and peroxide **41**, which were reduced by triphenylphosphine to litseaverticillol D (**4**) and litseaverticillols F (**6**), G (**7**), respectively. Similarly, litseaverticillol B (**2**) can be transformed to litseaverticillol E (**5**, proposed structure) and litseaverticillols I (**44**), J (**45**), respectively. Notably, litseaverticillols F (**6**)/G (**7**) and litseaverticillols I (**44**)/J (**45**) were all separated by flash chromatography.

The first enantioselective total synthesis of litseaverticillols A and B was disclosed by (Morita et al., 2006; Morita and Kuwahara, 2006). Therein an Evans asymmetric aldol reaction and a microwave-promoted cyclization of a stannylated thiol ester intermediate were employed as the key C–C bond-forming steps. As displayed in Figure 1C, the readily available acid **46** (a 3:1 *E*/*Z* mixture) was first converted to the oxazolidinone derivative **47**, which then reacted with aldehyde **48** via the *syn*-selective Evans aldol reaction to produce two separable aldol products **49** and **50** in 34% and 10% yields, respectively. The *E*-isomer **49** was transformed to the thiol ester **51**. Subsequently, the microwave-promoted cyclization of **51** was achieved in the presence of $PdCl_2(PPh_3)_2$, $(2\text{-furyl})_3P$ and CuTC, leading to compound **52** in 63% yield. After the desilylation of **52**, (1*R*,5*S*)-litseaverticillol A was afforded in 85% yield. By following the similar reaction sequences, the *Z*-isomer of aldol product **50** was converted to (1*R*,5*S*)-litseaverticillol B (**2**) in 66% yield over the three steps.

The first enantioselective synthesis towards the litseaverticillols C and K was reported by (Mohapatra et al., 2007). The synthesis utilized the ring-closing metathesis (RCM) and Wittig reactions as key steps. As shown in Figure 1D, the starting material, D-glucose (**53**), was converted to lactone **56** in 12 steps involving oxidation state adjustment and functional group transformations. Lactone **56** was then subjected to Grignard addition to produce alcohol **57**, which then underwent an *O*-methylation and a base-promoted Hoffmann elimination to give diene derivative **58**. Ring-closing metathesis of **58** proceeded effectively to give the cyclopentene core **59**, which was subsequently converted to enone **60** through a three-step sequence involving (1) reductive cleavage of the benzyl ethers, (2) selective protection of the primary hydroxyl group, and (3) oxidation of the allylic alcohol. After a two-step protection group transformation, the resultant **61** was oxidized to aldehyde, and then subjected to Wittig reaction with ylide **62** to give a mixture of *E*- and *Z*-isomers (**63a**/**63b**) in 35:65. Subsequent deketalisation of the **63a**/**63b** mixture under acidic conditions furnished keto derivatives **64a**/**64b**, which were separated by silica gel chromatography. Finally, hydrolysis of the methyl ether at C-1 of **64a**/**64b** would produce the desired litseaverticillols C and K. Unfortunately, the hydrolysis reaction was unsuccessful under various conditions.

## 5 Summary and outlook

Due to their unique structures and promising anti-HIV activities, natural products derived from *L. verticillata* have garnered significant interest from the chemical community. Among these, litseaverticillols serve as representative molecules and have been extensively studied for their bioactivity. Several natural molecules of this family exhibited potent anti-HIV activities, but also inhibited the growth of human cells (HOG.R5), leading to the selectivity indices (SI = $CC_{50}/IC_{50}$) for the most promising compound in the range of 2–3. This underscores the need for structural optimization to identify new drug leads. Inspired by the plausible biosynthetic pathways, three research groups have developed diverse synthetic approaches to access the litseaverticillols. Despite these pioneering efforts, there is still a need for more efficient synthetic approaches with high stereoselectivities. Furthermore, analog production and structure-activity relationships (SAR) analysis are required as well to explore new anti-HIV lead compounds. Looking ahead, we anticipate expansive research into the isolation, synthesis, and bioactivity studies of these natural products. It is hoped that this review will provide useful information for future research efforts on natural products from *Litsea verticillate*.

## Author contributions

J-LY: Writing–original draft, Writing–review and editing. HN: Writing–original draft. XF: Writing–original draft. X-EL: Writing–original draft. YJ: Writing–original draft. JL: Writing–review and editing.

## Funding

The author(s) declare that financial support was received for the research, authorship, and/or publication of this article. This work was supported by the Guangdong Department of Education (2021ZDJS097), the Guangdong Basic and Applied Basic Research Foundation (2022A1515110592, and 2023A1515012715), and the Jiangmen Basic and Applied Basic Research Project (202301003003140).

## Conflict of interest

The authors declare that the research was conducted in the absence of any commercial or financial relationships that could be construed as a potential conflict of interest.

## Publisher's note

All claims expressed in this article are solely those of the authors and do not necessarily represent those of their affiliated organizations, or those of the publisher, the editors and the reviewers. Any product that may be evaluated in this article, or claim that may be made by its manufacturer, is not guaranteed or endorsed by the publisher.

## References

Atanasov, A. G., Waltenberger, B., Pferschy-Wenzig, E.-M., Linder, T., Wawrosch, C., Uhrin, P., et al. (2015). Discovery and resupply of pharmacologically active plant-derived natural products: a review. *Biotechnol. Adv.* 33, 1582–1614. doi:10.1016/j.biotechadv.2015.08.001

Atanasov, A. G., Zotchev, S. B., Dirsch, V. M., Orhan, I. E., Banach, M., Rollinger, J. M., et al. (2021). Natural products in drug discovery: advances and opportunities. *Nat. Rev. Drug Discov.* 20, 200–216. doi:10.1038/s41573-020-00114-z

Chaachouay, N., and Zidane, L. (2024). Plant-derived natural products: a source for drug discovery and development. *Drugs Drug Candidates* 3 (1), 184–207. doi:10.3390/ddc3010011

Chopra, B., and Dhingra, A. K. (2021). Natural products: a lead for drug discovery and development. *Phytother. Res.* 35, 4660–4702. doi:10.1002/ptr.7099

Fauci, A. S. (1988). The human immunodeficiency virus: infectivity and mechanisms of pathogenesis. *Science* 239, 617–622. doi:10.1126/science.3277274

Guan, Y., Wang, D., Tan, G. T., Van Hung, N., Cuong, N. M., Pezzuto, J. M., et al. (2016). Litsea species as potential antiviral plant sources. *Am. J. Chin. Med.* 44, 275–290. doi:10.1142/S0192415X16500166

Hara, H., Fujihashi, T., Sakata, T., Kaji, A., and Kaji, H. (1997). Tetrahydronaphthalene lignan compounds as potent anti-HIV type 1 agents. *AIDS Res. Hum. Retroviruses.* 13, 695–705. doi:10.1089/aid.1997.13.695

Hoang, V. D., Tan, G. T., Zhang, H.-J., Tamez, P. A., Hung, N. V., Cuong, N. M., et al. (2002). Natural anti-HIV agents—part I: (+)-demethoxyepiexcelsin and verticillatol from Litsea verticillata. *Phytochemistry* 59, 325–329. doi:10.1016/S0031-9422(01)00454-X

Hu, C., Liang, B., Sun, J., Li, J., Xiong, Z., Wang, S.-H., et al. (2024). Synthesis and biological evaluation of indole derivatives containing thiazolidine-2,4-dione as α-glucosidase inhibitors with antidiabetic activity. *Eur. J. Med. Chem.* 264, 115957. doi:10.1016/j.ejmech.2023.115957

Kong, D.-G., Zhao, Y., Li, G.-H., Chen, B.-J., Wang, X.-N., Zhou, H.-L., et al. (2015). The genus Litsea in traditional Chinese medicine: an ethnomedical, phytochemical and pharmacological review. *J. Ethnopharmacol.* 164, 256–264. doi:10.1016/j.jep.2015.02.020

Larder, B. A., and Kemp, S. D. (1989). Multiple mutations in HIV-1 reverse transcriptase confer high-level resistance to zidovudine (AZT). *Science* 246, 1155–1158. doi:10.1126/science.2479983

Lepri, A. C., Sabin, C. A., Staszewski, S., Hertogs, K., Müller, A., Rabenau, H., et al. (2000). Resistance profiles in patients with viral rebound on potent antiretroviral therapy. *J. Infect. Dis.* 181, 1143–1147. doi:10.1086/315301

Li, M., Li, H., Min, X., Sun, J., Liang, B., Xu, L., et al. (2024). Identification of 1,3,4-thiadiazolyl-containing thiazolidine-2,4-dione derivatives as novel PTP1B inhibitors with antidiabetic activity. *J. Med. Chem.* 67, 8406–8419. doi:10.1021/acs.jmedchem.4c00676

Liang, B., Xiao, D., Wang, S.-H., and Xu, X. (2024). Novel thiosemicarbazide-based β-carboline derivatives as α-glucosidase inhibitors: synthesis and biological evaluation. *Eur. J. Med. Chem.* 275, 116595. doi:10.1016/j.ejmech.2024.116595

Mabberley, D. J. (1997). *The plant-book: a portable dictionary of the vascular plants*. The Edinburgh Building, Cambridge, UK: Cambridge University Press.

MacRae, W. D., and Towers, G. H. N. (1984). Biological activities of lignans. *Phytochemistry* 23, 1207–1220. doi:10.1016/S0031-9422(00)80428-8

Margaros, I., Montagnon, T., Tofi, M., Pavlakos, E., and Vassilikogiannakis, G. (2006). The power of singlet oxygen chemistry in biomimetic syntheses. *Tetrahedron* 62, 5308–5317. doi:10.1016/j.tet.2006.01.110

Mohapatra, D. K., Mondal, D., and Gurjar, M. K. (2007). Towards the enantioselective synthesis of anti-HIV agents litseaverticillols C and K from d-glucose. *Tetrahedron* 63, 2613–2621. doi:10.1016/j.tet.2007.01.037

Morita, A., Kiyota, H., and Kuwahara, S. (2006). Enantioselective synthesis of the (1S,5R)-Enantiomer of litseaverticillols A and B. *Biosci. Biotechnol. Biochem.* 70, 2564–2566. doi:10.1271/bbb.60253

Morita, A., and Kuwahara, S. (2006). Enantioselective total synthesis of litseaverticillols A and B. *Org. Lett.* 8, 1613–1616. doi:10.1021/ol053122a

Newman, D. J., and Cragg, G. M. (2020). Natural products as sources of new drugs over the nearly four decades from 01/1981 to 09/2019. *J. Nat. Prod.* 83, 770–803. doi:10.1021/acs.jnatprod.9b01285

Richman, D. D. (2001). HIV chemotherapy. *Nature* 410, 995–1001. doi:10.1038/35073673

Rimando, A. M., Pezzuto, J. M., Farnsworth, N. R., Santisuk, T., Reutrakul, V., and Kawanishi, K. (1994). New lignans from anogeissus acuminata with HIV-1 reverse transcriptase inhibitory activity. *J. Nat. Prod.* 57, 896–904. doi:10.1021/np50109a004

Soejarto, D. D., Gyllenhaal, C., Regalado, J. C., Pezzuto, J. M., Fong, H. H. S., Tan, G. T., et al. (1999). Studies on biodiversity of Vietnam and Laos: the UIC-based ICBG program. *Pharm. Biol.* 37, 100–113. doi:10.1076/1388-0209(200010)37:SUP;1-W;FT100

Tantillo, C., Ding, J., Jacobo-Molina, A., Nanni, R. G., Boyer, P. L., Hughes, S. H., et al. (1994). Locations of anti-AIDS drug binding sites and resistance mutations in the three-dimensional structure of HIV-1 reverse transcriptase: implications for mechanisms of drug inhibition and resistance. *J. Mol. Biol.* 243, 369–387. doi:10.1006/jmbi.1994.1665

Vassilikogiannakis, G., Margaros, I., and Montagnon, T. (2004). Biomimetic total synthesis of litseaverticillols B, E, I, and J and structural reassignment of litseaverticillol E. *Org. Lett.* 6, 2039–2042. doi:10.1021/ol0493610

Vassilikogiannakis, G., Margaros, I., Montagnon, T., and Stratakis, M. (2005). Illustrating the power of singlet oxygen chemistry in a synthetic context: biomimetic syntheses of litseaverticillols A–G, I and J and the structural reassignment of litseaverticillol E. *Chem. Eur. J.* 11, 5899–5907. doi:10.1002/chem.200401311

Vassilikogiannakis, G., and Stratakis, M. (2003). Biomimetic total synthesis of litseaverticillols A, C, D, F, and G: singlet-oxygen-initiated cascades. *Angew. Chem. Int. Ed.* 42, 5465–5468. doi:10.1002/anie.200352180

Wang, Y.-S., Wen, Z.-Q., Li, B.-T., Zhang, H.-B., and Yang, J.-H. (2016). Ethnobotany, phytochemistry, and pharmacology of the genus Litsea: an update. *J. Ethnopharmacol.* 181, 66–107. doi:10.1016/j.jep.2016.01.032

Xiao, D., Lu, L., Liang, B., Xiong, Z., Xu, X., and Chen, W.-H. (2023). Identification of 1,3,4-oxadiazolyl-containing β-carboline derivatives as novel α-glucosidase inhibitors with antidiabetic activity. *Eur. J. Med. Chem.* 261, 115795. doi:10.1016/j.ejmech.2023.115795

Zhang, H.-J., Hung, N. V., Cuong, N. M., Soejarto, D. D., Pezzuto, J. M., Fong, H. H. S., et al. (2005). Sesquiterpenes and butenolides, natural anti-HIV constituents from litsea verticillata. *Planta Med.* 71, 452–457. doi:10.1055/s-2005-864142

Zhang, H.-J., Tan, G. T., Hoang, V. D., Hung, N. V., Cuong, N. M., Soejarto, D. D., et al. (2001). Natural anti-HIV agents. Part 2: litseaverticillol A, a prototypic litseane sesquiterpene from Litsea verticillata. *Tetrahedron Lett.* 42, 8587–8591. doi:10.1016/S0040-4039(01)01852-4

Zhang, H.-J., Tan, G. T., Hoang, V. D., Hung, N. V., Cuong, N. M., Soejarto, D. D., et al. (2003a). Natural anti-HIV agents. Part 3: litseaverticillols A–H, novel sesquiterpenes from Litsea verticillata. *Tetrahedron* 59, 141–148. doi:10.1016/S0040-4020(02)01491-6

Zhang, H.-J., Tan, G. T., Santarsiero, B. D., Mesecar, A. D., Hung, N. V., Cuong, N. M., et al. (2003b). New sesquiterpenes from litsea verticillata. *J. Nat. Prod.* 66, 609–615. doi:10.1021/np020508a

# Frontiers in Pharmacology

**Explores the interactions between chemicals and living beings**

The most cited journal in its field, which advances access to pharmacological discoveries to prevent and treat human disease.

---

## Discover the latest Research Topics

See more →

**Frontiers**

Avenue du Tribunal-Fédéral 34
1005 Lausanne, Switzerland
frontiersin.org

**Contact us**

+41 (0)21 510 17 00
frontiersin.org/about/contact